

# COMPACTED OXIDE LAYER FORMATION UNDER CONDITIONS OF LIMITED DEBRIS RETENTION AT THE WEAR INTERFACE DURING HIGH TEMPERATURE SLIDING WEAR OF SUPERALLOYS

Ian A. Inman B.Sc. (Hons.), M.Sc.

A thesis submitted in partial fulfilment of the  
requirements for the degree of Doctor of Philosophy

funded by the EPSRC



School of Engineering and Technology  
Northumbria University

November 2003



# Contents

<b>1. INTRODUCTION</b>	<b>1</b>
<b>2. LITERATURE REVIEW</b>	<b>4</b>
2.1 Introduction	4
2.2 Friction	5
2.2.1 Definition of Friction	5
2.2.2 Observed Friction in Real Systems	8
2.2.3 Adhesion	8
2.2.4 Ploughing	10
2.2.5 Combination of Models	11
2.2.6 Complications with the Bowden and Tabor Model	12
2.3 Wear Theory	13
2.3.1 Archard and Hirst – Distinction between Mild and Severe Wear	13
2.3.2 Classification by Mechanism	17
2.4 ‘Two and Three Body’ Wear	30
2.4.1 Overview	30
2.4.2 Surface Films and Preoxidation – Third Body or Not?	34
2.4.3 Behaviour of Particles at the Interface	34
2.4.4 The Effect of Forces of Attraction between Third Bodies	38
2.5 Mild Wear and Mechanisms of Compact Oxide Formation	40
2.5.1 Introduction to Compacted Oxides or ‘Glazes’	40
2.5.2 Mechanisms for Generation of Oxide Debris and Compacted Oxide Layer Formation	41
2.5.3 Effects of Environmental Variables	44
2.5.4 Pre-treatment of Sliding Surfaces	48
2.5.5 Third Body Interaction in Relation to Compact Oxide Formation	53
2.5.6 Quinn’s Oxidational Wear Model	58
2.6 The Effects of Load and Sliding Speed	65
2.6.1 Early Work	65
2.6.2 Wear of Cobalt Based Alloys	72
2.7 Effect of a Second Phase on Wear	80
2.8 Material Transfer and Mechanical Alloying	83
2.9 Nano-scale Characterisation of Sliding Surfaces	85
2.10 Previous Work within the University of Northumbria	86

<b>3. INTRODUCTION TO THE CURRENT INVESTIGATION</b>	<b>89</b>
<b>4. EXPERIMENTAL</b>	<b>92</b>
4.1 Apparatus and Materials	92
4.1.1 Apparatus	92
4.1.2 Materials Used	96
4.2 Wear Testing	97
4.2.1 Room Temperature to 750°C, at 0.314 m.s <sup>-1</sup> and 0.905 m.s <sup>-1</sup>	97
4.2.2 Nimonic 80A versus Stellite 6 – In-depth Studies	99
4.2.3 Switching off reciprocation – Nimonic 80A versus Incoloy 800HT and Incoloy MA956 versus Incoloy 800HT at 510°C and 0.314 m.s <sup>-1</sup>	100
4.3 Structural Analysis	101
4.3.1 Scanning Electron Microscopy with Energy Dispersive Spectroscopy	101
4.3.2 X-ray Diffraction	101
4.3.3 Micro-hardness Tests	102
4.3.4 Nano-hardness Tests	102
4.3.5 Transmission Electron Microscopy (TEM)	103
4.3.6 Scanning Tunnelling Microscopy (STM)	103
<b>5. RESULTS</b>	<b>105</b>
5.1 Testing of Nimonic 80A versus Stellite 6 between Room Temperature and 750°C, at 0.314 and 0.905 m.s <sup>-1</sup>	106
5.1.1 Experimental Observations – Nimonic 80A versus Stellite 6	106
5.1.2 Optical and SEM Microscopy – Nimonic 80A versus Stellite 6	111
5.1.3 EDX Analysis – Nimonic 80A versus Stellite 6	120
5.1.4 Mapping using EDX – Nimonic 80A versus Stellite 6	123
5.1.5 Autopoint EDX Analysis – Nimonic 80A versus Stellite 6	126
5.1.6 XRD Analysis – Nimonic 80A versus Stellite 6	126
5.1.7 Micro-hardness Testing – Nimonic 80A versus Stellite 6	131
5.2 In-depth Studies of the Nimonic 80A versus Stellite 6 Wear Pair	134
5.2.1 Build up of Glaze with Time – Nimonic 80A versus Stellite 6 at 510°C and 750°C, Sliding Speed 0.314 m.s <sup>-1</sup>	134
5.2.2 Reversal of Sample and Counterface – Stellite 6 versus Nimonic 80A at 750°C	144
5.2.3 Substitution of Nimonic 80A with High Purity Nickel Nickel 200 <sup>TM</sup> versus Stellite 6 at 750°C	153



5.3	Testing of Incoloy MA956 versus Stellite 6 between Room Temperature and 750°C, at 0.314 and 0.905 m.s <sup>-1</sup>	161
5.3.1	Experimental Observations – Incoloy MA956 versus Stellite 6	161
5.3.2	Optical and SEM Studies – Incoloy MA956 versus Stellite 6	166
5.3.3	EDX Analysis – Incoloy MA956 versus Stellite 6	174
5.3.4	EDX Mapping – Incoloy MA956 versus Stellite 6	178
5.3.5	Autopoint EDX Analysis – Incoloy MA956 versus Stellite 6	182
5.3.6	XRD Analysis – Incoloy MA956 versus Stellite 6	183
5.3.7	Micro-hardness Testing – Incoloy MA956 versus Stellite 6	187
5.4	Testing of Nimonic 80A versus Incoloy 800HT between Room Temperature and 750°C, at 0.314 and 0.905 m.s <sup>-1</sup>	190
5.4.1	Experimental Observations – Nimonic 80A versus Incoloy 800HT	190
5.4.2	Optical and SEM Morphology – Nimonic 80A versus Incoloy 800HT	196
5.4.3	EDX Analysis – Nimonic 80A versus Incoloy 800HT	204
5.4.4	EDX Mapping – Nimonic 80A versus Incoloy 800HT	206
5.4.5	Autopoint EDX Analysis – Nimonic 80A versus Incoloy 800HT	209
5.4.6	XRD Analysis – Nimonic 80A versus Incoloy 800HT	211
5.4.7	Micro-hardness Testing – Nimonic 80A versus Incoloy 800HT	214
5.4.8	Sliding Without Reciprocation – Nimonic 80A versus Incoloy 800HT, 510°C and 0.314 m.s <sup>-1</sup>	219
5.5	Testing of Incoloy MA956 versus Incoloy 800HT between Room Temperature and 750°C, at 0.314 and 0.905 m.s <sup>-1</sup>	221
5.5.1	Experimental Observations – Incoloy MA956 versus Incoloy 800HT	221
5.5.2	Optical and SEM Morphology – Incoloy MA956 versus Incoloy 800HT	229
5.5.3	EDX Analysis – Incoloy MA956 versus Incoloy 800HT	236
5.5.4	EDX Mapping – Incoloy MA956 versus Incoloy 800HT	238
5.5.5	Autopoint EDX Analysis – Incoloy MA956 versus Incoloy 800HT	241
5.5.6	XRD Analysis – Incoloy MA956 versus Incoloy 800HT	245
5.5.7	Micro-hardness Testing – Incoloy MA956 versus Incoloy 800HT	250
5.5.8	Sliding Without Reciprocation – Incoloy MA956 versus Incoloy 800HT, 510°C and 0.314 m.s <sup>-1</sup>	254

5.6	In-depth Nano-characterisation – Nimonic 80A versus Stellite 6	256
5.6.1	Nano-indentation Testing – Nimonic 80A and Incoloy MA956 versus Stellite 6	257
5.6.2	Nano-scale studies of glaze layers formed on Nimonic 80A samples (slid against a Stellite 6 counterface) at 750°C and 0.314 m.s <sup>-1</sup> using TEM and STM	258
<b>6.</b>	<b>DISCUSSION</b>	<b>266</b>
6.1	Nimonic 80A versus Stellite 6	266
6.1.1	Nimonic 80A versus Stellite 6 between Room Temperature and 750°C, at 0.314 m.s <sup>-1</sup>	266
6.1.2	Nimonic 80A versus Stellite 6 between Room Temperature and 750°C, at 0.905 m.s <sup>-1</sup>	271
6.1.3	Wear Map for Nimonic 80A versus Stellite 6	275
6.1.4	Elimination of Alloying Elements – Nickel 200TM versus Stellite 6 at 750°C	277
6.2	Incoloy MA956 versus Stellite 6	278
6.2.1	Incoloy MA956 versus Stellite 6 between Room Temperature and 750°C, at 0.314 m.s <sup>-1</sup>	278
6.2.2	Incoloy MA956 versus Stellite 6 between Room Temperature and 750°C, at 0.905 m.s <sup>-1</sup>	281
6.2.3	Wear Map for Incoloy MA956 versus Stellite 6	284
6.3	Nimonic 80A versus Incoloy 800HT	287
6.3.1	Nimonic 80A versus Incoloy 800HT between Room Temperature and 750°C, at 0.314 m.s <sup>-1</sup>	287
6.3.2	Nimonic 80A versus Incoloy 800HT between Room Temperature and 750°C, at 0.905 m.s <sup>-1</sup>	292
6.3.3	Wear Map for Nimonic 80A versus Incoloy 800HT	296
6.4	Incoloy MA956 versus Incoloy 800HT	299
6.4.1	Incoloy MA956 versus Incoloy 800HT between Room Temperature and 750°C, at 0.314 m.s <sup>-1</sup>	299
6.4.2	Incoloy MA956 versus Incoloy 800HT between Room Temperature and 750°C, at 0.905 m.s <sup>-1</sup>	305
6.4.3	Wear Map for Incoloy MA956 versus Incoloy 800HT	310
6.5	Nano-scale Studies of High Temperature Wear – Nimonic 80A / Stellite 6 at 750°C and 0.314 m.s <sup>-1</sup>	312
6.5.1	Nano-hardness of Glaze Layers – Nimonic 80A versus Stellite 6 and Incoloy MA956 versus Stellite 6	312
6.5.2	Nano-scale Characterisation of Glaze Layers – Nimonic 80A / Stellite 6 at 0.314 m.s <sup>-1</sup> and 750°C	314

<b>7. SUMMARY</b>	<b>317</b>
7.1 Effect of Sliding Speed between Room Temperature and 750°C	317
7.1.1 Nimonc 80A versus Stellite 6	317
7.1.2 Incoloy MA956 versus Stellite 6	320
7.1.3 Nimonc 80A versus Incoloy 800HT	323
7.1.4 Incoloy MA956 versus Incoloy 800HT	327
7.2 In-depth and Nano-scale Studies of Nimonc 80A Samples worn against Stellite 6 at 750°C and 0.314 m.s <sup>-1</sup>	333
7.2.1 Nano-hardness of Glaze Layers – Nimonc 80A versus Stellite 6 and Incoloy MA956 versus Stellite 6	333
7.2.2 Nano-scale Characterisation of Glaze Layers – Nimonc 80A / Stellite 6 at 0.314 m.s <sup>-1</sup> and 750°C	334
<b>8. RECOMMENDATIONS FOR FURTHER WORK</b>	<b>335</b>
<b>REFERENCES</b>	<b>337</b>
<b>APPENDIX 1: Related Articles and Contacting the Author (not an official part of the thesis)</b>	<b>345</b>
A1.1 Contacting the Author	345
A1.2 Articles Directly Related to the Current Study	345
A1.3 Other Related Work	346

## List of Tables

<b>Table 2.1:</b>	Quinn's comparison of the various classifications of wear	19
<b>Table 2.2:</b>	Wear data for standard and alternatively processed superalloys	21
<b>Table 2.3:</b>	Wear rates of case hardened steels before and after implantation of oxygen ions, 400 m sliding distance	52
<b>Table 2.4:</b>	Wear rates of case hardened steels before and after implantation of oxygen ions, 100 m sliding distance	52
<b>Table 4.1:</b>	Standard conditions used in wear rig operation, unless stated elsewhere	95
<b>Table 4.2:</b>	Main wear pairs used during testing	96
<b>Table 4.3:</b>	Nominal compositions of alloys in wt%	96
<b>Table 4.5:</b>	Sliding times and equivalent distances for timed tests of Nimonic 80A versus Stellite 6	100
<b>Table 4.6:</b>	Key specifications for Hysitron Triboindenter used for nano-indentation tests	104
<b>Table 4.7:</b>	Nominal load parameters used for nano-indentation tests on Nimonic 80A samples slid against Stellite 6 at 510°C and 750°C, also Incoloy MA956 samples slid against Stellite 6 at 750°C	104
<b>Table 5.1:</b>	Hardness data for glaze and undeformed substrate, Nimonic 80A versus Stellite 6 slid at 750°C	134
<b>Table 5.2:</b>	Hardness data for glaze, for a Stellite 6 sample slid against a Nimonic 80A counterface at 0.314 m.s-1 and 750°C	151
<b>Table 5.3:</b>	Hardness data for glaze and undeformed substrate – Nickel 200TM versus Stellite 6 slid at 750°C	160
<b>Table 5.4:</b>	Hardness data for glaze and undeformed substrate, Incoloy MA956 versus Stellite 6 slid at 750°C	188
<b>Table 5.5:</b>	Hardness data for transfer layers between room temperature and 570°C, Nimonic 80A versus Incoloy 800HT	217
<b>Table 5.6:</b>	Hardness data for glaze and undeformed substrate, Nimonic 80A versus Incoloy 800HT slid at 750°C	218
<b>Table 5.7:</b>	Hardness data for transfer layers at room temperature and 270°C, Incoloy MA956 versus Incoloy 800HT	252
<b>Table 5.8:</b>	Hardness data for glaze and undeformed substrate, Incoloy MA956 versus Incoloy 800HT slid at 750°C	252
<b>Table 5.9:</b>	Nano-indentation data for glaze layers formed on Incoloy MA956 at 750°C, also Nimonic 80A at 510°C and 750°C when slid against Stellite 6	259
<b>Table 5.10:</b>	Selected Area Diffraction (SAD) indexing data for glaze layer, produced by wear of Nimonic 80A versus Stellite 6	262

<b>Table 6.1:</b>	Free energies of formation for key oxides at 727°C formed under conditions of static oxidation	270
<b>Table 6.2:</b>	Summary of mean micro-hardness values for glaze and deformed substrate for Nimonic 80A and Incoloy MA956 versus Stellite 6 at 750°C	284
<b>Table 6.3:</b>	Mean hardness values for glaze and deformed substrate for Nimonic 80A versus Incoloy 800HT at 750°C	290
<b>Table 6.4:</b>	Mean hardness values for glaze and deformed substrate for Incoloy MA956 versus Incoloy 800HT	301
<b>Table 6.5:</b>	Mean nano-hardness and modulus values for glaze – Nimonic 80A / Stellite 6 (510°C and 750°C) and Incoloy MA956 / Stellite 6 (750°C)	313

## List of Figures

<b>Figure 2.1:</b>	Modes of relative motion – sliding and rolling	5
<b>Figure 2.2:</b>	Coulomb's model for sliding friction	7
<b>Figure 2.3:</b>	Deformation during sliding, represented by the ploughing of the flat surface of a softer material by a rigid cone of harder material	12
<b>Figure 2.4:</b>	Wear surfaces produced during the sliding of Incoloy MA956 against Incoloy 800HT at 270°C and 750°C	15
<b>Figure 2.5:</b>	Variation in wear rate with sliding speed at 20, 300 and 400°C in air and also 300°C in pure oxygen for $\alpha/\beta$ brass sliding against steel	15
<b>Figure 2.6:</b>	Experimental Data from Archard and Hirst's Work on Like-on-Like Sliding at 1.8 m.s <sup>-1</sup>	17
<b>Figure 2.7:</b>	Archard and Hirst's Experimental Data	18
<b>Figure 2.8:</b>	Variation of 'normalised' wear rates of Al 12.3 wt. % Si alloy slid against Cu, Cu 4.6% Al and Cu 7.5% Al	22
<b>Figure 2.9:</b>	The three models of abrasive wear	23
<b>Figure 2.10:</b>	Abrasive wear as a result of an idealised cone sliding across a flat surface	28
<b>Figure 2.11:</b>	Wear particle formation by shear deformation of voids	28
<b>Figure 2.12:</b>	Idealised cell showing relative dimensions, from plan, side and end structures of cells in the wear surface	29
<b>Figure 2.13:</b>	Effectiveness of wear reduction on S45C plain carbon steel due to the introduction of Fe <sub>2</sub> O <sub>3</sub> particles	32
<b>Figure 2.14:</b>	Mechanisms of possible movement of particles during sliding of particulate materials	37
<b>Figure 2.15:</b>	Variation of coefficient of friction and wear rate of Fe 4.9%Cr with oxygen partial pressure during like on like sliding at 20°C	45
<b>Figure 2.16:</b>	Variation of wear and coefficient of friction as a function of relative humidity	48
<b>Figure 2.17:</b>	Effects of pre-oxidation and pre-sliding on wear of S45C at 20°C	49
<b>Figure 2.18:</b>	'Modified' version of Jiang's diagrammatic representation of sliding wear processes at various temperatures	56
<b>Figure 2.19:</b>	Oxygen transport between oxide plateaux and cracks in the oxides	62
<b>Figure 2.20:</b>	Variation in wear rate with sliding speed at 20, 300 and 400°C in air and also 300°C in pure oxygen for $\alpha/\beta$ brass sliding against steel	66

<b>Figure 2.21:</b>	Effect of sliding speed on wear rate / load – 0.52% carbon steel	67
<b>Figure 2.22:</b>	Effect of sliding speed on wear rate of Al 12.3 wt. % Si versus various counterface materials	69
<b>Figure 2.23:</b>	Wear transition map for steels showing regions of mild and severe wear – sliding conditions corresponding to different types of wear transitions observed are also indicated	71
<b>Figure 2.24:</b>	Variation in wear rate with sliding speed and load for the rubbing of laser clad Stellite 6 pins with AISI 4340 steel disks	75
<b>Figure 2.25:</b>	Binary phase diagram for cobalt and chromium, showing the transition temperature for 27% chromium	77
<b>Figure 2.26:</b>	Identification of grain boundary carbides by changes in distribution of cobalt and chromium in the Stellite 6 substrate	80
<b>Figure 4.1:</b>	Reciprocating high temperature block on cylinder wear rig, as used in the experimental programme	93
<b>Figure 4.2:</b>	Wear rig furnace, showing sample arm (with sample), shaft and counterface in position for testing	94
<b>Figure 4.3:</b>	Typical samples used for wear tests	95
<b>Figure 4.4:</b>	Loading profile for nano-indentation tests conducted on glaze layers	103
<b>Figure 5.1:</b>	Effect of temperature on weight change and wear rate – Nimonic 80A versus Stellite 6	108
<b>Figure 5.2:</b>	Temperature versus coefficient of friction – Nimonic 80A versus Stellite 6	109
<b>Figure 5.3:</b>	Sample wear scar optical images – Nimonic 80A / Stellite 6, 0.314 m.s <sup>-1</sup>	112
<b>Figure 5.4:</b>	Sample wear scar optical images – Nimonic 80A / Stellite 6, 0.905 m.s <sup>-1</sup>	113
<b>Figure 5.5:</b>	SEM micrographs for Nimonic 80A versus Stellite 6 – wear surface	114
<b>Figure 5.6:</b>	SEM micrographs for Nimonic 80A versus Stellite 6 showing change in wear scar morphology between 510°C and 690°C at 0.905 m.s <sup>-1</sup> / 4,522 m	115
<b>Figure 5.7:</b>	SEM micrographs for Nimonic 80A versus Stellite 6 – debris	116
<b>Figure 5.8:</b>	Counterface wear scar optical images – Nimonic 80A / Stellite 6, 0.314 m.s <sup>-1</sup>	117
<b>Figure 5.9:</b>	Counterface wear scar optical images – Nimonic 80A / Stellite 6, 0.905 m.s <sup>-1</sup>	117
<b>Figure 5.10:</b>	EDX data – variation of composition of loose debris and glaze layers (Nimonic 80A vs. Stellite 6), room temperature to 750°C, 0.314 m.s <sup>-1</sup>	122
<b>Figure 5.11:</b>	EDX data – variation of composition of loose debris (Nimonic 80A vs. Stellite 6), 570°C to 750°C, 0.905 m.s <sup>-1</sup>	122

<b>Figure 5.12:</b>	Cross sectional EDX element maps for Nimonic 80A worn against Stellite 6 subsequent to wear at $0.314 \text{ m.s}^{-1}$	124
<b>Figure 5.13:</b>	Data from Autopoint EDX analysis for Nimonic 80A slid against Stellite 6 at a sliding speed of $0.314 \text{ m.s}^{-1}$ and a temperature of $750^{\circ}\text{C}$	125
<b>Figure 5.14:</b>	XRD data – Nimonic 80A versus Stellite 6 at $0.314 \text{ m.s}^{-1}$	128
<b>Figure 5.15:</b>	XRD data – Nimonic 80A versus Stellite 6 at $0.905 \text{ m.s}^{-1}$	129
<b>Figure 5.16:</b>	Glancing Angle XRD data – Nimonic 80A versus Stellite 6 at $0.314 \text{ m.s}^{-1}$	131
<b>Figure 5.17:</b>	Subsurface layer hardness for samples slid at $0.314$ and $0.905 \text{ m.s}^{-1}$ , Nimonic 80A versus Stellite 6	133
<b>Figure 5.18:</b>	Change in weight and wear rate with time for Nimonic 80A versus Stellite 6 at $510^{\circ}\text{C}$ , $630^{\circ}\text{C}$ and $750^{\circ}\text{C}$	136
<b>Figure 5.19:</b>	Change in coefficient of friction with sliding distance for Nimonic 80A versus Stellite 6 at $510^{\circ}\text{C}$ and $750^{\circ}\text{C}$	137
<b>Figure 5.20:</b>	Glaze build up with time for Nimonic 80A versus Stellite 6 – optical	139
<b>Figure 5.21:</b>	Glaze build up with time for Nimonic 80A versus Stellite 6 – SEM low resolution images (X300)	140
<b>Figure 5.22:</b>	Glaze build up with time for Nimonic 80A versus Stellite 6 – SEM high resolution images (X3.0K)	141
<b>Figure 5.23:</b>	XRD data – Nimonic 80A versus Stellite 6 at $0.314 \text{ m.s}^{-1}$ / $510^{\circ}\text{C}$	142
<b>Figure 5.24:</b>	XRD data – Nimonic 80A versus Stellite 6 at $0.314 \text{ m.s}^{-1}$ / $750^{\circ}\text{C}$	143
<b>Figure 5.25:</b>	Weight change and wear rate versus sliding speed for Stellite 6 as the sample material worn against a Nimonic 80A counterface at $750^{\circ}\text{C}$	145
<b>Figure 5.26:</b>	Coefficient of friction versus temperature – Stellite 6 vs. Nimonic 80A	146
<b>Figure 5.27:</b>	Compacted oxide produced on Stellite 6 samples slid against a Nimonic 80A counterface at different sliding speeds – optical images	149
<b>Figure 5.28:</b>	Compacted oxide produced on Stellite 6 samples slid against a Nimonic 80A counterface at $0.314 \text{ m.s}^{-1}$ and $0.905 \text{ m.s}^{-1}$ – SEM images	150
<b>Figure 5.29:</b>	Backscatter image of the side profile of a Stellite 6 sample	150
<b>Figure 5.30:</b>	Variation in hardness with increasing distance from the sliding surface for both the cobalt rich matrix and the carbide precipitates in Stellite 6 slid against a Nimonic 80A counterface at $750^{\circ}\text{C}$	152
<b>Figure 5.31:</b>	Compacted oxide produced on a Nimonic 80A counterface slid against Stellite 6 samples at $0.314 \text{ m.s}^{-1}$ and $0.905 \text{ m.s}^{-1}$	153



<b>Figure 5.32:</b>	Weight change and wear rate versus sliding speed for Nickel 200 <sup>TM</sup> versus Stellite 6 at 0.314 m.s <sup>-1</sup> and 0.905 m.s <sup>-1</sup>	155
<b>Figure 5.33:</b>	Friction data for Nickel 200 <sup>TM</sup> versus Stellite 6 at 0.314 and 0.905 m.s <sup>-1</sup>	156
<b>Figure 5.34:</b>	Comparison of wear scars produced by wear of Nimonic 80A versus Stellite 6 and Nickel 200 <sup>TM</sup> versus Stellite 6	156
<b>Figure 5.35:</b>	SEM images of Nickel 200 <sup>TM</sup> samples slid against a Stellite 6 counterface at 0.314 and 0.905 m.s <sup>-1</sup>	158
<b>Figure 5.36:</b>	XRD Plots for glaze from Nickel 200 <sup>TM</sup> versus Stellite 6	159
<b>Figure 5.37:</b>	Subsurface layer hardness for samples slid at 0.314 and 0.905 m.s <sup>-1</sup> , Nickel 200 <sup>TM</sup> versus Stellite 6, 750°C	160
<b>Figure 5.38:</b>	Effect of temperature on weight change and wear rate – Incoloy MA956 versus Stellite 6	164
<b>Figure 5.39:</b>	Coefficient of friction versus temperature – Incoloy MA956 vs. Stellite 6	165
<b>Figure 5.40:</b>	Sample wear scar optical images – Incoloy MA956 / Stellite 6, 0.314 m.s <sup>-1</sup>	168
<b>Figure 5.41:</b>	Sample wear scar optical images – Incoloy MA956 / Stellite 6, 0.905 m.s <sup>-1</sup>	169
<b>Figure 5.42:</b>	SEM micrographs for Incoloy MA956 versus Stellite 6 – wear surface	170
<b>Figure 5.43:</b>	SEM micrographs for Incoloy MA956 versus Stellite 6 – debris	171
<b>Figure 5.44:</b>	Counterface wear scar optical images – Incoloy MA956 / Stellite 6, 0.314 m.s <sup>-1</sup>	172
<b>Figure 5.45:</b>	Counterface wear scar optical images – Incoloy MA956 / Stellite 6, 0.905 m.s <sup>-1</sup>	172
<b>Figure 5.46:</b>	EDX data – variation of composition of loose debris and glaze layers (Incoloy MA956 vs. Stellite 6), room temperature to 750°C, 0.314 m.s <sup>-1</sup>	177
<b>Figure 5.47:</b>	EDX Data – variation of composition of glaze layers (Incoloy MA956 vs. Stellite 6), 510°C to 750°C, 0.905 m.s <sup>-1</sup>	177
<b>Figure 5.48:</b>	Cross sectional EDX element maps for Incoloy MA956 worn against Stellite 6 subsequent to wear at 0.314 m.s <sup>-1</sup>	179
<b>Figure 5.49:</b>	Cross sectional EDX element maps for Incoloy MA956 worn against Stellite 6 subsequent to wear at 0.905 m.s <sup>-1</sup>	180
<b>Figure 5.50:</b>	Data from Autopoint EDX analysis for Incoloy MA956 slid against Stellite 6 at sliding speeds of 0.314 and 0.905 m.s <sup>-1</sup> and 750°C	181
<b>Figure 5.51:</b>	XRD for Incoloy MA956 versus Stellite 6 – 0.314 m.s <sup>-1</sup>	184
<b>Figure 5.52:</b>	XRD for Incoloy MA956 versus Stellite 6 – 0.905 m.s <sup>-1</sup>	185

<b>Figure 5.53:</b>	Glancing Angle XRD for Incoloy MA956 versus Stellite 6 – 0.314 m.s <sup>-1</sup>	186
<b>Figure 5.54:</b>	Subsurface layer hardness for samples slid at 0.314 and 0.905 m.s <sup>-1</sup> , Incoloy MA956 versus Stellite 6	189
<b>Figure 5.55:</b>	Effect of temperature on weight change and wear rate – Nimonic 80A versus Incoloy 800HT	192
<b>Figure 5.56:</b>	Temperature versus coefficient of friction for Nimonic 80A versus Incoloy 800HT	193
<b>Figure 5.57:</b>	Distance to transition in coefficient of friction from high variability (severe wear) to low variability (mild wear) at 630°C, 690°C and 750°C – Nimonic 80A versus Incoloy 800HT at 0.905 m.s <sup>-1</sup>	196
<b>Figure 5.58:</b>	Optical images for Nimonic 80A versus Incoloy 800HT at 0.314 m.s <sup>-1</sup>	198
<b>Figure 5.59:</b>	Optical Images for Nimonic 80A versus Incoloy 800HT at 0.905 m.s <sup>-1</sup>	199
<b>Figure 5.60:</b>	SEM micrographs for Nimonic 80A versus Incoloy 800HT – wear surface	200
<b>Figure 5.61:</b>	SEM micrographs for Nimonic 80A versus Incoloy 800HT – debris	201
<b>Figure 5.62:</b>	Counterface wear scar optical images – Nimonic 80A / Incoloy 800HT, 0.314 m.s <sup>-1</sup>	202
<b>Figure 5.63:</b>	Counterface wear scar optical images – Nimonic 80A / Incoloy 800HT, 0.905 m.s <sup>-1</sup>	202
<b>Figure 5.64:</b>	Cross sectional EDX element maps for Nimonic 80A worn against Incoloy 800HT subsequent to wear at 0.314 m.s <sup>-1</sup>	207
<b>Figure 5.65:</b>	Cross sectional EDX element maps for Nimonic 80A worn against Incoloy 800HT subsequent to wear at 0.905 m.s <sup>-1</sup>	208
<b>Figure 5.66:</b>	Data from Autopoint EDX analysis for Nimonic 80A versus Incoloy 800HT at sliding speeds of 0.314 and 0.905 m.s <sup>-1</sup> and 750°C	210
<b>Figure 5.67:</b>	XRD for Nimonic 80A versus Incoloy 800HT at 0.314 m.s <sup>-1</sup>	212
<b>Figure 5.68:</b>	XRD for Nimonic 80A versus Incoloy 800HT at 0.905 m.s <sup>-1</sup>	213
<b>Figure 5.69:</b>	Glancing Angle XRD for Nimonic 80A vs. Incoloy 800HT at 0.314 m.s <sup>-1</sup>	214
<b>Figure 5.70:</b>	Subsurface layer hardness for samples slid at 0.314 and 0.905 m.s <sup>-1</sup> , Nimonic 80A versus Incoloy 800HT	216
<b>Figure 5.71:</b>	Optical and SEM images of sample surfaces on sliding without reciprocation – Nimonic 80A versus Incoloy 800HT at 510°C and 0.314 m.s <sup>-1</sup>	220

<b>Figure 5.72:</b>	Coefficient of friction versus sliding distance for Nimonic 80A versus Incoloy 800HT at 510°C and 0.314 m.s <sup>-1</sup> without reciprocation	221
<b>Figure 5.73:</b>	Effect of temperature on weight change and wear rate – Incoloy MA956 vs. Incoloy 800HT	224
<b>Figure 5.74:</b>	Temperature versus coefficient of friction for Incoloy MA956 versus Incoloy 800HT	225
<b>Figure 5.75:</b>	Distance to transition in coefficient of friction from high variability (severe wear) to low variability (mild wear) at 630°C, 690°C and 750°C – Incoloy MA956 versus Incoloy 800HT at 0.314 m.s <sup>-1</sup> and 0.905 m.s <sup>-1</sup>	226
<b>Figure 5.76:</b>	Optical Images for Incoloy MA956 versus Incoloy 800HT at 0.314 m.s <sup>-1</sup>	230
<b>Figure 5.77:</b>	Optical Images for Incoloy MA956 versus Incoloy 800HT at 0.905 m.s <sup>-1</sup>	231
<b>Figure 5.78:</b>	SEM micrographs for Incoloy MA956 versus Incoloy 800HT – wear surfaces	232
<b>Figure 5.79:</b>	SEM micrographs for Incoloy MA956 versus Incoloy 800HT – debris	233
<b>Figure 5.80:</b>	Counterface wear scar optical images – Incoloy MA956 / Incoloy 800HT, 0.314 m.s <sup>-1</sup>	234
<b>Figure 5.81:</b>	Counterface wear scar optical images – Incoloy MA956/ Incoloy 800HT, 0.905 m.s <sup>-1</sup>	234
<b>Figure 5.82:</b>	Cross sectional EDX element maps for Incoloy MA956 worn against Incoloy 800HT subsequent to wear at 0.314 m.s <sup>-1</sup>	239
<b>Figure 5.83:</b>	Cross sectional EDX element maps for Incoloy MA956 worn against Incoloy 800HT subsequent to wear at 0.905 m.s <sup>-1</sup>	240
<b>Figure 5.84:</b>	Data from Autopoint EDX analysis for Incoloy MA956 versus Incoloy 800HT at sliding speeds of 0.314 and 0.905 m.s <sup>-1</sup> and 750°C	243
<b>Figure 5.85:</b>	XRD for Incoloy MA956 versus Incoloy 800HT – 0.314 m.s <sup>-1</sup>	246
<b>Figure 5.86:</b>	XRD for Incoloy MA956 versus Incoloy 800HT – 0.905 m.s <sup>-1</sup>	248
<b>Figure 5.87:</b>	Subsurface layer hardness for samples slid at 0.314 and 0.905 m.s <sup>-1</sup> , Incoloy MA956 versus Incoloy 800HT	253
<b>Figure 5.88:</b>	Optical and SEM images of sample surfaces on sliding without reciprocation Incoloy MA956 versus Incoloy 800HT at 510°C and 0.314 m.s <sup>-1</sup>	255
<b>Figure 5.89:</b>	Coefficient of friction versus sliding distance for Incoloy MA956 versus Incoloy 800HT at 510°C and 0.314 m.s <sup>-1</sup> without reciprocation	256
<b>Figure 5.90:</b>	TEM bright field image showing wear induced polycrystalline glaze layer and deformation of Nimonic 80A substrate	261

<b>Figure 5.91:</b>	TEM morphological and structural details of glaze layer on Nimonic 80A	262
<b>Figure 5.92:</b>	TEM-EDS patterns for glaze and Nimonic 80A substrate	263
<b>Figure 5.93:</b>	TEM image showing interface of glaze layer / deformed Nimonic 80A substrate	264
<b>Figure 5.94:</b>	STM surface line profile results on glaze layer formed on Nimonic 80A	265
<b>Figure 6.1:</b>	Wear processes for Nimonic 80A versus Stellite 6 from room temperature to 750°C at 0.314 m.s <sup>-1</sup>	268
<b>Figure 6.2:</b>	Mean Knoop hardness (hot hardness, 50 g load, 12 s dwell time) from room temperature to 510°C, with wear regimes with respect to temperature identified for the Nimonic 80A / Stellite 6 and Incoloy MA956 / Stellite 6 systems	269
<b>Figure 6.3:</b>	Wear processes for Nimonic 80A versus Stellite 6 from room temperature to 750°C at 0.905 m.s <sup>-1</sup>	273
<b>Figure 6.4:</b>	Wear map for Nimonic 80A versus Stellite 6	276
<b>Figure 6.5:</b>	Wear processes for Nickel 200™ slid against a Stellite 6 counterface at 750°C, for 0.314 and 0.905 m.s <sup>-1</sup>	278
<b>Figure 6.6:</b>	Wear processes for Incoloy MA956 versus Stellite 6 from room temperature to 750°C at 0.314 m.s <sup>-1</sup>	280
<b>Figure 6.7:</b>	Wear processes for Incoloy MA956 versus Stellite 6 from room temperature to 750°C at 0.905 m.s <sup>-1</sup>	283
<b>Figure 6.8:</b>	Wear map for Incoloy MA956 versus Stellite 6	286
<b>Figure 6.9:</b>	Wear processes for Nimonic 80A versus Incoloy 800HT from room temperature to 750°C at 0.314 m.s <sup>-1</sup>	288
<b>Figure 6.10:</b>	Layers formed on Nimonic 80A sample and Incoloy 800HT counterface at 750°C and 0.314 m.s <sup>-1</sup>	291
<b>Figure 6.11:</b>	Wear scar cross section on Incoloy 800HT counterface worn against a Nimonic 80A sample – 0.314 m.s <sup>-1</sup> and 0.905 m.s <sup>-1</sup>	291
<b>Figure 6.12:</b>	Wear processes for Nimonic 80A versus Incoloy 800HT from room temperature to 750°C at 0.905 m.s <sup>-1</sup>	293
<b>Figure 6.13:</b>	Distance to transition in coefficient of friction from high variability (severe wear) to low variability (mild wear) at 630°C, 690°C and 750°C – Nimonic 80A versus Incoloy 800HT at 0.905 m.s <sup>-1</sup>	295
<b>Figure 6.14:</b>	Layers formed on Nimonic 80A sample and Incoloy 800HT counterface at 750°C and 0.905 m.s <sup>-1</sup>	296
<b>Figure 6.15:</b>	Wear map for Nimonic 80A versus Incoloy 800HT	298
<b>Figure 6.16:</b>	Distance to transition in coefficient of friction from high variability (severe wear) to low variability (mild wear) at 630°C, 690°C and 750°C – Incoloy MA956 versus Incoloy 800HT at 0.314 m.s <sup>-1</sup> and 0.905 m.s <sup>-1</sup>	301

<b>Figure 6.17:</b>	Wear processes for Incoloy MA956 versus Incoloy 800HT from room temperature to 750°C at 0.314 m.s <sup>-1</sup>	303
<b>Figure 6.18:</b>	Layers formed on Incoloy MA956 sample and Incoloy 800HT counterface at 750°C and 0.314 m.s <sup>-1</sup>	304
<b>Figure 6.19:</b>	Wear scar cross section on Incoloy 800HT counterface worn against an Incoloy MA956 sample – 0.314 m.s <sup>-1</sup> and 0.905 m.s <sup>-1</sup>	305
<b>Figure 6.20:</b>	Wear processes for Incoloy MA956 versus Incoloy 80HT from room temperature to 750°C at 0.905 m.s <sup>-1</sup>	308
<b>Figure 6.21:</b>	Layers formed on Incoloy MA956 sample and Incoloy 800HT counterface at 750°C and 0.905 m.s <sup>-1</sup>	309
<b>Figure 6.22:</b>	Wear map for Incoloy MA956 versus Incoloy 800HT	312
<b>Figure 6.23:</b>	STM imaging of compacted oxide glaze formed during sliding wear of Nimonic 80A against Stellite 6	314
<b>Figure 6.24:</b>	Surface and sub surface layer micro-hardness for Nimonic 80A samples slid against Stellite 6 at 0.314 m.s <sup>-1</sup> and 750°C	316

## **ACKNOWLEDGEMENTS**

I would like to thank Prof. Santu Datta and Dr. Jim Burnell-Gray, my supervisors, for their help, advice and encouragement with this thesis.

I also wish to take the opportunity to thank other staff and research students within the Advanced Materials Research Institute and the School of Engineering, Science and Technology for all the help and assistance given. In particular, I wish to thank Bob Best for assistance and help with Scanning Electron Microscopy and Energy Dispersive X-Ray, and Ed Lancely, Clive Hartis and John Bagnall for help in the day-to-day running of this project.

Many thanks must be made also to my parents and friends who had to listen to all my tales of woe whilst I completed the write-up of this thesis. I also wish to pass on my gratitude to Sunderland Association Football Club where I am a season ticket holder; my trips to the Stadium of Light for football matches were at times the only break I had from my doctoral work.

I also wish to thank the EPSRC for their funding of this project.

This copy of this thesis has been supplied on condition that anyone who consults it is understood that its copyright rests with the author. No quotation from the thesis and no information derived from it may be published without the author's prior written permission.

## **DECLARATION**

I hereby declare that:

During the period I have been registered for the degree of Ph.D., for which this thesis is submitted, I have not been a registered candidate for any other award of a university.

Furthermore, I declare that I have attended relevant seminars within the University and presented papers at conferences and relevant meetings on the subject of high temperature wear.



# **Compacted Oxide Layer Formation under Conditions of Limited Debris Retention at the Wear Interface during High Temperature Sliding Wear of Superalloys**

By Ian A. Inman B.Sc. (Hons.), M.Sc.

## **ABSTRACT**

For many applications, including power generation, aerospace and the automobile industry, high temperature wear provides serious difficulties where two or more surfaces are able to move relative to one another. It is increasingly the case that with for example, aerospace applications, demands for ever more powerful and efficient engines that thus operate at higher temperatures, conventional lubrication is no longer sufficient to prevent direct contact between metallic surfaces and consequent accelerated wear.

One phenomenon that has been observed to reduce metallic contact and thus high temperature wear and friction is the formation of what are termed 'glazes', essentially layers of compacted oxide wear debris that becomes sintered together to form a low friction wear resistant oxide surface.

This thesis studies the nature of the wear encountered with four different combinations of Superalloys, slid together using a 'block-on-cylinder' configuration developed for accelerated simulation testing of car engine 'valve-on-valve-seat' wear. Predominantly, Nimonic 80A and Incoloy MA956 were used as sample materials and Stellite 6 and Incoloy 800HT were used as counterface materials.

The initial part of this study concentrates on sliding speed – during the current experimental programme, testing was conducted at  $0.314 \text{ m.s}^{-1}$  and  $0.905 \text{ m.s}^{-1}$ , between room temperature and  $750^{\circ}\text{C}$  – this supplemented previous testing conducted at  $0.654 \text{ m.s}^{-1}$ . When Nimonic 80A was slid against Stellite 6, lowering sliding speed to  $0.314 \text{ m.s}^{-1}$  between  $510^{\circ}\text{C}$  and  $750^{\circ}\text{C}$  lead to the formation of wear protective glaze layers consisting of cobalt and chromium oxides from the Stellite 6, whereas at  $0.905 \text{ m.s}^{-1}$  and during previous testing at  $0.654 \text{ m.s}^{-1}$ , only high wear was encountered with debris consisting of nickel and chromium oxides from the Nimonic 80A. When Incoloy MA956 was slid against Stellite 6 at the same sliding speeds and over the same temperature range, a wear protective layer readily formed regardless of sliding speed. However, the sliding speed was observed to affect the relative contributions to the glaze layer from sample and counterface – a shift was observed from largely cobalt and chromium oxides from the Stellite 6 at  $0.314 \text{ m.s}^{-1}$  to largely iron and chromium oxides from the Incoloy MA956 at  $0.905 \text{ m.s}^{-1}$ . Also, the use of a higher sliding speed was noted to promote glaze formation at lower temperature, with glaze appearing at  $450^{\circ}\text{C}$  for  $0.905 \text{ m.s}^{-1}$ , whereas only severe wear was observed for testing at  $0.654 \text{ m.s}^{-1}$ .

When Incoloy MA956 was worn against Incoloy 800HT, increasing the sliding speed from  $0.314 \text{ m.s}^{-1}$  to  $0.905 \text{ m.s}^{-1}$  had the opposite affect – the beginning of glaze formation was suppressed from  $630^{\circ}\text{C}$  to  $690^{\circ}\text{C}$ . Similar results were also observed when Nimonic 80A was slid against Incoloy 800HT, with the beginning of glaze formation suppressed from  $570^{\circ}\text{C}$  to  $630^{\circ}\text{C}$ . Thus whether sliding speed promotes or suppresses glaze formation is highly material dependant.

Additionally, both the Incoloy MA956 versus Incoloy 800HT and the Nimonic 80A versus Incoloy 800HT combinations were characterised by high degrees of metallic transfer and especially at room temperature and 270°C, adhesive wear – with Nimonic 80A versus Incoloy 800HT, the level of transfer, mostly from Incoloy 800HT to Nimonic 80A, was observed to increase with increasing sliding speed.

Further experimental studies concentrating on the sliding of Nimonic 80A versus Stellite 6 at 0.314 m.s<sup>-1</sup> and 750°C, indicated extremely rapid formation of glaze from Stellite 6-sourced debris – this consisted of an initial transfer of material from the harder Stellite 6 to the softer Nimonic 80A, followed by the steady development of a wear resistant glaze layer. The reversal of sample and counterface whilst varying sliding speed demonstrated that direction of transfer was more strongly influenced by material than configuration (i.e. which material was sample and which material was counterface). Finally, the substitution of Nimonic 80A with high purity nickel promoted the formation of glaze at not just 0.314 m.s<sup>-1</sup>, but also at 0.905 m.s<sup>-1</sup> – this was due to the elimination of chromium oxide (in the form of Cr<sub>2</sub>O<sub>3</sub>) from the predominantly nickel oxide (NiO) debris. This result, however, raises a number of queries yet to be answered. Firstly, why were nickel and chromium together readily able to form an oxide glaze with Nimonic 80A worn against Incoloy 800HT, but not so readily with Nimonic 80A worn against Stellite 6? Secondly, why did chromium readily form an oxide glaze with cobalt at 0.314 m.s<sup>-1</sup> with the Nimonic 80A versus Stellite 6 combination, but not so readily with nickel at higher sliding speed?

Finally, nano-characterisation studies were carried out on the glaze layers formed on Nimonic 80A samples slid against Stellite 6 at 0.314 m.s<sup>-1</sup> and 750°C. These glaze layers were shown to have a nano-scale grain structure, with a grain size of as little as 5 to 15 nm at the very surface of the glaze. A likely route of formation was established, starting with deformation of the surface, intermixing of debris from sample and counterface, oxidation of debris, further mixing and repeated welding and fracture – these processes are aided by high temperature oxidation and diffusion. The grain size is then refined by the formation of sub-grains, accompanied by increasing mis-orientation to give nano-structured grains - a non-equilibrium state results, with poorly defined and irregular grain boundaries. The presence of a nano-polycrystalline structure implies improved fracture toughness. However, the disorganised nature of the glaze layer suggests the production of a glaze is, overall, an inefficient process.

Analysis was performed using optical microscopy, SEM, EDX, EDX mapping and Autopoint, XRD, Glancing Angle XRD and extensive micro-hardness testing. Some preliminary nano-hardness testing was also carried out, that suggested glaze hardness levels not too far removed from bulk theoretical hardness values for chromium oxide and indicating low porosity and high levels of sintering within the glaze layers. Nano-characterisation studies were carried out using TEM and STM.

## 1. INTRODUCTION

Wear is an unavoidable and a potentially serious problem in all areas of engineering. Under normal conditions, good design practice along with appropriate materials selection and the use of an appropriate coating or lubricant system, may be sufficient to minimise wear of interacting surfaces or components to an acceptable level.

However, high temperature wear, particularly above 400°C, poses a problem in that protection by the use of lubricants is not available – the temperature capabilities of most hydrocarbon- or silicone-based lubricants are limited to 200°C and even solid lubricants such as molybdenum disulphide can only survive to at most 400°C. Thus for applications ranging from valve-on-valve seat wear in an internal combustion engine to turbines in aerospace and power generation, alternative approaches are required. Suitable materials are selected on the basis of their high temperature environmental resistance, and physical and mechanical properties – excellent chemical and oxidational resistance, high temperature strength and creep resistance are thus paramount. For these reasons, superalloy materials such as Nimonic 80A are popular for such applications. However, such properties do not always guarantee immunity against high temperature wear.

Coatings, pre-oxidation and surface modification of alloys can also give a greater degree of protection, especially during the extremely damaging ‘run-in’ period. However, the lifetime of the modified surfaces can be limited and once the underlying, unmodified material is exposed, wear rates are often very similar to the unprotected material from this point on. In addition to this, there is with time an increasing demand for greater operational efficiency and thus higher operational temperatures in aerospace applications and power generation. In such cases, traditional methods of surface protection are becoming less effective. An alternative approach would be to produce an in-situ surface layer, assisted by the events occurring during the wear process.

High temperature wear arises from and involves the simultaneous occurrence of two degradation processes – i) environmental interaction with faster kinetics and ii) damage due to wear – both processes taking place at the contacting surfaces under load. However, these two degradation processes can be used with benefits to generate a “glazed” layer on one or both surfaces, which minimises and can almost completely eliminate subsequent wear.

Clearly the key to the solution to high temperature wear lies in understanding the mechanisms behind the formation of these glazed surfaces.

Experimental work done in this laboratory [1-3] (concentrating on the use of dissimilar metals, specifically superalloys, in sliding contact) and elsewhere [4,5] has shown that the formation of this layer involves a number of processes – oxidation of the contacting surfaces, debris generation, debris transfer between contacting surfaces and repeated compaction and sintering of debris particles and fracture. The other important factor is the sustainability of the compacted layer. This is affected by the nature of the debris, specifically the size and shape of the generated particles, the adhesion of the debris particles and glaze to surfaces and also the deformation behaviour and hence the load-bearing capability of the material underneath the compacted layer necessary to support the compacted layer.

Research on high temperature wear has significantly improved understanding of some of the processes responsible for the formation of glazed layers. However, it is still not possible to predict the process variables and the materials systems, which will lead to the formation of wear resistant compacted oxide surfaces (glazes). Uncertainty exists concerning the influence of the properties of the materials (i.e. oxidation resistance, deformation characteristics) and the effect of speed and temperature. This project has thus been designed to gain further insight into the processes of glaze formation and achieve improved understanding of the mechanisms responsible for the development of glaze layers.

In this project, attention has been focussed on superalloys that possess superior resistance to oxidation. Another factor that is distinctive of this study has been the use of a wear rig, which only allows minimum debris retention between the wear surfaces. Bearing in mind that oxidation and the presence of debris are the necessary conditions for glaze formation, the project was planned to investigate the minimum conditions required for glaze formation, defined by the high oxidation resistance of the materials and minimum debris retention.

Several factors characterise the studies undertaken to elucidate the mechanisms of glaze formation, viz;

1. the sliding of different combinations of ‘unlike-on-unlike’ materials;

2. the limited debris retention of the ‘block-on-cylinder’ configuration;
3. the investigation of the influence of various tribological parameters in combination – these include load [1,2], temperature and during the current study, sliding speed;
4. substitution of one or other alloy with a pure metal (Nimonic 80A with nickel), to study the effects of eliminating alloying components; and
5. the use of Transmission Electron Microscopy (TEM) and Scanning Tunnelling Microscopy (STM), allowing preliminary nano-scale studies of the structures of the resulting high temperature glazes – it is thus hoped from these studies that a greater in-depth understanding of glazes and how they are formed will be gained.

The thesis is divided into eight chapters:

- **Chapter 2** (following this ‘Introduction’ chapter) contains a critical literature review, covering early wear theory, the effects of adhesion and abrasion as a result of contact during sliding (e.g. ploughing, cutting, wedge forming, delamination wear), third-body effects and current compacted oxide and glaze layer formation theory.
- **Chapter 3** is an introduction to the current experimental programme.
- **Chapter 4** contains the experimental methodology and the details of the equipment and various characterisation techniques used.
- **Chapter 5** reports on the experimental findings.
- **Chapter 6** is a discussion of these results.
- **Chapter 7** summarises the findings of the experimental work.
- **Chapter 8** makes a number of suggestions for further work.

## **2. LITERATURE REVIEW**

### **2.1 Introduction**

This chapter critically reviews the relevant literature related to unlubricated sliding wear at elevated temperatures. The review is divided into the following sections:

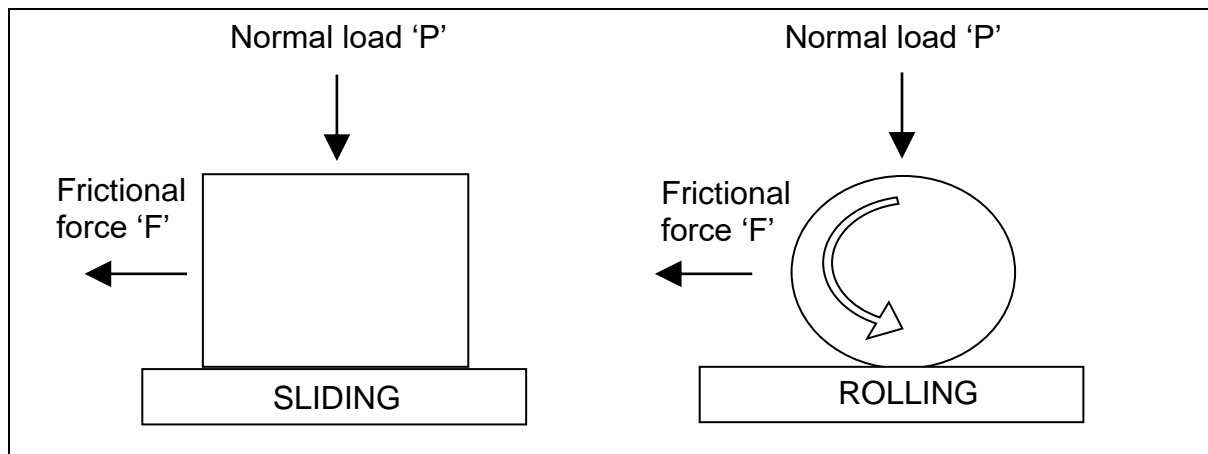
- Section 2.2 discusses the key aspects of frictional force.
- Section 2.3 deals with principal models of wear theory, including surface contact under load and under sliding conditions. The effects of surface contamination are also reviewed, along with the key mechanisms of wear – adhesive, abrasive, delamination and corrosive (oxidational) wear.
- Section 2.4 examines the effect of wear debris at the wear interface and on the wear process. This includes a comprehensive discussion of ‘two’ and ‘three’ body wear, focussing on the effect of retained debris on the key wear mechanisms.
- Section 2.5 looks at the key aspects of mild wear and the mechanisms of compact oxide and glaze formation during unlubricated wear at elevated temperatures. The effects of environmental variables, such as atmosphere, water vapour, humidity and the effects of pre-treatment are also considered.
- Section 2.6 discusses the effects of mechanical parameters such as load and sliding speed on the formation of compact oxide layers. Special attention with regard to load and sliding speed is paid to cobalt-based alloys such as Stellite 6 and to the presence of carbides in such alloys, effectively forming a second phase.
- Section 2.7 expands on the discussion of second phases – the possible effect of second phases present in the test alloys used in the current programme are considered.
- Section 2.8 examines material transfer and mechanical alloying during sliding wear.
- Section 2.9 looks at previous nano-characterisation work conducted on sliding surfaces.
- Section 2.10 concludes the literature review by examining previous work conducted on elevated temperature wear, within the Surface Engineering Research Group and the Advanced Materials Research Institute at Northumbria University.

## 2.2 Friction

### 2.2.1 Definition of Friction

The frictional force is defined as the resistance to movement produced when one body moves against another. Friction may be defined as sliding or rolling friction (Figure 2.1) [6]. Sliding friction can be said to occur where the interfaces of two rigid objects move relative to one another, whereas in rolling friction, one or both of the objects has freedom of movement other than that in the direction of the sliding action, allowing it to ‘rotate’ or ‘roll’. It is to be pointed out that due to other factors such as misalignment or relative movement of asperities past each other on interface surfaces, that an element of sliding friction will always be involved where rolling wear occurs.

**Figure 2.1: Modes of relative motion – sliding and rolling**



There are three widely accepted laws on friction. The first two laws of friction were defined by Leonardo da Vinci [7] and redefined by Amontons:

1. *Frictional force is proportional to normal load.*

This can be defined empirically as:

$$F = \mu P \quad \{2.1\}$$

where  $F$  is the frictional force,  $\mu$  is the coefficient of friction and  $P$  is the normal load. Redefining this in terms of coefficient of friction gives:

$$\mu = F/P \quad \{2.2\}$$

2. *Frictional force is independent of apparent area of contact.*

The third law of friction, normally attributed to Coulomb [6], additionally states:

3. *Frictional force is independent of sliding velocity.*

A further unstated law [6] is that ‘static’ friction (where there is no movement of the contacting surfaces) is greater than the ‘sliding’ friction (where the contacting surfaces move relative to each other), in other words, the frictional force required to initiate sliding is greater than that required to maintain it. Sliding friction in this case can alternatively be referred to as ‘kinetic’ friction (there is a change of state due to the resultant movement of the sliding surfaces).

The use of these laws has been observed to form a good fit with experimental data over a limited range of conditions, however, due to changes in the physical nature of materials directly as a result of wear or due to other factors, their uses can be restricted. For example, the oxidation or chemical alteration of the contacting surfaces involved may have a major influence and the adhesion properties of the sliding surfaces will also affect the overall coefficient of friction.

Other early work in the field of friction was conducted by Coulomb [6,8], whose approach was to use a simplified model of the surface of a material, in which the asperities were modelled by a repeating pattern of interlocking wedges and troughs. When one surface is moved relative to the other, in order to ‘unlock’ the surfaces, it is necessary to apply friction force  $F$  to overcome the normal load  $P$  (‘a’ to ‘b’ in Figure 2.2). In Coulomb’s model, the first law of friction can be redefined as:

$$\mu = \tan \theta = F / P \quad \{2.3\}$$

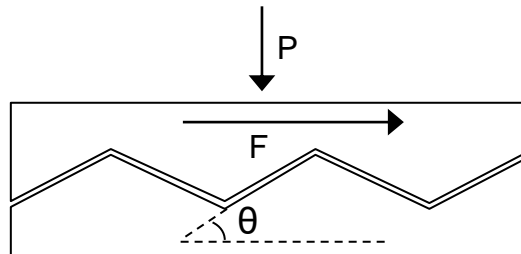
$\theta$  here defined as the average slope of the asperities and thus the applied or frictional force is proportional to load. Each of these models does not account for the adhesion or any



other interaction occurring on the materials' surfaces and therefore the independence of the frictional force from the area of contact can at this stage be assumed. However, on unlocking the asperities from one set of troughs, such that asperities are resting on asperities (Figure 2.2b), any further sliding action leads to the asperities sliding down the other side into the next set of troughs under the influence of the normal load (Figure 2.2c). No net work is therefore done within the system and with zero energy change, the Coulomb model cannot work. Clearly, for the movement or sliding action to occur, overall, energy must be put into the system.

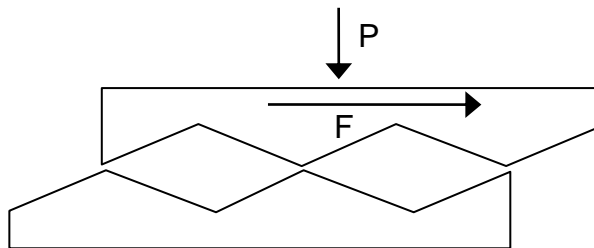
**Figure 2.2: Coulomb's model for sliding friction**

- (a) Initial state, with interlocking asperities, average slope  $\theta$ .

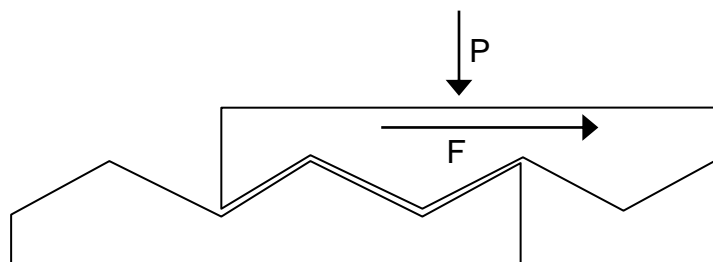


- (b) The work done in the sliding action is against the normal load ' $P$ ', giving rise to frictional force ' $F$ ', relationship  $F = P \tan \theta$ .

This means the coefficient of friction ' $\mu' = \tan \theta$  in Coulomb's model.



- (c) Coulomb's model fails as in the model he proposes, an equal amount of work is done by the normal load as the asperities re-interlock 'one asperity on' – they can be said to slide down the other side of the slope [7].



### **2.2.2 Observed Friction in Real Systems**

During sliding wear, typical friction values of between 0.002 and 0.1 in a lubricated system and 0.1 and 2.0 in an unlubricated system are normally encountered. In many real systems, the range of friction values can extend beyond this, from as much as 10 for a clean metallic surface to as little as  $1 \times 10^{-5}$  for a radially loaded ball bearing (where rotational friction is predominantly encountered). Specific design can reduce friction even further, a notable example being a hydrostatic bearing on a telescope, where friction levels can be as low as  $1 \times 10^{-5}$  [6].

### **2.2.3 Adhesion**

Adhesion is considered to originate from the action of intermolecular forces at surfaces or interfaces in close contact [6]. Clean surfaces show greater adhesion [1,6] and thus greater resistance to their relative movement to one another. Where a surface is free of oxide and other contamination or debris, close contact between the interface surfaces, especially at asperities, will allow ready bonding and the tendency towards the formation of metallic or covalent bonds will be high, thus adhesion will also be high. The presence of surface contamination will inhibit metallic contact and prevent these bonds from forming, thus any adhesion between the surfaces will be limited to the effects of weaker Van der Waals' forces between the surfaces, effective up to a distance of 10 nm. Friction is also affected by the surrounding atmosphere; adhesion in a vacuum is stronger [1].

When the surfaces are brought together, the contacts first take place at the high points of the asperities, which will deform elastically or plastically under the applied load. Because of the very low area of initial contact, in all but the most polished surfaces, deformation will be primarily plastic [10-12].

This deformation continues until there is sufficient area of contact between the two surfaces to sustain the load, i.e. the area of contact is such that the applied stress through any given point is reduced to a level, which is insufficient to continue the deformation process (assuming a constant applied load). In this case, the applied stress falls below the yield strength of the material. It is at these points of close contact that bonding occurs, in other words, the material at the contacting asperities may adhere.

It is also apparent from the above that the true area of contact is thus independent of the apparent area of contact. Given a particular surface asperity profile or configuration, it is not possible to predict the true or final area of contact, due to the combined effects of applied load and the deformation properties of both materials – the discussion here focuses on the softer material, assuming any deformation in the harder material to be negligible.

Thus, if  $H$  is the indentation hardness of the material,  $P$  is the applied load and  $A$  is the true area of contact [6]:

$$H = P/A \quad \{2.4\}$$

The greater the hardness of the softer material or the lower the applied load on the contacting surfaces, the lower the true area of contact will be. Rearranging equation {2.4} gives:

$$A = P/H \quad \{2.5\}$$

The frictional force due to adhesion  $F_{adh}$  at the points of contact (or alternatively, the force required to overcome this adhesion) is therefore a function of the shear strength  $s$  of these junctions, assuming these to be all of the same shear strength (there are no chemical or physical changes affecting the material), thus:

$$F_{adh} = As \quad \{2.6\}$$

Combining and substituting into equation {2.3}:

$$\mu_{adh} = \frac{F_{adh}}{P} \approx \frac{s}{H} \quad \{2.7\}$$

On applying a force to slide one surface over the other, the junction should fail by rupture of the weaker material. The shear strength of the weaker material  $s$  is considered to be the shear strength of the junction. In most metallic materials, the hardness  $H$  is approximately

three times the uniaxial yield stress  $Y$ , this itself being 1.7 to 2 times the yield value in pure shear.

$$H \approx 3Y \approx 5s \quad \{2.8\}$$

Substituting these values into equation {2.7}:

$$\mu_{adh} \approx \frac{s}{H} \approx \frac{s}{5s} = 0.2 \quad \{2.9\}$$

#### 2.2.4 Ploughing

Adhesion is only one component of the coefficient of friction, when relating the interaction of these asperities to the frictional force. Comparison with data shows a large discrepancy with the reported values of 0.1 to 2.0 for real systems [6]. This discrepancy is accounted for by physical deformation.

Bowden and Tabor [8] showed that as well as adhesion, the physical deformation due to a harder material ploughing through a softer material or rather the work required to carry this out, also contributed to the frictional force. This is referred to as “ploughing”.

The standard model used for deformation and ploughing is that of a cone of rigid material being pulled through the flat surface of a softer, more easily deformed material, as shown in Figure 2.3 along with the relevant parameters.

To displace the softer material by the rigid cone, the angle  $\alpha$  between the axis of the conical asperity and the outside slope, requires force  $F_{def}$ , referred to as the “flow pressure”. This can be calculated by multiplying the cross-sectional area of the groove by the indentation hardness:

$$F_{def} = Hax = Hx^2 \cdot \tan \alpha \quad \{2.10\}$$

The load supported through the asperity acts through an area of radius equivalent to half the width of the groove left behind by the asperity. The area supporting the load is  $\pi a^2$ , thus:

$$P = \frac{H\pi a^2}{2} = \frac{1}{2} \cdot H\pi x^2 \cdot \tan^2 \alpha \quad \{2.11\}$$

Returning to equation {2.3}

$$\mu = F / P$$

this gives the component of coefficient of friction from deformation:

$$\mu_{def} = \frac{F_{def}}{P} = \frac{2}{\pi} \cdot \cot \alpha \quad \{2.12\}$$

One potential difficulty with this model, is that it assumes that the hardened asperity will not deform, whereas in reality, some degree of deformation can be said to occur even when the asperity is significantly harder than the deformable material. For example, previous testing [1,2] has shown that the significantly harder Stellite 6 counterface will still suffer some damage when worn against a much softer material such as Incoloy MA956.

### 2.2.5 *Combination of Models*

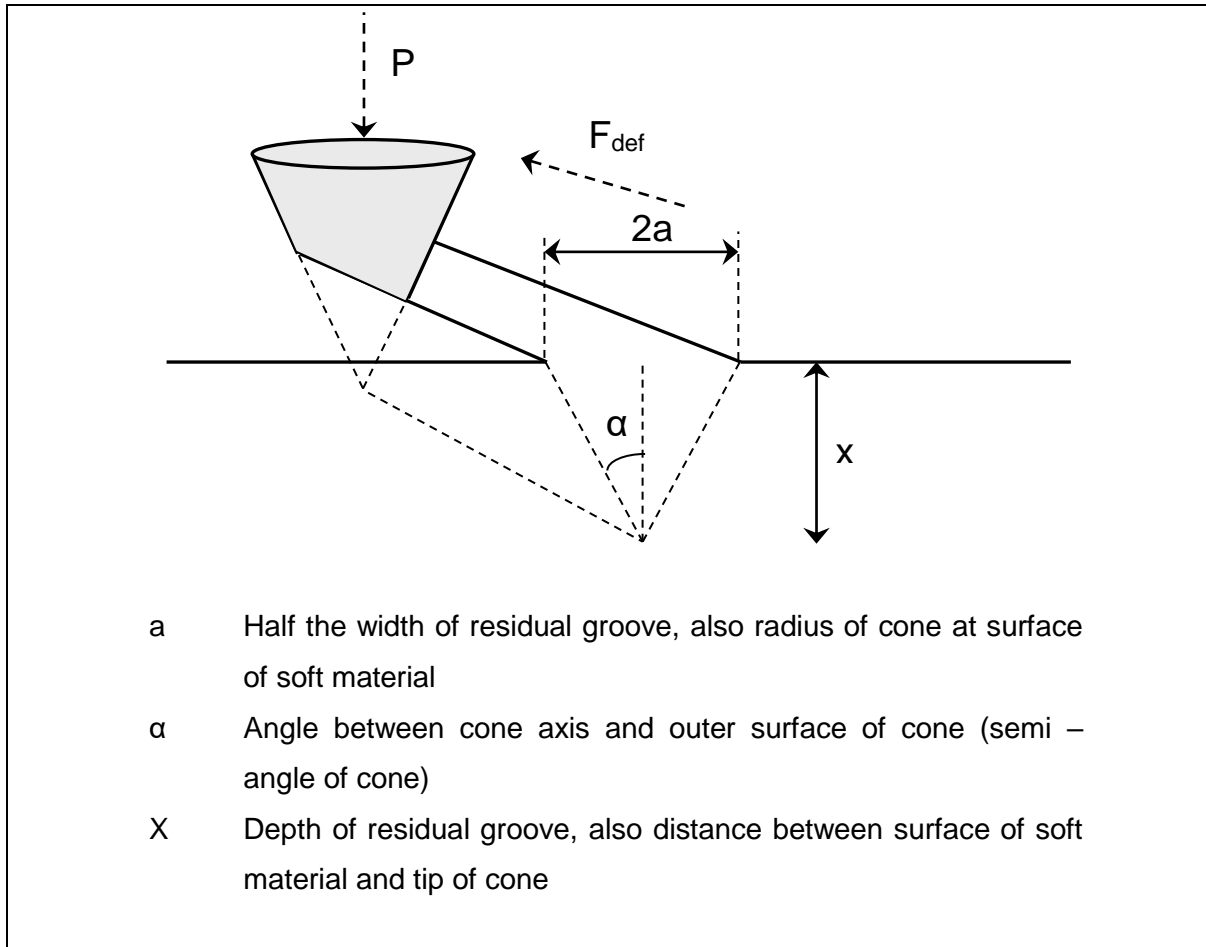
Bringing both adhesion and plastic deformation considerations together [8], if  $F_{adh}$  is the ‘frictional force due to adhesion’ (or alternatively, the force needed to overcome adhesion) and  $F_{def}$  is the ‘flow pressure’ (the force required to push the material ahead of the asperity out of the way), then the total frictional force (or force needed to overcome surface effects) is:

$$F_{total} = F_{adh} + F_{def} \quad \{2.13\}$$

As  $\mu = F/P$ , then this can be modified to:

$$\mu_{total} = \mu_{adh} + \mu_{def} \quad \{2.14\}$$

**Figure 2.3: Deformation during sliding, represented by the ploughing of the flat surface of a softer material by a rigid cone of harder material**



### 2.2.6 Complications with the Bowden and Tabor Model

These models represent an idealised situation, which assumes the continuous movement of one surface against another, and do not explain the observed discrepancies between the theory and experimental state. For example, on application of a tangential force and just before the beginning of moving or sliding, it is found that coefficients of friction are higher than during the sliding process [6] – in other words, the static coefficient of friction is higher than the dynamic coefficient of friction. This applied force causes further

deformation of asperity junctions and leads to '*junction growth*', increasing the true area of contact. How far this junction growth can go depends on and is limited by the ductility of the material and should be greater, say, for a ductile steel or a copper than for a titanium aluminide material. With a clean, uncontaminated surface, values of coefficient of friction can be at or in excess of unity, however, the adsorption of gases and other contaminants and the presence of lubricants act also to weaken these junctions and junction growth is limited. Much of the potential increase in coefficient in friction cannot therefore occur, restricting the values to the more commonly observed range of 0.1 to 1.0.

Another difficulty is that of 'stick-slip' [6], where during sliding (especially with a slow-moving system), surfaces will stick together until the force upon them is great enough for sliding to occur. On a localised level, this relates to the adherence of asperities and the required force needed to overcome the resulting junctions. Where motion is intermittent as with stick-slip, by inference, the problem may be further exacerbated by junction growth during the periods of non-motion, once again affecting the friction model.

Even accounting for these factors, there are other changes that can occur as a direct result of sliding, including chemical changes which can affect the sliding, lubrication and adhesion properties at the sliding interface. Oxidation is one such example.

## **2.3 Wear Theory**

### ***2.3.1 Archard and Hirst – Distinction between Mild and Severe Wear***

In 1956, Archard and Hirst [9, 13] categorised wear into two groups, mild wear and severe wear.

'Mild wear' occurs when the debris produced (generally oxide) prevents direct metal-to-metal contact. Although Quinn [14] does not specifically mention the oxidation reaction in his review of oxidational wear when discussing the definition of mild wear, the vast majority of studies into sliding wear to date have concentrated on the oxidation reaction. Debris produced is of very small size (less than 1  $\mu\text{m}$ ) and complete coverage is not necessarily achieved, with oxide in many cases only forming on load-bearing areas such as asperities. Electrical contact resistance is high, due to the presence of the oxide on the wear surface.

The absence of such layers allows contact between the metallic interfaces, with adhesion, plastic deformation and to varying degrees, material transfer between the surfaces. This is typical of the ‘severe wear’ situation, examples of which have already been observed in the lower temperature sliding wear of Incoloy MA956 against Incoloy 800HT in the work of Wood [1] and Rose [2] – the 270°C case shown in Figure 2.4 is one such example. Debris particles tend to be large, flat and angular, with sizes of up to 0.1 mm or greater. Contact resistance on surfaces that have undergone severe wear tends to be very low, due to the exposure of the metallic surface.

Temperature affects the nature of wear as it influences the kinetics of oxidation. Other factors such as relative humidity [15] and partial pressure of oxygen also affects the nature of wear as explained by Lancaster [17] and Stott *et al.* [18,19]. Figure 2.5 shows a reduced range of severe wear in an oxygen atmosphere at 300°C, compared to that with air.

The model that Archard and Hirst [9] proposed from their work assumes a true area of contact, occurring between a limited number of asperities on the contacting surfaces. The true area of contact can be calculated by equation {2.5}:

$$A = P/H$$

If  $W$  is the worn volume and  $L$  is the sliding distance producing the wear, then  $W/L$  is dependent on and is therefore proportional to the area of the friction junctions or true area of contact.

$$W/L \propto A \quad \text{or} \quad W/L = K_a A \quad \{2.16\}$$

This gives:

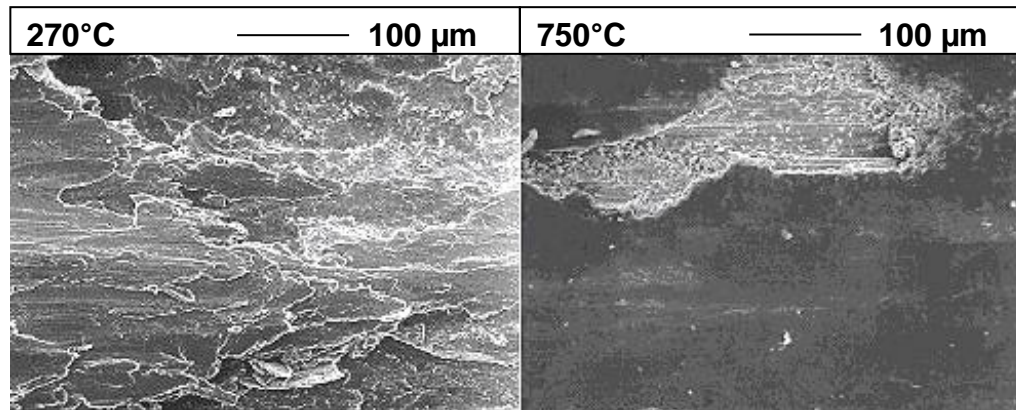
$$W/L = K_a P/H \quad \text{or} \quad W = K_a PL/H \quad \{2.17\}$$

the dimensionless parameter  $K_a$  being the constant of proportionality and also the probability of a wear particle being generated. It is also referred to as the “wear coefficient”. An alternative form ( $K_I = K_a/H$ ) is:



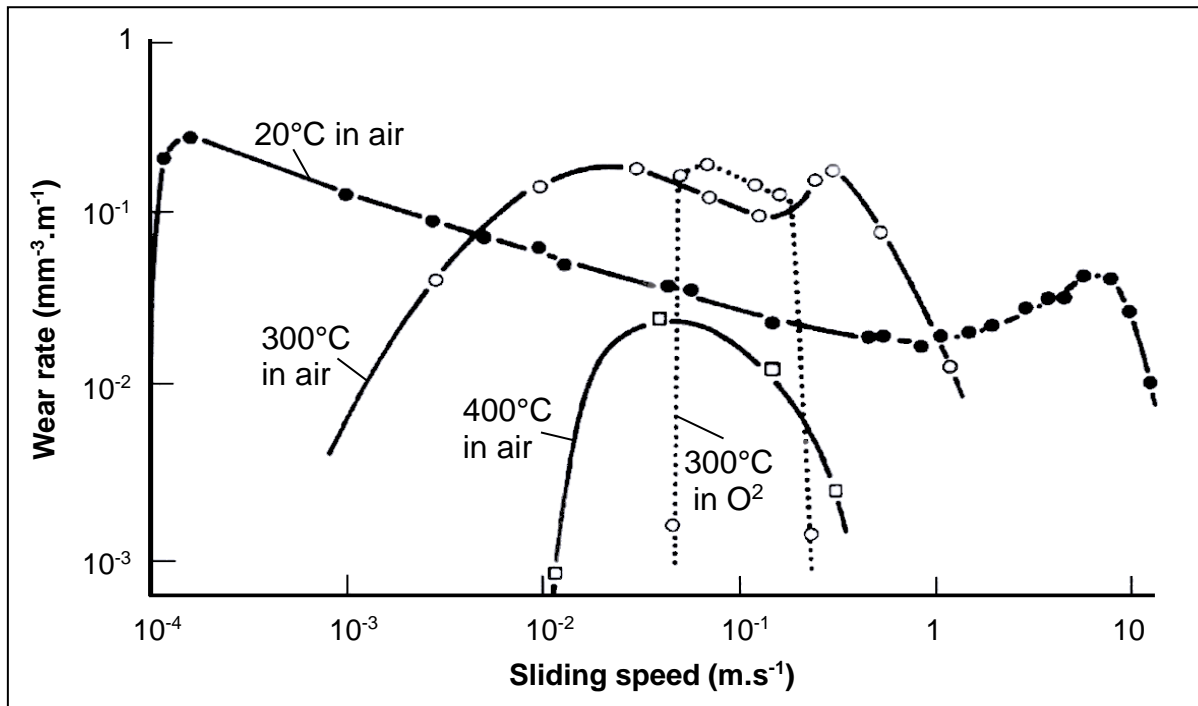
**Figure 2.4: Wear surfaces produced during the sliding of Incoloy MA956 against Incoloy 800HT at 270°C and 750°C [2]**

(load = 7N, sliding speed =  $0.654 \text{ m.s}^{-1}$ , sliding distance = 9,418 m)



At 270°C, a highly worn, heavily deformed surface is produced. There is direct metal-to-metal contact, allowing high levels of adhesion accompanied by plastic deformation, material transfer and the production of large flat angular debris. At 750°C, a compacted oxide layer has been created from the debris, giving physical protection via enhanced hardness and also separating the metallic surfaces, preventing contact and adhesion.

**Figure 2.5: Variation in wear rate with sliding speed at 20, 300 and 400°C in air and also 300°C in pure oxygen for  $\alpha/\beta$  brass sliding against steel [17]**



$$W = K_I PL \quad \{2.18\}$$

$K_I$  being referred to as the “ $K$  factor” [9]. Taking equation 2.5 and rearranging allows  $K_a$  to be expressed in terms of wear depth, sliding velocity and pressure. Dividing by the apparent area of contact gives:

$$d/L = p(K_a/H) \quad \{2.19\}$$

where  $d$  is the depth of wear (volume divided by area) and  $p$  is the mean pressure (load over area). If  $v$  is sliding speed and  $t$  is the time of sliding,  $L=vt$ . Thus:

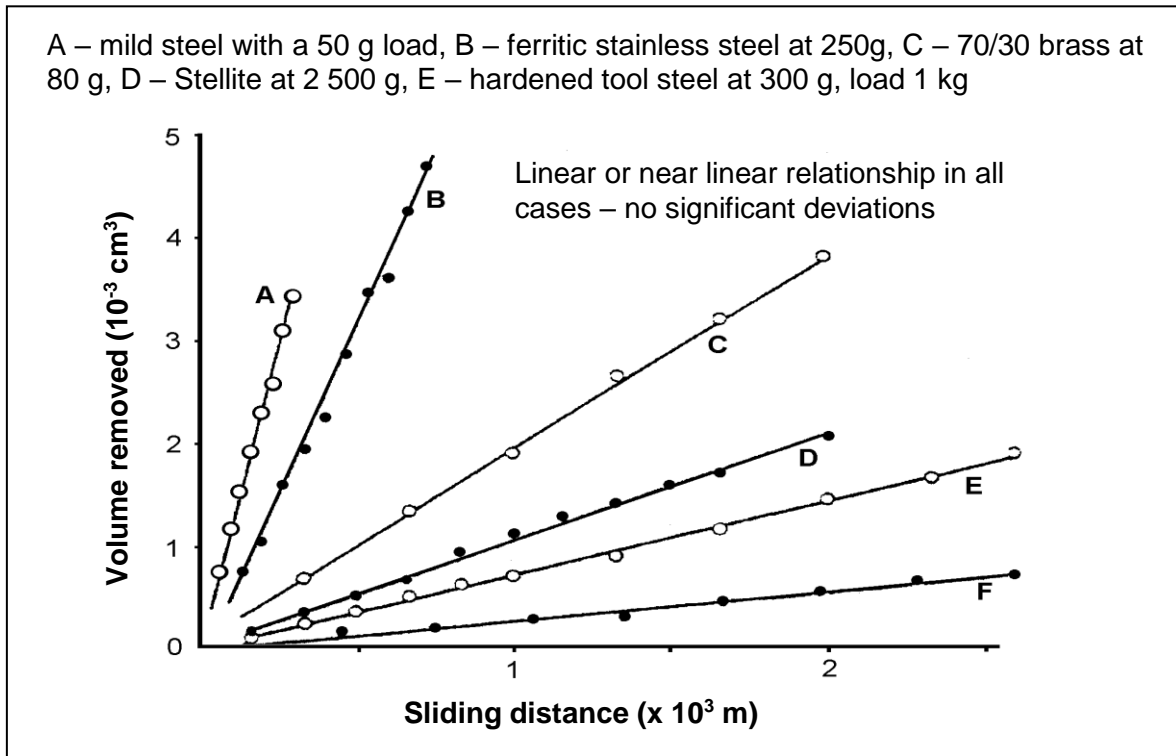
$$d/vt = p(K_a/H) \quad \text{or} \quad t = dH/K_a p v \quad \{2.20\}$$

$$K_a = dH/pvt \quad \{2.21\}$$

The above implies that the level of wear will be proportional to the sliding distance and applied load and work by Archard and Hirst showed this to be true over a limited range [9], as shown in Figures 2.6 and 2.7.

The Archard model [9] is effective assuming there are no changes in the wear surface as a result of the sliding process or otherwise. However, changes do occur in many cases, leading to changes in wear rate resulting from little or no variation in experimental or operational parameters [20-23] and thus changes in  $K_a$  value may be observed. Previous experimental work within AMRI [1,2] has demonstrated such changes can occur, with changes in friction coincident with a switch from early severe wear to mild oxidational wear observed in many cases, without any alteration of experimental parameters. This was usually denoted by reductions in coefficient of friction and in the variability of coefficient of friction. For example, during early severe wear at 750°C, values typically between 0.7 and 1 could be obtained for Nimonic 80A versus Incoloy 800HT. On switching to mild wear, values of between 0.4 and 0.5 were typically obtained.

**Figure 2.6: Experimental Data from Archard and Hirst's Work on Like-on-Like Sliding at  $1.8 \text{ m.s}^{-1}$  [9]**



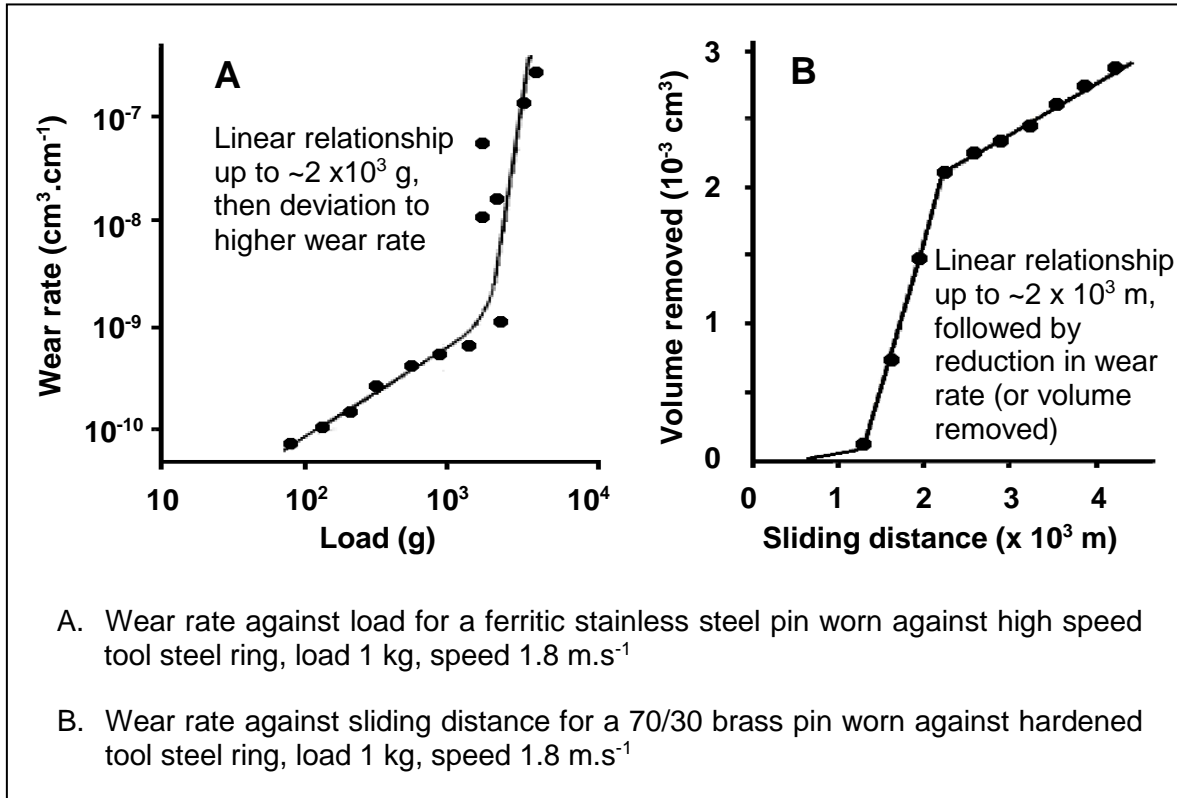
A direct link between hardness and wear rate is not always observed. Archard and Hirst themselves proposed the theory of mild and severe wear discussed in this section, to resolve these difficulties [9].

### 2.3.2 Classification by Mechanism

Many approaches to classifying wear have been attempted – Quinn's 1983 review [14] lists a number of these and tries to classify them under Archard and Hirst's mild and severe wear [9] headings (Table 2.1). For example, Burwell and Strang [24] propose seven different classifications of mild and severe wear, which Quinn argues are actually special cases of Archard and Hirst's mild and severe wear (with many of their classifications including elements of both) [9]. Ludema [25] talks in terms of "scuffing" ('roughening of surfaces by plastic flow, whether or not there is material loss or transfer') and "run-in", Quinn seeing "scuffing" as a form of adhesive wear and "run-in" as corrosive or mild wear (due to the generation of oxides on the wear surface). Finally, Tabor [26] does not distinguish between adhesive and corrosive wear, preferring to classify both as adhesive

wear, with Burwell and Strang's remaining mechanisms being referred to as "non-adhesive wear" (surface fatigue, abrasion and fretting) or a mixture of both (cavitation and erosion).

**Figure 2.7: Archard and Hirst's Experimental Data [9]**



The classification of wear mechanisms clearly remains a matter of debate amongst authors, although Quinn [14] proposes that each of the forms of wear described should be considered in terms of either mild or severe wear in any given situation. However, it is the view of the current author that it is not possible to talk simply in terms of mild and severe wear. For example, when material is lost by abrasion, the loss of material by the ploughing action of asperities on a wear surface does not necessarily require adhesion or corrosion to remove material. Also, loss of material by delamination wear is a fatigue-related process, caused by repeated loading and unloading of surface layers as asperities of the opposite surface pass over it, assisting the propagation of sub-surface cracks, eventually leading to material loss. Although adhesion or reaction with a corrosive environment may accelerate the process, again neither is necessary for fatigue and crack propagation to occur.

**Table 2.1: Quinn’s comparison of the various classifications of wear [14]**

Burwell and Strang [24]	Tabor	Ludema	Quinn [14 ]
<div>Adhesive wear</div> <div>Corrosive wear</div>	Adhesive wear	<div>Scuffing</div> <div>“Run-in”</div>	<div>Severe wear</div> <div>Mild wear</div>
<div>Surface fatigue (pitting)</div> <div>Abrasion</div> <div>Fretting</div>	Non-adhesive wear	Mechanisms of scuffing and “run-in”	Mechanisms of mild and severe wear
<div>Cavitation</div> <div>Erosion</div>	Mixtures of adhesive and non-adhesive wear	Not covered in Ludema’s review	

Another suggested classification system is that of Rabinowicz [27], who as well as adhesive and corrosive wear, identifies abrasive and fatigue wear as distinct categories of wear in their own right. Each of these four categories of wear shall now be discussed in turn.

### 2.3.2.1 Adhesive Wear

In the context of wear, adhesive wear occurs when contact is made between two surfaces moving or sliding past each other. Provided that the surfaces are clear of contaminants, oxides or other reaction products, the formation of a strong ionic or covalent bond can occur at these points of contacts, which most often are the raised asperities on the sliding surfaces. For sliding to continue, the applied force must be sufficient to lead to failure of the resulting junctions by shear. Where two dissimilar materials are in contact, the strength of the junction is usually the strength of the softer or weaker material, as the strength of the bond between the two is normally stronger than the cohesive strength of the softer material.

The ability of a material to deform can have a large influence on the level of adhesion, shown by the relationship between hardness and wear rate in Archard and Hirst's [9,13] wear model ( $W = K_a PL/H$  equation {2.17}), although where frictional heating affects the microstructure or heat treatments are used to enhance hardness, this rule does not apply. For example, Wood [1] examined the effects of processing on Nimonic 80A (as-cast and hot pressed at 1,200°C). In each case, the extra 'hot' processing imparted greater hardness on the alloy (Wood quotes hardness values of 308 Hv or 3.14 GPa for hot pressed Nimonic 80A compared to 223 Hv or 2.27 GPa for cast Nimonic 80A – a Vicker's micro indenter was used with a load of 500g), however, there was no clear evidence that the extra processing resulted in greater wear resistance and in many cases, the level of wear was actually worse than the standard alloy (Table 2.2).

The mutual solubility of the materials forming the wear pair also has an effect [9], the greater the solubility, the greater the level of adhesion. This was demonstrated by Subramanian [28-30] in sliding tests for aluminium 12.3 wt.% silicon alloys against various counterface materials. Of particular note [28] was a series of wear tests conducted between an aluminium-silicon alloy 'pin' sample and three 'ring' counterfaces (essentially a variation of 'pin-on-disk'), one of copper, one copper with 4.6% aluminium and the remainder copper with 7.5% aluminium. Wear rates were lower, the higher the percentage of aluminium in the counterface (Figure 2.8), which Subramanian concluded was due to decreasing solubility of the aluminium from the pin with higher percentage aluminium levels in the copper-based counterface – aluminium could less easily diffuse into the counterface material when in contact. With reduced solubility, adhesion was less and a lower amount of material was transferred to the counterface. Also noted was the increase in hardness that resulted from the additions of aluminium to copper for these experiments, also contributing to the reduction in wear.

### **2.3.2.2 Abrasive Wear**

Abrasive wear is the removal of surface material from an object by the action of a second agent or medium. This may be the surface of another object or by hard particles trapped between the two interacting surfaces – referred to as 'two body' and 'three body' abrasion respectively. The hard particles or surface must be 1.3 times harder than the softer

material undergoing abrasion, which Hutchings [8] and Ludema [31] note is the difference of one unit on Moh's scale of mineral hardness.

Hutchings [8] quotes three common models for abrasive wear via plastic deformation, these being *cutting*, *ploughing* and *wedge-forming*. These are illustrated in Figure 2.9. Adhesion can play a greater or lesser role in the model of abrasive wear observed.

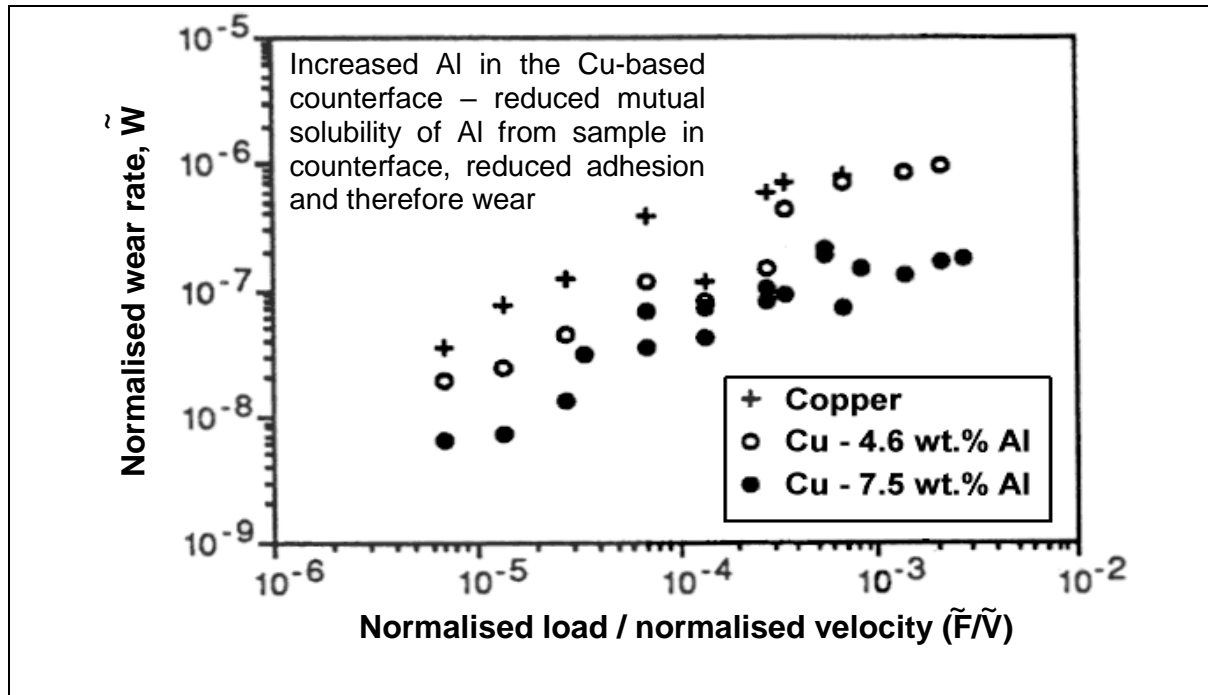
Abrasive wear can occur by either plastic deformation or brittle failure and in many cases occur together in the same wear system. However, the general approach is to consider them independently, one example being the consideration of the 'ploughing' model of abrasion discussed in the following [32].

**Table 2.2: Wear data for standard and alternatively processed superalloys [1]**

(Load = 7 N, Sliding Speed =  $0.654 \text{ m.s}^{-1}$ , Sliding Distance = 9,418 m)

Wood [1] tested the wear properties of Nimonic 80A in the 'as-cast' and 'hot pressed' forms, the latter being of greater hardness due to processing. The wear data shown here, collected by Wood, shows no evidence of enhanced hardness due to materials processing improving the wear properties of the Nimonic 80A. In three of the cases, the wear levels are actually greater for the processed material.		
	<b>Weight change (mg.cm<sup>-2</sup>)</b>	
<b>Counterface</b>	<b>Nimonic 80A (standard)</b>	<b>Nimonic 80A (hot pressed, 1,200°C, 30 kN)</b>
<b>Vickers hardness</b> (diamond indenter, 500 g load)	223	308
<b>Stellite 6</b> (Room Temp.)	-11.4	-20.5
<b>Stellite 6</b> (750°C)	-74.3	-113.6
<b>Incoloy 800HT</b> (Room Temp.)	+9.4	-3.2
<b>Incoloy 800HT</b> (750°C)	-1.3	+10.0

**Figure 2.8:** Variation of ‘normalised’ wear rates of Al-12.3 wt. % Si alloy slid against Cu, Cu-4.6% Al and Cu-7.5% Al [28]



### 1. Cutting

The movement of the asperity or third body over the softer material results in the creation of a deep groove upon the sample surface, with long strips of debris forming at the point of contact. This produces the deepest groove of all three models with the strongest adhesion.

### 2. Wedge-forming

Material is pushed up ahead of asperities on the counterface, resulting in a grooved wear scar with transverse cracks. Wear rates are lower than for the ‘cutting’ model, this mode tending to occur where adhesion between surface and counterface is strong.

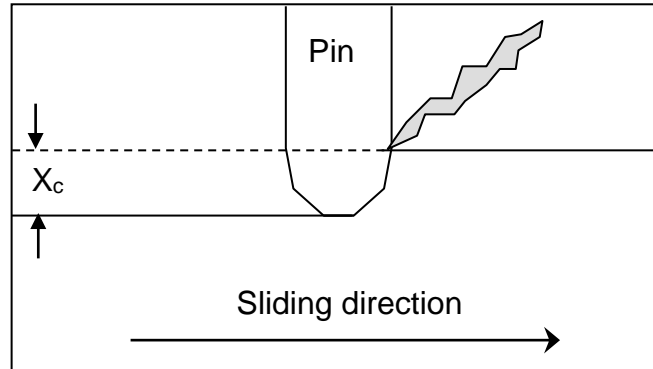
### 3. Ploughing

Adhesion between the harder and softer material is relatively weak and the grooves thus created are shallower, with lower penetration of the harder asperity or third body into the softer material. Formation of wear debris particles cannot be clearly seen at the point of contact.

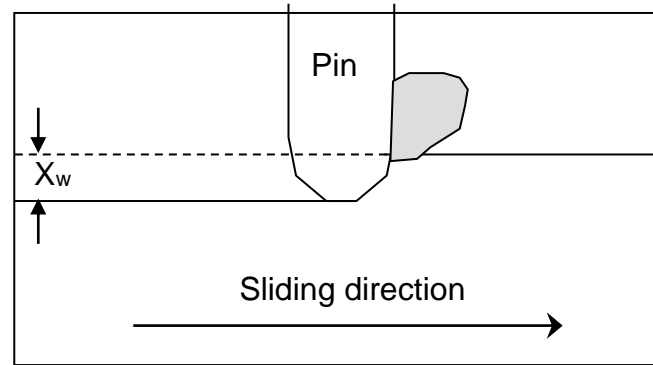


**Figure 2.9: The three models of abrasive wear [8]**

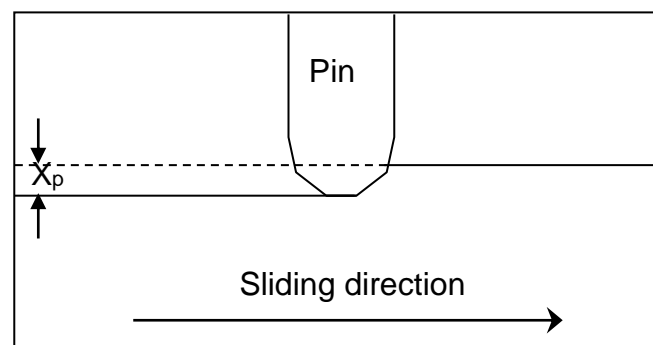
**(a) Cutting**



**(b) Wedge-forming**



**(c) Ploughing**



**Depth of penetration ( $X$ ):  $X_p < X_w < X_c$**

The idealised model [32] assumes a cone of semi-angle  $\alpha$  passing through the surface of a plastically deformable material (Figure 2.3). If the cone travels distance  $L$  through the surface of the material, then the volume of material removed is:

$$W = La^2 \cot \alpha \quad \{2.22\}$$

Assuming yielding of the softer material under normal load, each asperity will support a pressure of  $\pi a^2 Y/2$ ,  $Y$  being the yield strength (or pressure) of the softer material. Therefore the load  $P$  carried by  $N$  asperities is:

$$P = Y \cdot \frac{N\pi a^2}{2} \quad \{2.23\}$$

and combining the above with equation {2.22} gives a relationship between load and volume of lost material:

$$W = \frac{2 \cot \alpha \cdot PL}{\pi Y} \quad \{2.24\}$$

Equation {2.8} states that  $H=3Y$  (the hardness is three times the yield stress), thus:

$$W = \frac{6 \cot \alpha \cdot PL}{\pi H} \quad \{2.25\}$$

Substituting  $6 \cot \alpha / \pi$  with  $K_a$ , the Archard wear coefficient [9], gives equation {2.17} from the Archard and Hirst model:

$$W = K_a PL/H$$

In this case, the wear coefficient relates to the geometry of the wear particles or asperities by the angle of the idealised wearing element, rather than the probability of a wear particle being generated. Other than that, only the derivation route is different.

However, as has already been stated, in general plastic deformation and brittle failure in adhesion are often considered independently, despite it being the case that both may occur together. This model is one such example, with only plastic deformation being considered and brittle failure of material being ignored.

-----

Removal of material during abrasive wear of sliding surfaces occurs by either one or both of brittle fracture or plastic deformation – despite the fact that both occur together in many instances, work to date has normally only considered them as independent processes.

### ***2.3.2.3 Delamination (Fatigue) Wear***

The delamination or fatigue theory of wear was proposed by Suh [33], as an attempt to explain weaknesses in the Archard theory of adhesive wear [9]. Suh argued that:

- Archard's theory completely ignored the physics and physical metallurgy of metal deformation.
- Many of the assumptions employed in the mathematical model were arbitrary and unreasonable.
- The theory did not provide any insight to the wear of metals under different sliding conditions.

Suh's approach [33] was to base the observed wear mechanism on dislocation theory and plastic deformation and fracture of metals near a surface. Suh's reasoning behind the resulting delamination theory of wear was thus (illustrated in Figure 2.11):

1. During wear, the material at and very near the surface does not have a high dislocation density, due to the elimination of dislocations by the image force acting on those dislocations, which are parallel to the surface. Therefore, the material very near the surface work hardens less than that of the sub-surface layer.
2. With continued sliding, there will be pile-ups of dislocations a finite distance from the surface. In time, this will lead to the formation of voids. Void formation will be enhanced if the material contains a hard second phase for dislocations to pile

against. Voids form primarily by plastic flow of matrix around hard particles, when there are large secondary phase particles in the metal.

3. With time, the voids will coalesce, either by growth or shearing of the metal. The end result is a crack parallel to the wear surface.
4. When this crack reaches a critical length (material dependent), the material between the crack and the surface will shear, yielding a sheet-like particle.
5. The final observed shape of the particle will be dependent upon its length and internal strains.

Suh proposed the following mathematical model for the total volume of wear  $W$  produced by a hard surface sliding on a soft surface.

$$W = N_1 \frac{S}{S_{01}} A_1 h_1 + N_2 \frac{S}{S_{02}} A_2 h_2 \quad \{2.26\}$$

where:

- $1$  - material '1'
- $2$  - material '2'
- $N$  - number of wear sheets in material removed
- $S$  - total distance slid
- $S_o$  - critical sliding distance required to remove a complete layer of material
- $A$  - average area of delamination sheet
- $h$  - sheet thickness

For this model to work, the following assumptions need to be made:

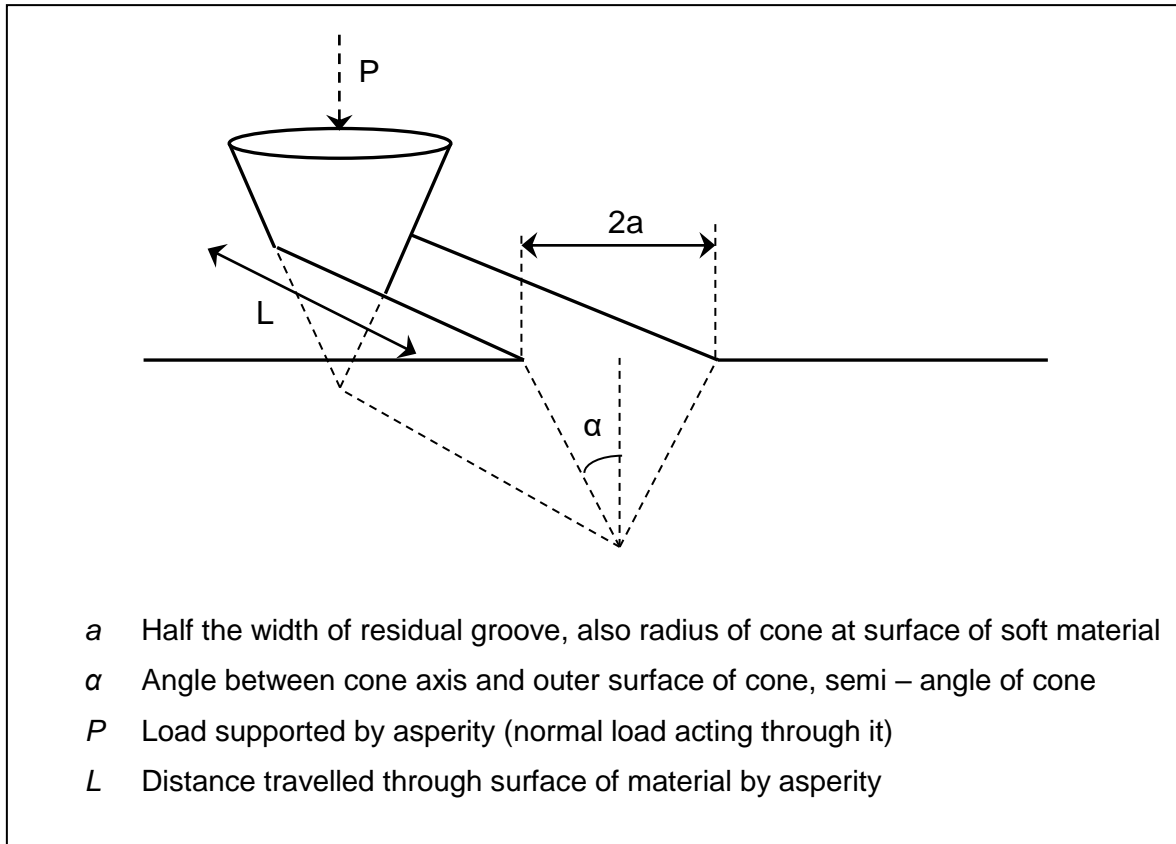
1. metals wear layer by layer, each layer comprising  $N$  wear sheets (or particles);
2. the number of wear sheets or particles per layer ( $N$ ) is proportional to the number of asperities in contact at any one time, between the contacting surfaces; and
3. the rate of void and crack nucleation can be expressed in terms of a critical distance parameter,  $S_o$ , defined as the interfacial sliding distance required for the complete removal of one layer of sheet.

The above model does succeed in providing a link between wear observations and microstructure; also, it takes into account wear of the harder surface, one thing Archard's model [9] does not – Archard's model always assumes wear debris being generated due to material loss only from the softer surface. However, Wood [1] correctly points out that parameters such as  $S_o$  are used in the model that are difficult to establish by empirical means.

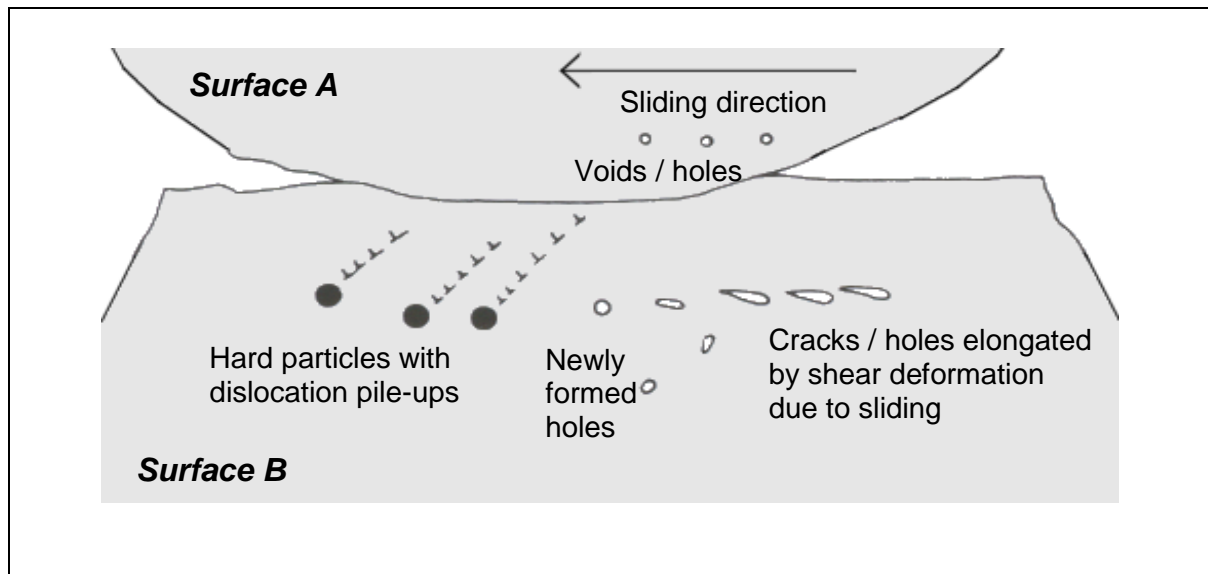
As three of the alloys in the current studies contain dispersions of a second phase (as detailed in Section 2.7), the levels of hard particles will be high. Wood [1] and Rose [2] in particular observed high levels of plate-like debris being generated under certain conditions, particularly at intermediate temperatures. The high level of these hard particles could thus explain the enhanced wear by delamination of these high strength superalloys. However, at high temperature, further complications occur due to oxidation. It could be argued that oxide will affect the degree of sub-surface stress.

Work continued on the delamination model [34-36], further refining the understanding of immediate sub-surface deformation and crack propagation. Rigney and Glasier [35] went on to suggest that the development of these plate-like debris could sometimes occur due to changes in microstructure of material in the highly deformed surface region. By repeated ploughing over the surface by asperities of the second material, the microstructure near the surface was converted to a 'cell-type' structure as a result of increased dislocation density (Figure 2.12), dependent on applied stress, temperature and stacking fault energy. Each cell is capable of accommodating large strains in the sliding direction and allows repeated deformation of the material surface. Crack propagation occurs along the cell boundaries, finally leading to the production of flake-like debris, similar in nature to that proposed in delamination wear. Rigney quotes a value of 0.3  $\mu\text{m}$  for these cells or 'sub-grains' [37] in the case of simple face-centred cubic metals, with increasing hardness as the substructure size decreases in most systems.

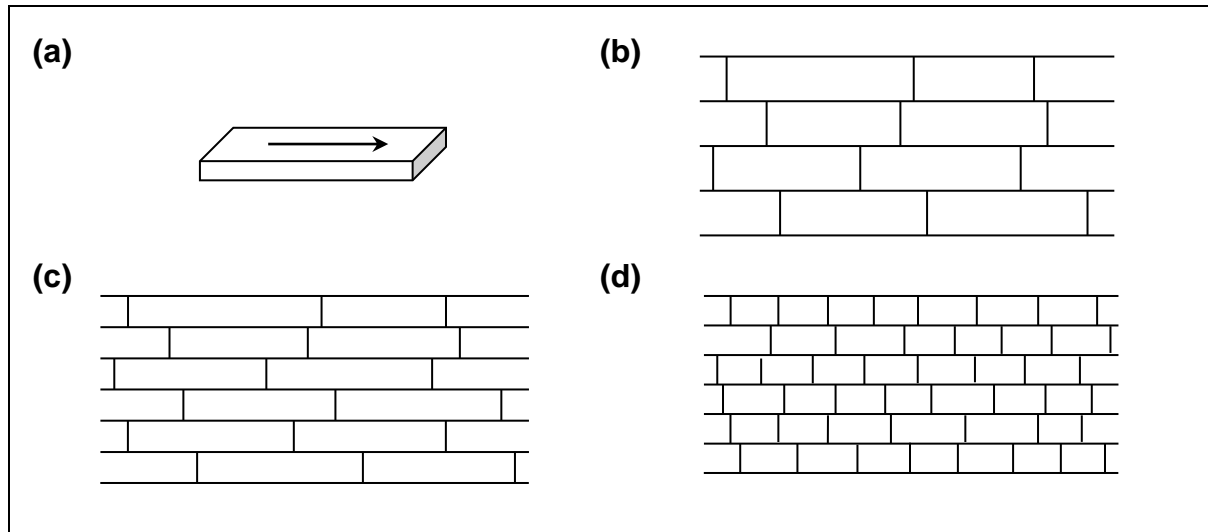
**Figure 2.10: Abrasive wear as a result of an idealised cone sliding across a flat surface**



**Figure 2.11: Wear particle formation by shear deformation of voids [33]**



**Figure 2.12: Idealised cell (a) showing relative dimensions, from plan (b), side (c) and end (c) structures of cells in the wear surface [35]**



#### 2.3.2.4 Corrosive Wear

Rabinowicz [27] defines corrosive wear as the removal of corrosion products by sliding, exposing a fresh surface on which new corrosion products may form. The corrosion products are formed due to reaction between the sliding surfaces and the environment, whether the environment is liquid or gaseous [14].

The corrosion products may act to separate the sliding surfaces (especially if removal is not complete) and thus prevent other mechanisms of wear, such as metallic adhesion, from operating – this more often than not leads to large-scale reductions in wear. This led Quinn to equate the corrosive wear categories of Burwell and Strang [24] with the mild wear category of Archard and Hirst [9,13], as discussed in Section 2.3 and the processes and reactions involved can be said to be analogous – a reactive agent interacts with the sliding interface to produce a corrosion product, which more often than not leads to reduced wear.

In most engineering applications, it is oxygen that is the main reactive agent in corrosive wear. Thus, the term ‘oxidational wear’ is a very often used term when talking about sliding wear, particularly dry sliding wear, where the lack of a lubricant allows ready environmental attack (although the lubricant itself may be the attacking agent or contain oxygen which can attack the wear surfaces) and high temperature sliding wear, where the

rate of oxidation is greatly accelerated. In both cases, the formation of oxide (the corrosive product) leading to mild wear may more readily occur. Oxidational wear is discussed in detail in Section 2.5.

## **2.4 ‘Two and Three Body’ Wear**

### **2.4.1 Overview**

Much of the discussion so far has been concerned with what happens when two surfaces move relative to one another, generating wear debris. The consideration of wear without the interaction of debris is referred to as ‘two body’ wear. However, the generation of debris particles introduces a ‘third body’ into the sliding process, which can then go on to have a significant effect on the wear process.

This debris may be retained within the interface area, where it may become an ‘active’ participant [38] in the wear process or may be ejected immediately after its formation, in which case, it is referred to as ‘passive’ debris. Active debris tends to be fine and may be a mixture of metallic and oxide particles. On the other hand, ‘passive’ debris particles are in general much larger and due to their immediate removal from the wear interface on formation, may retain much of their original form and structure. In metallic wear, ‘passive debris’ is more likely to be metallic.

The work of Rose [2] clearly illustrates this differentiation. If Rose’s work with Nimonic 80A and Incoloy MA956 versus Stellite 6 is taken into consideration, at lower temperatures (up to 390°C for Incoloy MA956 and 450°C for Nimonic 80A), debris tended to be of a fine nature and were usually oxide – the debris was largely retained at the interface, commuted and largely converted to a layer of oxide – the tendency at lower temperatures was for this layer to be in the form of loose, discrete oxide particles. The retention of this debris as a ‘third body’ then acted to keep the interfaces separate and wear values low. This is an example of ‘active’ debris.

At temperatures of between 510°C and 630°C for Nimonic 80A versus Stellite 6 and 450°C to 510°C for Incoloy MA956 versus Stellite 6, debris was ejected as larger metallic particles that did not remain at the wear interface and thus failed to separate the two wear surfaces. This is an example of ‘passive’ debris.



Higher temperatures saw the generation of larger amounts of fine oxide debris – in the case of Incoloy MA956 versus Stellite 6, this again acted to separate the interfaces and also formed a compacted oxide or glaze layer. Conversely, with Nimonic 80A versus Stellite 6, levels of wear increased due to the presence of the oxide debris acting as an abrasive agent against the Nimonic 80A. Both these are once again examples of ‘active’ debris.

As well as promoting mild wear, the negative effect of abrasion has also been noted – as with hard and soft surfaces in the two body wear models already discussed, for a third body to have an abrasive effect at the wear interface leading possibly to increased wear, it is normally expected that the third body will be 1.3 times the hardness or greater than of either of the contacting materials [14].

Active participation of third bodies has been noted by other researchers, notably Iwabuchi *et al.* [39-41], who studied the effects of the introduction of iron oxide ( $\text{Fe}_2\text{O}_3$ ) particles to the wear interface, noting that where the particles were supplied under fretting test conditions, the severe running in wear volume for a standard carbon steel (S45C), was reduced ten-fold [41]. Increased surface roughness also proved to be a positive factor in the presence of these introduced particles, in that the particles were more effectively retained. Introduction of a large enough quantity of  $\text{Fe}_2\text{O}_3$  particles managed to eliminate the severe wear running in stage.

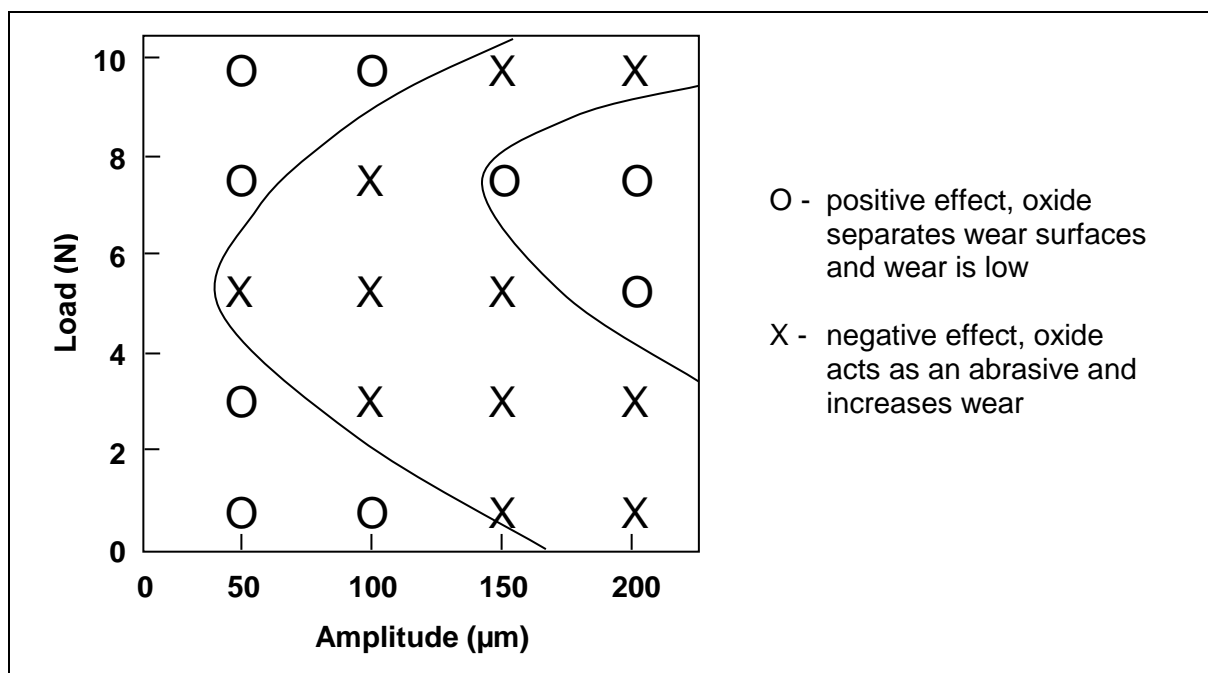
Iwabuchi also studied the effects of particle size [39] on wear and found that with a surface roughness of maximum asperity height  $20\mu\text{m}$ , a particle size of  $0.3\mu\text{m}$  was found to give the lowest wear rate in mild wear, the smallest particle size studied. However, particle sizes of  $1\mu\text{m}$  were observed to reduce the severe wear run-in stage the most. Ideally, the same size particle would result in both – for practical use to be made of such observations, clearly a compromise needs to be identified. It is also to be noted that Iwabuchi expressed uncertainty as to whether the  $0.3\mu\text{m}$  particle size is most effective only for the  $20\mu\text{m}$  maximum asperity height or for other asperity heights as well.

The current author suggests that this will be variable and also changing as the wear test proceeds, for the simple reason that as the larger asperities are removed, until such point as

an oxide layer forms, the particle size that can be contained in the recesses will also reduce. Conversely, during severe wear, damage to the wear surface so as to roughen it may allow for a larger particle size to be retained. A limiting factor on this is that there will probably be an upper limit of particle size, partially due to comminution and ejection of larger debris and also a limit to the size of particle that can convert from metal to oxide.

Iwabuchi also points out that the tendency to form a protective compacted layer of oxide is affected by other parameters – varying test parameters such as load and sliding speed showed that for certain conditions, the oxide particles acted as an abrasive and increased the wear rate. Figure 2.13 is a wear map of load versus amplitude, where different combinations of load and amplitude produce different outcomes as regards the influence of the introduced oxide particles [38]. For very low loads and amplitudes, the introduction of the oxide particles has a positive effect, lowering the level of wear. For medium loads and amplitudes, the oxides have a negative effect and wear levels are higher due to the abrasive action of the oxides. Yet increasing load for moderate amplitude or amplitude for moderately high load once again results in a positive influence from the introduced oxide and wear levels are once again low.

**Figure 2.13: Effectiveness of wear reduction on S45C plain carbon steel due to the introduction of  $\text{Fe}_2\text{O}_3$  particles [38]**



Leheup and Pendlebury [42] took a different approach, by the use of an interfacial air flow in a like-on-like ‘cup-on-flat surface’ sliding test at different temperatures for Fe-18% Cr, 9% Ni stainless steel. The effect of temperature was quite marked, with removal of the debris at room temperature leading to increased wear. At temperatures of 400°C and 500°C, formation of compacted oxide layers did still occur – this was considered to be due to the ready sintering and adherence of the loose oxide particles at these temperatures. The attractive effects of Van der Waals’ forces (acting to retain smaller particles between the wear surfaces) were also considered – this is detailed in Sections 2.4.3 and 2.4.4. Colombie *et al.* [43] obtained similar results with increased wear on blowing nitrogen through the wear interface at frequent intervals, the more frequent the intervals, the greater the observed wear. Magnetic fields can also have an effect with ferromagnetic materials – Hiratsukam *et al.* [44] showed that the field direction could influence whether debris was retained (thus reducing wear) or ejected (thus increasing wear).

Rigney [37] also questioned the validity of the traditional models of wear if they do not take into account third bodies resulting from transfer and mixing – as well as separating or screening ‘first bodies’ (sample and counterface), third bodies can have other effects as they are able to flow and transmit load, accommodate velocity gradients and are also created, destroyed and regenerated during sliding. Resulting behaviour can depend on dimensions, compositions (may be the same as either of the ‘first body’ materials or a mixture of both), properties (the materials may undergo stresses close to their mechanical limits) and hardness. Chemical composition is key to the observed properties of the third body.

Despite the evidence available, it is still the case that many models of wear do not take into account the action of the third body, with debris assumed to be ejected on formation. Much work has been done using experimental rigs in which debris is retained at the wear interface – this includes fretting wear and much of the pin-on-disk work [4, 5, 14, 18, 19, 39, 42, 47-49, 53, 54, 59-76, 86, 87, 89, 97, 99, 101, 102]. Even in situations where ejection is favoured, such as the block-on-cylinder approach used within AMRI [1,2], debris has remained at the interface and has played a significant part in the promotion of mild wear.

### ***2.4.2 Surface Films and Preoxidation – Third Body or Not?***

Also absent from the traditional models, is consideration of the effect of any surface films, adsorbed gases or other volatiles that may be present in most situations. Clearly, the wear process will be affected by the nature of the surfaces [45,46].

This is also true for pre-oxidised films [1,44,47,48], where early metal-to-metal contact has been reduced or eliminated to varying degrees, followed by earlier formation of compacted oxides in a number of cases. Although not a ‘third body’ in their own right (they are directly attached to one or both ‘first body’ surfaces at the beginning of sliding), the sliding action will create extra loose material from the surface oxidation layer, which will proceed to act as a third body where retention is preferred over ejection.

### ***2.4.3 Behaviour of Particles at the Interface***

The behaviour of third body material at the wear interface goes beyond just acting as an agent for separation of the sliding surfaces or removing material from them. Rigney’s observations [37] on load transmission, velocity gradients and debris particle creation, destruction and regeneration is one example of this.

In addition, the particles may undergo varying degrees of motion at the interface due to the movement of the sliding surfaces. Halliday and Hirst [49] noted accumulation and ‘rolling’ of debris particles during fretting corrosion tests on mild steel specimens, which they commented as being responsible for the reduction of friction during testing. They also noted that some sliding debris must also be present, as the observed coefficient of friction would have been in the region of 0.002 for rolling alone, rather than the values near or below 0.05 observed after the run-in phase was complete. Halliday and Hirst also established that the presence of the oxide particles prevented wear due to welding (adhesion) of the surfaces together.

Conversely, Suh and Sin [50] noted an increase in friction and wear by ploughing due to the presence of debris particles, this was confirmed by the removal of the debris, after which the coefficient of friction fell from a high ‘steady state’ value and gradually rose again as further debris was generated. It is to be commented here, that Suh and Sin used a unidirectional crossed rotating-cylinder-on-stationary-cylinder-configuration, whilst

Halliday and Hirst conducted tests with a oscillatory cylinder on two block fretting wear configuration. Thus, it would have been likely that debris retention in Halliday and Hirst's work would have been much greater, allowing for the observed generation of  $\text{Fe}_2\text{O}_3$  oxide particles.

Also, Suh and Sin's work [50] largely describes a metal-metal interaction, with most testing carried out in a purified argon atmosphere. Even where an inert atmosphere is not used (as with AISI 1020 steel), there is nothing to suggest the generation of oxide debris and thus all interactions can be assumed to be metal-metal in their case. Thus a direct comparison between their work and that of Halliday and Hirst may not be wholly appropriate. However, Rose [2] reports high levels of wear for Nimonic 80A versus Stellite 6 at elevated temperature, where only oxide debris was generated during all but the earliest part of the sliding process. Here, it is the oxide debris acting as a third body and aiding material removal.

The work of Rice *et al.* [51] shows that the effects of debris parameters on coefficient of friction are more important than asperity parameters. On modelling the influence of variation of density and size parameters for particles at the interface and asperities on coefficient of friction, the sensitivity of coefficient of friction to changes in particle density and size was much greater.

If the particle parameters alone are considered, it was observed that increases in density lead to a much faster increase in coefficient in friction to a high steady state value. Increased particle size also lead to increases in coefficient of friction values, or conversely, smaller particle sizes were preferred for a lower friction regime. Of most interest in the work of Rice *et al.* [51], was the observation that if particle density was increased whilst particle size was decreased (which could be regarded as analogous to particle break-down early in the wear process), then there was a sharp increase in friction, followed by a steady decrease with time.

It is to be noted that as with Suh and Sin [50], Rice *et al.* [51] did not consider the movement of debris, as in Rice's words, the debris is 'entrapped'. However, the approach of Rice *et al.* [51] does allow for estimation of friction where particle size means that

movement is not a primary consideration – Hesmat [52] proposes a lower size limit of 20  $\mu\text{m}$  for debris to be a contributor to abrasive wear, above which the work of Shu and Sin [50] and Rice *et al.* [51] is therefore more applicable.

Debris movement for smaller particle sizes is clearly a key consideration, as the fall in friction due to for instance, rolling, invalidates any models that fail to consider it. Jiang, Stott and Stack [53] proposed the following series of mechanisms for wear debris movement under sliding conditions, each mechanism accounting for a different mode of perceived particle movement (Figure 2.14).

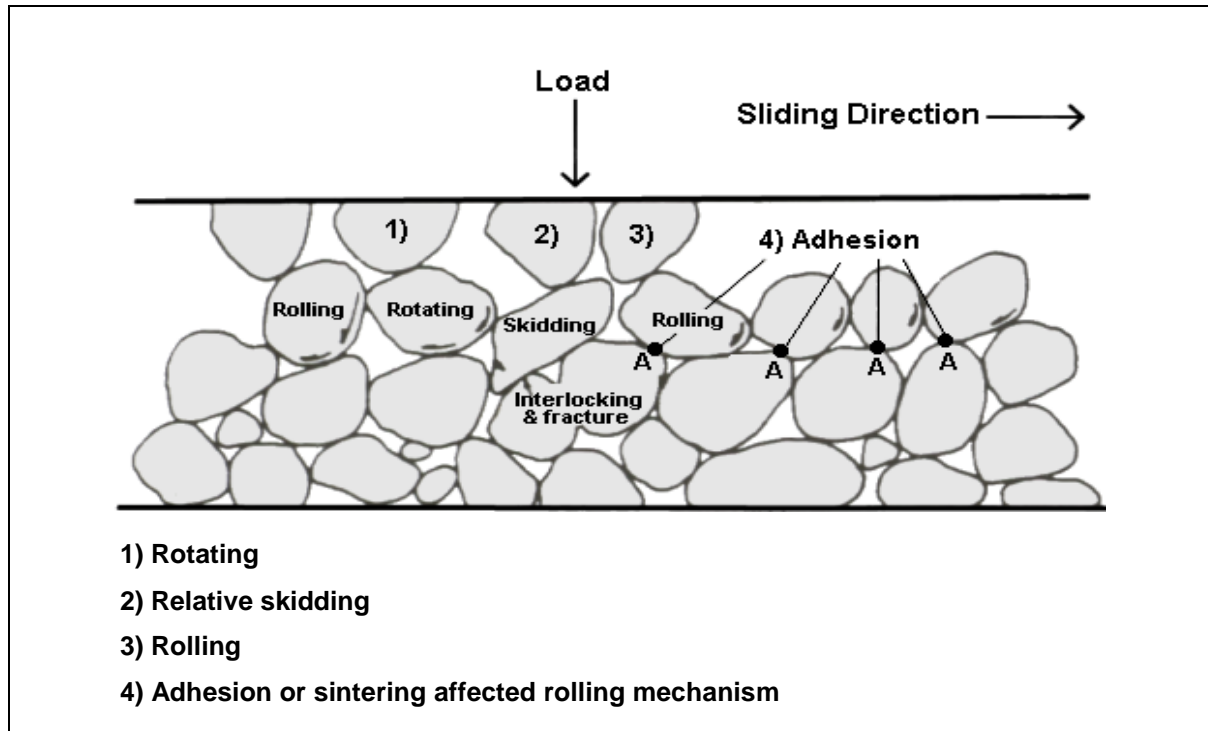
1. **Rotating:** a particle is entrapped in front of another fixed or immovable particle or object. It cannot move from its current position when impacted by an asperity from the opposite surface and is only able to rotate around its own centre.
2. **Relative skidding:** a fixed or locked grain in one half of the sliding pair slides or ‘skids’ against a fixed grain attached to the opposite surface.
3. **Rolling:** the particles are able to freely move or roll along with the opposite sliding surface (and are not entrapped by it as with the ‘rotation’ mechanism).
4. **Adhesion or sintering affected rolling mechanism:** adhesion developing between adjacent particles hinders rolling of particles, affecting (increasing) friction compared to the ‘free’ rolling mechanism.

The mechanisms of movement can change and any particle may be subject to a different mechanism at different times. It is also possible that a particle will become ‘interlocked’ or as Stott later states ‘entrapped’ [54] and unable to move and thus be liable to fracture, due to a build-up of stress upon it. Later appraisal of these mechanisms by Stott [54] does not specifically mention the fourth mechanism, with adhesion and sintering general factors affecting the resulting particle layer as a whole.

It is also possible that for a given range of particle sizes, powder ‘flow’ may be observed. Hesmat [52] observes that particles of an intermediate size, between 5  $\mu\text{m}$  and 20  $\mu\text{m}$  may undergo ‘*quasi-hydrodynamic flow*’ under sliding conditions. Larger particles will behave as in-situ elastic bodies and contribute to abrasive wear, whilst smaller particles will compact and behave as a nearly solid body, moving along with the ‘first body’ interface

and protecting it. At these smaller sizes, Van der Waals' forces and other attractive forces will become important factors and inhibit the flow process.

**Figure 2.14: Mechanisms of possible movement of particles during sliding of particulate materials [53]**



However, it is to be pointed out that the debris produced using the block-on-cylinder configuration [1,2], in the  $5\text{ }\mu\text{m}$  to  $20\text{ }\mu\text{m}$  size range specified by Hesmat for flow, were noted to be highly irregular in shape, reported as being 'flat and angular' as the result of delamination wear. Secondly, they were metallic, meaning that adhesion between metallic surfaces would also be a major influence – Hesmat's work was with oxide particles. The combination of these influences would thus inhibit any flow process and eliminate the '*quasi-hydrodynamic flow*' region – high levels of metallic wear were observed [1,2] during the 'severe wear' phases, with associated high levels of adhesion due to transfer and back-transfer of material between metallic interfaces. Where oxidative wear did occur, particles were  $5\text{ }\mu\text{m}$  in size or less, where as Hesmat points out, Van der Waals' and other attractive forces and compaction come into play. This means that '*quasi-hydrodynamic flow*' cannot play a significant part in the sliding wear process, as observed between the selected test alloys in the current configuration, favouring ejection of material from the

wear interface. Hesmat's lower limit of 20  $\mu\text{m}$  for abrasive wear could therefore be revised downwards to the 5  $\mu\text{m}$  upper limit for forces of attraction and compaction.

#### 2.4.4 *The Effect of Forces of Attraction between Third Bodies*

As already noted [52], attractive forces such as Van der Waals' forces become a factor when considering very small particle sizes (for oxides, 5  $\mu\text{m}$  or less). Electrostatic forces between particles, and between particles and tribosurfaces, also exist, but these are only about 1% of Van der Waals' forces for non-conductive solids [31].

If ' $F$ ' is the force of attraction and assuming the particle is spherical, this can be directly related to particle size by:

$$F = \frac{AR}{6r^2} \quad \{2.27\}$$

where:

- $A$  - Hamaker constant;
- $R$  - radius of the particle or sphere;
- $r$  - equilibrium separation.

The Hamaker constant [52] is dependent on the surface energy of the sphere:

$$A = 9\pi^2\gamma \quad \{2.28\}$$

Where:

- $\underline{r}$  - distance affecting mutual action of Van der Waals' forces  
(which can be estimated at 0.3  $\mu\text{m}$  to 0.5  $\mu\text{m}$ );
- $\gamma$  - surface energy.

Van der Waals' forces are extremely short range in nature, produced by dipole induction between neighbouring bodies. This accounts for the attraction observed between the smaller sized wear particles (less than 5 $\mu\text{m}$  [52]) and the wear surfaces [55].



Surface energy is temperature-dependent, thus making the Hamaker ‘constant’ and the force of attachment  $F$  temperature-dependent. An Arrhenius relationship exists between surface energy and temperature:

$$\gamma = \gamma_o \cdot \exp\left(-\frac{E}{RT}\right) \quad \{2.29\}$$

Where:

- $R$  - gas constant;
- $E$  - activation energy for ‘bonding’;
- $T$  - absolute temperature.

The amount of work done in relationship to wear is fairly minimal, compared to the formation of compacted oxides and ‘glazes’ to be discussed in Section 2.5., with the work of Hesmat [52] being one of the more comprehensive studies of the potential behaviour of debris and particles at the wear interface in relation to particle size. It is suggested, here, that the role of Van der Waals’ forces in the accumulation and grouping together of particles is perhaps more important, especially at more elevated temperatures. For sintering and fusion of finer oxide particles to form glazes, an attractive force must be present to hold the particles in position long enough to allow significant sintering reactions to occur.

The importance of sintering in the formation of debris layers in itself cannot be ignored. Zhou *et al.* [56] showed that for iron, nickel and iron-25% nickel powders, significant sintering can occur on raising the temperature above room temperature (denoted by the significant shrinkage of specially prepared compacts), where the particle size is defined as ‘ultra-fine’, in this case, 30 to 40 nm. In comparison, more traditional fine particle sizes of around 5  $\mu\text{m}$  did not show a significant response (in terms of shrinkage) until above 500°C. This does not mean to say sintering did not occur with the larger particles – it is more a case of a more noticeable response was obtained from the smaller particle sizes due to their greater relative surface area and therefore, contact area. With particle sizes detected of 300 to 400 nm, a ready sintering response may be detectable in a wear situation.

Another comment worth noting is the shrinkage of the compacts, as occurs in all powder compacts on sintering. As sintering and thus shrinkage will undoubtedly occur in accumulations of wear debris at not necessarily that greatly elevated temperatures, this will no doubt have an influence on the formation of compacted oxide layers during the wear process. To date, no attempt has been made to address this issue or its importance on the sliding wear process.

## **2.5 Mild Wear and Mechanisms of Compact Oxide Formation**

### ***2.5.1 Introduction to Compacted Oxides or ‘Glazes’***

As stated in Section 2.3.1, Archard and Hirst [9,13] were amongst the earliest researchers to categorise wear into mild and severe wear. They defined mild wear as that occurring where the surface is extremely smooth and consisting partially or wholly of the reaction product, between the material under sliding and the surrounding atmosphere or fluid. An oxidation reaction is required for the creation of the corrosion product, although as already stated, the corrosion product itself need not necessarily be an oxide.

The term ‘glaze’ is a misleading one, as it implies a glassy amorphous material, which was thought to be the case until Lin, Stott and Wood [4] proved them to be crystalline by means of electron diffraction – the term ‘compacted oxide layer’ is a more accurate description. ‘Glaze’ and ‘compacted oxide’ tend to be used fairly interchangeably throughout literature, despite the crystalline nature of these oxide wear surfaces being established – the term ‘glaze’ has remained in common use. More recently Datta *et al.* [118, 120] have demonstrated the compacted oxide layers formed in some systems and under certain conditions are of nano-crystalline structure and are highly disordered – this is discussed further in Section 6.3.

Compacted oxide layers tend to form under conditions of moderately high temperature, low loading and usually low sliding speed. For a compacted oxide layer to form and a resultant reduction in wear to occur, many researchers specify that a minimum temperature must be exceeded, dependent upon conditions and alloy composition. With increasing temperature, the formation of these compacted oxides becomes more rapid, with a consequent reduction of a ‘severe wear’ running in period, the debris from which can be a major source of material needed for the formation of the compacted oxide layers.

Compacted oxide formation is not just restricted to low sliding speed, as the effect of frictional heating due to high sliding speed can raise the temperature above the critical temperature required for the formation of the compacted oxide layers.

Many researchers have extensively studied the reduction of wear by the formation of compacted oxides at high temperatures. As well as Archard and Hirst [9,13], others such as Lancaster [17], Bhansali [57], Razavizadeh and Eyre [58], Stott *et al.* [4, 5, 18, 19, 53, 59-72], Quinn [14, 73-76] and Garcia [77] amongst others, have contributed to the knowledge base on compacted oxide formation. The work conducted within AMRI in recent years [1-3] has additionally concentrated on the sliding of dissimilar interfaces and effects of this on the mode of wear. The key issues on oxide formation are discussed below.

Wear that is dependent on the tendency to oxidation is highly dependent on temperature. The tendency to oxidation with respect to temperature can be described by the following Arrhenius type equation:

$$K_p = A_p e^{Q_p / RT_o} \quad \{2.30\}$$

where  $K_p$  is oxidation rate,  $A_p$  is the Arrhenius constant,  $Q_p$  is the activation energy (for oxidation),  $R$  is the gas constant and  $T_o$  is the absolute temperature in Kelvin.

### **2.5.2 Mechanisms for Generation of Oxide Debris and Compacted Oxide Layer Formation**

Studying a range of alloys of varying composition in like-on-like sliding, mainly nickel or nickel-iron-based with significant quantities of chromium and in some cases, cobalt, it was established by Stott *et al.* [4] that the oxides retained composition varying little from the original base alloys. It was thus concluded that the observed low wear and friction arise from the physical properties and condition of the glaze, rather than their chemical composition.

Stott, Lin and Wood [4, 5, 59-63], on carrying out a series of fretting wear tests on a number of nickel-chromium alloys (two of which had a high percentage of cobalt),

identified these conditions, influenced by the materials properties and sliding temperature, marking the formation or non-formation of the compacted oxide layers.

1. In the first condition, transient oxides form and build-up on the alloy surface [78]. Continued oxidation of the substrate surface, caused by diffusion of oxygen to the substrate-oxide interface and through physical defects, maintain or thicken the oxide layer formed.
2. In the second condition, the early stages of wear are masked by the formation of an insufficiently thick glaze layer due to unfavourable temperatures and low alloy strength. This may involve an extended 'pre-glaze' or severe wear run-in period, when larger debris particles are generated which undergo continued break-down and consolidation until a sufficiently thick sintered surface layer is formed to prevent any further mechanical damage to the underlying alloy. Further oxide generation then proceeds as for the first mechanism.
3. In the third condition, the glaze does not remain stable during sliding and areas of compacted oxide continually break down and reform.

Stott *et al.* [5, 54, 64-66] later produced a further set of three modified mechanisms, based on their studies of the elevated temperature (200-600°C) fretting wear of iron-based alloys. These mechanisms were seen as limiting cases for oxide debris generation, after which the build-up of oxide to form compacted layers continued:

1. **Oxidation – scrape – reoxidation** This involves a two-stage process. In the first step, oxide generation takes place in the areas of contact between the two sliding surfaces, with general oxidation over the apparent sliding area of contact and also, at asperity contacts where temperatures exceed the general temperature in the region of the sliding area of contact. In the second stage, this oxide is removed by subsequent traversals of the sliding interfaces, exposing fresh metal for further oxidation. The debris formed may then be either completely removed from the interface, act as a third body abrasive, contributing to the wear process or compacted to form a wear-protective oxide layer.

2. **Total oxidation** Under certain conditions, particularly high ambient temperatures, oxide generated during sliding or even present prior to the commencement to sliding, is not completely removed by subsequent traversals of the sliding interfaces, allowing oxide thickening with time. Provided this layer is coherent and adherent to the metal substrate and can withstand the stresses of sliding, a plastically deformed wear-protective oxide layer can develop.
3. **Metal debris** Debris particles generated during the early stages of wear are broken up by the sliding action, with any fresh areas of exposed metal being subject to further oxidation. There may be a high level of oxidation of the debris surfaces, due to the relatively large exposed surface area of metal. For example, a limiting oxide thickness of 2 nm on such particles is achieved in under 0.1 seconds at 20°C for iron or steel, meaning that for iron particles of 0.1  $\mu\text{m}$  diameter, 6% of the debris is oxidised in a fraction of a second at this temperature [54].

Enhanced oxidation is promoted by heat of deformation and increased energy of particles due to increased defect density and surface energy (remembering that the exposed surface area of debris material will increase as particle size decreases). There is also an input due to the heat of oxidation and it is therefore possible that very fine metallic particles may undergo complete, spontaneous oxidation under certain circumstances. The resulting oxide can later develop into a wear-protective layer.

This could help to explain the appearance of oxide during low temperature wear [53], also noted by researchers in AMRI [1,2].

The third mechanism proposed in Stott's original work is similar to that of Lin and Wood [4], both depending on the generation of larger debris from the wear substrate and the comminution of this debris to fine oxide particles as the wear process continues to develop.

The one major difficulty with these mechanisms is that they were developed from work on low speed reciprocating sliding wear, where frictional heating is not such an important

factor [66]. At sliding speeds of greater than  $1 \text{ m.s}^{-1}$  [81], frictional heating increasingly becomes an issue. This is discussed in Section 2.6.

### 2.5.3 Effects of Environmental Variables

#### 2.5.3.1 Oxygen Levels and Partial Pressure

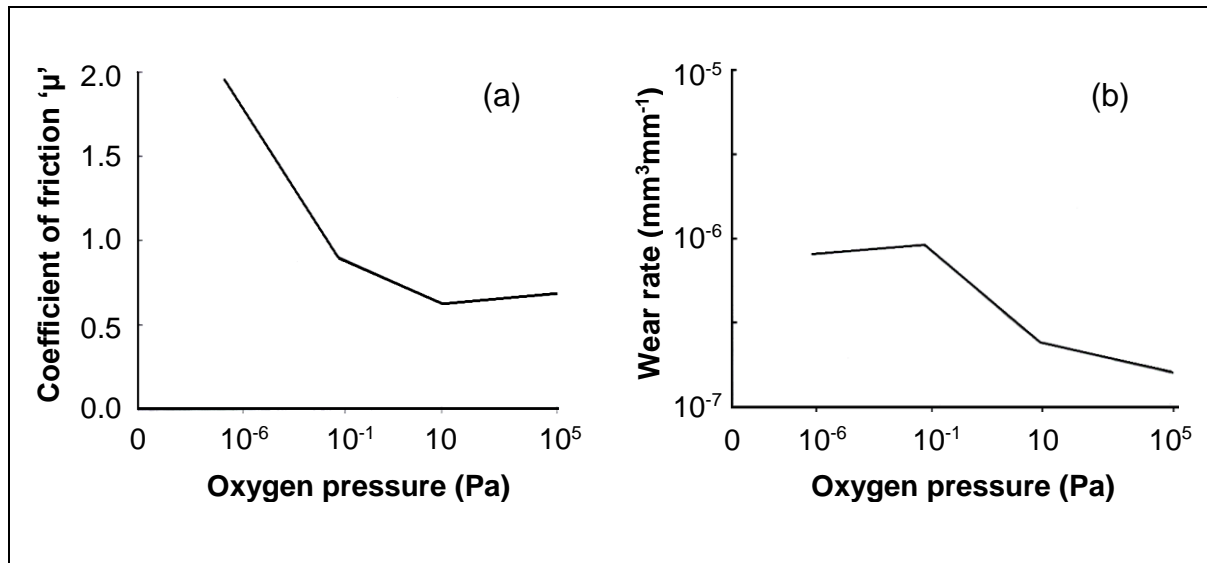
Even in environments with low oxygen partial pressure [18,67] (effectively removing much of the oxygen from the system), stable oxide layers are still able to form. Under vacuum, increasing pressure from high vacuum conditions to  $10^{-2} \text{ Pa}$  was enough to result in a reduction in friction in the sliding wear of an iron-chromium alloy. Buckley [80] noted during the like-on-like sliding of clean iron that a pressure of 400 Pa (or 3 Torr) was sufficient to prevent seizure. Lancaster [17] noted that at  $300^\circ\text{C}$ , that the range of sliding speeds over which severe wear was observed when a 60/40 brass slid against tool steel was greatly reduced in an oxygen atmosphere compared to the level of wear observed in air (Figure 2.5).

Barnes *et al.* [67-69] undertook an investigation into the effects of partial pressure, initially from  $10^{-6}$  to  $10^{-4} \text{ Pa}$ , on a range of iron-chromium alloys ranging from pure iron, to iron 40% chromium (Figure 2.15). Initial work indicated high friction levels and seizure at  $450^\circ\text{C}$  for iron and between  $500\text{-}600^\circ\text{C}$  (rising slightly with chromium content) for the various iron-chromium alloys, the only exception being Fe-40%Cr, with which there was no seizure up to the maximum test temperature of  $850^\circ\text{C}$ . This may be associated with Fe-40%Cr being dual phase [68, 97], consisting of the solid solution ' $\alpha$ ' phase and the FeCr intermetallic ' $\sigma$ ' phase – the probable presence of this more brittle, less ductile phase may be to reduce plastic flow and adhesion during sliding in high vacuum conditions.

Adhesive wear and seizure (here defined as the coefficient of friction rising above a nominal value of 3.5) was dominant at partial pressures of oxygen of  $10^{-6}$  and  $10^{-5} \text{ Pa}$ , despite there apparently being sufficient oxygen present to prevent this. On raising the partial pressure of oxygen  $10^{-4} \text{ Pa}$ , significant amounts of oxide were observed and areas of compacted debris had developed. These 'islands' were specified as the reason for a switch between severe and mild wear, with more rapid development of these oxides being observed on raising the partial pressure of oxygen to  $10^{-1} \text{ Pa}$ . Examination of the compacted debris showed it to be either completely oxidised or oxide covered metallic

debris. This was accompanied by significant decreases in friction (Figure 2.15), though despite the presence of oxide debris, the wear rate remained high until the oxygen partial pressure reached 1 Pa with a value of  $10^{-6} \text{ mm}^3.\text{mm}^{-1}$  at this partial pressure, dropping to circa  $1.8 \times 10^{-7} \text{ mm}^3.\text{mm}^{-1}$  at 10 Pa.

**Figure 2.15: Variation of coefficient of friction (a) and wear rate (b) of Fe-4.9%Cr with oxygen partial pressure during like-on-like sliding at 20°C [67]**



Changes in partial pressure were also made during sliding tests [67], with oxygen in some cases being removed from the wear system (the pressure was reduced from  $10^{-1}$  Pa to  $10^{-6}$  Pa). When this occurred, the oxide debris and the compacted oxide layers remained at the wear interface once they were formed, showing continued stability and wear resistance, even without a continued supply of oxygen.

Comment is also made that the shape of the stylus Barnes *et al.* [67] used may have influenced the results. The use of a hemispherical stylus during sliding tests trapped more wear debris than the use of a conical stylus, thus promoting a greater level of formation of islands of compacted oxide debris. Also, the more ready destruction of these islands can be put down to the higher contact pressures that would occur with a conical stylus, because of the smaller area of contact.

The work of Barnes *et al.* [66-68] clearly demonstrated that compacted oxide or ‘glaze’ layers were formed from oxide debris which later rebonded to the surface, discounting earlier theories of wear in which the glaze formed directly from oxides forming on metallic surfaces [4, 5, 59-63].

#### ***2.5.3.2 Effect of Water Vapour and Relative Humidity***

The presence of water vapour in the atmosphere can have a positive or negative effect on oxide development, depending on relative humidity levels and materials being tested. With mild steel, it has been observed that there is a reduction in wear levels with increasing relative humidity under fretting conditions [81,82] and similarly with carbon steel under sliding wear conditions [15]. It was further suggested [83], that adsorbed moisture might have a dual effect, in that the moisture on the surface of debris particles might possibly act as a lubricant, promoting speedier debris dispersal and thus less abrasive wear (though how this dispersal occurs is not specified by the authors). From this, it was proposed that the hydrated form of the iron oxide developing in the presence of the moisture might in itself be a less abrasive medium. This hypothesis seems to assume that the presence of oxide will by default increase wear due to abrasion and fails to mention the reduction in wear due to the separation of the metallic interfaces. Thus, it is conceivable that if the moisture assists in the dispersion of the debris, there are circumstances in which the wear rate would increase due to the presence of water vapour – the removal of debris may allow direct contact between wear surfaces, allowing material removal by adhesive, abrasive and delamination mechanisms.

Further experimental work by Bill [84] in fact showed that this could be the case, with the relationship between relative humidity and wear rates becoming quite complex. 99.9% Fe was observed to show a significant increase in wear rate due to a rise in relative humidity from 0 to 10%, followed by a rapid decrease and minimum values in the region of 50 to 70%, followed by a small rise towards atmospheric saturation. In the same study, titanium showed increasing wear up to 30% relative humidity, followed by an erratic decline in wear values up to saturation levels. Nickel showed a sharp decrease in wear levels between 0 and 10% relative humidity, followed by increasing wear with relative humidity up to saturation. One note of caution is that these datum are fretting wear datum and the



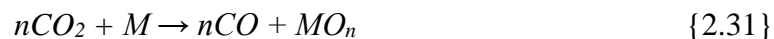
behaviour with higher speed unidirectional sliding wear may be different – decreased debris retention is very likely to have a significant effect.

Experiments by Oh *et al.* [15] with sliding wear suggested a transition from severe to mild wear with increasing relative humidity with a number of carbon steels (Figure 2.16). At low relative humidity, severe wear was encountered with high wear rates, with total losses amounting to between 0.130g and 0.190g. This remained the case until circa 50% relative humidity was reached. The level of wear dropped rapidly after this ‘transition point’, with very low levels of wear and a mild wear regime existing at relative humidity levels of 70% and losses totalling no more than 0.0006g to 0.002g. Levels of carbon in the steel were observed to affect this transition, this being observed at higher values with increasing carbon content. Friction levels were also observed to fall rapidly, from between 0.62 and 0.68 at 35% relative humidity to between 0.44 and 0.48 at 70% relative humidity.

### 2.5.3.3 Other Atmospheres

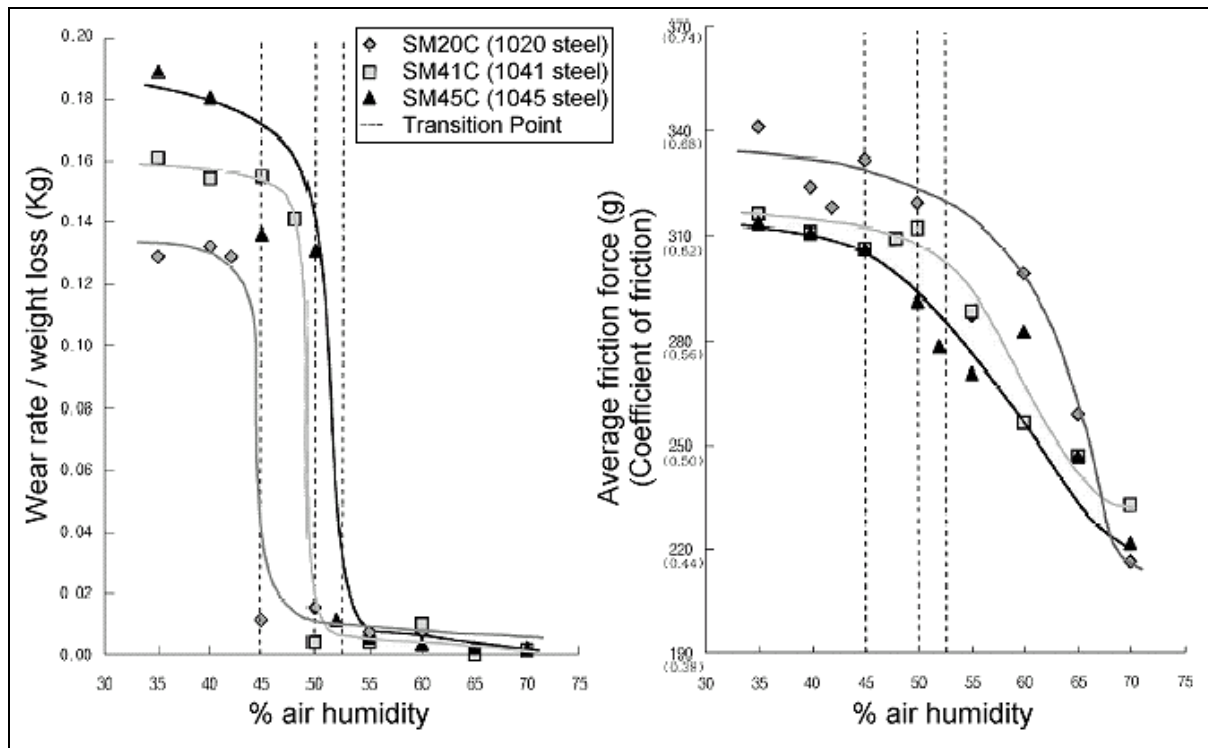
The wear process in atmospheres other than air or oxygen will depend on whether the atmosphere is oxidising or reducing. In most practical situations, corrosion product will not form in a reducing (non-oxidising) atmosphere, thus the production of wear protective layers is not possible. Only the presence of adsorbed gases and other volatiles will act to separate the wear surfaces, reduce adhesion and therefore levels of wear and friction [8].

As for oxidising atmospheres, only carbon dioxide has been looked at to any great degree. Studies by Sullivan and Granville [48] showed that a compacted oxide layer was formed when a Fe-9%Cr steel was tested with a pin-on-disk rig in carbon dioxide, between 200 and 550°C. Smith [85] observed the formation of compacted oxides on testing 316 stainless steel in carbon dioxide between 20°C and 600°C. The carbon dioxide acted as the oxidising agent in each case:



with the wear mechanisms very close to or the same as that of standard air.

**Figure 2.16: Variation of wear and coefficient of friction as a function of relative humidity [15]**



As for oxidising atmospheres without oxygen, research is extremely limited. Bill [84] obtained 'prodigious amounts of black debris' on testing titanium in pure dry nitrogen. It may be that this is removed adherent oxide present prior to sliding or even a mixture of metallic titanium and oxide. The possibility of titanium nitride is extremely unlikely if not impossible, due to testing being carried out at room temperature. However, no attempt was made to analyse the debris or explain the result.

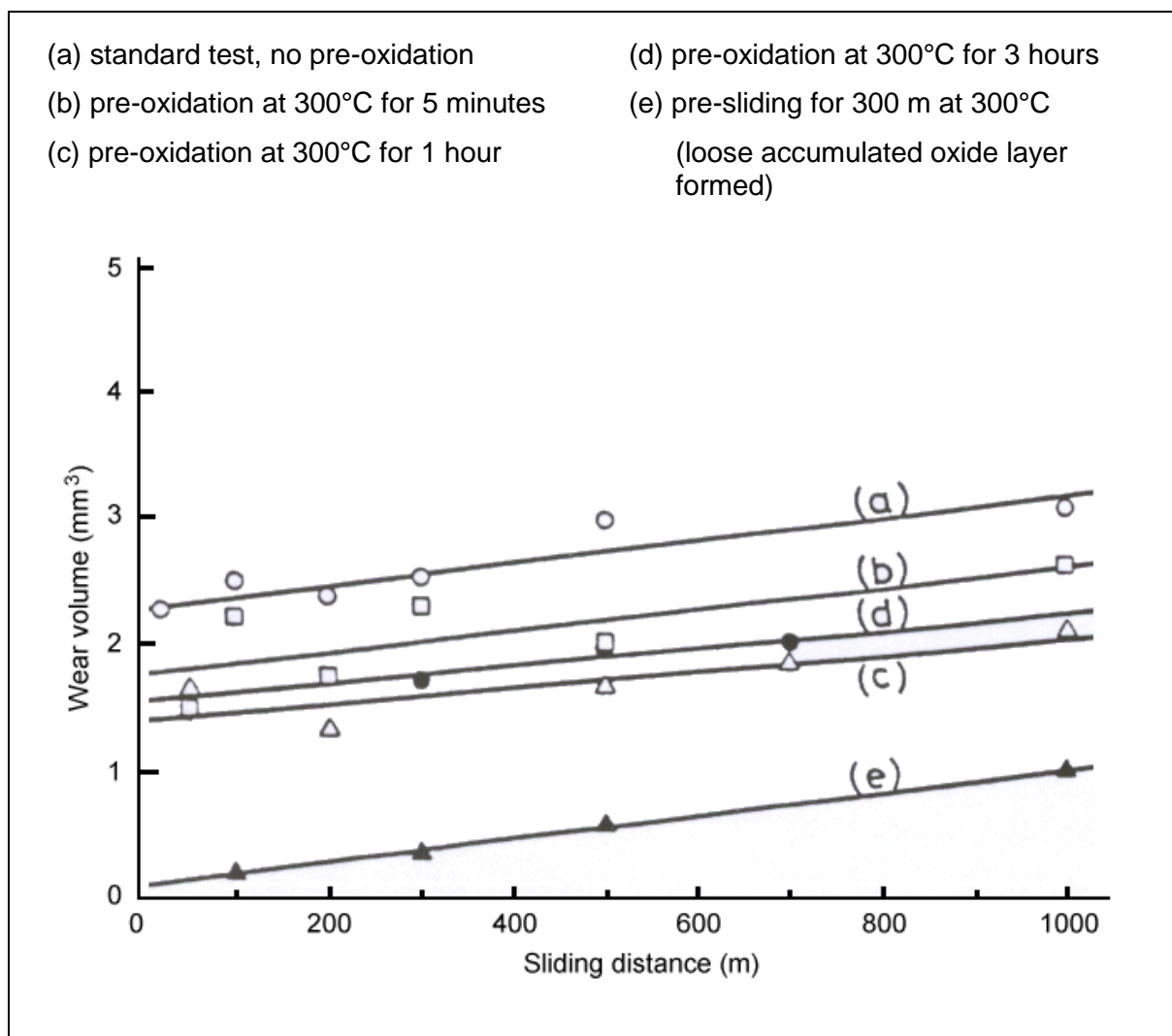
## 2.5.4 Pre-treatment of Sliding Surfaces

### 2.5.4.1 Pre-oxidation

Stott and Mitchell [47] also carried pre-oxidation on Jethete M152 (a high chromium steel) and 321 stainless steel, which on sliding indicated elimination of metal-to-metal contact in the case of Jethete M152 and also the immediate establishment of compacted oxide in the case of the 321 stainless steel. They concluded that the pre-oxidation provided an extra supply of oxide debris that led to the more rapid establishment of glaze surfaces.

Iwabuchi *et al.* [86] studied the effects of pre-oxidation of a number of samples of S45C carbon steel – for each sliding test, a moving disk specimen was rotated against a fixed ring specimen, with both pre-oxidised samples and unoxidised samples undergoing unidirectional sliding for 1,000 m at room temperature. The pre-oxidation treatment was carried out at a temperature of 300°C for times of 5 minutes, 1 hour and 3 hours for different batches of samples. Pre-oxidation times of 5 minutes and one hour did result in progressive reductions in wear (Figure 2.17), however, increasing pre-oxidation time to 3 hours produced no evidence of further improvement. The observed reductions in wear occurred because of the break-down of the oxide layer to form debris, the presence of which prevented metal contact and adhesion.

**Figure 2.17: Effects of pre-oxidation and pre-sliding on wear of S45C at 20°C [86]**



Iwabuchi *et al.* conducted similar experiments with 304 stainless steel specimens [86], with specimen configurations identical to those for S45C plain carbon steel. Pre-oxidation was again carried out at 300°C for times of up to 10 hours – a test temperature of 300°C was used in all cases. Although there was some scatter of data after 300 m of sliding, there was no evidence of any effect of pre-oxidation on overall wear, regardless of the time of pre-oxidation and Iwabuchi *et al.* concluded that pre-oxidation had no effect under the prescribed test conditions.

Pre-oxidation was also noted to be ineffective in reducing the initial severe wear rate of 304 stainless steel, even with pre-oxidation times of up to 10 hours. This was due to ‘selective oxidation’ of chromium at the surface reducing the overall level of oxidation of the stainless steel, with the end result being that there was insufficient oxide to reduce severe wear rate by debris generation from this layer.

Thus although pre-oxidation can reduce or eliminate early metal-metal contact, this cannot be guaranteed. Under certain circumstances, possibly due to variations in alloy composition affecting the nature of the surface oxidation, the production of suitable surface oxide required for the promotion of early glaze formation may not occur.

#### **2.5.4.2 Pre-sliding**

Iwabuchi *et al.* [86] additionally looked at samples of S45C carbon steel that had undergone pre-sliding at 300°C and 300m, sufficient to create an accumulated loose oxide layer. Subsequent tests indicated the complete elimination of the severe wear regime (Figure 2.17), with only mild wear being observed, regardless of test temperature. In the case of pre-oxidation, the oxide layer served only to reduce the severe wear “run-in” phase (Section 2.5.4.1).

A reduction in severe wear was also observed when 304 stainless steel underwent pre-sliding for 100 m at room temperature, due again to the presence of an accumulated loose oxide layer. In both cases, the availability of pre-existing oxide debris acted to prevent contact between the metallic interfaces.

Pre-sliding was additionally carried out for 304 stainless steel over a distance of 300 m at room temperature, 200°C and 400°C (at which temperature the oxide layer formed was a glaze), with the severe wear stage being eliminated in each case during subsequent sliding. The presence of accumulated oxide from pre-sliding did not, however, lead to a reduction in the rate of wear during mild wear.

#### **2.5.4.3 Ion Implantation**

Langguth *et al.* [87] carried out oxygen ion implantation on a series of chromium and carbon steels (AISI 52100, AISI 440B, AISI M2) and also 321 stainless steel, followed by a series of sliding speed experiments using a pin-on-disk rig, disks of diameter  $30 \times 10^{-3}$  m. A sliding speed of  $28 \times 10^{-3} \text{ m.s}^{-1}$  was used over a sliding distance of 400 m, with relative humidity set at 30% or 80%.

In general, recorded levels of wear for the ion-implanted samples were far lower than for their untreated equivalents (Table 2.3). This was due to the presence of the oxygen in the surface layers assisting the formation of oxidised debris and thus reducing the initial severe wear period. Certain aspects of heat treatment of the alloys and the sliding conditions were observed to affect this. For example, in the case of the chromium and carbon steels, the improvement in wear resulting from oxygen ion implantation was noticeably less for AISI 52100 and AISI 440B in the annealed form compared to the martensitic form – this can be seen by comparing the data in Tables 2.3 and 2.4. Relative humidity has a marked effect on this, as can be seen in the case of AISI 52100 steel, where the oxygen ion implanted material actually undergoes a higher level of wear than the untreated material. These observations were attributed to the higher sample plasticity of the annealed samples.

A change in the form of the debris was also observed, from a smooth oxide layer with the martensitic samples to loose debris with the annealed samples. The one exception to this was with AISI 440B steel, where the reduction was greater in the annealed state and accompanied by a change in the state of the oxide debris from the loose form to the oxide layer form seen with the martensitic samples.

**Table 2.3: Wear rates of case-hardened steels before and after implantation of oxygen ions, 400 m sliding distance [87]**

(ion implantation conditions  $5 \times 10^{17} \text{ cm}^{-2}$ , 50 keV; test conditions in air at 30% or 80% relative humidity RH,  $28 \times 10^{-3} \text{ m.s}^{-1}$ )

	Wear rate ( $10^{-16} \text{ m}^3.\text{m}^{-1}$ )			
	Steel ball		Tungsten carbide ball	
	30% RH	80% RH	30% RH	80% RH
<b>AISI 52100</b>				
Untreated	1,000	100	17.5	17.5
Implanted	1	3.4	1.8	0.3
<b>AISI 440B</b>				
Untreated	19	25	34	85
Implanted	1.4	2.5	2.8	1.8
<b>AISI M2</b>				
Untreated	11.5	2.9	11.2	20
Implanted	3.3	1.9	1.6	3.3

**Table 2.4: Wear rates of case-hardened steels before and after implantation of oxygen ions, 100 m sliding distance [87]**

(ion implantation conditions  $5 \times 10^{17} \text{ cm}^{-2}$ , 50 keV – 100 keV in case of AISI 52100; test conditions in air at 30% or 80% relative humidity RH,  $28 \times 10^{-3} \text{ m.s}^{-1}$ )

	Wear rate ( $10^{-16} \text{ m}^3.\text{m}^{-1}$ )			
	Steel ball		Tungsten carbide ball	
	30% RH	80% RH	30% RH	80% RH
<b>AISI 52100</b>				
Untreated	611	7.7	38	1.5
Implanted	68	11.2	38	2.2
Oxidised	1.1	0	0.8	0.8
<b>AISI 321</b>				
Untreated	1,400	72	4,000	32
Implanted	215	72	2,000	16
Oxidised	140	72	0	32
<b>AISI 440B</b>				
Untreated	98	9.1	42	42
Implanted	33	0.2	84	42

In comparison to standard pre-oxidation (Table 2.4), wear tended to be less, with the exception of annealed AISI 52100, where the pre-oxidised samples produced superior results, regardless of the levels of relative humidity.

Langguth *et al.* note also that implantation has been tried with a range of different ions, including nitrogen, carbon and boron with varying degrees of success, though not to the same degree of success as oxygen, as these alternatives do not promote wear track oxidation.

### ***2.5.5 Third Body Interaction in Relation to Compact Oxide Formation***

In Section 2.4.3, a brief discussion was made of four mechanisms of particle behaviour at the sliding interface, as proposed by Jiang *et al.* [53] – these included **(1) rotation**, **(2) skidding**, **(3) rolling** and **(4) adhesion / sintering affected rolling**. Jiang *et al.* observed that the friction levels for mechanism (4) is highly dependent on the adhesion force between particles in the sliding system. While this adhesion force is weak, friction levels for mechanism (4) are lower than that for mechanism (2), however, increasing this adhesion force above a critical level results in a situation where the reverse is the case. Skidding then becomes the dominant mechanism, with no relative movement between neighbouring particles – an increase in adhesion force locks them in place. A stable compact layer can result and at higher temperatures, a wear resistant ‘glaze type’ layer is possible (with the particles locked together, there is sufficient time for sintering). Stott’s later modification of this approach [54] (the inclusion of adhesion and sintering effects in rotation, skidding and rolling mechanisms) better recognises the fact that adhesion and sintering has a more general effect on the various particles making up the particle layer, regardless of if they are entrapped or in relative motion.

Adhesive forces and sintering tend to take effect at more elevated temperatures and this is demonstrated by experimental work carried out by Jiang *et al.* [70] on the sliding wear of Nimonic 80A at 20, 150 and 250°C. At 20°C, a thick layer of compacted, fine wear debris was formed, with some evidence of solidification and sintering in some areas. However, ultrasonic cleaning in acetone showed the layers formed to be still particulate in nature. There is a transition from metal-metal wear to contact between these primarily oxide particle layers, at which point increases in contact resistance and decreases in levels

of wear are coincident. At 250°C, sintering becomes a significant factor and there is a tendency to form smooth glaze layers on top of these compacted oxide layers. The 150°C case was intermediate, with some development of smooth load-bearing areas between the particulate layers. Removal of this more loosely compacted material by ultrasonic cleaning in acetone left behind the more compacted debris, load-bearing areas.

The observations described above clearly indicate that temperature is a major driving force for adhesion between particles and formation of load-bearing compacted debris layers. This was demonstrated further [70] by the heating of samples that had undergone previous sliding at 20°C, to 600°C for 90 minutes. The compacted layers formed during the sliding phase of the test became solidly sintered together as a result of the subsequent heating of the samples. The effect of a very small particle size would be to increase the available surface energy, due to the resultant increase in relative surface area. This would act to drive the adhesion and sintering process and allow for observable sintering at temperatures where sintering of larger particle sizes used in powder technology applications would not be noticeable. As adhesion itself is temperature dependent, increases in temperature due to ambient or frictional heating would accelerate the adhesion and therefore the sintering process. The effect of temperature on adhesion follows an Arrhenius relationship [73], analogous to that for oxidation (equation {2.30}):

$$K_p = A_p e^{-Q_p/RT_o}$$

The layers that sintered together when the temperature was increased to 600°C were subject to high thermal stresses (due to differences in thermal expansion coefficient) and cracked on cooling partially as a result of this and also due to shrinkage from the sintering process.

From experimental observations made, Jiang *et al.* proposed a descriptive model of the sliding wear process [54, 71]. Figure 2.18 shows this diagrammatically, with possible modifications to it for the reincorporation of debris for broken-down compacted oxide and ‘glaze’ layers:



1. wear debris particles are generated, due to the relative movement of the metal surfaces;
2. some are removed from the wear tracks to form loose wear particles;
3. others are retained within the wear track;
4. those retained are initially comminuted by repeated plastic deformation and fracture while freely moving between the rubbing surfaces – as this occurs, such particles can undergo partial or even complete oxidation, due to continued exposure of fresh metallic surfaces during comminution;
5. when fragmented to a small enough size, these particles are then agglomerated at various sites on the wear surfaces, due to adhesion forces between solid surfaces originating from surface energy, to form relatively stable compact layers.

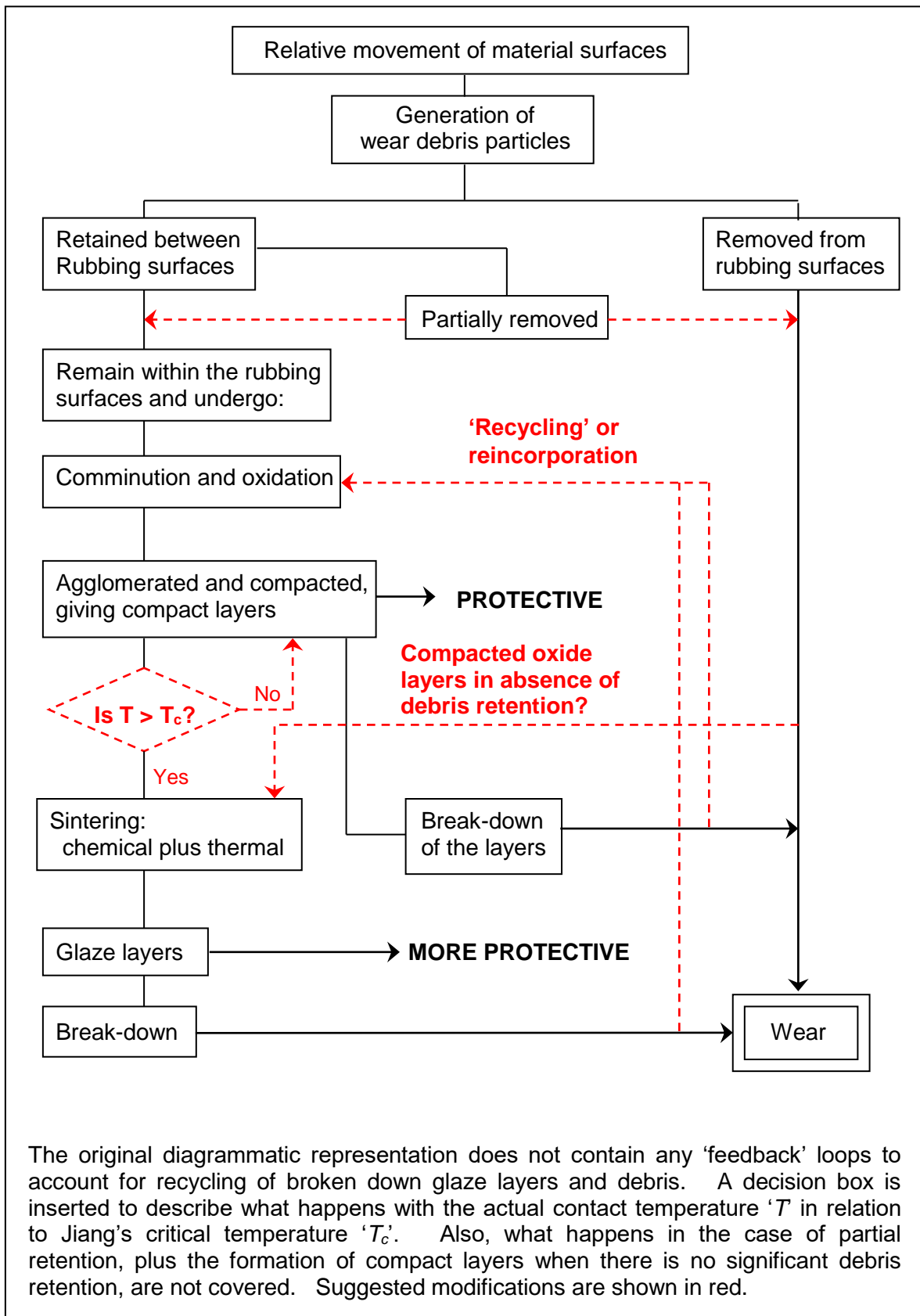
This has two effects, viz:

- i. Firstly, material loss is reduced by a material recycling effect of the wear debris particles. Material breaking away from the compacted debris may rejoin it.
- ii. Secondly, due to heavy deformation and oxidation of the wear debris particles, the layers formed are hard and wear-protective.

Two competitive processes then occur during subsequent sliding, i.e.:

- a. The compacted layers are continually broken-down, the debris from which may promote wear (though again, reincorporation may occur).
- b. Continuing sintering and cold welding between particles within the layers, leading to further consolidation.

**Figure 2.18: ‘Modified’ version of Jiang’s diagrammatic representation of sliding wear processes at various temperatures [71]**



For the latter case to predominate, the temperature must be high enough to encourage the sintering processes required to ensure a solid wear-protective layer forms on top of the compacted particle layers before the layers are broken-down. Jiang states that the temperature must be above a critical or transition temperature for these glaze layers to form. The effects of this can be seen in the experimental work of Jiang *et al.* – at 20°C, this critical temperature was not reached, thus the debris, although compaction was observed, did not sinter to form a ‘glaze’ layer. At 250°C, ‘glaze’ was clearly visible, whilst at 150°C, closer to and possibly not too far above the transition temperature, more limited sintering processes meant that whilst some ‘glaze’ areas formed, there were also substantial areas of loose debris still present.

Also of note is the formation of compacted debris layers close to the centre of wear scars, where debris retention would be at its greatest [72]. Away from the centre of the point of contact, there would be more scope for removal of debris, by being pushed out from the sides of the contact area. Coverage by high resistance compacted layers was estimated to be 20 to 50%, although this was reduced slightly by ultrasonic cleaning of the worn sample, which removed some of the more loosely compacted layers.

Jiang estimated also that to cause a transition from severe to mild wear, only 20% of the surface needed to be covered by ‘glaze’-type layers, compared to a value of greater than 30% for non-glaze compacted layers, demonstrating that ‘glaze’ layers offer more physical protection.

Jiang’s model is based on experimental work done on fretting wear systems and Rose [2] questioned the applicability of Jiang’s model in a low debris retention system. However, Jiang does account for debris removal from the system leading to wear, as would occur in, for example, higher speed unidirectional sliding. Also, in Rose’s own ‘reciprocating-block-on-rotating-cylinder’ experimental work (a higher speed unidirectional sliding configuration), examples of debris retention with glaze and compacted layer formation do occur (i.e. Incoloy MA956 versus Stellite 6), despite the more adverse sliding conditions. But as Rose points out, there are examples where compacted oxide layers do form and there is no significant third body debris retention [1,42], thus suggesting that Jiang’s model requires further modification to account for this (some proposals are made in Figure 2.18).

### 2.5.6 Quinn's Oxidational Wear Model

Quinn [73] proposed a model for mild oxidative wear, stating that wear rate was dependent upon the rate of formation of oxide films on the wear interface. However, once a critical thickness  $\xi$  was reached, then the oxide layers would no longer be able to withstand the forces acting tangentially on them and would fail and break away. On combining Quinn's work with that of Archard [9], it has been shown that the critical thickness can be used to relate the rate of wear to material oxidation rate, showing an increase in wear rate with temperature.

In Archard's wear equation {2.17}:

$$W = \frac{K_a PL}{H} \quad \text{or} \quad W = K_a AL \quad \left( A = \frac{P}{H} \right)$$

$W$  is the wear volume,  $P$  is the applied normal load and  $L$  is the total sliding distance (unit sliding distance is assumed for the following derivation, making  $W$  the wear rate).  $K_a$  can thus be regarded as the probability of a wear particle being generated in any given encounter. This being the case, then  $1/K_a$  is the number of encounters required to produce a wear particle.

In oxidational wear, a wear particle cannot be produced until the critical thickness for mechanical stability  $\xi$  is reached, thus  $1/K_a$  is the number of encounters required to generate an oxide layer of this thickness. If  $t$  is the time required to grow the layer and  $\tau$  is the length of time of each encounter, then:

$$t = \frac{\tau}{K_a} \quad \{2.32\}$$

If  $V$  is the sliding speed and  $d$  is the distance along which the sliding contact is maintained, then:

$$\tau = \frac{d}{V} \quad \{2.33\}$$

and equation {2.32} can be modified to:

$$t = \frac{d}{VK_a} \quad \{2.34\}$$

In a given time period  $t$ , the growth of oxide per unit area will be  $\Delta m$ . As oxidation is normally parabolic:

$$\Delta m^2 = K_p t \quad \{2.35\}$$

where  $K_p$  is the parabolic rate constant. If  $f$  is the mass fraction of oxide that is of oxygen and  $\rho$  is the oxide average density, then:

$$\Delta m = f \xi \rho \quad \{2.36\}$$

and:

$$f^2 \xi^2 \rho^2 = K_p t \quad \{2.37\}$$

Substituting {2.37} into {2.34} gives:

$$K_a = \frac{dK_p}{V f^2 \xi^2 \rho^2} \quad \{2.38\}$$

The rate constant can normally be calculated using an Arrhenius relationship, as described by equation {2.30}:

$$K_p = A_p e^{-Q_p/RT_o}$$

where  $A_p$  is the Arrhenius constant,  $Q_p$  is the activation energy (in this case for oxidation),  $R$  is the gas constant and  $T_o$  is the absolute temperature of reaction. Thus:

$$K_a = \frac{dA_p e^{-Q_p/RT_o}}{Vf^2 \xi^2 \rho^2} \quad \{2.39\}$$

Substituting into Archard's equation [9] gives a final expression for wear rate:

$$W = \frac{dAA_p e^{-Q_p/RT_o}}{Vf^2 \xi^2 \rho^2} \quad \{2.40\}$$

This expression relates directly to the oxidational properties of the materials, plus the critical environmental variables affecting the wear process, such as temperature at the interface at the time of contact and sliding speed relative to the opposing interface, as well as the critical thickness of the oxide. Quinn proposes that as the critical thickness of the oxide can be measured microscopically [73] and with information on the static oxidation properties of the wearing materials, wear rate prediction should be easily achieved.

It is to be noted, however, that the estimation of temperature at the wear interface is extremely difficult and even more so when oxide is present at the wear interface. On the whole, oxides are of much lower thermal conductivity than the metal on which they form [16]. This will have the effect of slowing the flow of heat away from the wear interface and raising the temperature above what may be expected. As the alloys used were iron-based [73], Quinn made use of the oxide produced to estimate the temperature of oxidation – iron oxidises to certain oxides depending on the oxidation temperature [14]. Up to 200°C, iron oxidises to the trivalent state and Fe<sub>2</sub>O<sub>3</sub> is produced. Between 200 and 500°C, iron is oxidised to both the trivalent and bivalent states, giving the spinel structure, Fe<sub>3</sub>O<sub>4</sub>. Above 500°C, the bivalent state is dominant, giving the Wüstite structure, FeO (though it is to be pointed out that iron is a prime example in which elevated temperature oxidation can lead to the formation of multi-scale layers).

Another complication is the effect of the state of the surface and the presence of defects (i.e. dislocations and voids) in the material within the area of contact [14,88]. The wear process has a very strong effect on the formation of these and increasing levels of defects will also increase the value of the Arrhenius constant. The effect of this is to increase the rate of tribo-oxidation above that of static oxidation.

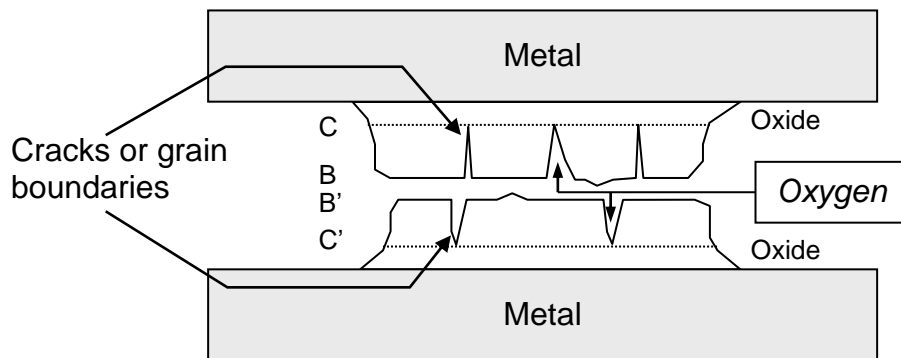
The reasoning behind this [76, 88] is greater ‘activation’ of wear surfaces due to the wear process, as a result of a higher level of dislocations at the surface of the deformed metal. These dislocations act as sinks for metal ion ‘vacancies’ diffusing to the metal / oxide interface, preventing the formation of pores at the interface [88]. In standard oxidation, the presence of such pores is believed to inhibit ion diffusion through the oxide layer and slow the rate of oxidation – oxides created during tribo-oxidation have been observed not to have these pores, thus giving a possible reason for the more rapid oxidation observed. The continued disruption of the oxide as it forms will also contribute to enhanced oxidation during sliding wear [88] – the continued removal of oxide leads either to exposure of fresh metal or a reduced thickness of oxide layer across which diffusion can logically more easily occur.

The effects of flaws and grain boundaries are also important [88]. Cracks and grain boundaries in the outer layers of the forming oxide may act as routes for the passage of oxygen ions and in the latter case, molecular oxygen species may be able to pass along the more significant flaws in the oxide layer. Where these flaws exist, it is the distance between the flaw tips and the metal / oxide interface that is more important than the actual overall thickness of the oxide layer (Figure 2.19). The tendency will be for increased oxidation rate due to such flaws.

The transfer of oxides between the wear surfaces also complicates matters, with transferred material either adhering to the opposite interface (for example, the adherence of high level nickel oxide to Stellite 6 as a sample material, when worn against Nimonic 80A at  $0.654 \text{ m.s}^{-1}$  [2]) or the debris particles embedding themselves within the oxide layers of the second wear surface. Also, Quinn himself points out that oxidation will continue whilst the surfaces are out of contact [74] and this is especially the case at elevated temperatures where the materials would oxidise under static conditions without the effect of the action of sliding. Quinn’s original assumption was that oxidation only occurred at the elevated temperatures resulting from asperity interaction. Additionally, Quinn’s model assumes continuous tribological contacts are maintained. This is rarely the case and whilst in a typical sliding test, for example ‘pin-on-disk’, continuous contact may be assumed for the pin, at any given moment only a small proportion of the disk is in contact. This is discussed further in Section 2.5.6.1.

**Figure 2.19: Oxygen transport between oxide plateaux and cracks in the oxides [88]**

Quinn's oxidation model supposes that any oxygen species would have to diffuse right from the surface of the oxide (B or B') to the metal. The presence of cracks and grain boundaries act as points of ingress for oxygen ions and in the case of cracks, molecular oxygen. This means that the distance for diffusion is significantly less where cracks in the outer layers of oxide are prevalent. Diffusion need only take place across the underlying oxide from the crack tips (C and C') to the metal and thus the rate of oxidation is greater.



The effects of variation in the nature of oxide scale are also not accounted for. For example, when iron undergoes oxidation at elevated temperatures (typically above 600°C), it is possible for multi-scale layers to form, with  $\text{Fe}_2\text{O}_3$  forming the outer layer,  $\text{Fe}_3\text{O}_4$  forming a middle layer and  $\text{FeO}$  forming underneath at the metal / oxide interface. This will affect the diffusion of species through the oxide that enable any reaction to proceed. With iron, the outer  $\text{Fe}_2\text{O}_3$  containing layers will have a lower diffusivity than those formed in contact with the metal (species can diffuse more readily through the  $\text{Fe}_3\text{O}_4$  and  $\text{FeO}$  making up the remaining oxide). Wear further complicates this situation, as it is extremely likely that the outer layers will fracture, thus increasing the overall rate of oxidation.

#### **2.5.6.1 Modification of Quinn's Oxidational Wear Model for Discontinuous Contact**

For Quinn's model of mild oxidational wear to give an accurate assessment of wear in a system, tribological contact must be maintained between the two contacting surfaces. During 'pin-on-disk' wear, although this may be a near accurate description for the contact state of the pin, only a small proportion of the wear track of the disk is in contact at any given time. For example, Garcia *et al.* [77] observed that when balls of corundum were



slid against disks of TiN-coated steel, the wear rate of the disks was more greatly influenced by contact frequency than sliding speed and the wear rate of the disks was inversely proportional to contact frequency. It was concluded that these results were not consistent with the mild oxidational model of Quinn, leading to its modification to relate wear rate to contact frequency.

For this modified model, it is assumed that  $1/K_a$  contact events are required for  $\xi$ , the critical oxide thickness, to be achieved – this is the same as for Quinn’s model. However, in this case, the time required to reach this critical thickness depends on the contact frequency  $F$ , which is the inverse of the elapsed time between two contacts at a given point between the contacting surfaces - whilst this can clearly be related to sliding speed, the frequency of contact can also be changed by varying the length of the wear track without any need to vary sliding speed. It is clear that each asperity is not going to make contact each time the disk rotates, however, Garcia [77] comments that the probability of a contact (and hence a wear particle being generated) is included in the statistical meaning of the wear coefficient,  $K_a$ .

Therefore:

$$t = \frac{1/K_a}{F} = \frac{1}{FK_a} \quad \{2.42\}$$

The constant of proportionality  $K_a$  in Archard and Hirst’s model [9] is thus defined by:

$$K_a = \frac{K_p}{Ff^2\xi^2\rho^2} \quad \{2.43\}$$

and once again substituting the rate constant, as defined by equation {2.28} gives:

$$K_a = \frac{A_p e^{-Q_p/RT_o}}{Ff^2\xi^2\rho^2} \quad \{2.44\}$$

Substituting into Archard's equation {2.17}:

$$W = \frac{K_a PL}{H} \quad \text{or} \quad W = K_a AL \quad \left( A = \frac{P}{H} \right)$$

gives a final expression for wear rate (again as sliding distance  $L$  is assumed to be 1, then the wear volume  $W$  can be taken to represent the wear rate), this time with the frequency of contact events being the determining parameter for the input of energy for oxide growth, rather than sliding speed:

$$W = \frac{AA_p e^{-Q_p/RT_o}}{Ff^2 \xi^2 \rho^2} \quad \{2.45\}$$

Garcia *et al.* [77] reported that relating wear to contact frequency as an independent parameter gave results of reduced scatter compared to the large spread of data frequently encountered with sliding speed in literature. However, Quinn's model [73] is still valid where a wear surface remains in continuous contact – the determining parameter in such cases is the duration of each individual wear event at a given asperity and hence sliding speed and asperity size are once again the determining parameters for the input energy for oxide growth.

One criticism of Garcia's modification [77] to Quinn's model is in incorporating the probability of a contact into Archard and Hirst's [9] constant of proportionality  $K_a$ , which is effectively the probability that a wear particle will be generated on any given contact. For this to work it is necessary for a wear particle to be generated each time a contact is made – this in itself is highly improbable. However, the lower level of data scatter achieved by Garcia's discontinuous contact model, indicates that this alternative frequency based approach provides a good approximation in circumstances where Quinn's model is not as effective in predicting rates of wear (i.e. where contact is not maintained).

## 2.6 The Effects of Load and Sliding Speed

### 2.6.1 Early Work

Work by Lancaster [17] showed a transition from severe to mild wear when testing 60/40 brass against a tool steel (load 30N, at temperatures of 20, 300 and 400°C in air, also 300°C in O<sub>2</sub>), coupled with the oxidation of surface material preventing intermetallic contact. This work also demonstrated that this transition only occurred above a certain critical temperature (influenced externally or by frictional heating) and that this temperature could be influenced by variables such as load and speed. Increased load had the effect of raising this temperature, as a greater rate of oxidation had to be achieved to prevent intermetallic contact (i.e. to prevent the penetration of metallic asperities through the oxide layers). Increasing sliding speed in the case of brass and tool steel had the effect of decreasing this critical temperature, as although it was noted by Lancaster that the rate of oxidation was dependent on the time available between repeated contacts (in other words, inversely dependent on the sliding speed), the rate of oxidation increased as a direct result of increased frictional heating at higher sliding speeds.

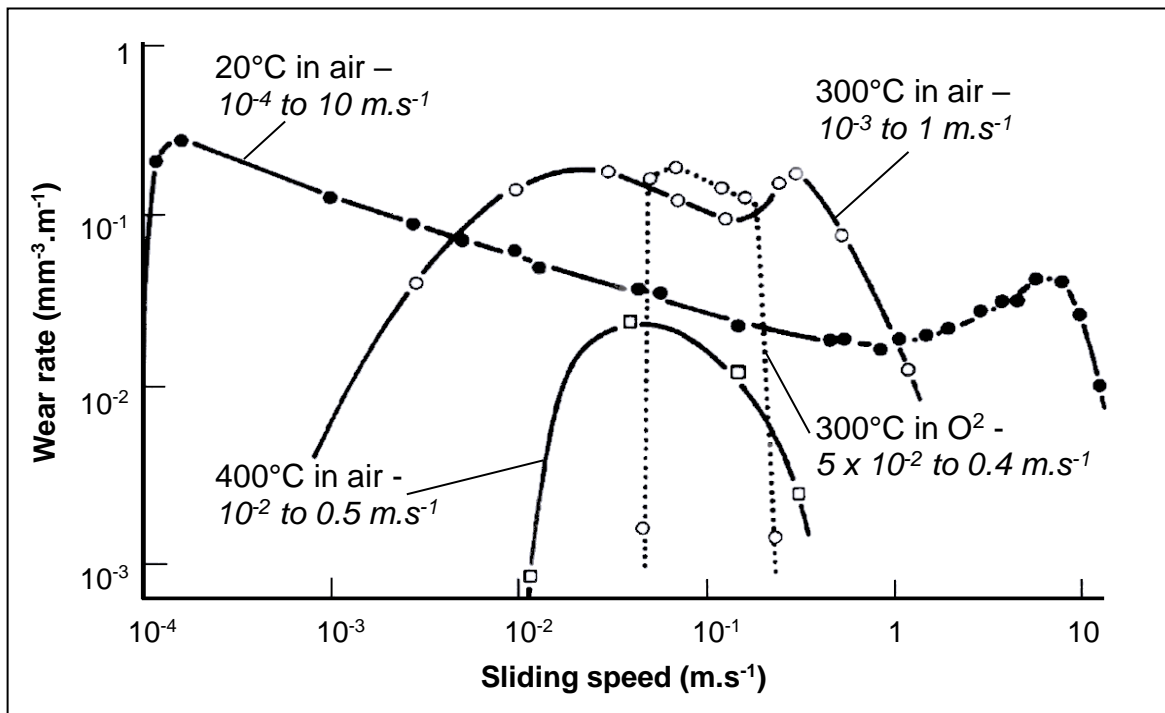
Lancaster also observed an intermediate range of severe wear, with mild wear observed at low and high sliding speeds (Figure 2.20). Increasing temperature was noted to reduce the range of speeds over which this severe wear was observed – at 20°C, severe wear was observed from 10<sup>-4</sup> m.s<sup>-1</sup> to 10 m.s<sup>-1</sup>, reducing to between approximately 10<sup>-3</sup> m.s<sup>-1</sup> and 1 m.s<sup>-1</sup> at 300°C, and approximately 10<sup>-2</sup> m.s<sup>-1</sup> and 0.5 m.s<sup>-1</sup> at 400°C. Testing in a pure oxygen atmosphere rather than air at 300°C reduced the range further to between approximately 5 x 10<sup>-2</sup> m.s<sup>-1</sup> and 0.4 m.s<sup>-1</sup> – the effects of oxygen availability and partial pressure are discussed in more detail in Section 2.5.3.1.

Welsh [22, 23] carried out an extensive series of studies into the effects of hardness, load, sliding speed and alloying elements on the wear process in various low carbon steels, using a pin-on-rotating ring (cylinder) configuration, loads of up to 2 kg.f and speeds of up to 2.66 m.s<sup>-1</sup>. On increasing sliding speed or applied load, two transitions were observed in the wear process, firstly from mild wear at low speeds and loads to severe wear at intermediate speeds or loads (T<sub>1</sub>), followed by a further transition from severe to mild wear at much higher speeds or loads (T<sub>2</sub>). Furthermore, it was noted that increasing the sliding speed lowered the critical load at which these transitions occurred (Figure 2.21), with the

lower transition being eliminated in some cases, leaving only the severe wear to mild wear transition. In extreme cases, these transitions could be lowered enough so as to be eliminated from the experimental data – mild wear could be observed over the whole range. The variation in the upper transition from the intermediate severe wear back to higher speed mild wear, was observed to be the more sensitive to sliding speed.

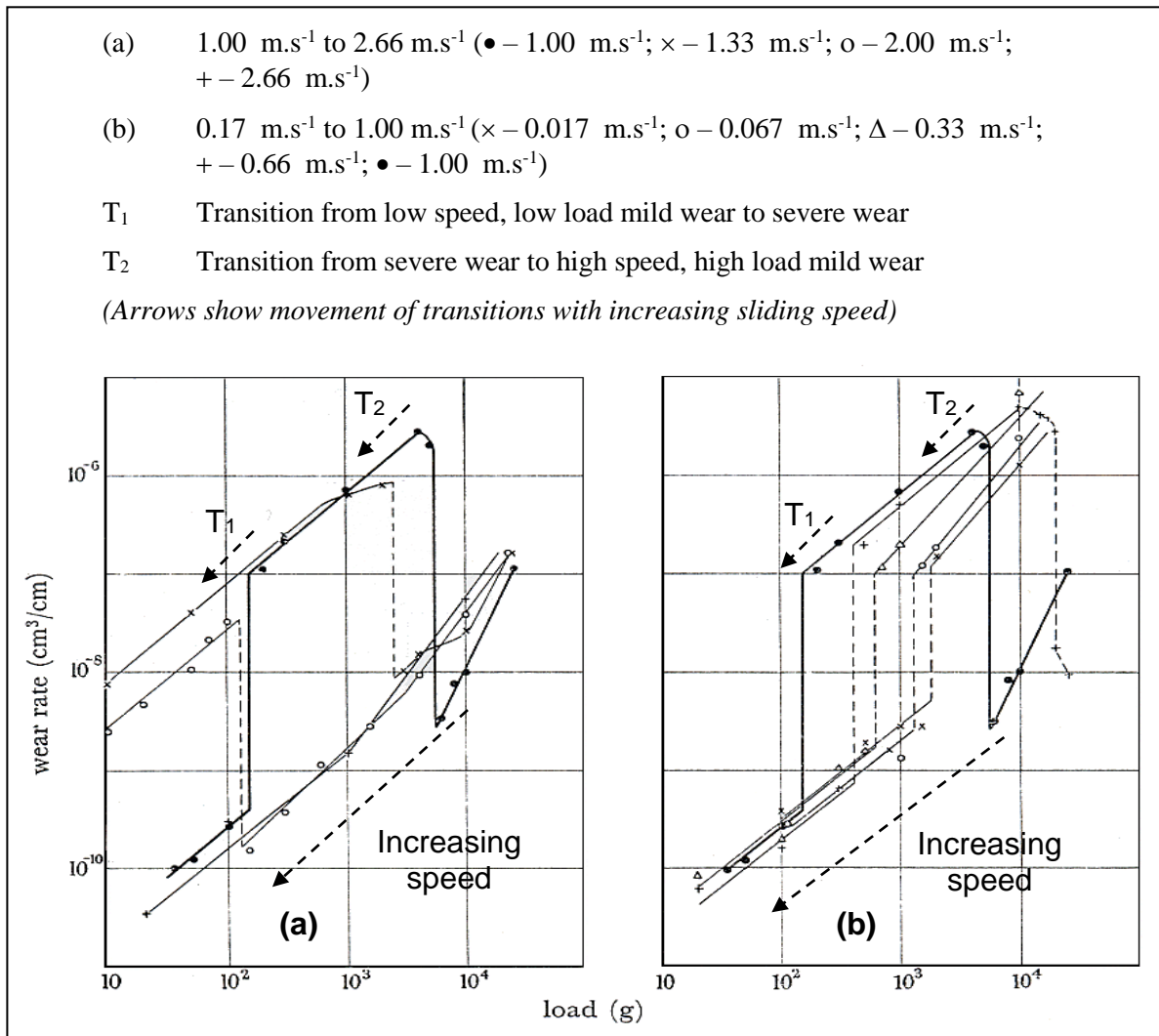
**Figure 2.20: Variation in wear rate with sliding speed at 20, 300 and 400°C in air and also 300°C in pure oxygen for  $\alpha/\beta$  brass sliding against steel [17]**

(Approximate sliding speed ranges for severe wear at each temperature given in *italics*)



Low speed, low load mild wear was attributed to the presence of loose oxide debris at the sliding interface and intermediate severe wear being due to direct metal-to-metal wear. The mild wear encountered at high speed and high load was attributed to hardening, accompanied by the development of an adherent oxide film, as a result of frictional heating. The hardening came about as a result of the low carbon steels undergoing phase changes, due to high localised temperatures around points of contact being sufficient to produce a transformation to austenite, followed by rapid cooling by conduction of heat into the bulk metal producing a structure at the surface not too dissimilar to martensite. Welsh uses the term ‘self induced quench hardening’ to describe this.

**Figure 2.21: Effect of sliding speed on wear rate / load – 0.52% carbon steel [22]**



A critical hardness had to be exceeded by these phase changes for mild wear to be re-established under high speed, high load conditions – the transition back from severe wear to mild wear is in fact a two part transition, with  $T_2$  referring to the point where sufficient phase hardening occurs to suppress severe wear without the intervention of an oxide film (the development of which further acts to protect the wear surface) and a  $T_3$  transition approximately matching the point where permanent phase change hardening occurs. The term ‘mild wear’ again here, can be considered a misnomer, as Welsh himself states that at loads and speeds slightly above the observed ranges of conditions, due to increased thermal softening, pin wear rate increases dramatically with large scale transfer of material from the pin to the ring.

Subramanian [28] conducted a series of sliding tests of an Al-12.3 wt. % Si alloy in pin form against various rotating ‘ring’ counterfaces, including mild steel in the rolled condition, quenched and tempered die steel and copper with varying levels of aluminium, during which the sliding speed was increased at various times. The wear rate of the Al-12.3 wt. % Si alloy pin (Figure 2.22) decreased with increased sliding speed up to a critical value of usually  $1 \text{ m.s}^{-1}$ , regardless of counterface material or applied pressure used. Further increases in speed above this critical value led to progressive increases in wear.

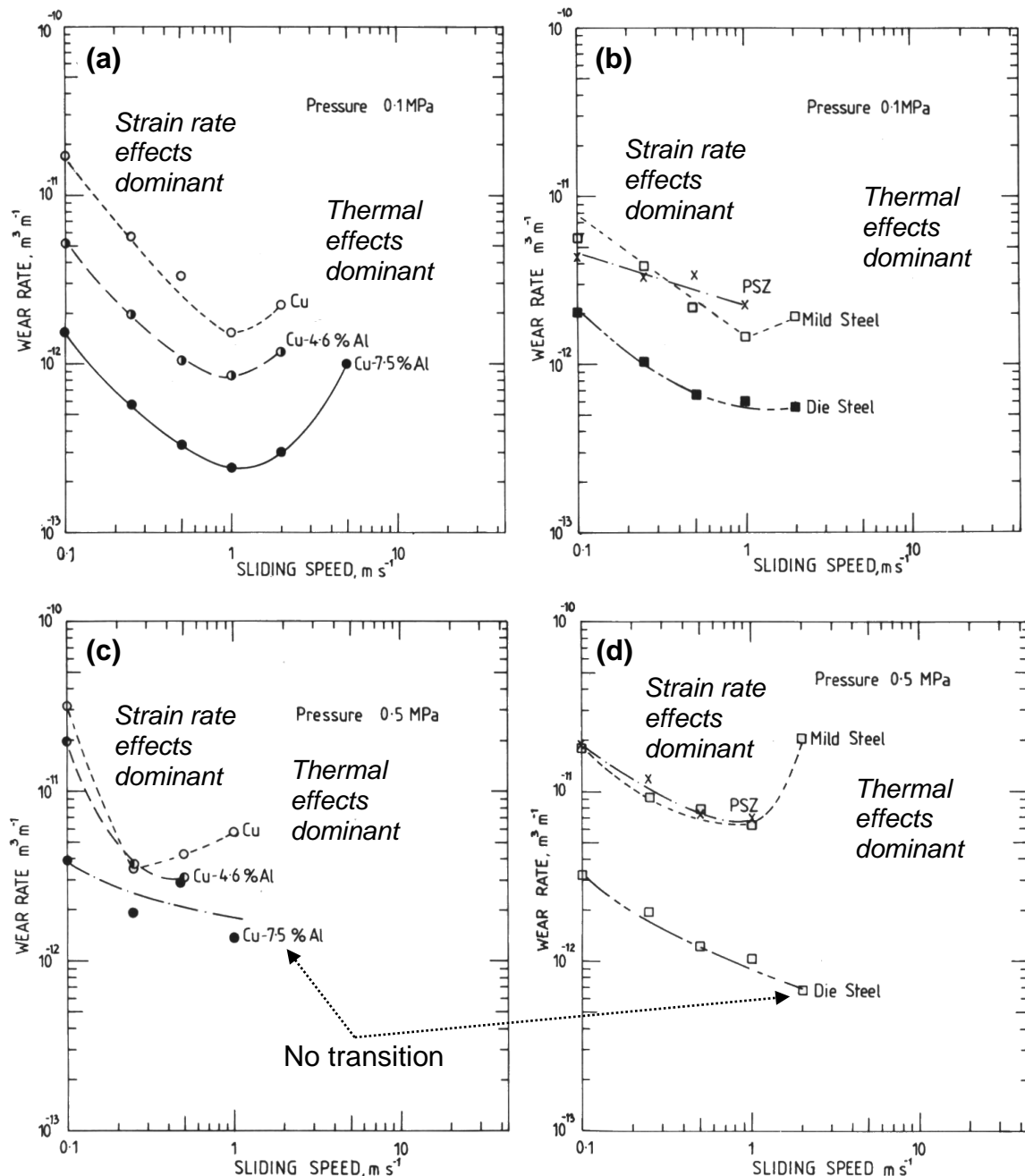
Subramanian explains the decrease in wear with increasing sliding speed due to increasing strain rates and due to increased hardness and flow strength of the wear surface. The true area of contact is thus reduced and with a lower level of contacts between the wearing surfaces, a lower wear rate results. In competition with this is the effect of increased temperature due to frictional heating (which was observed to occur), softening the material at the wear interface. This results in an increase in the true area of contact and thus an increase in the wear rate. Subramanian does not go into detail with his reasoning, however, the softening of the material must allow for deformation and ‘spreading’ of asperities and also increased contact at other points due to this. Also, no explanation is offered for absence of transitions and the continued decrease in wear rates of Cu-7.5% Al or die steel at an applied pressure of 0.5 MPa.

Changes in wear mechanism were observed with Subramanian’s ‘ $1 \text{ m.s}^{-1}$ ’ transition, with equiaxed particles produced below this critical or ‘transition’ speed, compaction of these particles and delamination of the compacted particles around the transition speed and delamination or plastically deformed material above this. It is not stated whether the particles produced at any particular speed are metallic or oxide.

The critical speed was observed to be dependent on counterface material and a higher transition was noted for harder, more thermally conductive alloys. Reduced mutual solubility also led to a higher transition speed.

**Figure 2.22: Effect of sliding speed on wear rate of Al-12.3 wt. % Si versus various counterface materials**

- (a) Cu, Cu-4.6 wt. % Al and Cu-7.5 wt% Al counterfaces, applied pressure 0.1 MPa
- (b) Mild steel, die steel and partially stabilised zircona counterfaces, applied pressure 0.1 MPa
- (c) Cu, Cu-4.6 wt. % Al and Cu-7.5 wt% Al counterfaces, applied pressure 0.5 MPa
- (d) Mild steel, die steel and partially stabilised zircona counterfaces, applied pressure 0.5 MPa

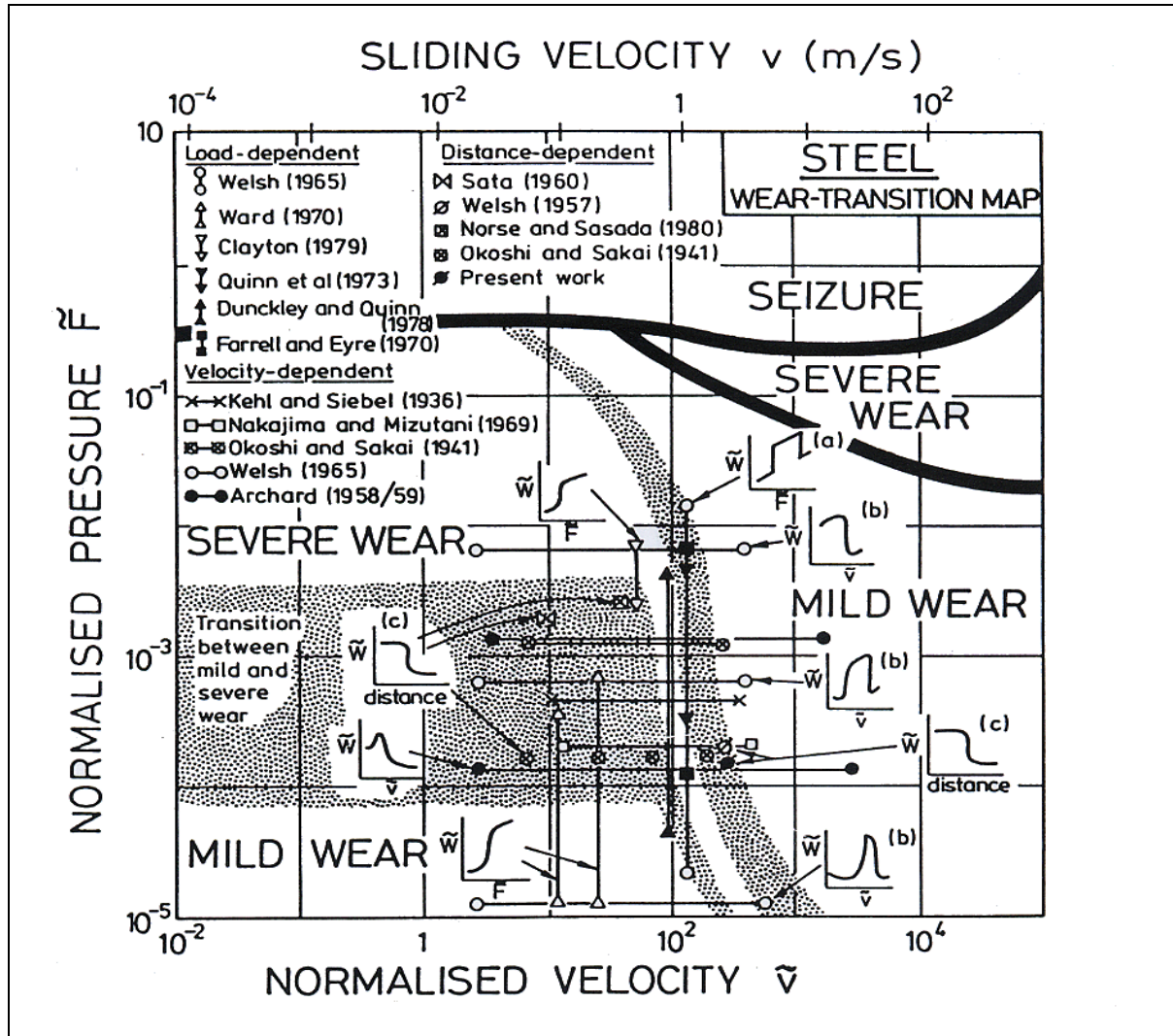


Welsh [22,23] discusses the existence of lower limits of load and speed, marking the transition from mild to severe wear and also an upper limit, marking the transition back to mild wear. So [90] on the other hand only discusses a single limit or critical value for both load and speed for the transition from mild wear at low speeds and loads, to severe wear at high speeds and loads. Comparison with the work of Welsh would make So's transition equivalent to the lower transition, with no mention of an upper transition despite the use of higher sliding speeds. So quotes values of 400°C and 5 MPa contact pressure as being limiting conditions for mild wear for many steels. In one test of note, a high carbon steel sample underwent a mild-to-severe wear transition at a contact pressure of 4.43 MPa, on raising the sliding speed from 3 to 4 m.s<sup>-1</sup>. A Stellite sample remained in the mild wear state at a contact pressure of 8.85 MPa (just under twice as much pressure) under similar conditions. As So used a pin-on-disk configuration, compared to the pin-on-rotating-cylinder configuration of Welsh, this may account for the differences in results – the pin-on-disk configuration may not have generated sufficiently severe conditions for the upper transition to occur.

The complexity of the situation is made apparent in Lim's review of wear maps [91], where it can be seen that the effects of the load and sliding speed parameters can give different apparent results, depending on the experimental parameters used (Figure 2.23). If reference is made to Figure 2.23, it can be seen that if a relatively high fixed load (referred to as a normalised pressure by Lim) is used with increasing sliding speed, a transition from severe-to-mild wear is observed (Welsh [22]). At lower loads, more complex forms may result from increasing sliding speeds to much higher values (Archard [13] and Welsh [22]). Similarly, if speed is fixed at an arbitrarily low value, increasing load may see a switch from mild to severe wear (Ward [91]) or at a higher fixed value of speed may give a more complex curve once again (Welsh [22]). The start and end parameters may also affect the final result – the complexity of what happens when two surfaces are worn against each other has led to a variety of apparently contradictory results.



**Figure 2.23: Wear transition map for steels showing regions of mild and severe wear – sliding conditions corresponding to different types of wear transitions observed are also indicated [91]**



Lim [91], Childs [92] and others attempted to resolve this by the use of wear maps, the objective being to allow for the prediction of what will happen under certain conditions of load and sliding speed – as can be seen from Figure 2.23, the possible outcomes depending on the values of these two parameters alone can make prediction difficult even just for room temperature wear. Wear maps need not necessarily be for just speed and load, with Kato and Hokkirigawa [93] opting for an abrasive wear map, using ‘degree of penetration (of asperities)’ and ‘shear strength at the contact interface’ as the key parameters.

Most load and sliding speed work to date has concentrated on what happens at room temperature, with little work at elevated temperature. One quotable example is the work of Rose [2], where a series of experiments was conducted at 750°C with loads varying between 7 and 25 N, during which an apparent transition from mild-to-severe wear was noted at 15 N, when Nimonic 80A was worn against Incoloy 800HT. Also when Incoloy MA956 was worn against Stellite 6 or Incoloy 800HT, at 25 N, the glaze layer formed on the Incoloy MA956 was beginning to show signs of breaking away.

### **2.6.2 Wear of Cobalt-Based Alloys**

Amongst the most comprehensive work carried out on the sliding wear of cobalt was that by Buckley [94], who compared the sliding wear in vacuum of cobalt with that of copper. Lower friction and adhesion levels were noted for the cobalt – this was attributed to its hexagonal close-packed structure, compared to the copper’s face-centred cubic structure. During sliding, friction with cobalt was noted to remain at a low, steady value, whilst that of copper was observed to rise with increased sliding distance. A similar pattern was noted in the values of adhesion measured before and after testing.

When cobalt was tested at above 300°C, friction and adhesion values were observed to rise, with complete welding at 450°C. This was attributed to phase changes within the cobalt with increasing temperature from hexagonal close-packed to face-centred cubic. This is lower than the quoted value of 417°C for cobalt [94, 95], which Buckley attributed to frictional heating due to increased sliding speeds used during testing.

The differences between the sliding behaviour of metals in hexagonal close-packed phase and face-centred cubic phase were attributed to the greater number of active slip systems available in the latter structure. There are twelve primary slip systems within a typical face-centred cubic metal (4 slip planes each with three slip directions), which are all crystallographically similar. By comparison, there are only three primary slip systems in cobalt, these being based on the basal plane with the highest atomic density (i.e. 1 slip plane with 3 slip directions). Cross slip is also more difficult, as with hexagonal close-packed structures such as cobalt, screw dislocations are required to move out of the primary basal glide plane onto planes that unlike face-centred cubic structures, are crystallographically different. Hexagonal close-packed materials are thus less deformable.

In addition, recrystallisation under more extreme conditions (e.g. temperature, load) and alignment of this basal plane in grains at the sliding surface allow for regions of extended easy glide and thus less force should be required for localised fracture than for face-centred cubic structures. This leads to reduced shear being needed to overcome junction formation during sliding, hence observed values of friction and adhesion are also lower. With face-centred cubic metals, strain of adhered or welded junctions will result in increased shear stress, due to work hardening. This work hardening is a result of the interaction of slip plane and slip plane dislocations forming barriers to other dislocation slip plane movement and thus a greater stress is needed to overcome these barriers.

Buckley [94] also observed that because of the extremely low coefficient of friction during the sliding of cobalt, the formation of oxides on the sliding surfaces did not necessarily reduce friction values and increases in friction could actually be observed.

Stott, Stevenson and Wood [96] observed the formation of compacted oxide layers during like-on-like fretting wear tests of cobalt-based Stellite 31 between room temperature and 800°C (293 K to 1,074 K). The formation of these oxides was by a similar route to that observed for iron-based and nickel-based alloys, with alloying components present in the oxides to roughly the same proportions as the original alloy.

At temperatures between room temperature and 300°C, Stellite 31 undergoes a much lower level of wear compared to various nickel- and iron-based alloys, which Stott also attributes to the lower number of slip planes in the hexagonal close-packed structure of cobalt. Stott specifies an initial period of low wear for up to an hour, followed by the production of bright, rough metallic wear scars showing characteristics of abrasion and evidence of material transfer. This he attributes to a probable change in phase from hexagonal close-packed to face-centred cubic and thus a loss in wear resistance. Later, the bright worn surface is lost with increasing amounts of oxide being produced, although the load-bearing areas remain metallic.

Both the 'phase changes' and oxide production have been attributed to temperature increases at the wear interface. However, the phase transformation temperature of cobalt is at 417°C – Stellite 31 contains 26% chromium, which has the effect of significantly

raising the hexagonal close-packed to face-centred cubic transition temperature – Stott himself states that 20% Cr will raise the transition temperature to 1,120K or 847°C (expressing uncertainty as to the effects of the other alloying components). This suggests a far greater influence due to frictional heating and localised flash temperatures due to asperity interactions – for a phase change to readily happen, the temperature at the immediate interface would have to reach 500°C above ambient. As a fretting wear combination is used, it is difficult to see how this could occur.

However, the level of alteration of temperature for any phase transitions will also depend on the effects of other alloying components on cobalt-based alloys. As already stated, chromium will raise the transition temperature quite dramatically. Other references [94,97] suggest that tungsten and molybdenum will also raise this transition, whilst nickel and iron will have the effect of stabilising the higher temperature face-centred cubic structure and suppressing this transition. It may be that the presence of nickel to 10.5% and iron to 2% may be sufficient to retard the effect of the chromium and 7.5% tungsten to a much lower level. Thus a much smaller increment in temperature due to frictional heating and flash temperatures may be needed to effect any phase transition and Stott's conclusion that the damage observed can be attributed to phase changes and thus a reduction in resistance to deformation, may indeed be valid.

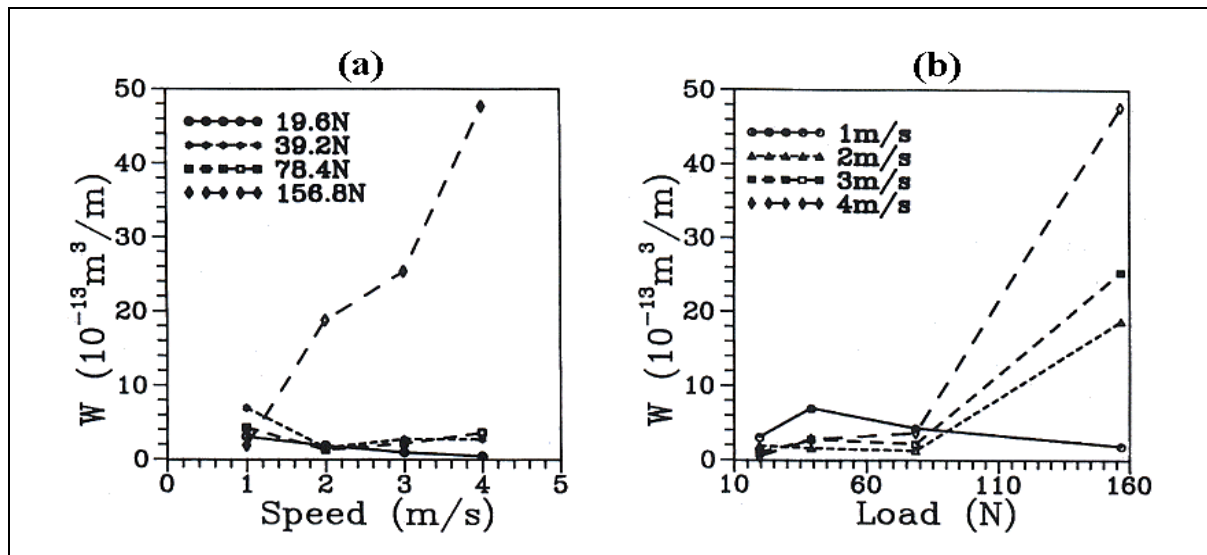
At elevated temperatures, Stott [96] observed that compacted oxide formation was not accompanied by any falls in friction that were observed during similar experimentation with nickel-based alloys. With friction levels already low due to the hexagonal close-packed structure, it is simply a case of there being no significant difference between the friction levels before and after the elimination of metallic contact by the higher temperature glaze formation. Also, it is likely that glaze formation occurred before any transition from a hexagonal close-packed to a face-centred cubic structure could have a significant effect on the wear process.

#### ***2.6.2.1 The Effect of Load and Sliding Speed – Stellite 6***

Following on from So's previously discussed work (Section 2.6.1) with a Stellite material [90], So *et al.* went on to test Stellite 6 clad mild steel against AISI 4140 and 4340 steels in the martensitic phase, first as the pin material (4.75 mm in diameter) then the disk material

[98]. Measured hardness values were 580 VHN for the Stellite 6 layer and 750 VHN for the steels, rising to 970 VHN after an unspecified heat treatment followed by water quenching, with test loads of up to 156.8 N and sliding speeds of up to 4 m.s<sup>-1</sup> used. After sliding for up to 10,000 m, the Stellite 6 layer was observed to be mostly covered by an oxide layer, consisting of W<sub>3</sub>O, CrO and Co<sub>2</sub>O<sub>3</sub>. Where this oxide layer spalled, a new oxide film was observed to readily replace it. This applied for all combinations of loads (19.6, 39.2, 78.4 and 156.8 N) and sliding speeds (1, 2, 3 and 4 m.s<sup>-1</sup>), with the exception of the most severe tested combination, 156.8 N and 4 m.s<sup>-1</sup>, when severe wear was observed for the Stellite 6 as the pin material. The experimental data obtained from these tests are presented in Figure 2.24.

**Figure 2.24: Variation in wear rate (W) with sliding speed (a) and load (b) for the rubbing of laser-clad Stellite 6 pins with AISI 4340 steel disks [98]**



The steels underwent increased wear compared to the Stellite 6, despite being of much greater hardness and So *et al.* concluded that the oxide layer formed on the Stellite 6 must be tougher than that formed on the steels. When used as a disk material, only a thin layer of oxide material was formed on the AISI 4340, compared to the thicker layer formed on the Stellite 6 – the wear rate of the steel was seven times that of the Stellite 6 laser-clad pin. As the pin material, severe wear was observed with the AISI 4140 steel, the rate of wear being 10 times higher than the Stellite 6 laser-clad disk. For all but the highest load, the wear rate of the Stellite 6 as the pin material actually decreased when the sliding speed

was increased from 1 to 2 m.s<sup>-1</sup>, with only a slight increase at intermediate loads on raising the sliding speed to 4 m.s<sup>-1</sup> (Figure 2.24). At the lowest load used, the decrease in wear continued up to 4 m.s<sup>-1</sup>.

The increasing wear rate for specimens under 156.8 N load was ascribed to softening of material due to the higher flash temperatures encountered, especially at higher sliding speed. The higher flash temperatures also led to changes in the observed oxide phases that formed on the respective wear surfaces, with a shift from Fe<sub>2</sub>O<sub>3</sub> to FeO on the steels and from W<sub>3</sub>O, through Co<sub>2</sub>O<sub>3</sub>, CrO, Cr<sub>2</sub>O<sub>3</sub> to Cr<sub>5</sub>O<sub>12</sub> on the laser-clad Stellite 6 layer with increasing temperature – this was accompanied with a reduction in friction. So does not offer an explanation for the change in oxide with temperature, though as with the oxidation of iron (Section 2.5.6), it appears that this can be attributed to changes in oxidation state of the chromium in Stellite 6, with preferential oxidation of tungsten and cobalt respectively at lower temperatures. It is curious to note here, that in the work of Wood [1] and Rose [2], that no such shift was observed with Stellite 6, with Cr<sub>2</sub>O<sub>3</sub>, Co<sub>3</sub>O<sub>4</sub> or a combined oxide of the two being consistently observed from XRD results. No evidence of tungsten phases was found, although this could be attributed to the sensitivity of the measurement and characterisation equipment.

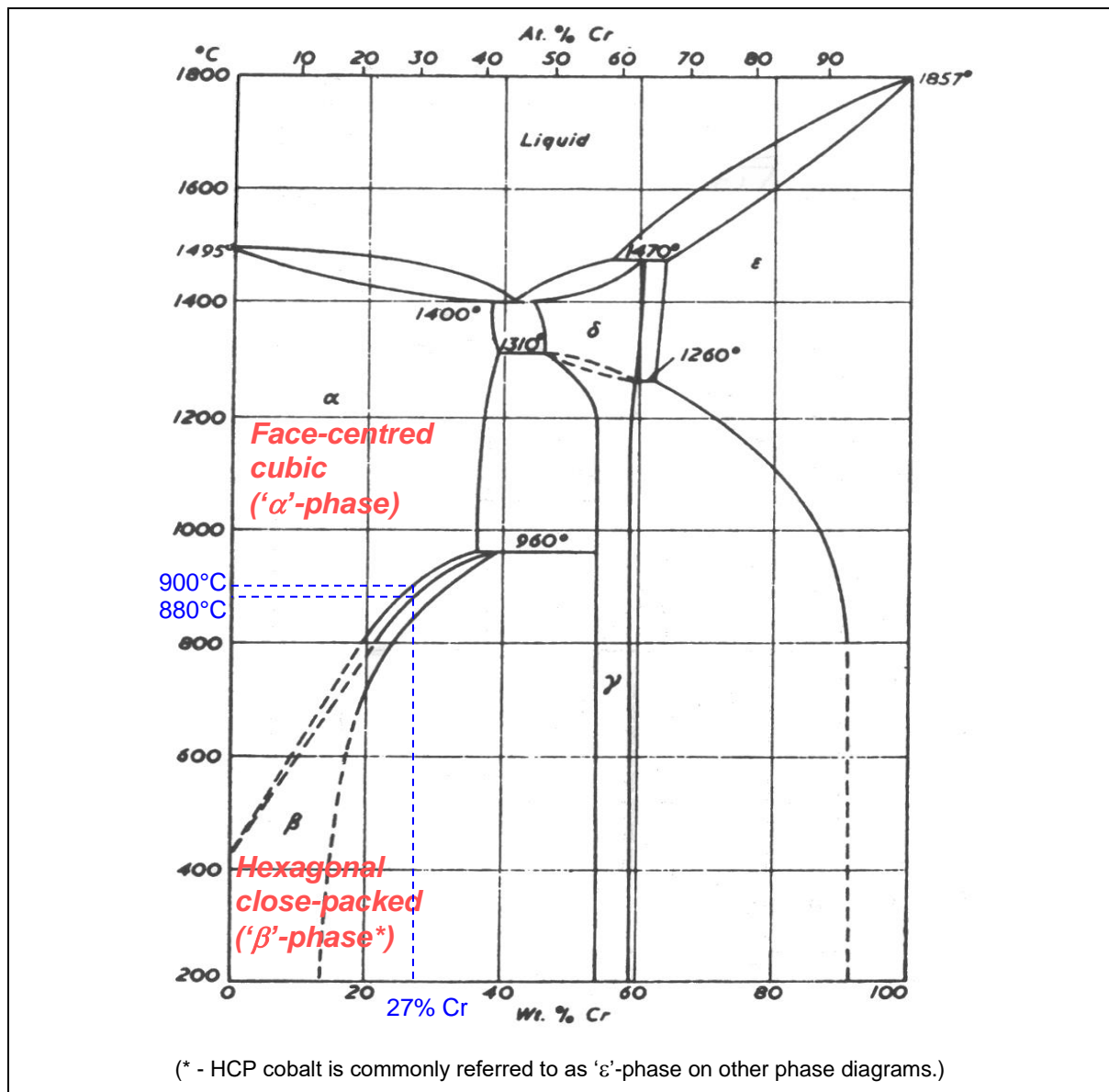
Also of note was the fact that the oxide layers formed in So's work, were more reminiscent of those created at higher ambient temperature in the work of Wood and Rose (510°C plus), indicating extremely high temperatures at the point of contact and So's measurements indicate a rapid rise in temperature with increasing load and speed (speed having less of an effect than load). So comments that under the most severe conditions (156.8 N and 4 m.s<sup>-1</sup>), the mean surface temperature at the point of contact reaches over 700°C and because of this, wear becomes severe due to softening. This may be more to do with the load and speed conditions rather than the temperature (even accounting for phase transitions), as Wood and Rose both tested Incoloy MA956 and Nimonic 80A against Stellite 6 at an ambient temperature of 750°C, with oxide layers being obtained in both cases on the Stellite 6 counterface.

This implies that So has underestimated the temperature at the sliding interface in this case. The softening may again be attributable to phase changes from hexagonal close-packed to



face-centred cubic. In the case of Stellite 6, there are far fewer alloying additions to offset the effects of chromium (present to 27%) and tungsten (present to 5%) on this transition. Figure 2.25 shows a binary phase diagram for the cobalt-chromium system [95], with the transition between the two phases for 27% chromium between approximately 880°C and 900°C. This is up to 200°C higher than So's 700°C estimate.

**Figure 2.25: Binary phase diagram for cobalt and chromium, showing the transition temperature for 27% chromium [95]**



Crook and Li [99] carried out a comparative 'like-on-like' sliding study of Stellite 6 and a number of other hard-facing alloys of varying cobalt content, including Stellite 1 (with

higher levels of carbon, chromium and tungsten than Stellite 6), Stellite 2006 (a 33% cobalt-iron-chromium alloy), Haynes No. 716 (a nickel-iron-chromium alloy with 11% cobalt) and Haynes No. 6 (a nickel-chromium alloy with no cobalt). They observed that in general, the higher the cobalt content, the better was the resistance to metal-metal wear up to 750°C. Where no cobalt was present within the alloy, wear rates were observed to be higher. Above this temperature (at 1,000°C), all alloys examined exhibited low wear with a protective oxide layer forming across the wear surface. Increases in wear were observed for all combinations with increased contact pressure, though at high load, increases became less severe for cobalt-chromium and cobalt-iron-chromium alloys. Of particular note is the response to increasing the sliding speed by an order of ten from the  $7.06 \times 10^{-4} \text{ m.s}^{-1}$  used for all their other tests, to  $7.88 \times 10^{-3} \text{ m.s}^{-1}$ , carried out at 500°C and 20.69 MPa. For the high cobalt-chromium alloys including Stellite 1 and Stellite 6, there was a slight decrease in the observed wear rate. Where cobalt levels were low or non-existent, the converse was true and increases in wear were observed.

Crook and Li [99] attributed the superior wear resistance of the cobalt-chromium alloys, firstly to the superior galling resistance and secondly to the tendency of alloys when in the face-centred cubic form, to undergo phase changes and become hexagonal close-packed, which as discussed earlier is less prone to deformation, due to a smaller number of available slip planes. Conversely, they point out that high nickel alloys have a poor galling resistance, yet specifically quote the work of Stott *et al.* [59, 60, 62] as examples of nickel-chromium alloys in particular exhibiting low levels of wear and developing glaze during the wear process at high temperature.

In both experimental programmes, a low amplitude ‘button-on-disk’ system suitable for fretting wear studies was used. However, Stott *et al.* concentrated solely on one material (Nimonic 80A), whereas Crook and Li’s comparative work on a range of alloys showed that although wear was still low for nickel-chromium alloys, the wear levels were inferior to cobalt-containing alloys. In both cases, it is not possible to say that in an extreme high wear environment (e.g. high speed, high load) that similar observations of low wear would be made. In the case of Stellite 6, So’s work [98] does indicate continued low wear under moderately high speed, high load uni-directional sliding wear (up to 156.8 N and  $4 \text{ m.s}^{-1}$ , with frictional temperatures of up to 700°C generated), however, if the work of Wood [1]



and Rose [2] are considered, high levels of wear are observed with Nimonic 80A at elevated temperature (750°C, 0.654 m.s<sup>-1</sup>, 7N, 9,418 m sliding distance) when undergoing uni-directional wear against a Stellite 6 counterface. Even in a like-on-like situation [2], wear properties of Nimonic 80A are inferior to those of Stellite 6.

#### ***2.6.2.2 The Presence of Carbides in Stellite 6***

In both the work of Stott [96] and So [90], no mention was made of the effect of the grain boundary carbides that would have formed with both Stellite 31 and especially Stellite 6, carbon being present to 0.5% and 1.1% respectively. This carbon combines with chromium to form a chromium carbide phase at the grain boundaries – in Stellite alloys, these are of the form M<sub>7</sub>C<sub>3</sub> and M<sub>23</sub>C<sub>6</sub> [98].

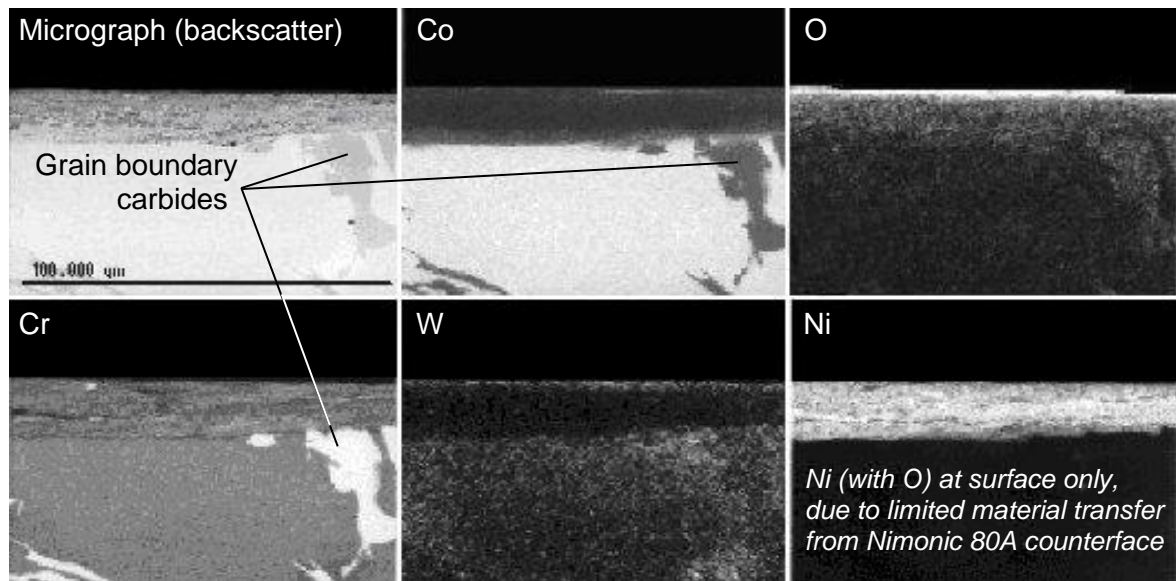
Although not discussed at the time, the carbides can be seen on the following cross-sectional EDX (Energy Dispersive X-Ray) map taken from the work of Rose [2] (Figure 2.26), for the reversal of sample and counterface for ‘Nimonic 80A versus Stellite 6’ (also evident for ‘Incoloy MA956 versus Stellite 6’ – not shown here [2]). Although carbon itself is not detectable by EDX without light element analysis or WDS (Wave Dispersive Spectroscopy), the use of backscatter and the changes in distribution of cobalt and chromium in the substrate are effective tools for their identification.

The presence of these hard, difficult-to-deform carbides may have had a number of effects on both sets of experimental work. Firstly, they may have further inhibited deformation of the mainly cobalt matrix during sliding wear, over and above the effect expected from the hexagonal close-packed structure, blocking the operation of the fewer slip planes present. Secondly, the removal of material from the Stellite alloys may have released some of these carbides into the sliding interface, increasing the levels of wear observed due to increased abrasion effects. The enhanced wear of the AISI 4140 and 4340 steels, when worn against Stellite 6 clad mild steel in So’s work [98] may have in addition been partially attributable to this.

There is also the possibility that the carbides (up to 30µm in size) within the Stellite 6 may affect the formation of glaze (only a few µm thick) on wear surfaces as the Stellite 6 is worn down and the carbides are exposed – this is discussed in more detail in Section 2.7.

**Figure 2.26: Identification of grain boundary carbides by changes in distribution of cobalt and chromium in the Stellite 6 substrate**

*(0.654 m.s<sup>-1</sup> / 9,418 m, 750°C, 7N – Stellite 6 sample slid against Nimonic 80A counterface [2])*



## 2.7 Effect of a Second Phase on Wear

The role of second phases in the wear process is one area often neglected in wear studies. In the vast majority of studies, experimentation has concentrated only on single-phase alloys. However, second phases are used in many alloys for various reasons, notably including enhancement of strength and creep resistance, especially in high temperature systems where the properties of the metallic matrix can become less robust.

During the wear process, where second phases are harder than the matrix material, it is not sufficient to assume that their presence will have no effect on the wear process and that they will simply be ‘worn away’ with the matrix as sliding proceeds (this only occurring if the second phase is of similar or lesser hardness). Vardavoulas [100] conducted a series of studies on a number of steels, into which via a powder metallurgy route, hard ceramic phases of different sizes were introduced – these included titanium carbide (modified to a much finer carbonitride phase by nitrogen annealing), copper phosphide and alumina. It is assumed in the following that the substrate metal is being oxidised and is thus the main source of supply for the compacted oxide or oxide debris and thus, the oxide / metal interface is effectively moving into the metal.

If the sizes of the particles forming the second phase are less than the critical oxide thickness ( $\xi$  from Quinn's oxidative wear theory [73]), then the second phase particles pass into the oxide layer as the metal oxidises. As their diameter is less than the critical thickness, they may not protrude above the surface of the oxide layer and thus cannot directly protect the matrix or impinge on the counterface material. The second phase particles are lost as the oxide layer breaks up at critical thickness to form debris. The only contribution may be to enhance the load-carrying capacity of the metallic matrix in supporting the oxide film.

Where the second phase particle size is only slightly greater than the critical oxide thickness (between  $\xi$  and  $3\xi$ ), there is a transition in the wear mechanism – this is referred to as the 'first stage'. Whilst a small quantity of the second phase may be removed with the oxide, as the oxide breaks up, most will remain embedded in the substrate or matrix. These particles protrude above the nominal surface of the interface and the counterface will slide over them. This continues until the oxide layer can reform and during this stage of wear, the matrix cannot influence the wear process – this is the 'second stage'.

The mechanical properties of the second phase influence what happens next during the 'second stage'. If the second phase particles are able to resist the sliding action and thus wear of these particles is low, then the matrix will be protected for a prolonged period and the 'second stage' will be extended. Enhanced wear of the counterface material by abrasion may occur at this stage. If they are not able to resist the sliding process and fail under the load from the counterface, then contact between matrix and counterface is quickly restored and the 'first stage' of wear will repeat itself. A further possibility is the detachment of the second phase particles as the oxide breaks up, with the presence of these particles as loose debris at the interface acting as third body abrasives – this occurs where cohesion between the matrix and the second phase is poor.

If the mean particle size is much greater than the critical oxide thickness, the particles show increased efficiency in providing oxidative wear protection to the material subject to wear. After break-up of the oxide layer (end of the 'first stage'), the harder second phase particles remain embedded in the matrix. Again, the main interaction is between the second phase particles and the counterface and it is this process, which controls the wear

mechanism – the matrix plays no direct part. The majority of the second phase particle is surrounded by the matrix, thus break-up is more difficult and detachment is almost impossible. Whilst this means that the matrix is well protected against wear, the counterface may undergo high rates of wear and thus becomes the main source of debris. The inference is here, that the first stage cannot resume until these larger particles have been worn near to the level of the rest of the sample surface and as other second phase particles will continue to be exposed elsewhere on the surface, first stage wear with the formation of a protective oxide layer cannot readily happen and severe wear will continue.

The four alloys in the current study are examples, viz:

1. Incoloy MA956 is an oxide dispersion strengthened (ODS) alloy in a body-centred cubic matrix of iron, chromium and some aluminium. The dispersoids [101] have been shown to consist of mixed yttrium and aluminium oxides in monoclinic ( $3Y_2O_3.5Al_2O_3$ ) and tetragonal ( $2Y_2O_3.Al_2O_3$ ) form, measured in this case as having diameters between 3 nm and 60 nm, the mean diameter being 9 nm. Elsewhere [103], an average diameter of 24 nm is quoted.
2. Nimonic 80A contains what is termed the  $\gamma'$  phase, normally very fine precipitates of the intermetallic  $Ni_3AlTi$  in a face-centred cubic matrix. The size of these precipitates can vary with heat treatment, with Fujita *et. al* [102] demonstrating an increase in size from 30 nm after 24 hours at 720°C to 125 nm after the same period at 875°C with Nimonic 80A. Precipitation can also occur on the grain boundaries [101], with precipitates apparent in the work of Fujita *et. al* [102] of up to 700 nm.
3. As already discussed, Stellite 6 consists of chromium carbides of the form  $M_7C_3$  and  $M_{23}C_6$  [97] in what is normally a cobalt-chromium hexagonal close-packed matrix. These should also form fine precipitates, however, grain boundary precipitates are observable in Figure 2.26, up to 30  $\mu m$  across.
4. The Incoloy 800HT matrix [105] also contains a fine dispersion of titanium nitrides, titanium carbides and chromium carbides of between 1  $\mu m$  and 3  $\mu m$  in size, in an austenitic face-centred cubic matrix. These are very few in number and concentration.

Glaze layers at most are only a few microns thick, however, with Incoloy MA956 and Nimonic 80A, comparisons with the studies of Vardavoulias [100] indicates that the second phase in each case is too small to affect the glaze forming process. However, if the greatly enlarged grain boundary carbide precipitates (up to 30  $\mu\text{m}$  across) are forming within the Stellite 6, then any material worn against the Stellite 6 should show poor relative wear properties. The work of Wood [1] and Rose [2] has given mixed results in this respect, with Incoloy MA956 readily forming a glaze layer and Nimonic 80A showing high levels of wear. The size of the carbide precipitates in Incoloy 800HT suggests it is borderline whether or not their presence will have any effect on glaze formation – their scarcity may limit any effect they may have. The continued formation of glaze on the sliding wear of either Incoloy MA956 or Nimonic 80A against Incoloy 800HT at and above 630°C [2] suggests no significant effect on glaze formation. The same applies for the like-on-like sliding of Incoloy 800HT at 750°C [2] – Rose’s friction data in each case show no sudden increases indicating a large-scale failure of the glaze layer.

## **2.8 Material Transfer and Mechanical Alloying**

Transfer of materials between wear surfaces is well reported in the literature and one clear example in previous work in AMRI is that reported by Rose [2], where Incoloy 800HT counterface material was transferred to the surfaces of Nimonic 80A samples at 270°C and 510°C.

Kerridge and Lancaster [106] reported, from tests using radioactive brass pins against hard steel rings, that the rate of transfer was equal to the rate of pin wear and that the wear debris was sourced from the transfer layer and not from the pin directly. Agglomeration was noted due to patches of transferred material on the ring surface being larger than individual transfer particles and the transfer particles were similar in size to the real areas of contact, thus the actual numbers of contacts was relatively small. The contact areas would be at the peaks of a small number of larger asperities, resulting from agglomeration of transfer particles on the wear surface.

Sawa and Rigney [107] studied the sliding of dual phase steels in air and under vacuum conditions, both self-mated and against molybdenum. A three-stage process was mapped out:

1. The first stage involved smooth sliding with low friction. Towards the end of the first stage, some fluctuations were noted – these were associated with discrete transfer events. These events indicated that larger scale transfer was about to occur.
2. The beginning of the second stage was indicated by a large increase in friction, followed by a gradual decrease, but with fluctuations still greater than for the initial stage. This marked the beginning of larger scale transfer and mixing.
3. Friction levels eventually approached an intermediate level with only moderate fluctuations. This indicated stage 3, with continuing mixing and transfer.

Sawa and Rigney [107] commented that spreading of transfer material and mixing with base material occurred during stages 2 and 3 (apparently neglecting the discrete transfer events during stage 1). The major transfer event at the beginning of stage 2 marked the start of this larger scale transfer, with the system only able to tolerate a certain critical amount of transfer before this major change occurred.

If it is considered that material transfer can occur due to debris from one surface attaching itself to the other, if debris is being generated by both interfaces, and that this debris is of a fine size, then a process similar to mechanical alloying via powder metallurgy methods is therefore possible. Where an alloy is produced deliberately via this route, in simple terms, the constituent parts are mixed in powder form in the proportions required in the final alloy. The powder is milled down and then sintered in the required shape [107,109]. Analogies can be seen with this in the sliding wear process, with the sliding surfaces providing the ‘milling’ action on the newly produced debris. Assuming atmospheric interaction to be minimal, these particles may adhere to one another and to the wear surfaces, producing a mechanically mixed layer. However, there are obvious differences between the two

Firstly, the proportions of material are not controlled and thus the mechanically mixed layer produced may be any proportion between the two. Although a 1:1 ratio is possible

for some combinations [35], a bias one way or the other is also likely – for example, copper worn against various steels [110] has been observed to produce a mostly copper nano-crystalline material with a relatively small number of iron crystals mechanically mixed in. The geometry of the wear arrangement may have a strong influence on this, with for example pin-on-disk configurations favouring transfer to the disk, in cases where hardness values are similar. Secondly, there is no control over the mixing process and therefore the composition of the mechanically mixed layer may vary over relatively short distances. It is possible for all stages of the process to occur simultaneously [35], thus some debris may have structures consistent with the early stages of the wear process when mixing is still incomplete. This mixture of compositions will also be detected in the debris produced from the mechanically mixed layer (which are limited in size to the thickness of this layer).

Chen [110] examined transfer under vacuum conditions for a number of simple metallic combinations. Initial ‘transfer events’ were demonstrated to involve discrete fragments of 1 to 30  $\mu\text{m}$ , these appearing after only a few millimetres of sliding. A lamellar structure was noted in the transfer debris, which would shear in the direction of sliding. Further work with copper and aluminium by Rigney [37] indicated a lamellar thickness of 0.3  $\mu\text{m}$  (noted in Section 2.3.2.3 on ‘Delamination and Fatigue Wear’), about the same thickness as the deformation subgrain structure adjacent to the surface – Rigney notes that it seems that the substructure developing during plastic deformation provides sufficient heterogeneity to allow shear instability, this forming part of the transfer process. The use of TEM allowed a much finer nano-crystalline substructure to be seen.

Rigney [37] further comments that transfer can be in either direction, although transfer in one direction may dominate – this will depend on the respective materials forming the wear pair. It is also commented that the transfer material tends to be patchy and continuous film on the surface rarely forms – high wear with fluctuating friction or smooth sliding with low wear may result.

## **2.9 Nano-scale Characterisation of Sliding Surfaces**

Nano-scale studies of sliding surfaces to date have been extremely limited and no attempt has yet been made to study high temperature glaze layers, using Scanning Tunnelling



Microscopy, Transmission Electron Microscopy or other similar techniques. However, the potential usefulness of TEM has been demonstrated by the study of the room temperature wear of PVD TiAlN/CrN super-lattice coatings [112], where crystallite sizes of  $11\pm 5$  nm were observed after wear. Atomic Force Microscopy studies made of wear tracks produced by the sliding of alumina in a humid environment [113], established that the resulting tribologically formed aluminium hydroxide film consisted of particles of size 20 to 50 nm – a likely formation route was deduced from  $\alpha$ -alumina debris particles of the same size.

TEM and STM characterisation work within AMRI [116, 118] on glaze layers of  $3.5\text{ }\mu\text{m}$  formed at high temperature (Nimonic 80A versus Stellite 6 at  $750^{\circ}\text{C}$ , block on cylinder configuration) has suggested that there is a variation in grain size with depth, starting at 5 to 15 nm up to  $1\text{ }\mu\text{m}$  depth, increasing to between 10 and  $50\text{ }\mu\text{m}$  between  $1\text{ }\mu\text{m}$  and the glaze-substrate interface at  $2.5\text{ }\mu\text{m}$ . A series of initial processes is proposed for the generation of the glaze layer, including deformation of the surface, intermixing of the debris from the sample and counterface surfaces undergoing wear, oxidation of the debris, further mixing and repeated welding and fracture. This is followed by the development of a highly mis-oriented grain structure and the development of nano-sized grains within the glaze layer. This is discussed in more detail in Section 6.3.

## **2.10 Previous Work within the University of Northumbria**

Most of the previous work in the area of high temperature wear ( $200^{\circ}\text{C}$  and above) has concentrated on wear systems consisting of two similar materials in contact. Work within the Surface Engineering Research Group (SERG) by Wood [1,3] and the Advanced Materials Research Institute (AMRI) by Rose [2] involved studies of high temperature wear (up to  $750^{\circ}\text{C}$ ) in systems consisting of dissimilar materials combinations, over a wide range of conditions and temperatures. Wood showed that the combination of materials used strongly influenced the ease with which glaze formation resulted. The use of the high cobalt-chromium alloy Stellite 6 as a counterface material in contact with iron-chromium-based Incoloy MA956 in particular, was shown to promote glaze and compacted oxide formation, keeping wear to very low levels, compared to other combinations where cobalt was absent. Also, regardless of the combinations used,



geometry was apparently an important factor in the wear process, with transfer of material from the counterface to the sample being the preferred option.

Work on the influence of temperature by both Wood and particularly by Rose, showed a variation in wear behaviour with temperature. Rose showed that at lower temperatures (below 450°C), the presence of cobalt in Stellite 6 again promoted the formation of oxide debris leading to reduced wear in combination with iron-chromium-based Incoloy MA956 and also Nimonic 80A, a high nickel-chromium alloy, in the form of loose debris which separated the interfaces and prevented metal-to-metal contact. The use of an alternative counterface (Incoloy 800HT, an iron-nickel-chromium alloy with a small amount of aluminium) resulted in radically different behaviour, specifically the transfer of metal to form a work hardened layer on the surface of the sample, with no oxide present to separate the interfaces.

Intermediate temperatures (450°C for Incoloy MA956 / Stellite 6, 450°C and above for Nimonic 80A / Stellite 6 and up to 630°C for Incoloy MA956 / Incoloy 800HT and Nimonic 80A / Incoloy 800HT) in all cases brought about a severe wear regime with exposed metal at the wear interface and metallic debris production. Higher temperatures resulted in increased oxidation promoting glaze formation, although only on Stellite 6 with continued high wear in the case of Nimonic 80A / Stellite 6. Rose [2] explained this intermediate region of severe wear in terms of loss of strength of the metal substrate.

However, it is to be pointed out that in two cases (Nimonic 80A / Incoloy 800HT and Incoloy MA956 / Stellite 6), the metal substrate was able to support the oxide 'glaze' formed, at even higher temperatures when it would be expected for the metal substrate to offer even less support. The apparent absence of the oxide debris from the metal surfaces is also not explained, where severe wear occurs at intermediate temperatures. Rose does make comment that at temperatures just below this severe wear region, some smearing of oxide particles is observed – this indicates a possibility that these particles fail to support the applied load and thus allow contact of the wear interfaces. Non-detection of this oxide under conditions where a severe wear mechanism was dominant may be explained by the continual removal of metallic debris from the wear surfaces, removing any traces of oxide with the debris and preventing any significant build-up of oxide.

At the highest temperatures tested (up to 750°C), Rose reported that all combinations except for the Nimonic 80A / Stellite 6 combination showed glaze formation covering the sample surfaces, accompanied by oxide debris production, albeit with some enhanced wear for the Incoloy MA956 / Incoloy 800HT combination. For Nimonic 80A / Stellite 6 there were apparent contradictions in the findings of Wood and Rose, with Wood [1] reporting traces of glaze on the Nimonic 80A sample, but no accumulation to form glaze platforms, whilst Rose [2] reported an absence of glaze-type material from the sample (only appearing in a patchy unstable form, that was readily visible on the Stellite 6 counterface) with only trace amounts of nickel oxide present on the sample wear scar. Also, Wood did not report a glaze from the Incoloy MA956 / Incoloy 800HT combination, but did report a mixed oxide layer of aluminium, iron and chromium. Rose on the other hand, reported a glaze consisting of iron-chromium oxide.

A further difficulty arises when considering the work of Vardavoulas [100] in relation to the sliding experiments with Stellite 6 [1,2]. With carbide grain boundary precipitates of up to 30 µm across (Figure 2.26), compared to glaze layers of only a few microns, then any material worn against Stellite 6 should have exhibited high levels of wear and failed to form a glaze layer. Incoloy MA956 readily developed a glaze layer, including material from the Stellite 6. No glaze formation was reported by Rose [2] in the case of Nimonic 80A either as the sample or counterface material, with a glaze layer developing only on the Stellite 6. This was attributed to a combination of insufficient adhesion of the oxides formed, combined with ‘ploughing’ and ‘abrasive effects’ of hard particles in the Stellite 6. However, the formation of a protective layer on the Stellite 6 itself, developing from material largely sourced from the Nimonic 80A suggests that any embedded carbides would have had an extremely limited effect. This suggests that the carbides may have been to some degree, sealed off by formation of this layer and thus any effect they may have had, was probably restricted to the very early stages of sliding.

The present work has been designed to extend the high temperature wear work involving studies of different combinations of materials and process variables taking into account many of the unexplained phenomena arising from the work of Wood and Rose.

### 3. INTRODUCTION TO THE CURRENT INVESTIGATION

The literature review presented in Chapter 2 indicates that much work has been done on the formation of compacted oxides / glazes. Glaze formation has been observed to accompany the process for fretting wear involving like-on-like systems and low amplitude sliding wear. Stott, Lin and Wood [4] established that these ‘glazes’ were in fact fine crystalline materials, formed from the oxide debris generated during sliding wear. Mechanisms have been proposed to explain the formation of glaze layers during high temperature wear which included the ‘total oxidation’, ‘oxidation-scrape-reoxidation’ and ‘metal debris’ mechanisms [62] detailed in the literature review (Chapter 2) and later work [70] addressed the generation of the ‘glazes’ from the debris present on the surface.

Until recently, such work has been largely concentrated on ‘like-on-like’ systems. There have also been few systematic studies involving a range of temperatures and speed. A further weakness in the field of high temperature wear has been that such studies did not explore the critical conditions necessary for the formation of glazes – minimum amount of debris required, the extend of the ability of the material involved to undergo oxidation (oxidation resistance) and the required temperature and speed ranges. Key examples include work carried out by Leheup and Pendlebury [42], and Colombie *et al.* [43], where a flow of air or nitrogen reduced oxide debris retention at low temperature, but did not prevent glaze formation at higher temperature. Similar results were obtained by Wood [1] and Rose [2], using a ‘block-on-cylinder’ configuration that does not encourage high debris residency at the wear interface (Figures 4.1 and 4.2 show this ‘block-on-cylinder’ configuration, also used in current study) – glaze layers were observed to form under varying conditions of load at high temperature (510°C to 750°C).

The studies of Wood [1] and Rose [2] were additionally carried out on unlike-on-unlike superalloy systems, which also have been little studied. However, these limited debris retention, variable load, high temperature (up to 750°C) studies have not to date examined the effect of sliding speed under such conditions.

The most important weakness has been the lack of detailed structural investigations, particularly at the nano-scale using TEM and STM.

The current work was undertaken to address some of these gaps. Firstly, the testing into the effect of variation of physical variables started by Rose was expanded upon, by looking at the effects of sliding speed on the wear process. As with Rose [2], the four alloy pairs chosen as representative by Wood [1] as exhibiting complex wear behaviour were used, these being Incoloy MA956 and Nimonic 80A as sample materials worn against Stellite 6 and Incoloy 800HT counterfaces. Selected sliding speeds both faster and slower than the  $0.654 \text{ m.s}^{-1}$  used by Wood [1] and Rose [2] were used ( $0.314 \text{ m.s}^{-1}$  and  $0.905 \text{ m.s}^{-1}$ ), with observations concentrating on the effect this has on compact oxide formation – previous work has suggested enhanced glaze formation due to frictional heating [23, 70, 79], break-down and enhanced or severe wear [90], or a complex relationship where both are seen dependent on the combination of conditions [2, 16, 17, 22, 29, 91, 92, 98].

With reference to the experimental data obtained, one sliding combination (Nimonic 80A versus Stellite 6) was selected for further study, including:

- 1) Testing over a range of sliding distances / times at one sliding speed, to more closely study the development of oxide and glaze layers. This study was conducted at two different temperatures (again selected with reference to experimental data), to study the effect of temperature on the glaze-forming process.
- 2) Reversal of sample and counterface, to enable greater study of the changes of wear mechanism with relation to the second member of the wear combination with relation to sliding speed.
- 3) Substitution of one of the alloys with a pure metal, to examine the effects of the elimination of alloying components from the wear process.

Most importantly in this study, Transmission Electron Microscopy and Scanning Tunnelling Microscopy have been used to characterise glaze and debris layers at the nano-scale level (formed during the sliding of Nimonic 80A versus Stellite 6 at  $750^{\circ}\text{C}$  and  $0.314 \text{ m.s}^{-1}$ ) and provide far more detailed structural information. Such techniques have been used not only to study the morphology and topography of the grains, but also the sub-grain structure, grain orientation and dislocation distribution within the glaze and debris layers. In support of these nano-scale studies, preliminary nano-hardness testing

was conducted, in order to more accurately ascertain the true hardness levels of some of the glaze layers formed.

## 4. EXPERIMENTAL

### 4.1 Apparatus and Materials

#### 4.1.1 Apparatus

The rig was basically a ‘block-on-cylinder’ arrangement, as shown in Figures 4.1 and 4.2, the cylinder being referred to as the ‘counterface’ and the block being the ‘sample’. The samples used were rectangular in shape of dimensions 45 mm x 5 mm x 5 mm, while the counterface had a diameter of 50 mm and also a length of 50 mm (Figure 4.3). The counterface was attached to a rotating shaft powered by a variable speed electric motor, the rotational speed of this ‘counterface’ shaft nominally set to  $0.314 \text{ m.s}^{-1}$  (120 r.p.m.), although it was possible to set to any speed between  $0.314 \text{ m.s}^{-1}$  (120 r.p.m.) and  $0.905 \text{ m.s}^{-1}$  (320 r.p.m.). A digital torque transducer was used to calibrate the setting for each speed used.

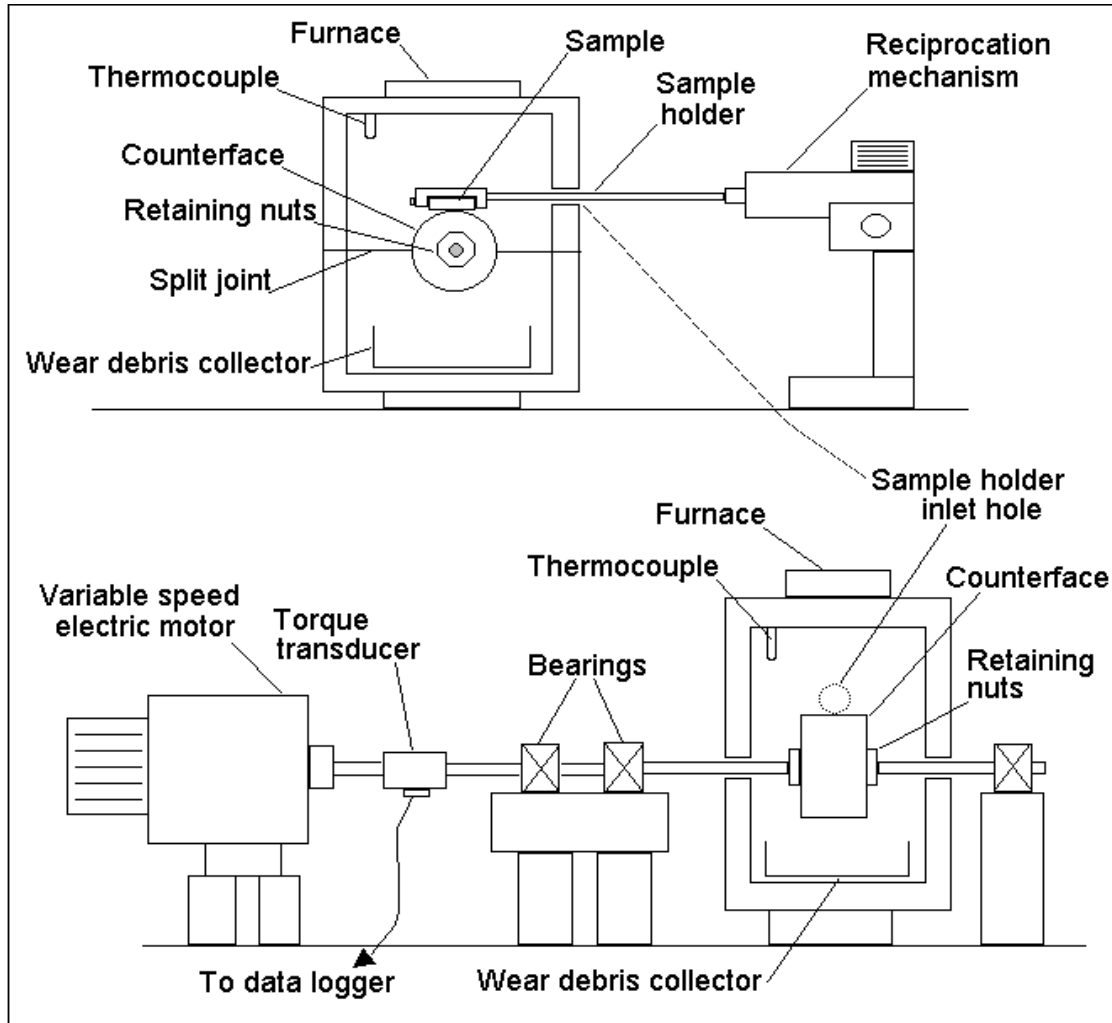
The sample was held in a holder ‘arm’, capable of reciprocation back and forth approximately 12 mm, 3 times a minute. Normal load at the point of contact on the counterface of this sample arm was 7 N, but addition of weights attached by a holder can increase this to 25 N. The sample and counterface were retained within a furnace capable of operating between room temperature and  $750^{\circ}\text{C}$ . A debris collection tray was placed in the bottom of this furnace, to catch any debris ejected from the sample or counterface during testing.

The rig was operated under the conditions shown in Table 4.1, unless experimental requirements dictated that some or all of these parameters had to be varied.

Each sample was weighed before and after testing, using a *Sartorius analytical microbalance* model number *MC210SN*. The ‘after test’ weight was subtracted from the ‘before test’ weight to obtain the weight change, which was converted to a mean wear rate covering the duration of the test using:

$$w = \frac{\Delta M \times 10^6}{d} \quad \{4.1\}$$

**Figure 4.1: Reciprocating high temperature block-on-cylinder wear rig, as used in the experimental programme**



where:

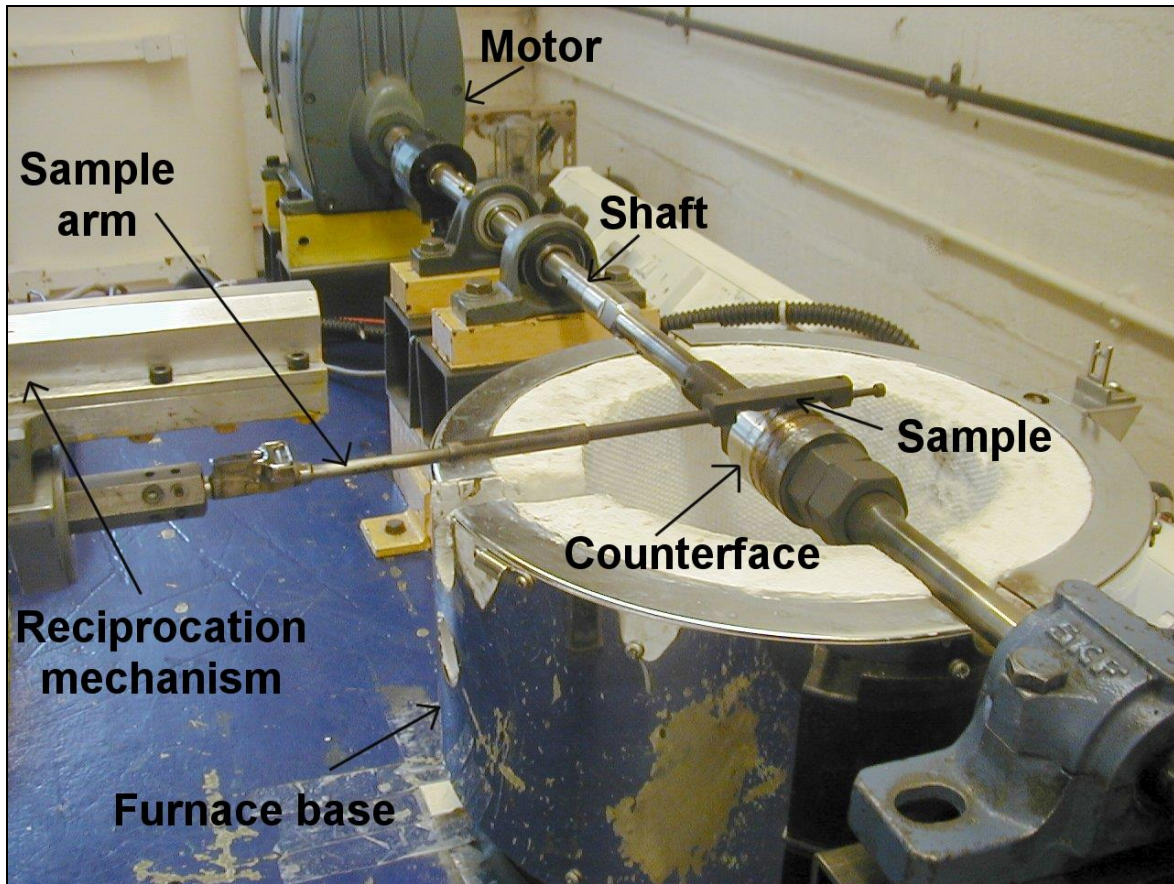
- $w$  - wear rate in micrograms per metre or  $\mu\text{g.m}^{-1}$ ;
- $\Delta M$  - change in weight or mass of sample in grams;
- $d$  - total sliding distance in metres.

To obtain the wear rate for a given segment of sliding distance (between distance  $d_1$  and  $d_2$ ) during a sliding test, this is modified to:

$$w_{d_1 \text{ to } d_2} = \frac{(\Delta M_2 - \Delta M_1) \times 10^6}{d_2 - d_1} \quad \{4.2\}$$



**Figure 4.2:** Wear rig furnace, showing sample arm (with sample), shaft and counterface in position for testing



For example, if the total sliding distance is 13,032 m and only the wear rate between 4,522 m and 13,032 m (say after glaze formation) is required, then equation {4.2} becomes:

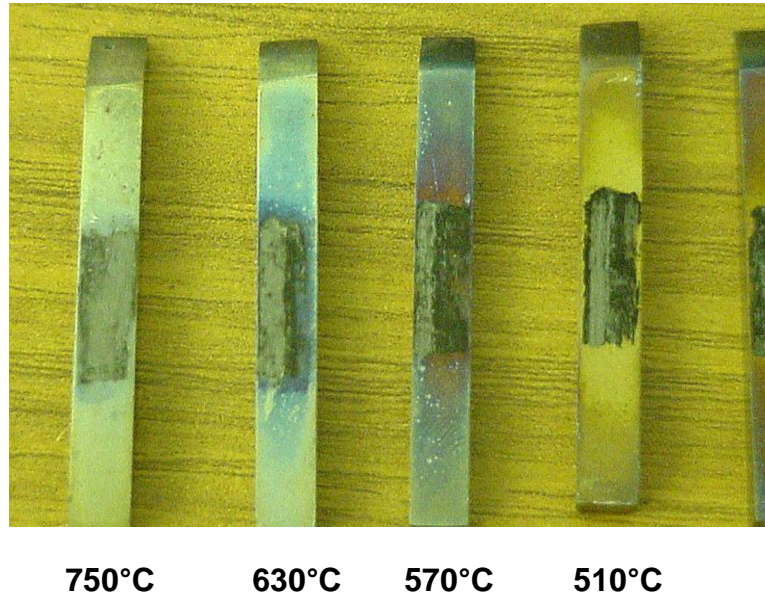
$$W_{4,522m \text{ to } 13,032m} = \frac{(\Delta M_{13,032m} - \Delta M_{4,522m}) \times 10^6}{13,032 - 4,522} \quad \{4.3\}$$

The coefficient of friction data were collected by a *Melbourne type TRP-50* torque transducer attached to the ‘counterface’ shaft, the output being shown in millivolts by a *Thurlby multimeter and data logger*, model number 1905a. These values were converted to coefficient of friction by the following formula {4.4}, either manually or via spreadsheet on a standard PC compatible microcomputer.



**Figure 4.3:** Typical samples used for wear tests

The examples shown are Nimonic 80A wear tested against Stellite 6 (load = 7N, sliding speed =  $0.314 \text{ m.s}^{-1}$ , sliding distance = 4,522 m), test temperatures indicated. Each sample is of dimensions 45 x 5 x 5 mm.



**Table 4.1:** Standard conditions used in wear rig operation, unless stated elsewhere

<b>Temperature:</b>	750°C (also used at room temperature, 270°C, 390°C, 450°C, 510°C, 570°C, 630°C and 690°C)
<b>Load:</b>	7 N
<b>Counterface rotational speed:</b>	$0.314 \text{ m.s}^{-1}$ ( $0.905 \text{ m.s}^{-1}$ for high sliding speed tests)
<b>Sliding distance:</b>	4,522 m at $0.314 \text{ m.s}^{-1}$ 4,522 m and 13,032 m at $0.905 \text{ m.s}^{-1}$
<b>Environment:</b>	Air
<b>Reciprocation:</b>	On, but can be switched to “off” for non-reciprocation tests

$$V_{\omega metal} = V - \left( \left( 1 - \frac{t}{t_f} \right) V_o + \frac{t}{t_f} V_f \right) \quad \text{then} \quad \mu = \frac{F}{W} = \frac{T/r}{W} = \left( \frac{V_{\omega metal} \times 3.02}{r} \right) / W \quad \{4.4\}$$

where  $\mu$  is the coefficient of friction,  $F$  is frictional force,  $W$  is applied load,  $T$  is torque in Nm,  $r$  is counterface radius in m,  $t$  is the current time,  $t_f$  is the final time,  $V$  is the data logger reading in millivolts, with  $V_f$  and  $V_o$  being the readings in millivolts at the beginning and end of testing. 3.02 is an equipment-specific correction factor to convert voltage readings into torque.

#### 4.1.2 Materials Used

The four main wear pairs used for experimentation are detailed in Table 4.2. The compositions of each of these materials are as detailed in Table 4.3.

**Table 4.2: Main wear pairs used during testing**

Sample	Counterface
Nimonic 80A	Stellite 6
Incoloy MA956	Stellite 6
Nimonic 80A	Incoloy 800HT
Incoloy MA956	Incoloy 800HT

**Table 4.3: Nominal compositions of alloys in wt%**

	Fe	Ni	Cr	Al	Ti	Mn	W	Co	Si	C	Yt O
Incoloy MA956	74	-	20	4.5	0.5	0.05	-	-	-	-	0.5
Nimonic 80A	0.7	75.8	19.4	1.4	2.5	-	-	-	0.1	0.08	-
Stellite 6	2.5 max	2.5 max	27	-	-	1	5	60	1	1	-
Incoloy 800HT	43.8	32.5	21.0	0.37	0.37	1.5 max	-	-	0.4	0.1 max	-

## 4.2 Wear Testing

### 4.2.1 Room Temperature to 750°C, at 0.314 m.s<sup>-1</sup> and 0.905 m.s<sup>-1</sup>

The four main wear pairs detailed in Table 4.2 each underwent testing at sliding speeds of 0.314 and 0.905 m.s<sup>-1</sup>, at temperatures of 20 (room temperature), 270, 390, 450, 510, 570, 630, 690 and 750°C. The sliding distance was fixed at 4,522 m, corresponding to 4 hours at 0.314 m.s<sup>-1</sup>. Friction values were taken every 94.2 m, corresponding to one time interval every 300 seconds (5 minutes) at 0.314 m.s<sup>-1</sup>. At 0.905 m.s<sup>-1</sup>, the total sliding time and time interval between friction readings were 1 hour 23 minutes and 104 seconds respectively. Tests were all replicated twice, with further tests conducted where results were dubious or extra tests on slid samples were required (i.e. micro-hardness, nano-scale characterisation) – further replication was usually unnecessary, due to the generally good reproducibility of weight change and coefficient of friction data.

The following observations were made:

- range of low temperature oxidational wear (if any);
- range of intermediate severe wear (if any);
- range of high temperature oxidational wear (if any);
- weight change of sample;
- mean wear rate of sample over total sliding distance for test, with the exception of 0.905 m.s<sup>-1</sup>, 13,032 m, where the wear rates between 0 and 4,522 m, and between 4,522 and 13,032 m were calculated – this enabled the effect of change of wear mode on wear rate to be observed, should a change in wear mode be observed during sliding.

From the data obtained, estimates of transition temperature between each range were made and studies were carried out, using a range of characterisation techniques (further details are provided in Section 4.2.2):

- *Scanning Electron Microscopy (SEM)*

Used to study the morphology of the wear surfaces and changes in morphology resulting from changes in sliding parameters.

- *Energy Dispersive X-ray Spectroscopy (EDX), EDX mapping and Autopoint EDX*

Used to provide data on composition of surface deposits. Mapping and Autopoint were used to study variations in composition, creating composition profiles.

- *Standard X-ray Diffraction (XRD) and Glancing Angle XRD (where appropriate)*

Used in conjunction with EDX to determine the phases of material present. Glancing Angle XRD was used on selected samples, to study potential variation of phases with depth within any surface deposits formed.

- *Micro-hardness*

Depth profiles for micro-hardness data at room temperature, were made for samples slid at room temperature, 270°C, 510°C and 750°C for each main test combination (0.314 m.s<sup>-1</sup> and 0.905 m.s<sup>-1</sup>). Micro-hardness data was also obtained for the glaze layers and surface deposits formed for each main test combination (0.314 m.s<sup>-1</sup> and 0.905 m.s<sup>-1</sup>) at 750°C and also for any work-hardened metallic transfer layers formed at lower temperatures (to ascertain the level of work-hardening).

- *Transmission Electron Microscopy (TEM) and Scanning Tunnelling Microscopy (STM)*

Experimental work carried out during the early stages of this project indicated that Nimonic 80A worn against Stellite 6 from 510°C upwards, resulted in glaze formation only with the least severe sliding conditions covered by the experimental work (0.314 m.s<sup>-1</sup>, 4,522 m). In order to obtain further information about glaze and compacted oxide formation, the 750°C case was selected for further study using these techniques. The use of TEM and STM allowed the study of the glazes at nano-scale level.

These characterisation techniques were used to study and observe the predominant factors during each type of wear and the effect of temperature and sample and counterface materials on these factors. Emphasis was put on the study of glaze and debris composition, to observe the key components of the oxides formed and thus those components most likely to encourage glaze formation.

Additionally, further tests were carried out at  $0.905 \text{ m.s}^{-1}$  over an increased sliding distance of 13,032 m (equivalent to 4 hours sliding time), to compare weight losses between reduced and extended sliding. This was used as a confirmatory test, to find in the case of a glaze forming on a sample, the effect of glaze formation on weight loss and wear rate, compared to samples tested at 1 hour 23 minutes. The four-hour data were also used for the comparison of friction at different sliding speeds, due to the greater time period available after the initial period of severe wear. This allowed time for the friction readings to settle and give a better estimate of friction for each of the tests done at  $0.905 \text{ m.s}^{-1}$ . Friction readings for these 13,032 m samples were carried out once again at intervals of 300 seconds, equivalent to a sliding distance between friction readings of 271.5 m.

#### ***4.2.2 Nimonic 80A versus Stellite 6 – In-depth Studies***

##### ***4.2.2.1 Build-Up of Glaze with Time***

Based upon test information obtained, supplementary testing was carried out at temperatures of  $510^{\circ}\text{C}$  and  $750^{\circ}\text{C}$  at a sliding speed of  $0.314 \text{ m.s}^{-1}$  over the time intervals listed in Table 4.5, to study the build-up of any glaze layers formed. Listed alongside are the equivalent sliding distances.

The wear rate data in this case was calculated between each test distance and the previous one using equation {4.2}, to allow for an accurate assessment of the amount of wear occurring at any given stage of the sliding process.

##### ***4.2.2.2 Reversal of Sample and Counterface – Stellite 6 versus Nimonic 80A at $750^{\circ}\text{C}$***

The sliding tests for the Stellite 6 / Nimonic 80A system at  $750^{\circ}\text{C}$ , were repeated using the same sliding conditions as for the main test programme (7N load, over a sliding distance of 4,522 m) at sliding speeds of  $0.314 \text{ m.s}^{-1}$  and  $0.905 \text{ m.s}^{-1}$ , however, with the Stellite 6 as the sample material and the Nimonic 80A as the counterface material. The wear surfaces and changes in wear scar morphology of the surface of the Stellite 6 were then studied using SEM, with EDX and XRD used to study compositional information of any surface deposits formed. The effects (if any) of the carbide second phase in the Stellite 6 were also investigated.

**Table 4.5: Sliding times and equivalent distances for timed tests of Nimonic 80A versus Stellite 6**

(load = 7N, sliding speed =  $0.314 \text{ m.s}^{-1}$ , temperature =  $510^{\circ}\text{C} / 750^{\circ}\text{C}$ )

Sliding time (minutes)	Sliding distance (metres)
2	38
10	188
15	283
20	377
30	565
60	1,130
120	2,261
240	4,522

#### 4.2.2.3 Nickel 200<sup>TM</sup> versus Stellite 6 at $750^{\circ}\text{C}$

Nickel 200<sup>TM</sup> (99% purity nickel – replacing the Nimonic 80A and thus eliminating the chromium content) was slid against Stellite 6 at  $750^{\circ}\text{C}$  at sliding speeds of  $0.314 \text{ m.s}^{-1}$  and  $0.905 \text{ m.s}^{-1}$ , over a distance of 4,522 m. Note was made of the differences in wear scar morphology and debris composition between Nickel 200<sup>TM</sup> and Nimonic 80A as the sample material.

#### 4.2.3 Switching off reciprocation – Nimonic 80A versus Incoloy 800HT and Incoloy MA956 versus Incoloy 800HT at $510^{\circ}\text{C}$ and $0.314 \text{ m.s}^{-1}$

Based upon test information obtained, the sliding of both Nimonic 80A versus Incoloy 800HT and Incoloy MA956 versus Incoloy 800HT at  $510^{\circ}\text{C}$  and  $0.314 \text{ m.s}^{-1}$ , over a sliding distance of 4,522 m under an applied load of 7N was repeated, but with the reciprocation mechanism in the sample arm switched off throughout testing. By switching off the reciprocation mechanism, it was hoped to enhance the debris retention sufficiently to allow the development of oxide layers, under a set of conditions where previously oxide had been observed but had not developed into glaze.

### 4.3 Structural Analysis

#### 4.3.1 *Scanning Electron Microscopy with Energy Dispersive Spectroscopy*

The primary method of characterisation used for wear scar and debris was scanning electron microscopy, using an *Hitachi SM2400* scanning electron microscope. This was also used to conduct Energy Dispersive X-Ray Spectroscopy (EDX) to determine wear scar deposit and debris compositions.

EDX ‘Digimaps’ (plots of concentration of a selected element) and Autopoint data (EDX at regularly spaced intervals) were also used to study the variation in composition of cross-sectional profiles of selected samples. During the current experimental programme, particular emphasis was placed upon the 750°C samples, as these contained the best deposits for analysis [1,2]. The purpose of this was to ascertain the composition of each of the layers created during sliding, leading to glaze formation. Oxygen was not included in the Autopoint EDX analysis data, in order to see clearly the variations of alloy components with respect to each other through the glaze and mixed debris layers. A profile for overall oxygen content was obtained in each case, however, due to limitations of the EDX facilities within AMRI (oxygen was on the lower limit of what could be detected), the data provided could only be regarded as a rough guide to the presence of oxygen at any point of measurement.

#### 4.3.2 *X-ray Diffraction*

X-ray Diffraction (XRD) was used to determine the phases present on the wear scar, utilising a *Siemens Diffraktometer 5000* diffractometer. Standard XRD diffractograms were collected with a locked detector tube, between ‘ $2\theta$ ’ angles of 10 to 90° (‘ $\theta$ ’ being the angle of incidence of the X-rays), with interpretation of the data carried out using the associated *DIFAC-DOS/DIFAC+* software and diffraction pattern database.

Glancing angle XRD was conducted on selected 750°C samples (where previous testing [1,2] indicated that the best ‘glaze’ layers were formed) in order to achieve a depth profile of phases present through the glaze layer. In practice, the need for a ‘flat surface’ for effective Glancing Angle XRD meant that experimentation was restricted to the 0.314 m.s<sup>-1</sup> samples. Samples were selected which had a smooth flat wear surface, these giving the clearest noise-free plots for a reasonable  $2\theta$  dwell time (i.e. 3 seconds, giving a

total test time of 16 hours), from which usable sets of results could be obtained. The ' $2\theta$ ' range of angles in this case was  $10^\circ$  to  $100^\circ$ , with successive runs being conducted at detector tube angles of  $1^\circ$ ,  $2^\circ$ ,  $3^\circ$ ,  $5^\circ$ ,  $7^\circ$  and  $9^\circ$ .

#### 4.3.3 Micro-hardness Tests

Micro-hardness tests were carried out using a *Buehler Micromet II* micro-hardness tester, on cross-sections of samples of all four material combinations, slid for 4,522 m at  $0.314 \text{ m.s}^{-1}$  and  $0.905 \text{ m.s}^{-1}$  respectively and at room temperature,  $270^\circ\text{C}$ ,  $510^\circ\text{C}$  and  $750^\circ\text{C}$ . Testing started just below the surface and continued up to 1 mm depth into the sample, at intervals of approximately  $30\mu\text{m}$  for the first  $150\mu\text{m}$ ,  $50\mu\text{m}$  up to  $300\mu\text{m}$ , then intervals of  $100\mu\text{m}$  thereafter. A Vickers diamond indenter was used, with a test load of 50 g and a dwell time of 12 seconds. Samples were polished to  $0.25\mu\text{m}$  using a diamond paste.

Additionally, further micro-hardness tests were carried out using the same test parameters on any surface deposits formed on the  $750^\circ\text{C}$  samples and also on any metallic transfer layers formed at lower temperatures (typically, these formed at room temperature and  $270^\circ\text{C}$ ), to ascertain the degree of work-hardening.

Results are presented in GPa, which can be converted to standard Vickers hardness numbers (in  $\text{kg.mm}^{-2}$ ) by dividing by 1,000 and multiplying by 9.81.

#### 4.3.4 Nano-hardness Tests

A number of nano-indentation tests were carried out using a Hysitron nano-indenter with a 150 nm Berkovich three-sided pyramidal indenter at the University of Newcastle upon Tyne (key specifications in Table 4.6), on glaze layers formed during high temperature sliding wear. The samples used for these tests were Incoloy MA956 samples slid at  $0.314 \text{ m.s}^{-1}$  and  $750^\circ\text{C}$ , and Nimonic 80A samples slid at  $0.314 \text{ m.s}^{-1}$  for temperatures of  $510^\circ\text{C}$  and  $750^\circ\text{C}$ . The values obtained were compared with those obtained for micro-hardness, the objective being to show the greater usefulness of nano-hardness data in determining glaze layer properties. The test time in each case was ten seconds, with a five second ramp up period to maximum load and five second ramp down period back to zero load (Figure 4.4). The maximum load used varied between  $500\mu\text{N}$  and  $10,000\mu\text{N}$ ,



the higher loads used more especially on the first batch of samples tested, the Incoloy MA956. This was to ascertain the maximum load that could be used without the nano-indenter penetrating the glaze layer, into the substrate or in some cases, the powdery layer beneath. The full set of loading parameters are presented in Table 4.7, with obtained experimental data in Table 5.9.

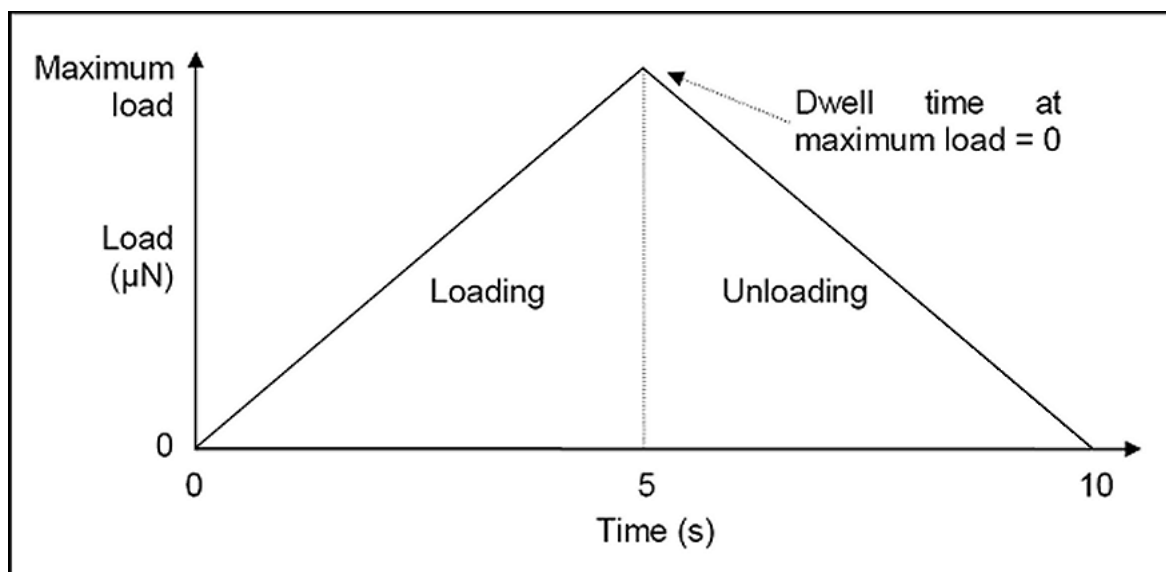
#### 4.3.5 Transmission Electron Microscopy (TEM)

A Phillips CH 20 Transmission Electron Microscope, based at Sheffield Hallam University, was used to determine the structures and sub-structures of the glazed layers formed between Nimonic 80A and Stellite 6 during sliding at  $0.314 \text{ m.s}^{-1}$  / 4,522 m and  $750^\circ\text{C}$ . The Transmission Electron Microscope was operated at 200 kV with an ‘ $\omega$ ’ filament. Further single point EDX studies were carried out in conjunction with this.

#### 4.3.6 Scanning Tunnelling Microscopy (STM)

STM was conducted on glaze layers formed between Nimonic 80A and Stellite 6 during sliding at  $0.314 \text{ m.s}^{-1}$  / 4,522 m and  $750^\circ\text{C}$ , using a commercial variable temperature VT-STM/AFM system in UHV condition (Omicron GmbH, Germany). The experiments were performed in constant current mode (1 nA) with a base pressure of  $2 \times 10^{-5} \text{ N.m}^{-2}$ . The tips used during experimentation were prepared by the mechanical cutting of 90%Pt-10%Ir alloy wires.

**Figure 4.4:** Loading profile for nano-indentation tests conducted on glaze layers



**Table 4.6: Key specifications for Hysitron Triboindenter used for nano-indentation tests**

Indenter:	Berkovich, 150 nm
Transducer:	
Z-Axis (Vertical):	
Maximum force:	30 mN
Load resolution:	<1 nN
Load noise floor:	100 nN
Maximum displacement:	30 $\mu\text{m}$
Displacement resolution:	0.0002 nm
Displacement noise floor:	0.2 nm
Thermal drift:	<0.05 nm.s <sup>-1</sup>

**Table 4.7: Nominal load parameters used for nano-indentation tests on Nimonic 80A samples slid against Stellite 6 at 510°C and 750°C, also Incoloy MA956 samples slid against Stellite 6 at 750°C**

Sample Material	Test 1 ( $\mu\text{N}$ )	Test 2 ( $\mu\text{N}$ )	Test 3 ( $\mu\text{N}$ )	Test 4 ( $\mu\text{N}$ )	Test 5 ( $\mu\text{N}$ )	Test 6 ( $\mu\text{N}$ )
<b><i>Incoloy MA956 (750°C)</i></b>	1,000	5,000	10,000	500	1,000	10,000
<b><i>Nimonic 80A (510°C)</i></b>	5,000	5,000	5,000	5,000	-	-
<b><i>Nimonic 80A (750°C)</i></b>	5,000	5,000	5,000	1,000	-	-

## 5. RESULTS

This chapter is divided into three main sections:

- **Section 5.1** reports on the wear testing of Nimonic 80A as the sample material versus Stellite 6 as the counterface at sliding speeds of  $0.314 \text{ m.s}^{-1}$  and  $0.905 \text{ m.s}^{-1}$ , discussing the collected friction and weight change data. Also covered is associated characterisation work, including optical microscopy, SEM, EDX (including Autopoint), XRD (including Glancing Angle) and micro-hardness testing.
- **Section 5.2** discusses the more in-depth study of the Nimonic 80A versus Stellite 6 combination. This begins with a closer study of what happens when the sample and counterface materials are reversed at  $0.314 \text{ m.s}^{-1}$  and  $0.905 \text{ m.s}^{-1}$ . Other studies look at the development of compacted oxides at  $510^{\circ}\text{C}$  and  $750^{\circ}\text{C}$  with increasing distance / time at  $0.314 \text{ m.s}^{-1}$  and the effect of the substitution of Nimonic 80A with Nickel 200<sup>TM</sup> (99% purity nickel) when slid against Stellite 6 at  $750^{\circ}\text{C}$ .
- **Section 5.3** reports on the wear testing of Incoloy MA956 as the sample material versus Stellite 6 as the counterface at sliding speeds of  $0.314 \text{ m.s}^{-1}$  and  $0.905 \text{ m.s}^{-1}$ , again looking at the collected friction and weight change data. Information collected from optical microscopy, SEM, EDX (including Autopoint), XRD (including Glancing Angle) and micro-hardness testing are once again examined.
- **Section 5.4** does likewise for Nimonic 80A versus Incoloy 800HT.
- **Section 5.5** discusses identical testing for the Incoloy MA956 versus Incoloy 800HT wear pair.
- **Section 5.6** examines the nano-characterisation work carried out on the glaze formed on Nimonic 80A, when slid against Stellite 6 at  $0.314 \text{ m.s}^{-1}$  and  $750^{\circ}\text{C}$  – results are presented for TEM and STM. This section also discusses initial studies of nano-hardness for glaze layers formed at both  $510^{\circ}\text{C}$  and  $750^{\circ}\text{C}$ , by the sliding of Nimonic 80A against Stellite 6 and also at  $750^{\circ}\text{C}$  for the Incoloy MA956 / Stellite 6 (counterface) system, both combinations again slid at  $0.314 \text{ m.s}^{-1}$ .

## 5.1 Testing of Nimonic 80A versus Stellite 6 between Room Temperature and 750°C, at 0.314 and 0.905 m.s<sup>-1</sup>

### 5.1.1 Experimental Observations – Nimonic 80A versus Stellite 6

Figure 5.1 shows the variation of weight loss (in grams) and wear rate (defined in this thesis as  $\mu\text{g.m}^{-1}$ ) with temperature for the Nimonic 80A / Stellite 6 (counterface) system, in the room temperature to 750°C temperature range. The weight loss and wear rate behaviour observed at 0.314 m.s<sup>-1</sup> (after 4,522 m of sliding) and 0.905 m.s<sup>-1</sup> (after 4,522 m and 13,032 m of sliding) is described in this section.

#### a) Weight change and wear rate data at 0.314 m.s<sup>-1</sup> / 4,522 m

Extremely low weight losses from the Nimonic 80A as the sample material were recorded at all temperatures between room temperature and 390°C at 0.314 m.s<sup>-1</sup> / 4,522 m, with a largest mean change of -0.002(4) g at 270°C (the negative value of weight change indicates it is a weight loss). Slight gains in Nimonic 80A sample weight were observed for all test temperatures between 450°C and 750°C, with maximum mean values at 510°C and 630°C of 0.001(1) g and 0.001(4) g respectively. One exception to this was a loss at 570°C, with a mean change of -0.003(3) g.

The wear rate data (in  $\mu\text{g.m}^{-1}$ ) at 0.314 m.s<sup>-1</sup> / 4,522 m followed a profile indicating highest wear rates matching the largest weight losses from the Nimonic 80A over the range of studied temperatures (room temperature to 750°C). Mean wear rate values for 0.314 m.s<sup>-1</sup> remained very small between room temperature and 390°C (decreasing from 0.626  $\mu\text{g.m}^{-1}$  at room temperature to 0.539  $\mu\text{g.m}^{-1}$  at 270°C and 0.184  $\mu\text{g.m}^{-1}$  at 390°C) in line with the very low weight losses over this temperature range (-0.002(8) at room temperature, -0.002(4) g at 270°C and -0.000(8) at 390°C). Small negative values for wear rate were observed between 450°C and 750°C where weight gains were recorded (0.000(2) g at 450°C, 0.001(1) g at 510°C, 0.001(4) g at 630°C, negligible weight change at 750°C). At 450°C, a mean wear rate of -0.051  $\mu\text{g.m}^{-1}$  was recorded, at 510°C the wear rate was -0.196  $\mu\text{g.m}^{-1}$ , falling to -0.312  $\mu\text{g.m}^{-1}$  at 630°C, then rising on increasing the temperature to 750°C at which wear rate levels were negligible. The only exception to this trend of small or negative wear rates was at 570°C, where a larger positive wear rate of 0.522  $\mu\text{g.m}^{-1}$  was recorded, matching up with a small negative weight change of -0.003(3) g (i.e. a small weight loss).

### ***b) Coefficient of friction data at 0.314 m.s<sup>-1</sup>***

The coefficient of friction values (Figure 5.2) measured during each of the tests at 0.314 m.s<sup>-1</sup> showed an initial unsettled period, before, in many cases, settling into a ‘steady state’ with reduced variation. In addition, there was also a clear downward trend of friction values with temperature, both for peak values during the unsettled ‘run-in’ period and during the later ‘steady state’ wear period. For example, at 0.314 m.s<sup>-1</sup>, values of friction during the unsettled period rose from zero to as high as 1.14 at room temperature, 0.78 at 270°C, 0.7 at 510°C and 0.63 at 750°C. On achieving steady state sliding, values settled to ~0.8 for room temperature, 0.7 to 0.8 at 270°C, 0.6 to 0.7 at 510°C and ~0.5 for 750°C – during steady state sliding, the variation observed was much reduced, being no more than approximately 12% of the mean value over the full range of test temperatures (room temperature to 750°C).

### ***c) Weight change and wear rate data at 0.905 m.s<sup>-1</sup> / 4,522 m***

At 0.905 m.s<sup>-1</sup> / 4,522 m, weight change and wear rate of the Nimonic 80A at room temperature (weight change -0.001(6) g – a negative value of weight change indicates a weight loss; wear rate 0.350 µg.m<sup>-1</sup> between 0 and 4,522 m) and 270°C (weight change -0.000(4) g; wear rate 0.097 µg.m<sup>-1</sup>) remained extremely low.

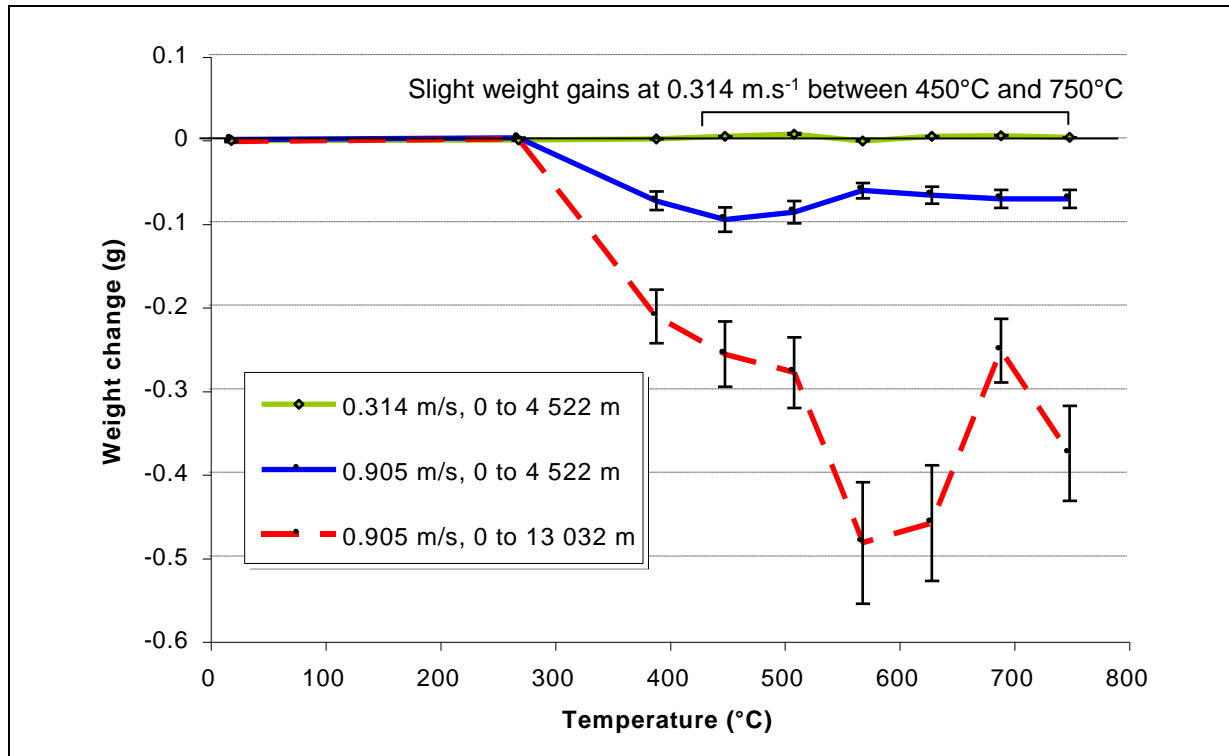
Between 390°C and 510°C, weight loss and wear rate of the Nimonic 80A increased rapidly. At 390°C, the weight change was measured at -0.075 g and wear rate at 16.586 µg.m<sup>-1</sup>. At 450°C, weight change was -0.097(8)g and the wear rate was 21.612 µg.m<sup>-1</sup>. At 510°C, weight loss and wear rate were slightly less than at 450°C, with weight change and wear rate values of -0.088(7) g and 19.604 µg.m<sup>-1</sup> respectively.

Wear levels remained high at 0.905 m.s<sup>-1</sup> / 4,522 m between 570°C and 750°C – weight change measurements indicated a steady increase in weight loss from the Nimonic 80A with temperature, with values of -0.062(9) at 570°C, -0.068(5) g at 630°C, -0.072(8) g at 690°C and -0.079(8) at 750°C. Over the same temperature range, wear rate between 0 and 4,522 m increased from 13.907 µg.m<sup>-1</sup> at 570°C, 15.174 µg.m<sup>-1</sup> at 630°C, 16.092 µg.m<sup>-1</sup> at 690°C and 17.653 µg.m<sup>-1</sup> at 750°C.

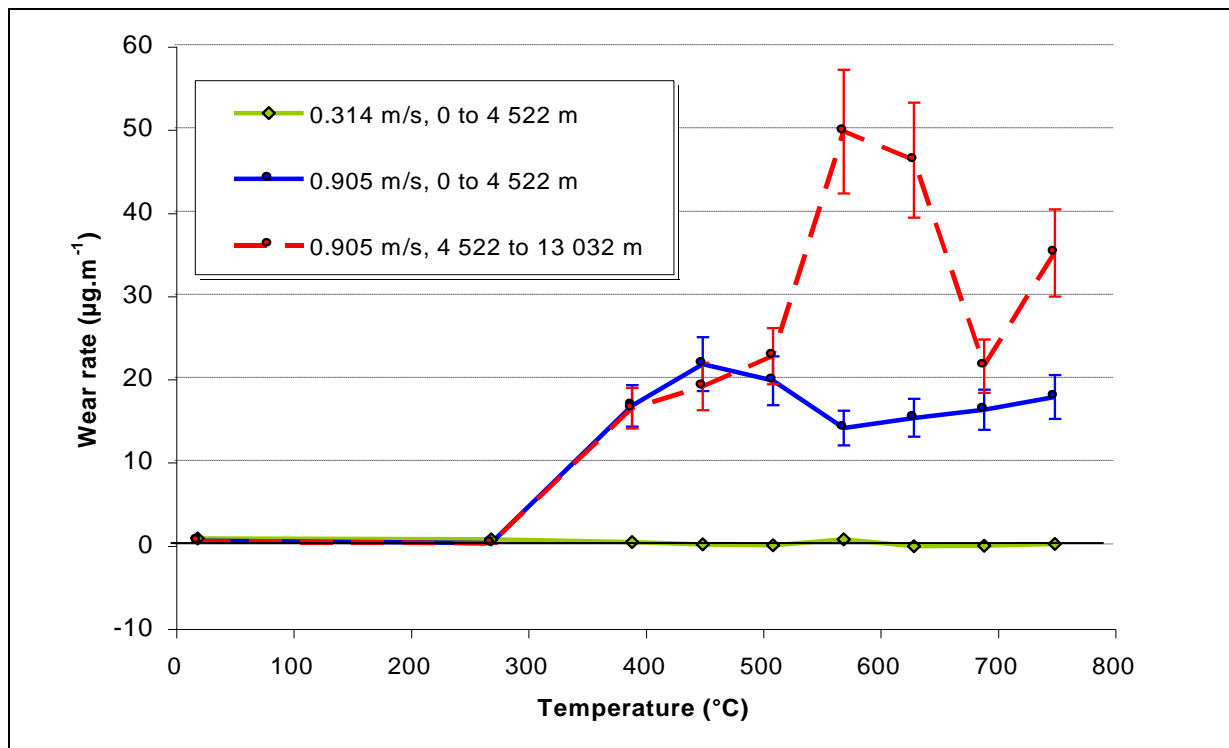
**Figure 5.1: Effect of temperature on weight change and wear rate – Nimonic 80A versus Stellite 6**

(load = 7N, sample size = 3)

(a) Weight change versus temperature



(b) Wear rate versus temperature

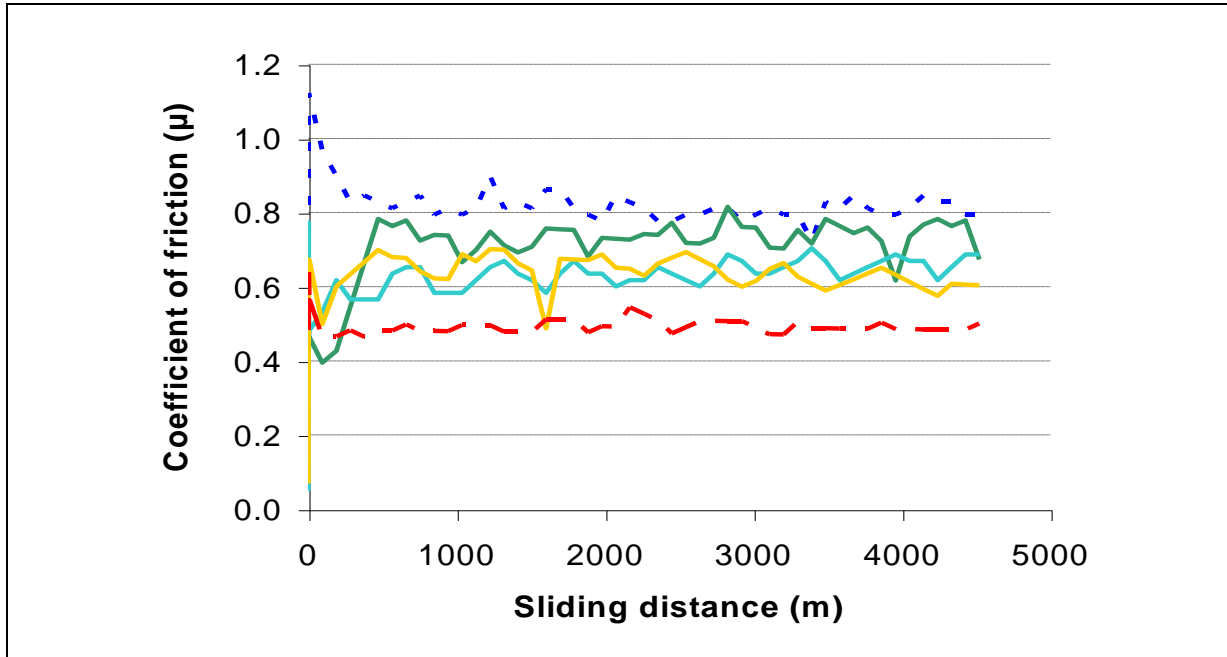


**Figure 5.2: Temperature versus coefficient of friction – Nimonic 80A versus Stellite 6**

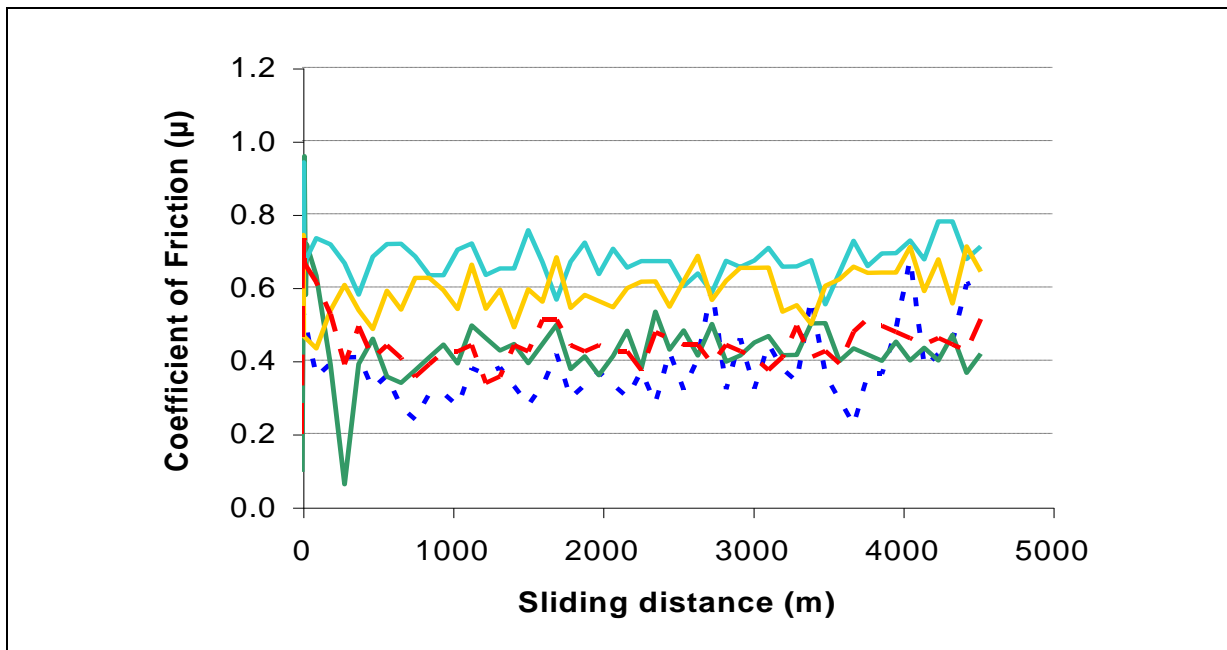
(load = 7N, sample size = 3)

..... Room temp.    — 270°C    — 450°C    — 510°C    - - 750°C

(a)  $0.314 \text{ m.s}^{-1} / 4,522 \text{ m}$



(b)  $0.905 \text{ m.s}^{-1} / 4,522 \text{ m}$



***d) Weight change and wear rate data at 0.905 m.s<sup>-1</sup> / 13,032 m***

At 0.905 m.s<sup>-1</sup>, Nimonic 80A sample weight loss values remained extremely low after 13,032 m of sliding at room temperature (weight change -0.004(4) g) and 270°C (weight change -0.000(7) g). Wear rates (between 4,522 and 13,032 m) also remained low, with record values of 0.334 µg.m<sup>-1</sup> at room temperature and 0.029 µg.m<sup>-1</sup> at 270°C. These values were little different to those observed after 4,522 m.

Between 390°C and 510°C, weight loss and wear rate of the Nimonic 80A samples were observed to increase. At 390°C, weight change was measured at -0.213(7) g and wear rate between 4,522 m and 13,032 m at 16.299 µg.m<sup>-1</sup>. At 510°C, weight change and wear rate values were -0.096(5) g and 21.537 µg.m<sup>-1</sup> (4,522 to 13,032 m) respectively. However, despite the increase in wear with temperature, the rates of wear of the Nimonic 80A between 390°C and 510°C were again little changed to those observed after 4,522 m of sliding (i.e. 16.586 µg.m<sup>-1</sup> at 390°C and 19.604 µg.m<sup>-1</sup> at 510°C).

This was not the case at 570°C and above, with the wear rates of the Nimonic 80A between 4,522 m and 13,032 m showing much higher values. 570°C was the most severe case, with a mean wear rate of 49.563 µg.m<sup>-1</sup> between 4,522 and 13,032 m compared to 13.907 µg.m<sup>-1</sup> up to 4,522 m. The increase in wear rate was less severe at 690°C (21.360 µg.m<sup>-1</sup> compared to 16.092 µg.m<sup>-1</sup> up to 4,522 m), though there was a moderate rise in wear rate with extended sliding between 4,522 m and 13,032 m at 750°C (34.963 µg.m<sup>-1</sup> compared to 17.653 µg.m<sup>-1</sup> between 0 and 4,522 m). There was also a shift in the peak wear rate of the Nimonic 80A from 450°C to 570°C, on increasing the sliding distance from 4,522 m to 13,032 m (Figure 5.1b). Weight losses were also observed to increase, with weight change values of -0.484(6) g at 570°C, -0.460(8) g at 570°C, -0.254(6) g at 690°C, -0.377(4) g at 750°C recorded after 13,032 m of sliding. These compared with values of -0.062(9) g at 570°C, -0.068(5) g at 630°C, -0.072(8) g at 690°C and -0.079(8) g at 750°C after 4,522 m.

***e) Coefficient of friction data at 0.905 m.s<sup>-1</sup>***

The coefficient of friction values (Figure 5.2) measured during each of the tests once again showed an initial unsettled period at 0.905 m.s<sup>-1</sup> as they did for 0.314 m.s<sup>-1</sup>. Once again, this unsettled period was followed by a more settled 'steady state', though with higher







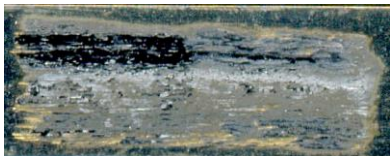

variance at  $0.905 \text{ m.s}^{-1}$  (in general within a 20% band, although this could be up to 50% at room temperature) than for  $0.314 \text{ m.s}^{-1}$  (~12%). No clear trend with temperature could be observed at  $0.905 \text{ m.s}^{-1}$ , either with the unsettled ‘run-in’ values or the ‘steady state’ values. During run-in, values of friction rose from 0 to 0.53 at room temperature, 0.95 at  $270^\circ\text{C}$ , 0.72 at  $510^\circ\text{C}$  and 0.73 at  $750^\circ\text{C}$ . Values of friction during steady state varied between 0.23 and 0.60 at room temperature, 0.35 and 0.50 at  $270^\circ\text{C}$ , 0.48 and 0.68 at  $510^\circ\text{C}$ , and then decreased to between 0.35 and 0.50 at  $750^\circ\text{C}$ .

Measured coefficient of friction values tended to be higher at  $0.314 \text{ m.s}^{-1}$ , however, it is to be noted that the higher levels of vibration encountered at  $0.905 \text{ m.s}^{-1}$  may well have reduced contact time between the sample and the counterface, thus actual coefficient of friction values at  $0.905 \text{ m.s}^{-1} / 13,032 \text{ m}$  were likely to have been much higher. This may have also accounted for the lack of any clear trends in the data, lost due to or hidden by the high levels of variance.







### ***5.1.2 Optical and SEM Microscopy – Nimonic 80A versus Stellite 6***

The use of optical microscopy (Figures 5.3 and 5.4) and SEM (Figure 5.5) indicated that regardless of sliding speed ( $0.314 \text{ m.s}^{-1}$  or  $0.905 \text{ m.s}^{-1}$ ), patches of oxidised debris were observed to form across the Nimonic 80A sample wear scar at room temperature and  $270^\circ\text{C}$ , allowing only very limited metal-to-metal contact between the sample and the Stellite 6 counterface. Monitoring of room temperature tests indicated that this metal-to-metal contact was mostly limited to the very early stages of wear and did not tend to occur once the oxide debris was formed. Only a small amount of this debris, of size in general between  $300 \text{ nm}$  and  $1 \mu\text{m}$  (with some particles up to  $3 \mu\text{m}$  and the occasional particle of up to  $5 \mu\text{m}$ ) was ejected during sliding (Figure 5.7). As reported in previous work [2], this material appeared to ‘smear’ at  $270^\circ\text{C}$ , especially at  $0.905 \text{ m.s}^{-1}$ . Above  $270^\circ\text{C}$ , the behaviour at  $0.314 \text{ m.s}^{-1}$  and  $0.905 \text{ m.s}^{-1}$  diverged dramatically.

**Figure 5.3:** Sample wear scar optical images – Nimonic 80A / Stellite 6, 0.314 m.s<sup>-1</sup>

	<p><b>Room temperature, 4,522 m</b>  <i>(wear scar = 14 x 5 mm)</i>          Loose oxide debris covering most of wear scar</p>
	<p><b>270°C, 4,522 m</b>  <i>(wear scar = 14 x 5 mm)</i>          Loose oxide debris with a little smearing</p>
	<p><b>390°C, 4,522 m</b>  <i>(wear scar = 14 x 5 mm)</i>          Loose oxide debris with increased smearing and traces of sintering</p>
	<p><b>450°C, 4,522 m</b>  <i>(wear scar = 14 x 5 mm)</i>          Highly smeared oxide, some sintering with first traces of glaze</p>
	<p><b>510°C, 4,522 m</b>  <i>(wear scar = 14 x 5 mm, also 570°C, 630°C)</i>          Patchy glaze coverage with little metallic wear</p>
	<p><b>750°C, 4,522 m</b>  <i>(wear scar = 14 x 5 mm, also 690°C)</i>          More extensive glaze coverage</p>

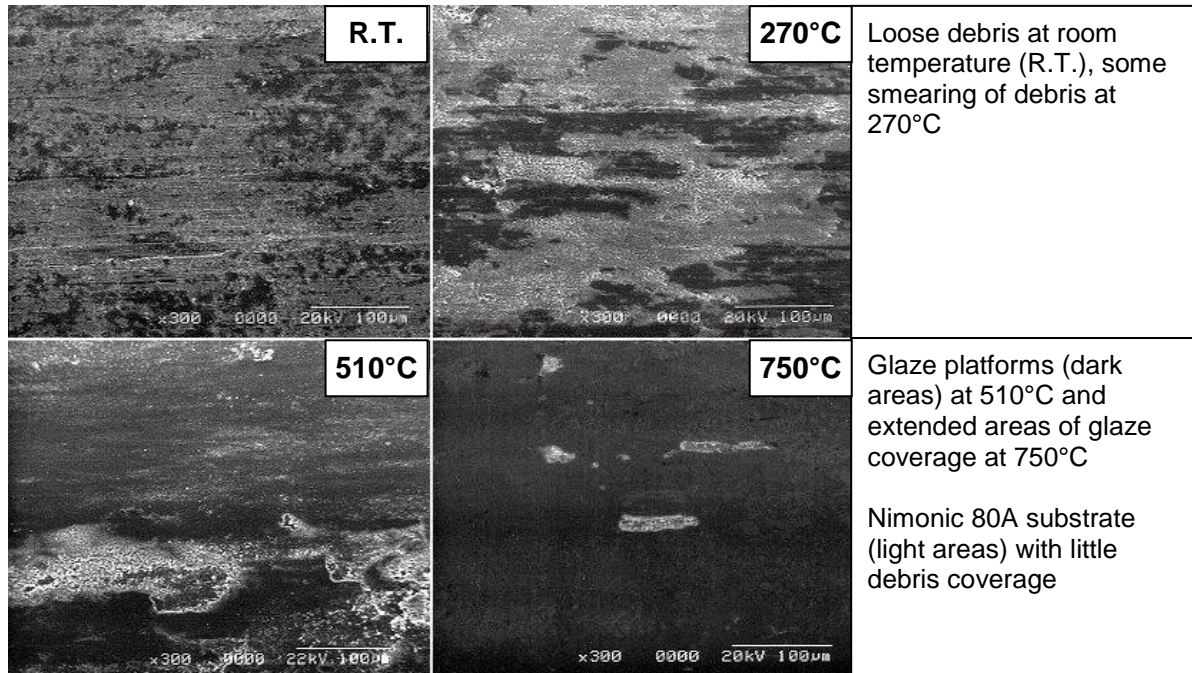
**Figure 5.4:** Sample wear scar optical images – Nimonic 80A / Stellite 6,  $0.905 \text{ m.s}^{-1}$   
*(Observations made after 13,032 m of sliding follow the same pattern as 4,522 m)*

	<p><b>Room temperature, 4,522 m</b>  <i>(wear scar = <math>14 \times 5 \text{ mm}</math>)</i>  Loose oxide debris covering most of wear scar</p>
	<p><b>270°C, 4,522 m</b>  <i>(wear scar = <math>15 \times 5 \text{ mm}</math>)</i>  Loose oxide debris with smearing</p>
	<p><b>390°C, 4,522 m</b>  <i>(wear scar = <math>17 \times 5 \text{ mm}</math>, also 450°C)</i>  Severe wear, substrate metal exposed, no oxide evident</p>
	<p><b>510°C, 4,522 m</b>  <i>(wear scar = <math>17 \times 5 \text{ mm}</math>, also 570°C)</i>  Severe wear, substrate metal exposed</p>
	<p><b>630°C, 4,522 m</b>  <i>(wear scar = <math>17 \times 5 \text{ mm}</math>)</i>  Severe wear, substrate metal exposed, limited smearing of oxide onto wear scar surface</p>
	<p><b>750°C, 4,522 m</b>  <i>(wear scar = <math>17 \times 5 \text{ mm}</math>, also 690°C)</i>  Highly worn wear scar covered by extremely thin oxide layer with a little loose debris – torn metallic appearance replaced by parallel markings in direction of sliding</p>

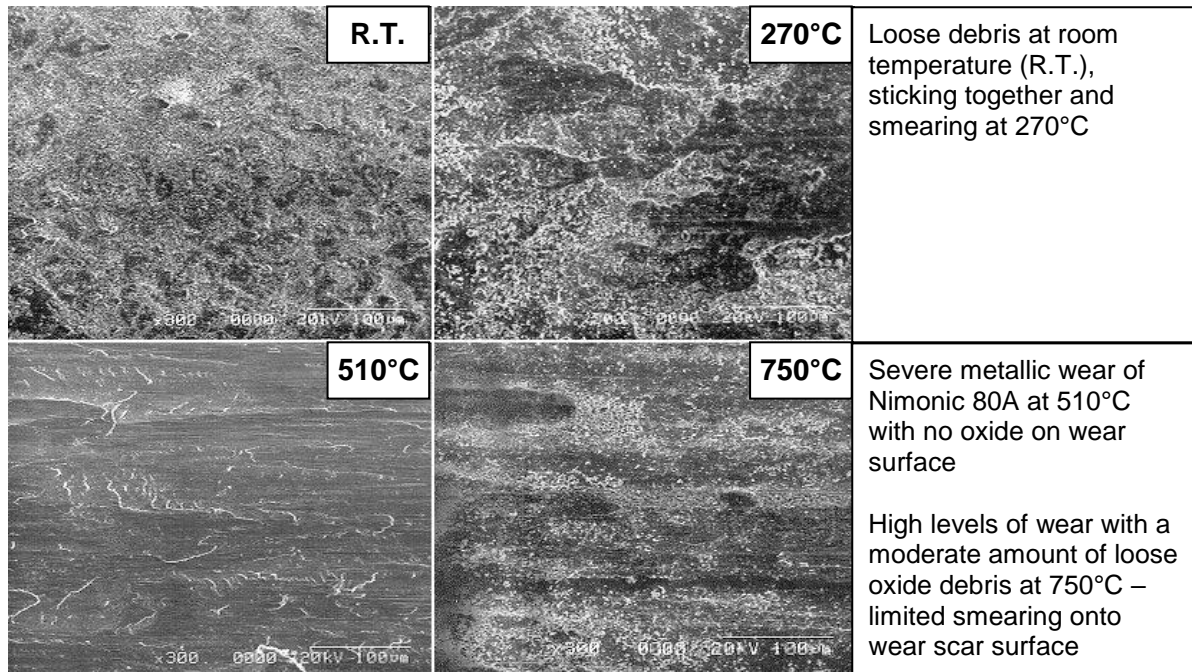


**Figure 5.5: SEM micrographs for Nimonic 80A versus Stellite 6 – wear surface**

(a)  $0.314 \text{ m.s}^{-1} / 4,522 \text{ m}$  – room temperature,  $270^\circ\text{C}$ ,  $510^\circ\text{C}$  and  $750^\circ\text{C}$

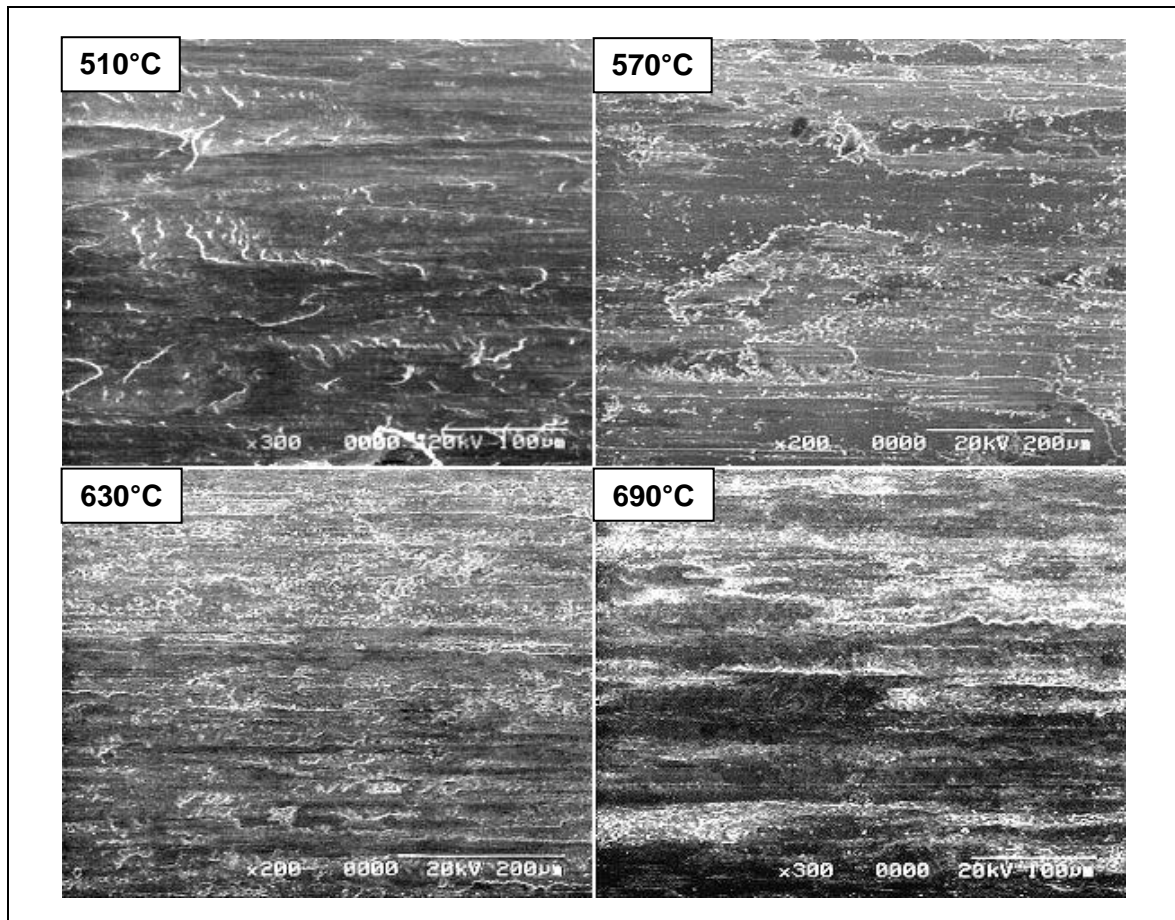


(b)  $0.905 \text{ m.s}^{-1} / 4,522 \text{ m}$  – room temperature,  $270^\circ\text{C}$ ,  $510^\circ\text{C}$  and  $750^\circ\text{C}$



Same pattern of observations made after 13,032 m of sliding at  $0.905 \text{ m.s}^{-1}$  as for (b)

**Figure 5.6:** SEM micrographs for Nimonic 80A versus Stellite 6 showing change in wear scar morphology between 510°C and 690°C at 0.905 m.s<sup>-1</sup> / 4,522 m



At 510°C, the sample wear scar had a highly torn metallic surface.

At 570°C, parallel marking began to appear on the wear scar as the level of oxide in the debris increased.

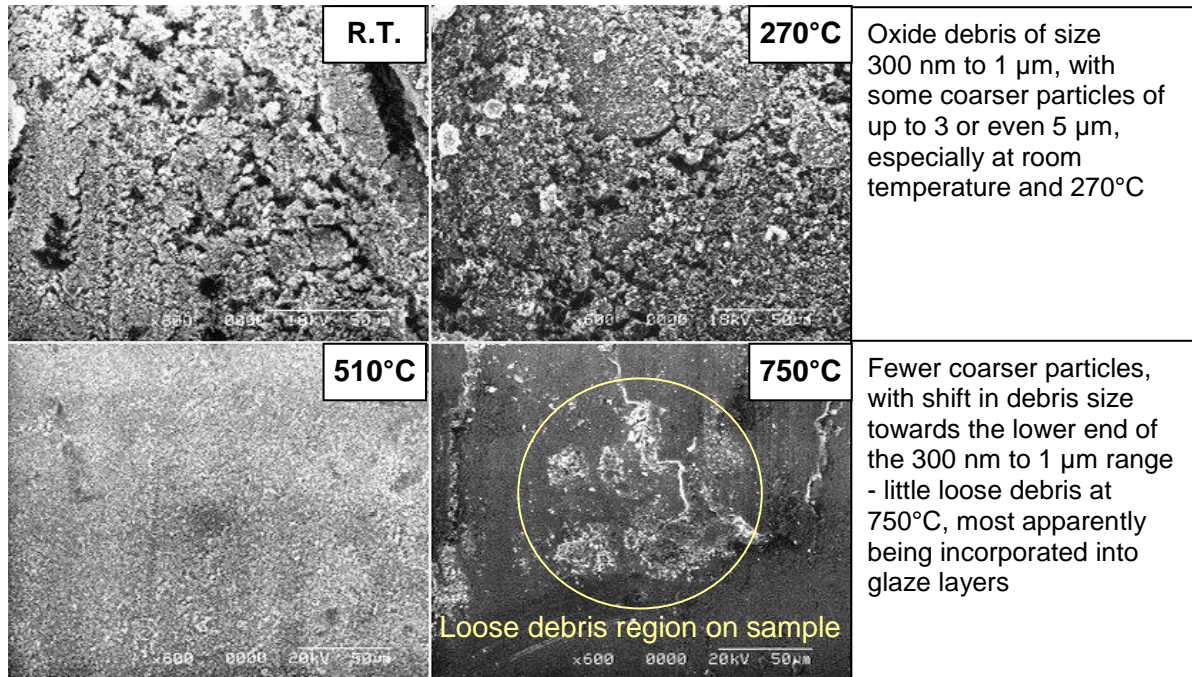
At 630°C and 690°C (also 750°C – Figure 5.5), the wear scar no longer had a torn metallic surface, with surface damage consisting of parallel marks in the direction of sliding. There was no build-up into glaze platforms due to the poor sintering characteristics of the oxide, with at best a small amount of smearing of oxide onto the exposed metallic surfaces of the Nimonic 80A.

There was no evidence of a reduction in wear rate coinciding with the appearance of this oxide. Instead, the presence of the oxide debris coincided with increases in weight loss and wear rate between 4,522 and 13,032 m of sliding at 0.905 m.s<sup>-1</sup> (compared to that observed between 0 and 4,522 m – Figure 5.1).

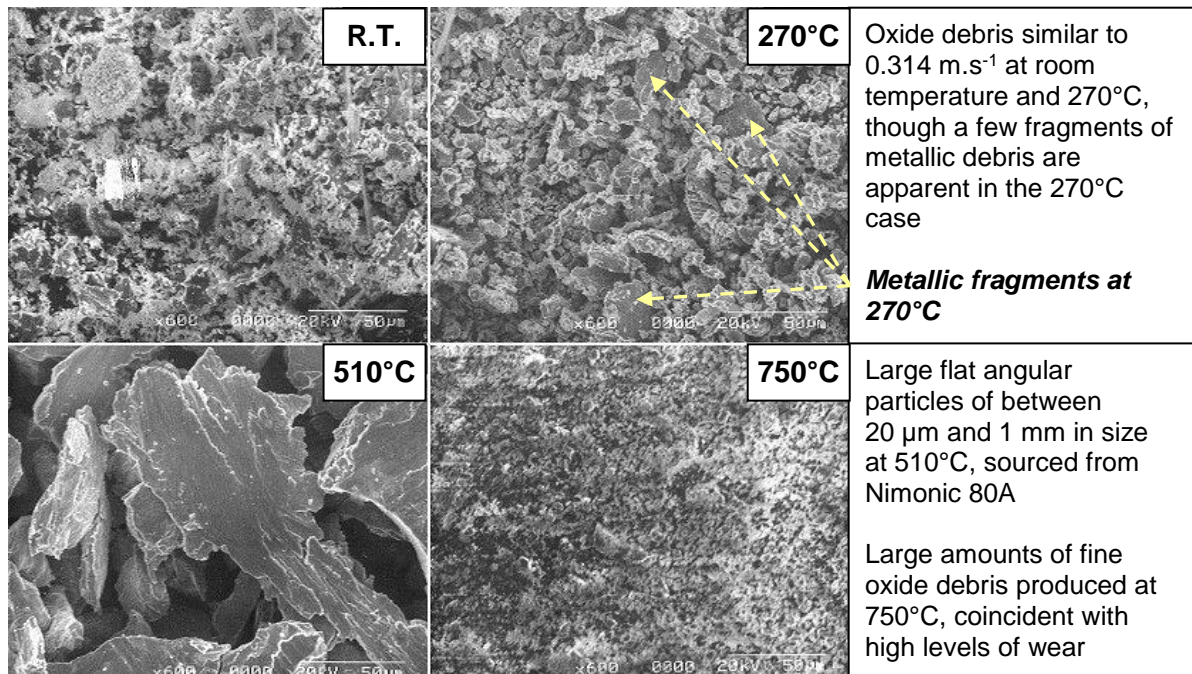


**Figure 5.7: SEM micrographs for Nimonic 80A versus Stellite 6 – debris**

(a)  $0.314 \text{ m.s}^{-1} / 4,522 \text{ m}$  – room temperature,  $270^\circ\text{C}$ ,  $510^\circ\text{C}$  and  $750^\circ\text{C}$

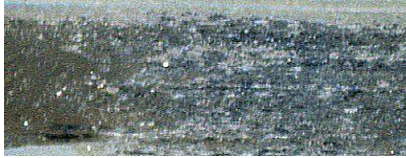
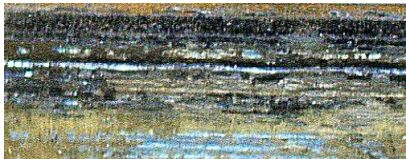
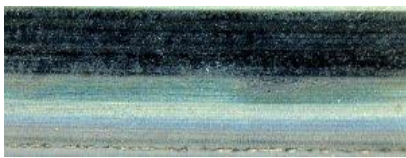


(b)  $0.905 \text{ m.s}^{-1} / 4,522 \text{ m}$  – room temperature,  $270^\circ\text{C}$ ,  $510^\circ\text{C}$  and  $750^\circ\text{C}$






Same pattern of observations made after 13,032 m of sliding at  $0.905 \text{ m.s}^{-1}$  as for (b)

**Figure 5.8: Counterface wear scar optical images – Nimonic 80A / Stellite 6, 0.314 m.s<sup>-1</sup>**

	<p><b>270°C, 4,522 m</b> (<i>section = 15 x 5 mm, applicable to between room temperature and 450°C</i>)</p> <p>Loose oxide debris, some smearing at 390°C and 450°C</p>
	<p><b>510°C, 4,522 m</b> (<i>section = 15 x 5 mm, applicable also at 570°C</i>)</p> <p>Patchy glaze covering contact areas</p>
	<p><b>750°C, 4,522 m</b> (<i>section = 15 x 5 mm, applicable to between 630°C and 750°C</i>)</p> <p>Smooth glaze covering contact areas</p>

**Figure 5.9: Counterface wear scar optical images – Nimonic 80A / Stellite 6, 0.905 m.s<sup>-1</sup>**

(Observations made after 13,032 m of sliding follow the same pattern as 4,522 m)

	<p><b>270°C, 4,522 m</b></p> <p>(<i>section = 15 x 5 mm, applicable also at room temperature</i>)</p> <p>Loose oxide debris with smearing, especially at 270°C</p>
	<p><b>510°C, 4,522 m</b></p> <p>(<i>section = 15 x 5 mm, applicable between 390°C and 570°C</i>)</p> <p>Worn surface free of debris and glaze</p>
	<p><b>750°C, 4,522 m</b></p> <p>(<i>section = 15 x 5 mm, applicable also at 690°C</i>)</p> <p>Patchy glaze layer covered in loose debris</p>

At  $0.314 \text{ m.s}^{-1}$ , the debris observed at room temperature and  $270^{\circ}\text{C}$  was also present at  $390^{\circ}\text{C}$  and  $450^{\circ}\text{C}$ . Smearing also continued to be observed at  $390^{\circ}\text{C}$  and  $450^{\circ}\text{C}$ , and was noticeably more pronounced than at  $270^{\circ}\text{C}$ . At  $390^{\circ}\text{C}$  and  $450^{\circ}\text{C}$  (Figure 5.3), the debris on the surface additionally showed evidence of particles ‘sticking’ or sintering together, accompanied by the formation at  $450^{\circ}\text{C}$  of a few isolated patches of glaze-like material. Damage due to metal-to-metal contact between the Nimonic 80A sample and Stellite 6 counterface remained extremely limited.

At  $510^{\circ}\text{C}$  and above (sliding speed  $0.314 \text{ m.s}^{-1}$ ), comprehensive glaze formation became more evident with increasing sliding temperature (Figures 5.3 and 5.5). Areas of fully developed glaze platforms seemed to show greater evidence of more complete sintering, with fewer areas of porosity and less loose debris at  $750^{\circ}\text{C}$  (where glaze coverage was observed to be most extensive) compared to  $510^{\circ}\text{C}$  (Figure 5.5). Evidence of damage due to metal-to-metal contact between the Nimonic 80A sample and Stellite 6 counterface became progressively less with increasing temperature as glaze formation became more comprehensive.

The formation of glaze at  $510^{\circ}\text{C}$  and above coincided with a significant reduction in the loose debris produced, with much of the debris apparently being incorporated into the glaze. The distribution of debris particle sizes seemed also to shift towards the lower end of the  $300 \text{ nm}$  to  $1 \mu\text{m}$  range, with possibly some debris of size below this range and fewer larger particles above  $1 \mu\text{m}$  (Figure 5.7) present.

At  $0.905 \text{ m.s}^{-1} / 4,522 \text{ m}$  and  $0.905 \text{ m.s}^{-1} / 13,032 \text{ m}$ , the first evidence of a transition in wear was the presence of the occasional fragment of metallic debris in amongst the oxide debris at  $270^{\circ}\text{C}$  (Figure 5.7). From  $390^{\circ}\text{C}$  up to  $510^{\circ}\text{C}$  (Figure 5.4), the wear surfaces exhibited a high degree of metallic damage typical of severe wear, accompanied by the production of high levels of larger metallic debris particles between  $20 \mu\text{m}$  and  $1 \text{ mm}$  in size, with little evidence of finer oxide debris. The flat angular platelet nature of this metallic debris indicated the operation of a delamination mechanism [2] in the surface layers of the wear sample.



At 570°C and above (sliding speed 0.905 m.s<sup>-1</sup>), the highly worn wear scar on the Nimonic 80A samples showed signs of an extremely thin film of smeared oxide, plus an increasing proportion of oxide in the debris produced (first observed at 510°C). This oxide showed very little tendency to undergo agglomeration and sintering, with no accompanying evidence that this oxide was building up into glaze layers after either 4,522 m or 13,032 m of sliding.

The increasing presence of the oxide with rising sliding temperature amongst the debris at 0.905 m.s<sup>-1</sup> coincided with a progressive change in the morphology of the Nimonic 80A wear scar (Figure 5.6). Instead of a randomly torn surface characteristic of severe metallic wear (510°C), a pattern of fine parallel grooves developed in the direction of sliding in the presence of loose oxide. At 570°C, the torn surface was still evident, but with some grooves parallel to the direction of sliding. At 630°C and 690°C, the torn surface had been completely replaced by this pattern of fine parallel grooves.

The oxide debris produced at 0.905 m.s<sup>-1</sup> and temperatures of between 630°C and 750°C, were once again very fine, with particle sizes in the range 300 nm to 1 µm and only a few larger particles outside this range. The green colour indicated a high level of nickel oxide in this debris.

#### ***5.1.2.1 Stellite 6 Counterface Wear Scar Morphology***

Wear on the Stellite 6 counterface showed similar patterns to that of the samples. At 0.314 m.s<sup>-1</sup>, the loose debris observed on the Nimonic 80A sample between room temperature and 450°C was also present on the Stellite 6 counterface (which showed very little damage due to the loose debris preventing metal-to-metal contact with the Nimonic 80A sample). At 510°C and above, patchy glaze formation was noted on the Stellite 6 counterface, becoming more continuous between 630°C and 750°C (Figure 5.8 – metallic damage between 510°C and 750°C became progressively less).

At 0.905 m.s<sup>-1</sup>, loose oxide debris was again observed on the Stellite 6 counterface, but only up to 270°C (Figure 5.9). Between 390°C and 570°C, all evidence of this oxide disappeared and the wear scar on the counterface had a bright, metallic, worn surface typical of severe wear (the 510°C example is shown in Figure 5.9). 630°C / 0.905 m.s<sup>-1</sup> showed

some evidence of limited oxide coverage, the green colour of which again indicated a high level of nickel oxide. Isolated patches of glaze appear to have formed on some asperities in the counterface wear track under these conditions, evident by the shiny surfaces upon them (not shown).

Clearly defined but patchy glaze layers were observed only on the Stellite 6 counterface for temperatures of 690°C and 750°C (Figure 5.9) at 0.905 m.s<sup>-1</sup> – this glaze was still accompanied by a little remaining loose debris on the counterface surface, some of which became embedded in the surface of the glaze. This glaze could be easily dislodged from the surface of the Stellite 6, which showed evidence of only a small amount of damage beneath the glaze layer.

### 5.1.3 EDX Analysis – Nimonic 80A versus Stellite 6

The EDX analysis for the 0.314 m.s<sup>-1</sup> samples showed that the fine oxide debris covering wear scar surfaces at room temperature, 270°C and 390°C consisted of varying levels of nickel, chromium and cobalt; some location specific variation was observed. Selection of an area high in fine oxide debris particles gave varying levels of cobalt (up to 50%) and nickel (up to 60%, coincident with falls in cobalt levels to less than 10%). Areas relatively free of particles consistently indicated a higher level of nickel from the Nimonic 80A sample metal beneath (up to 60%), which showed no evidence of transfer of metal between the counterface and the sample (EDX indicated no Stellite 6-sourced cobalt in the exposed metal). The small amount of oxide debris that was ejected from the wear interface gave results similar to the loose debris on the sample wear scar, though cobalt- and chromium-based debris sourced from the Stellite 6 were usually dominant.

From 450°C upwards (Figure 5.10) at 0.314 m.s<sup>-1</sup>, with the oxide debris smearing together and glaze forming, cobalt levels in glaze-covered regions were higher, although still fairly variable at between 35 and 55 %. The levels of nickel detected dropped to less than 10% within the glaze, although some spot EDX values reached between 15 and 18%. This was most noticeable at 570°C, where glaze coverage was incomplete (thus the collected data may have been affected by the Nimonic 80A substrate) and particularly at 750°C, where standard EDX indicated more general nickel levels of 18%. Chromium levels in the glaze

remained high throughout at between 30 to 35%, compared to measured chromium levels in the Nimonic 80A sample of ~25%. Silicon was present in the transferred glaze material at between 1 and 6.5%, in general higher than the nominal 1% silicon content in metallic Stellite 6. Standard EDX detected no significant quantities of any other elements.

The high levels of cobalt and chromium at  $0.314 \text{ m.s}^{-1}$  between  $450^{\circ}\text{C}$  and  $750^{\circ}\text{C}$  indicate that most of the oxide forming the glaze was sourced from the Stellite 6 counterface. The very low levels of nickel indicate only a limited contribution from the Nimonic 80A sample.

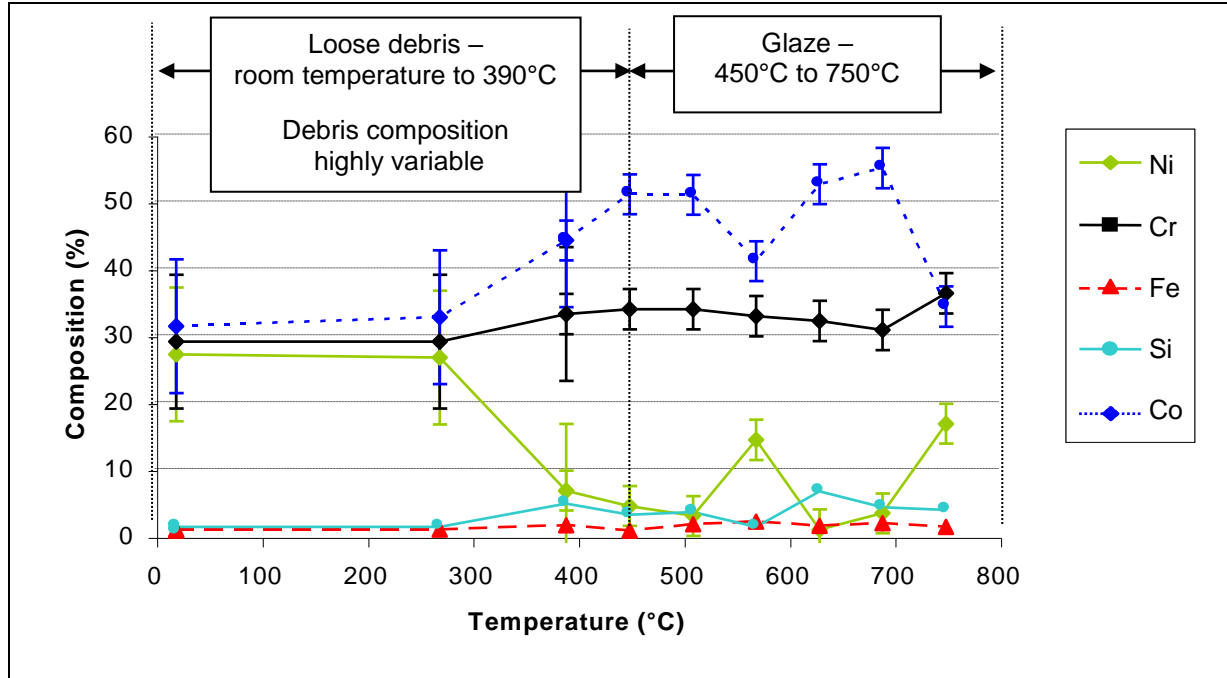
The little loose oxide debris ejected from the wear interface between  $450^{\circ}\text{C}$  and  $750^{\circ}\text{C}$  at  $0.314 \text{ m.s}^{-1}$  was at times swamped by contamination from the alumina furnace lining (up to 60% aluminium). Despite this, high levels of cobalt (between 40 and 50%) and chromium (32 to 25%) were still detected, with varying but low levels of nickel (between 2 and 15%) and silicon (between 1 and 6.5%). This data thus indicates that the primary source of the debris was also the Stellite 6 counterface.

At  $0.905 \text{ m.s}^{-1}$ , the EDX results at room temperature and  $270^{\circ}\text{C}$  (after both 4,522 m and 13,032 m of sliding) were similar to those for  $0.314 \text{ m.s}^{-1}$ , with areas high in fine particle debris showing high cobalt levels (up to 50%, indicating transfer from the Stellite 6 counterface) and areas relatively free of particles, giving higher nickel levels (up to 60%) from the Nimonic 80A sample material beneath. The little loose oxide debris ejected from the wear interface up to  $270^{\circ}\text{C}$  gave similar results.

From  $390^{\circ}\text{C}$  upwards, where retained debris was completely absent from the surface of the Nimonic 80A samples slid at  $0.905 \text{ m.s}^{-1}$ , nickel was consistently high at around 70%, in line with Nimonic 80A alloy composition (irrespective of whether sliding had been conducted up to 4,522 or 13,032 m). Cobalt levels remained almost negligible, showing no evidence of material transfer (metallic or oxide) from the Stellite 6 counterface at or above this temperature, nor was there any significant trace of cobalt in the ejected metallic debris produced. The chromium levels dropped from ~35% with the oxide debris present at  $270^{\circ}\text{C}$ , to ~25% with both the metallic debris and the exposed substrate from  $390^{\circ}\text{C}$  upwards (again roughly in line with Nimonic 80A alloy composition).

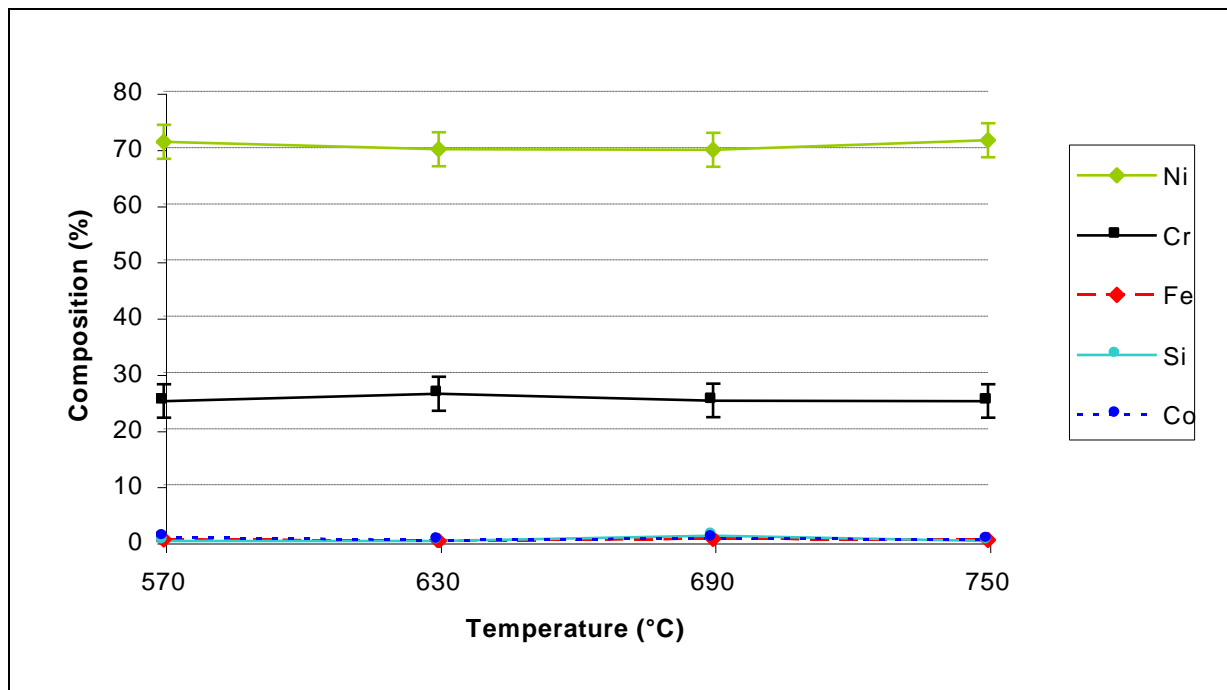
**Figure 5.10: EDX data – variation of composition of loose debris and glaze layers (Nimonic 80A vs. Stellite 6), room temperature to 750°C, 0.314 m.s<sup>-1</sup>**

(load = 7N, sliding distance = 4,522 m, sample size = 3)



**Figure 5.11: EDX data – variation of composition of loose debris (Nimonic 80A vs. Stellite 6), 570°C to 750°C, 0.905 m.s<sup>-1</sup>**

(load = 7N, sliding distance = 4,522 m, sample size = 3)



Same pattern of observations made after 13,032 m of sliding

The appearance of the very fine oxide layer on the surfaces of the Nimonic 80A samples from 570°C upward (Figure 5.11) at 0.905 m.s<sup>-1</sup> (after both 4,522 m and 13,032 m of sliding) had no effect on the results of the EDX analysis. The high levels of oxide debris produced consisted of ~70% nickel and ~25% chromium (not too dissimilar to the composition of the Nimonic 80A sample), again with no significant amounts of cobalt present. Minor constituents present in the Nimonic 80A accounted for the remaining 5%.

The easily dislodged, patchy glaze that formed upon the surface of the Stellite 6 counterface at 0.905 m.s<sup>-1</sup> (after both 4,522 m and 13,032 m of sliding) and temperatures of 690°C and 750°C, was of composition very similar to the large amounts of loose oxide debris formed under the same conditions. The glaze consisted of on average ~68% nickel, 25% chromium and only ~1% cobalt after 4,522 m and ~69% nickel, 25% chromium and negligible amounts of cobalt after 13,032 m, indicating the Nimonic 80A sample to be the primary source of the oxide forming the glaze.

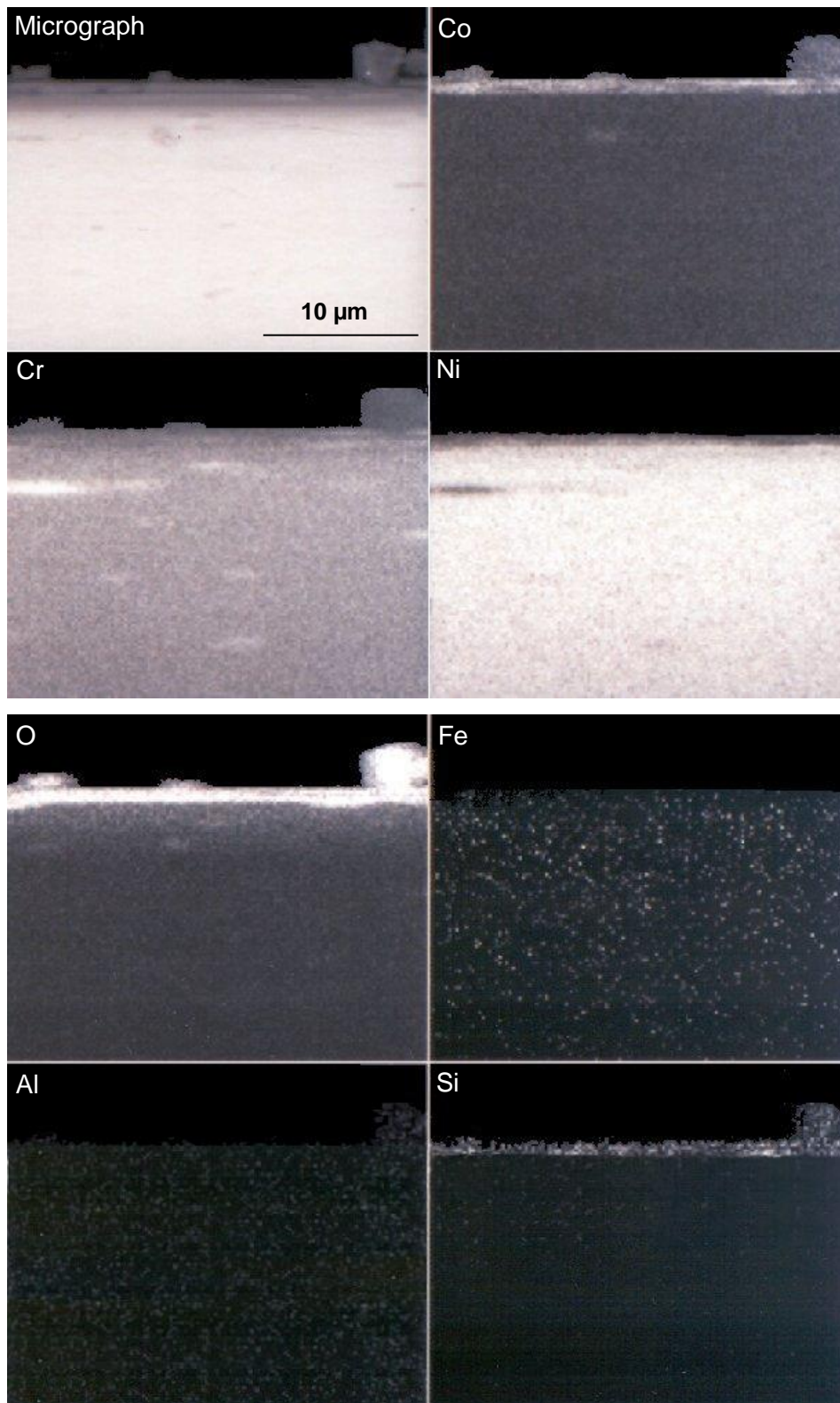
In comparison, the glaze layers formed at 690°C and 750°C on the Stellite 6 counterface at 0.314 m.s<sup>-1</sup> were highly adherent and insufficient glaze could be removed to carry out an effective EDX analysis. Information on the composition of the glaze was obtained only by sliding Stellite 6 as the sample against Nimonic 80A as the counterface – the experimental results for this work are reported in Section 5.2.2.

#### ***5.1.4 Mapping using EDX – Nimonic 80A versus Stellite 6***

Due to lack of deposit on Nimonic 80A samples slid at 0.905 m.s<sup>-1</sup>, only the composition maps at 750°C for 0.314 m.s<sup>-1</sup> are shown (Figure 5.12 is a representative example, other samples giving near identical results) - this test combination was selected, as it was at 750°C that the most complete compacted oxide layers were formed.

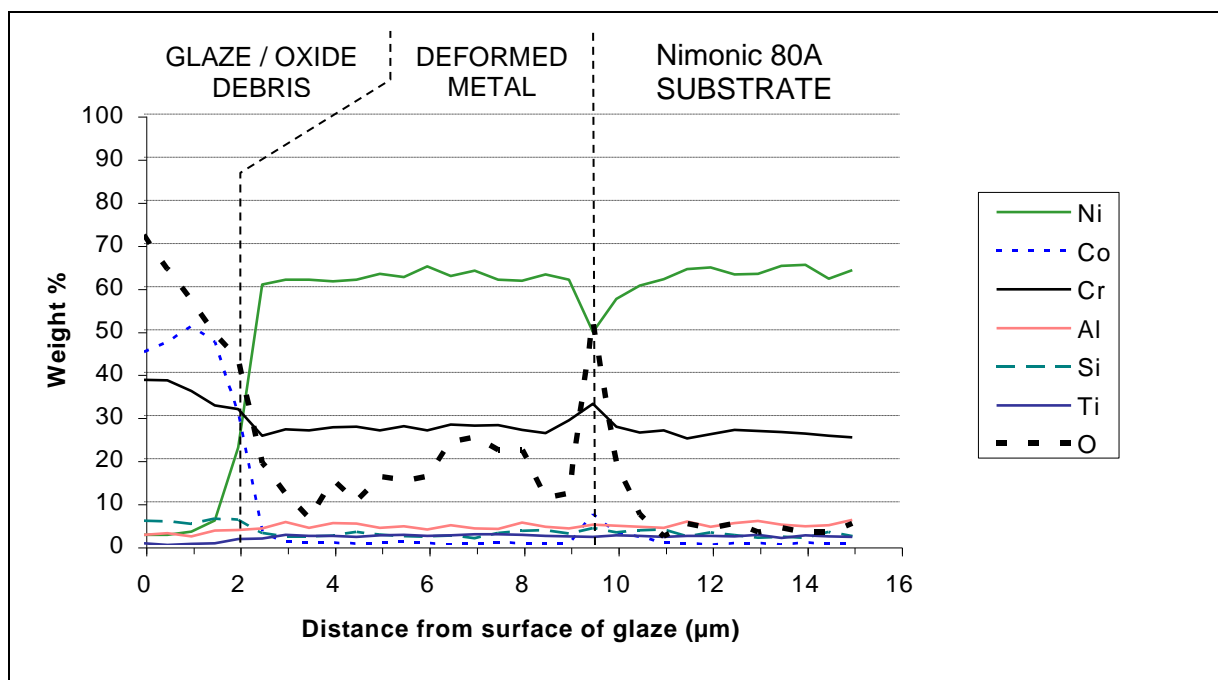
**Figure 5.12: Cross-sectional EDX element maps for Nimonic 80A worn against Stellite 6 subsequent to wear at  $0.314 \text{ m.s}^{-1}$**

*(load = 7N, sliding distance = 4,522 m, temperature =  $750^\circ\text{C}$ , sample size = 3)*



**Figure 5.13: Data from Autopoint EDX analysis for Nimonic 80A slid against Stellite 6 at a sliding speed of  $0.314 \text{ m.s}^{-1}$  and a temperature of  $750^\circ\text{C}$**

Amounts of each substance present are expressed in terms of percentage of the non-oxygen content. Amount of oxygen is expressed in terms of percentage of the overall content. Data (sample size = 3) are for samples slid for a distance of 4,522 m.



The maps for  $0.314 \text{ m.s}^{-1} / 750^\circ\text{C}$  showed that cobalt and oxygen were concentrated together in the glaze and oxide debris layers formed on the surface of the Nimonic 80A and completely absent from the bulk of the Nimonic 80A substrate, indicating transfer from the Stellite 6 counterface. Chromium was present in both the surface layer and the substrate – due to it being a significant component in both Nimonic 80A and Stellite 6, no conclusions can be drawn from the maps alone about the possible source of the chromium in the surface layers. However, mapping also indicated an absence of nickel from these surface areas, thus showing that nickel, only present in significant quantities in the Nimonic 80A, was not a primary constituent of the compacted oxide.

As for minor constituents, silicon was also concentrated within the glaze layer region – as this is only present in any measurable quantities within the Stellite 6, it has clearly been transferred to the surface of the Nimonic 80A with the cobalt. No clear patterns were observable within the aluminium and iron maps, from which any conclusions can be drawn.



### 5.1.5 Autopoint EDX Analysis – Nimonic 80A versus Stellite 6

The lack of deposits formed on the  $0.905 \text{ m.s}^{-1}$  samples also meant that like the EDX maps, Autopoint EDX was only feasible for samples slid at  $0.314 \text{ m.s}^{-1}$ , with the  $750^\circ\text{C}$  samples again being of most interest due to the more complete nature of the glaze layers formed. Figure 5.13 is a representative example of the Autopoint EDX data obtained for the  $0.314 \text{ m.s}^{-1} / 4,522 \text{ m} / 750^\circ\text{C}$  samples, all 3 samples undergoing Autopoint testing giving very similar results.

At  $0.314 \text{ m.s}^{-1} / 750^\circ\text{C}$ , the glaze or compacted oxide debris layer was present to an apparent average depth of  $2 \mu\text{m}$  on the surface of the Nimonic 80A, showing levels of cobalt and chromium (at just below 50% and  $\sim 30\%$  respectively of the non-oxygen content) not too far removed from the levels seen in Stellite 6. The Stellite 6 was the dominant source of material in the glaze layer. Nickel was present in the glaze at levels of no more than approximately 2%, indicating no significant contribution from the Nimonic 80A. The overall oxygen content was between 40 and 70% in this layer.

The next region up to between  $7 \mu\text{m}$  and  $11 \mu\text{m}$  depth ( $\sim 9 \mu\text{m}$  in the shown example – Figure 5.13) depending on the sample, corresponds to a deformed metallic layer (which the glaze layer overlies) relating to what appeared to be metal that may have been removed from and redeposited on the Nimonic 80A. This removal and redeposition is indicated by the presence of occasional areas of cobalt from the Stellite 6 counterface (Figure 5.13 is one such example) entrapped at the interface between the deformed layer and the undeformed Nimonic 80A sample material. Nimonic 80A was identified as the primary source of this deformed layer, due to the high levels of nickel ( $\sim 62$  to  $63\%$ ) and chromium ( $\sim 25$  to  $27\%$ ) and negligible levels of cobalt within the layer, at no more than  $\sim 2\%$ . The development of the stable, high-cobalt glaze layer on top of this deformed metal layer indicates that the deformed metal layer was formed earlier during the sliding process, prior to glaze formation.

### 5.1.6 XRD Analysis – Nimonic 80A versus Stellite 6

XRD analysis indicated a Stellite 6-sourced cobalt-containing phase in the surface deposits in a number of the  $0.314 \text{ m.s}^{-1}$  samples – specifically at room temperature,  $270^\circ\text{C}$ ,  $510^\circ\text{C}$  (Figure 5.14a),  $630^\circ\text{C}$  and  $750^\circ\text{C}$  (Figure 5.14b) – this could have been either  $\text{Co}_3\text{O}_4$  or  $\text{CoCr}_2\text{O}_4$  (both have near identical diffraction patterns, though is identified as  $\text{CoCr}_2\text{O}_4$  on



the XRD scans). With both cobalt and chromium identified by EDX, mapping and Autopoint, and cobalt levels as high as 55%, both phases are likely to have been present.  $\text{Ni}_{2.9}\text{Cr}_{0.7}\text{Fe}_{0.36}$  showed the strongest signal, this being in line with the Nimonic 80A substrate, although not stoichiometrically consistent as the phase suggested has much higher levels of iron than with Nimonic 80A.

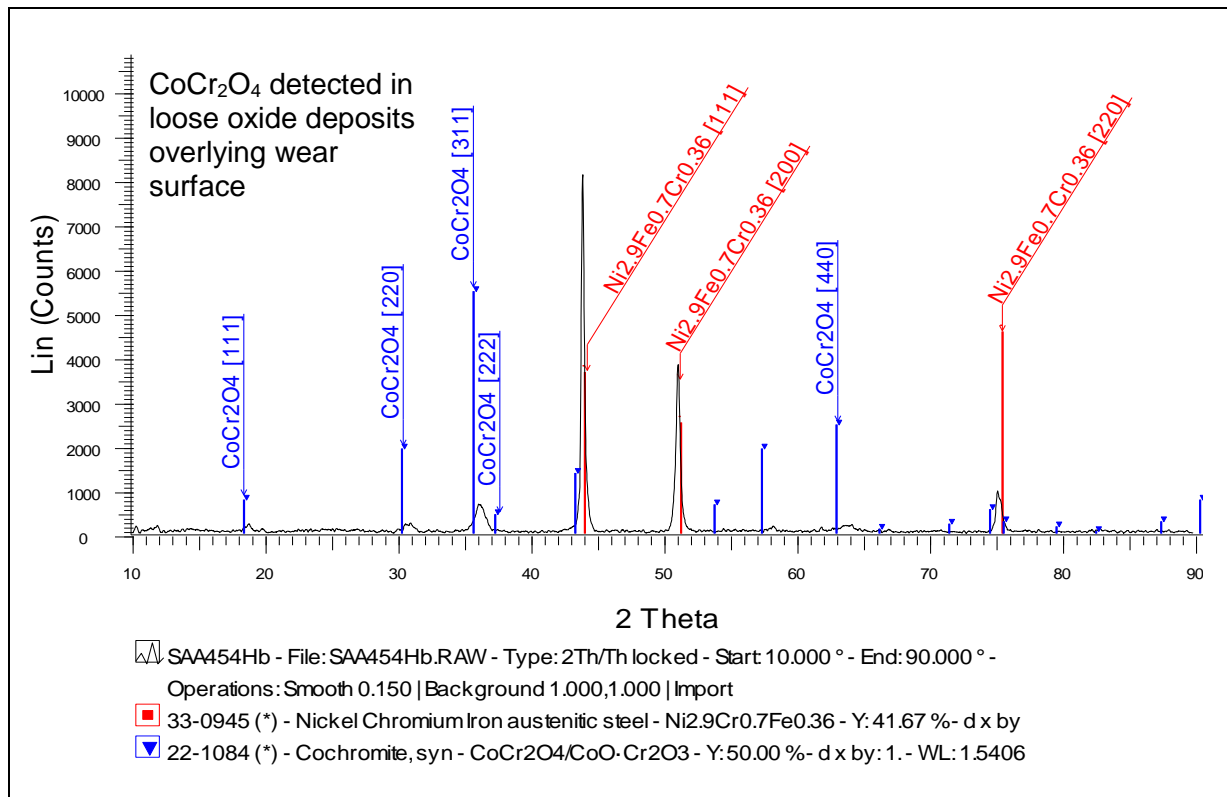
XRD on the  $0.905 \text{ m.s}^{-1}$  samples identified a clear pattern for  $\text{Ni}_{2.9}\text{Cr}_{0.7}\text{Fe}_{0.36}$  for a number of samples, again at room temperature,  $270^\circ\text{C}$ ,  $510^\circ\text{C}$ ,  $630^\circ\text{C}$  and  $750^\circ\text{C}$  (Figure 5.15). XRD failed to detect any phases apart from this in the powdery deposits identified on the samples at room temperature (Figure 5.15a) and  $270^\circ\text{C}$ , nor were any extra phases identified on samples between  $390^\circ\text{C}$  and  $630^\circ\text{C}$  (Figure 5.15b shows the  $510^\circ\text{C}$  example), where there had been high levels of wear.

A hint of NiO was detected on the  $750^\circ\text{C}$  samples tested at  $0.905 \text{ m.s}^{-1}$  (Figure 5.15c). However, the best results were obtained by the use of XRD on the collected debris samples at  $630^\circ\text{C}$ ,  $690^\circ\text{C}$  and  $750^\circ\text{C}$  (Figure 5.15d) – the Nimonic 80A versus Stellite 6 samples at  $0.905 \text{ m.s}^{-1}$  were the only cases where sufficient oxide debris was collected to enable effective XRD. Three phases were detected, the metallic phase  $\text{Ni}_{2.9}\text{Cr}_{0.7}\text{Fe}_{0.36}$ , plus the oxide phases NiO and  $\text{Cr}_2\text{O}_3$ .

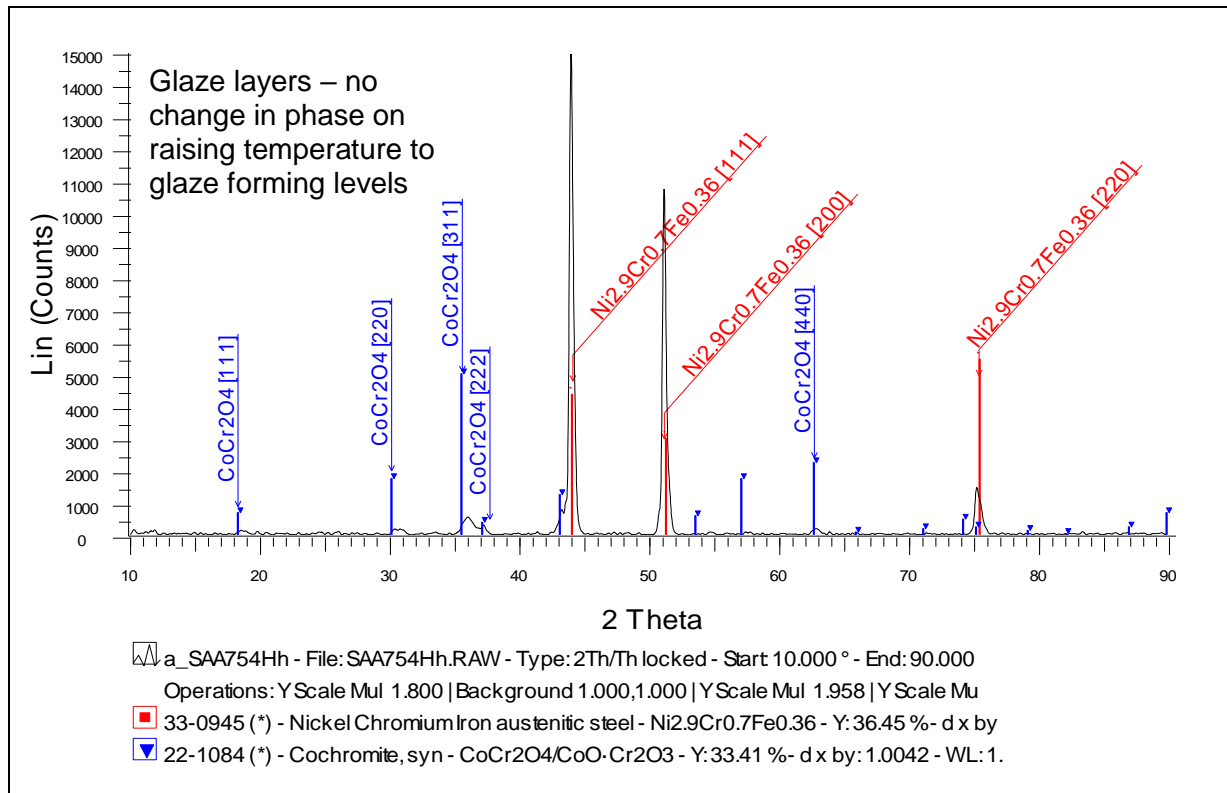
Glancing Angle XRD on selected  $0.314 \text{ m.s}^{-1} / 4,522 \text{ m}$  samples slid at  $750^\circ\text{C}$  again confirmed the presence of  $\text{Ni}_{2.9}\text{Cr}_{0.7}\text{Fe}_{0.36}$  and one of the two phases,  $\text{Co}_3\text{O}_4$  or  $\text{CoCr}_2\text{O}_4$ . It was additionally noted that the  $\text{Ni}_{2.9}\text{Cr}_{0.7}\text{Fe}_{0.36}$  peaks were actually dual peaks over intermediate angles and the composite plot in Figure 5.16 seems to indicate two peaks very close together in each case. It is to be noted that the diffraction angles for the crystallographic planes within face-centred cubic Co are very close to those of the same Miller indices within  $\text{Ni}_{2.9}\text{Cr}_{0.7}\text{Fe}_{0.36}$ , thus this might possibly indicate the presence of metallic cobalt within the surface layers that has transferred from the Stellite 6 and undergone a phase change from the expected hexagonal close-packed structure.

**Figure 5.14: XRD data – Nimonic 80A versus Stellite 6 at 0.314 m.s<sup>-1</sup>**

(a) Room temperature to 450°C, load = 7N, sliding distance = 4,522 m, wear surface

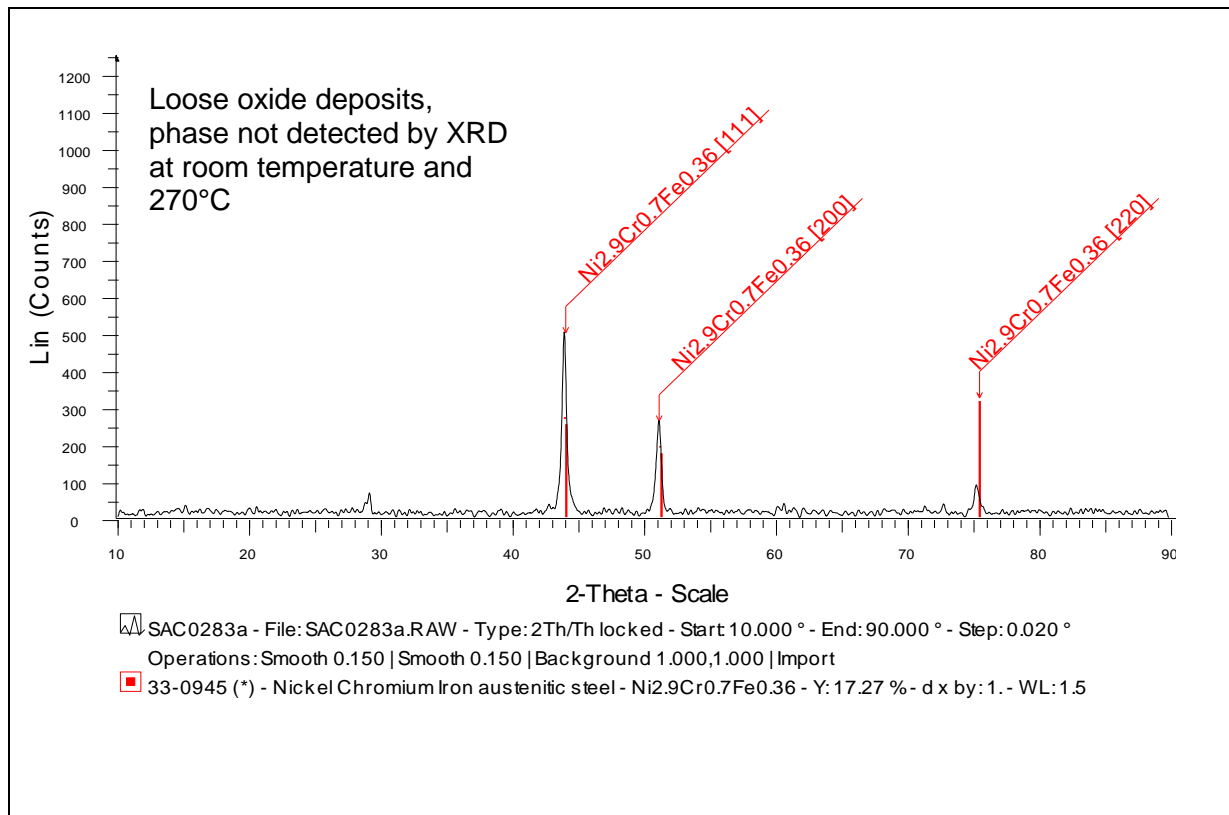


(b) 510°C to 750°C, load = 7N, sliding distance = 4,522 m, wear surface

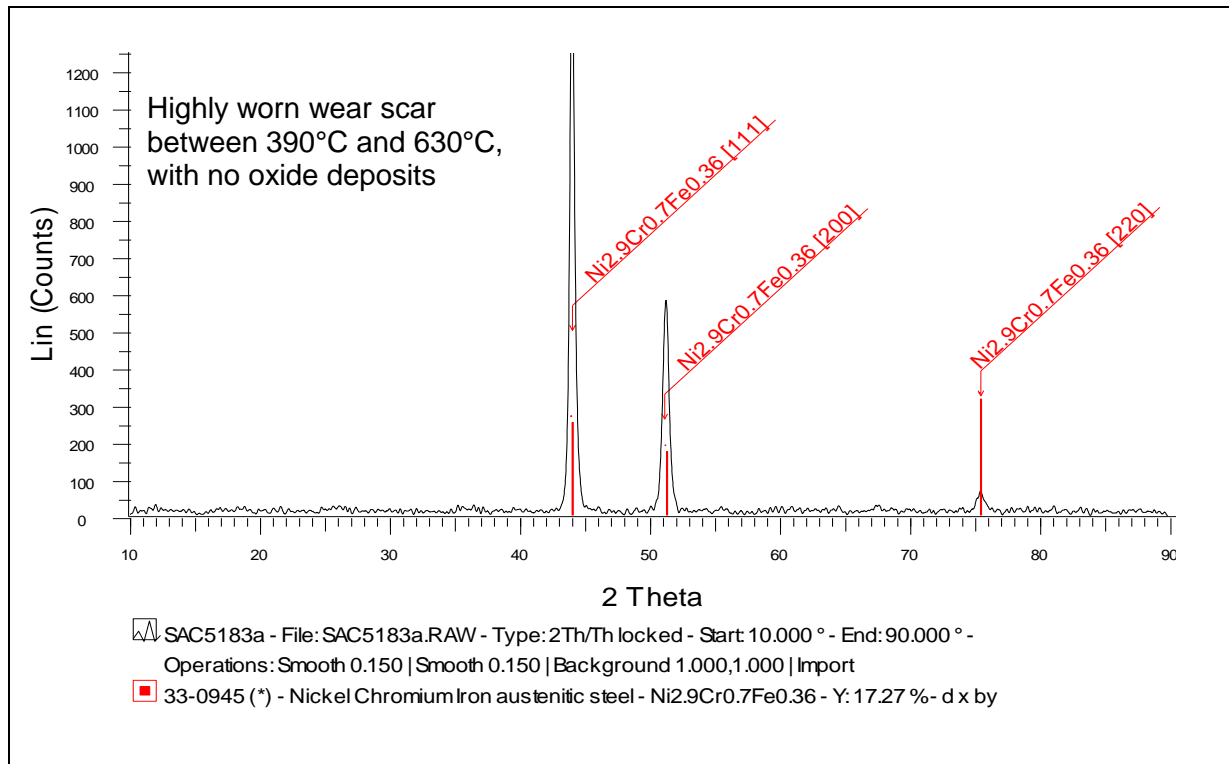


**Figure 5.15: XRD data – Nimonic 80A versus Stellite 6 at 0.905 m.s<sup>-1</sup>**

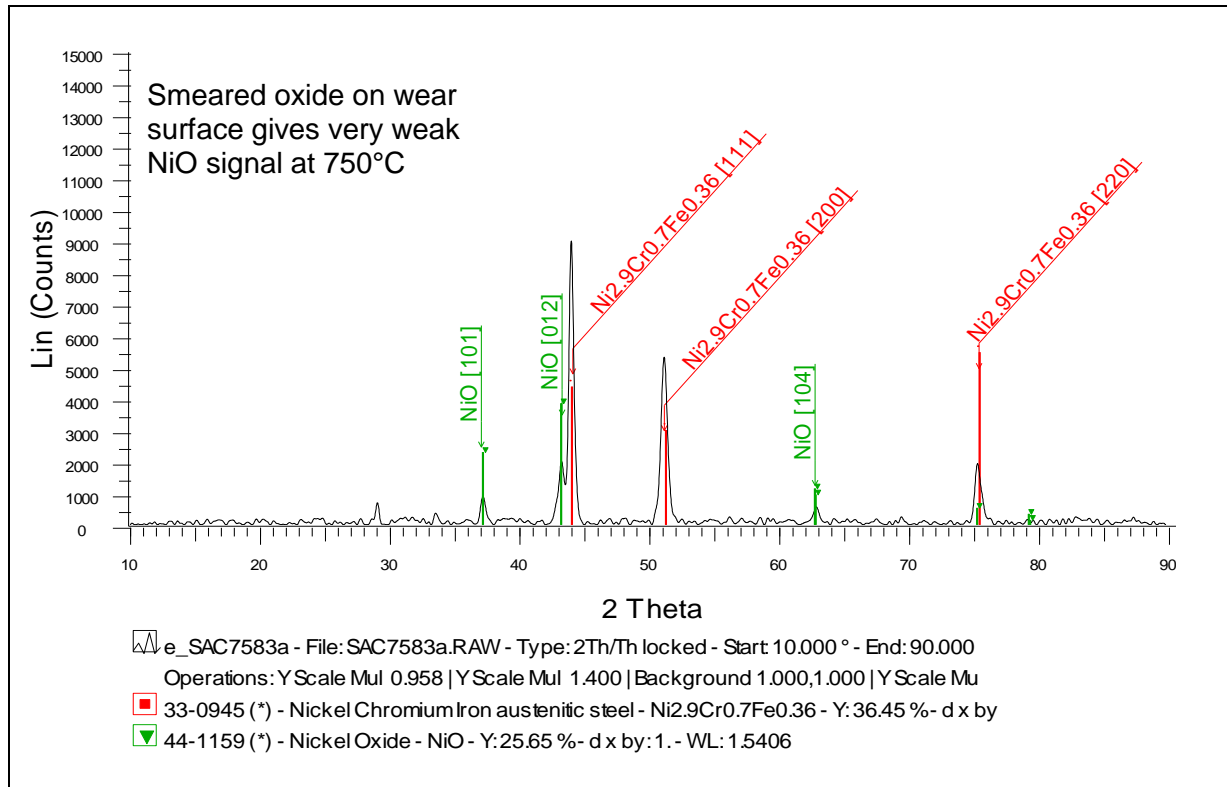
(a) Room temperature and 270°C, load = 7N, sliding distance = 4,522 m / 13,032 m, wear surface



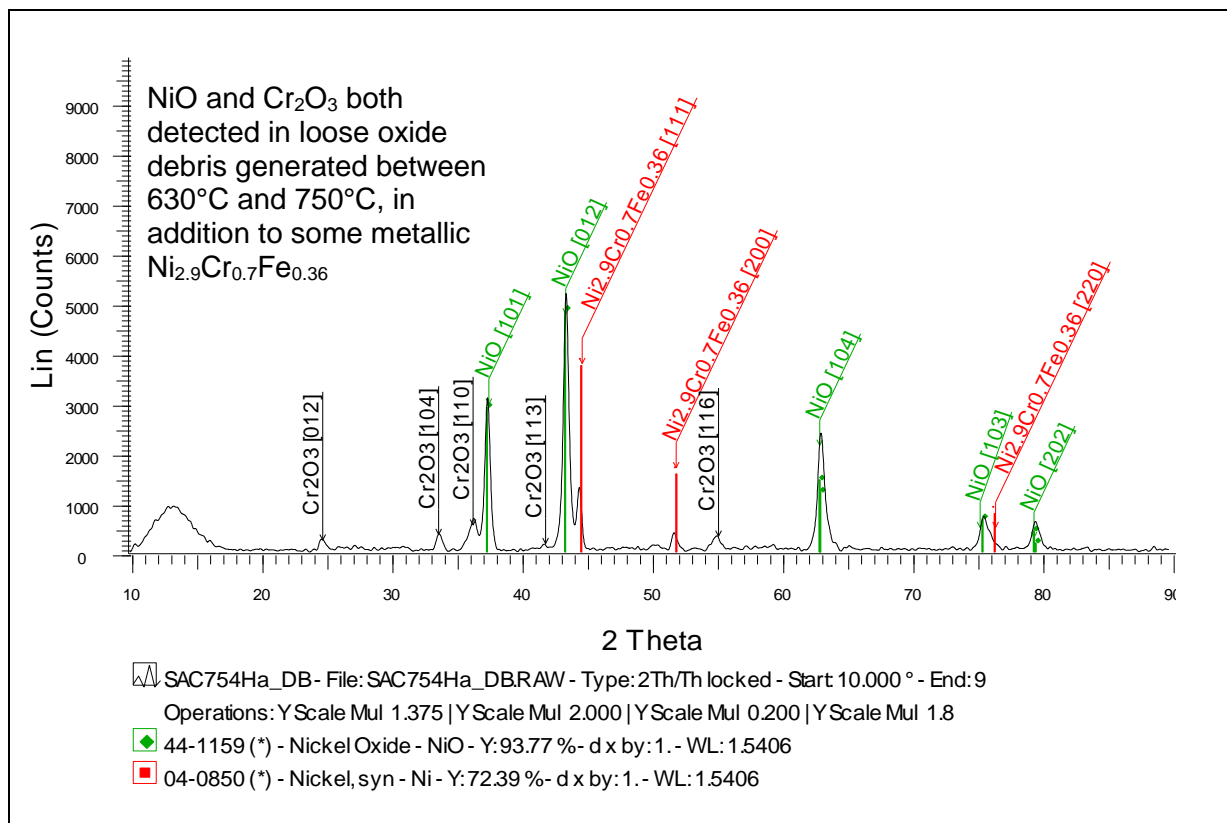
(b) 390°C to 690°C, load = 7N, sliding distance = 4,522 m / 13,032 m, wear surface



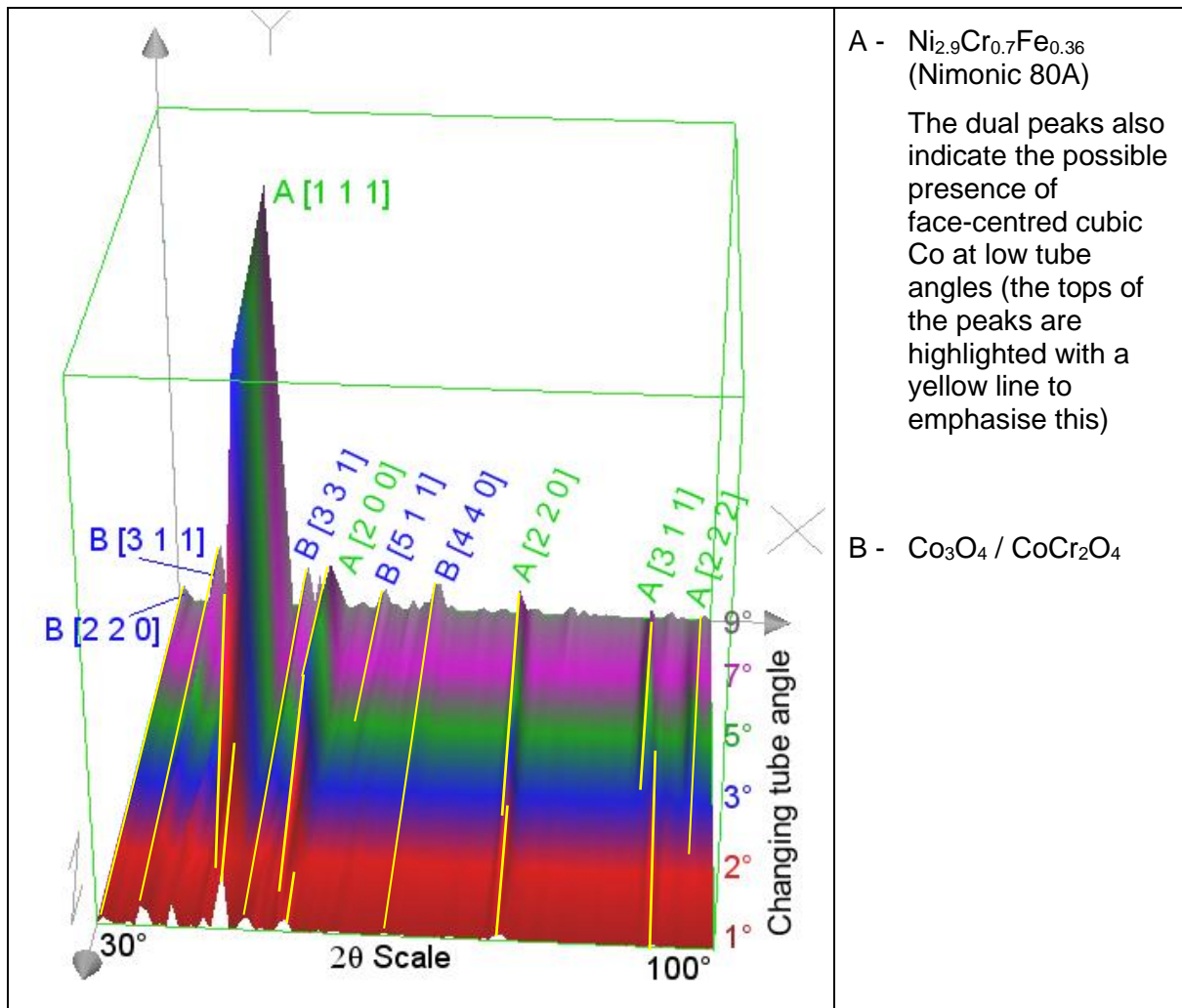
(c) 750°C, load = 7N, sliding distance = 4,522 m / 13,032 m, wear surface



(d) 630°C to 750°C, load = 7N, sliding distance = 4,522 m / 13,032 m, loose debris



**Figure 5.16: Glancing Angle XRD data – Nimonic 80A versus Stellite 6 at 0.314 m.s<sup>-1</sup> (750°C, load = 7N, sliding distance = 4,522 m)**



### 5.1.7 Micro-hardness Testing – Nimonic 80A versus Stellite 6

At 0.314 m.s<sup>-1</sup>, an area of greater hardness (Figure 5.17a shows representative depth hardness profiles taken from samples slid at room temperature, 270°C, 510°C and 750°C) was observed in the substrate immediately adjacent to the wear scar, accompanied by a rapid decrease in hardness with increasing depth into the sample – this pattern was observed at three of the key test temperatures – room temperature, 270°C, 510°C and 750°C.

At room temperature and 270°C, hardness values in the subsurface area adjacent to the wear scar were some 25% higher than in the main bulk of the substrate. Values of Vicker's

hardness fell from just over 4.9 GPa within the first 0.1 mm of the surface, to in general between 3.2 GPa and 3.6 GPa at depths between 0.1 mm and 1 mm below the surface. At 510°C, hardness values fell from peak values of ~5.0 GPa within the first 0.1 mm below the wear scar surface to between 3.0 GPa and 4.5 GPa between 0.1 mm and 1 mm depth. At 750°C, hardness values in the subsurface areas were between 15 to 30% higher than in the bulk of the substrate, falling from as high as 6.0 GPa within the first 0.1 mm depth to in general between 4.3 GPa and 5.2 GPa at depths between 0.1 mm and 1 mm.

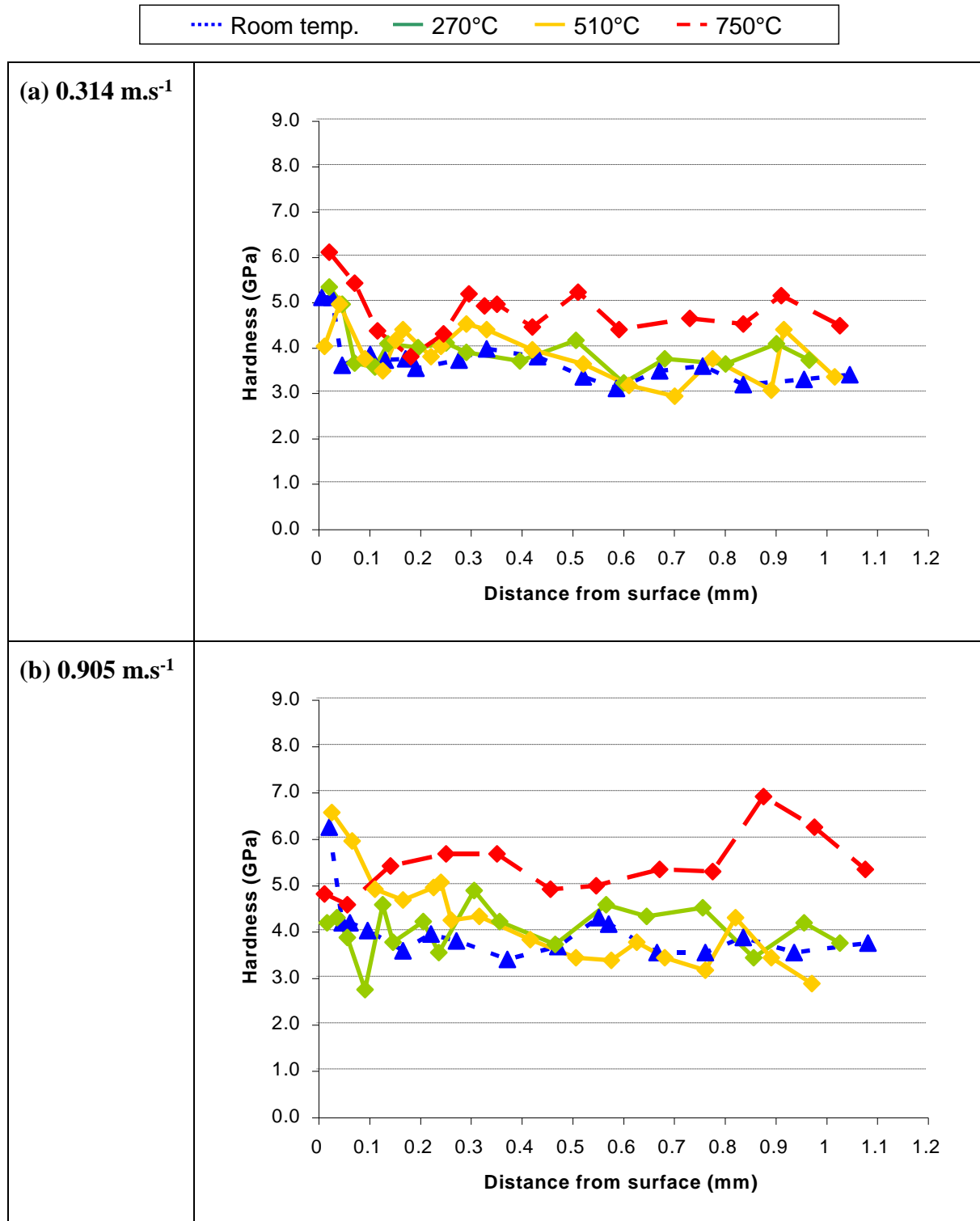
At 0.905 m.s<sup>-1</sup> / 4,522 m, the situation was more complicated (Figure 5.17b shows representative depth hardness profiles taken from samples slid at room temperature, 270°C, 510°C and 750°C), with the pattern of high subsurface hardness followed by clear decreases only observed at room temperature and 510°C. At room temperature, subsurface hardness reached levels of ~6.2 GPa within the first 0.1 mm below the surface, falling to in general between 3.4 to 3.9 GPa after ~0.1 mm and remaining in this range up to 1 mm depth. At 510°C, subsurface hardness fell from levels as high as 6.6 GPa within the first 0.1 mm, settling to between 2.9 to 4.1 GPa at depths of between 0.1 mm and 1 mm.

At 270 and 750°C, no clear trend was apparent between hardness levels and depth. At 270°C, hardness values remained in general between 3.4 and 4.4 GPa. Hardness values at 750°C were highly erratic with no sign of sub-surface hardening, varying between 4.5 GPa and 7.0 GPa.

Hardness testing of the glaze surface produced at 0.314 m.s<sup>-1</sup> and 750°C gave an average of 6.4 GPa, compared to 5.2 GPa for the Nimonic 80A substrate (Table 5.1). It is to be noted that difficulties were encountered with the glaze fragmenting at times during micro-hardness testing, with the glaze breaking-up in places to sometimes reveal underlying powdery debris – actual hardness levels of the glaze may have thus been much higher than the measured values suggest.

**Figure 5.17: Subsurface layer hardness for samples slid at 0.314 and 0.905 m.s<sup>-1</sup>, Nimonic 80A versus Stellite 6**

(load = 7N, sliding distance = 4,522 m, hardness values in GPa, Vickers micro-indenter - 50g, sample size = 3)



**Table 5.1: Hardness data for glaze and undeformed substrate, Nimonic 80A versus Stellite 6 slid at 750°C**

(load = 7N, sliding distance = 4,522 m, hardness values in GPa, Vickers micro-indenter - 50g, sample size = 5)

Unworn substrate (preheated to 750°C for 4 hours)		Glaze formed at 0.314 m.s <sup>-1</sup>		Nimonic 80A surface at 0.905 m.s <sup>-1</sup>
4.95	Mean = 5.23 GPa	5.98	Mean = 6.45 GPa	No glaze formed - surface too rough for measurements
5.77		6.99		
5.10		6.50		
5.73		7.32		
4.61		5.46		

## 5.2 In-depth Studies of the Nimonic 80A versus Stellite 6 Wear Pair

### 5.2.1 Build-up of Glaze with Time – Nimonic 80A versus Stellite 6 at 510°C and 750°C, Sliding Speed 0.314 m.s<sup>-1</sup>

#### 5.2.1.1 Experimental Observations – Glaze Build-up at 510°C and 750°C, 0.314 m.s<sup>-1</sup>

During the sliding of Nimonic 80A against Stellite 6 at a sliding speed of 0.314 m.s<sup>-1</sup> and temperatures of 510°C and 750°C, initial weight gains were observed for the Nimonic 80A sample within the first 38 m (2 minutes) of sliding at both temperatures (0.000(4) g at 510°C and 0.008(8) g at 750°C). After these initial weight gains, sample weight change showed very little variation up to 4,522 m (240 minutes) of sliding, regardless of temperature or sliding distance / time.

**510°C:** A very slight positive weight gain of 0.000(4) g was observed for the Nimonic 80A after 38 m sliding distance or two minutes sliding time, equating to a negative wear rate of -10.614 µg.m<sup>-1</sup>. Weight loss values did not show much change, showing a very slight upward and erratic trend to a maximum value of 0.001(2) g after 2,261 m (120 minutes) of sliding. There was a very slight loss on continued sliding to 4,522 m (240 minutes), with a recorded mean weight change value of 0.000(8) g.

After a large negative wear rate of -10.614 µg.m<sup>-1</sup> between 0 and 38 m (the first 2 minutes of sliding), wear rate values remained near negligible up to 4,522 m or 240 minutes (at most



1.061  $\mu\text{g.m}^{-1}$  between 38 m and 188 m, and -1.274  $\mu\text{g.m}^{-1}$  between 283 m and 377 m). This indicates a large transfer in material (the negative value indicating transfer to the sample) occurred at the very beginning of sliding (0 to 38 m), after which there was little gain or loss of material.

The coefficient of friction values (Figure 5.19) measured during each of the tests at 510°C showed a very brief initial unsettled period, before rapidly settling into a ‘steady state’ with reduced variation. At 510°C, values during the initial unsettled period rose from zero to typically ~0.7 (variability ~20%), before settling down to between 0.6 and 0.7 (variability ~12%).

**750°C:** After two minutes sliding time or 38 metres sliding distance at 750°C, a slight mean positive weight change of 0.001(0) g was obtained for the Nimonic 80A. After this early initial gain in weight, weight change values decreased very slightly with time, indicating a very gradual loss of material from the Nimonic 80A sample. After 240 minutes or 4,522 m, a negligible value for weight change was obtained.

Presenting this data in terms of wear rate (Figure 5.18b) between each measurement point shows the effect of the material build-up on the Nimonic 80A sample even more clearly. A large negative magnitude wear rate of -26.448  $\mu\text{g.m}^{-1}$  was obtained in the first 38 m (2 minutes), indicating rapid initial build-up of material on the sample. After this, wear rate became very low very rapidly, as indicated by the 0.700  $\mu\text{g.m}^{-1}$  value between 38 m (2 minutes) and 188 m (10 minutes). Values after this remained very close to and in general, very slightly above zero wear rate, indicating a very gradual loss of material from the glaze surface. Wear remained extremely low for the remainder of the test period.

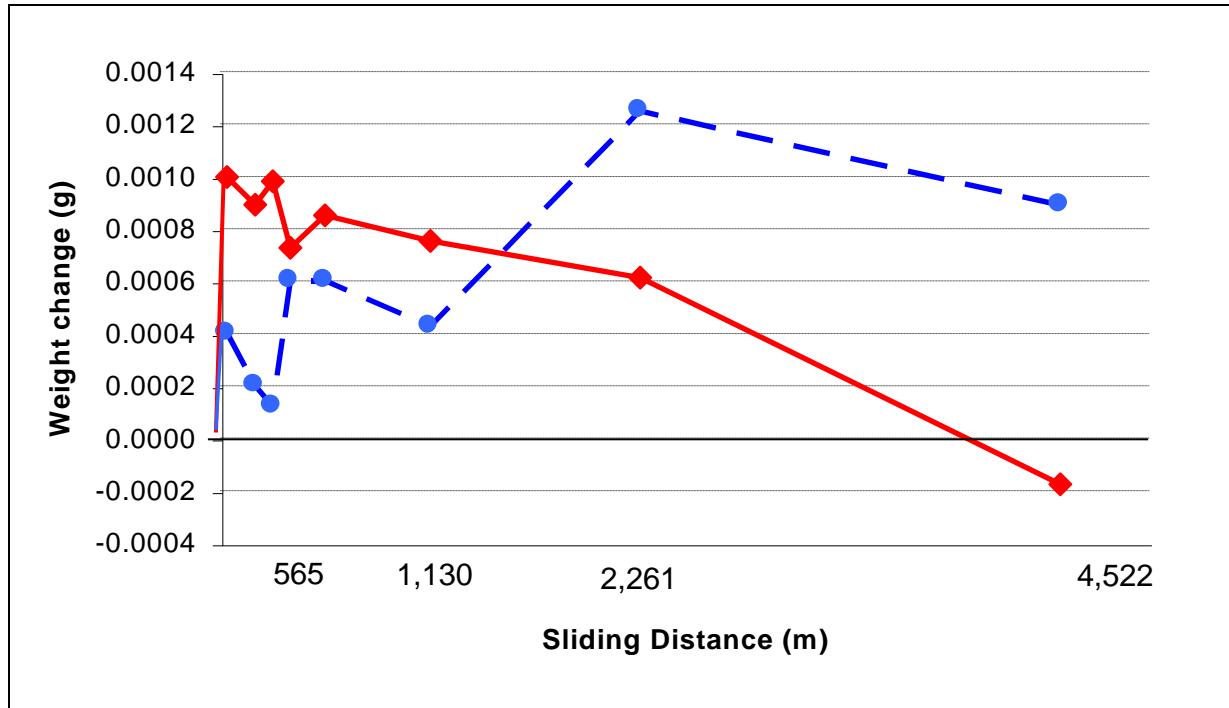
At 750°C, coefficient of friction values (Figure 5.19) followed the same pattern as observed at 510°C, with a brief unsettled run-in period at the very beginning of sliding followed by a very rapid transition to reduced variation steady state sliding. Recorded values of coefficient of friction were lower at 750°C – during the unsettled run-in phase, the coefficient of friction rose from zero to typically 0.5 to 0.55 (variability ~20% – this compares with ~0.7 at 510°C), settling down to ~0.5 (variability ~10%) during steady state sliding (compared to between 0.6 and 0.7 at 510°C).

**Figure 5.18: Change in weight and wear rate with time for Nimonic 80A versus Stellite 6 at 510°C, 630°C and 750°C**

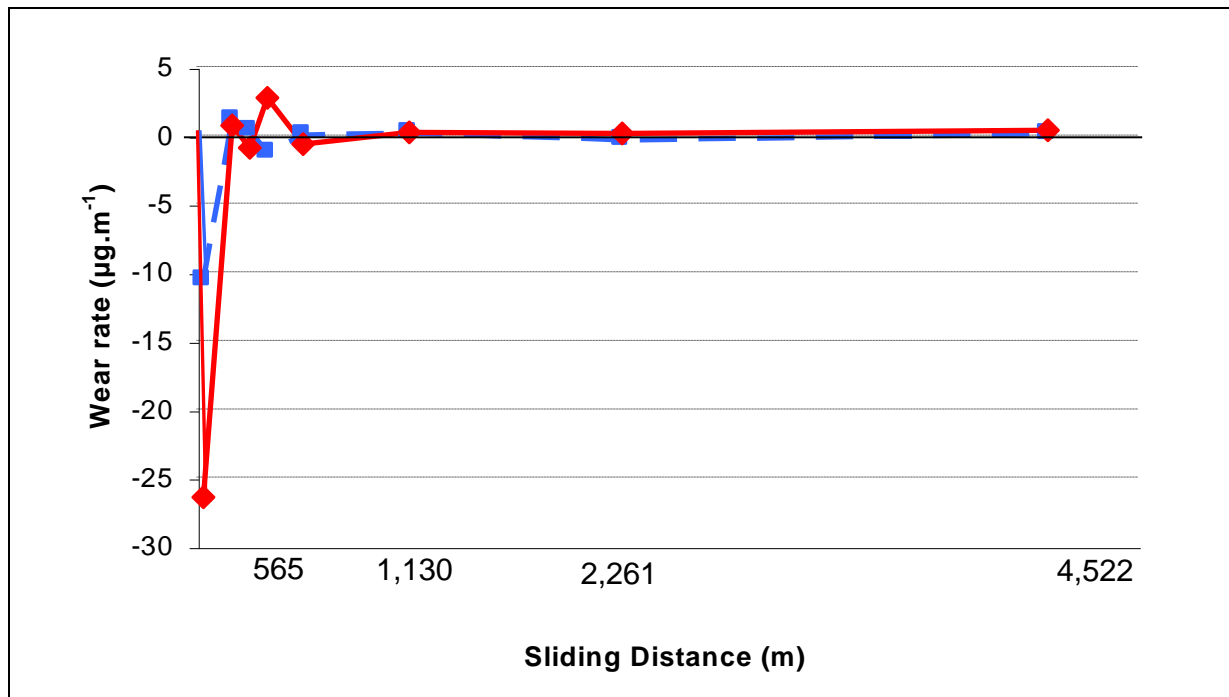
(load = 7N, sliding speed =  $0.314 \text{ m.s}^{-1}$ , sample size = 3)



(a) Weight change



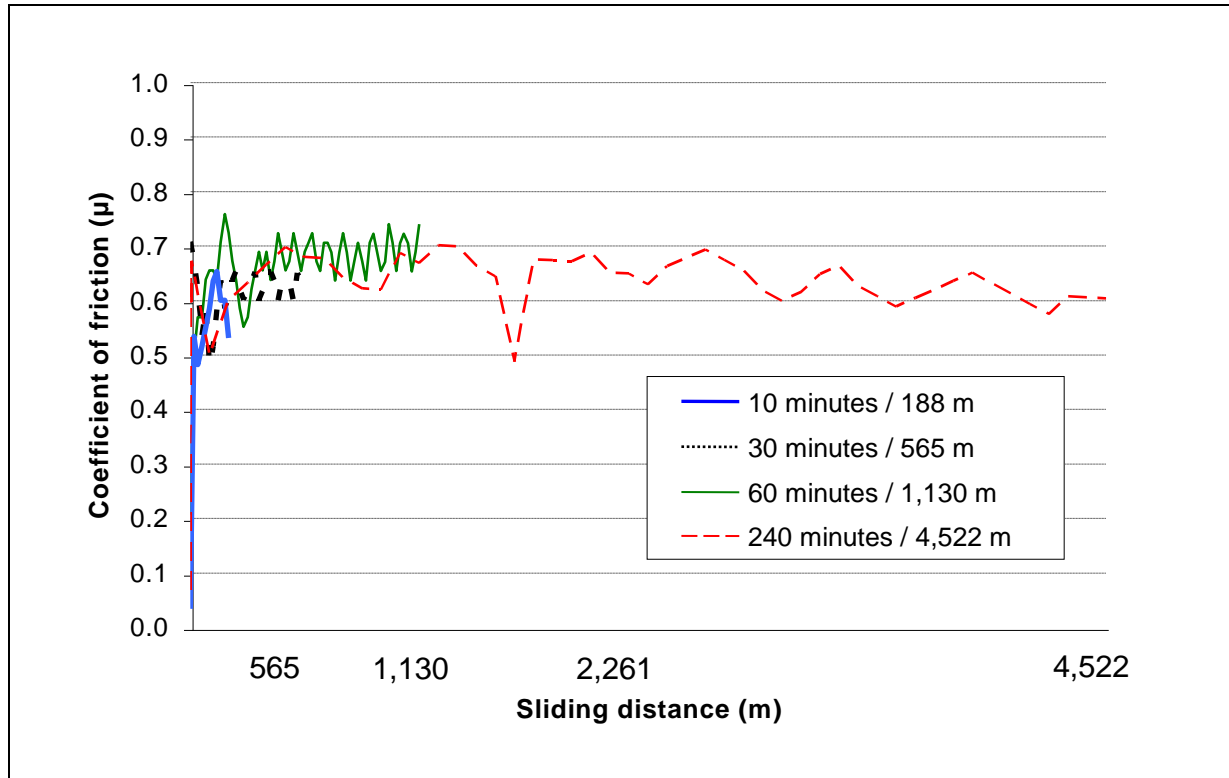
(b) Wear rate



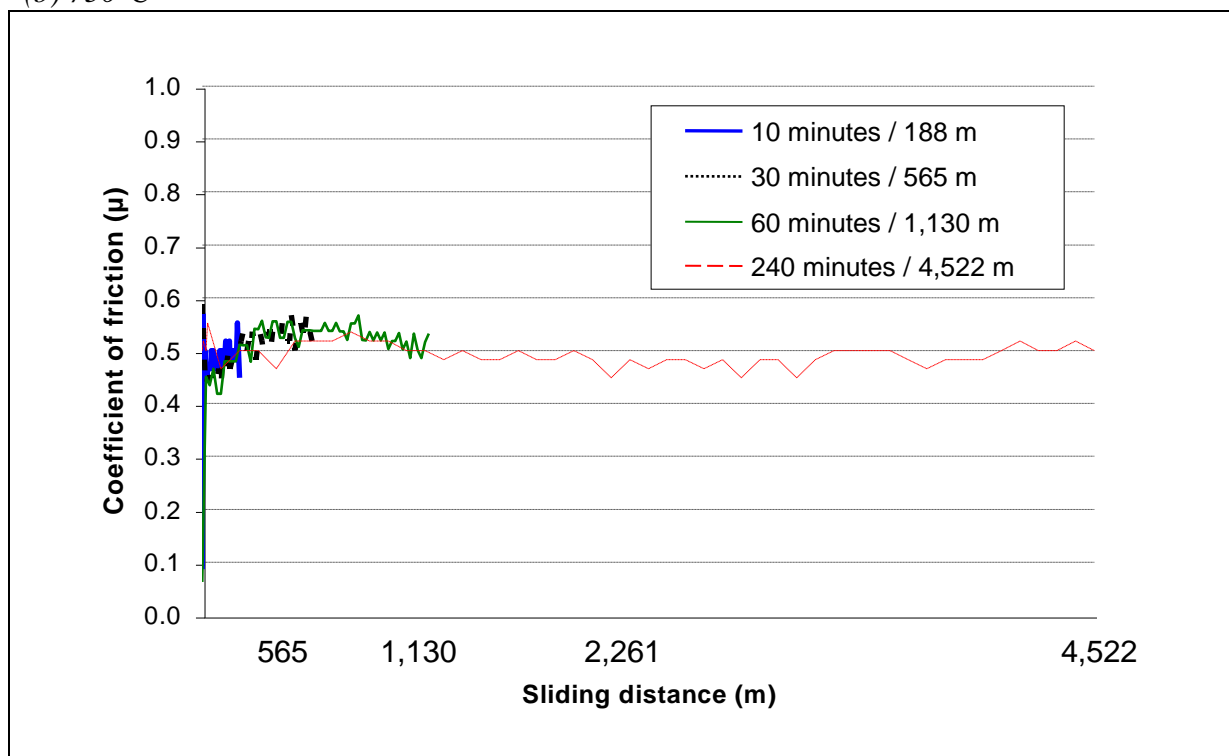
**Figure 5.19: Change in coefficient of friction with sliding distance for Nimonic 80A versus Stellite 6 at 510°C and 750°C**

(load = 7N, sliding speed =  $0.314 \text{ m.s}^{-1}$ , sample size=5)

(a) 510°C



(b) 750°C



### ***5.2.1.2 Optical and SEM Studies – Glaze Build-up at 510°C and 750°C, 0.314 m.s<sup>-1</sup>***

At 510°C, the formation of oxide layers and glaze platforms on the surface of the Nimonic 80A were observed after only 38 m or 2 minutes of sliding, accompanied by a very limited amount of damage to the Nimonic 80A (Figures 5.20a and 5.21a) and virtually no damage to the Stellite 6 counterface (not shown). The level of glaze coverage then increased on sliding up to 188 m (10 minutes), with only a very slight increase in metallic damage. However, although a reduction in porosity was observed with increasing sliding distance, the glaze layers continued to show some porosity after 4,522 m / 240 minutes of sliding.

Further sliding resulted in an increase in glaze coverage with no extra damage to the Nimonic 80A. However, at 510°C, the glaze was always observed to be patchy and highly porous with evidence of some breakaway of sections of glaze at all sliding distances up to 4,522 m (4 hours) of sliding (Figure 5.22) and a small amount of accompanying black oxide powder debris generation – this loose oxide debris was usually in the size range 300 nm to 1 µm, with a few particles of size up to 3 µm.




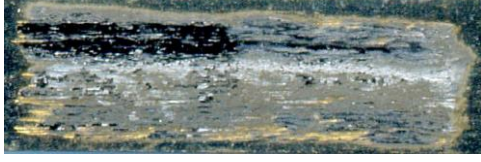
The rapid formation of a patchy glaze was again observed at 750°C, with oxide layers and glaze platforms once again visible after only 38 metres or 2 minutes of sliding, with very little damage to the Nimonic 80A substrate (Figures 5.20b and 5.21b) or to the Stellite 6 counterface (not shown). Examination of samples slid for longer distances indicated no further significant damage to either, with the initially patchy glaze developing into a smooth glaze layer after 4,522 m (240 minutes). Glaze layers were observed to be more complete and less porous at 750°C than at 510°C (Figure 5.22) – the level of porosity seemed to reduce significantly with sliding distance, with glaze layers formed after both 2,261 m / 120 minutes and 4,522 m / 240 minutes apparently very smooth and with extended areas of very low porosity.

At 750°C, losses in terms of breakaway of material from the glaze and debris formation were minimal and less than at 510°C. Debris produced were always in the form of black oxide powder, particle sizes normally in the range 300 nm to 1 µm with a few particles up to 3 µm.




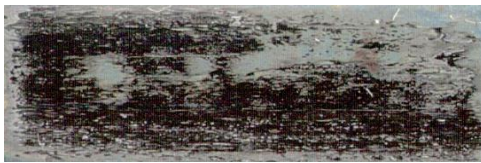
**Figure 5.20: Glaze build-up with time for Nimonic 80A versus Stellite 6 – optical**

(load = 7N, sliding speed = 0.314 m.s<sup>-1</sup>, wear scars = 14 x 5 mm)

(a) 510°C

	<p><b>2 minutes, 38 metres</b></p> <p>A little surface damage, some oxide build-up and glaze formation (darker banded areas) already occurring</p>
	<p><b>10 minutes, 188 metres</b></p> <p>Oxide debris and patchy glaze formation over a greater percentage of the surface (dark grey)</p>
	<p><b>120 minutes, 2,261 metres</b></p> <p>Glaze formation still patchy with some limited removal</p>
	<p><b>240 minutes, 4,522 metres</b></p> <p>Patchy glaze coverage persists up to 750°C, though with slightly greater coverage of wear scar</p>

(b) 750°C

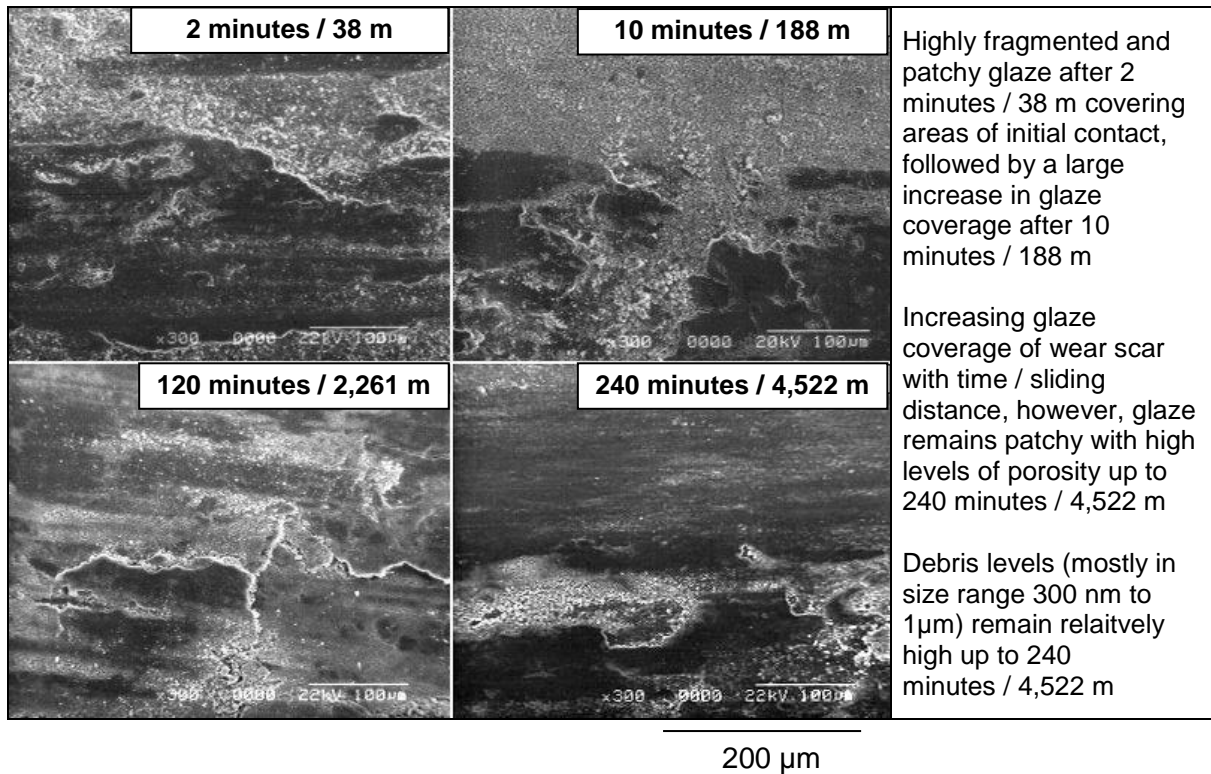
	<p><b>2 minutes, 38 metres</b></p> <p>Slight surface damage, substantial glaze (grey colour) formation already occurring, less powdery than at 510°C</p>
	<p><b>10 minutes, 188 metres</b></p> <p>Patchy glaze formation over a greater percentage of the surface (dark grey) with some removal (lighter areas) and limited loose oxide formation</p>
	<p><b>120 minutes, 2,261 metres</b></p> <p>Glaze formation still patchy with some limited removal</p>
	<p><b>240 minutes, 4,522 metres</b></p> <p>Glaze coverage now accounting for most of wear scar area, with a less broken, smooth surface – minimal loose debris</p>



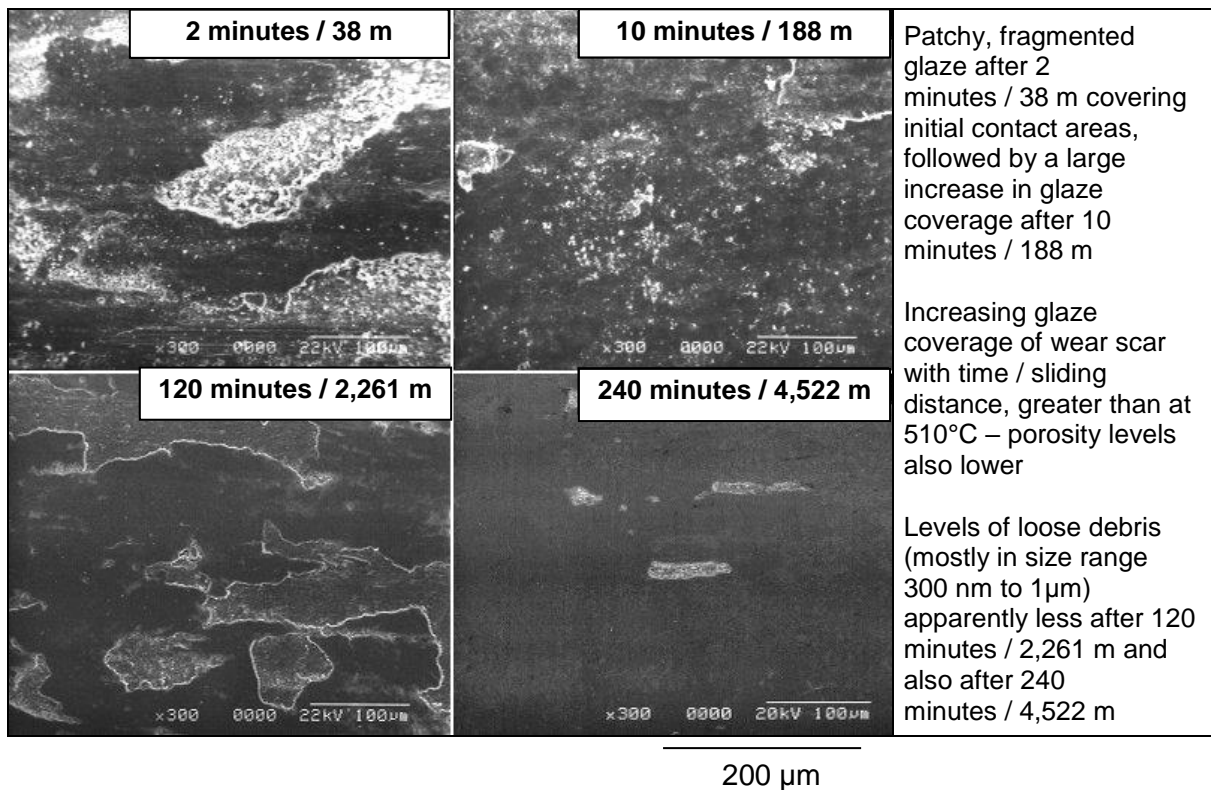
**Figure 5.21: Glaze build-up with time for Nimonic 80A versus Stellite 6 – SEM low resolution images (X300)**

(load = 7N, sliding speed =  $0.314 \text{ m.s}^{-1}$ , wear scars =  $14 \times 5 \text{ mm}$ )

(a)  $510^\circ\text{C}$

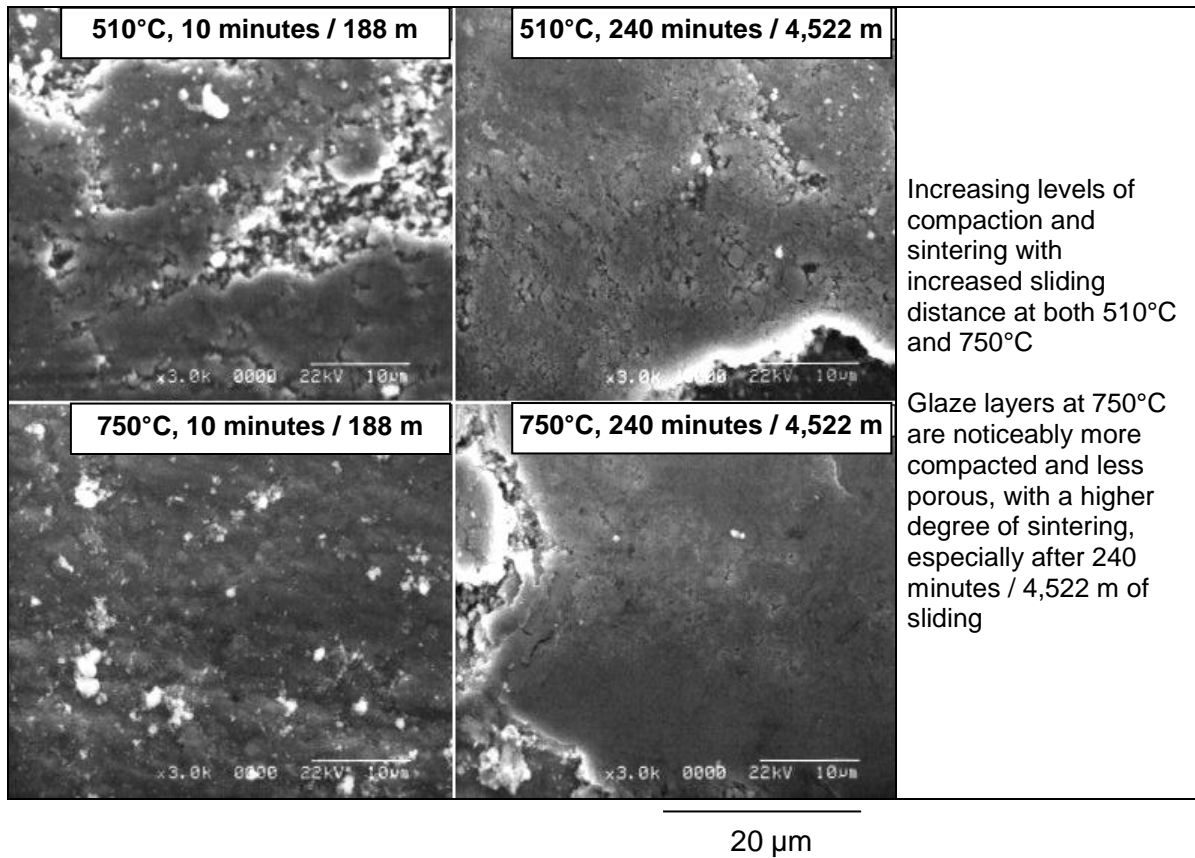


(b)  $750^\circ\text{C}$



**Figure 5.22: Glaze build-up with time for Nimonic 80A versus Stellite 6 – SEM high resolution images (X3.0K)**

(load = 7N, sliding speed =  $0.314 \text{ m.s}^{-1}$ , wear scars =  $14 \times 5 \text{ mm}$ )

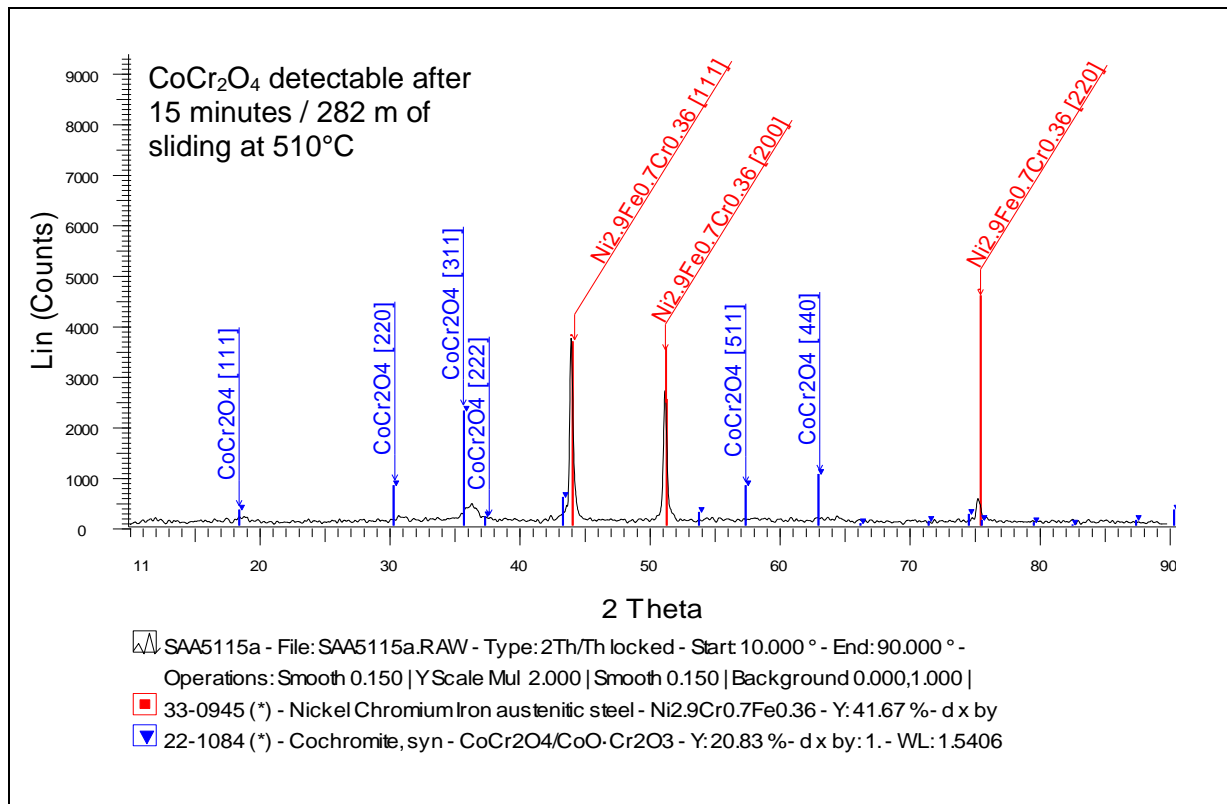


### 5.2.1.3 EDX Analysis – Glaze Build-up at 510°C and 750°C, $0.314 \text{ m.s}^{-1}$

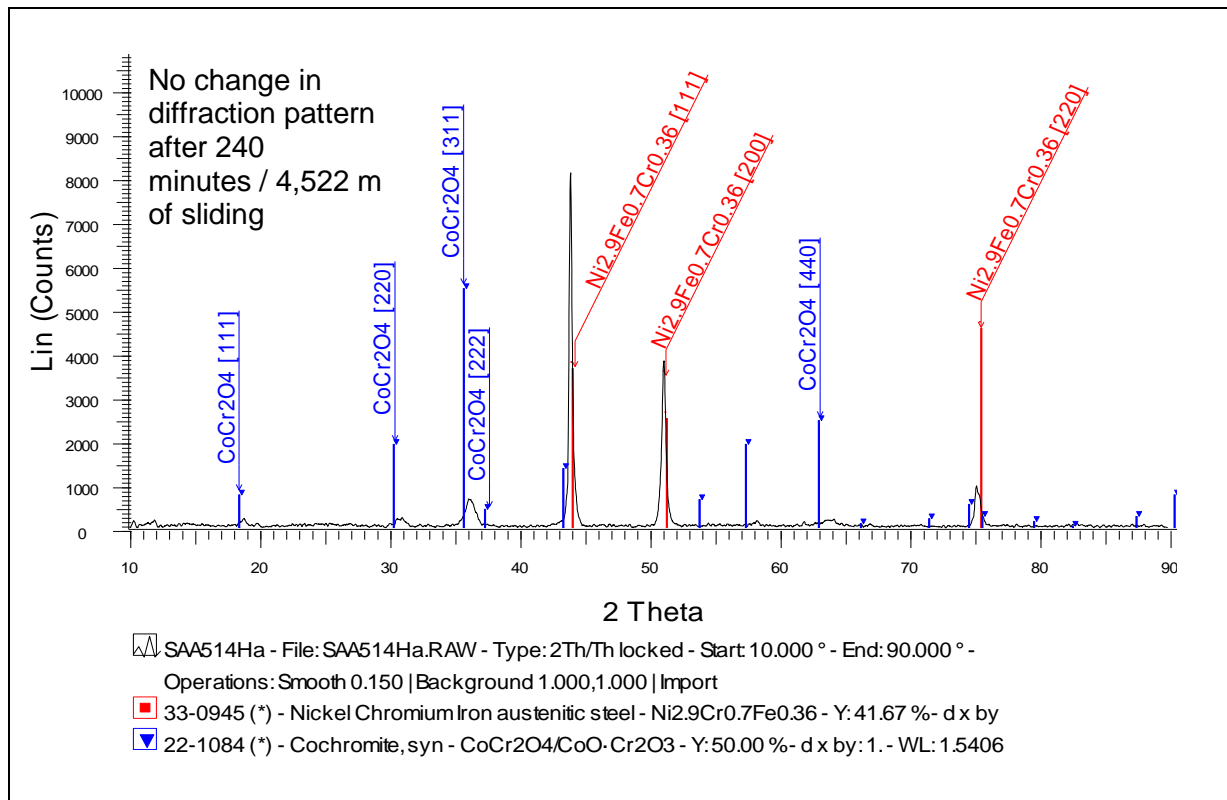
The use of EDX on samples slid at 510°C, indicate very high levels of cobalt and chromium in the glaze layers, with only a small amount of nickel. After 38 metres / 2 minutes, the oxide consisted on average of ~59% cobalt, ~28% chromium and ~7% nickel. After 2,261 metres / 240 minutes, there was very little change composition (~62% Co, ~30% Cr, ~2% Ni). After 4,522 m / 240 minutes of sliding, there was a very slight decrease in cobalt levels to ~51%, with nickel levels remaining low at ~3% and chromium levels unchanged at ~34%. The high cobalt levels and low nickel levels indicate the source of the glaze was almost exclusively the Stellite 6 counterface.

**Figure 5.23: XRD data – Nimonic 80A versus Stellite 6 at 0.314 m.s<sup>-1</sup> / 510°C**

(a) load = 7N, sliding distance = 282 m (15 minutes), wear surface



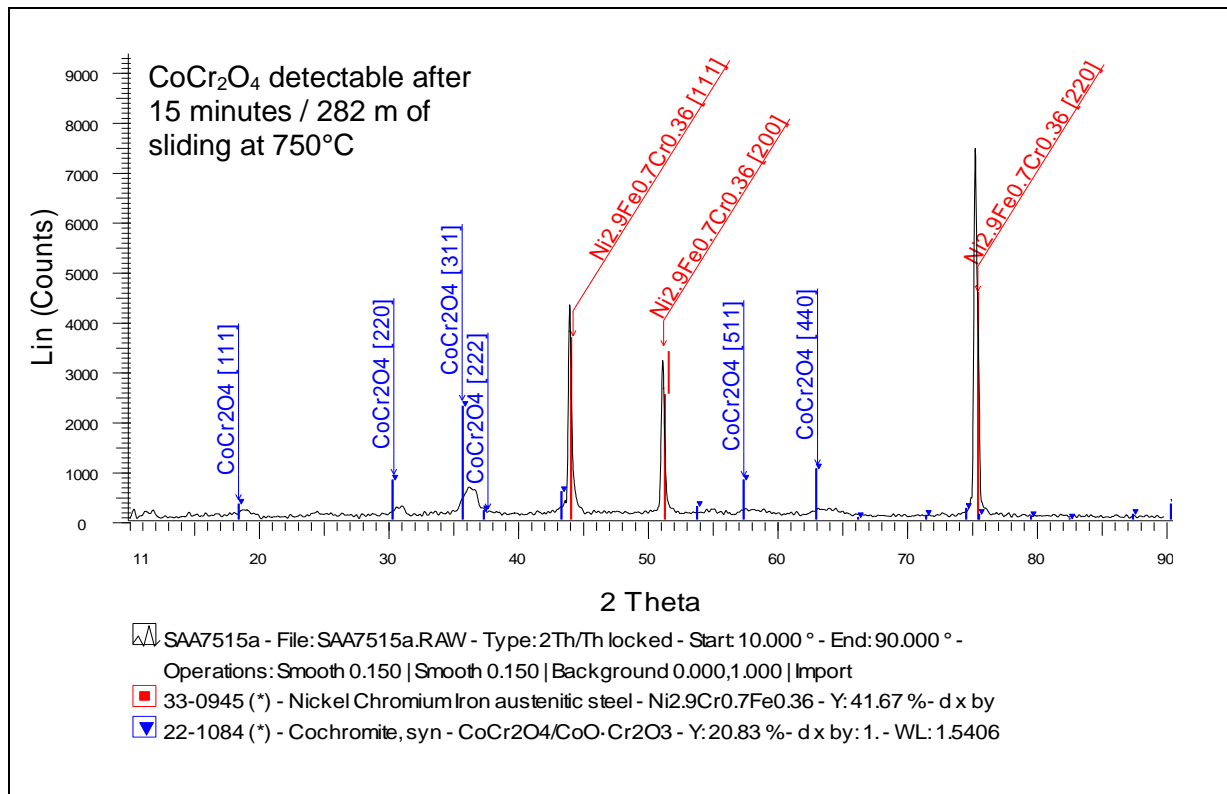
(b) load = 7N, sliding distance = 4,522 m (240 minutes), wear surface



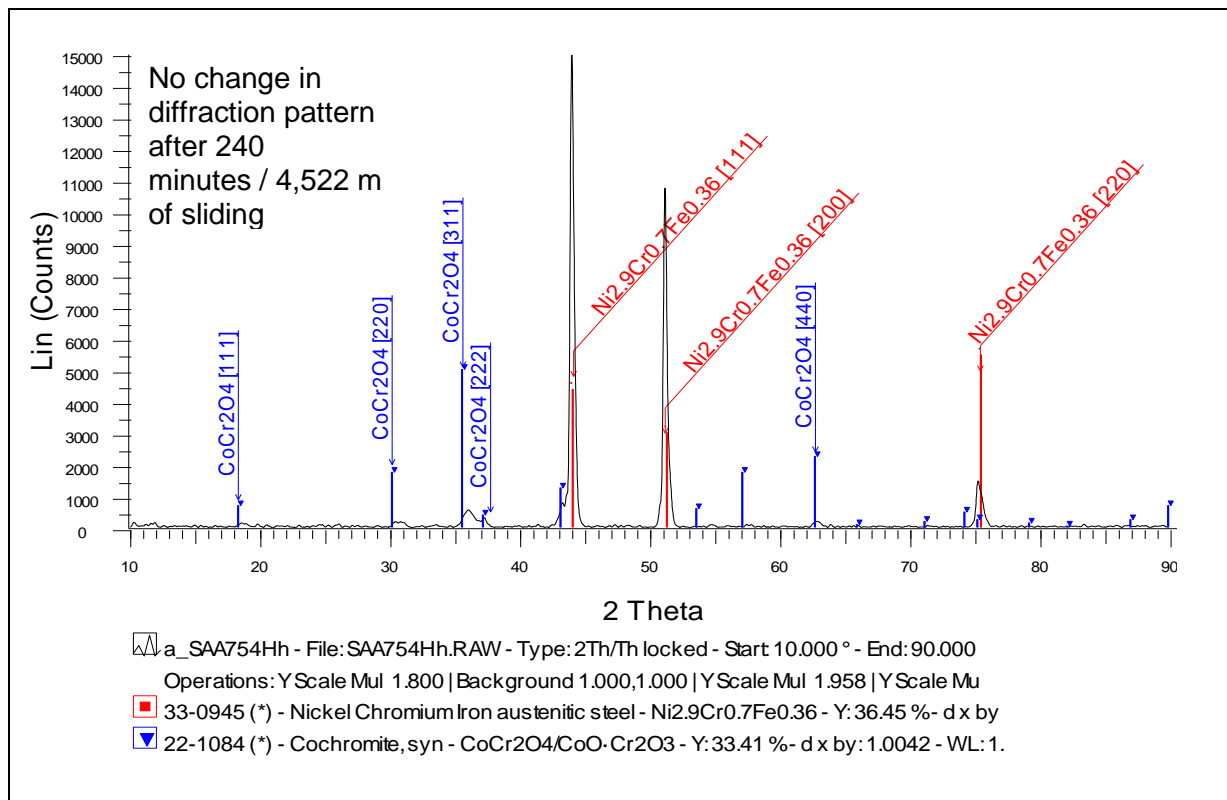


**Figure 5.24: XRD data – Nimonic 80A versus Stellite 6 at  $0.314 \text{ m.s}^{-1}$  /  $750^\circ\text{C}$**

(a) load = 7N, sliding distance = 282 m (15 minutes), wear surface



(b) load = 7N, sliding distance = 4,522 m (240 minutes), wear surface



At 750°C, EDX of the oxide material forming the glaze layers indicated that the majority of this oxide was transferred from the Stellite 6, but with a more significant (although still small) contribution from the Nimonic 80A (indicated by the presence of Ni) than seen at 510°C. The contribution from the Nimonic 80A became greater with increasing sliding distance / time - after 38 metres / 2 minutes, the mean composition of the glaze was ~55% cobalt, ~28% chromium and ~9% nickel. After 2,261 metres / 120 minutes, cobalt levels decreased to ~50%, and nickel levels increased to ~18% (chromium levels remained at ~27%). After 4,522 metres / 240 minutes, cobalt accounted for only ~34%, with nickel levels rising to ~17% and chromium levels rising to ~36%.

The EDX data at 750°C also indicated a high degree of variability in the glaze composition, most noticeably after 2,261 m / 120 minutes and 4,522 m / 240 minutes of sliding. This was most evident from highly erratic values of cobalt (between ~40 % and ~60%) and nickel (between ~7% and ~25%) obtained after sliding for both distances / times.

#### ***5.2.1.4 XRD Analysis – Glaze Build-up at 510°C and 750°C, 0.314 m.s<sup>-1</sup>***

XRD on samples slid at both 510°C and 750°C indicated the presence of CoCr<sub>2</sub>O<sub>4</sub> and / or Co<sub>3</sub>O<sub>4</sub> on samples slid for 15 minutes or more (Figures 5.23 and 5.24) – given the high levels of cobalt detected by EDX, the presence of both phases was likely. The high cobalt content further indicated that the Stellite 6 was the primary source of the debris forming the glaze layers.

No extra phases or changes of phase were observed, regardless of temperature or sliding distance / time.

### ***5.2.2 Reversal of Sample and Counterface - Stellite 6 versus Nimonic 80A at 750°C***

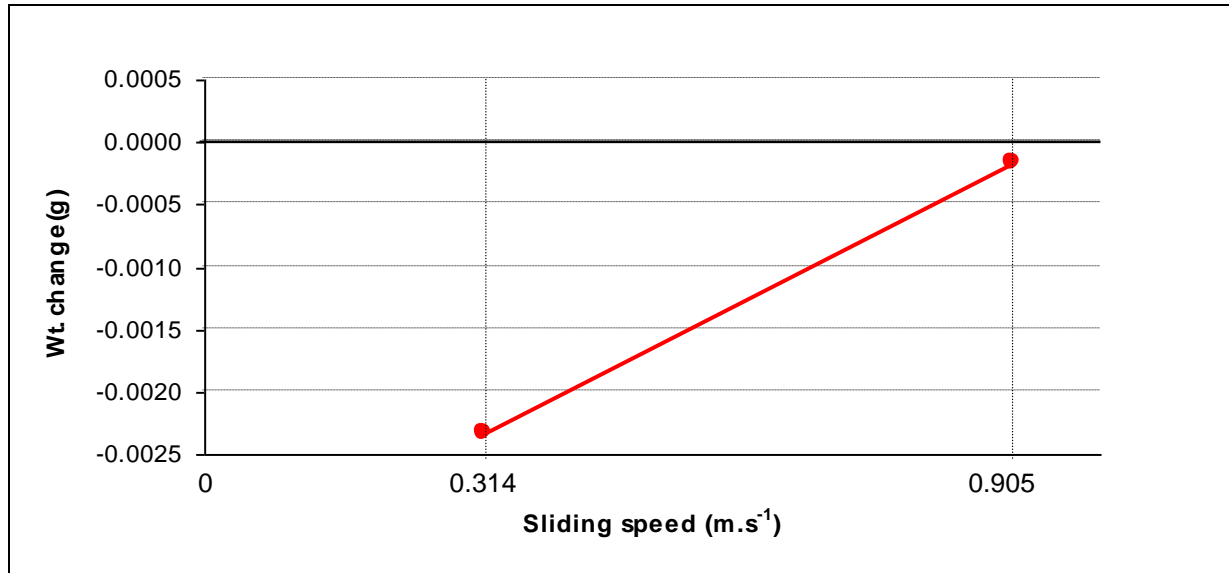
#### ***5.2.2.1 Experimental Observations – Stellite 6 versus Nimonic 80A***

With Stellite 6 as the sample and Nimonic 80A as the counterface, weight change values tended to be minimal, with a tendency to decreasing weight loss from the Stellite 6 sample with increasing sliding speed. Figure 5.25 shows the observed change in weight versus sliding speed, changing from -0.002(4) g at 0.314 m.s<sup>-1</sup> to near-negligible at 0.905 m.s<sup>-1</sup>. Figure 5.25b shows a decrease in wear rate on increasing sliding speed from 0.521 µg.m<sup>-1</sup> at 0.314 m.s<sup>-1</sup> to near negligible levels at 0.905 m.s<sup>-1</sup>.

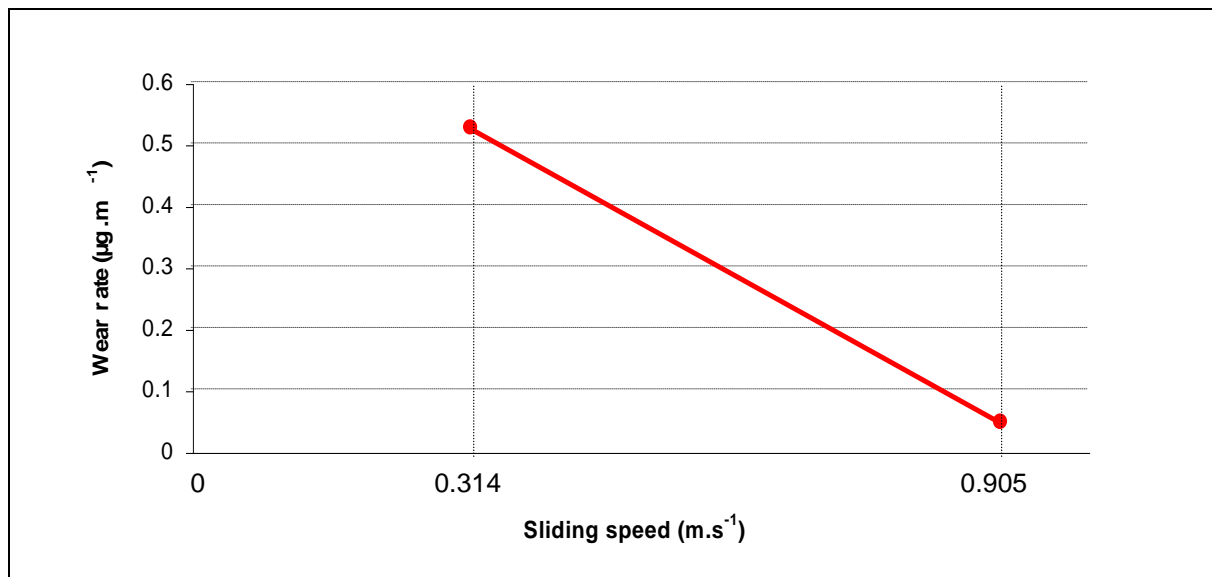
**Figure 5.25: Weight change and wear rate versus sliding speed for Stellite 6 as the sample material worn against a Nimonic 80A counterface at 750°C**

(load = 7N, sliding distance = 4,522 m, sample size = 3)

(a) Weight change

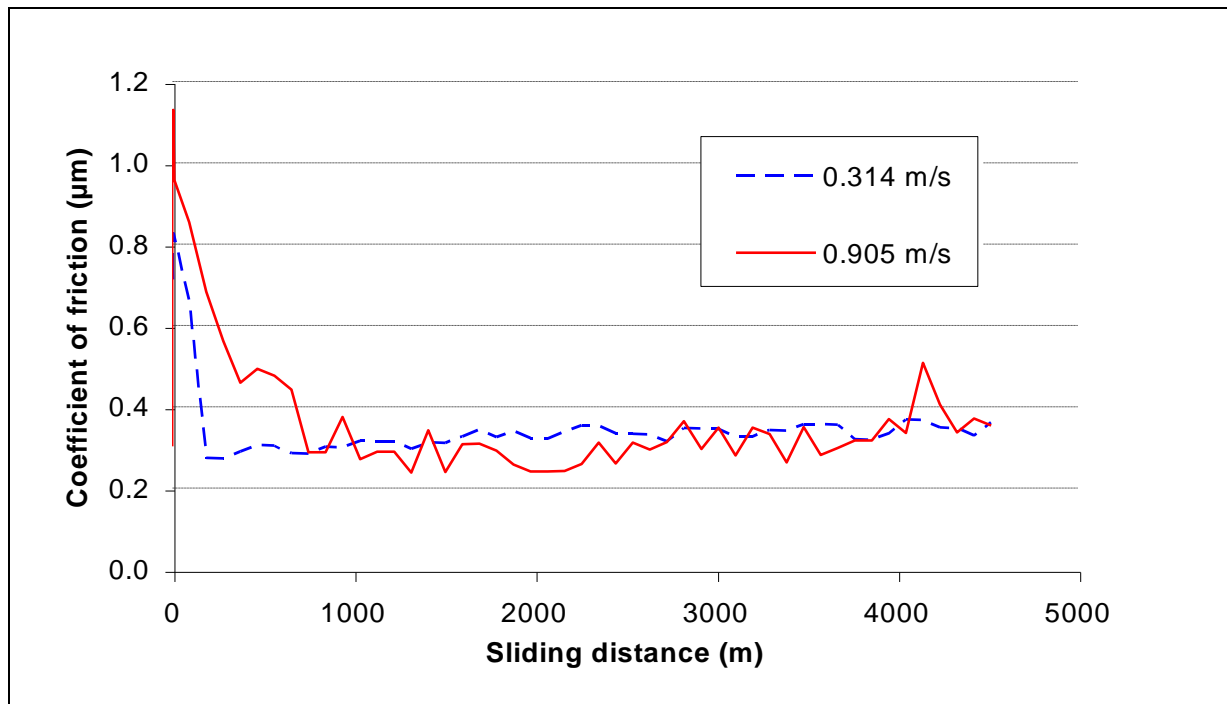


(b) Wear rate



**Figure 5.26: Coefficient of friction versus temperature – Stellite 6 vs. Nimonic 80A**

(load = 7N, sliding distance = 4,522 m, sample size = 3)



Coefficient of friction values (Figure 5.26) indicated the presence of an unsettled run-in period during the early stages of sliding, which regardless of sliding speed, rapidly gave way to more settled steady state sliding without any further major variations— this occurred after  $\sim 188$  m at  $0.314 \text{ m.s}^{-1}$  and  $\sim 750$  m at  $0.905 \text{ m.s}^{-1}$ . During the unsettled run-in period, friction values rose to higher values at  $0.905 \text{ m.s}^{-1}$  (a maximum value of 1.14 was observed almost immediately after the start of sliding) than at  $0.314 \text{ m.s}^{-1}$  (the maximum value achieved was 0.83, again almost immediately after the start of sliding). Coefficient of friction values at  $0.314 \text{ m.s}^{-1}$  tended to be slightly higher during steady state sliding at between 0.3 and 0.35, compared to between 0.25 and 0.35 at  $0.905 \text{ m.s}^{-1}$ . Variability at  $0.314 \text{ m.s}^{-1}$  was also less at  $\sim 15\%$ , compared to  $\sim 20\%$  at  $0.905 \text{ m.s}^{-1}$ .

It is to be noted that although coefficient of friction values tended to be slightly lower at  $0.905 \text{ m.s}^{-1}$  than at  $0.314 \text{ m.s}^{-1}$  during steady state sliding, the greater levels of vibration observed at  $0.905 \text{ m.s}^{-1}$  and resulting reductions in contact time mean that actual coefficient of friction values at  $0.905 \text{ m.s}^{-1}$  were likely to have been much higher. For this reason, caution must be observed on drawing any conclusions from the  $0.905 \text{ m.s}^{-1}$  coefficient of friction data.

### 5.2.2.2 Optical and SEM Microscopy – Stellite 6 versus Nimonic 80A

Compacted oxide formation was observed to form regardless of the sliding speed used (Figures 5.27 and 5.28 show the optical and SEM images respectively), however, the nature of the glaze was noted to change. At  $0.314 \text{ m.s}^{-1}$ , a smooth glaze surface of between  $\sim 4.5$  and  $\sim 5.5 \mu\text{m}$  thickness was formed, though one sample was observed to have a small strip of material of rougher morphology along the middle of the wear scar, approximately 2 mm across. At  $0.905 \text{ m.s}^{-1}$  where more material had been transferred, the rougher morphology high transfer region covered almost the entire wear scar, with a greenish powder evident identical to the loose debris observed at  $750^\circ\text{C} / 0.905 \text{ m.s}^{-1}$  when Nimonic 80A was the sample (Figure 5.4). This indicated the presence of nickel oxide.

Some patches of transferred metal were also evident underlying the glaze layer on the Stellite 6 samples at  $0.905 \text{ m.s}^{-1}$ , indicating they had been deposited early during the sliding process.

The use of backscatter to study the worn Stellite 6 indicated the presence of carbides concentrated in grain boundary regions as large as  $10 \mu\text{m}$  to  $15 \mu\text{m}$  in thickness (Figure 5.29). However, despite their size, no effect on the wear process could be identified, with the carbides showing no evidence of protruding beyond the surface of the Stellite 6 into the wear region or the overlying glaze layers. Similar observations were made with the  $0.905 \text{ m.s}^{-1}$  sample.

### 5.2.2.3 EDX Analysis – Stellite 6 versus Nimonic 80A

EDX analysis of the oxide deposits on the Stellite 6 samples indicated a variation in the source material for the two different observed regions of glaze deposit (the smoother low transfer region and rougher high transfer region). Also, regardless of region morphology, there was an overall shift towards higher nickel levels and lower cobalt levels with increased sliding speed, indicating a shift in source from the Stellite 6 sample at  $0.314 \text{ m.s}^{-1} / 750^\circ\text{C}$  to the Nimonic 80A counterface at  $0.905 \text{ m.s}^{-1} / 750^\circ\text{C}$ . Figure 5.27, showing the optical images obtained for each of the three sliding speeds, shows also the EDX data obtained in each case, with values given for low transfer (smooth) and high transfer (rough) regions in each case. At  $0.314 \text{ m.s}^{-1}$ , the smoother low transfer regions accounting for most of the wear scar consisted of high levels of cobalt (mean value of 37.35%) and low levels of nickel

(14.45%), indicating that the source of the majority of the material was the Stellite 6 sample – transfer from the Nimonic 80A counterface was fairly low. The rougher high transfer region gave higher nickel (31.45%) and lower cobalt (23.60%) levels indicating a shift towards the source material being the Nimonic 80A counterface, albeit with a high degree of mixing with Stellite 6 sample material.

Increasing the sliding speed to  $0.905 \text{ m.s}^{-1}$  was sufficient to almost eliminate cobalt from the rougher high transfer region (nickel 61.67%, cobalt 4.2% – there was less mixing in this area). An increasing proportion of nickel (nickel 37.55%, cobalt 20.90%) also indicated a larger Nimonic 80A contribution and increased mixing in the smoother low transfer region.

The lack of influence of swapping of the sample and counterface materials on the direction of material transfer indicated that sliding speed had a greater influence. At  $0.314 \text{ m.s}^{-1}$ , the Stellite 6 has remained the primary source of material, whether as the sample or the counterface. At  $0.905 \text{ m.s}^{-1}$ , the Nimonic 80A has remained the main source of material.

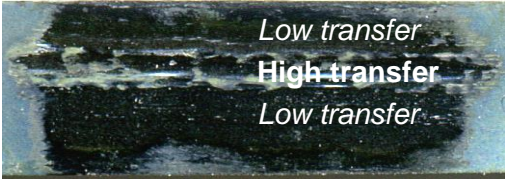
#### **5.2.2.4 Hardness Data – Stellite 6 versus Nimonic 80A**

No clear variations in hardness could be identified in the sub-surface layers of the Stellite 6 samples slid at either  $0.314 \text{ m.s}^{-1} / 750^{\circ}\text{C}$  or  $0.905 \text{ m.s}^{-1} / 750^{\circ}\text{C}$  (Figure 5.30 shows representative hardness profiles for samples slid at  $0.314 \text{ m.s}^{-1}$  and  $0.905 \text{ m.s}^{-1}$ ), that could be attributed to sub-surface work-hardening near the wear surface. However, there was a significant difference in hardness between matrix and high carbide regions, with matrix values of between  $\sim 3.8$  and  $6.3 \text{ GPa}$  and high carbide concentration areas of between  $6.9$  and  $14.7 \text{ GPa}$  at  $0.314 \text{ m.s}^{-1}$ . At  $0.905 \text{ m.s}^{-1}$ , matrix hardness values were between  $4.0 \text{ GPa}$  and  $6.3 \text{ GPa}$  and high carbide concentration areas gave values of between  $5.8 \text{ GPa}$  and  $18.0 \text{ GPa}$ . It is to be noted that the actual hardness of the carbides may well have been higher than the obtained data suggests (the theoretical hardness of chromium carbide is  $18.7 \text{ GPa}$  [116]), as it was extremely difficult to position the Vickers micro-indenter over a carbide-only region. The thickness of the carbides at between  $10 \mu\text{m}$  and  $15 \mu\text{m}$  were insufficient to allow this to be done consistently.

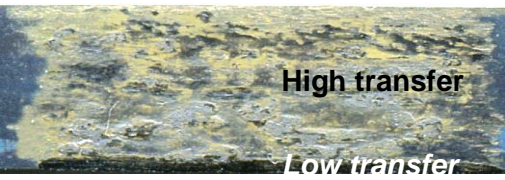
**Figure 5.27: Compacted oxide produced on Stellite 6 samples slid against a Nimonic 80A counterface at different sliding speeds – optical images**

(load = 7N, sliding distance = 4,522 m, temperature = 750°C, sample size = 3)

(a)  $0.314 \text{ m.s}^{-1}$

 <p>Low transfer High transfer Low transfer</p> <p>Mostly smooth compacted oxide layer, black in colour, high in cobalt, low in nickel. Small strip of nickel rich, cobalt depleted oxide. (wear scar 14 mm)</p>									
	Ni	Cr	Fe	Al	Co	Ti	Mn	Si	W
Low transfer	14.45	38.35	1.00	1.30	37.35	37.35	0.15	2.15	0.70
High transfer	31.45	38.45	0.95	0.75	23.60	1.15	0.30	0.90	2.65
Nimonic 80A as sample	16.70	36.20	1.30	0.50	34.20	0.90	0.80	3.80	5.60

(b)  $0.905 \text{ m.s}^{-1}$

 <p>High transfer Low transfer</p> <p>Nickel-rich, cobalt depleted material covering almost all of wear scar – some early metallic transfer. Thin strip of higher cobalt material along 'bottom' edge. (wear scar 16 mm)</p>									
	Ni	Cr	Fe	Al	Co	Ti	Mn	Si	W
Low transfer	37.55	35.05	1.40	3.10	20.90	1.05	0.80	0.85	1.60
High transfer	61.67	27.57	0.63	2.13	4.20	1.93	0.13	0.67	0.43
Nimonic 80A as sample	71.30	24.90	0.20	2.20	0.20	1.80	0.00	0.00	0.00

'Low transfer' refers to areas where there has not been large-scale transfer of material from the Nimonic 80A counterface to the Stellite 6 sample.

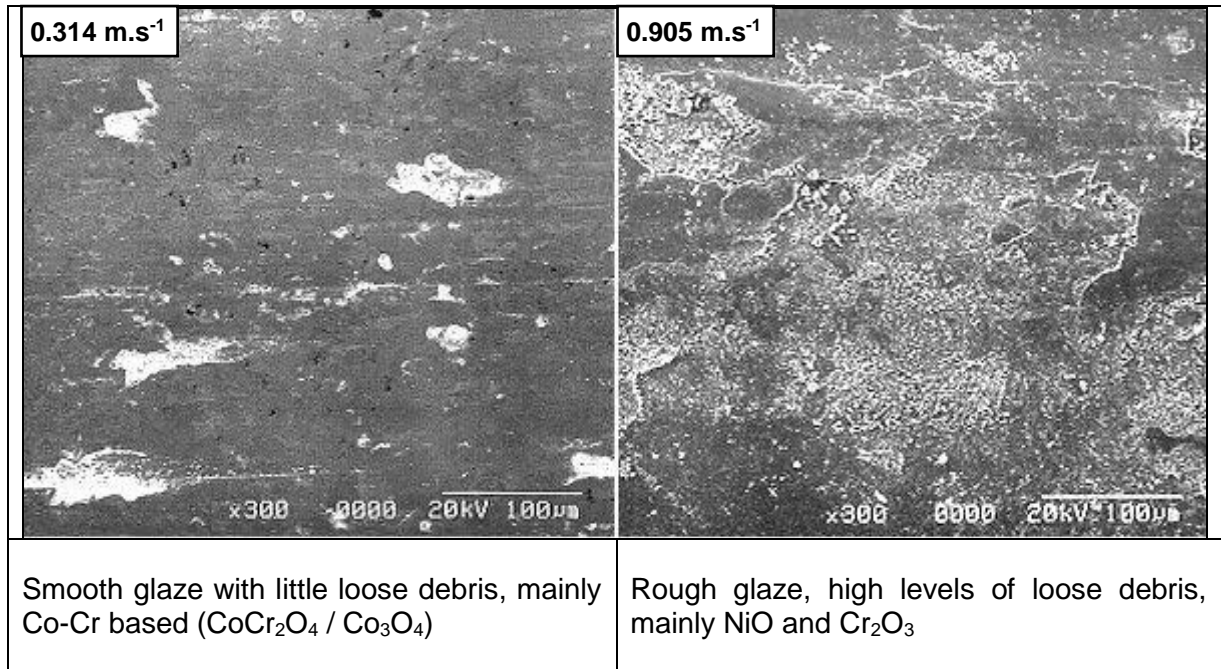
'High transfer' is where greater levels of transfer from the Nimonic 80A counterface have clearly occurred, the transferred material forming a mixed layer at  $0.314 \text{ m.s}^{-1}$ , becoming predominantly nickel-based at  $0.905 \text{ m.s}^{-1}$ .

'Nimonic 80A as sample' refers to data collected in earlier testing (Section 5.1) by the sliding of Nimonic 80A as the sample against a Stellite 6 counterface and is shown here for comparative purposes.



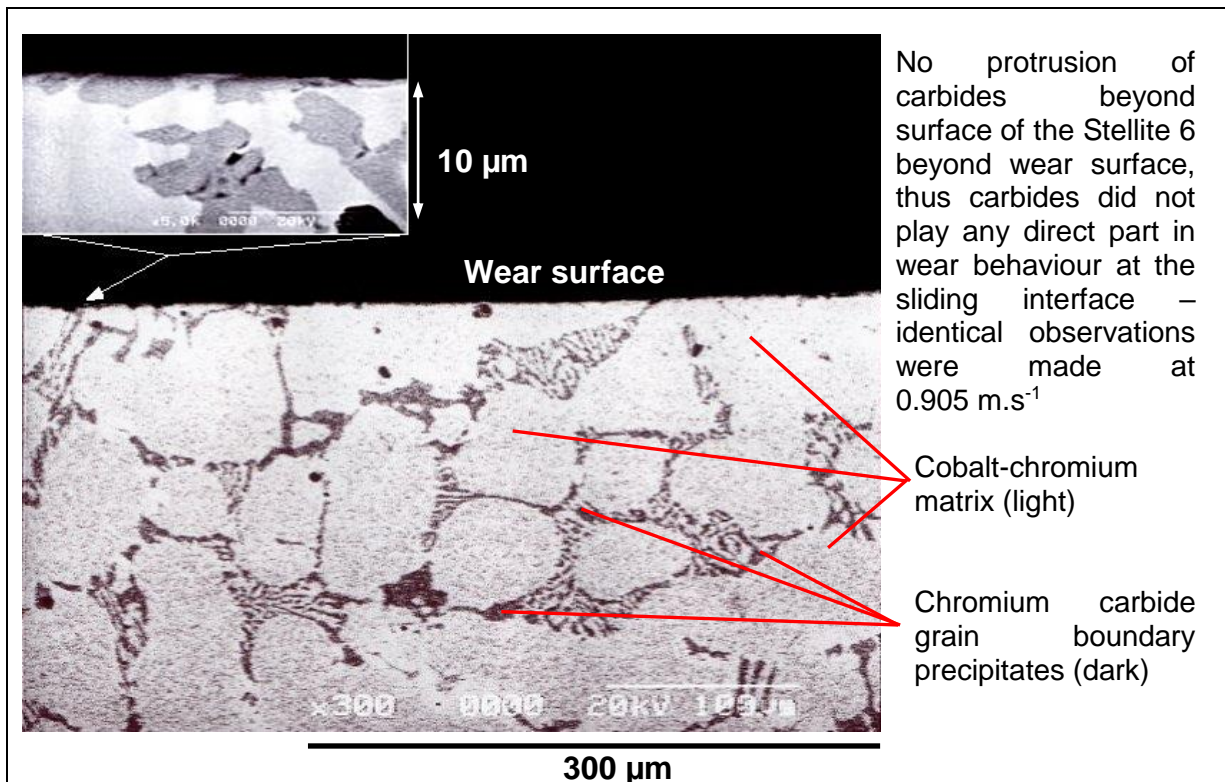
**Figure 5.28: Compacted oxide produced on Stellite 6 samples slid against a Nimonic 80A counterface at  $0.314 \text{ m.s}^{-1}$  and  $0.905 \text{ m.s}^{-1}$  – SEM images**

(load = 7N, sliding distance = 4,522 m, temperature =  $750^\circ\text{C}$ )



**Figure 5.29: Backscatter image of the side profile of a Stellite 6 sample**

(load = 7N, sliding speed =  $0.314 \text{ m.s}^{-1}$ , sliding distance = 4,522 m, temperature =  $750^\circ\text{C}$ )





Hardness levels of glaze layers formed at  $0.314 \text{ m.s}^{-1} / 750^{\circ}\text{C}$  on the Stellite 6 surface (Table 5.2 – mean value 11.22 GPa) tended to be higher than that of the Stellite 6 matrix (mean hardness 5.19 GPa) and in general harder than that of the areas of high carbide concentration (mean hardness 9.45 GPa). However, the Vickers micro-indenter, even with a 50g load, was able to penetrate the extremely thin glaze layers (between  $\sim 4.5$  and  $\sim 5.5 \mu\text{m}$ ) into the underlying Stellite 6 material. Thus it is likely that the obtained values for glaze hardness were significantly less than the glaze layers' true levels of hardness.

No hardness vales are presented for the glaze layers formed on the Stellite 6 surface at  $0.905 \text{ m.s}^{-1} / 750^{\circ}\text{C}$  – no reliable data could be obtained due to the high roughness of the glaze surfaces at  $0.905 \text{ m.s}^{-1}$ .

#### 5.2.2.5 Nimonic 80A Counterface – Stellite 6 versus Nimonic 80A

At  $0.314 \text{ m.s}^{-1}$  and  $750^{\circ}\text{C}$  (Figure 5.31), a patchy dark glaze formed over the surface of the Nimonic 80A counterface wear scar, identical to the smooth high chromium-cobalt glaze present on the wear scar of the Stellite 6 sample. This glaze was easily removed from some areas of the wear scar, the high cobalt content of which (32% Co, 38% Cr, 19% Ni), indicating that the main source of this glaze was the Stellite 6. The greenish high nickel oxide from the Nimonic 80A counterface was observable only in the gaps in the glaze layer on the counterface.

**Table 5.2: Hardness data for glaze, for a Stellite 6 sample slid against a Nimonic 80A counterface at  $0.314 \text{ m.s}^{-1}$  and  $750^{\circ}\text{C}$**

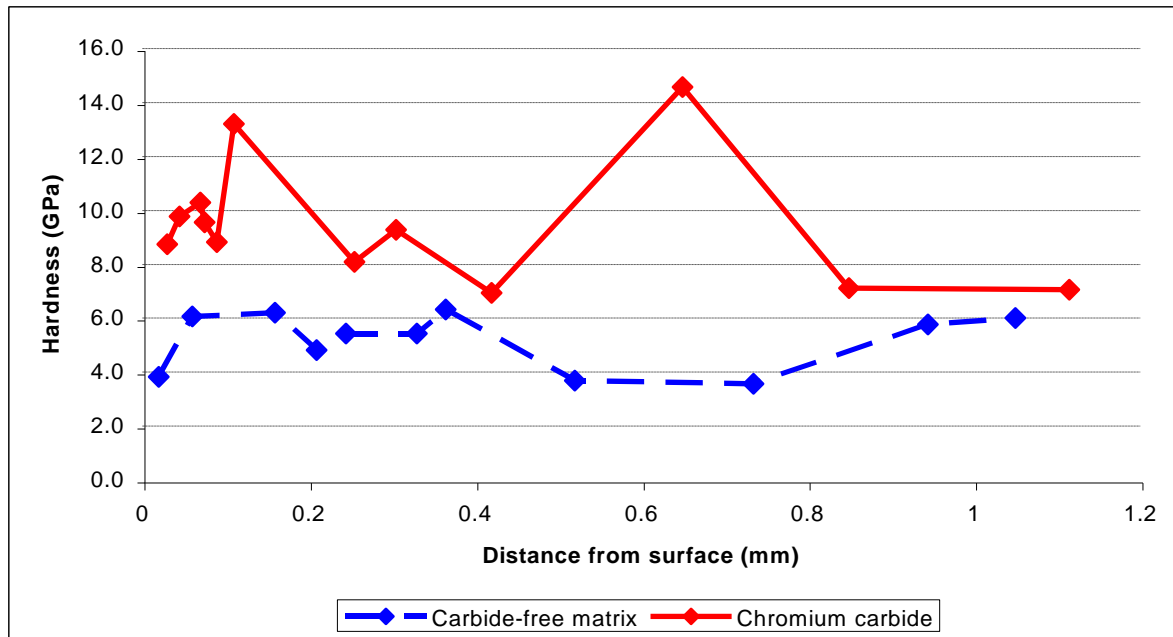
(load = 7N, sliding distance = 4,522 m, hardness values in GPa, Vickers micro-indenter - 50g, sample size = 5)

11.88	<b>Mean hardness of glaze = 11.22 GPa</b>
10.63	
10.63	
12.45	
10.51	

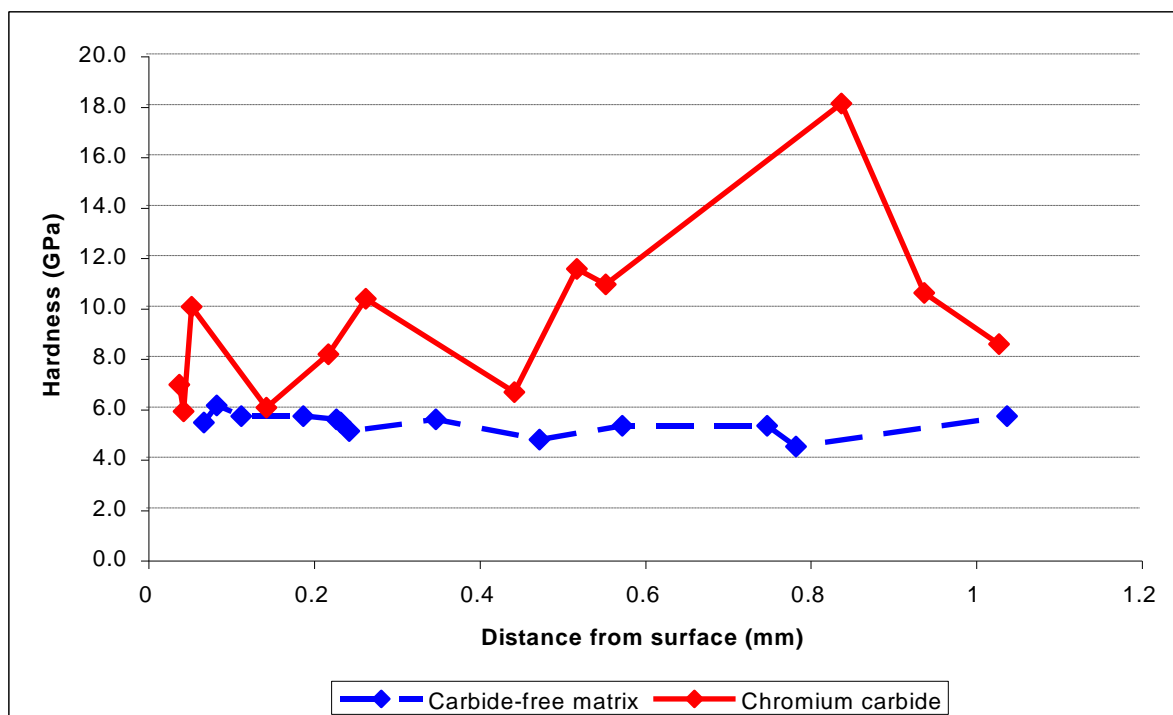
**Figure 5.30: Variation in hardness with increasing distance from the sliding surface for both the cobalt rich matrix and the carbide precipitates in Stellite 6 slid against a Nimonic 80A counterface at 750°C**

(load = 7N, sliding distance = 4,522 m, hardness values in GPa, Vickers micro-indenter – 50g, sample size = 3)

(a)  $0.314 \text{ m.s}^{-1}$





(b)  $0.905 \text{ m.s}^{-1}$



**Figure 5.31: Compacted oxide produced on a Nimonic 80A counterface slid against Stellite 6 samples at  $0.314 \text{ m.s}^{-1}$  and  $0.905 \text{ m.s}^{-1}$**

(load = 7N, sliding distance = 4,522 m, temperature =  $750^\circ\text{C}$ , wear sections =  $15 \times 5 \text{ mm}$ )

	<p><b><math>0.314 \text{ m.s}^{-1}</math></b></p> <p>Patchy smooth glaze, similar to that observed on Stellite 6 sample, greenish colour in glaze-free areas indicates high levels of NiO</p>
	<p><b><math>0.905 \text{ m.s}^{-1}</math></b></p> <p>High wear and damage to counterface on lower part of sample, lighter colour of debris indicating high NiO levels, darker area is region of limited glaze.</p>

At  $0.905 \text{ m.s}^{-1}$  and  $750^\circ\text{C}$ , an area of darker glaze like material formed down the centre of the Nimonic 80A counterface wear scar. As at this sliding speed, the oxide on the Stellite 6 sample wear scar was primarily nickel-based with some chromium (i.e. indicating transfer from the Nimonic 80A counterface to the Stellite 6 sample), then the glaze-like layer formed on the counterface was also likely to be of similar composition. Insufficient glaze could be collected for a reliable analysis.

The level of damage on the counterface was greater for increased sliding speed - no significant metallic damage was observed at  $0.314 \text{ m.s}^{-1}$ , compared to a moderate level of damage at  $0.905 \text{ m.s}^{-1}$ .

### **5.2.3 Substitution of Nimonic 80A with High Purity Nickel - Nickel 200<sup>TM</sup> versus Stellite 6 at $750^\circ\text{C}$**

#### **5.2.3.1 Experimental Observations – Nickel 200<sup>TM</sup> versus Stellite 6**

Weight change values for the Nickel 200<sup>TM</sup> samples slid against Stellite 6 at  $750^\circ\text{C}$  were extremely low, with an average gain of  $0.001(1) \text{ g}$  at  $0.314 \text{ m.s}^{-1}$ , and negligible changes ( $0.000(8) \text{ g}$ ) at  $0.905 \text{ m.s}^{-1}$  (Figure 5.32). This was reflected by the similarly low wear rate data ( $-0.252 \mu\text{g.m}^{-1}$  between 0 and 4,522 m of sliding at  $0.314 \text{ m.s}^{-1}$  and  $-0.184 \mu\text{g.m}^{-1}$

between 0 and 4,522 m at  $0.905 \text{ m.s}^{-1}$  – Figure 5.32a). This contrasts with the large jump seen in weight loss (from  $-0.000(2) \text{ g}$  to  $-0.072(7) \text{ g}$ ) and wear rate (from  $0.039 \mu\text{g.m}^{-1}$  to  $16.084 \mu\text{g.m}^{-1}$ ) on increasing sliding speed from  $0.314 \text{ m.s}^{-1}$  to  $0.905 \text{ m.s}^{-1}$ , for the Nimonic 80A / Stellite 6 (counterface) system at  $750^\circ\text{C}$  (shown for comparison purposes).

Coefficient of friction data was highly erratic, with steady state values varying between 0.3 and 0.6 at both  $0.314 \text{ m.s}^{-1}$  and  $0.905 \text{ m.s}^{-1}$  (Figure 5.33). At both  $0.314 \text{ m.s}^{-1}$  and  $0.905 \text{ m.s}^{-1}$  unsettled ‘run-in’ values (as high as  $\sim 0.85$ ) gave way to ‘steady state’ values after about 500 m of sliding – sliding speed neither increased or reduced this distance.

### 5.2.3.2 Optical and SEM Microscopy – Nickel 200<sup>TM</sup> versus Stellite 6

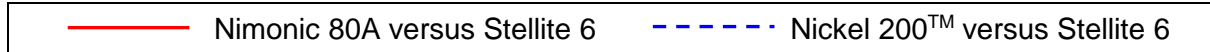
Optically (Figure 5.34), the smooth surfaces produced during the sliding of Nickel 200<sup>TM</sup> against Stellite 6 seemed to indicate a stable, adherent glaze, with no real evidence of severe wear noted on either sample or counterface. SEM of the  $0.314 \text{ m.s}^{-1}$  sample (Figure 5.35) also showed a relatively smooth glaze, but not quite as smooth as with Nimonic 80A or Incoloy MA956 versus Stellite 6 at the same speed. At  $0.905 \text{ m.s}^{-1}$ , there was still glaze coverage across the entire wear scar with low overall wear. However, there was more evidence of breakaway at  $0.905 \text{ m.s}^{-1}$ , but accompanied by continued ready glaze-platform formation from the loose debris.

This break-away did not expose the underlying substrate (no evidence of any enhanced damage to the Nickel 200<sup>TM</sup> sample could be found), with SEM indicating the continued formation and break-up of glaze platforms over previously deposited oxide material (Figure 5.35).

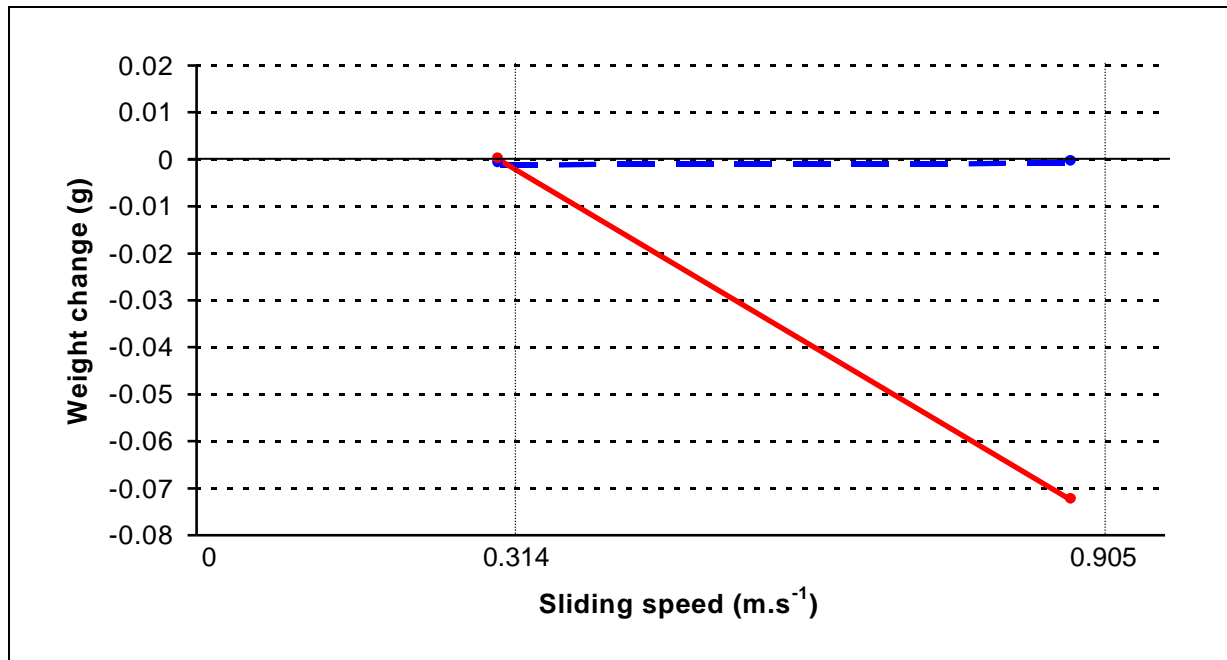
Only a small amount of loose oxide debris was produced during sliding at both  $0.314 \text{ m.s}^{-1}$  and  $0.905 \text{ m.s}^{-1}$ . This debris was of average particle size in the range 300 nm to  $1 \mu\text{m}$ , with only a few particles of size above this, no bigger than  $3 \mu\text{m}$ . Many of the larger particles were clumped and sintered together from smaller particles. Debris typical of that produced is shown in the X6.0K micrograph of the  $0.905 \text{ m.s}^{-1}$  sample (Figure 5.35). Here, debris has been compacted together, with some sintering together and some refracturing.

**Figure 5.32: Weight change and wear rate versus sliding speed for Nickel 200™ versus Stellite 6 at 0.314 and 0.905 m.s<sup>-1</sup>**

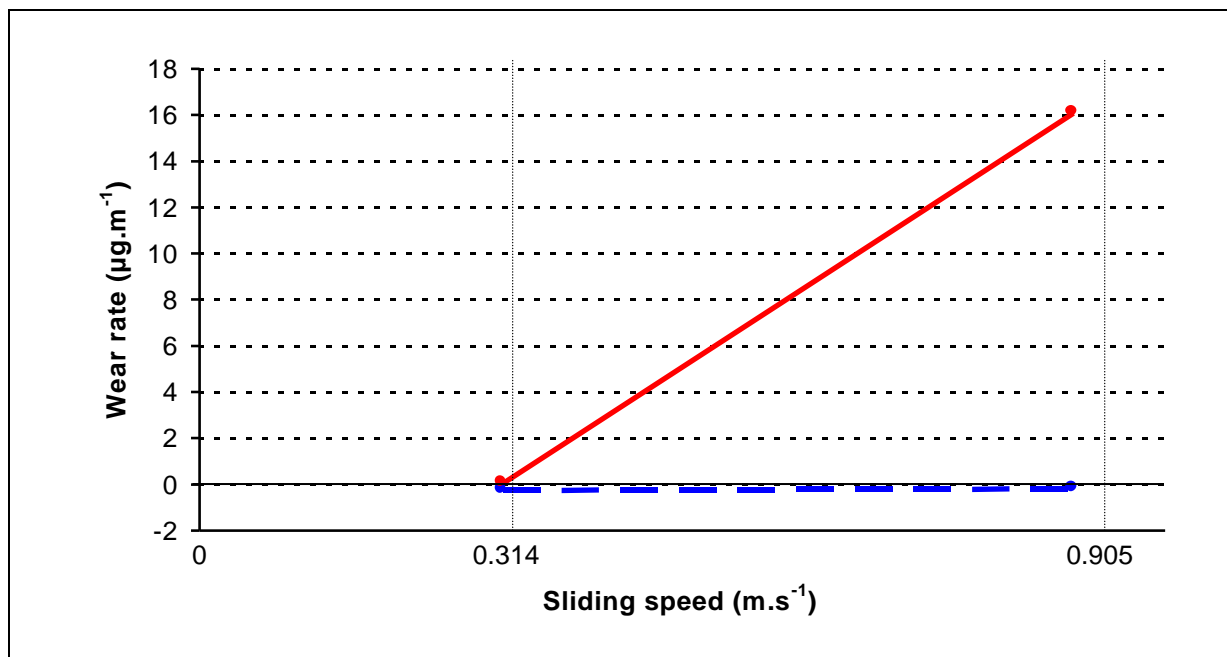
(load = 7N, sliding distance = 4,522 m, temperature = 750°C, sample size = 3)



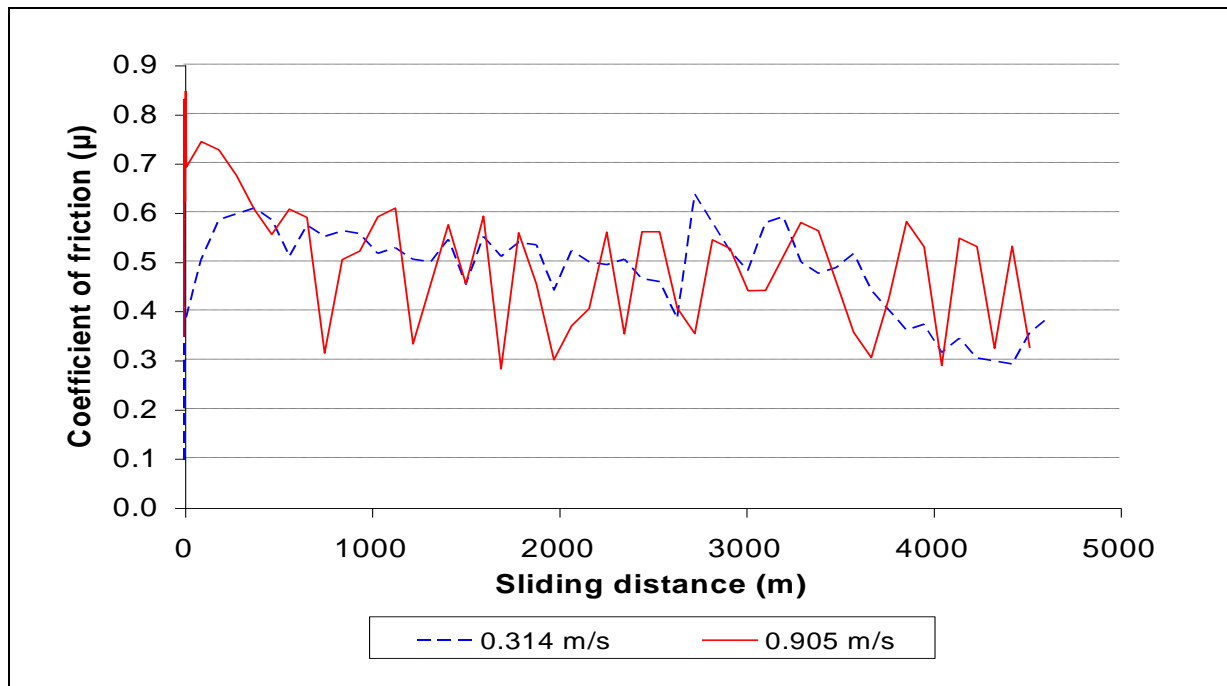
(a) Weight change



(b) Wear rate

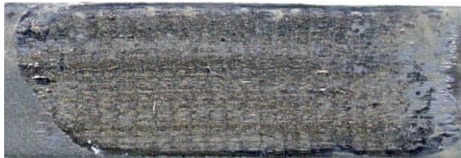


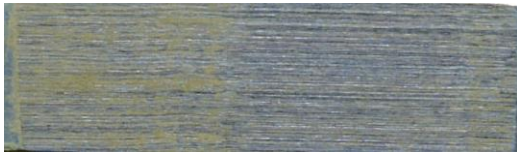


**Figure 5.33: Friction data for Nickel 200™ versus Stellite 6 at 0.314 and 0.905 m.s<sup>-1</sup>**  
(load = 7N, sliding distance = 4,522 m, temperature = 750°C, sample size = 3)



**Figure 5.34: Comparison of wear scars produced by wear of Nimonic 80A versus Stellite 6 and Nickel 200™ versus Stellite 6**

(load = 7N, sliding distance = 4,522 m, temperature = 750°C, wear scars are 5 mm across)

	<p><b>Nickel 200™ versus Stellite 6, 0.314 m.s<sup>-1</sup></b></p> <p>Low wear with a nickel oxide (NiO) glaze layer, not as smooth as for Nimonic 80A versus Stellite 6 at 0.314 m.s<sup>-1</sup>. Very little loose nickel oxide debris.</p>
	<p><b>Nimonic 80A versus Stellite 6, 0.314 m.s<sup>-1</sup></b></p> <p>Low wear, smooth cobalt chromium oxide (CoCr<sub>2</sub>O<sub>4</sub>) rich glaze layer, very little Co-Cr oxide loose debris.</p>
	<p><b>Nickel 200™ versus Stellite 6, 0.905 m.s<sup>-1</sup></b></p> <p>Low wear, nickel oxide (NiO) glaze layer, slightly grooved in direction of sliding. Very little loose nickel oxide debris produced.</p>
	<p><b>Nimonic 80A versus Stellite 6, 0.905 m.s<sup>-1</sup></b></p> <p>High wear, grooved and worn surface, some NiO debris on wear scar, large amount of NiO and Cr<sub>2</sub>O<sub>3</sub> debris ejected, no glaze formed.</p>

← 15 mm →

### 5.2.3.3 EDX and XRD Analysis – Nickel 200<sup>TM</sup> versus Stellite 6

XRD detected only the presence of the phase NiO in the glaze layer, with EDX indicating the dominance of nickel (~98% Ni – other elements were only present to trace levels), regardless of whether sliding was conducted at 0.314 m.s<sup>-1</sup> or 0.905 m.s<sup>-1</sup> – no significant levels of cobalt (or chromium) from the Stellite 6 counterface could be detected (even at 0.314 m.s<sup>-1</sup>). This contrasts with the cobalt-chromium based glaze produced at 0.314 m.s<sup>-1</sup> with Nimonic 80A as the sample material and the high levels of wear observed at 0.905 m.s<sup>-1</sup>, where high levels of nickel-based and chromium-based oxide were produced.

The little loose oxide debris that was produced was also of nickel oxide (~98%), again regardless of sliding speed.

### 5.2.3.4 Micro-hardness Testing – Nickel 200<sup>TM</sup> versus Stellite 6

Micro-hardness profiles for both 0.314 and 0.905 m.s<sup>-1</sup> gave no clear trends (Figure 5.37 shows representative depth hardness profiles taken from samples slid at 0.314 m.s<sup>-1</sup> and 0.905 m.s<sup>-1</sup>, sliding temperature 750°C), with Nickel 200<sup>TM</sup> sample values beneath the wear scar little different from the undeformed Nickel 200<sup>TM</sup> values. Hardness values tended to be highly variable, at between 1.4 and 1.8 GPa.

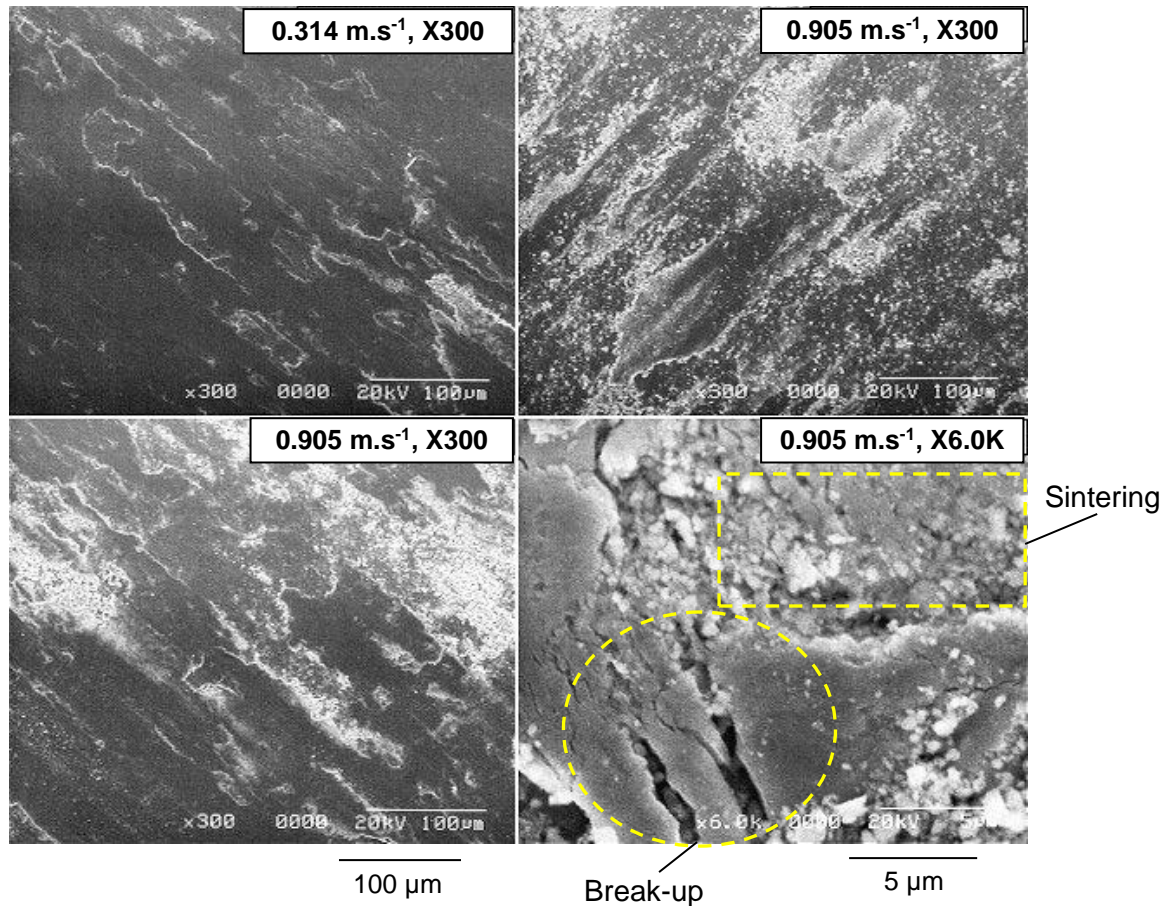
Glaze data (Table 5.3) did, however, show variations in hardness depending on the nature of the glaze. In general, the glaze formed only a very thin layer (no more than 1 µm) on the surface of the Nickel 200<sup>TM</sup> (especially at 0.905 m.s<sup>-1</sup>), with the micro-hardness indenter penetrating through the layer into the substrate beneath and giving relatively low values. At 0.314 m.s<sup>-1</sup>, values of between 3.0 and 6.0 GPa were obtained, compared to values of between 2.0 and 3.1 GPa (with one exception at 6.4 GPa) for 0.905 m.s<sup>-1</sup>.

In contrast a few areas, where a thicker glaze was obtained, gave very high levels of hardness – these again proved to be variable. Values for 0.314 m.s<sup>-1</sup> again were on average higher than for 0.905 m.s<sup>-1</sup> (with mean values of 22.6 and 16.0 GPa respectively), though the difficulty in obtaining data meant only a small number of values could be obtained. More often than not, the glaze layer broke up on attempting micro-hardness testing, regardless of test load (normally 50g for 12 seconds – 10 and 25 g were also tried), exposing a loose underlying nickel oxide debris layer.



**Figure 5.35: SEM images of Nickel 200™ samples slid against a Stellite 6 counterface at 0.314 and 0.905 m.s<sup>-1</sup>**

(load = 7N, sliding distance = 4,522 m, temperature = 750°C)



**0.314 m.s<sup>-1</sup>:**

Relatively smooth glaze with limited breakaway.

**0.905 m.s<sup>-1</sup>:**

Glaze coverage of the wear scar is still comprehensive, however, glaze platforms are more fragmented than at 0.314 m.s<sup>-1</sup>, with slightly more loose debris.

**0.905 m.s<sup>-1</sup>, X6.0K:**

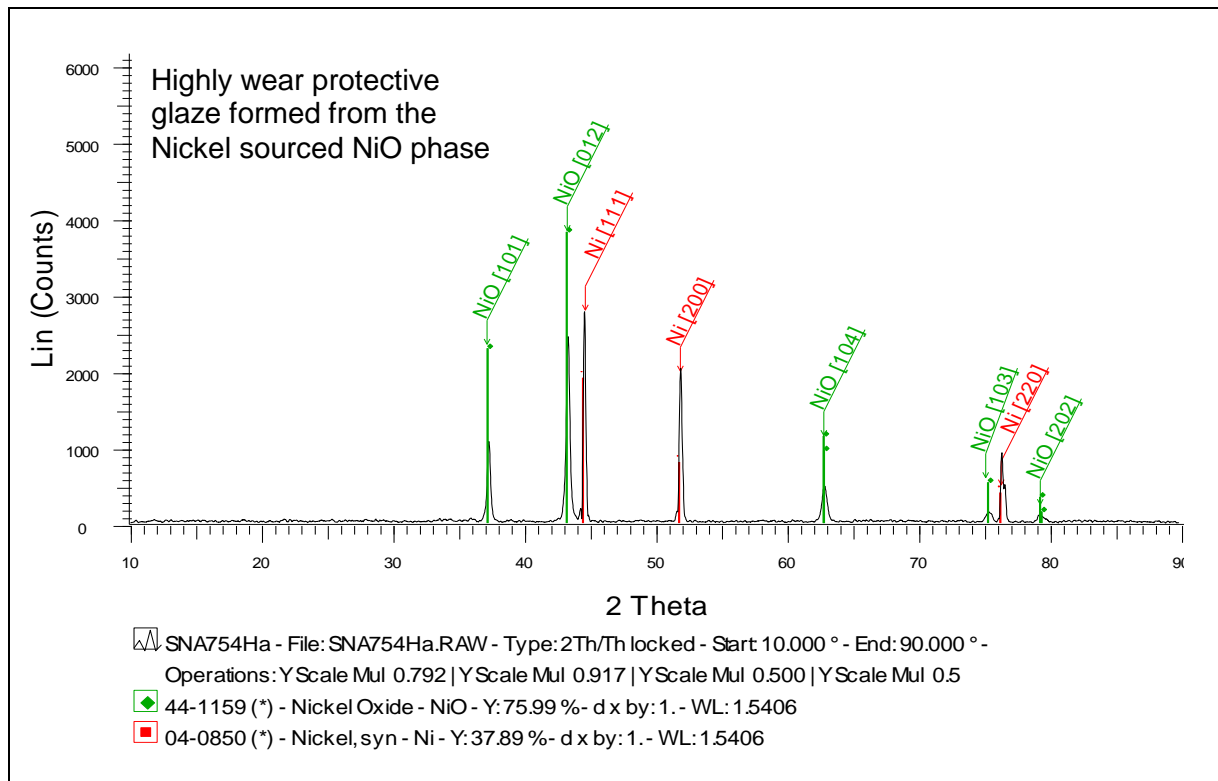
Both glaze forming and break-up processes are visible, with cracks developing in the glaze platform in the bottom left of the picture and loose debris joining and sintering together in the top right.



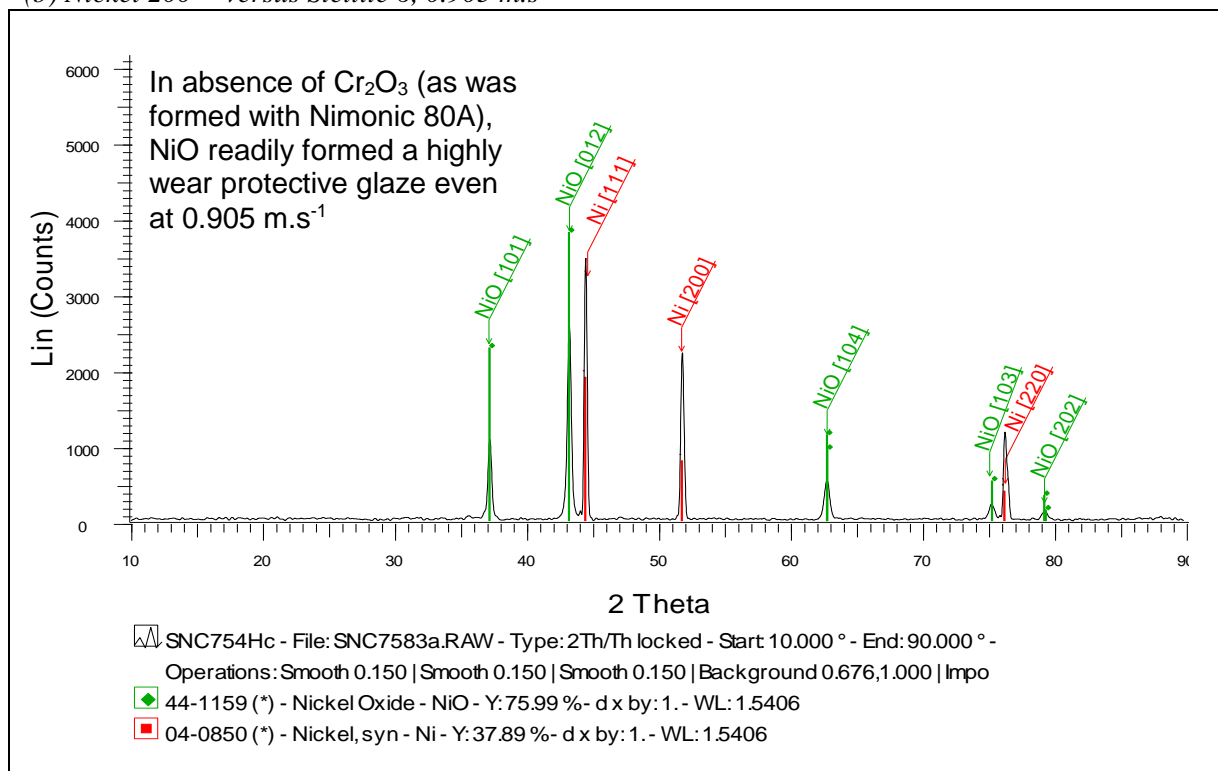
**Figure 5.36: XRD Plots for glaze from Nickel 200™ versus Stellite 6**

(load = 7N, sliding distance = 4,522 m, temperature = 750°C)

(a) Nickel 200™ versus Stellite 6, 0.314 m.s<sup>-1</sup>



(b) Nickel 200™ versus Stellite 6, 0.905 m.s<sup>-1</sup>



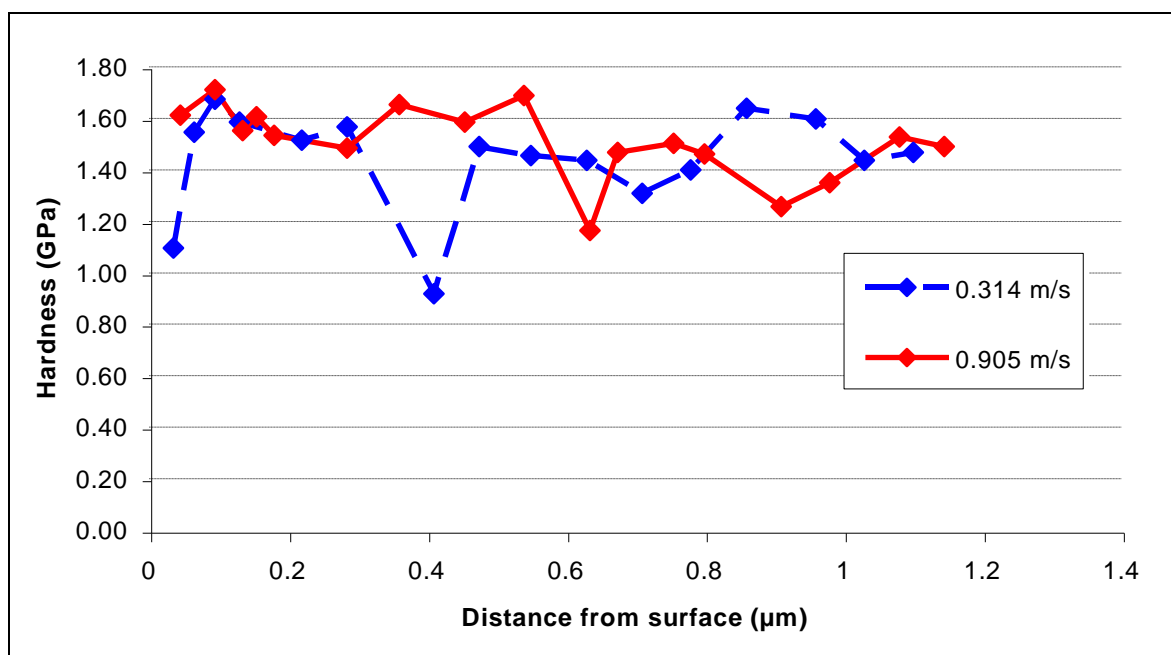
**Table 5.3: Hardness data for glaze and undeformed substrate – Nickel 200™ versus Stellite 6 slid at 750°C**

(load = 7N, sliding distance = 4,522 m, hardness values in GPa, Vickers micro-indenter - 50g, sample size = 5)

Substrate (preheated to 750° for 4 hours)		0.314 m.s <sup>-1</sup>		0.905 m.s <sup>-1</sup>	
1.78 1.52 1.57 1.51 1.61	Mean = 1.60 GPa	Thinned glaze		Thinned glaze	
		5.98	Mean = 4.61 GPa	2.59	Mean = 3.29 GPa
		3.05		1.96	
		2.35		2.38	
		6.28		3.14	
		5.38		6.38	
		Thicker glaze platforms		Thicker glaze platforms	
		25.31	Mean = 22.56 GPa	11.87	Mean = 15.99 GPa
		24.05		17.22	
		15.30		19.62	
		21.47		14.76	
		27.07		16.38	

**Figure 5.37: Subsurface layer hardness for samples slid at 0.314 and 0.905 m.s<sup>-1</sup>, Nickel 200™ versus Stellite 6, 750°C**

(load = 7N, sliding distance = 4,522 m, Vickers micro-indenter - 50g, sample size = 3)



### 5.3 Testing of Incoloy MA956 versus Stellite 6 between Room Temperature and 750°C, at 0.314 and 0.905 m.s<sup>-1</sup>

#### 5.3.1 Experimental Observations – Incoloy MA956 versus Stellite 6

Figure 5.38 shows the variation of weight loss (in grams) and wear rate (defined in this thesis as  $\mu\text{g.m}^{-1}$ ) with temperature for the Incoloy MA956 / Stellite 6 (counterface) system, from room temperature to 750°C. The weight loss and wear rate behaviour observed at 0.314 m.s<sup>-1</sup> (after 4,522 m of sliding) and 0.905 m.s<sup>-1</sup> (after 4,522 m and 13,032 m of sliding) is described in this section.

##### a) Weight change and wear rate data at 0.314 m.s<sup>-1</sup>

The weight change profile for Incoloy MA956 versus Stellite 6 at 0.314 m.s<sup>-1</sup> (after 4,522 m of sliding), was very similar to that obtained with Nimonic 80A. The Incoloy MA956 underwent very low levels of weight loss up to 450°C (largest mean change of -0.002(5) g at 390°C) and very slight gains from 510°C to 750°C (largest mean change of 0.001(5) g at 630°C). Wear rate values for the Incoloy MA956 (between 0 and 4,522 m) also remained extremely low at 0.314 m.s<sup>-1</sup>, rising from 0.136  $\mu\text{g.m}^{-1}$  at room temperature, up to 0.545  $\mu\text{g.m}^{-1}$  at 390°C. Values for wear rate then decreased, with negative values between 510°C (-0.130  $\mu\text{g.m}^{-1}$ ) and 750°C (-0.150  $\mu\text{g.m}^{-1}$ ). The largest negative magnitude value was -0.335  $\mu\text{g.m}^{-1}$  at 630°C.

##### b) Coefficient of friction data at 0.314 m.s<sup>-1</sup>

Measured coefficient of friction values (Figure 5.39) for the Incoloy MA956 / Stellite 6 (counterface) system at 0.314 m.s<sup>-1</sup> showed two clear phases of frictional behaviour. At the very beginning of sliding, there was an initial unsettled or ‘run-in’ period, with high levels of variance (~20%), which rapidly gave way to a more settled ‘steady state’ with reduced variation (~12%), persisting for the remainder of each sliding test.

A downward trend in coefficient of friction with temperature for the Incoloy MA956 / Stellite 6 system at 0.314 m.s<sup>-1</sup>, was visible in both the data for the unsettled ‘run-in’ period and the ‘steady state’ period (Figure 5.39). This became less pronounced at higher temperatures, with no significant difference in either case between the friction data at 510°C and 750°C. Peak values for the run-in data fell from 1.05 at room temperature, to 0.75 at 270°C, 0.64 at 510°C and 0.66 at 750°C – in each case a sharp rise

from zero friction was observed at the beginning of testing. ‘Steady state’ values showed a steady decrease from between 0.93 - 1.05 at room temperature, to between 0.66 - 0.76 at 270°C, 0.58 - 0.65 at 510°C and 0.55 - 0.67 at 750°C.

***c) Weight change and wear rate data at 0.905 m.s<sup>-1</sup> / 4,522 m***

At 0.905 m.s<sup>-1</sup> / 4,522 m, weight loss from the Incoloy MA956 remained low at room temperature (weight change -0.002(1) g – the negative value indicates a weight loss) and 270°C (weight change -0.001(9) g). The wear rate of the Incoloy MA956 also remained low, with recorded values of 0.462 µg.m<sup>-1</sup> (between 0 and 4,522 m) at room temperature and 0.411 µg.m<sup>-1</sup> at 270°C.

At 390°C and 450°C, there was a rapid increase in weight loss from the Incoloy MA956 samples, with recorded values for weight change -0.075(4) g at 390°C and -0.147(8) g at 450°C (representing the highest losses observed after 4,522 m of sliding). Wear rate values between 0 and 4,522 m of 16.681 µg.m<sup>-1</sup> at 390°C and 32.675 µg.m<sup>-1</sup> at 450°C indicate a very large increase in wear.

Between 510°C and 750°C, there was a steady decrease in weight loss and wear rate. At 510°C, weight change and wear rate values of -0.082(8) g and 18.330 µg.m<sup>-1</sup> (between 0 and 4,522 m) were obtained. At 630°C, recorded weight change and wear rate values were -0.007(7) g and 1.694 µg.m<sup>-1</sup>. At 750°C, weight change and wear rate values were minimal at -0.000(7) g and 0.146 µg.m<sup>-1</sup> respectively.

***d) Weight change and wear rate data at 0.905 m.s<sup>-1</sup> / 13,032 m***

At 0.905 m.s<sup>-1</sup> / 13,032 m, values of weight loss and wear rate (between 4,522 and 13,032 m) for the Incoloy MA956 remained low at room temperature (weight change -0.008(0) g; wear rate 0.618 µg.m<sup>-1</sup> between 4,522 and 13,032 m) and 270°C (weight change -0.004(0) g; wear rate 0.225 µg.m<sup>-1</sup> between 4,522 and 13,032 m). These values showed little difference to those observed after 4,522 m.

At 390°C, there was a large increase in weight loss – the very high levels of weight loss from the Incoloy MA956 observed after 4,522 m (weight change -0.075(4) g) were also observed after 13,032 m (weight change -0.374(2) g, representing the highest weight losses

recorded after 13,032 m), indicating continuing high wear on extended sliding. However, at 450°C, the weight change value at 450°C after 13,032 m of sliding (-0.147(7) g) was little different to that observed after 4,522 m (-0.147(2) g). These data indicated two changes in wear behaviour with increasing temperature, firstly to a high wear situation at 390°C regardless of sliding distance, then to a ‘two stage’ wear process at 450°C, with early high level wear followed by a later period of minimal wear.

The use of wear rate data clearly showed that changes in wear behaviour were occurring on raising the temperature firstly to 390°C then to 450°C. A wear rate value of 35.107  $\mu\text{g.m}^{-1}$  at 390°C, indicated continued high wear between 4,522 and 13,032 m – this wear rate was higher than that observed between 0 and 4,522 m (16.681  $\mu\text{g.m}^{-1}$ ). However, at 450°C, a very low wear rate of -0.064  $\mu\text{g.m}^{-1}$  was obtained between 4,522 m and 13,032 m, compared to 32.675  $\mu\text{g.m}^{-1}$  between 0 and 4,522 m.

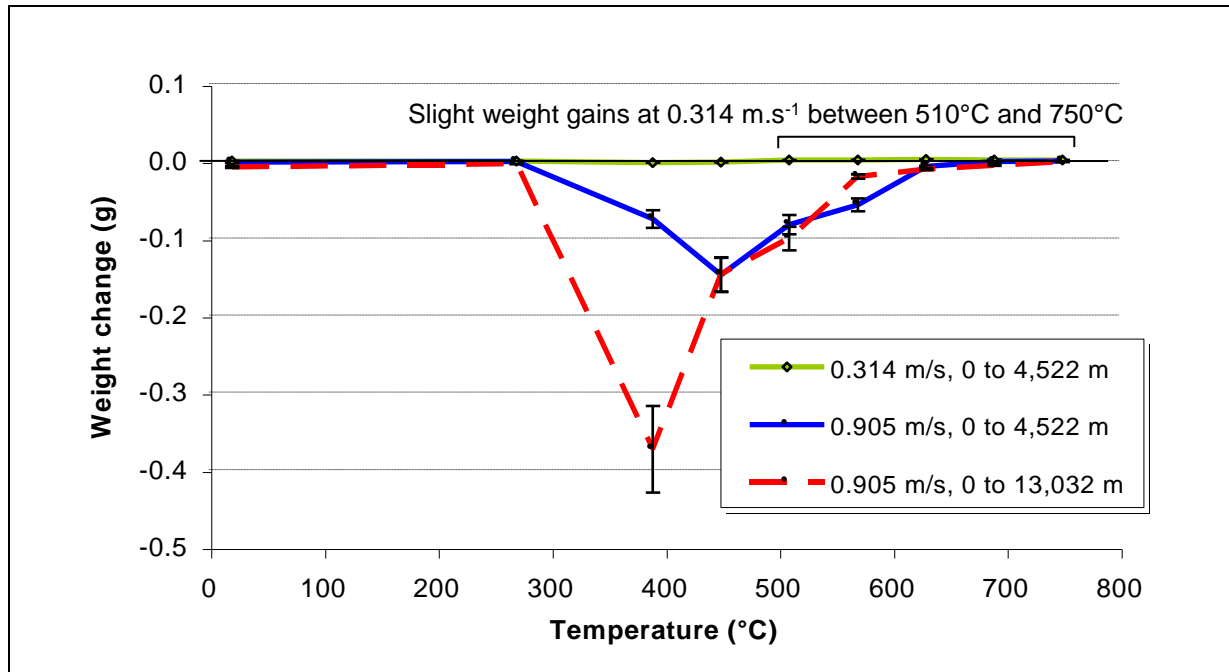
The same ‘two stage’ weight change profile was exhibited at 510°C, with most losses from the Incoloy MA956 restricted to the first 4,522 m of sliding. At 510°C, the mean weight change value after 4,522 m was -0.082(9) g (the wear rate between 0 and 4,522 m was 18.330  $\mu\text{g.m}^{-1}$ ), compared to -0.100(8) g after 13,032 m (the wear rate between 4,522 and 13,032 m was 4.318  $\mu\text{g.m}^{-1}$ ). Similar patterns of wear were exhibited at 570°C and 630°C (Figure 5.38).

This pattern broke down only on reaching 690°C and 750°C, with extremely low values for Incoloy MA956 weight change and wear rate after both 4,522m and 13,032 m of sliding. At 690°C, weight change values of -0.001(1) g after 4,522 m and -0.005(8) g after 13,032 m of sliding were obtained. At the same temperature, wear rates of 0.243  $\mu\text{g.m}^{-1}$  up to 4,522 m and 0.553  $\mu\text{g.m}^{-1}$  between 4,522 and 13,032 m now indicated slightly increased but still very low wear rate for extended sliding. Weight change and wear rate were near-negligible at 750°C, with values for weight change of -0.000(6) g for 4,522 m and -0.001(5) g for 13,032 m. Wear rate values at this temperature were 0.146  $\mu\text{g.m}^{-1}$  up to 4,522 m and 0.113  $\mu\text{g.m}^{-1}$  between 4,522 and 13,032 m respectively, indicating no significant change in wear behaviour.

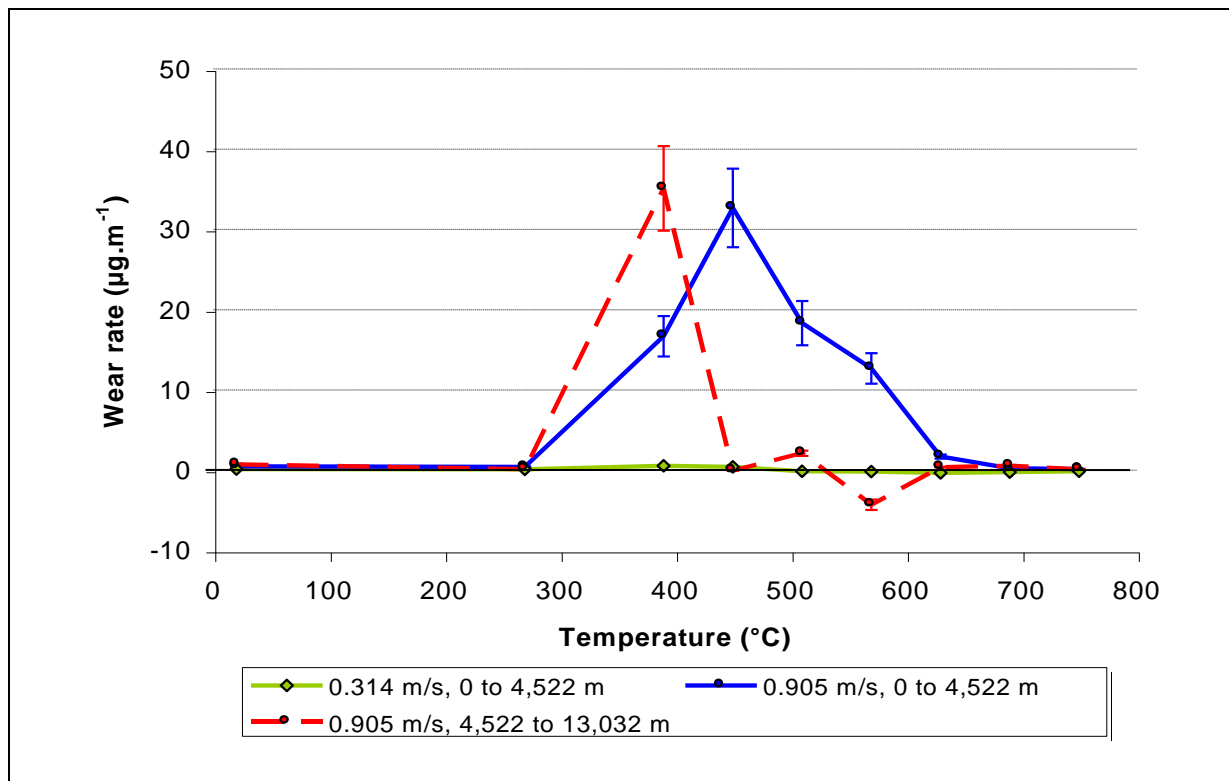
**Figure 5.38: Effect of temperature on weight change and wear rate – Incoloy MA956 versus Stellite 6**

(load = 7N, sample size =5)

(a) Weight change versus temperature



(b) Wear rate versus Temperature

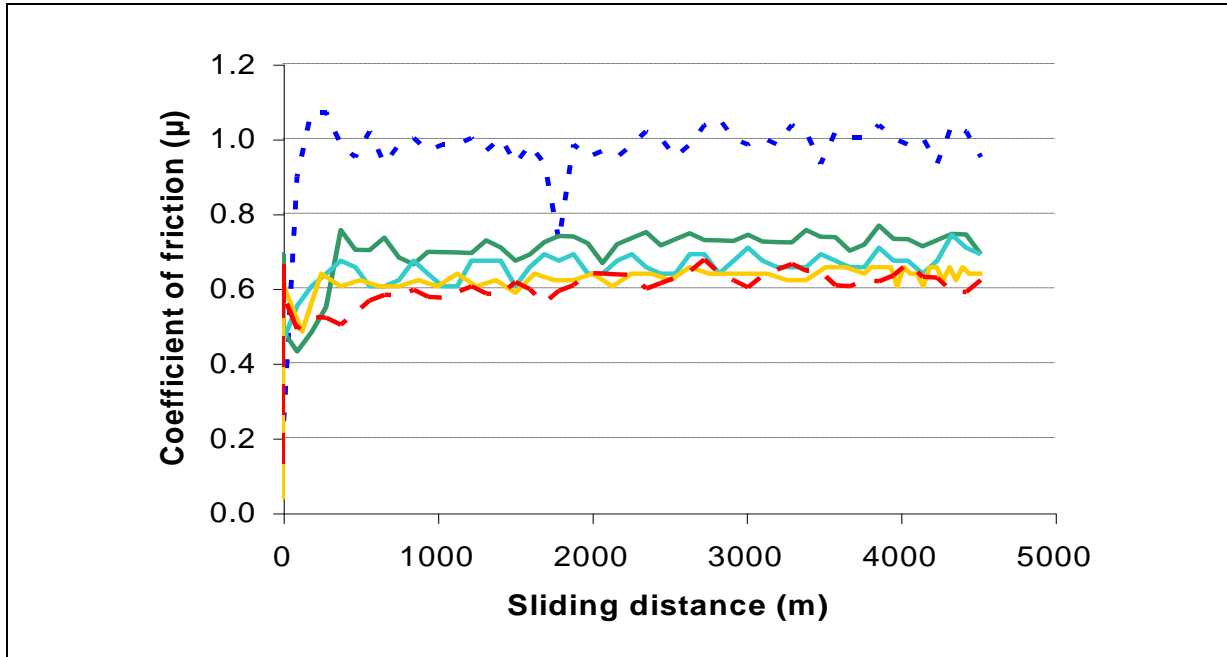


**Figure 5.39: Coefficient of friction versus temperature – Incoloy MA956 vs. Stellite 6**

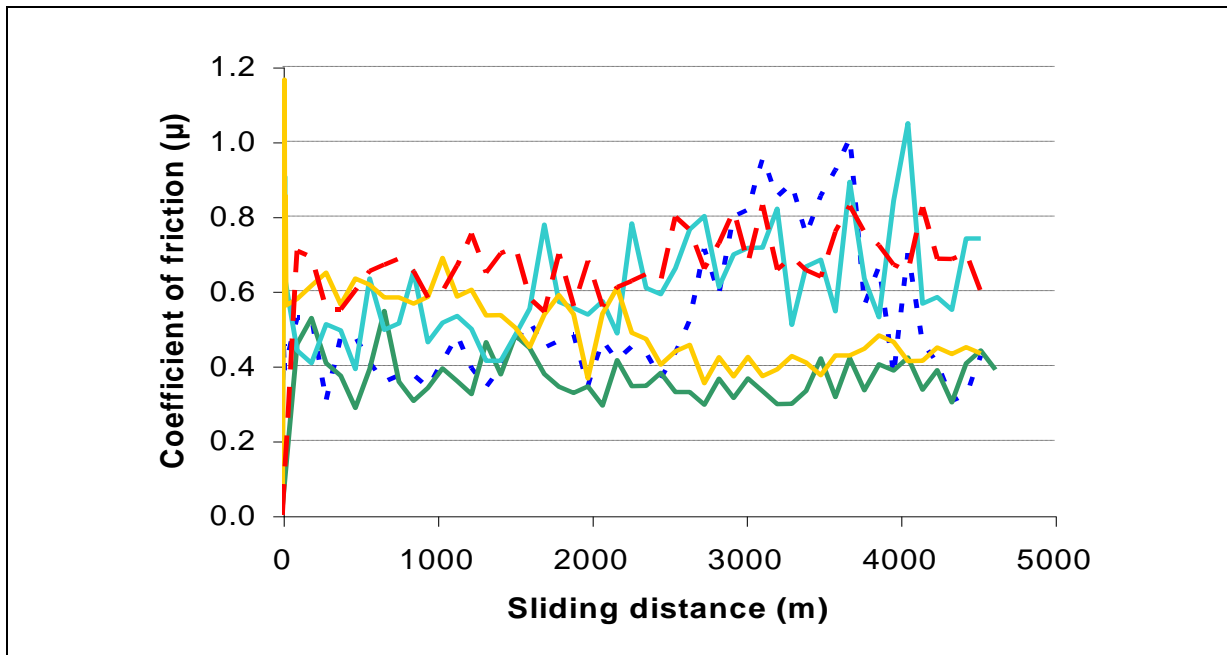
(load = 7N, sample size = 3)

..... Room temp.    — 270°C    — 450°C    — 510°C    - - 750°C

(a)  $0.314 \text{ m.s}^{-1} / 4,522 \text{ m}$



(b)  $0.905 \text{ m.s}^{-1} / 4,522 \text{ m}$



***e) Coefficient of friction data at 0.905 m.s<sup>-1</sup>***

The 0.905 m.s<sup>-1</sup> coefficient of friction data were extremely variable and did not tend to settle down readily into a steady state. As such, any unsettled run-in period was in general hard to distinguish from the later data, though early increases on average from zero to 0.52 at room temperature, 0.63 at 270°C, 1.16 at 510°C and 0.71 at 750°C were noted.

At 0.905 m.s<sup>-1</sup>, steady state variations for Incoloy MA956 versus Stellite 6 (where identifiable) of between 20% and 33% were observed, with actual recorded variations of between 0.34 and 0.52 at room temperature, 0.41 and 0.65 at 270°C, 0.36 and 0.68 at 510°C, and 0.55 and 0.81 at 750°C. In some cases, however, especially at room temperature and 270°C, there were occasional large increases or variations in friction (for example, at room temperature, there was a rapid increase in friction from 0.37 after 2,449 m of sliding to 0.95 after 3,109 m).

Coefficient of friction values once again tended to be lower for 0.905 m.s<sup>-1</sup> than for 0.314 m.s<sup>-1</sup>, however, given the greater levels of vibration and resulting reductions in contact time at this higher sliding speed, actual coefficient of friction values at 0.905 m.s<sup>-1</sup> were likely to have been much higher. For this reason, it is difficult to draw any clear conclusions from the 0.905 m.s<sup>-1</sup> data.

***5.3.2 Optical and SEM Studies – Incoloy MA956 versus Stellite 6***

Observation of samples slid at 0.314 m.s<sup>-1</sup> using optical microscopy (Figure 5.40) and SEM (Figure 5.42) indicated a pattern of behaviour similar to that seen with Nimonic 80A versus Stellite 6 up to 270°C, with loose oxidised debris present on the wear scar surface; this once again became increasingly smeared with temperature. This loose debris continued to be present up to 450°C for 0.314 m.s<sup>-1</sup> (Figure 5.40), at which temperature, there was an increase in the sintering and agglomeration of the debris and isolated areas of glaze-like material began to form. Evidence of metal-to-metal contact between room temperature and 450°C was extremely limited for the Incoloy MA956 / Stellite 6 (counterface) system. Monitoring of room temperature tests indicated that this metal-to-metal contact was mostly limited to the very early stages of wear, tending not to occur once the loose oxide debris had formed.








Between 510°C and 750°C at 0.314 m.s<sup>-1</sup> (Figures 5.40 and 5.42a), increasing levels of glaze formation were observed with increasing sliding temperature up to 750°C – these glaze layers formed tended to become more extensive and contain less porosity as the sliding temperature increased. Evidence of damage due to metal-to-metal contact between the Incoloy MA956 sample and Stellite 6 counterface was also less at glaze forming temperatures (between 510°C and 750°C) and became progressively less evident on increasing the temperature towards 750°C.

The oxide debris (Figure 5.43) produced at all temperatures between room temperature and 750°C at 0.314 m.s<sup>-1</sup>, were in general between 300 nm and 1 µm in size, with some larger particles of up to 3 µm – a few particles above and below this size range were also observed. There were fewer larger particles at glaze-forming temperatures (>450°C), apart from the occasional larger fragment of broken-off glaze.










At 0.905 m.s<sup>-1</sup>, loose oxide debris was observed on the Incoloy MA956 sample wear scar surface only at room temperature and 270°C (Figure 5.41 – Figure 5.42b additionally shows the SEM micrograph for room temperature and 0.905 m.s<sup>-1</sup>), with only limited evidence of damage due to metal-to-metal contact between the Incoloy MA956 sample and Stellite 6 counterface. Monitoring of testing at room temperature indicated this contact to be largely restricted to the early stages of wear (as at 0.314 m.s<sup>-1</sup>), tending not to happen once the loose oxide debris had formed. At 270°C, some smearing of the oxide was observed and some small fragments of metallic debris, suggesting increasing levels of metal-to-metal contact between sample and counterface, were noted in amongst the oxide debris (Figure 5.43b).

At 390°C (Figures 5.41 and 5.42b) and 0.905 m.s<sup>-1</sup>, all traces of oxide debris on the surface of the Incoloy MA956 samples had disappeared and a bright metallic, highly worn, wear scar was observed at both 4,522 m and 13,032 m, typical of severe wear. Debris produced was metallic in nature and the flat angular platelet-like particles of size between 20 µm and 1 mm suggested a delamination wear mechanism was in operation.

**Figure 5.40: Sample wear scar optical images – Incoloy MA956 / Stellite 6, 0.314 m.s<sup>-1</sup>**

	<p><b>Room temperature, 4,522 m</b>  <i>(wear scar = 14 x 5 mm)</i>          Loose debris covering most of wear scar</p>
	<p><b>270°C, 4,522 m</b>  <i>(wear scar = 14 x 5 mm, also 390°C)</i>          Loose debris, a little smearing</p>
	<p><b>450°C, 4,522 m</b>  <i>(wear scar = 14 x 5 mm)</i>          Highly smeared oxide, some sintering with first traces of glaze</p>
	<p><b>510°C, 4,522 m</b>  <i>(wear scar = 14 x 5 mm, also 570°C)</i>          Patchy glaze formation</p>
	<p><b>750°C, 4,522 m</b>  <i>(wear scar = 14 x 5 mm, also 630°C, 690°C)</i>          Glaze formation – spalling on cooling</p>

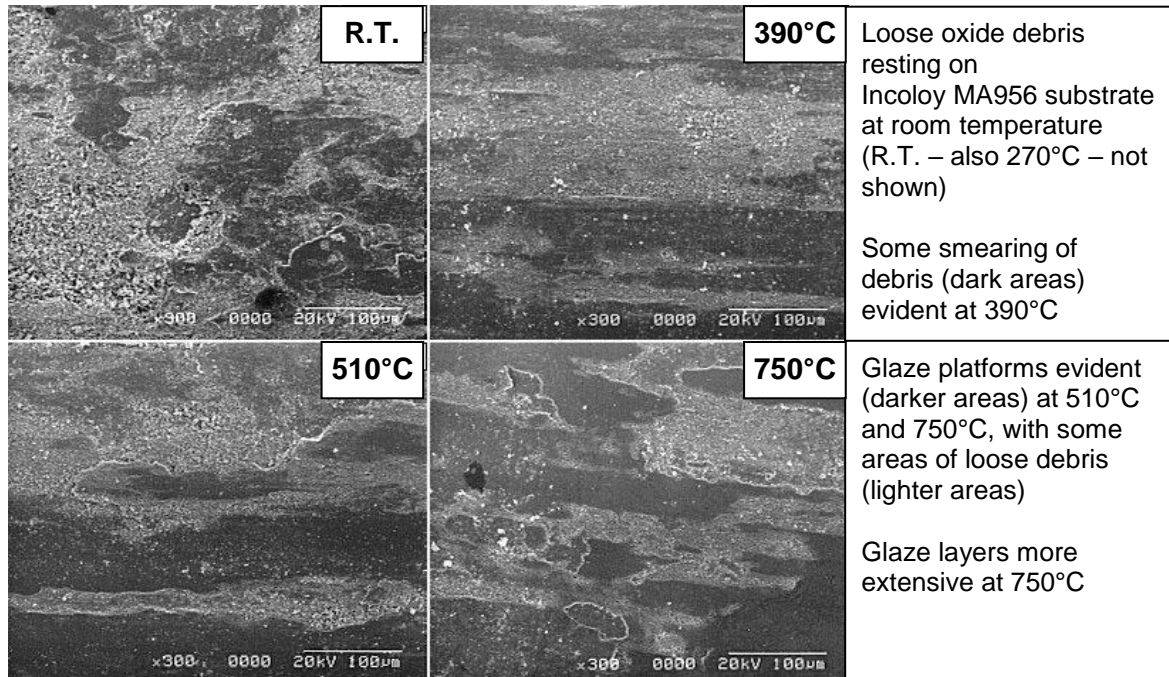
**Figure 5.41: Sample wear scar optical images – Incoloy MA956 / Stellite 6, 0.905 m.s<sup>-1</sup>**  
*(Observations made after 13,032 m of sliding follow the same pattern as 4,522 m where not shown)*

	<b>Room temperature, 4,522 m</b> (wear scar = 14 x 5 mm) Loose debris covering most of wear scar
	<b>270°C, 4,522 m</b> (wear scar = 14x 5 mm) Loose debris with some smearing
	<b>390°C, 4,522 m</b> (wear scar = 18 x 5 mm) Severe wear with no glaze
	<b>390°C, 13,032 m</b> (wear scar = 19 x 5 mm) Severe wear with no glaze
	<b>450°C, 4,522 m</b> (wear scar = 19 x 5 mm) Severe wear with no glaze
	<b>450°C, 13,032 m</b> (wear scar = 19 x 5 mm) Glaze development only after extended sliding
	<b>510°C, 4,522 m</b> (wear scar = 18 x 5 mm, also 570°C) Early severe wear followed by glaze formation
	<b>510°C, 13,032 m</b> (wear scar = 18 x 5 mm, also 570°C) Further glaze development with extended sliding
	<b>750°C, 4,522 m</b> (wear scar = 14 x 5 mm, also 630°C, 690°C) Comprehensive glaze formation

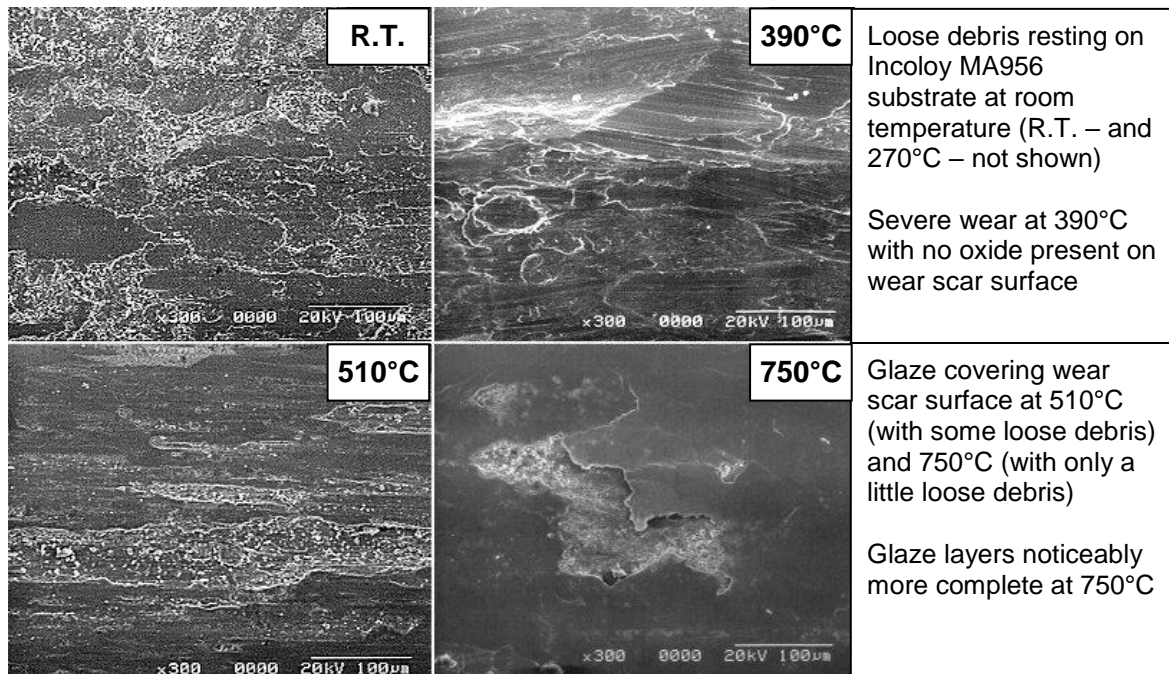


**Figure 5.42: SEM micrographs for Incoloy MA956 versus Stellite 6 – wear surface**

(a)  $0.314 \text{ m.s}^{-1} / 4,522 \text{ m}$  – room temperature,  $390^{\circ}\text{C}$ ,  $510^{\circ}\text{C}$  and  $750^{\circ}\text{C}$



(b)  $0.905 \text{ m.s}^{-1} / 4,522 \text{ m}$  – room temperature,  $390^{\circ}\text{C}$ ,  $510^{\circ}\text{C}$  and  $750^{\circ}\text{C}$

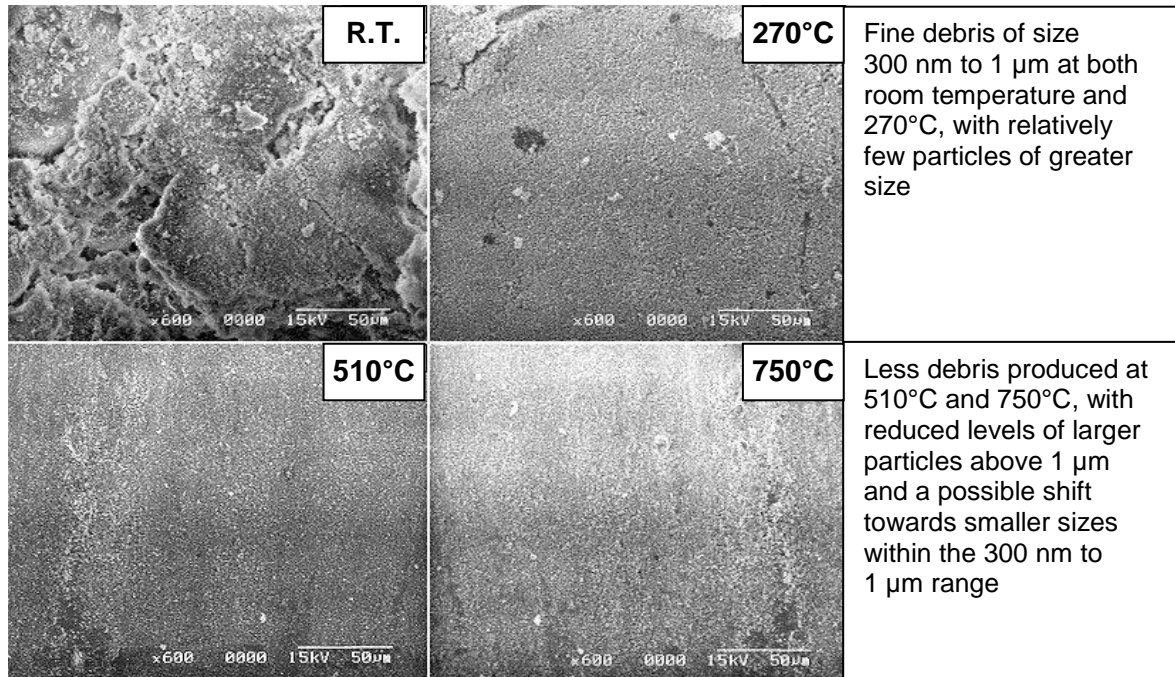


Same pattern of observations made after 13,032 m of sliding at  $0.905 \text{ m.s}^{-1}$

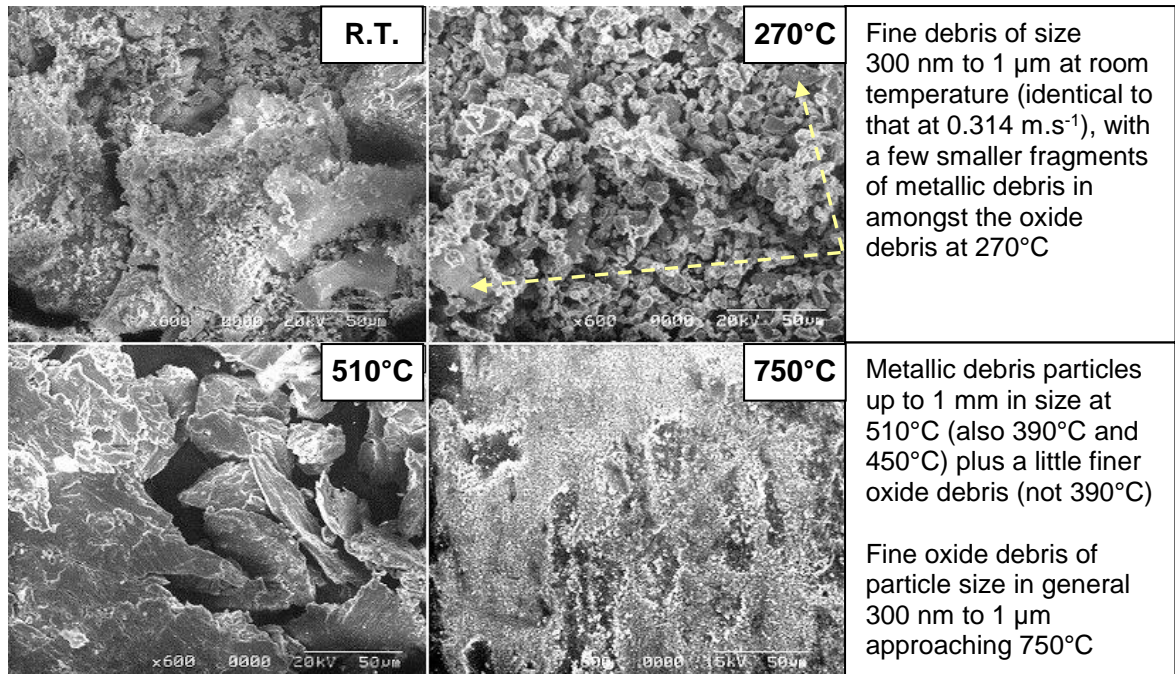


**Figure 5.43: SEM micrographs for Incoloy MA956 versus Stellite 6 – debris**

(a)  $0.314 \text{ m.s}^{-1} / 4,522 \text{ m}$  – room temperature,  $270^\circ\text{C}$ ,  $510^\circ\text{C}$  and  $750^\circ\text{C}$


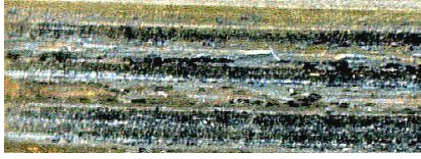
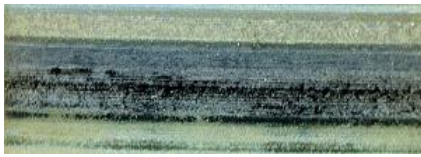


(b)  $0.905 \text{ m.s}^{-1} / 4,522 \text{ m}$  – room temperature,  $270^\circ\text{C}$ ,  $510^\circ\text{C}$  and  $750^\circ\text{C}$




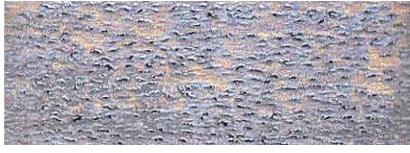
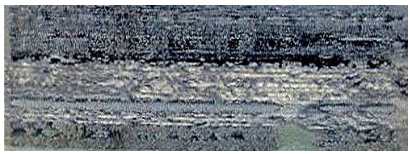

Same pattern of observations made after 13,032 m of sliding at  $0.905 \text{ m.s}^{-1}$

**Figure 5.44: Counterface wear scar optical images – Incoloy MA956 / Stellite 6, 0.314 m.s<sup>-1</sup>**

	<b>270°C, 4,522 m</b> <i>(section = 15 x 5 mm, applicable also at room temperature, 390°C and 450°C)</i> Loose oxide debris, some smearing at 390°C and 450°C
	<b>510°C, 4,522 m</b> <i>(section = 15 x 5 mm, applicable also at 570°C)</i> Patchy glaze covering contact areas
	<b>750°C, 4,522 m</b> <i>(section = 15 x 5 mm, applicable also at 630°C and 690°C)</i> Smooth glaze covering contact areas

**Figure 5.45: Counterface wear scar optical images – Incoloy MA956 / Stellite 6, 0.905 m.s<sup>-1</sup>**

*(Observations made after 13,032 m of sliding follow the same pattern as 4,522 m)*

	<b>270°C, 4,522 m</b> <i>(section = 15 x 5 mm, applicable also at room temperature)</i> Loose oxide debris with smearing, especially at 270°C
	<b>510°C, 4,522 m</b> <i>(section = 15 x 5 mm, applicable also at 390°C and 450°C)</i> Worn surface free of debris and glaze
	<b>570°C, 4,522 m</b> <i>(section = 15 x 5 mm, applicable also at 630°C)</i> Patchy glaze layer covered in loose debris
	<b>750°C, 4,522 m</b> <i>(section = 15 x 5 mm, applicable also at 690°C)</i> Comprehensive glaze formation – spalling on cooling



The ‘severe wear only’ phase at  $0.905 \text{ m.s}^{-1}$  was limited to  $390^\circ\text{C}$  for the Incoloy MA956 / Stellite 6 system. At  $450^\circ\text{C}$ , severe wear continued to dominate the early wear process, with a bright, highly worn wear surface on the  $0.905 \text{ m.s}^{-1}/4,522 \text{ m}$  samples (Figure 5.41). Continuing sliding up to  $13,032 \text{ m}$  at  $450^\circ\text{C}$  did result in the development of a glaze layer, covering most of the wear scar. This pattern continued at  $510^\circ\text{C}$  (Figures 5.41 and 5.42b) and  $570^\circ\text{C}$  with comprehensive glaze formation on the  $13,032 \text{ m}$  samples, compared to only limited glaze formation at  $4,522 \text{ m}$ .

At  $0.905 \text{ m.s}^{-1}$ , damage to the Incoloy MA956 samples became noticeably less as glaze formation became more comprehensive with increasing temperature. The depth and extent of the wear scar on the Incoloy MA956 sample became less pronounced, with the  $690^\circ\text{C}$  and  $750^\circ\text{C}$  (Figures 5.41 and 5.42b) samples showing very little evidence of severe wear prior to glaze formation. The larger metallic debris was increasingly replaced by finer oxide debris in the  $300 \text{ nm}$  to  $1 \mu\text{m}$  range as sliding temperature increased and severe wear was increasingly restricted to the early stages of sliding.

#### ***5.3.2.1 Stellite 6 Counterface Wear Scar Morphology***

An identical pattern of wear to that observed on the Incoloy MA956 sample at  $0.314 \text{ m.s}^{-1}$  was also observed on the Stellite 6 counterface (Figure 5.44). Between room temperature and  $450^\circ\text{C}$ , loose oxide debris covered the Stellite 6 counterface wear scar surface. Between  $510^\circ\text{C}$  and  $750^\circ\text{C}$ , the counterface wear scar surface was increasingly covered by glaze. Damage due to metal-to-metal contact of the Stellite 6 counterface with the Incoloy MA956 sample was extremely limited, particularly at glaze forming temperatures ( $510^\circ\text{C}$  to  $750^\circ\text{C}$ ).

A similar pattern of wear was observed on the Stellite 6 counterface to that on the Incoloy MA956 sample at  $0.905 \text{ m.s}^{-1}$  (Figure 5.45). At room temperature and  $270^\circ\text{C}$ , patches of loose oxide debris were observed across the surfaces of the wear scars, with very little accompanying damage to the counterface. A phase of severe wear was observed up to  $510^\circ\text{C}$ , with moderately worn wear scars that were highly damaged and metallic in nature. At  $570^\circ\text{C}$  and  $630^\circ\text{C}$ , patchy glaze formation occurred, this becoming more continuous at  $690^\circ\text{C}$  and  $750^\circ\text{C}$ . As glaze formation increased with temperature ( $570^\circ\text{C}$  to  $750^\circ\text{C}$ ), damage to the counterface decreased.

At  $0.905 \text{ m.s}^{-1}$ , the glaze formation on the Stellite 6 counterface was delayed until  $570^{\circ}\text{C}$ , despite glaze formation on samples of Incoloy MA956 at temperatures as low as  $450^{\circ}\text{C}$ .

### 5.3.3 EDX Analysis – Incoloy MA956 versus Stellite 6

The oxide debris and surface deposits formed on Incoloy MA956 samples that underwent sliding at  $0.314 \text{ m.s}^{-1}$ , showed a fairly consistent composition profile under EDX analysis from room temperature up to  $750^{\circ}\text{C}$  (Figure 5.46) with the Stellite 6 acting as the primary source of debris. Between room temperature and  $390^{\circ}\text{C}$ , there were slight decreases in cobalt levels ( $\sim 38\%$  to  $\sim 34\%$ ) within the loose oxide debris observed on the Incoloy MA956 wear scars. Iron levels in the same debris rose from  $\sim 16$  to  $25\%$  (indicating a limited contribution from the Incoloy MA956), with chromium levels remaining fairly steady between  $30$  and  $35\%$ .

Between  $390^{\circ}\text{C}$  and  $750^{\circ}\text{C}$ , with the onset of glaze formation on the Incoloy MA956 samples, the amount of cobalt within the glaze increased to  $\sim 40\%$ , with iron levels dropping to between  $15$  and  $20\%$ . Again chromium levels remained fairly steady between  $30$  and  $35\%$ . Thus, at all temperatures (room temperature to  $750^{\circ}\text{C}$ ), the high levels of cobalt-based oxide indicated that at  $0.314 \text{ m.s}^{-1}$  the Stellite 6 acted as the primary source of debris, along with a small but significant contribution of iron / chromium oxides from the Incoloy MA956.

All other elements remained at negligible or near-negligible levels at  $0.314 \text{ m.s}^{-1}$ , regardless of sliding temperature or whether or not glaze formation was observed.

The data from EDX at  $0.905 \text{ m.s}^{-1} / 4,522 \text{ m}$  indicated a change in the main source of debris to the Incoloy MA956. At room temperature and  $270^{\circ}\text{C}$ , the loose oxide debris that separated the Incoloy MA956 and Stellite 6 wear surfaces was highly variable in composition. At room temperature, iron levels were on average  $\sim 56\%$ , compared to  $\sim 28\%$  chromium and only  $\sim 8.5\%$  cobalt. At  $270^{\circ}\text{C}$ , iron and cobalt levels were on average both  $\sim 30\%$ , with a jump in chromium levels to  $36\%$ . Despite the high variability in the oxide debris composition observed at both temperatures, more often than not, the debris contained high levels of iron and low levels of cobalt, indicative of Incoloy MA956 acting as the main source of debris.



At 390°C and 450°C (0.905 m.s<sup>-1</sup>), where no significant oxide debris was observed and severe wear dominated, EDX of the wear scar surfaces were consistent with the Incoloy MA956 substrate – there was no evidence of transfer of material from the Stellite 6. The debris was also of high iron composition (~62% Fe, ~28% Cr, 0.1%-0.4% Co), indicating the metallic debris was generated almost exclusively from the Incoloy MA956.

The highest levels of iron at 0.905 m.s<sup>-1</sup> were observed in the glaze layers formed between 510°C and 630°C (~66% at 510°C and ~67% at 630°C) – with chromium levels remaining at ~32% and no significant evidence of cobalt, this EDX data indicated that the glaze forming between 510°C and 630°C was sourced solely from the Incoloy MA956. However, for glaze material produced above 630°C, cobalt transfer from the Stellite 6 again became a factor and cobalt levels rose from negligible levels between 450°C and 630°C to ~15% at 750°C. There was a consequent reduction of Incoloy MA956-sourced iron levels from ~67% at 630°C to ~48% at 750°C (although the relative quantities of iron and cobalt indicated that the Incoloy MA956 remained the main source of material forming the glaze), however, chromium remained at ~32%. Loose debris produced at 0.905 m.s<sup>-1</sup> gave similar results, within a band 2-3% either side of the values obtained for the 'glaze' oxide – this was also primarily Incoloy MA956-sourced.

EDX of samples and debris slid at 0.905 m.s<sup>-1</sup> / 13,032 m gave similar results to those slid for a distance of 4,522 m. At room temperature and 270°C, iron levels of ~58%, chromium levels of ~28% and cobalt levels on average no higher than ~5% indicated that Incoloy MA956 remained the main source of oxide debris after 13,032 m, with only a limited amount of variation in composition (approximately ±5% in iron and chromium levels).

At 390°C, EDX indicated that the oxide-free wear surfaces observed to form on the Incoloy MA956 at 0.905 m.s<sup>-1</sup> / 13,032 m, were absent of Stellite 6-sourced material (~62% Fe, ~28% Cr and negligible Co) – this indicated that continued sliding to 13,032 m had not led to any transfer. The ejected metallic debris produced at 390°C was of a composition very similar to that of the Incoloy MA956 itself (~63% Fe, ~29%Cr and negligible Co), indicating little evidence of material removal from the Stellite 6.

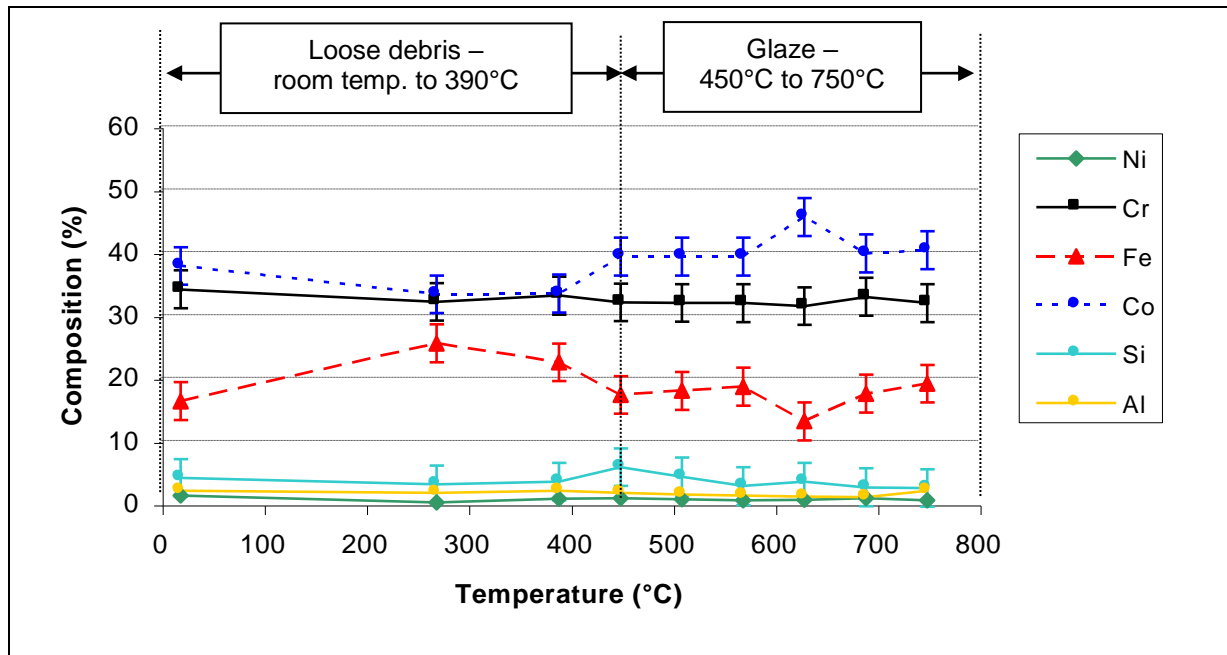
The glaze layers observed to be forming on the  $0.905 \text{ m.s}^{-1}$  / 13,032 m Incoloy MA956 samples at  $450^{\circ}\text{C}$  were also of a high iron (~61%) / chromium (~26%) composition with negligible cobalt – once again, the primary source of the oxide debris forming the glaze layers was the Incoloy MA956. This continued to be the case on increasing the temperature up to  $750^{\circ}\text{C}$ . However, as had been the case after 4,522 m of sliding, cobalt reappeared in the glaze above  $570^{\circ}\text{C}$ , indicating increased levels of transfer from the Stellite 6 counterface – between  $570^{\circ}\text{C}$  and  $750^{\circ}\text{C}$ , cobalt levels rose from ~1.5% to ~20%. Over the same range of temperatures, the level of iron in the glaze fell from ~64% to ~40% and the level of chromium remained roughly the same, values rising slightly from ~27.5% to ~32%.

Other elements remained at negligible levels at  $0.905 \text{ m.s}^{-1}$  with the exception of aluminium, which at glaze forming temperatures ( $450^{\circ}\text{C}$  and  $750^{\circ}\text{C}$ ) was present to between 5% and 8%. Increasing the sliding distance from 4,522 m to 13,032 m had no significant effect.

The glaze that formed upon the Stellite 6 counterface at  $750^{\circ}\text{C}$  (the glaze was removed for analysis) was generally of a composition close to the glaze examined on the wear scar of Incoloy MA956 as a sample, depending on the sliding speed. For samples slid at  $0.314 \text{ m.s}^{-1}$ , a mean composition of ~41% cobalt, ~32% chromium and ~17% iron was obtained, indicating that the material forming the glaze was sourced primarily from the Stellite 6. For samples slid at  $0.905 \text{ m.s}^{-1}$  / 4,522 m and  $750^{\circ}\text{C}$ , the glaze removed from the Stellite 6 counterface was primarily sourced from the Incoloy MA956 sample, as indicated by the high levels of iron (mean ~45%) and low levels of cobalt (mean ~15%) – chromium levels were recorded at a mean level of ~28%. Very similar values were obtained after 13,032 m, albeit with slightly higher levels of cobalt (~19%) and lower levels of iron (~41%) – chromium levels remained the same (~28%).

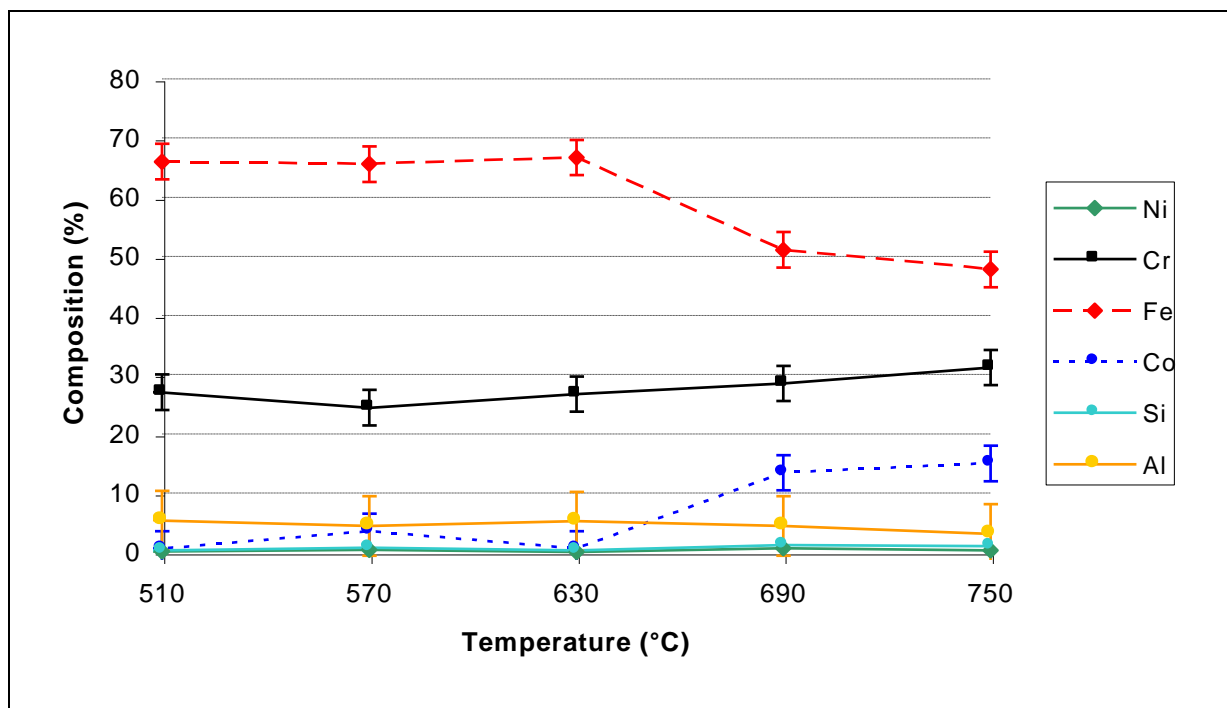
**Figure 5.46: EDX data – variation of composition of loose debris and glaze layers (Incoloy MA956 vs. Stellite 6), room temperature to 750°C, 0.314 m.s<sup>-1</sup>**

(load = 7N, sliding distance = 4,522 m, sample size = 3)



**Figure 5.47: EDX Data – variation of composition of glaze layers (Incoloy MA956 vs. Stellite 6), 510°C to 750°C, 0.905 m.s<sup>-1</sup>**

(load = 7N, sliding distance = 4,522 m, sample size = 3)



Same pattern of observations made after 13,032 m of sliding

### 5.3.4 EDX Mapping – Incoloy MA956 versus Stellite 6

At  $0.314 \text{ m.s}^{-1} / 4,522 \text{ m}$ , there was a high concentration of cobalt, plus an increased concentration of chromium in the glaze layer for samples slid at  $750^{\circ}\text{C}$  (Figure 5.48 is representative of samples slid at  $0.314 \text{ m.s}^{-1}$  and  $750^{\circ}\text{C}$ ) - Stellite 6 was the only possible source of this cobalt. Iron was exclusively restricted to the Incoloy MA956 sample with no evidence of migration into the glaze layer. This suggests that the high cobalt-chromium glaze consisted of material primarily transferred from the Stellite 6 counterface against which Incoloy MA956 was worn. Aluminium was almost completely absent for this combination ( $0.314 \text{ m.s}^{-1} / 4,522 \text{ m}$ ,  $750^{\circ}\text{C}$ ). Stellite 6-sourced silicon was restricted to the glaze layer region.

Also present near the base of the compacted oxide layer on the Incoloy MA956 samples slid at  $0.314 \text{ m.s}^{-1}$ , were isolated fragments of unoxidised high-cobalt metal. These indicate very limited transfer of metallic Stellite 6 to the Incoloy MA956 before a significant oxide layer formed on the Incoloy MA956 surface.

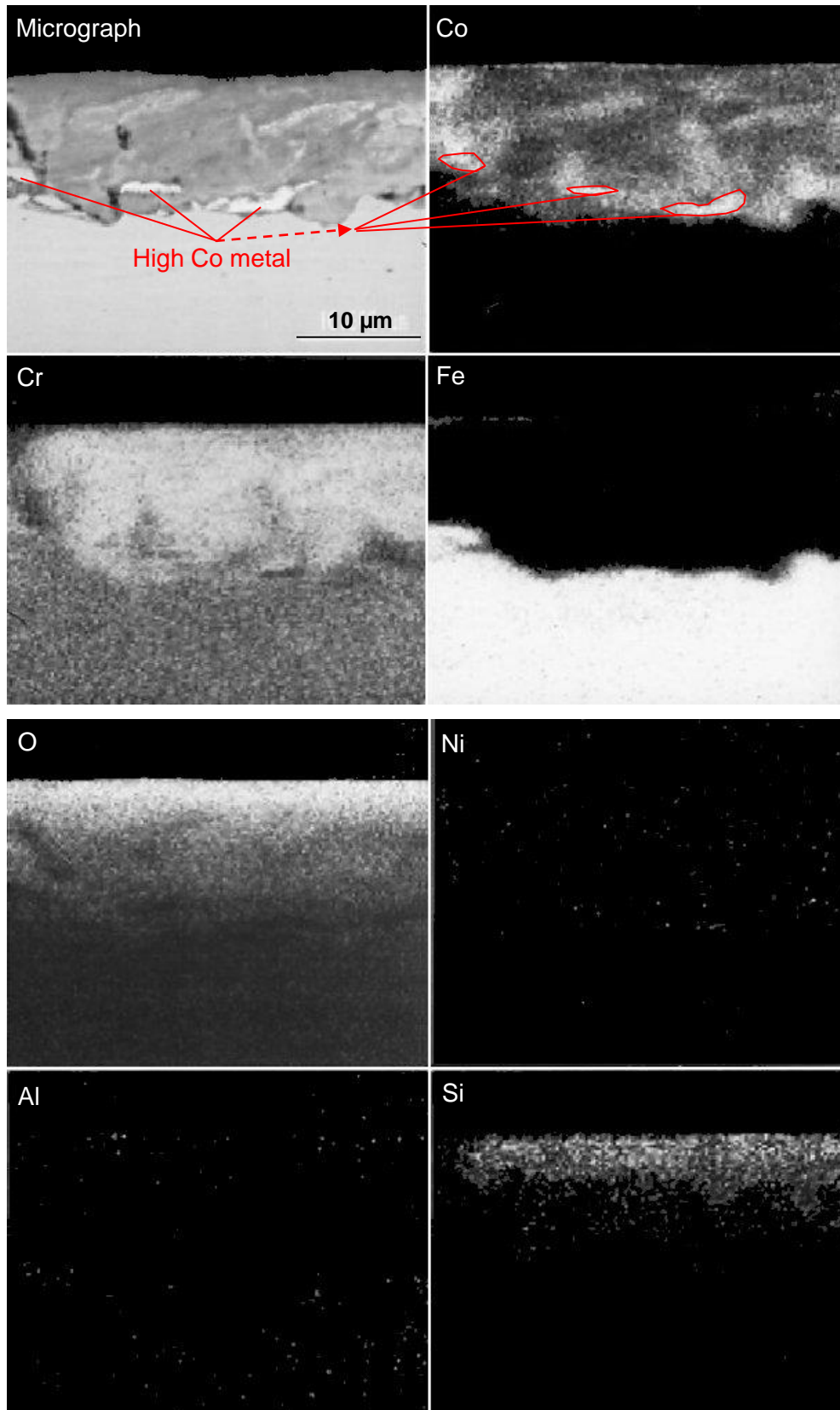
EDX mapping of Incoloy MA956 samples slid against Stellite 6 at  $0.905 \text{ m.s}^{-1} / 4,522 \text{ m}$  and  $750^{\circ}\text{C}$ , showed only very low amounts of cobalt in the glaze layer (Figure 5.49 is representative of samples slid at  $0.905 \text{ m.s}^{-1} / 4,522 \text{ m}$  and  $750^{\circ}\text{C}$ ). Chromium was still present, but at reduced levels compared to  $0.314 \text{ m.s}^{-1}$ . These were replaced at  $0.905 \text{ m.s}^{-1}$  to a certain extent by iron and aluminium from the Incoloy MA956 – the very high concentration of aluminium close to the Incoloy MA956-debris interface suggests additional movement of aluminium by diffusion.

There was also a strong signal for Stellite 6-sourced silicon in the surface layers of the  $0.905 \text{ m.s}^{-1} / 4,522 \text{ m}$  samples, despite the reduced levels of cobalt and chromium indicating decreased transfer from the Stellite 6 counterface at higher sliding speeds. This was again restricted to the glaze layers, as it had been at  $0.314 \text{ m.s}^{-1}$ .

No fragments of unoxidised cobalt metal were observed at  $0.905 \text{ m.s}^{-1}$ , indicating no significant metal transfer from the Stellite 6 counterface to the Incoloy MA956 sample.

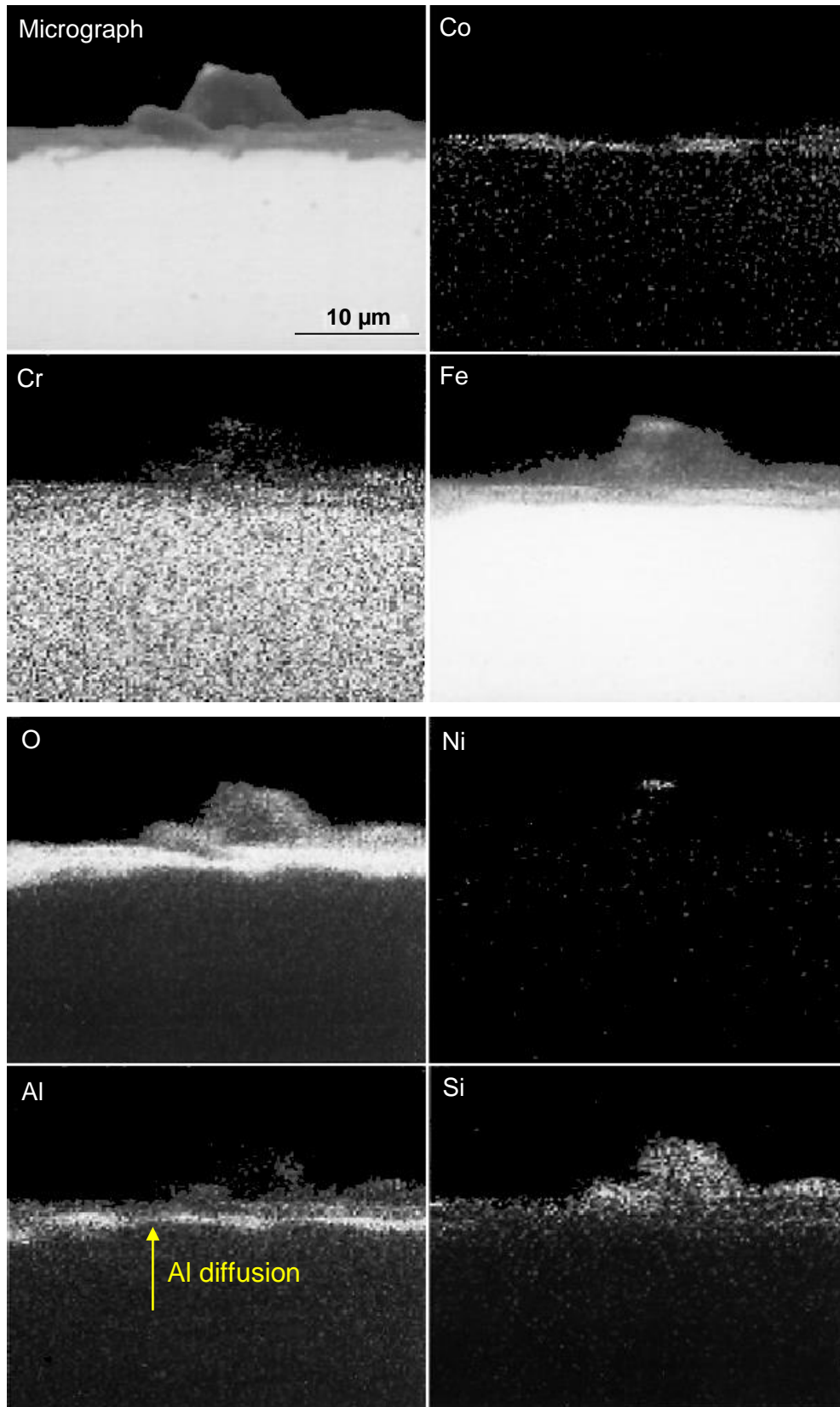
**Figure 5.48:** Cross-sectional EDX element maps for Incoloy MA956 worn against Stellite 6 subsequent to wear at  $0.314 \text{ m.s}^{-1}$

(load = 7N, sliding distance = 4,522 m, temperature =  $750^\circ\text{C}$ , sample size = 3)



**Figure 5.49: Cross-sectional EDX element maps for Incoloy MA956 worn against Stellite 6 subsequent to wear at  $0.905 \text{ m.s}^{-1}$**

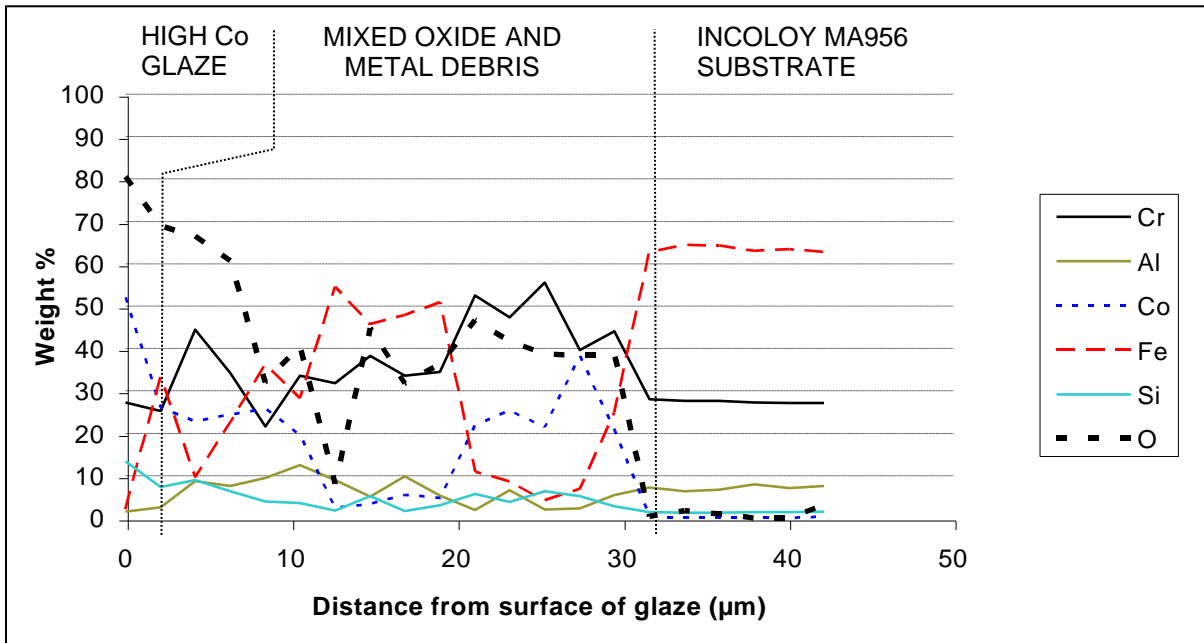
*(load = 7N, sliding distance = 4,522 m, temperature =  $750^\circ\text{C}$ , sample size = 3)*



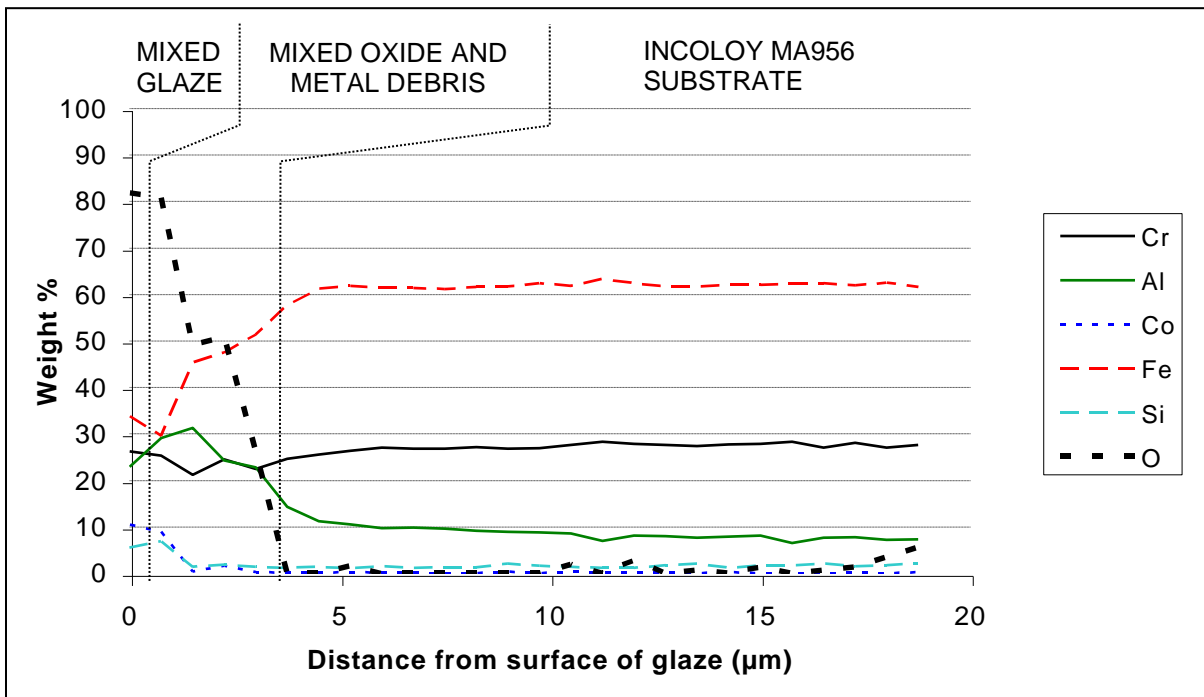
**Figure 5.50: Data from Autopoint EDX analysis for Incoloy MA956 slid against Stellite 6 at sliding speeds of 0.314 and 0.905 m.s<sup>-1</sup> and 750°C**

Amounts of each substance present are expressed in terms of percentage of the non-oxygen content. Amount of oxygen is expressed in terms of percentage of the overall content. Data (sample size = 3) are for samples slid for a distance of 4,522 m.

(a) 0.314 m.s<sup>-1</sup>



(b) 0.905 m.s<sup>-1</sup>





### 5.3.5 Autopoint EDX Analysis – Incoloy MA956 versus Stellite 6

Presented in Figure 5.50 is a representative example of the Autopoint EDX data obtained from Incoloy MA956 samples slid against a Stellite 6 counterface at  $0.314 \text{ m.s}^{-1}$  / 4,522 m and  $750^{\circ}\text{C}$ , all samples giving very similar results. For each sample studied, the data indicated that the glaze layer was on average  $\sim 2 \mu\text{m}$  thickness at  $0.314 \text{ m.s}^{-1}$  and  $\sim 1 \mu\text{m}$  thickness at  $0.905 \text{ m.s}^{-1}$ , overlying a debris layer beneath. The depth of the debris layer was observed to be greater at  $0.314 \text{ m.s}^{-1}$  (between 30 to  $40 \mu\text{m}$ ) than at  $0.905 \text{ m.s}^{-1}$  (no more than 4 to  $5 \mu\text{m}$ ).

At  $0.314 \text{ m.s}^{-1}$  / 4,522 m, the  $\sim 2 \mu\text{m}$  thickness glaze layer was high in cobalt ( $\sim 53\%$ ) and low in iron ( $\sim 2\%$ ), indicating that it was sourced from the Stellite 6 counterface (Figure 5.50). The 30 to  $40 \mu\text{m}$  thick debris layer beneath the glaze consisted of areas of mixed metal and oxide material all the way to the Incoloy MA956-debris interface. No clear indication could be obtained of whether the Incoloy MA956 sample or the Stellite 6 counterface was the primary source of material in the debris layer. Large fluctuations were observed in Incoloy MA956-sourced iron (between 3 and  $55\%$ ), Stellite 6-sourced cobalt (between 2 and  $38\%$ ) and chromium from both (between 22 and  $55\%$ ). Additionally, no correlation was observed between overall oxygen content and the amount present of any of the metallic components at  $0.314 \text{ m.s}^{-1}$ .

The formation of the stable, high-cobalt glaze layer over the top of this mixed metal-oxide debris layer at  $0.314 \text{ m.s}^{-1}$  / 4,522 m indicates additionally that the mixed metal-oxide layer can only have been formed earlier during sliding, prior to glaze formation.

At  $0.905 \text{ m.s}^{-1}$  / 4,522 m and  $750^{\circ}\text{C}$ , again a thin glaze layer of up to  $2 \mu\text{m}$  thickness was present at the surface. Cobalt accounted for only  $\sim 10\%$  of the glaze composition, with iron ( $\sim 33\%$ ), chromium ( $\sim 28\%$ ) and aluminium ( $\sim 22\%$ ) now dominant. As with the standard EDX results, this change in glaze layer composition indicates a change in the primary source of debris for the glaze to the Incoloy MA956, with reduced transfer of material from the Stellite 6 counterface.

The underlying debris layer was greatly reduced at  $0.905 \text{ m.s}^{-1}$ , forming a layer of thickness no more than 4 or  $5 \mu\text{m}$ . The debris layer was once again mixed metal and oxide, however,

the high iron levels (between ~30% and 57%), and negligible cobalt levels indicated that the Incoloy MA956 was the sole source of this debris. Again, the formation of a stable glaze layer over the top of this mixed metal-oxide debris layer indicated that the mixed metal-oxide debris layer can only have formed earlier during sliding. The presence of cobalt only within the glaze layer at  $0.905 \text{ m.s}^{-1}$  indicated that the very limited transfer of material from the Stellite 6 counterface only occurred once the primarily Incoloy MA956-sourced glaze layer has started forming.

The high concentrations of aluminium observed in the surface layers with the EDX element maps (Figure 5.49) were also highly evident in the Autopoint EDX data for samples slid at  $0.905 \text{ m.s}^{-1}$ . High levels of aluminium in both the debris layer (between 15 and 31%, replacing iron which fell to as low as ~30%) and in the glaze layer (as high as 24% in some areas) were observed. With aluminium not present to any significant level in the Stellite 6, this high concentration can only be accounted for by diffusion of aluminium from the Incoloy MA956 into the debris layers and glaze during sliding.

### 5.3.6 XRD Analysis – Incoloy MA956 versus Stellite 6

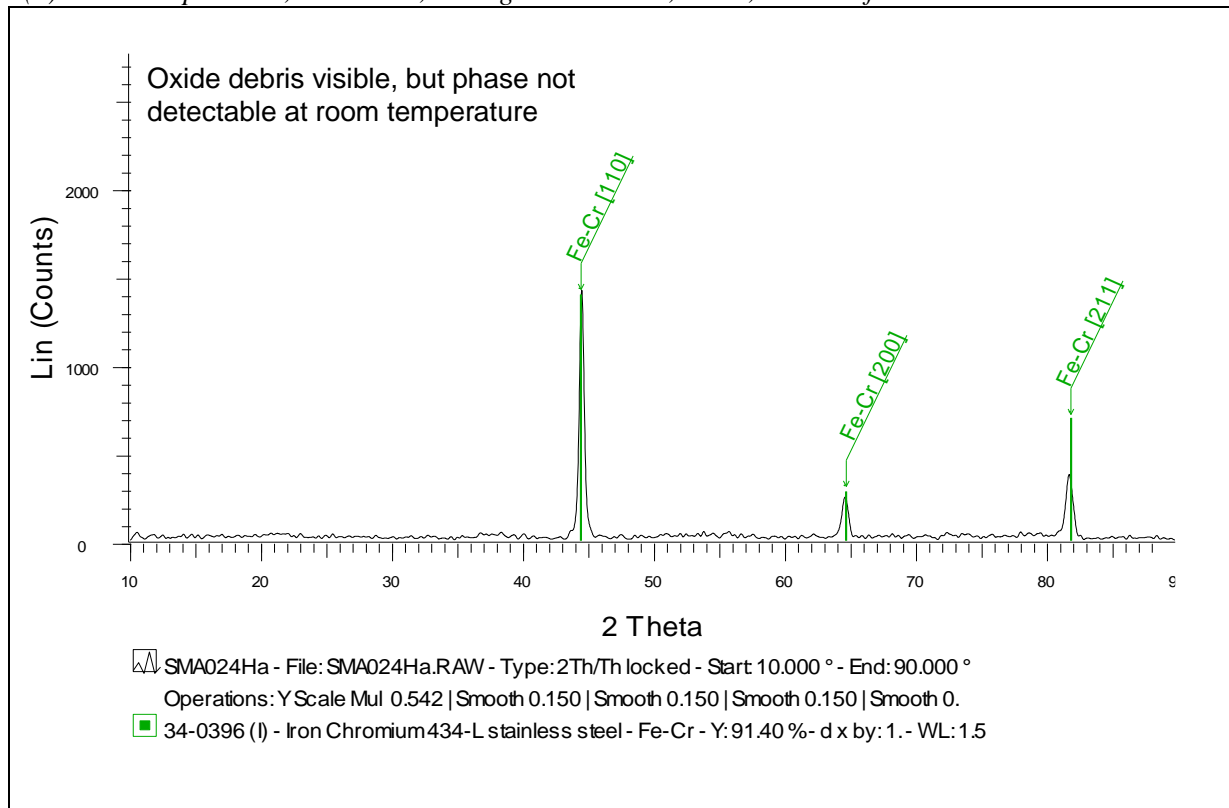
At  $0.314 \text{ m.s}^{-1}$ , XRD analysis suggested the presence of only Fe-Cr as a phase for room temperature (Figure 5.51a), despite the presence of oxide debris (Figure 5.42). At all other temperatures up to  $750^\circ\text{C}$ , the presence of either or both of  $\text{CoCr}_2\text{O}_4$  and  $\text{Co}_3\text{O}_4$  was indicated alongside Fe-Cr, weakly at  $270^\circ\text{C}$  and  $390^\circ\text{C}$  and more strongly at  $450^\circ\text{C}$  and above (Figure 5.51b shows the  $750^\circ\text{C}$  case).

Comparison of the XRD data with the physical evidence shows that the apparent absence or weak indication of  $\text{CoCr}_2\text{O}_4$  corresponded to temperatures (room temperature to  $390^\circ\text{C}$ ) where only powdery oxide debris was present on the wear scar. The stronger signal corresponded to temperatures ( $450^\circ\text{C}$  to  $750^\circ\text{C}$ ) over which glaze formation was observed.

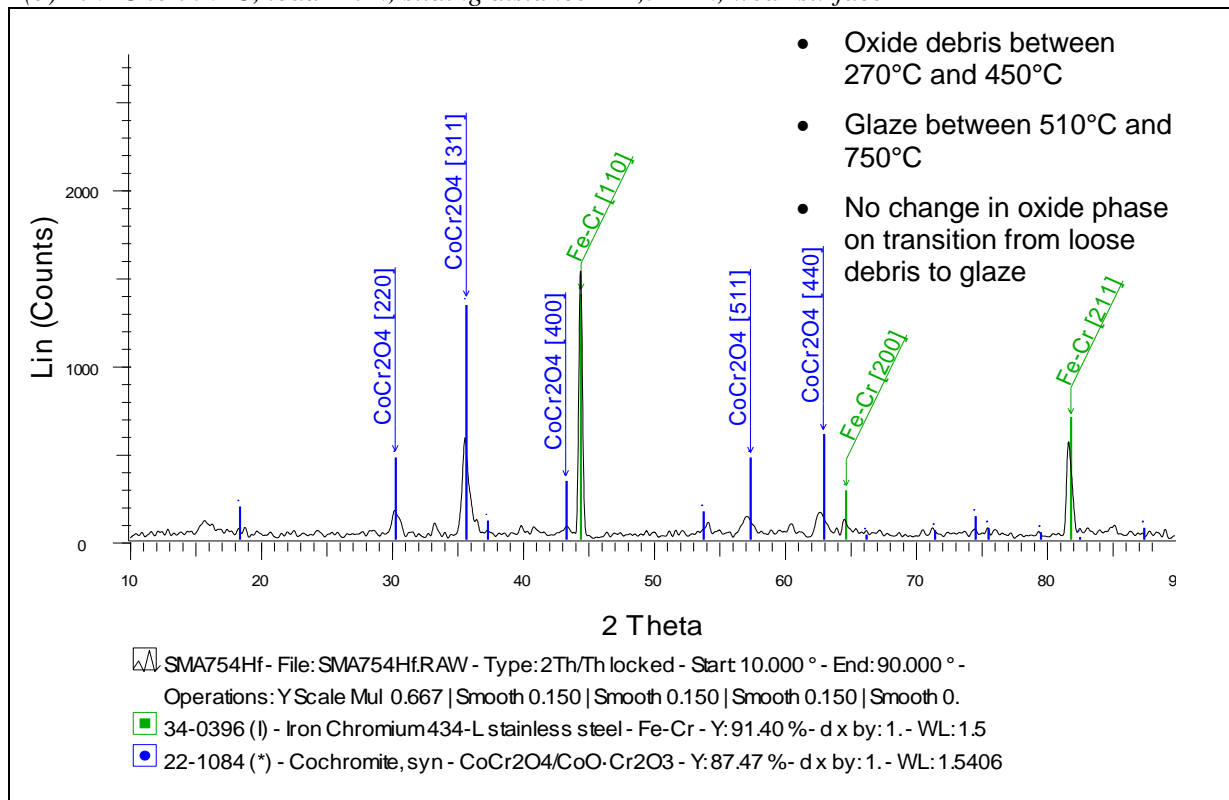
At  $0.905 \text{ m.s}^{-1}$ , Fe-Cr was the only phase detected up to  $450^\circ\text{C}$  – this was regardless of whether the Incoloy MA956 surface was covered in a fine powdery oxide deposit (room temperature and  $270^\circ\text{C}$  – Figure 5.52a) or completely devoid of oxide ( $390^\circ\text{C}$  and  $450^\circ\text{C}$  /  $4,522 \text{ m}$  – Figure 5.52b).

**Figure 5.51: XRD for Incoloy MA956 versus Stellite 6 – 0.314 m.s<sup>-1</sup>**

(a) Room temperature, load = 7N, sliding distance = 4,522 m, wear surface

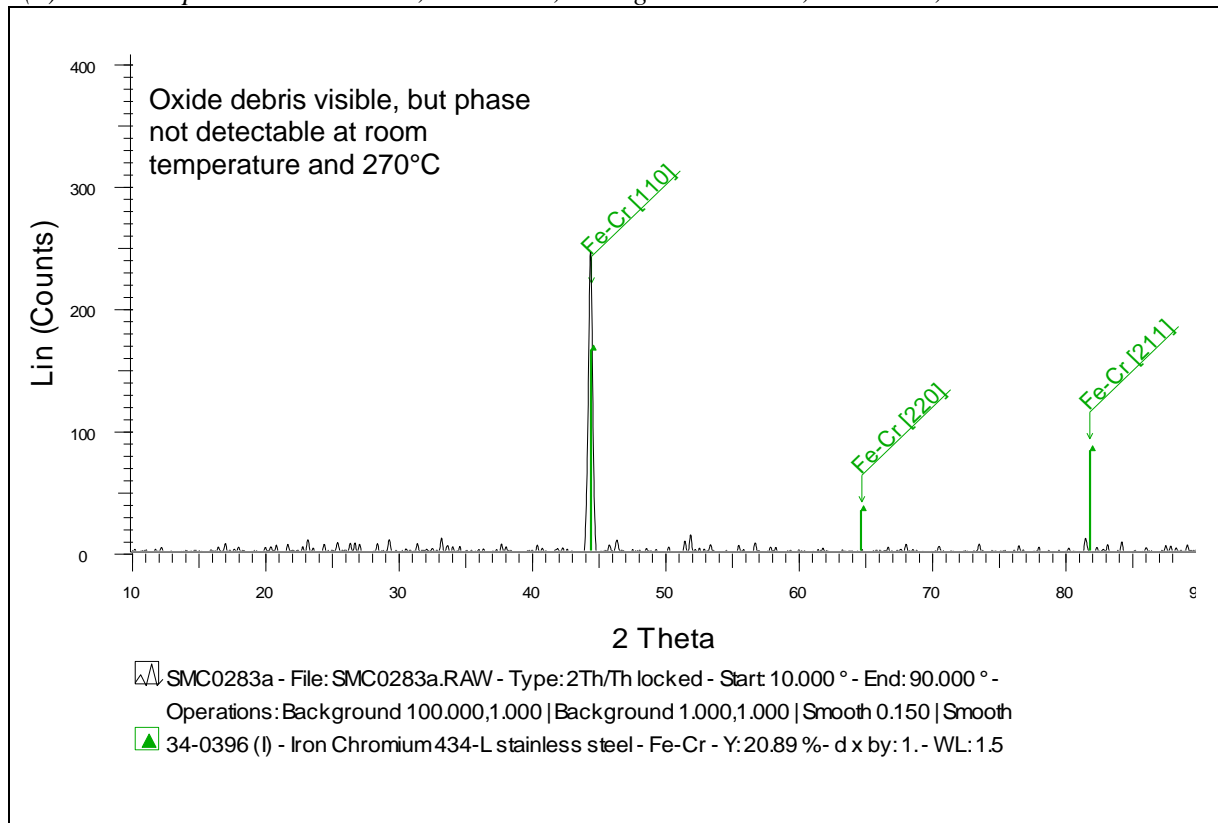


(b) 270°C to 750°C, load = 7N, sliding distance = 4,522 m, wear surface

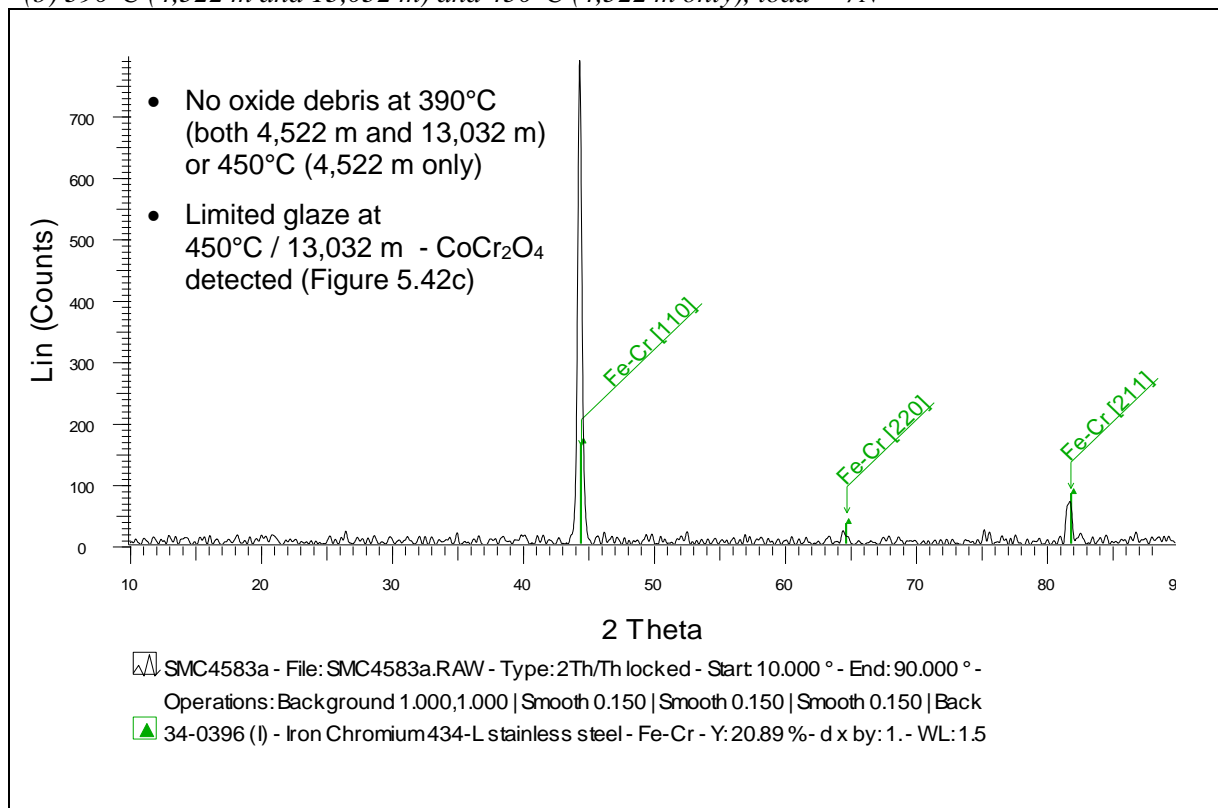


**Figure 5.52: XRD for Incoloy MA956 versus Stellite 6 –  $0.905 \text{ m.s}^{-1}$**

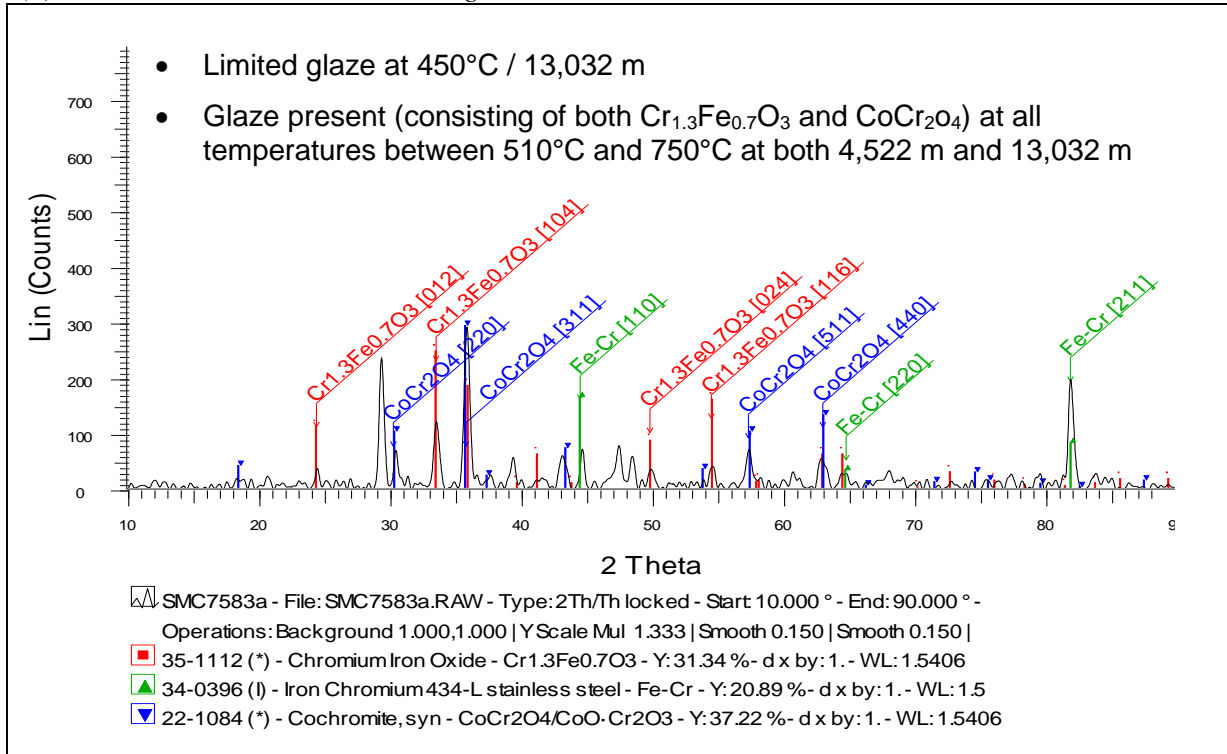
(a) Room temperature and  $270^\circ\text{C}$ , load = 7N, sliding distance = 4,522 m / 13,032 m



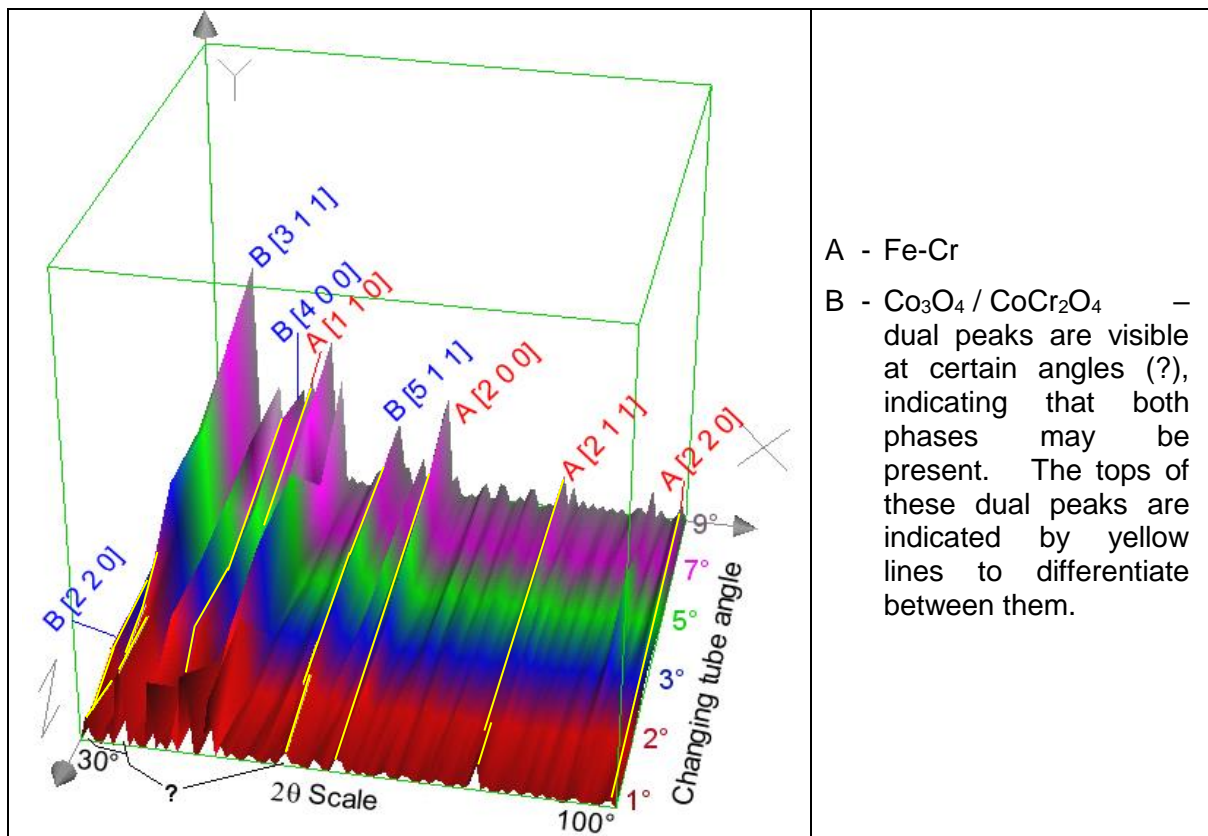
(b)  $390^\circ\text{C}$  (4,522 m and 13,032 m) and  $450^\circ\text{C}$  (4,522 m only), load = 7N



(c) 510°C to 750°C, load = 7N, sliding distance = 4,522 m / 13,032 m, also 450°C and 13,032 m



**Figure 5.53: Glancing Angle XRD for Incoloy MA956 versus Stellite 6 – 0.314 m.s<sup>-1</sup>**  
(750°C, load = 7N, sliding distance = 4,522 m, glancing angle XRD)



At 450°C / 13,032 m and temperatures of 510°C and greater (for sliding distances of both 4,522 m and 13,032 m) as glaze layers started to develop, XRD detected the iron-chromium phase  $\text{Cr}_{1.3}\text{Fe}_{0.7}\text{O}_3$  and one or both of the cobalt containing phases,  $\text{CoCr}_2\text{O}_4$  and  $\text{Co}_3\text{O}_4$  (Figure 5.52c).  $\text{Co}_3\text{O}_4$  was less likely than  $\text{CoCr}_2\text{O}_4$  as a cobalt-containing phase, due to the shift in source from the cobalt rich Stellite 6 counterface to the Incoloy MA956 sample on sliding at 0.905  $\text{m.s}^{-1}$ , indicated by EDX.

Glancing angle XRD of 0.314  $\text{m.s}^{-1}$  / 4,522m / 750°C samples (Figure 5.53) once again confirmed the presence of the Fe-Cr metallic phase and the  $\text{CoCr}_2\text{O}_4$  and / or  $\text{Co}_3\text{O}_4$  oxide phases. However, a dual peak was observed at some angles for  $\text{CoCr}_2\text{O}_4$  /  $\text{Co}_3\text{O}_4$ , this possibly indicating the presence of both phases in the glaze layers. The dual peak was absent from standard XRD, possibly due to the higher cobalt  $\text{Co}_3\text{O}_4$  being restricted to the extreme surface of the glaze layer (where it was in direct contact with the Stellite 6 counterface). Glancing angle XRD of 0.905  $\text{m.s}^{-1}$  samples slid at 750°C (for either 4,522 m or 13,032 m) did not give a conclusive result.

### 5.3.7 Micro-hardness Testing – Incoloy MA956 versus Stellite 6

No clear trends were visible at 0.314  $\text{m.s}^{-1}$  for the Incoloy MA956 / Stellite 6 system, regardless of the test temperature and there was no trace of a hardened sub-surface in any of the samples studied after testing (room temperature, 270°C, 510°C and 750°C – Figure 5.54a is representative of the data obtained from samples slid at each temperature). Compared to a mean hardness for the unworn Incoloy MA956 of 4.1 GPa, values for Incoloy MA956 samples at all temperatures in general remained between 2.6 and 4.3 GPa with no real indication of any increase or decrease in hardness with increasing depth.

There was, however, some evidence of increased subsurface hardness with the 0.905  $\text{m.s}^{-1}$  / 4,522 m samples at room temperature, 270°C and 510°C (Figure 5.54b shows representative depth hardness profiles obtained from samples slid at room temperature, 270°C, 510°C and 750°C) – a slight downward trend in hardness with increasing temperature was indicated by the collected hardness data. At room temperature, peak values of hardness of ~4.8 GPa were obtained at depths of between 0 and 0.1 mm, with hardness values decreasing at greater depths to in general between 3.5 GPa and 4.2 GPa.

Slightly higher peak values of ~5.1 GPa were obtained for depths of between 0 mm and 0.1 mm at 270°C, decreasing at greater depths to between 3.9 and 4.4 GPa. The lower value peaks in hardness for 510°C observed between 0 mm and 0.1 mm were less pronounced at 4.2 and 4.4 GPa respectively, dropping to in general between 3.4 and 3.9 GPa at depths between 0.1 mm and 1 mm. There was no indication of greater sub-surface hardness for samples slid at 750°C. Testing of samples slid at 750°C and 0.905 m.s<sup>-1</sup> gave in general the lowest values of hardness of between 2.9 and 3.9 GPa.

These results indicate a lower tendency for sub-surface hardening for Incoloy MA956 slid against Stellite 6 than was observed for Nimonic 80A slid against Stellite 6 (Figure 5.17).

It was not possible to measure the hardness of the glaze on the 0.314 m.s<sup>-1</sup> samples at 750°C (Table 5.4), due to the glaze continually breaking up whenever a hardness test was attempted. Each time, the glaze layer would fail to reveal a powdery layer underlying it. No such problems occurred with the primarily Incoloy MA956-sourced glaze layer formed on the 0.905 m.s<sup>-1</sup> samples, with very high values of on average 16.63 GPa obtained. Reduced underlying debris observed during Autopoint EDX testing (Figure 5.50b) seems to have allowed greater support of the Cr<sub>1.3</sub>Fe<sub>0.7</sub>O<sub>3</sub> / CoCr<sub>2</sub>O<sub>4</sub> glaze layer produced at 0.905 m.s<sup>-1</sup>.

**Table 5.4: Hardness data for glaze and undeformed substrate, Incoloy MA956 versus Stellite 6 slid at 750°C**

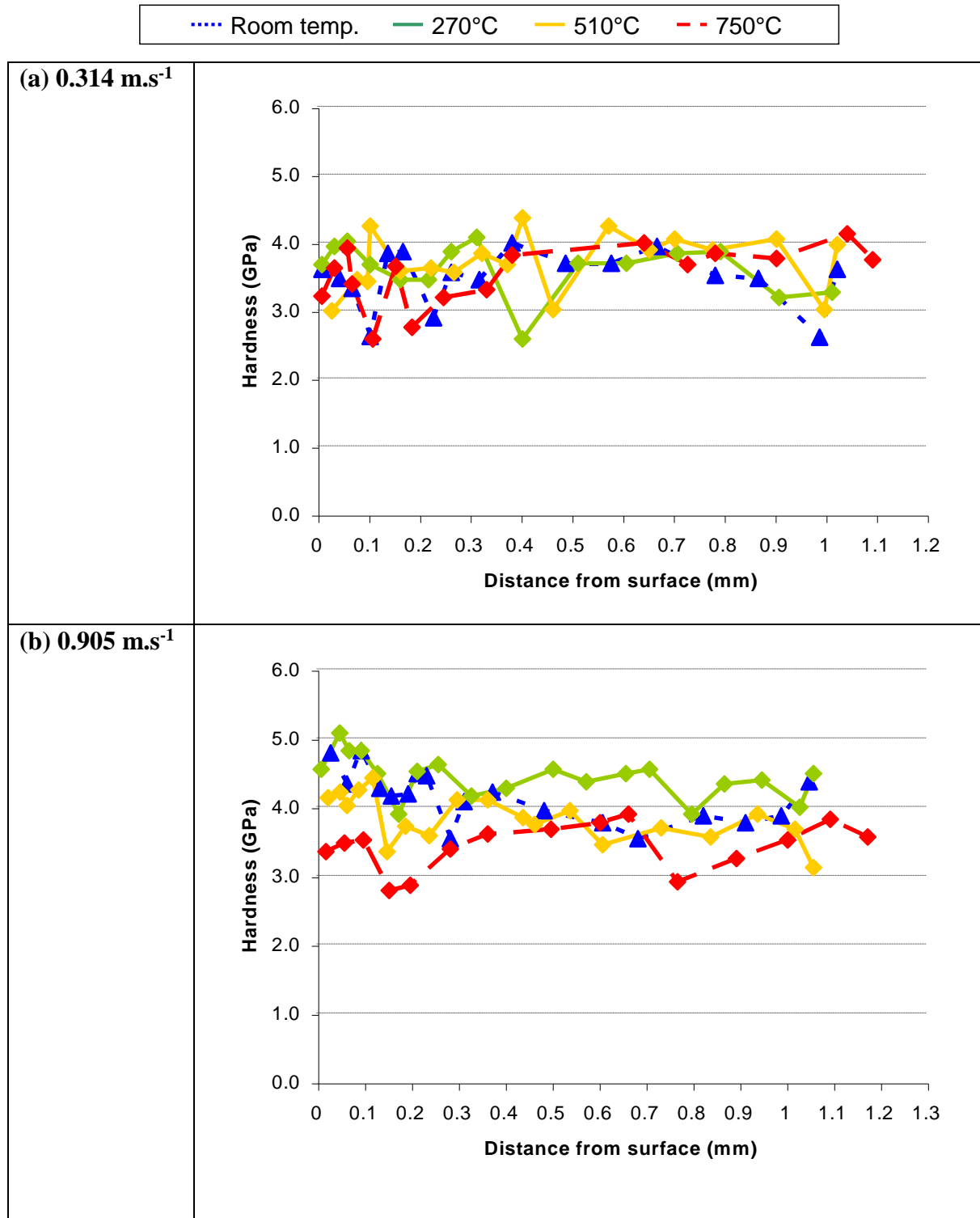
(load = 7N, sliding distance = 4,522 m, hardness values in GPa, Vickers micro-indenter - 50g, sample size = 5)

Unworn substrate (preheated to 750°C for 4 hours)		Glaze formed at 0.314 m.s <sup>-1</sup>	Glaze formed at 0.905 m.s <sup>-1</sup>	
4.48	Mean = 4.13 GPa	Glaze Layer collapses on the taking of measurements	16.38	Mean = 16.63 GPa
3.67			14.75	
3.91			14.20	
4.24			20.26	
4.36			17.44	



**Figure 5.54: Subsurface layer hardness for samples slid at 0.314 and 0.905 m.s<sup>-1</sup>, Incoloy MA956 versus Stellite 6**

(load = 7N, sliding distance = 4,522 m, hardness values in GPa, Vickers micro-indenter - 50g, sample size = 3)



## 5.4 Testing of Nimonic 80A versus Incoloy 800HT between Room Temperature and 750°C, at 0.314 and 0.905 m.s<sup>-1</sup>

### 5.4.1 Experimental Observations – Nimonic 80A versus Incoloy 800HT

Figure 5.55 shows the variation of weight loss (in grams) and wear rate (defined in this thesis as  $\mu\text{g.m}^{-1}$ ) with temperature for the Nimonic 80A / Incoloy 800HT (counterface) system, in the room temperature to 750°C temperature range. The weight loss and wear rate behaviour observed at 0.314 m.s<sup>-1</sup> (after 4,522 m of sliding) and 0.905 m.s<sup>-1</sup> (after 4,522 m and 13,032 m of sliding) is described in this section.

#### a) Weight change and wear rate data at 0.314 m.s<sup>-1</sup>/ 4,522 m

At 0.314 m.s<sup>-1</sup>, extremely small changes in sample weight and low levels of wear rate were observed throughout the entire test temperature range (room temperature to 750°C – Figure 5.55). This was especially the case at room temperature (weight change -0.003(0) g – the negative value indicating weight loss, wear rate 0.652  $\mu\text{g.m}^{-1}$  between 0 and 4,522 m) and 270°C (weight change -0.007(5) g, wear rate 1.656  $\mu\text{g.m}^{-1}$ ).

At 390°C, steep rises in weight loss (the recorded weight change was -0.055(0) g) and wear rate (12.370  $\mu\text{g.m}^{-1}$  up to 4,522 m) were observed, the highest for any temperature at 0.314 m.s<sup>-1</sup>. Weight loss and wear rate remained high (albeit with a slight downward trend) up to 570°C – for example, at 510°C, a wear rate of 8.694  $\mu\text{g.m}^{-1}$  was recorded (weight change -0.039(3) g). At 570°C, the recorded wear rate was 6.454  $\mu\text{g.m}^{-1}$  (weight change -0.029(2) g).

A small rise in Nimonic 80A weight loss (weight change -0.042(2) g) was observed at 630°C, with an accompanying wear rate of 9.341  $\mu\text{g.m}^{-1}$ . Weight loss and wear rate then showed a clear decrease on raising the temperature up to 750°C, with values of 0.001(8) g for weight change and -0.402  $\mu\text{g.m}^{-1}$  for wear rate indicating a slight net weight gain.

#### b) Coefficient of friction data at 0.314 m.s<sup>-1</sup>

An unsettled ‘run-in’ period was observed for the Nimonic 80A / Incoloy 800HT (counterface) system at the beginning of sliding at 0.314 m.s<sup>-1</sup>, which quickly gave way to

a more settled ‘steady state’ phase. There was no indication of a clear trend for the unsettled run-in data with rising temperature (Figure 5.56) – at the beginning of testing, values rose almost immediately from zero to a mean of  $\sim 1.12$  at room temperature,  $\sim 1.38$  at  $270^{\circ}\text{C}$  and  $510^{\circ}\text{C}$  and  $\sim 1.13$  at  $750^{\circ}\text{C}$ , with considerable sample-to-sample variation (up to  $\sim 20\%$ ).

However, a clear downward trend was observed with temperature for the steady state data – the friction values for  $0.314\text{ m.s}^{-1}$  decreased from between 0.81 and 0.875 at room temperature to  $\sim 0.6$  at  $270$  and  $510^{\circ}\text{C}$ , reaching a minimum at  $630^{\circ}\text{C}$  of between 0.42 and 0.5, before rising back to between 0.55 and 0.66 at  $750^{\circ}\text{C}$ . The level of variation in the coefficient of friction data remained fairly low at  $0.314\text{ m.s}^{-1}$ , being no more than 8 to 10% at all temperatures.

***c) Weight change and wear rate data at  $0.905\text{ m.s}^{-1}$  / 4,522 m***

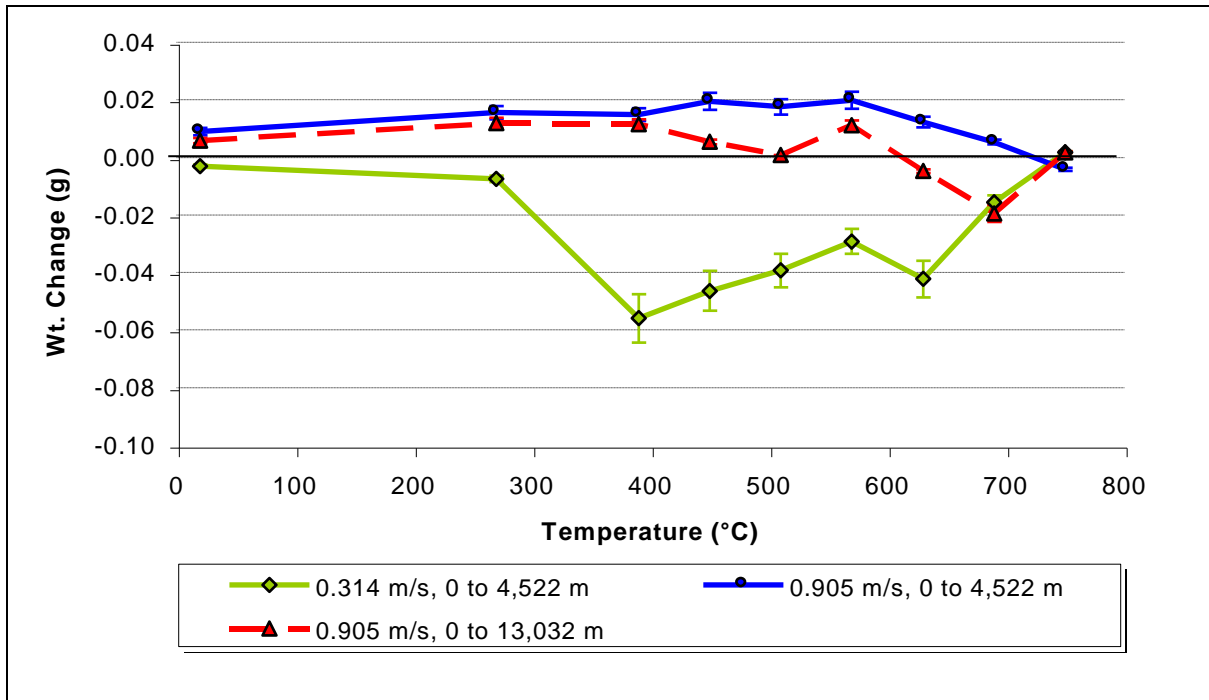
At  $0.905\text{ m.s}^{-1}$  / 4,522 m, there was evidence of small weight gains for the Nimonic 80A across almost the entire range of test temperatures (room temperature to  $750^{\circ}\text{C}$ ), starting at  $0.009(0)\text{ g}$  at room temperature and rising to maximum values of  $0.019(6)\text{ g}$  at  $450^{\circ}\text{C}$  and  $0.019(9)\text{ g}$  at  $570^{\circ}\text{C}$ . ‘Negative’ wear rates were obtained as a result of these weight gains, with typical values of  $-1.988\text{ }\mu\text{g.m}^{-1}$  at room temperature,  $-3.438\text{ }\mu\text{g.m}^{-1}$  at  $270^{\circ}\text{C}$ ,  $-4.324\text{ }\mu\text{g.m}^{-1}$  at  $450^{\circ}\text{C}$  and  $-4.397\text{ }\mu\text{g.m}^{-1}$  at  $570^{\circ}\text{C}$ . Above  $570^{\circ}\text{C}$ , there was a decrease in weight gain, with a small loss being recorded at  $750^{\circ}\text{C}$  – the weight change at this temperature was  $-0.004(1)\text{ g}$  with an accompanying positive wear rate of  $0.924\text{ }\mu\text{g.m}^{-1}$ .

These results in general indicate a build-up of material on the surface of the Nimonic 80A during sliding at  $0.905\text{ m.s}^{-1}$  up to 4,522 m, most particularly at  $450^{\circ}\text{C}$  and  $570^{\circ}\text{C}$ .

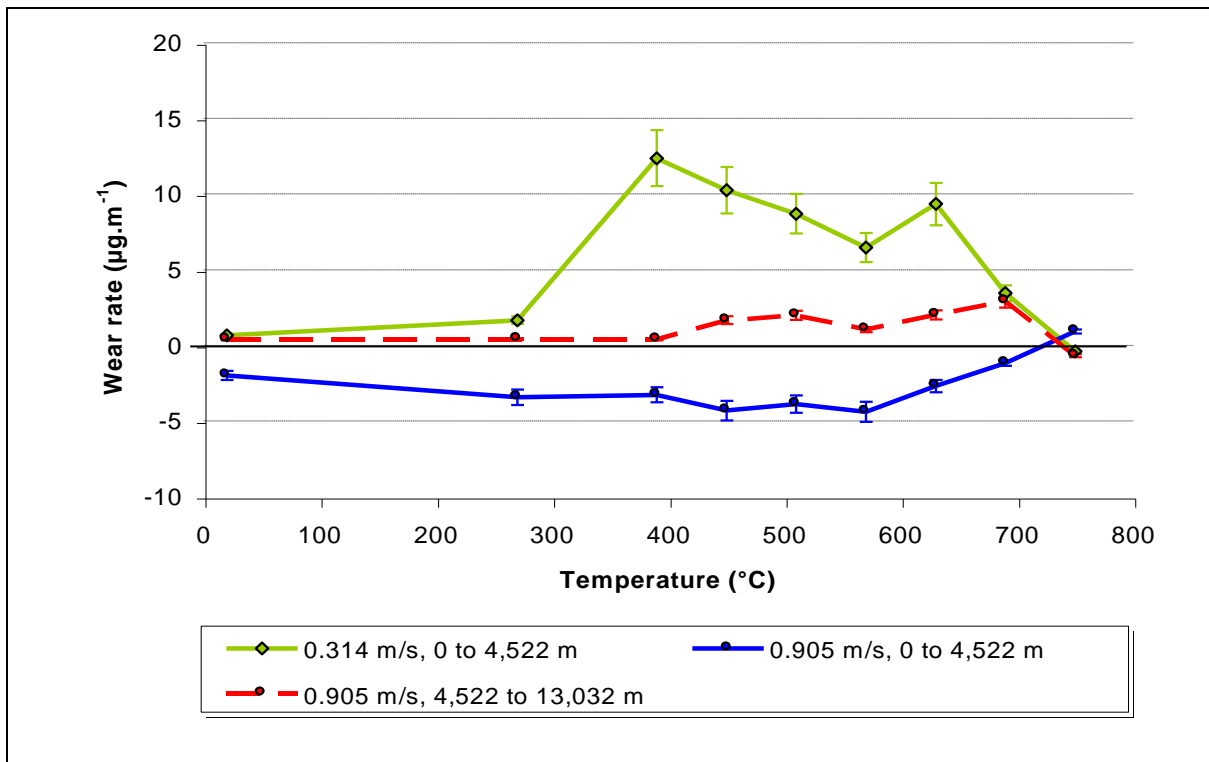
**Figure 5.55: Effect of temperature on weight change and wear rate – Nimonic 80A versus Incoloy 800HT**

(load = 7N, sample size = 3)

(a) Temperature versus weight change



(b) Temperature versus wear rate

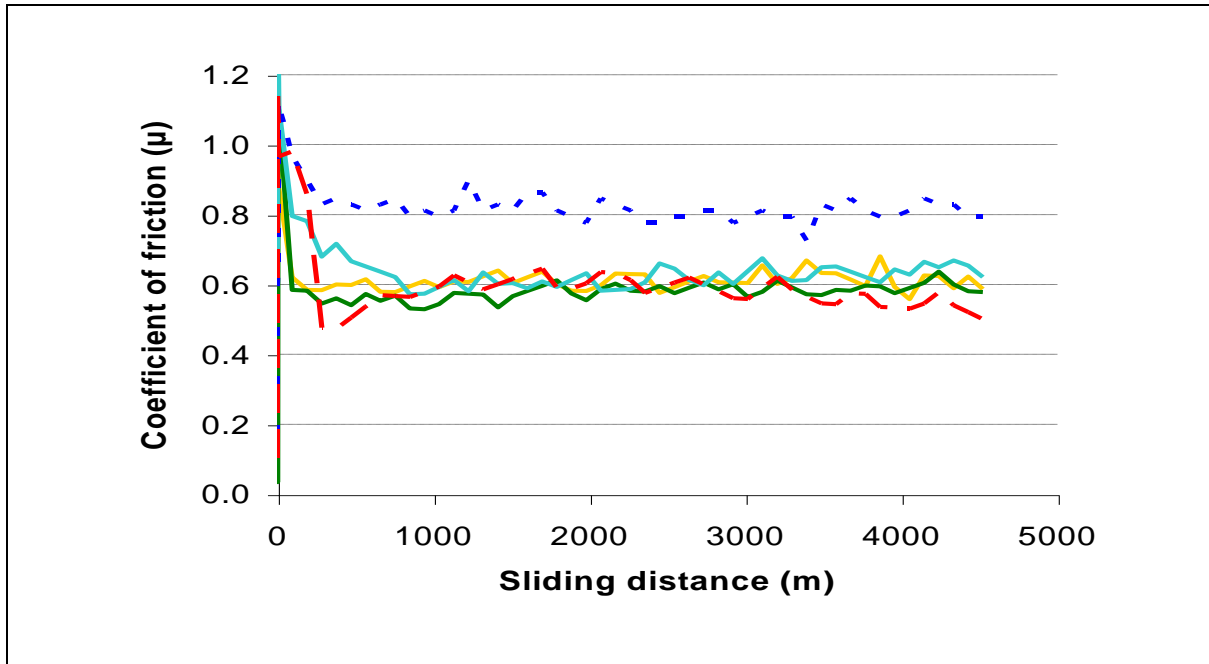


**Figure 5.56: Temperature versus coefficient of friction for Nimonic 80A versus Incoloy 800HT**

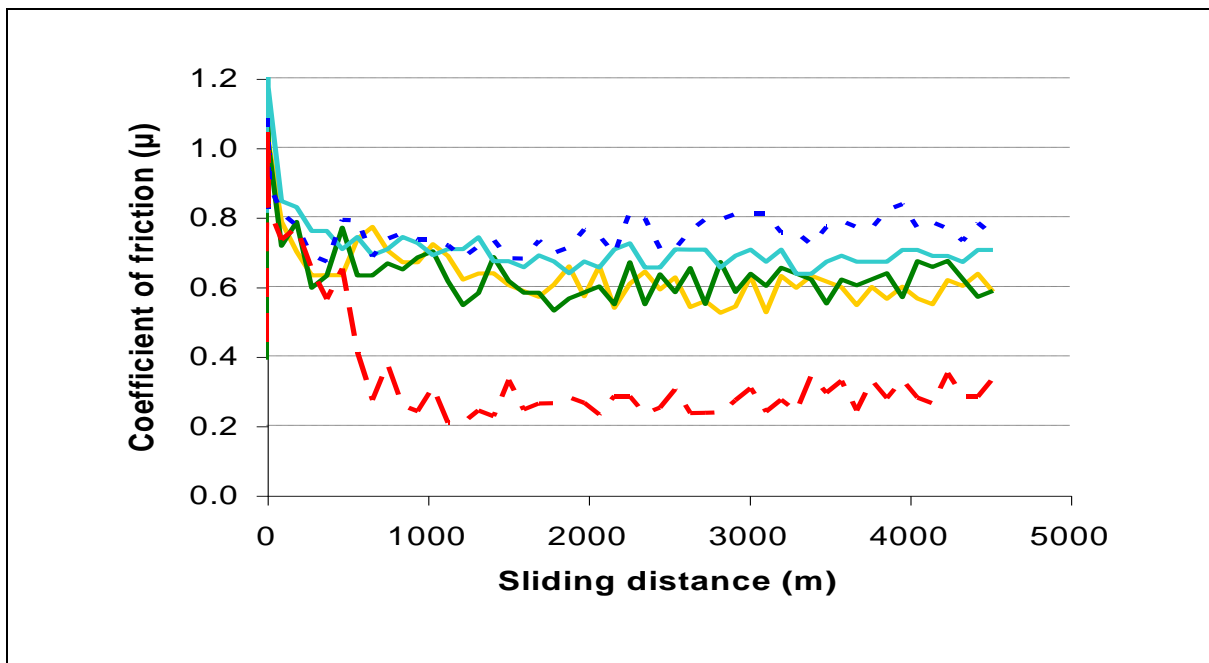
(load = 7N, sample size = 3)

Room temp. 270°C 450°C 510°C 750°C

(a)  $0.314 \text{ m.s}^{-1} / 4,522 \text{ m}$



(b)  $0.905 \text{ m.s}^{-1} / 13,032 \text{ m}$



***d) Weight change and wear rate data at 0.905 m.s<sup>-1</sup>/ 13,032 m***

Continued sliding up to 13,032 m at 0.905 m.s<sup>-1</sup> resulted in some weight losses from the Nimonic 80A, after initial recorded weight gains across almost the entire range of test temperatures (room temperature to 750°C) after 4,522 m of sliding. At room temperature, the weight gain after 13,032 m was 0.005(8) g, compared to 0.009(0) g after 4,522 m (there was thus a negative weight change – a loss in weight – between 4,522 and 13,032 m of -0.003(2) g). The highest values of weight change were recorded at 0.012(0) g after 13,032 m at 270°C (compared to 0.015(6) g after 4,522 m, representing a weight change between 4,522 and 13,032 m of -0.003(6) g) and 0.011(2) g at 570°C (compared to 0.020(9) g after 4,522 m, the weight change between 4,522 and 13,032 m being -0.009(7) g).

The most noticeable reductions in weight change at 0.905 m.s<sup>-1</sup> were at 510°C, 630°C and 690°C – at 510°C, recorded mean weight change values were 0.017(6) g after 4,522 m, dropping to 0.000(7) g after 13,032 m (a weight change between 4,522 and 13,302 m of -0.016(9) g). At 630°C, the shift was so great that negative weight change values (indicating a loss) were obtained after 13,032 m – the shift in weight change values was from 0.012(2) g after 4,522 m of sliding to -0.004(8) g after 13,032 m (a weight change between 4,522 and 13,302 m of -0.029(1) g). There was also a shift from positive values to negative values at 690°C, from 0.005(3) g after 4,522 m to -0.019(5) g after 13,032 m (a weight change between 4,522 and 13,302 m of -0.024(8) g).

750°C once again proved to be an exception to the rule, with a shift from weight loss to weight gain with increased sliding distance – recorded weight change values were -0.004(1) g after 4,522 m, compared to 0.001(8) g after 13,032 m (giving a now positive weight change between 4,522 and 13,302 m of 0.028(9) g).

These slight losses between 4,522 m and 13,032 m after the initial weight gains in the first 4,522 m, were reflected in the wear rates between 4,522 and 13,032 m, which because of these losses once again became positive. For example, at room temperature, the wear rate between 4,522 and 13,032 m was calculated as being 0.375 µg.m<sup>-1</sup> compared to -1.988 µg.m<sup>-1</sup> between 0 and 4,522m. At 270°C, wear rates of 0.421 µg.m<sup>-1</sup> (4,522 m to 13,032 m) compared to -3.438 µg.m<sup>-1</sup> (0 to 4,522 m) were obtained. At 450°C, the wear

rates were calculated at  $1.659 \mu\text{g.m}^{-1}$  (4,522 to 13,032 m) compared to  $-4.324 \mu\text{g.m}^{-1}$  (0 to 4,522 m). However, the very low wear rates indicate that these later losses were extremely limited.

At  $630^{\circ}\text{C}$  and above, the difference in wear rates began to decrease. Wear rates at  $630^{\circ}\text{C}$  of  $1.997 \mu\text{g.m}^{-1}$  (4,522 to 13,032 m), compared to  $-2.702 \mu\text{g.m}^{-1}$  (0 to 4,522 m). Convergence of the two values occurred at  $750^{\circ}\text{C}$ , with a small negative value for wear rate between 4,522 and 13,032 m of  $-0.697 \mu\text{g.m}^{-1}$ , compared to a small positive wear rate of  $0.924 \mu\text{g.m}^{-1}$  between 0 and 4,522 m (a switch to ‘loss then gain’ rather than ‘gain then loss’ as observed at other temperatures).

***e) Coefficient of friction data at  $0.905 \text{ m.s}^{-1}$***

The coefficient of friction data at  $0.905 \text{ m.s}^{-1}$  clearly showed two stages of behaviour (Figure 5.56b), an unsettled ‘run-in’ period followed by a more settled ‘steady state’ period, regardless of temperature. During the unsettled ‘run-in’ period, there was no clear trend with increasing temperature – friction values rose from zero to 1.08 at room temperature, 1.22 at  $270^{\circ}\text{C}$ , 1.33 at  $510^{\circ}\text{C}$  and 1.04 at  $750^{\circ}\text{C}$  with considerable sample-to-sample variation (~20%).

However, during the more settled ‘steady state’ sliding, friction values at  $0.905 \text{ m.s}^{-1}$  for the Nimonic 80A / Incoloy 800HT system, showed a clear downward trend with increasing temperature – values varied between 0.68 and 0.83 at room temperature, 0.65 and 0.74 at  $270^{\circ}\text{C}$ , 0.52 and 0.65 at  $510^{\circ}\text{C}$ , and 0.20 and 0.35 at  $750^{\circ}\text{C}$  (coinciding with the formation of glaze at this temperature). Variation can be said to increase with temperature, being no more than around 10% at room temperature and  $270^{\circ}\text{C}$ , rising to 25% at  $510^{\circ}\text{C}$  and  $750^{\circ}\text{C}$ . That said, the higher estimates of variation may be attributed to the very low recorded levels of friction at higher temperatures, especially the extremely low values at  $750^{\circ}\text{C}$ .

The variation in friction appeared to be higher for  $0.905 \text{ m.s}^{-1}$  than for  $0.314 \text{ m.s}^{-1}$ , however, as with other test combinations, this can be put down to the higher levels of vibration reducing contact time between sample and counterface at the higher sliding speed. For this reason, the true values of friction may actually be much higher for  $0.905 \text{ m.s}^{-1}$ .



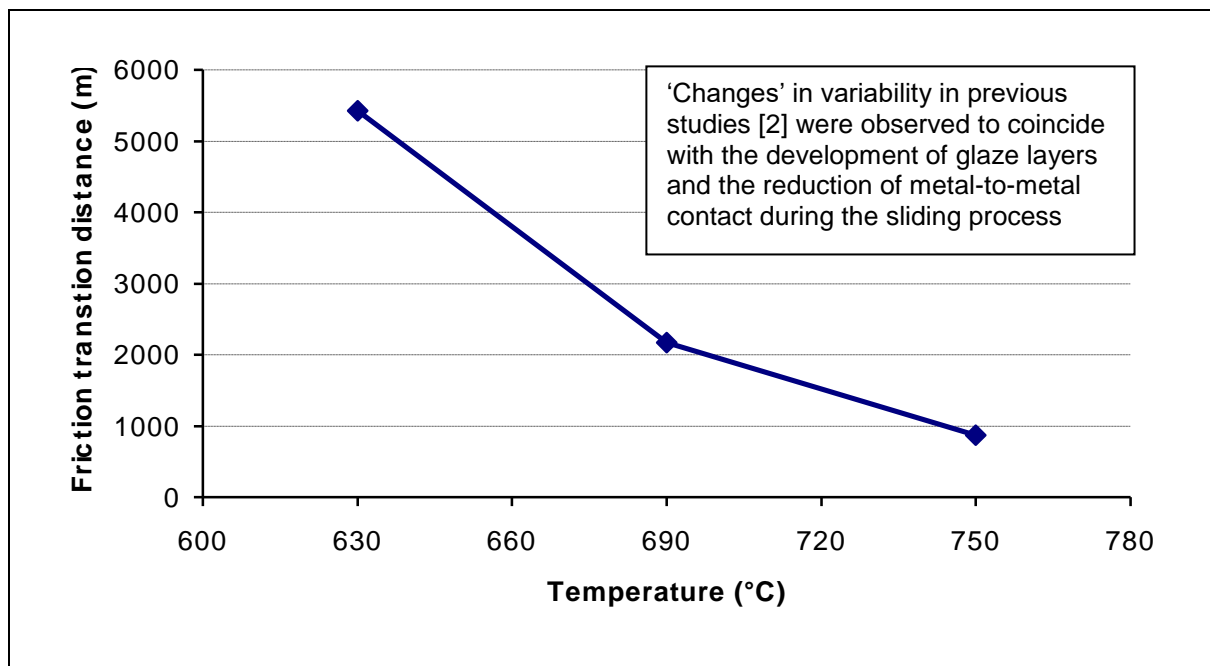
At  $0.905 \text{ m.s}^{-1}$ , particularly large drops in friction (from greater than 1 to between typically 0.3 and 0.5) were observed at the end of the ‘run-in’ period and the beginning of ‘steady state’ sliding at  $630^\circ\text{C}$ ,  $690^\circ\text{C}$  and  $750^\circ\text{C}$ . Such observations have been attributed to the onset of mild oxidational wear and the formation of glaze layers [2]. The time to this transition decreased with temperature (Figure 5.57):

- 100 minutes (5,430 m) at  $630^\circ\text{C}$ ;
- 40 minutes (2,172 m) at  $690^\circ\text{C}$  and;
- 16 minutes (869 m) at  $750^\circ\text{C}$ .

Such a pattern was not observed at  $0.314 \text{ m.s}^{-1}$ .

**Figure 5.57: Distance to transition in coefficient of friction from high variability (severe wear) to low variability (mild wear) at  $630^\circ\text{C}$ ,  $690^\circ\text{C}$  and  $750^\circ\text{C}$  – Nimonic 80A versus Incoloy 800HT at  $0.905 \text{ m.s}^{-1}$**

(load = 7N, sample size = 3)



#### 5.4.2 Optical and SEM Morphology – Nimonic 80A versus Incoloy 800HT

Optical (Figure 5.58) and SEM (Figure 5.60) examinations showed evidence of severe wear (wear surfaces were bright, metallic and highly damaged) at  $0.314 \text{ m.s}^{-1}$  with high levels of metal transfer at room temperature and  $270^\circ\text{C}$ . Transfer layers were formed on





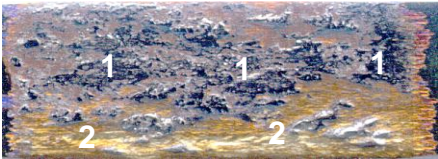
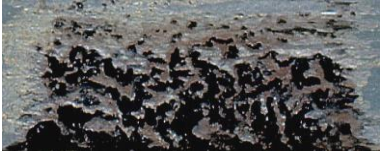
the wear surfaces of the Nimonic 80A as a result (Figure 5.58). SEM micrographs of debris generated at both room temperature and 270°C (Figure 5.60) show the debris particles to be flat, metallic, irregular in shape and platelet-like in nature, suggesting a delamination mechanism was in operation. These debris were in general of size between 20  $\mu\text{m}$  and 1 mm across.

The presence of transferred metal at 0.314  $\text{m.s}^{-1}$  became much reduced at higher temperatures, with only a few patches of transferred material present between 390°C and 570°C on a largely exposed wear scar (Figure 5.58 – Figure 5.60a also shows the wear surface at 510°C under SEM). This decrease in transfer coincided with increasing surface oxidation of the Nimonic 80A wear scar, visible as discolouration at 390°C and 510°C (Figure 5.58), as the sliding temperature was increased at 390°C and above (note that this oxide did not form into compacted oxide layers).








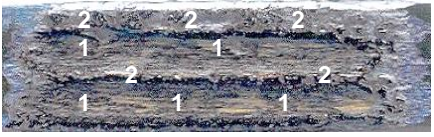
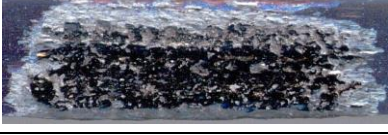

The first traces of glaze at 0.314  $\text{m.s}^{-1}$  appeared at 570°C, however, significant development of glaze layers only occurred at 630°C and above (coinciding with decreasing levels of wear – Figure 5.55). A transferred layer of metal did reappear in these cases (630°C and above), with the glaze overlying the transferred metal. There was still a substantial portion of debris that was flat, metallic, platelet-like and of irregular shape (indicative of delamination wear – debris size remained in the range 20  $\mu\text{m}$  and 1 mm), but this was accompanied by increasing levels of oxide debris from 570°C upwards. This oxide debris was very fine in nature, being of size less than 1  $\mu\text{m}$  and in some cases less than 300 nm – the oxide debris was just noticeable on the surfaces of the larger metallic debris at 750°C (Figure 5.61a).

At 0.905  $\text{m.s}^{-1}$ , a transferred metal layer was clearly visible at all test temperatures from room temperature to 630°C, with comprehensive coverage of the wear scar by this layer regardless of the sliding temperature. The presence of surface oxidation (most visible as discolouration on the wear scar surfaces at 390°C and above) did not apparently affect metallic transfer at 0.905  $\text{m.s}^{-1}$ .

**Figure 5.58: Optical images for Nimonic 80A versus Incoloy 800HT at 0.314 m.s<sup>-1</sup>**

	<p><b>Room Temperature, 4,522 m</b>  <i>(wear scar = 15 mm)</i>  Metallic transfer layer covering 90% of wear scar</p>
	<p><b>270°C, 4,522 m</b>  <i>(wear scar = 17 mm)</i>  Metallic transfer layer covering 80% of wear scar</p>
	<p><b>390°C, 4,522 m</b>  <i>(wear scar = 18 mm, also 450°C)</i>  Reduced transfer (35% coverage), now in more isolated patches, with very slight discolouration due to oxidation</p>
	<p><b>510°C, 4,522 m</b>  <i>(wear scar = 18 mm)</i>  Reduced transfer (15% coverage) in more isolated patches, increased discolouration due to oxidation</p>
	<p><b>570°C, 4,522 m</b>  <i>(wear scar = 19 mm)</i>  Patchy glaze formation (1) on asperities, a few isolated areas of transferred material (2)</p>
	<p><b>750°C, 4,522 m</b>  <i>(wear scar = 14 mm, also 630°C, 690°C)</i>  Glaze layer overlying a limited amount of transferred material</p>

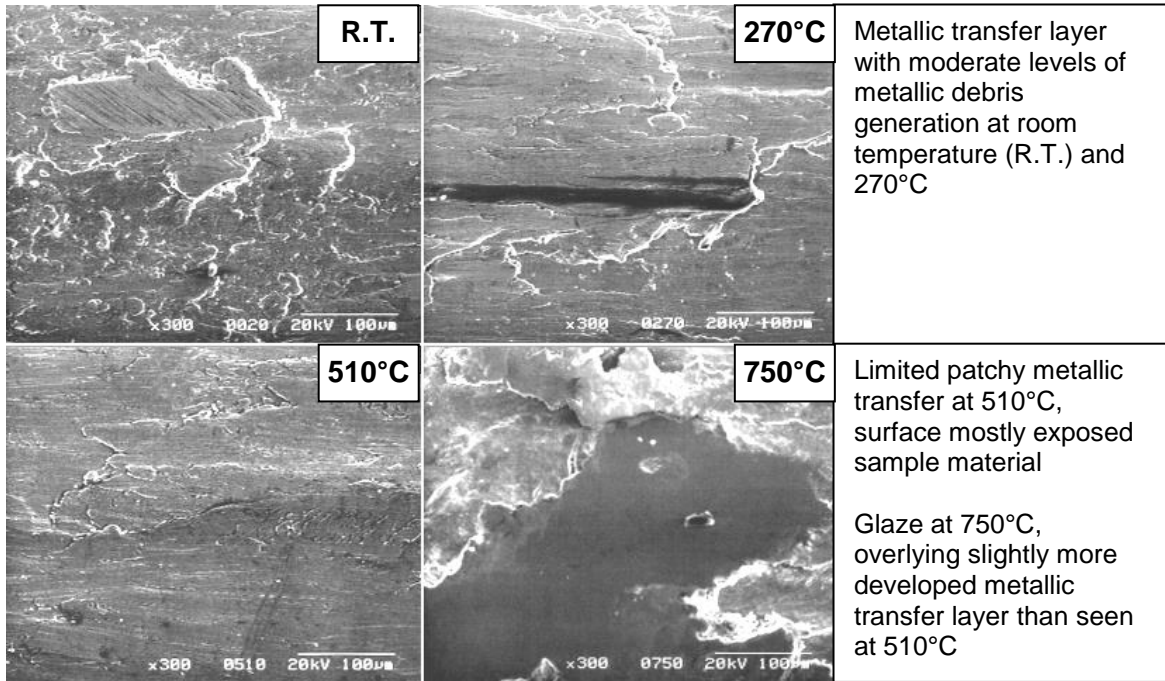
**Figure 5.59: Optical Images for Nimonic 80A versus Incoloy 800HT at 0.905 m.s<sup>-1</sup>**  
*(Observations after 13,032 m of sliding follow same pattern as 4,522 m where not shown)*

	<b>Room Temperature, 4,522 m</b> <i>(wear scar = 15 mm, also 270°C)</i> Metallic transfer layer covering 90% of wear scar
	<b>390°C, 4,522 m</b> <i>(wear scar = 18 mm)</i> Metallic transfer layer similar to room temperature – surface oxidation not inhibiting transfer
	<b>390°C, 13,032 m</b> <i>(wear scar = 18 mm)</i> Extra sliding has not led to significant removal of transfer layer
	<b>510°C, 4,522 m</b> <i>(wear scar = 18 mm)</i> Metallic transfer layer similar to room temperature – surface oxidation not inhibiting transfer
	<b>510°C, 13,032 m</b> <i>(wear scar = 18 mm)</i> Extra sliding has not led to significant removal of transfer layer
	<b>570°C, 4,522 m</b> <i>(wear scar = 18 mm)</i> Metallic transfer layer similar to room temperature – surface oxidation not inhibiting transfer – no glaze
	<b>630°C, 4,522 m</b> <i>(wear scar = 17 mm)</i> Metallic transfer layer (exposed areas in troughs on surface – '1') with some patchy glaze formation (2).
	<b>630°C, 13,032 m</b> <i>(wear scar = 17 mm)</i> Metallic transfer layer (exposed areas in troughs on surface – '1') with enhanced glaze formation (2).
	<b>750°C, 4,522 m</b> <i>(wear scar = 14 mm, applicable also to 690 °C)</i> Glaze layer overlying transferred material
	<b>750°C, 13,032 m</b> <i>(wear scar = 14 mm, applicable also to 690 °C)</i> No change in morphology after extra sliding

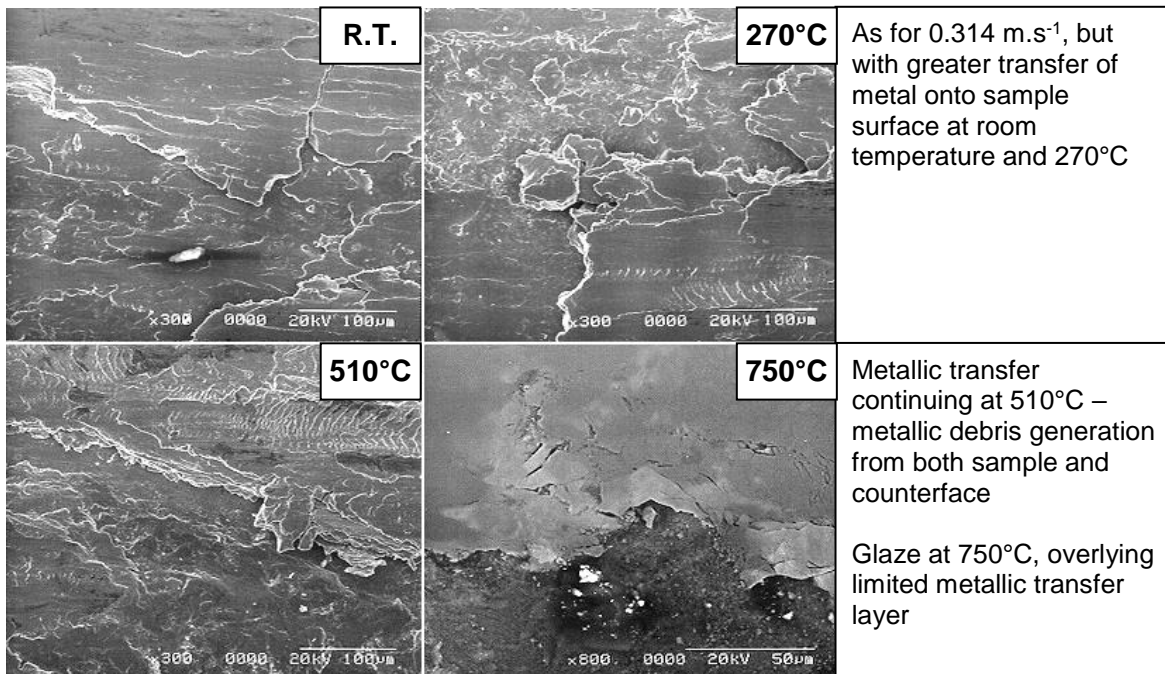


**Figure 5.60: SEM micrographs for Nimonic 80A versus Incoloy 800HT – wear surface**

(a)  $0.314 \text{ m.s}^{-1} / 4,522 \text{ m}$  – room temperature,  $270^\circ\text{C}$ ,  $510^\circ\text{C}$  and  $750^\circ\text{C}$



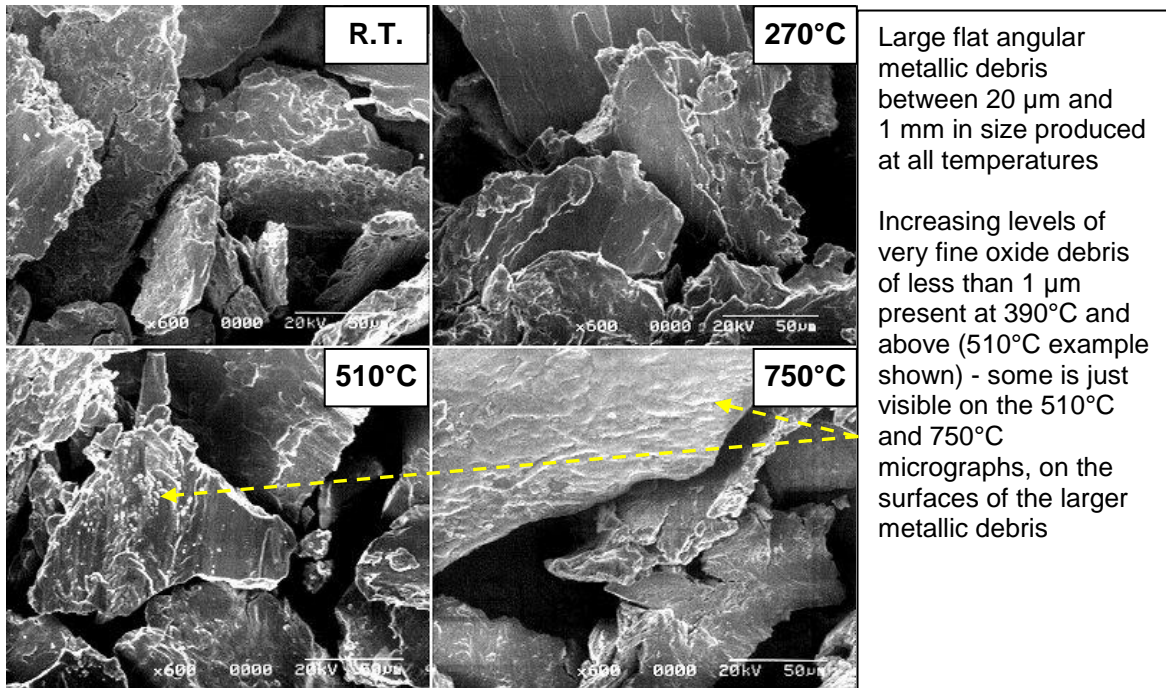
(b)  $0.905 \text{ m.s}^{-1} / 4,522 \text{ m}$  – room temperature,  $270^\circ\text{C}$ ,  $510^\circ\text{C}$  and  $750^\circ\text{C}$



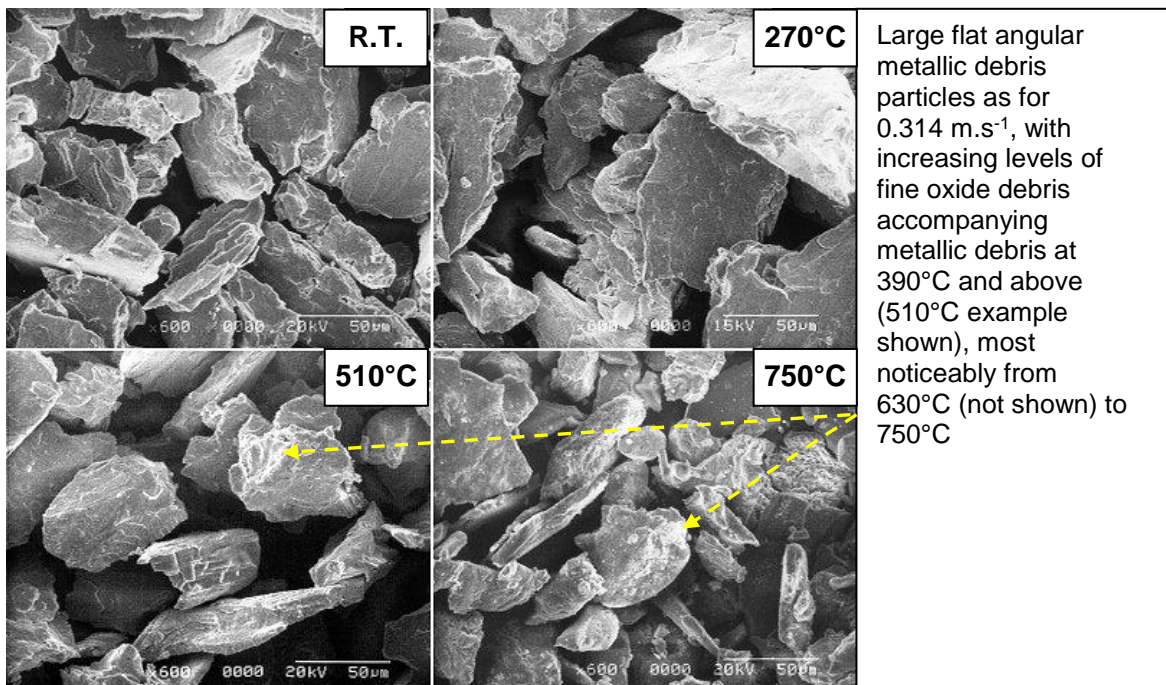
Same pattern of results observed after 13,032 m of sliding at  $0.905 \text{ m.s}^{-1}$

**Figure 5.61: SEM micrographs for Nimonic 80A versus Incoloy 800HT – debris**

(a)  $0.314 \text{ m.s}^{-1} / 4,522 \text{ m}$  – room temperature,  $270^\circ\text{C}$ ,  $510^\circ\text{C}$  and  $750^\circ\text{C}$






(b)  $0.905 \text{ m.s}^{-1} / 4,522 \text{ m}$



Same pattern of observations made after  $13,032 \text{ m}$  of sliding at  $0.905 \text{ m.s}^{-1}$






**Figure 5.62: Counterface wear scar optical images – Nimonic 80A / Incoloy 800HT, 0.314 m.s<sup>-1</sup>**

	<b>Room Temperature, 4,522 m</b> <i>(section = 16 mm, representative up to 510°C)</i> Highly worn wear scar with limited metallic transfer
	<b>630°C, 4,522 m</b> <i>(section = 16 mm)</i> Back transferred asperities in deeply grooved wear scar, with glaze on asperity peaks only
	<b>750°C, 4,522 m</b> <i>(section = 16 mm, applicable also to 690°C)</i> Back transferred asperities in deeply grooved wear scar, with glaze on asperity peaks only

**Figure 5.63: Counterface wear scar optical images – Nimonic 80A / Incoloy 800HT, 0.905 m.s<sup>-1</sup>**

*(Observations after 13,032 m of sliding follow same pattern as 4,522 m)*

	<b>Room Temperature, 4,522 m</b> <i>(section = 16 mm, representative up to 570°C)</i> Highly worn wear scar with limited metallic transfer
	<b>630°C, 4,522 m</b> <i>(section = 16 mm)</i> Back transferred asperities in deeply grooved wear scar, with glaze on asperity peaks only
	<b>750°C, 4,522 m</b> <i>(section = 16 mm, applicable also to 690 °C)</i> Back transferred asperities in deeply grooved wear scar, with glaze on asperity peaks only



Metallic debris production up to 630°C, again flat, platelet-like and of size between 20 µm and 1 mm (again typical of delamination wear), was at 0.905 m.s<sup>-1</sup> not at a significantly different level to that observed at 0.314 m.s<sup>-1</sup>. Only trace amounts of oxide debris were observed amongst the metallic debris and then only at 390°C and above, coinciding with increasing wear scar discoloration at these higher temperatures.

At 630°C and above, a glaze layer was once again observed to be overlying the transferred metal layer at 0.905 m.s<sup>-1</sup> (Figure 5.59). At 630°C, there was only limited glaze formation after 4,522 m, with more substantial glaze layers developing only after 13,032 m of sliding. At 690°C and especially 750°C (Figures 5.59 and 5.60b), comprehensive glaze layer development was observed after only 4,522 m of sliding. Oxide debris production was observed to increase also – the pattern of metallic debris with increasing oxide debris seen at 0.314 m.s<sup>-1</sup> was once again observed at 0.905 m.s<sup>-1</sup> with increasing temperature between 630°C and 750°C. As these glaze layers developed, the level of metallic transfer was observed to slightly decrease, particularly at 750°C.

#### ***5.4.2.1 Incoloy 800HT Counterface Wear Scar Morphology***

A grooved, worn surface was observed on the Incoloy 800HT counterface wear scar at all temperatures between room temperature and 750°C, regardless of whether the sliding speed was 0.314 m.s<sup>-1</sup> or 0.905 m.s<sup>-1</sup> (Figures 5.62 and 5.63). Between room temperature and 450°C, the counterface underwent a high level of wear with limited transfer layers forming on the resulting wear scar - the presence of these transfer layers indicated transfer and back-transfer of metallic material between the Nimonic 80A sample and the Incoloy 800HT counterface. The appearance of discoloration on the wear scar surfaces due to limited oxidation at 390°C and 450°C, coincided with a reduction in the development of these transfer layers.

At 510°C and above, discrete asperities of metallic material began to appear in the counterface wear track (the depth of which was sometimes up to 1.5 mm into the counterface surface), the quantity of which increased with temperature. The height of these asperities was sometimes as great as 1.5 mm above the level of the original counterface surface between 630°C and 750°C – a slightly lower concentration of asperities was observed at 0.905 m.s<sup>-1</sup>. Glaze formation was observed on the peaks of these

asperities at 570°C or greater at 0.314 m.s<sup>-1</sup> and 630°C or greater at 0.905 m.s<sup>-1</sup> – these temperatures matched those where glaze first appeared on the Nimonic 80A.

Large quantities of easily dislodged loose oxide debris were observed lying in the trough of Incoloy 800HT counterface wear track at temperatures of 570°C or greater at 0.314 m.s<sup>-1</sup> and 630°C or greater at 0.905 m.s<sup>-1</sup>, coinciding with glaze formation on the asperity peaks.

#### **5.4.3 EDX Analysis – Nimonic 80A versus Incoloy 800HT**

The EDX data obtained for the 0.314 m.s<sup>-1</sup> samples varied depending on whether or not a transferred layer of metal was present on the surface. At room temperature, the composition of the surface layers closely matched that of the Incoloy 800HT counterface (average figures of ~44% iron, ~30% nickel, ~23% chromium), with only minimal changes in composition at 270°C (~41% Fe, ~30% Ni, ~24% Cr). There was no clear evidence of any mixing, with debris compositions also matching that of Incoloy 800HT.

Between 390°C and 570°C, only the limited areas of transferred materials formed at 0.314 m.s<sup>-1</sup> gave compositions different from the mostly exposed and highly worn Nimonic 80A substrate. For example at 510°C, exposed areas of substrate gave compositions averaging 51% nickel, 29% chromium and 13% iron, compared to 40% iron, 29% nickel and 25% chromium for the transferred patches of metallic material. The composition of these transferred patches was closer to that of the Incoloy 800HT than the Nimonic 80A, indicating only a small amount of mixing.

Those samples worn at 630°C and above (sliding speed 0.314 m.s<sup>-1</sup>), where glaze formed overlying a limited transferred metallic layer, gave values for the glaze once again typical of the Incoloy 800HT counterface (42% Fe, 31% Cr, 23% Ni). Exposed areas of metallic transfer layer gave a composition intermediate between the Nimonic 80A and the Incoloy 800HT (~20% Fe, ~34% Cr and ~32% Ni).

The composition of the accompanying metallic debris formed during sliding at 0.314 m.s<sup>-1</sup> was more variable, with some debris matching that of the Incoloy 800HT counterface (which remained the main source of material) and some of a more intermediate composition between the two materials, depending on the debris particle or particles chosen

for analysis. Metallic debris composition was most variable (and most likely to be of intermediate composition between that of Nimonic 80A and Incoloy 800HT) at mid-range temperatures (390°C, 450°C and 510°C), where transfer layers on the sample were incomplete (nickel levels varied between ~23% and ~51% and iron levels varied between ~14% and 41% – chromium levels remained at around ~28%) – the same applied to the trace amounts of oxide debris produced at these temperatures. The composition of the increasing proportions of oxide debris present from 570°C upward closely matched that of the Incoloy 800HT (~40% Fe, ~30% Cr, ~25% Ni).

At 0.905 m.s<sup>-1</sup> / 4,522 m, where metal transfer was physically observed at all temperatures (room temperature to 750°C), compositions of the transfer layers continued to closely match the composition of Incoloy 800HT, with iron levels of between 37 and 41%, nickel levels rising slightly from 23 to 28%, and chromium levels dropping slightly from 32 to 26%. The glaze layers formed at 690°C and 750°C were of very similar composition to the Incoloy 800HT sourced-transfer layers they overlay on the Nimonic 80A sample.

Increasing the sliding distance up to 13,032 m (at 0.905 m.s<sup>-1</sup>) resulted in a more mixed metallic transfer layer composition at all temperatures, on average typically 35% nickel, 29% chromium and 30% iron (with 2 to 3% variation). The only exception to this was at 750°C, where the composition of the glaze and the transfer layer (both ~41% iron, ~31% chromium, ~23% nickel) matched that of the Incoloy 800HT counterface. The metallic debris composition was very close to that of the Incoloy 800HT, although once again some debris particles did show a higher level of nickel (up to ~35%), indicating a contribution from the Nimonic 80A – as at 0.314 m.s<sup>-1</sup>, the same applied to the trace amounts of oxide debris up to 570°C. The composition of the loose oxide debris present from 630°C upward, matched that of the Incoloy 800HT counterface material (~42% Fe, ~31% Cr, ~24% Ni).

The composition of the glaze layers formed upon the asperities within the Incoloy 800HT counterface wear track at 750°C (the glaze was removed for analysis), were similar to those of the glaze layers formed on the Nimonic 80A as a sample – the compositions indicated were not too dissimilar to that of the Incoloy 800HT, regardless of the sliding speed used. For samples slid at 0.314 m.s<sup>-1</sup>, a mean composition of ~29% nickel, 23% chromium and

45% iron was obtained. For samples slid at  $0.905 \text{ m.s}^{-1}$  / 4,522 m, the glaze removed from the counterface was of mean composition ~24% nickel, ~30% chromium and ~41% iron – the glaze composition after 13,032 m was almost identical.

#### **5.4.4 EDX Mapping – Nimonic 80A versus Incoloy 800HT**

Figures 5.64 and 5.65 show representative EDX maps for Nimonic 80A versus Incoloy 800HT, slid at  $750^{\circ}\text{C}$  and speeds of  $0.314 \text{ m.s}^{-1}$  and  $0.905 \text{ m.s}^{-1}$  respectively (there was little variation between samples). In both cases, iron was only present to any significant concentration in the surface layers only. Nickel was present in the surface layers, but at much reduced levels compared to the Nimonic 80A substrate. The high concentration of iron and low concentration of nickel in the surface layers point towards this surface layer being sourced primarily from the Incoloy 800HT counterface.

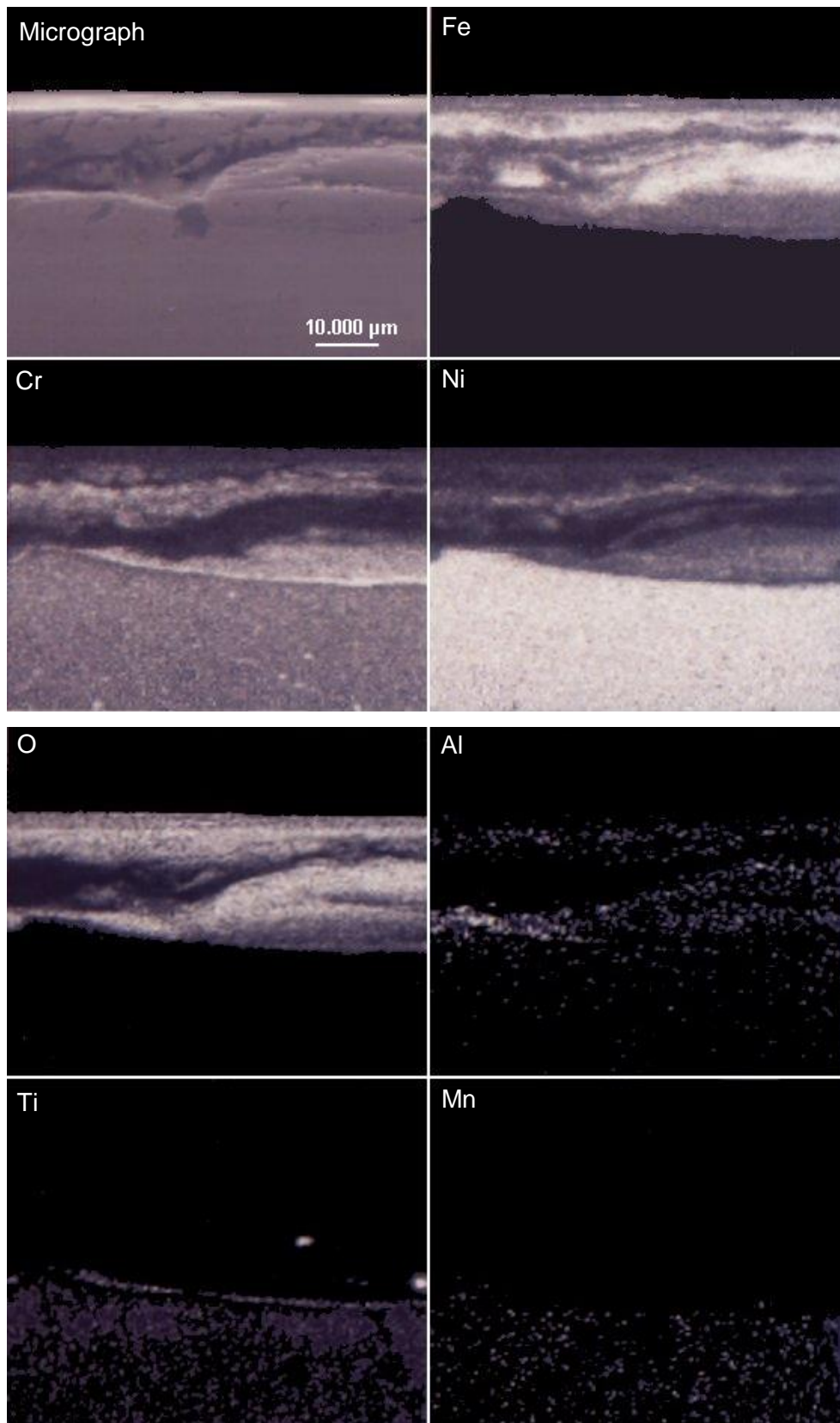
Chromium was also present in both the surface layers and the Nimonic 80A substrate. Chromium concentrations seemed to be slightly higher in some areas of the surface layers at  $0.314 \text{ m.s}^{-1}$ , indicating possible movement of chromium to the debris layer at this sliding speed. However, it was not possible to draw any conclusions about the behaviour of chromium at  $0.905 \text{ m.s}^{-1}$ , as no distinction was observed between chromium levels in the Nimonic 80A substrate and the surface layers.

Oxygen was also concentrated in this layer, however, on the  $750^{\circ}\text{C}$  sample at  $0.905 \text{ m.s}^{-1}$  there were large areas of the transferred layer which were not oxidised. This indicated that there had been a large-scale transfer of material from the Incoloy 800HT in the metallic phase, with subsequent compacted oxide generation occurring on top of this – the majority of the oxygen was concentrated above this mainly metallic layer.

A trace amount of oxygen was present at times along the interface between the transferred metal and the substrate (for example, the slight separation of the surface layer from the Nimonic 80A visible near the surface on the micrograph in Figure 5.65) on the featured  $750^{\circ}\text{C} / 0.905 \text{ m.s}^{-1}$  sample (other samples showed similar features), indicating some limited oxidation prior to this transfer during the earlier stages of wear.

**Figure 5.64: Cross-sectional EDX element maps for Nimonic 80A worn against Incoloy 800HT subsequent to wear at  $0.314 \text{ m.s}^{-1}$**

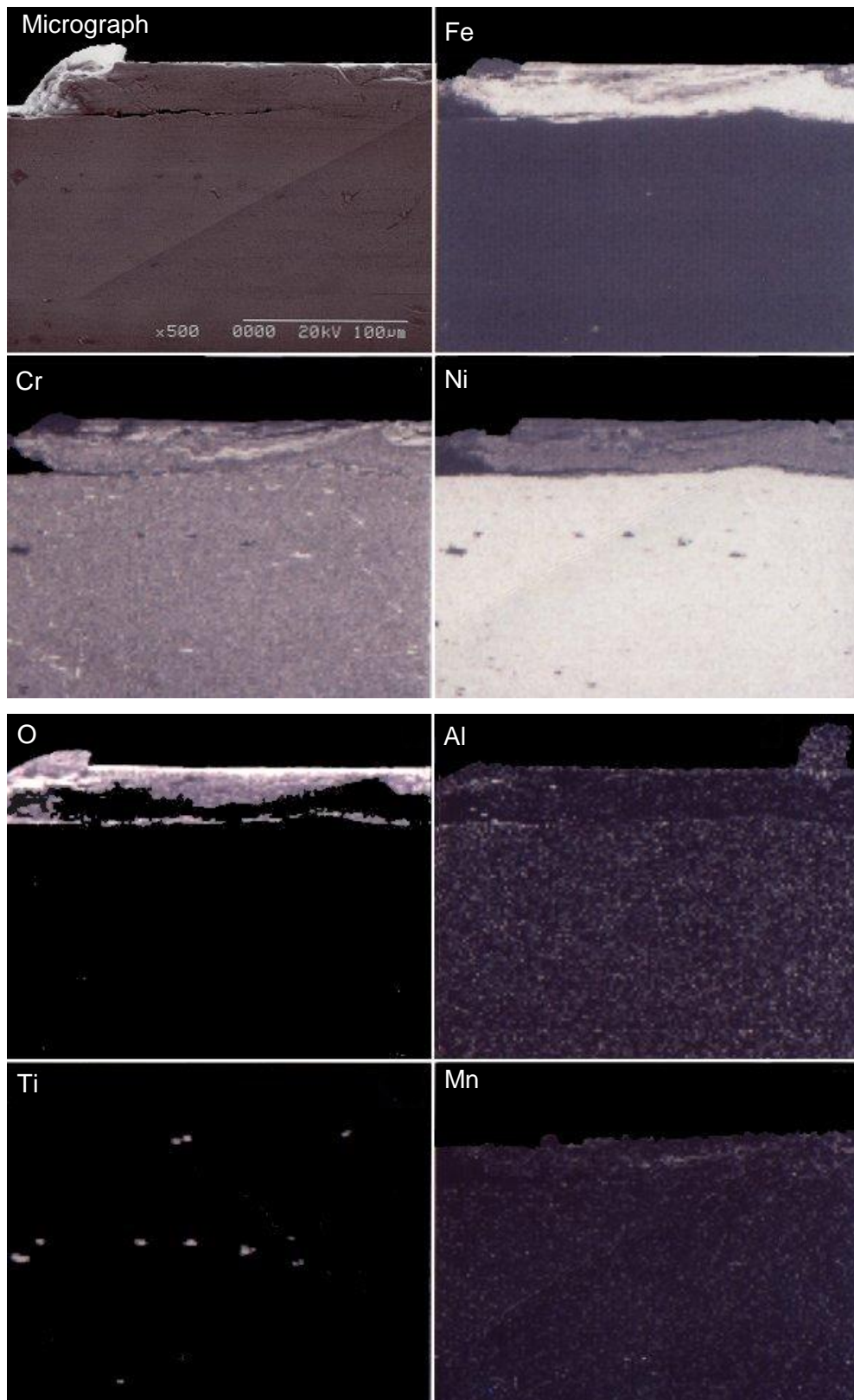
*(load = 7N, sliding distance = 4,522 m, temperature =  $750^{\circ}\text{C}$ , sample size = 3)*





**Figure 5.65: Cross-sectional EDX element maps for Nimonic 80A worn against Incoloy 800HT subsequent to wear at  $0.905 \text{ m.s}^{-1}$**

*(load = 7N, sliding distance = 4,522 m, temperature =  $750^\circ\text{C}$ , sample size = 3)*



#### 5.4.5 Autopoint EDX Analysis – Nimonic 80A versus Incoloy 800HT

Data collected by Autopoint EDX analysis, carried out on cross-sections of Nimonic 80A samples worn against Incoloy 800HT at 750°C ( $0.314 \text{ m.s}^{-1}$  / 4,522 m and  $0.905 \text{ m.s}^{-1}$  / 13,032 m), indicated proportions of nickel, chromium and iron not too far removed from Incoloy 800HT values within the  $\sim 1 \mu\text{m}$  thick glaze layer (Ni  $\sim 24\%$ , Cr  $\sim 27\%$ , Fe  $\sim 40\%$  for samples slid at  $0.314 \text{ m.s}^{-1}$  and Ni  $\sim 22\%$ , Cr  $\sim 27\%$ , Fe  $\sim 38\%$  for samples slid at  $0.905 \text{ m.s}^{-1}$ ), signifying material transfer from the Incoloy 800HT counterface (Figure 5.66 is representative of the Autopoint data obtained at both  $0.314 \text{ m.s}^{-1}$  and  $0.905 \text{ m.s}^{-1}$ , with little variation in the pattern of data obtained between samples).

At  $0.314 \text{ m.s}^{-1}$ , the glaze overlay a mixed metallic and oxide layer, with compositions intermediate between Nimonic 80A and Incoloy 800HT - this mixed layer extended to between  $32 \mu\text{m}$  and  $37 \mu\text{m}$  depth ( $34 \mu\text{m}$  in the shown example – Figure 5.66a), after which there was only Nimonic 80A substrate. Nickel levels varied between 25 and 70%, iron between 5 and 22% and chromium between 10 and 55% – the mixing within this layer was incomplete, with some areas matching the composition of the Nimonic 80A sample material and other areas of intermediate composition. For example, in the shown Autopoint EDX profile (Figure 5.66a), there is an area of material of similar composition to the Nimonic 80A ( $\sim 69\%$  Ni,  $\sim 12\%$  Cr and  $\sim 10\%$  Fe) at  $4 \mu\text{m}$  depth. An area of intermediate composition is present at  $\sim 30 \mu\text{m}$  depth ( $\sim 28\%$  Ni,  $\sim 52\%$  Cr and  $\sim 5\%$  Fe), near the bottom of the mixed layer.

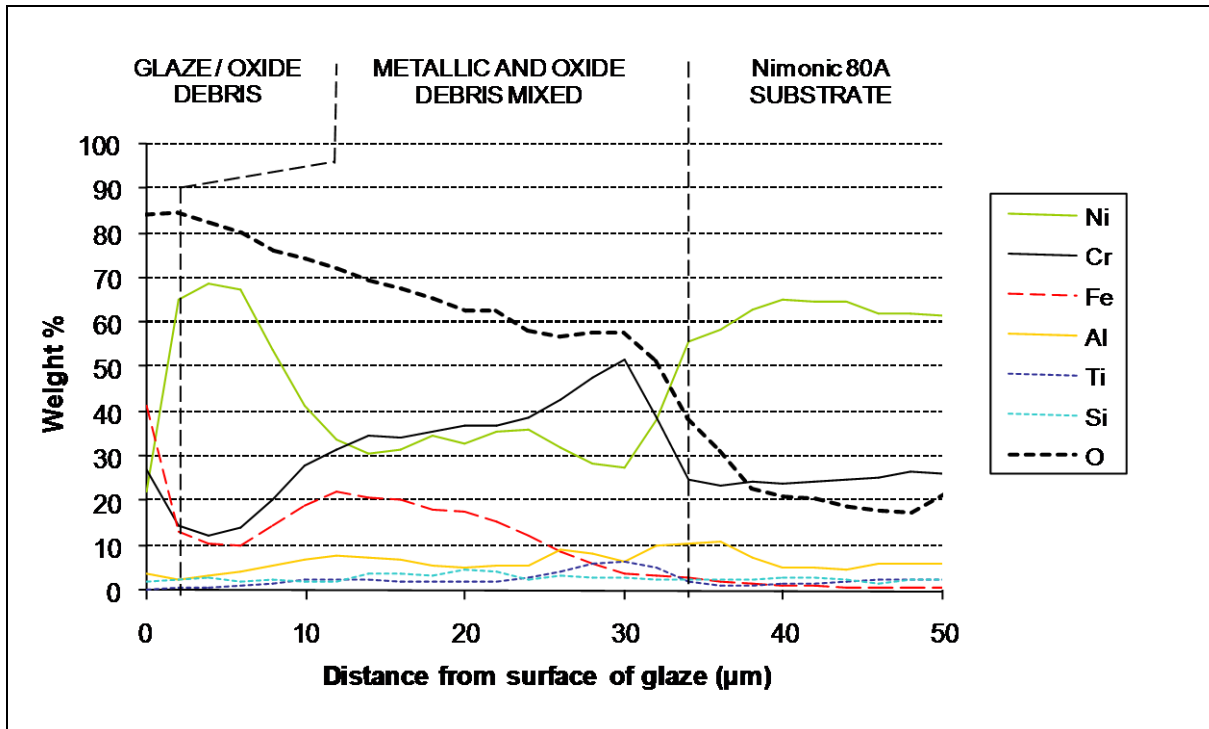
At  $0.905 \text{ m.s}^{-1}$ , the  $1 \mu\text{m}$  thick glaze layer overlay an oxide-only layer existing up to between  $10 \mu\text{m}$  to  $14 \mu\text{m}$  depth ( $14 \mu\text{m}$  in the shown example – Figure 5.66b), matching the Incoloy 800HT in composition. From here up to between  $40 \mu\text{m}$  and  $45 \mu\text{m}$  depth ( $41 \mu\text{m}$  in the given example – Figure 5.66b), there existed a mixed metal / oxide layer again in general not too far removed in composition from the Incoloy 800HT. Some variation was observed, possibly indicating some very limited mixing with the Nimonic 80A (Ni varied between 22 and 31%, Fe between 24 and 41% and Cr between 20 and 43%). Significant deviation from this and a greater contribution from the Nimonic 80A only began to occur after  $\sim 33 \mu\text{m}$  depth, with  $40 \mu\text{m}$  to  $45 \mu\text{m}$  (this varied between samples) marking the beginning of the Nimonic 80A substrate.



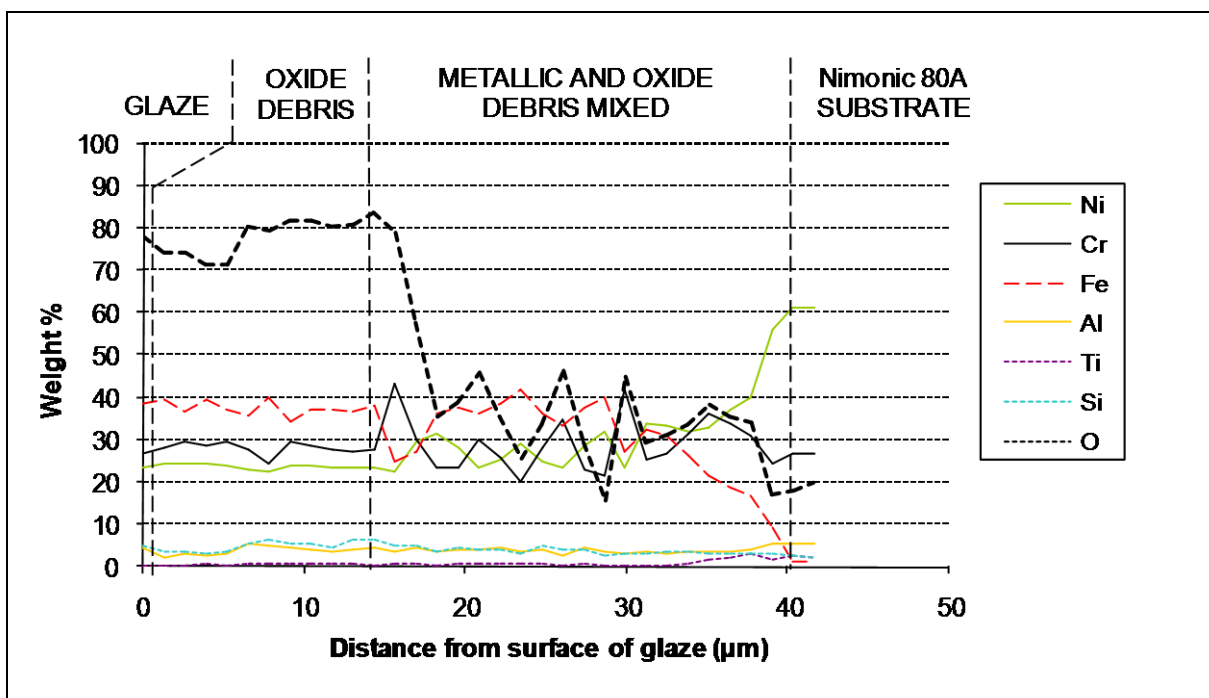
**Figure 5.66: Data from Autopoint EDX analysis for Nimonic 80A versus Incoloy 800HT at sliding speeds of 0.314 and 0.905 m.s<sup>-1</sup> and 750°C**

Amounts of each substance present are expressed in terms of percentage of the non-oxygen content. Amount of oxygen is expressed in terms of percentage of the overall content. Data (sample size = 3) are for samples slid for a distance of 4,522 m.

(a) 0.314 m.s<sup>-1</sup>



(b) 0.905 m.s<sup>-1</sup>



#### 5.4.6 XRD Analysis – Nimonic 80A versus Incoloy 800HT

$\text{Ni}_{2.9}\text{Cr}_{0.7}\text{Fe}_{0.36}$  was detected as a metallic phase for all samples from all test combinations, regardless of sliding speed or temperature (Figures 5.67 and 5.68). As this phase was detected for both the metallic phases of Nimonic 80A and Incoloy 800HT, it was not possible to determine which was the source of the transferred layer (and therefore whether it was transferred or back-transferred) from XRD alone.

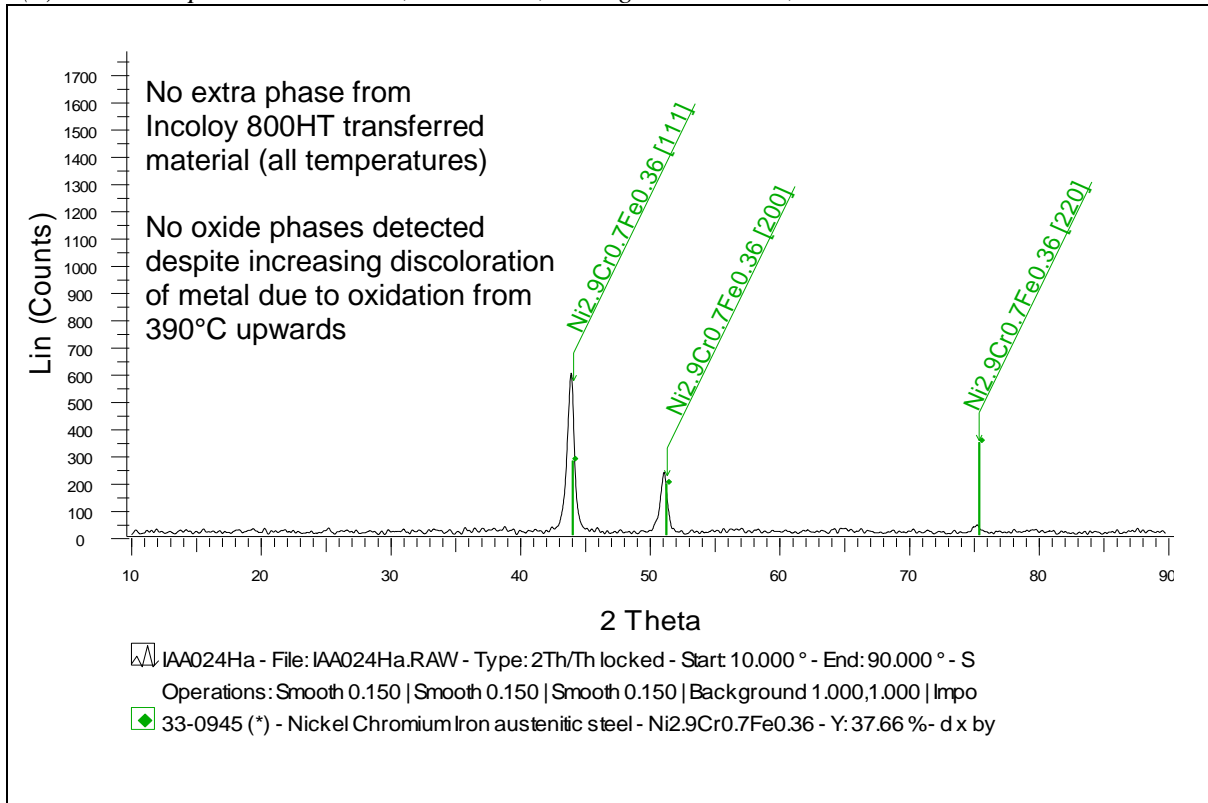
No oxide phase was detected between room temperature and  $510^{\circ}\text{C}$  at either  $0.314 \text{ m.s}^{-1}$  or  $0.905 \text{ m.s}^{-1}$  – this was despite increasing discoloration of wear scar surfaces due to limited oxidation at and above  $390^{\circ}\text{C}$ . At temperatures where glaze formation took place ( $570^{\circ}\text{C}$  and above at  $0.314 \text{ m.s}^{-1}$  – Figure 5.67b;  $630^{\circ}\text{C}$  and above at  $0.905 \text{ m.s}^{-1}$  – Figure 5.68b), the oxide phase  $\text{NiCr}_2\text{O}_4$  was detected, indicating that the glaze layers formed were of a nichromate-phase. However, the use of XRD alone again could not determine if the source material for the glaze was the Nimonic 80A sample or the Incoloy 800HT counterface – both contained high levels of nickel and chromium.

The use of standard and Autopoint EDX did indicate levels of nickel, chromium and iron similar to that for Incoloy 800HT within much of the transferred metal and within the glaze layers formed between  $570^{\circ}\text{C}$  ( $630^{\circ}\text{C}$  at  $0.905 \text{ m.s}^{-1}$ ) and  $750^{\circ}\text{C}$ . With iron present to an indicated level of 40% for both  $0.314$  and  $0.905 \text{ m.s}^{-1}$  /  $4,522 \text{ m}$ , this should appear strongly within the oxide phase of the glaze. Why this is not the case, at this time is uncertain. However, the use of EDX data to supplement XRD did clearly indicate that the primary source of the nichromate-phase glaze was the Incoloy 800HT.

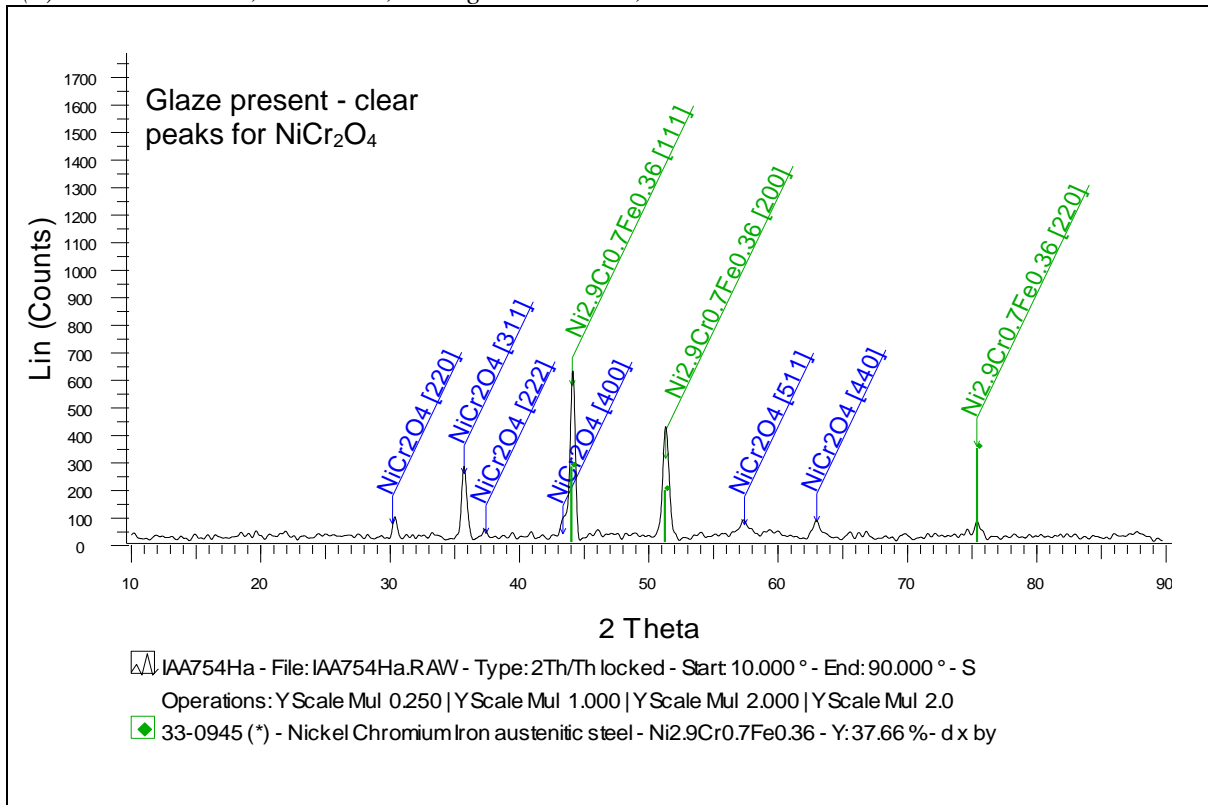
Glancing angle XRD for  $0.314 \text{ m.s}^{-1}$  /  $4,522 \text{ m}$  slid at  $750^{\circ}\text{C}$  (Figure 5.69) did not indicate any extra phases, only serving to confirm the presence of  $\text{Ni}_{2.9}\text{Cr}_{0.7}\text{Fe}_{0.36}$  and  $\text{NiCr}_2\text{O}_4$  phases detected during standard XRD testing. Similar results were obtained for Glancing Angle XRD for samples slid at  $0.905 \text{ m.s}^{-1}$  /  $4,522 \text{ m}$  and  $750^{\circ}\text{C}$ .

**Figure 5.67: XRD for Nimonic 80A versus Incoloy 800HT at 0.314 m.s<sup>-1</sup>**

(a) Room Temperature to 510°C, load = 7N, sliding distance = 4,522 m

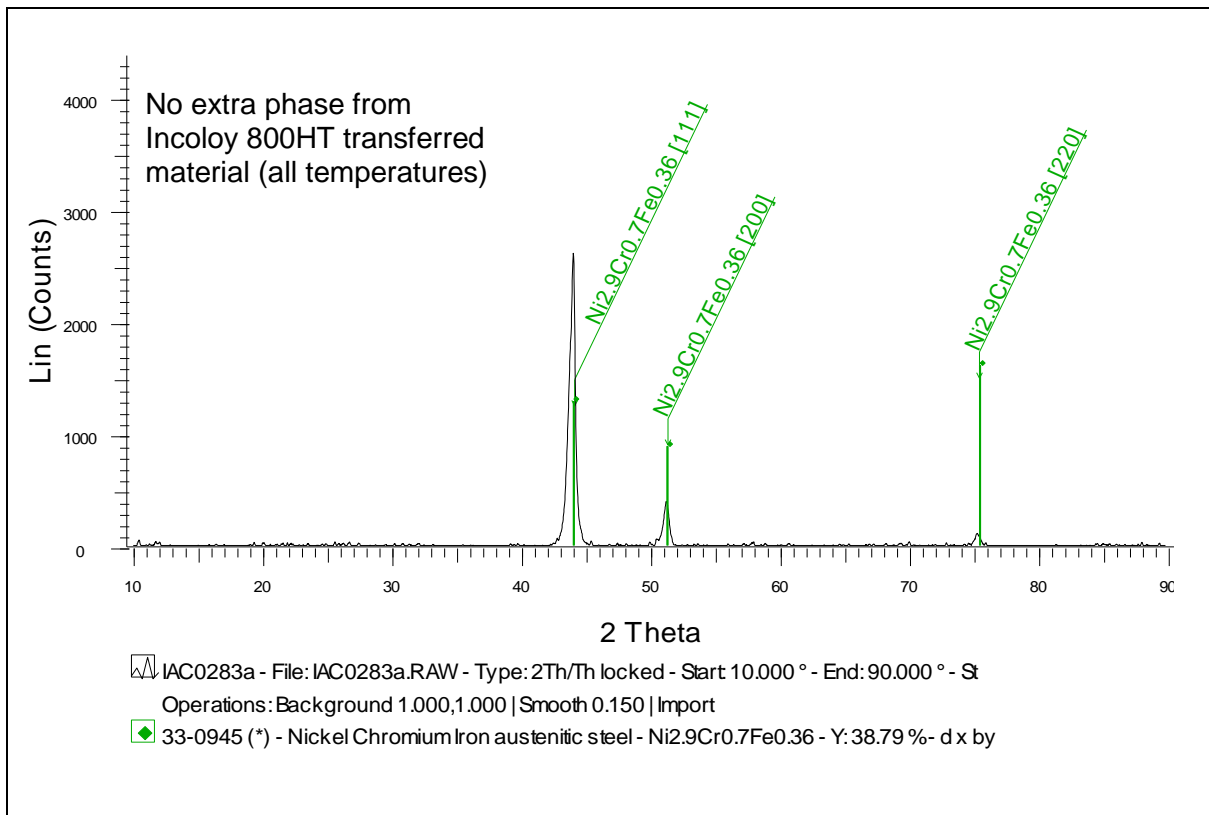


(b) 570°C to 750°C, load = 7N, sliding distance = 4,522 m

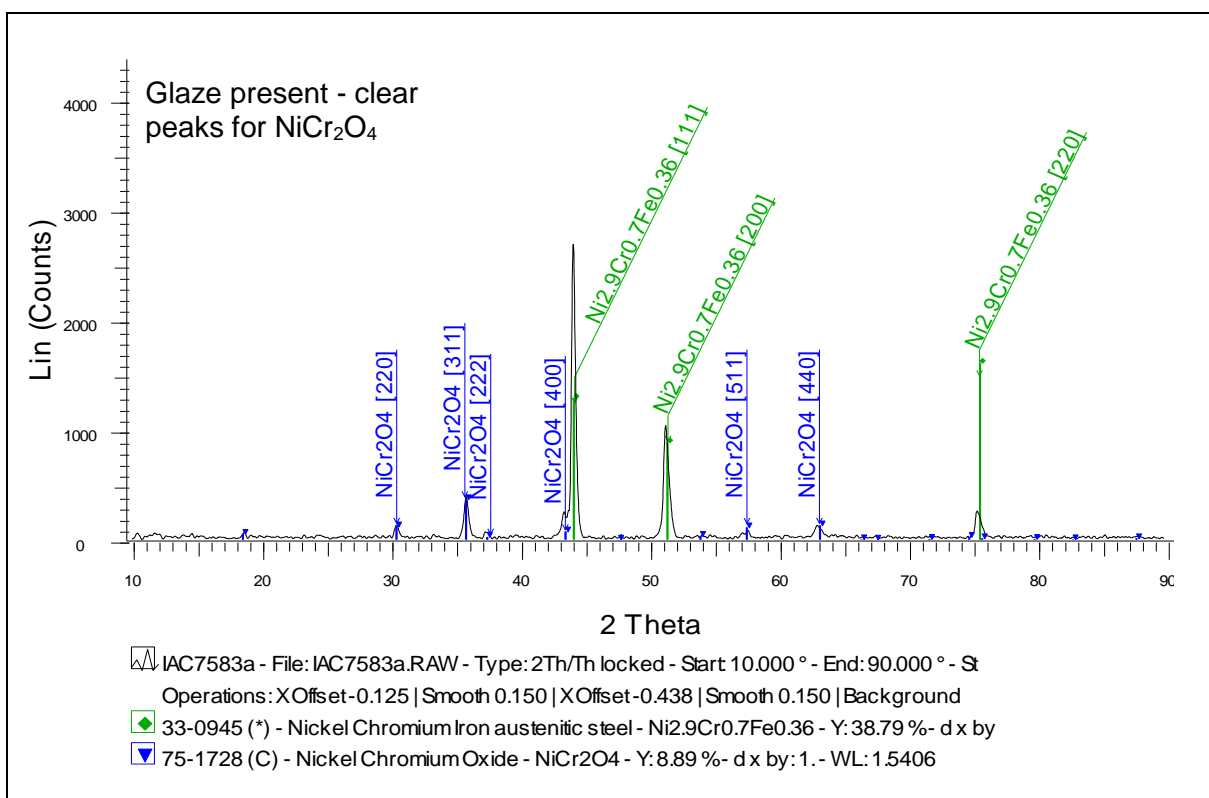


**Figure 5.68: XRD for Nimonic 80A versus Incoloy 800HT at 0.905 m.s<sup>-1</sup>**

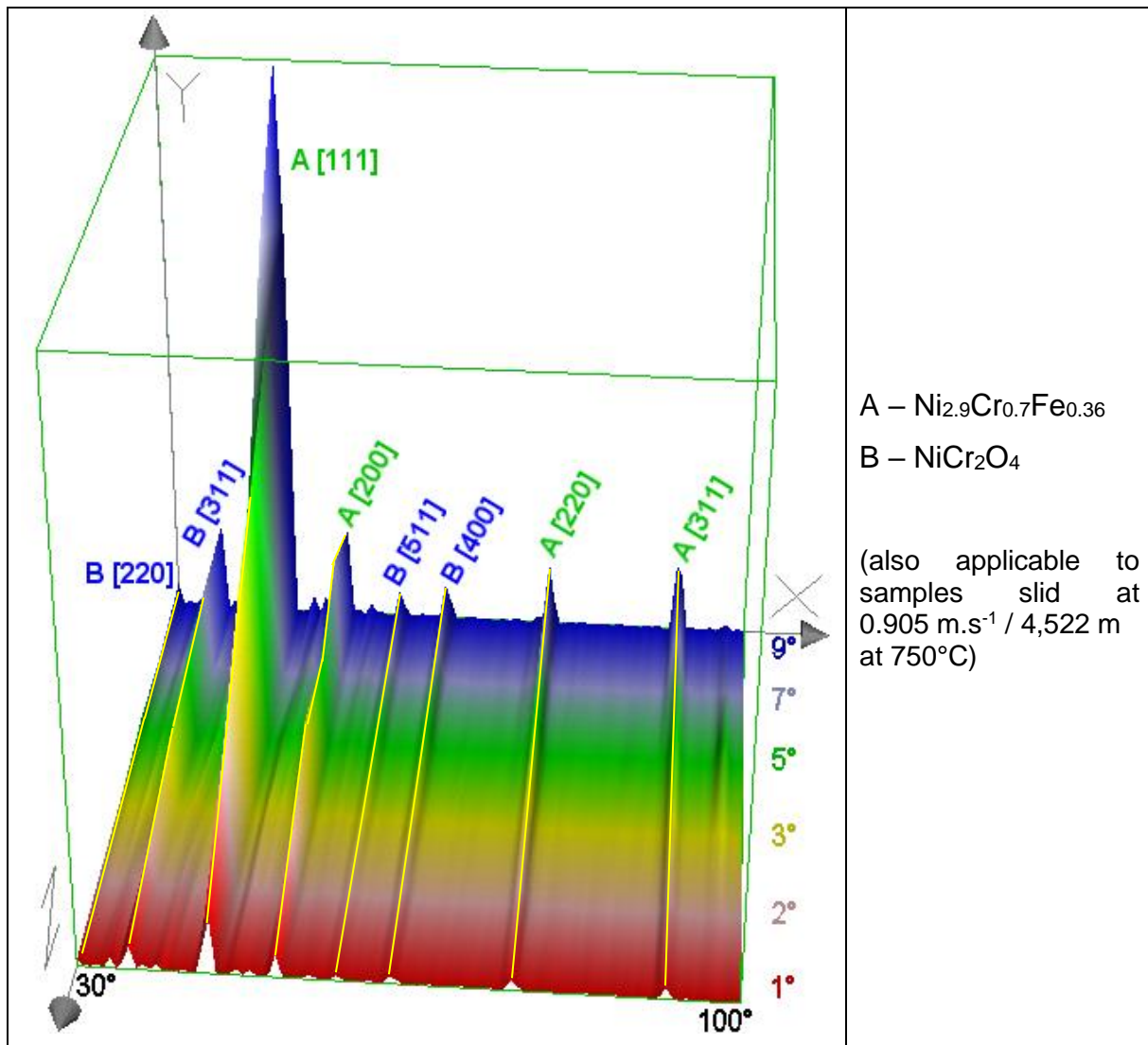
(a) Room Temperature to 570°C, load = 7N, sliding distance = 4,522 m / 13,032 m



(b) 630°C to 750°C, load = 7N, sliding distance = 4,522 m / 13,032 m



**Figure 5.69: Glancing Angle XRD for Nimonic 80A vs. Incoloy 800HT at  $0.314 \text{ m.s}^{-1}$**   
( $750^\circ\text{C}$ , load = 7N, sliding distance = 4,522 m, glancing angle)



#### 5.4.7 Micro-hardness Testing – Nimonic 80A versus Incoloy 800HT

At  $0.314 \text{ m.s}^{-1}$ , the hardness profile on all samples (Nimonic 80A slid against Incoloy 800HT) was the same, regardless of temperature (Figure 5.70a shows representative depth hardness profiles obtained from samples slid at room temperature,  $270^\circ\text{C}$ ,  $510^\circ\text{C}$  and  $750^\circ\text{C}$ ), with high initial values within the first 0.1 mm of the surface – peak values of 5.9 GPa were obtained with samples slid at room temperature, 3.9 GPa at  $270^\circ\text{C}$ , 4.8 GPa at  $510^\circ\text{C}$  and 7.1 GPa at  $750^\circ\text{C}$ . These high initial values were followed by sharp drops in hardness, levelling off at depths between 0.1 mm and 1 mm – hardness levels for room temperature samples decreased and remained close to  $\sim 4.0 \text{ GPa}$ ,  $270^\circ\text{C}$

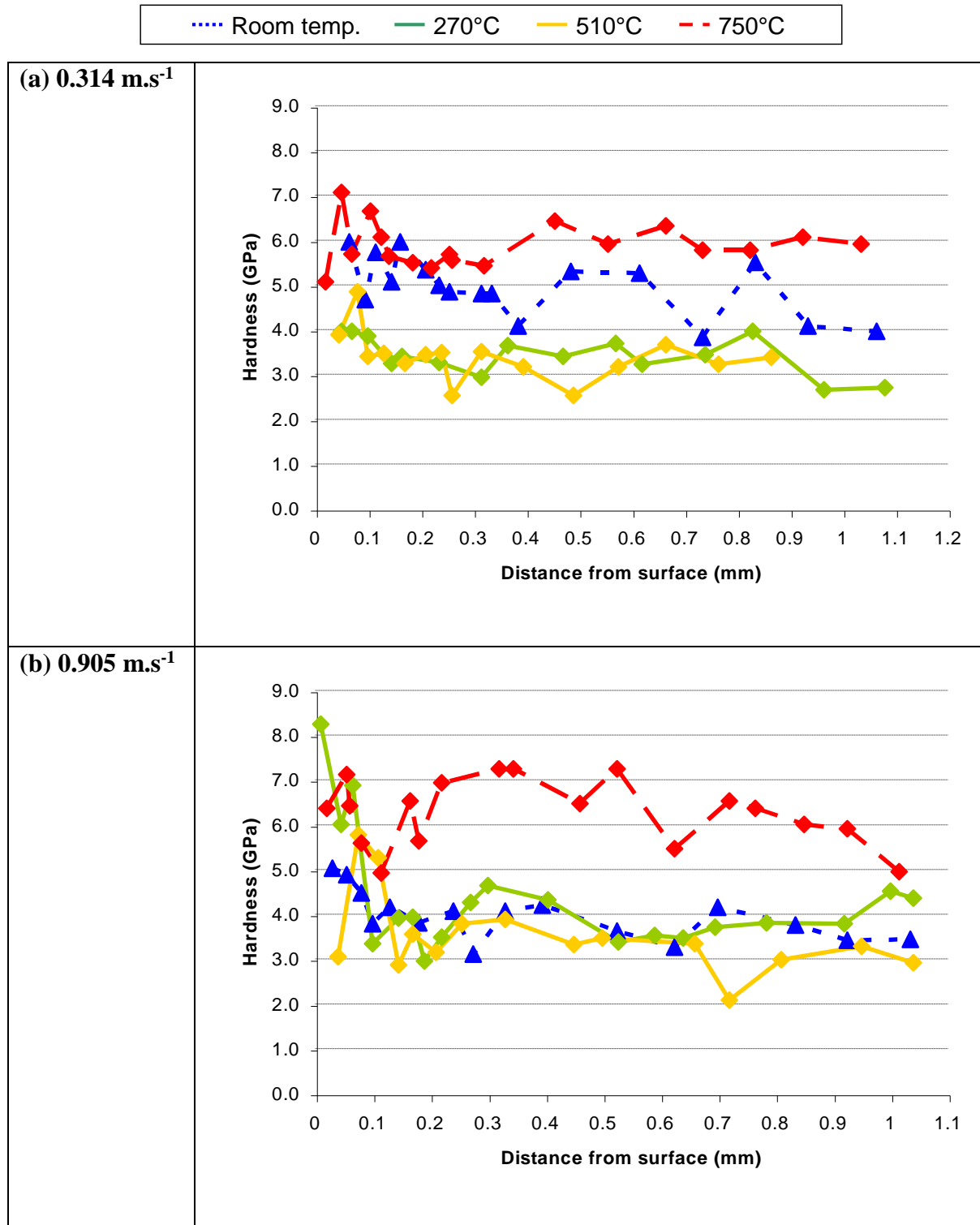
values settled between 2.9 and 3.7 GPa and 510°C values settled between 2.55 to 3.7 GPa. At 750°C, hardness values settled out at between 5.5 and 6.4 GPa. It can be seen from these quoted values, that the 750°C values were the highest, with room temperature values not much lower. 270°C and 510°C values were considerably lower – there appears to be no evidence of a temperature influenced trend on subsurface hardening.

The same pattern was observable at 0.905 m.s<sup>-1</sup> with high initial values within 0.1 mm of the wear scar surface at all test temperatures except for 750°C (Figure 5.70b shows representative depth hardness profiles obtained from samples slid at room temperature, 270°C, 510°C and 750°C). At room temperature, peak values of as high as 4.9 GPa were obtained. At 270°C, peak values were 8.2 GPa, with further peak values of 5.8 GPa at 510°C and 7.2 GPa at 750°C. There was a rapid decrease within 0.1 to 0.15 mm of the surface, before hardness values levelled off. At room temperature, values settled to between 2.9 and 4.1 GPa, at 270°C between 2.9 and 4.6 GPa and at 510°C between 2.9 and 3.9 GPa. The 750°C values tended not to follow this pattern and were highly erratic, varying between 4.3 and 7.3 GPa – there was no clear subsurface peak in hardness. The quoted data again indicated that for Nimonic 80A samples slid at 0.905 m.s<sup>-1</sup>, the highest hardness values were obtained at 750°C (despite the lack of a peak in hardness in the subsurface region) – room temperature and 270°C data were roughly equivalent and 510°C values were the lowest. There was no discernable temperature-influenced trend at 0.905 m.s<sup>-1</sup>, as had been the case at 0.314 m.s<sup>-1</sup>.

The mean hardness values for the transfer layers formed at room temperature and 270°C of 5.29 GPa (room temperature / 0.314 m.s<sup>-1</sup>), 5.62 GPa (270°C / 0.314 m.s<sup>-1</sup>) and 7.05 GPa (270°C / 0.905 m.s<sup>-1</sup> / 4,522 m) were in general not that much greater than the 5.23 GPa obtained for the unworn Nimonic 80A substrate (Table 5.5) – hardness values at room temperature / 0.905 m.s<sup>-1</sup> were in fact lower than the Nimonic 80A substrate at 4.97 GPa. However, EDX data indicated that the transfer layers formed on each of the Nimonic 80A samples were of composition indicating that they were largely transferred from the Incoloy 800HT counterface (Section 5.4.3). As the hardness of the unworn Incoloy 800HT was on average 2.15 GPa, the quoted hardness values for the transfer layers covering the Nimonic 80A wear scars indicated a high degree of hardening of the transferred Incoloy 800HT material.

**Figure 5.70: Subsurface layer hardness for samples slid at 0.314 and 0.905 m.s<sup>-1</sup>, Nimonic 80A versus Incoloy 800HT**

(load = 7N, sliding distance = 4,522 m, hardness values in GPa, Vickers micro-indenter - 50g, sample size = 3)





**Table 5.5: Hardness data for transfer layers between room temperature and 570°C, Nimonic 80A versus Incoloy 800HT**

(load = 7N, sliding distance = 4,522 m, hardness values in GPa, Vickers micro-indenter - 50g, sample size = 5)

(a) Room temperature and 270°C – 0.314 m.s<sup>-1</sup> and 0.905 m.s<sup>-1</sup>

Room temp. / 0.314 m.s <sup>-1</sup>		Room temp. / 0.905 m.s <sup>-1</sup>	
5.499	Mean = 5.29 GPa	4.847	Mean = 5.62 GPa
5.770		5.678	
5.534		5.641	
4.720		5.552	
4.950		6.399	
270°C / 0.314 m.s <sup>-1</sup>		270°C / 0.905 m.s <sup>-1</sup>	
5.295	Mean = 4.97 GPa	6.578	Mean = 7.05 GPa
4.084		8.943	
5.499		6.789	
4.720		5.587	
5.246		7.348	

(b) 390°C to 570°C – 0.905 m.s<sup>-1</sup> only (no transfer layer formed at 0.314 m.s<sup>-1</sup>)

390°C / 0.905 m.s <sup>-1</sup>		450°C / 0.905 m.s <sup>-1</sup>	
6.533	Mean = 6.16 GPa	6.228	Mean = 6.16 GPa
5.983		6.960	
5.924		5.789	
6.421		5.752	
5.943		6.083	
510°C / 0.905 m.s <sup>-1</sup>		570°C / 0.905 m.s <sup>-1</sup>	
6.022	Mean = 6.18 GPa	7.189	Mean = 6.69 GPa
7.010		6.377	
6.861		6.601	
4.222		7.035	
6.789		6.228	

(Mean hardness of unworn Nimonic 80A (sample) = 5.23 GPa,  
mean hardness of unworn Incoloy 800HT (counterface) = 2.15 GPa)

**Table 5.6: Hardness data for glaze and undeformed substrate, Nimonic 80A versus Incoloy 800HT slid at 750°C**

(load = 7N, sliding distance = 4,522 m, hardness values in GPa, Vickers micro-indenter - 50g, sample size = 5)

Unworn substrate (preheated to 750°C for 4 hours)		Glaze formed at 0.314 m.s <sup>-1</sup>		Glaze formed at 0.905 m.s <sup>-1</sup>	
4.95	<b>Mean = 5.23 GPa</b>	16.83	<b>Mean = 19.97 GPa</b>	21.20	<b>Mean = 18.06 GPa</b>
5.77		21.86		26.12	
5.10		13.86		12.30	
5.73		29.52		8.83	
4.61		17.79		21.86	

Hardness values remained high where comprehensive transfer layers continued to form on the 0.905 m.s<sup>-1</sup> / 4,522 m samples between 390°C and 570°C (Table 5.5). Hardening of the transferred Incoloy 800HT metallic material overlying the Nimonic 80A wear scar continued to occur despite the increasing sliding temperatures.

Due to the absence of transfer layers on the 0.314 m.s<sup>-1</sup> samples between 390°C and 570°C (where only isolated or patchy transfer was observed), no data is presented for this lower sliding speed in Table 5.5.

The hardness of surface glaze layers formed during sliding wear at 750°C was extremely high, with values on average of 20.0 GPa on samples slid at 0.314 m.s<sup>-1</sup> and 18.1 GPa at 0.905 m.s<sup>-1</sup> / 4,522 m. These values compared with an average of 5.2 GPa for the unworn substrate (Table 5.6). No collapse of the glaze layers was noted in this case and the indentation did not reveal an underlying powder layer.

#### **5.4.8 Sliding Without Reciprocation – Nimonic 80A versus Incoloy 800HT, 510°C and 0.314 m.s<sup>-1</sup>**


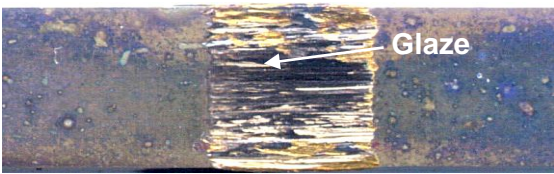
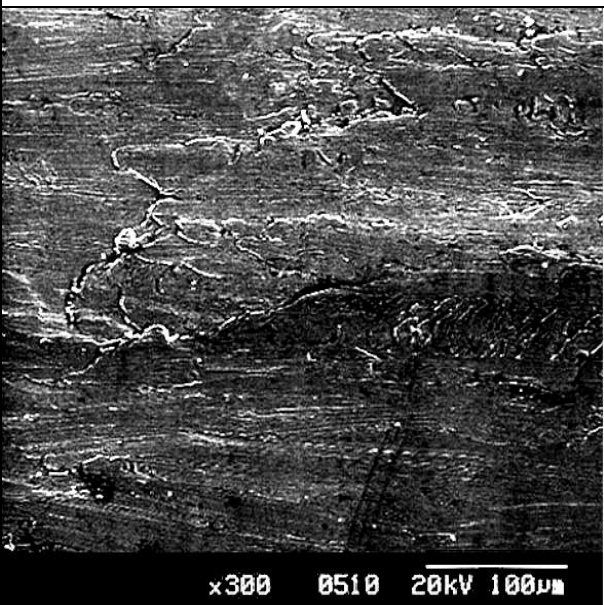
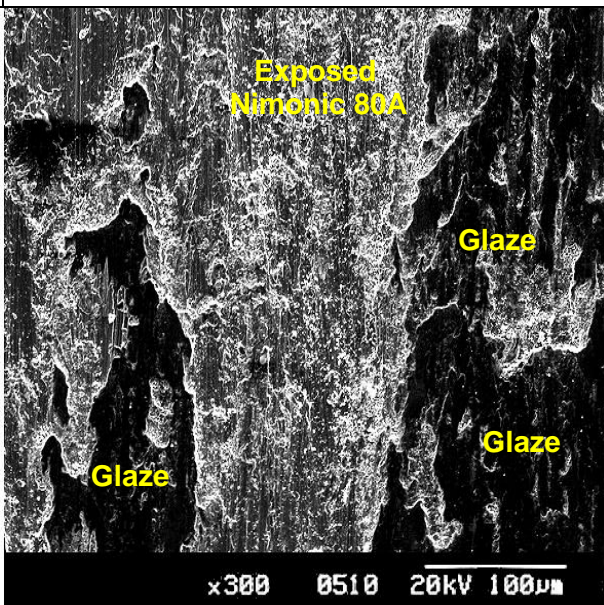
The sliding of Nimonic 80A at 510°C without reciprocation against an Incoloy 800HT counterface rotating at 0.314 m.s<sup>-1</sup> (sample size 5), resulted in the formation of a patchy glaze layer over parts of the Nimonic 80A wear scar surface (Figure 5.71). Coincident with this, there was a significant drop in weight loss (and also wear rate) – without reciprocation and only the counterface rotating, a mean weight change of -0.016(3) g (the negative value indicating a loss) was recorded after 4,522 m of sliding (mean wear rate between 0 and 4,522 m, 3.605 µg.m<sup>-1</sup>), compared to -0.039(3) g when using sample reciprocation (wear rate 8.691 µg.m<sup>-1</sup>).

A brief period of unsettled run-in wear at the beginning of sliding gave a mean peak value for coefficient of friction of 1.17 (Figure 5.72). This was followed by a rapid fall in coefficient of friction values for sliding without reciprocation to ‘steady state’ values of in general between 0.50 and 0.65. This compared to coefficient of friction values with reciprocation of between 0.56 and 0.68 – friction levels were only slightly less when the patchy glaze layer formed in the absence of reciprocation. No transition in the nature of the friction data was observed during sliding, despite the formation of glaze without reciprocation, thus it was not possible to ascertain the sliding distance required to promote the formation of glaze.

EDX data indicated a composition for the glaze consistent with the Incoloy 800HT counterface, (~41% Fe, ~30% Cr, ~24% Ni), pointing to transfer of material from the counterface to the Nimonic 80A sample to form the glaze. XRD indicated that this glaze layer was of a nichromate-phase (NiCr<sub>2</sub>O<sub>4</sub>), identical to that seen when using sample reciprocation at 0.314 m.s<sup>-1</sup> between 570°C and 750°C.

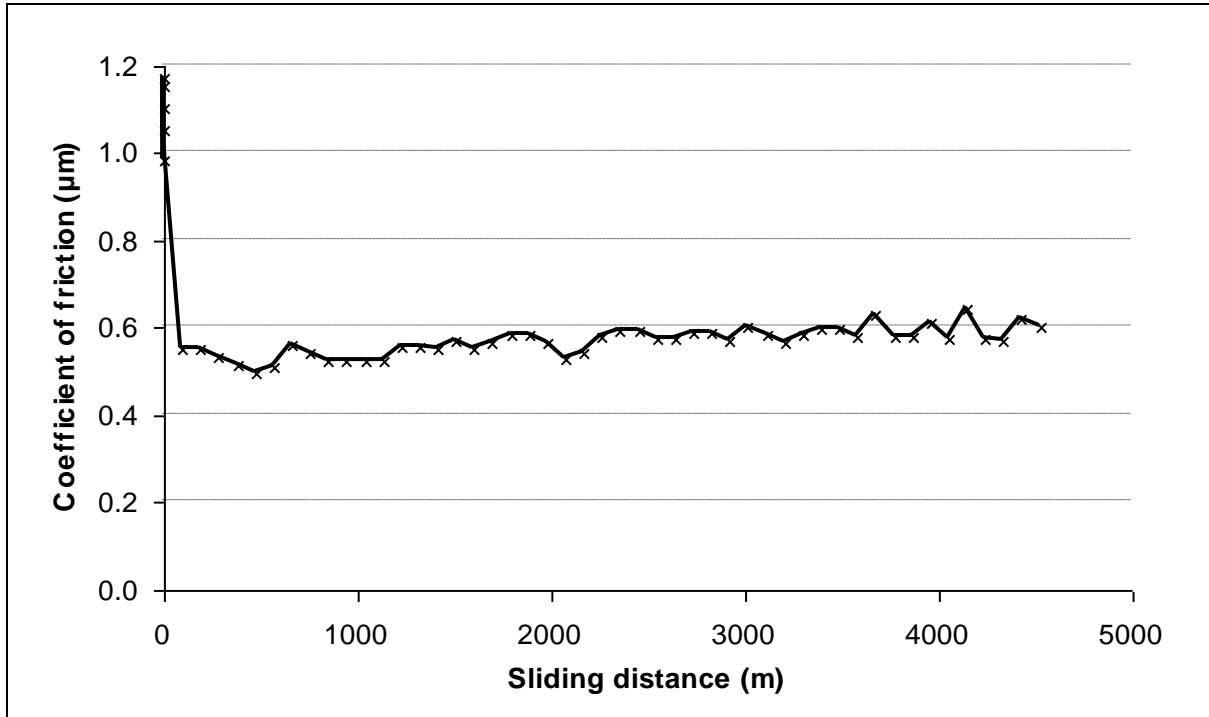
**Figure 5.71: Optical and SEM images of sample surfaces on sliding without reciprocation – Nimonic 80A versus Incoloy 800HT at 510°C and 0.314 m.s<sup>-1</sup>**

(load = 7N, sliding distance = 4,522 m)

<p><b>With reciprocation</b></p> <p>No evidence of glaze build-up on either the optical image or the SEM micrograph – only sufficient oxide to discolour wear scar surface present</p> <p>Mean weight change = -0.039(3) g</p> <p>Coefficient of friction = 0.56 to 0.68</p>	<p><b>Without reciprocation</b></p> <p>Patchy oxide build-up and NiCr<sub>2</sub>O<sub>4</sub> glaze formation, covering ~50% of wear scar.</p> <p>Mean weight change = -0.016(3) g</p> <p>Coefficient of friction = 0.50 to 0.65</p>
 <p style="text-align: center;">18 mm</p>	 <p style="text-align: center;">5 mm</p>
	

**Figure 5.72: Coefficient of friction versus sliding distance for Nimonic 80A versus Incoloy 800HT at 510°C and 0.314 m.s<sup>-1</sup> without reciprocation**

(load = 7N, sliding distance = 4,522 m, sample size = 3)



## 5.5 Testing of Incoloy MA956 versus Incoloy 800HT between Room Temperature and 750°C, at 0.314 and 0.905 m.s<sup>-1</sup>

### 5.5.1 Experimental Observations – Incoloy MA956 versus Incoloy 800HT

Figure 5.73 shows the variation of weight loss and wear rate (in  $\mu\text{g.m}^{-1}$ ) with temperature for the Incoloy MA956 / Incoloy 800HT (counterface) system, from room temperature to 750°C. The weight loss and wear rate behaviour observed at 0.314 m.s<sup>-1</sup> (after 4,522 m of sliding) and 0.905 m.s<sup>-1</sup> (after 4,522 m and 13,032 m of sliding) is described in this section.

#### a) Weight change and wear rate data at 0.314 m.s<sup>-1</sup>/ 4,522 m

A steady increase in Incoloy MA956 mean weight loss and wear rate was observed with increasing temperature up to 630°C at 0.314 m.s<sup>-1</sup> / 4,522 m. Weight change and wear rate values for 0.314 m.s<sup>-1</sup> remained fairly low between room temperature (-0.002(9) g, negligible wear rate) and 390°C (-0.066(8) g, wear rate 14.769  $\mu\text{g.m}^{-1}$  between 0 and 4,522 m) and did not increase greatly on raising the temperature to 510°C (-0.108(0) g, wear rate

23.893  $\mu\text{g.m}^{-1}$ ). Large increases in weight loss from the Incoloy MA956 were then observed, with increasing negative weight change values obtained for 630°C (-0.202(7) g) and 690°C (-0.282(6) g). Over this temperature range, wear rate increased from 23.893  $\mu\text{g.m}^{-1}$  at 510°C to 44.829  $\mu\text{g.m}^{-1}$  at 630°C and 62.501  $\mu\text{g.m}^{-1}$  at 690°C. At 750°C, weight loss and wear rate figures decreased, reaching final values of -0.090(3) g and 17.962  $\mu\text{g.m}^{-1}$  respectively.

***b) Coefficient of friction data at 0.314 m.s<sup>-1</sup>***

Coefficient of friction values for the Incoloy MA956 / Incoloy 800HT system at 0.314 m.s<sup>-1</sup> showed two distinct phases of behaviour, an unsettled ‘run-in’ period, followed by a more settled ‘steady state’ period. Typical variation of these coefficient of friction values was ~20% during run-in, falling to ~12% during steady state sliding – steady state conditions were normally established with 1,000 m of sliding (~53 minutes).

At 0.314 m.s<sup>-1</sup>, there was no clear indication of any trend in the early peak ‘run-in’ values of coefficient of friction as sliding temperature was increased. Coefficient of friction values rose rapidly at the beginning of testing from zero to 1.09 at room temperature, 1.15 at 270°C, 1.29 at 510°C and 1.18 at 750°C. However, a clear downward trend in coefficient of friction data (Figure 5.74) was observed for steady state values with increasing temperature, starting at between 0.75 and 0.85 at room temperature, falling to between 0.6 and 0.75 at 270°C, then 0.6 and 0.7 at 510°C and finally 0.4 and 0.6 between 630°C and 750°C.

Observable in the 0.314 m.s<sup>-1</sup> data at glaze forming temperatures (630°C to 750°C) was the change from more to less erratic values of coefficient of friction during steady state sliding (there was a drop in variability from ~12% to ~8%). This was observed to occur earlier with increasing temperature (Figure 5.75):

- At 630°C, the change from more to less erratic values of friction was observed after 155 minutes or 2,920 m of sliding.
- At 690°C, less erratic values appeared after 162.5 minutes or 3,062 m of sliding.



- At 750°C, this change to less erratic values was observed after 55 minutes or 1,036 m of sliding.

These ‘changes’ in variability in previous studies were observed to coincide with the development of substantial glaze layers and the reduction of metal-to-metal contact [2].

***c) Weight change and wear rate data at 0.905 m.s<sup>-1</sup> / 4,522 m***

Between room temperature and 630°C, the pattern of wear behaviour at 0.905 m.s<sup>-1</sup> / 4,522 m followed a pattern similar to that at 0.314 m.s<sup>-1</sup>, with a steady increase in weight loss and wear rate once again observed. The increases in weight loss from the Incoloy MA956 at 0.905 m.s<sup>-1</sup> / 4,522 m were gradual between room temperature and 510°C, with weight change values decreasing from -0.004(7) g to -0.062(0) g. Wear rates between 0 and 4,522 m increased from 1.045 µg.m<sup>-1</sup> to 13.703 µg.m<sup>-1</sup> over the same temperature range.

Between 510°C and 630°C, there was a significant acceleration in weight loss and wear rate at 0.905 m.s<sup>-1</sup> / 4,522 m. There was a decrease in weight change values (an increase in weight loss) after 4,522 m of sliding, from -0.062(0) g at 510°C to -0.131(2) g at 630°C, with wear rate increasing from 13.703 µg.m<sup>-1</sup> to 41.477 µg.m<sup>-1</sup> over the same test temperature range.

It was additionally observed that between 390°C and 630°C, wear rates at 0.905 m.s<sup>-1</sup> (after 4,522 m) were less than those obtained at 0.314 m.s<sup>-1</sup>. For example, at 390°C, the wear rate decreased from 14.769 µg.m<sup>-1</sup> at 0.314 m.s<sup>-1</sup> to 9.928 µg.m<sup>-1</sup> at 0.905 m.s<sup>-1</sup>. At 510°C, the decrease in wear rate was from 23.893 µg.m<sup>-1</sup> at 0.314 m.s<sup>-1</sup> to 13.703 µg.m<sup>-1</sup> at 0.905 m.s<sup>-1</sup>. At 570°C, the decrease in wear rate was from 33.523 µg.m<sup>-1</sup> at 0.314 m.s<sup>-1</sup> to 18.573 µg.m<sup>-1</sup> at 0.905 m.s<sup>-1</sup>.

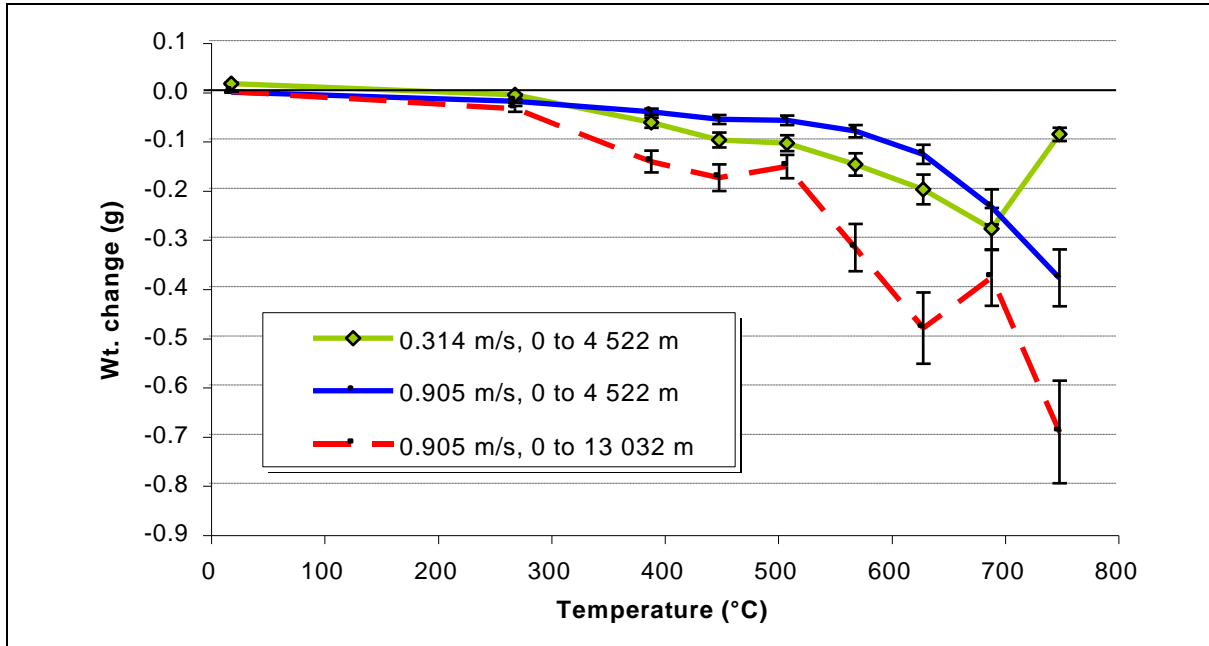
At 690°C and 750°C, weight loss and wear rate continued to increase at 0.905 m.s<sup>-1</sup> with increasing temperature. The mean recorded weight change values were -0.257(6) g at 690°C and -0.332(0) g at 750°C respectively. Recorded wear rate values after 4,522 m were 56.970 µg.m<sup>-1</sup> at 690°C and 73.413 µg.m<sup>-1</sup> at 750°C.



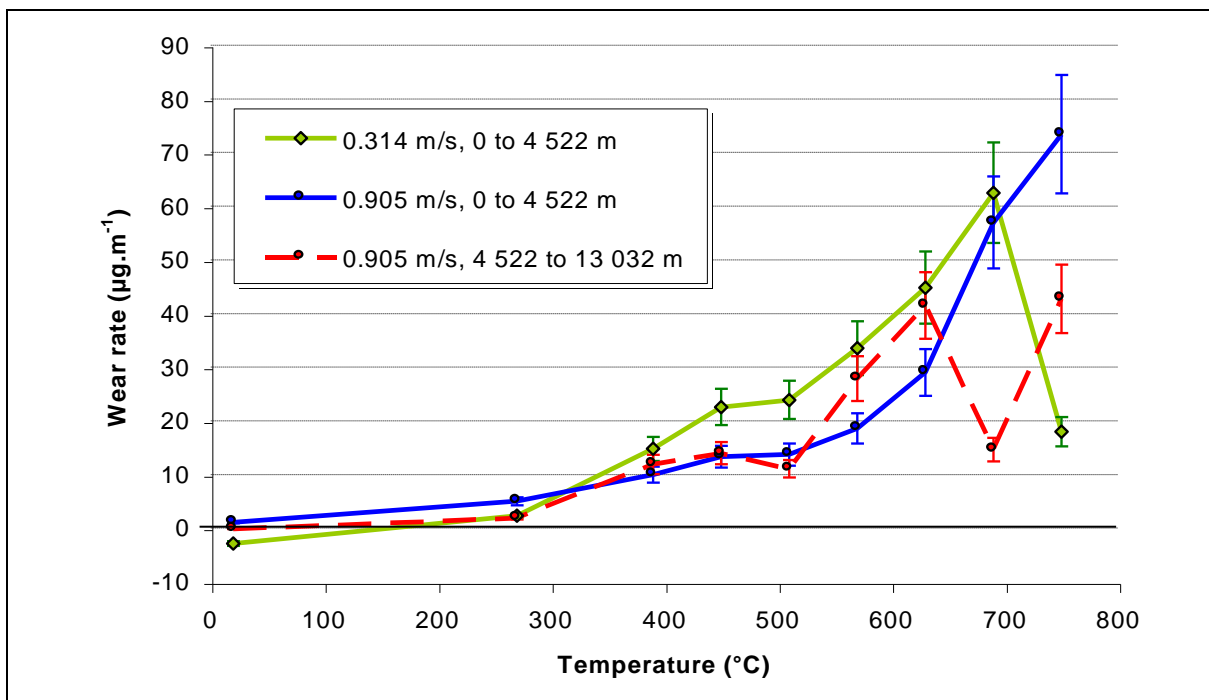
**Figure 5.73: Effect of temperature on weight change and wear rate – Incoloy MA956 vs. Incoloy 800HT**

(load = 7N, sample size = 3)

(a) Temperature versus weight change



(b) Temperature versus wear rate

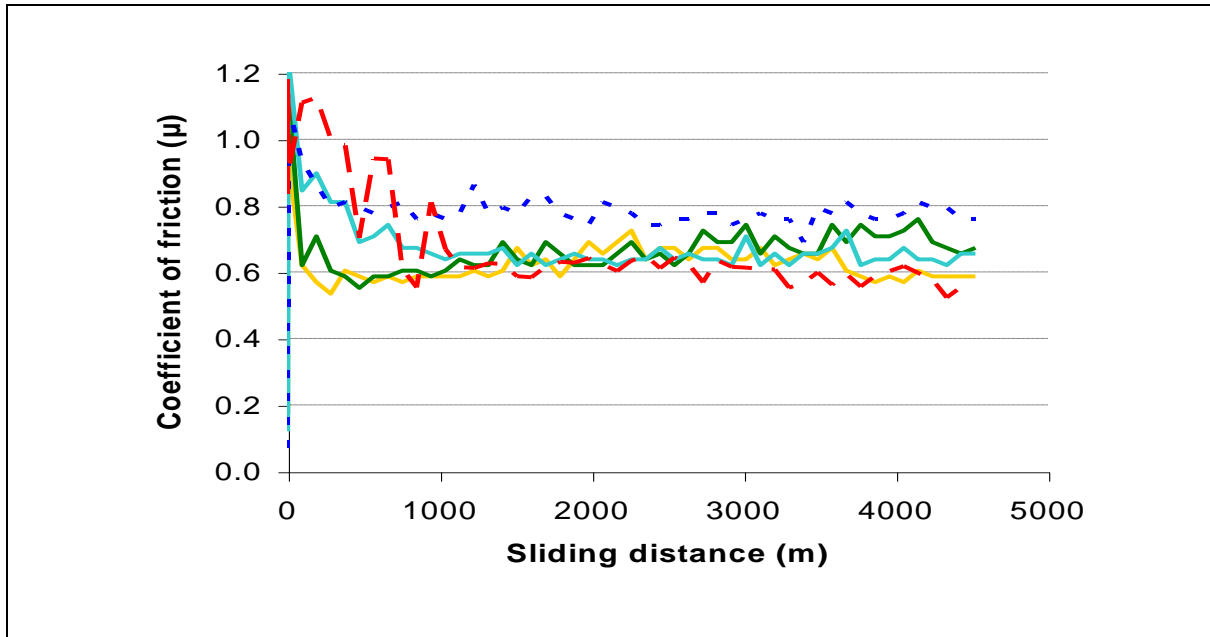


**Figure 5.74: Temperature versus coefficient of friction for Incoloy MA956 versus Incoloy 800HT**

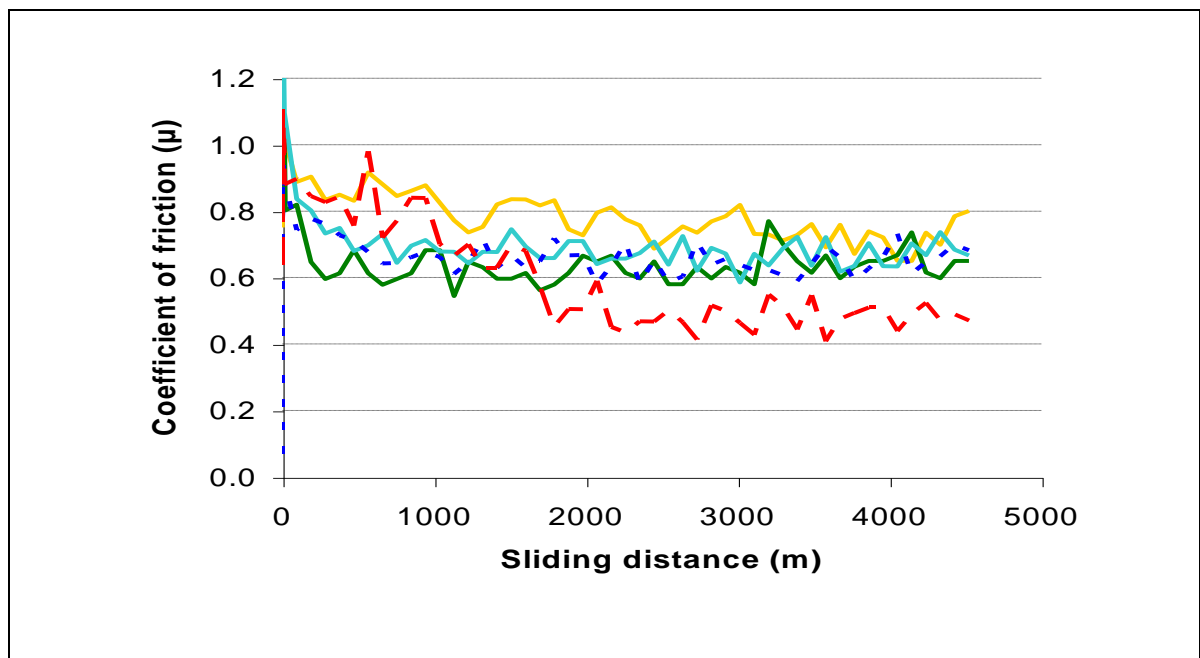
(load = 7N, sample size = 3)

Room temp. 270°C 450°C 510°C 750°C

(a)  $0.314 \text{ m.s}^{-1} / 4,522 \text{ m}$

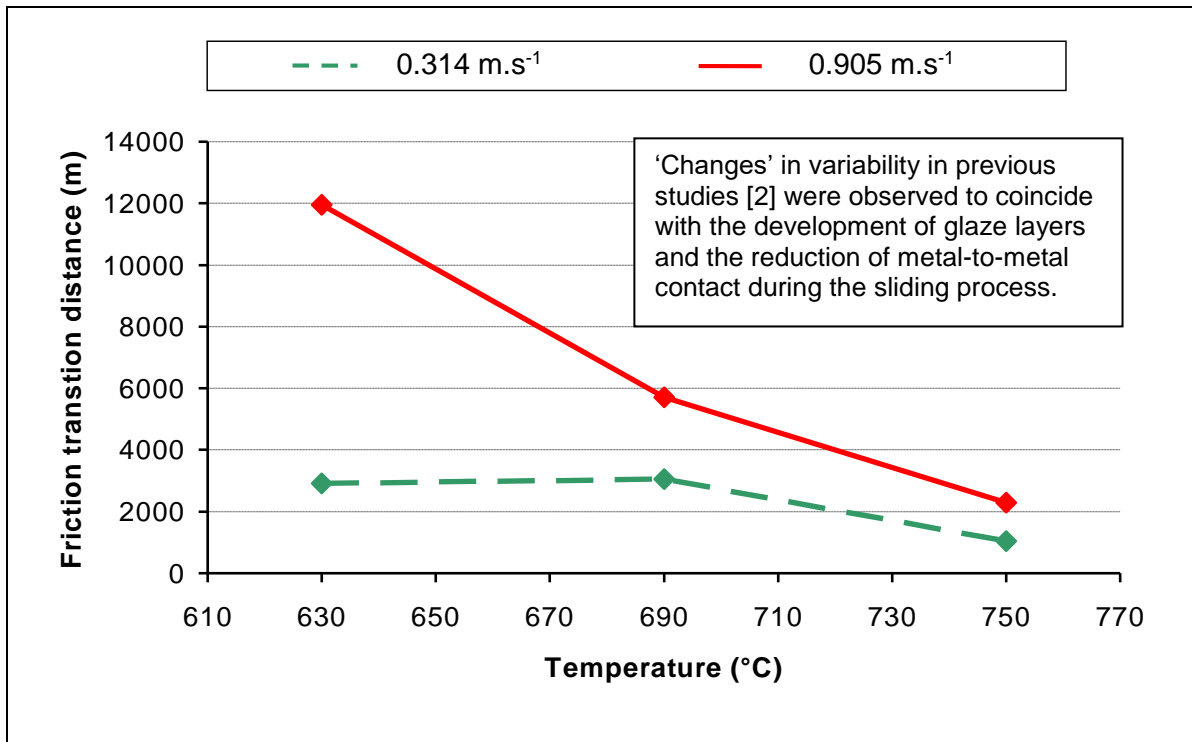


(b)  $0.905 \text{ m.s}^{-1} / 4,522 \text{ m}$



**Figure 5.75: Distance to transition in coefficient of friction from high variability (severe wear) to low variability (mild wear) at 630°C, 690°C and 750°C – Incoloy MA956 versus Incoloy 800HT at 0.314 m.s<sup>-1</sup> and 0.905 m.s<sup>-1</sup>**

(load = 7N, sample size = 3)



**d) Weight change and wear rate data at 0.905 m.s<sup>-1</sup> / 13,032 m**

At room temperature and 270°C, weight losses from the Incoloy MA956 after 13,032 m of sliding at 0.905 m.s<sup>-1</sup> were not too dissimilar to, albeit slightly greater than those obtained after 4,522 m, with weight change values recorded at -0.003(6) g at room temperature and -0.038(5) g at 270°C. A fall in wear rate data did indicate a slight change in behaviour at room temperature and 270°C with extended sliding to 13,032 m. At room temperature, the wear rate fell from 1.045 µg.m<sup>-1</sup> between 0 and 4,522 m to -0.134 µg.m<sup>-1</sup> between 4,522 and 13,032 m. At 270°C, the decrease in wear rate was from 5.024 µg.m<sup>-1</sup> to 1.850 µg.m<sup>-1</sup>. This clearly indicates that most wear occurred early during sliding (within the first 4,522 m).

Weight loss values from the Incoloy MA956 after 13,032 m between 390°C and 510°C indicated a slow increase in wear with temperature – weight change values for 0.905 m.s<sup>-1</sup> / 13,032 m decreased from -0.145(9) g at 390°C to -0.156(0) g at 510°C (the

negative values indicating a weight loss). There was no significant fall in wear rate on extended sliding to 13,032 m between 390°C and 510°C, with the 0 to 4,522 m values and the 4,522 to 13,032 m values being very similar. At 390°C, wear rate values rose very slightly from 9.928  $\mu\text{g.m}^{-1}$  between 0 and 4,522 m to 11.866  $\mu\text{g.m}^{-1}$  between 4,522 and 13,032 m. At 510°C, there was only a very slight decrease in wear rates from 13.703  $\mu\text{g.m}^{-1}$  to 11.054  $\mu\text{g.m}^{-1}$ .

On extended sliding up to 13,032 m at 570°C and 630°C, the increase in wear compared to that observed between 0 and 4,522 m became more rapid with weight change values indicating very substantial losses at both temperatures. There was also a clear upward trend in weight loss and wear rate with increasing temperature. At 570°C, the weight change values decreased from -0.084(0) g after 4,522 m to -0.320(9) g after 13,032 m (indicating increasing weight loss). At 630°C, the decrease in weight change values was greater from -0.131(2) g to -0.484(2) g. The wear rate data clearly indicate that wear of the Incoloy MA956 actually accelerated at both temperatures. At 570°C, the wear rate increased from 18.573  $\mu\text{g.m}^{-1}$  between 0 and 4,522 m to 27.838  $\mu\text{g.m}^{-1}$  between 4,522 and 13,032 m. At 630°C, the increase in wear rate was from 29.011  $\mu\text{g.m}^{-1}$  to 41.477  $\mu\text{g.m}^{-1}$ .

On raising the sliding temperature from 630°C to 690°C, there was a significant decrease in weight loss for samples slid for 13,032 m, with weight change values increasing from -0.484(2) g to -0.381(9) g. Wear rates between 4,522 and 13,032 m of sliding decreased from 41.477  $\mu\text{g.m}^{-1}$  at 630°C to 14.601  $\mu\text{g.m}^{-1}$  at 690°C.

At 690°C and 750°C, a significant fall in wear rate was recorded with extended sliding to 13,032 m. At 690°C, the wear rate fell from 56.970  $\mu\text{g.m}^{-1}$  between 0 and 4,522 m to 14.601  $\mu\text{g.m}^{-1}$  between 4,522 and 13,032 m. At 750°C, the wear rate fell from 73.413  $\mu\text{g.m}^{-1}$  to 42.728  $\mu\text{g.m}^{-1}$ .

However, it was also apparent that on raising the sliding temperature from 690°C to 750°C, there was a significant increase in the '4,522 to 13,032 m' mean wear rate values, from 14.601  $\mu\text{g.m}^{-1}$  to 42.728  $\mu\text{g.m}^{-1}$ .

*e) Coefficient of friction data at 0.905 m.s<sup>-1</sup>*

Coefficient of friction values for the Incoloy MA956 / Incoloy 800HT system at 0.905 m.s<sup>-1</sup> (Figure 5.74b) again showed an initial unsettled run-in period, followed by a more settled 'steady-state', as observed at 0.314 m.s<sup>-1</sup>. Variation of these coefficient of friction values was higher at 0.905 m.s<sup>-1</sup> than at 0.314 m.s<sup>-1</sup>, typically as high as ~30% during run-in and ~20% during steady state (this compared to ~20% during run-in and ~12% during steady state at 0.314 m.s<sup>-1</sup>).

No clear trend with increasing temperature was identifiable in the coefficient of friction data for samples slid at 0.905 m.s<sup>-1</sup>, either with the unsettled 'run-in' data or the 'steady-state' values, although steady state values were substantially lower at 750°C. During 'run-in', values of friction rose from 0 to 1.04 at room temperature, 1.25 at 270°C, 1.16 at 510°C and 1.10 at 750°C – this points to a slight downward trend, but not a significant one with ~30% variability in the 'run-in' values. Values of coefficient of friction during 'steady-state' sliding varied between 0.58 - 0.72 at room temperature and 270°C, 0.65 - 0.82 at 510°C, and 0.4 - 0.55 at 750°C.

The change from more to less erratic values of coefficient of friction during steady state sliding observed between 630°C and 750°C at 0.314 m.s<sup>-1</sup>, was also observed at 0.905 m.s<sup>-1</sup> (there was a drop in variability from ~20% to between 12% and 15%). This again occurred earlier with increasing temperature (Figure 5.75):

- At 630°C, the reduction in variability occurred only towards the end of sliding after 220 minutes or 11,946 m of sliding.
- At 690°C, less erratic values appeared after 105 minutes or 5,702 m of sliding.
- At 750°C, this reduction in variation was observed after 42 minutes or 2,285 m of sliding.

As with similar observations at 0.314 m.s<sup>-1</sup>, these 'changes' in variability in previous studies [2] were observed to coincide with the development of glaze layers and the reduction of metal-to-metal contact during the sliding process.

### 5.5.2 Optical and SEM Morphology – Incoloy MA956 versus Incoloy 800HT

Optical and SEM examination (Figures 5.76, 5.77 and 5.78) indicated that at room temperature and 270°C, Incoloy MA956 sample wear surfaces were metallic and highly damaged (indicative of severe wear), with a very high degree of metal transfer onto the surface of the Incoloy MA956 at both 0.314 m.s<sup>-1</sup> and 0.905 m.s<sup>-1</sup>. The resulting metallic transfer layer covered almost the entire wear scar.





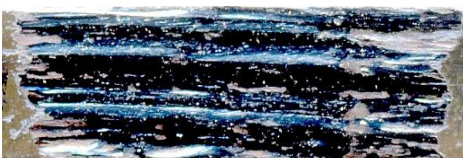
Transfer levels at both 0.314 m.s<sup>-1</sup> and 0.905 m.s<sup>-1</sup> were much lower at temperatures of 390°C and above. The decreasing transfer coincided with increasing discolouration of the wear scar surface between 390°C and 570°C, due to very limited oxidation of the exposed metallic surfaces (Figures 5.76 and 5.77 – this oxide did not build up into wear protective oxide layers). At 0.314 m.s<sup>-1</sup>, only isolated areas of transferred metallic material were formed on the wear scar surfaces at 0.314 m.s<sup>-1</sup>, covering at most between 5 to 10% of the wear surface area. Metallic transfer at 0.905 m.s<sup>-1</sup> was slightly higher and limited, patchy metallic transfer layers were able to form, covering up to 50% of the wear scar surface.

At 570°C and 630°C, the transfer layers formed at 0.905 m.s<sup>-1</sup> during the first 4,522 m were removed on extended sliding up to 13,032 m (Figure 5.76 shows the 630°C case). The level of damage to the Incoloy MA956 samples was observed to be significantly greater after 13,032 m of sliding, compared to that after 4,522 m.

Glaze formation at 0.314 m.s<sup>-1</sup> was first observed at 630°C (Figures 5.76 and 5.78), covering approximately 70% of the wear scar. On increasing the sliding temperature up to 690°C and 750°C, the observed glaze layers became more comprehensive, covering more than 90% of the wear scar in both cases (Figures 5.76 and 5.78 show the 750°C case).




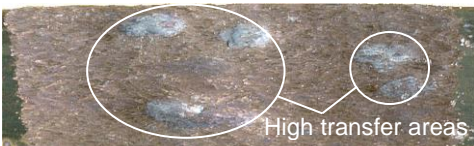
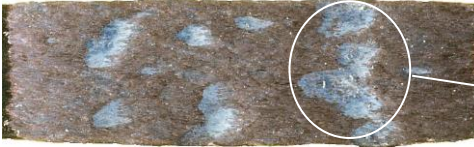


At 0.905 m.s<sup>-1</sup>, significant (albeit limited) build-up of oxide into platforms was first observed on the Incoloy MA956 samples, most noticeably after 13,032 m of sliding at 630°C (Figure 5.77) and then only covering ~25% of the wear scar. Comprehensive glaze formation was not observed until 690°C at 0.905 m.s<sup>-1</sup> and only after 13,032 m – only a few isolated patches were formed after 4,522 m. Glaze development was much more substantial at 750°C, but as at 690°C, only after 13,032 m of sliding (Figure 5.77) – after 4,522 m of sliding at 750°C, glaze formation was still incomplete (Figures 5.77 and 5.78), covering only 40 to 50% of the wear scar surface.

**Figure 5.76: Optical Images for Incoloy MA956 versus Incoloy 800HT at 0.314 m.s<sup>-1</sup>**

	<p><b>Room Temperature, 4,522 m – sample</b>  <i>(wear scar = 15 x 5 mm)</i>  Transfer layer covering 90% of wear scar</p>
	<p><b>270°C, 4,522 m – sample</b>  <i>(wear scar = 17 x 5 mm)</i>  Transfer layer covering 80% of wear scar</p>
	<p><b>510°C, 4,522 m – sample</b>  <i>(wear scar = 18 x 5 mm, also 390, 450, 570°C)</i>  Reduced transfer (10%), now in more isolated patches – discoloration due to limited oxidation of wear surface</p>
	<p><b>630°C, 4,522 m – sample</b>  <i>(wear scar = 20 x 5 mm)</i>  Glaze covering large areas of highly worn wear scar, with no evidence of metallic transfer</p>
	<p><b>750°C, 4,522 m – sample</b>  <i>(wear scar = 19 x 5 mm, also 690°C)</i>  Glaze covering most of wear scar, no evidence of metallic transfer</p>

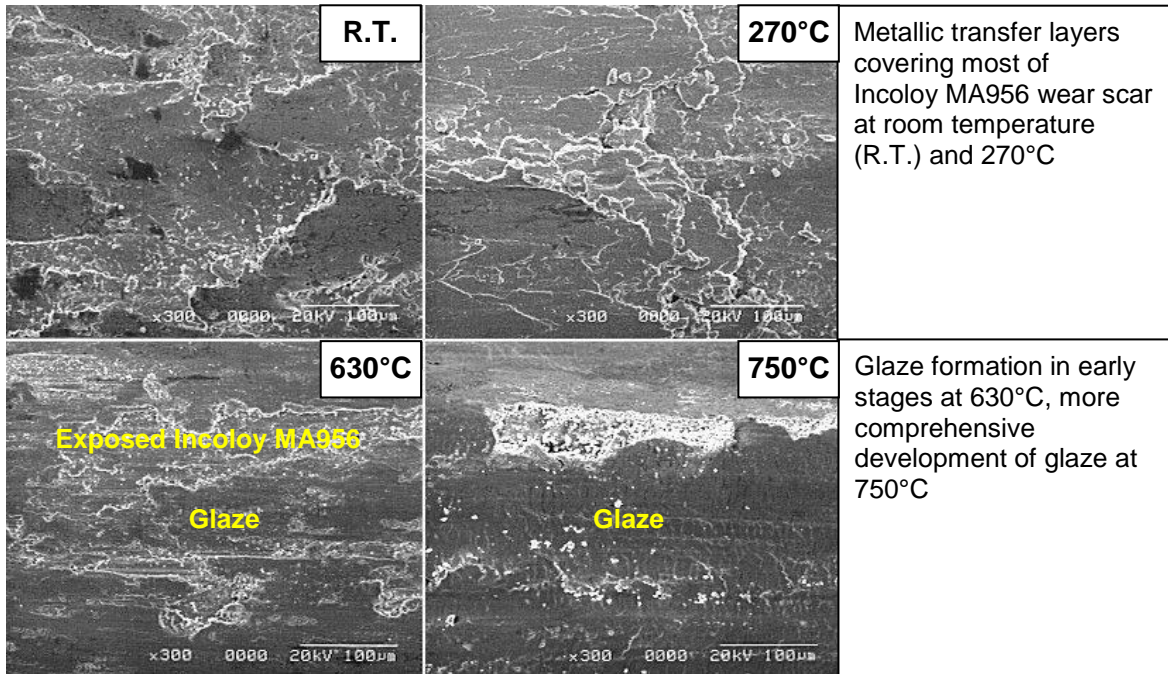


**Figure 5.77: Optical Images for Incoloy MA956 versus Incoloy 800HT at 0.905 m.s<sup>-1</sup>**  
*(Observations made after 13,032 m of sliding follow the same pattern as 4,522 m where not shown)*

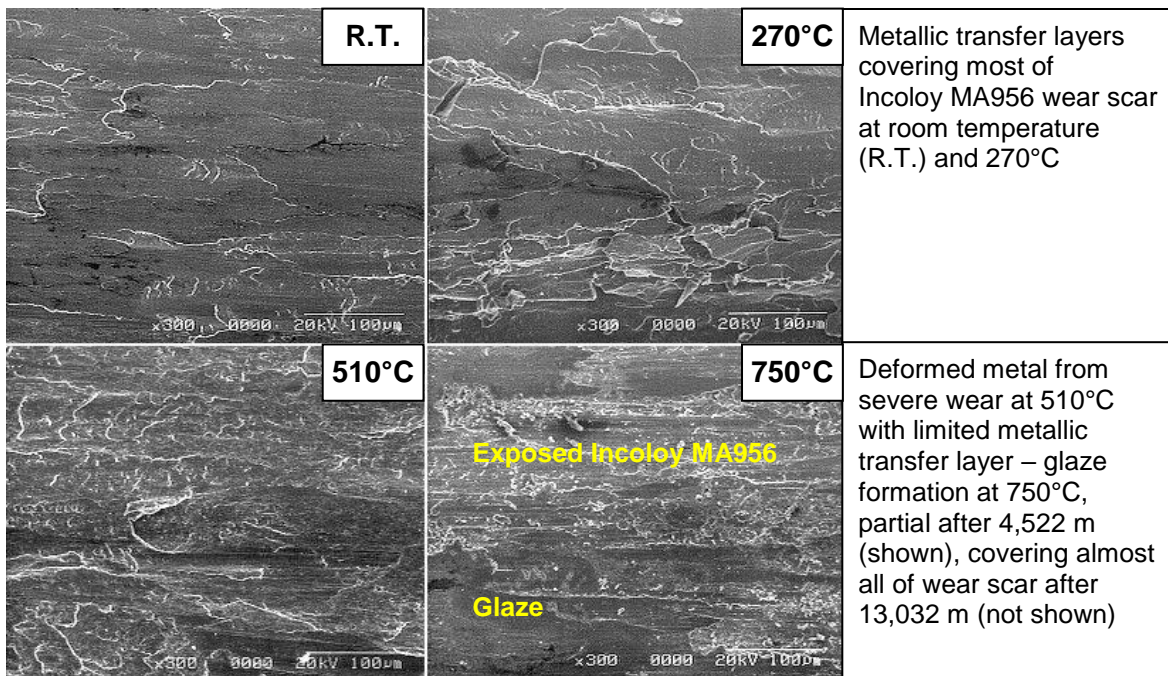
	<b>Room Temperature, 4,522 m – sample</b> (wear scar = 15 x 5 mm) Transfer layer covering 90% of wear scar
	<b>270°C, 4,522 m – sample</b> (wear scar = 15 x 5 mm) Transfer layer covering 75% of wear scar
	<b>510°C, 4,522 m – sample</b> (wear scar = 18 x 5 mm, also 390, 450, 570°C) Reduced metallic transfer with incomplete transfer layers (50%), though greater than at 0.314 m.s <sup>-1</sup> – increasing discoloration of wear surfaces due to limited oxidation
	<b>630°C, 4,522 m – sample</b> (wear scar = 19 x 5 mm) Isolated areas of increased oxidation on asperities (raised areas) of transferred material
	<b>630°C, 13,032 m – sample</b> (wear scar = 20 x 5 mm) No evidence of metallic transfer after 13,032 m, sample more highly worn – also increased oxide build-up on raised areas of sample, beginning to spread across surface
	<b>750°C, 4,522 m – sample</b> (wear scar = 18 x 5 mm, also 690°C) Evidence of significant plastic deformation of the Incoloy MA956, oxide build-up beginning to spread out from asperities
	<b>750°C, 13,032 m – sample</b> (wear scar = 18 x 5 mm) Evidence of significant plastic deformation of the Incoloy MA956, oxide glaze covering almost all of wear scar after continuing sliding up to 13,032 m

**Figure 5.78: SEM micrographs for Incoloy MA956 versus Incoloy 800HT – wear surfaces**

(a)  $0.314 \text{ m.s}^{-1} / 4,522 \text{ m}$  – room temperature,  $270^\circ\text{C}$ ,  $630^\circ\text{C}$  and  $750^\circ\text{C}$



(b)  $0.905 \text{ m.s}^{-1} / 4,522 \text{ m}$  – room temperature,  $270^\circ\text{C}$ ,  $510^\circ\text{C}$  and  $750^\circ\text{C}$

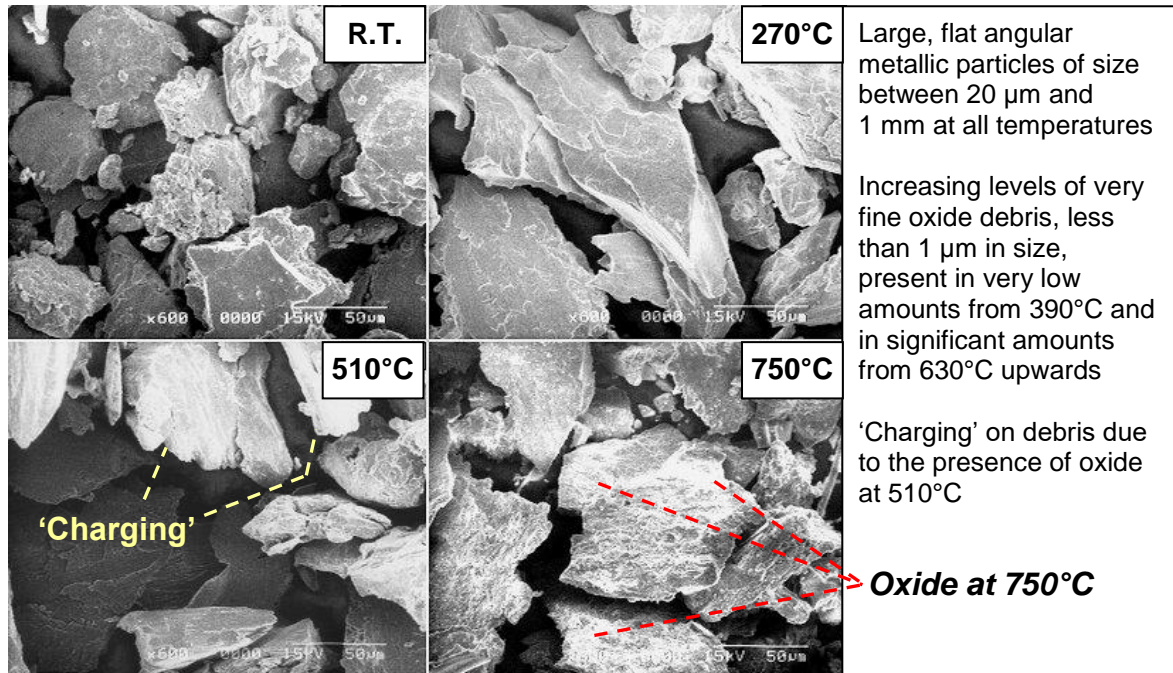


Same pattern of observations made after 13,032 m of sliding, with exception of enhanced glaze formation at  $750^\circ\text{C}$

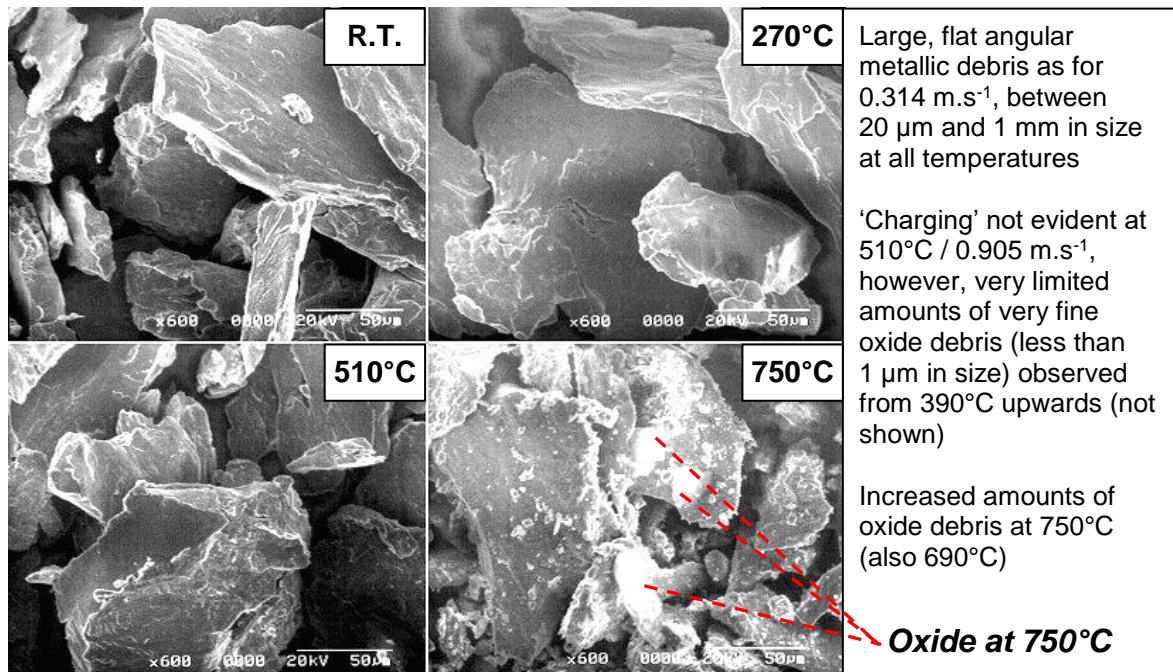


**Figure 5.79: SEM micrographs for Incoloy MA956 versus Incoloy 800HT – debris**

(a)  $0.314 \text{ m.s}^{-1} / 4,522 \text{ m}$  – room temperature,  $270^\circ\text{C}$ ,  $510^\circ\text{C}$  and  $750^\circ\text{C}$






(b)  $0.905 \text{ m.s}^{-1} / 4,522 \text{ m}$  – room temperature,  $270^\circ\text{C}$ ,  $510^\circ\text{C}$  and  $750^\circ\text{C}$






Same pattern of observations made after  $13,032 \text{ m}$  of sliding at  $0.905 \text{ m.s}^{-1}$

**Figure 5.80: Counterface wear scar optical images – Incoloy MA956 / Incoloy 800HT, 0.314 m.s<sup>-1</sup>**

	<p><b>Room Temperature, 4,522 m – counterface</b>  <i>(section = 5 x 15 mm, representative up to 450°C)</i>          Highly worn wear scar with limited transfer layer</p>
	<p><b>570°C, 4,522 m – counterface</b>  <i>(section = 15 x 5 mm, applicable between 510°C and 690°C)</i>          Deeply grooved wear scar, glaze free asperities formed due to transfer and / or back-transfer of metallic debris</p>
	<p><b>750°C, 4,522 m – counterface</b>  <i>(section = 15 x 5 mm, also applicable at 690°C)</i>          Deeply grooved wear scar, glaze forming only on tops of transferred / back-transferred asperities</p>

**Figure 5.81: Counterface wear scar optical images – Incoloy MA956/ Incoloy 800HT, 0.905 m.s<sup>-1</sup>**

*(Observations after 13,032 m of sliding follow same pattern as 4,522 m)*

	<p><b>Room Temperature, 4,522 m – counterface</b>  <i>(section = 15 x 5 mm, applicable up to 450°C)</i>          Highly worn wear scar with limited transfer layer</p>
	<p><b>570°C, 4,522 m – counterface</b>  <i>(section = 15 x 5 mm, applicable between 510°C and 630°C)</i>          Deeply grooved wear scar, glaze free asperities formed due to transfer and / or back-transfer of metallic debris</p>
	<p><b>750°C, 4,522 m - counterface</b>  <i>(section = 15 x 5 mm, also applicable to 690°C)</i>          Wear scar similar to 0.314 m.s<sup>-1</sup>, though slightly fewer asperities (glaze forming on asperity peaks)</p>

At 750°C, there was evidence of material softening and plastic deformation of the Incoloy MA956, the clearest indication of this being 'rims' of material pushed out from sides of the wear interface. These were most apparent on the 0.905 m.s<sup>-1</sup> / 4,522 m and 0.905 m.s<sup>-1</sup> / 13,032 m samples (Figure 5.77).

The large flat platelet-type metallic debris particles typical of delamination wear (Figure 5.79), were produced at both 0.314 m.s<sup>-1</sup> and 0.905 m.s<sup>-1</sup> over the entire range of test temperatures (room temperature to 750°C) – the size range for these particles was anywhere between 20 µm and 1 mm. No oxide was present amongst this metallic debris at room temperature and 270°C. At 390°C, 450°C, 510°C and 570°C, some oxide debris was observed, but only in trace amounts amongst the overwhelmingly metallic debris – this coincided with the discolouration of wear scar surfaces due to very limited oxidation at these temperatures. Further evidence of this limited oxidation (not sufficient to form oxide layers) at lower temperatures, was hinted at by charring on the surfaces of the metallic debris produced at 510°C (Figure 5.79) and 0.314 m.s<sup>-1</sup> during SEM.

Significant levels of oxide debris only became clearly observable in amongst this metallic debris at 630°C and above, which coincided with glaze formation observed at both 0.314 m.s<sup>-1</sup> and 0.905 m.s<sup>-1</sup> – this oxide debris tended to be of size between 300 nm and 1 µm. The level of oxide debris produced increased with temperature between 630°C and 750°C, however, the larger, flattened platelet-like metallic debris (of size 20 µm to 1 mm) was also still clearly observable (Figure 5.79).

#### ***5.5.2.1 Incoloy 800HT Counterface Wear Scar Morphology***

Evidence of severe wear on the Incoloy 800HT counterface (worn against the Incoloy MA956 sample) at both 0.314 m.s<sup>-1</sup> (Figure 5.80) and 0.905 m.s<sup>-1</sup> (Figure 5.81) was observed throughout the range of test temperatures (the patterns of wear were similar to those observed on the Incoloy 800HT counterface when worn against Nimonic 80A). Between room temperature and 450°C, the counterface wear scar was highly worn with a limited transfer layer forming upon it, indicating possible transfer and back-transfer of metallic material between the Incoloy MA956 sample and the counterface. A reduction in this transfer was observed at 390°C and 450°C, coinciding with the appearance of discoloration of the wear surfaces due to limited oxidation.



At 510°C and above, the wear track on the Incoloy 800HT counterface formed a deep groove of up to 1.5 mm depth into the counterface material. Asperities were present on the heavily worn surface of this wear track (slightly fewer asperities were observed at 0.905 m.s<sup>-1</sup>), with asperity-peak height reaching up to 1.5 mm above the level of the unworn surface of the counterface from 570°C upwards. There was no glaze formation until 690°C and then only on asperity-peaks – this matched with the more substantial formation of glaze observed on the wear surfaces of the Incoloy MA956 samples at 690°C and 750°C, at both 0.314 m.s<sup>-1</sup> and 0.905 m.s<sup>-1</sup>.

A large amount of easily dislodged loose oxide debris was observed to be lying in the counterface wear track at 630°C and above, at both 0.314 m.s<sup>-1</sup> and 0.905 m.s<sup>-1</sup>.

### 5.5.3 EDX Analysis – Incoloy MA956 versus Incoloy 800HT

EDX analysis of 0.314 m.s<sup>-1</sup> / 4,522 m samples slid at room temperature indicated clear evidence of transfer of metallic material from the Incoloy 800HT counterface and mixing with the Incoloy MA956 sample material, forming a mechanically mixed transfer layer. This transfer layer, overlying the surface of the Incoloy MA956, had a composition (at room temperature averaging 18% nickel, 29% chromium and 47% iron) intermediate between the Incoloy MA956 and Incoloy 800HT, indicating the level of mechanical mixing to be high. However, the composition was still highly variable (some areas gave compositions close to either the Incoloy MA956 or the Incoloy 800HT), indicating that the mixing process was incomplete.

For samples slid at 0.314 m.s<sup>-1</sup> and temperatures of between 390°C and 570°C, analysis of remaining areas of transferred metallic material indicated a reduction in the nickel present to ~10%, showing a reduced contribution to the transferred material from the Incoloy 800HT counterface. The remaining areas of the wear scar without significant transfer layers, gave values consistent with the Incoloy MA956 sample.

Analysis of the glaze formed at 630°C and above (sliding speed 0.314 m.s<sup>-1</sup>) gave proportions of chromium (26-28%) and iron (60-62%) consistent with the Incoloy MA956, showing the oxidised glaze material at 0.314 m.s<sup>-1</sup> to be sourced almost entirely from the Incoloy MA956 sample – there was very little trace of nickel (0-3%). Aluminium levels

within the glaze layers between 630°C and 750°C were also observed to be higher than expected, on average at around ~7.5% compared to ~4.5% within the unworn Incoloy MA956 alloy.

The 0.905 m.s<sup>-1</sup> samples (slid for both 4,522 m and 13,032m) followed the same pattern as that observed at 0.314 m.s<sup>-1</sup>. A mechanically mixed metallic layer was again formed at room temperature, with material present from both the Incoloy MA956 and Incoloy 800HT (the mean levels of the primary components present were ~19% Ni, ~29% Cr and ~43% Fe). However, the compositions of these layers were still highly heterogeneous – mixing was still incomplete and some areas of the transfer layer were similar in composition to either the Incoloy MA956 or the Incoloy 800HT.

Where transfer was reduced at 390°C and above (sliding speed 0.905 m.s<sup>-1</sup>), surface compositions did not vary too far from that of the Incoloy MA956 sample. Nickel was present to no more than ~3% in remaining areas of deposited material after 4,522 m of sliding (~2% after 13,032 m of sliding), with iron present to ~60% and chromium present to ~27%. This remained the case with similar levels of nickel, chromium and iron on samples slid at temperatures up to and including 630°C, indicating that transfer from the Incoloy 800HT counterface and metallic deposition on the Incoloy MA956 was limited – any metallic deposits present were primarily readhered Incoloy MA956.

At 0.905 m.s<sup>-1</sup>, the Incoloy MA956 substrate remained the primary source of oxide debris from which the glaze formed at 630°C (~0.5% Ni, 25% Cr, ~68% Fe), 690°C (~1% Ni, ~23% Cr, ~67% Fe) and 750°C (~0.5% Ni, ~27% Cr, ~67% Fe), with data very similar for samples slid for 4,522 m and 13,032 m. The increase in sliding speed to 0.905 m.s<sup>-1</sup> did not affect the composition or encourage extra transfer from the Incoloy 800HT. Higher than expected amounts of aluminium were detected between 630°C and 750°C at 0.905 m.s<sup>-1</sup> as they had at 0.314 m.s<sup>-1</sup> – levels of aluminium were recorded at between ~8% and ~11%.

At both 0.314 m.s<sup>-1</sup> (after sliding to 4,522 m) and 0.905 m.s<sup>-1</sup> (after sliding to 4,522 m and 13,032 m), analysis of the metallic debris formed due to sliding between room temperature and 390°C gave mixed results, with composition varying between that of the



Incoloy MA956 sample and that of the Incoloy 800HT counterface depending on the debris particles selected. With debris formed at 390°C and 450°C, the composition tended to match that of the Incoloy MA956, coinciding with the reduction of transfer at these temperatures. With no significant transfer from the Incoloy 800HT evident at either 0.314 m.s<sup>-1</sup> or 0.905 m.s<sup>-1</sup>, Incoloy MA956 remained the almost exclusive source of metallic debris between 510°C and 750°C. Iron levels in the metallic debris varied between ~59% and ~67%, chromium levels varied between ~23% and ~28%, aluminium levels varied between ~5% and ~10%, with nickel levels never exceeding 2.5%. As nickel was only present in the Incoloy 800HT counterface, the data showed that between 390°C and 750°C, there was very little contribution from the Incoloy 800HT counterface to the debris.

Incoloy MA956 was also the near-exclusive source for the loose oxide debris generated at both 0.314 m.s<sup>-1</sup> and 0.905 m.s<sup>-1</sup> (after both 4,522 m and 13,032 m of sliding) for temperatures of 630°C, 690°C and 750°C – levels of iron, chromium and nickel were very similar to those for the metallic debris and the unworn Incoloy MA956 sample material.

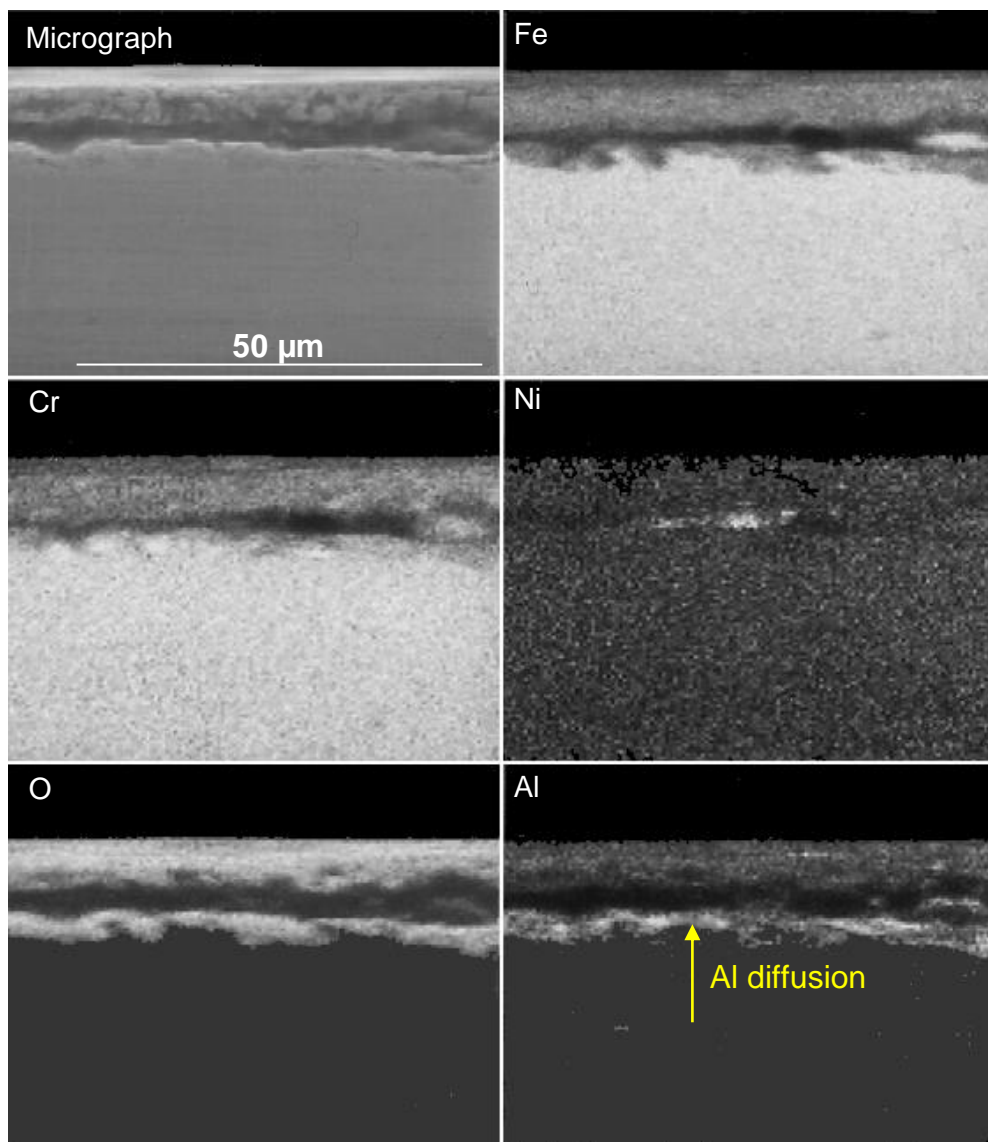
The glaze that formed upon the asperities on the Incoloy 800HT counterface wear track at 750°C and both 0.314 m.s<sup>-1</sup> and 0.905 m.s<sup>-1</sup> (the glaze was removed for analysis), was of a composition intermediate between the counterface and the Incoloy MA956 sample. For samples slid at 0.314 m.s<sup>-1</sup>, a mean composition of ~18% nickel, 20% chromium and 58% iron was obtained. For samples slid at 0.905 m.s<sup>-1</sup>, nickel levels of ~16%, chromium levels of ~21% and iron levels of ~58% were recorded after 4,522 m, with values after 13,032 m near-identical.

#### **5.5.4 EDX Mapping – Incoloy MA956 versus Incoloy 800HT**

Mapping produced similar results, irrespective of the sliding speed used – representative maps for 0.314 m.s<sup>-1</sup> / 4,522 m and 0.905 / 4,522 m, both at 750°C, are shown in Figures 5.82 and 5.83 respectively. Immediately apparent from the mapping was the presence of iron and chromium throughout – as part of the surface layers and the substrate. Nickel was only present as a trace element in the glaze layers at the surface, this indicating only very slight transfer from the Incoloy 800HT counterface.

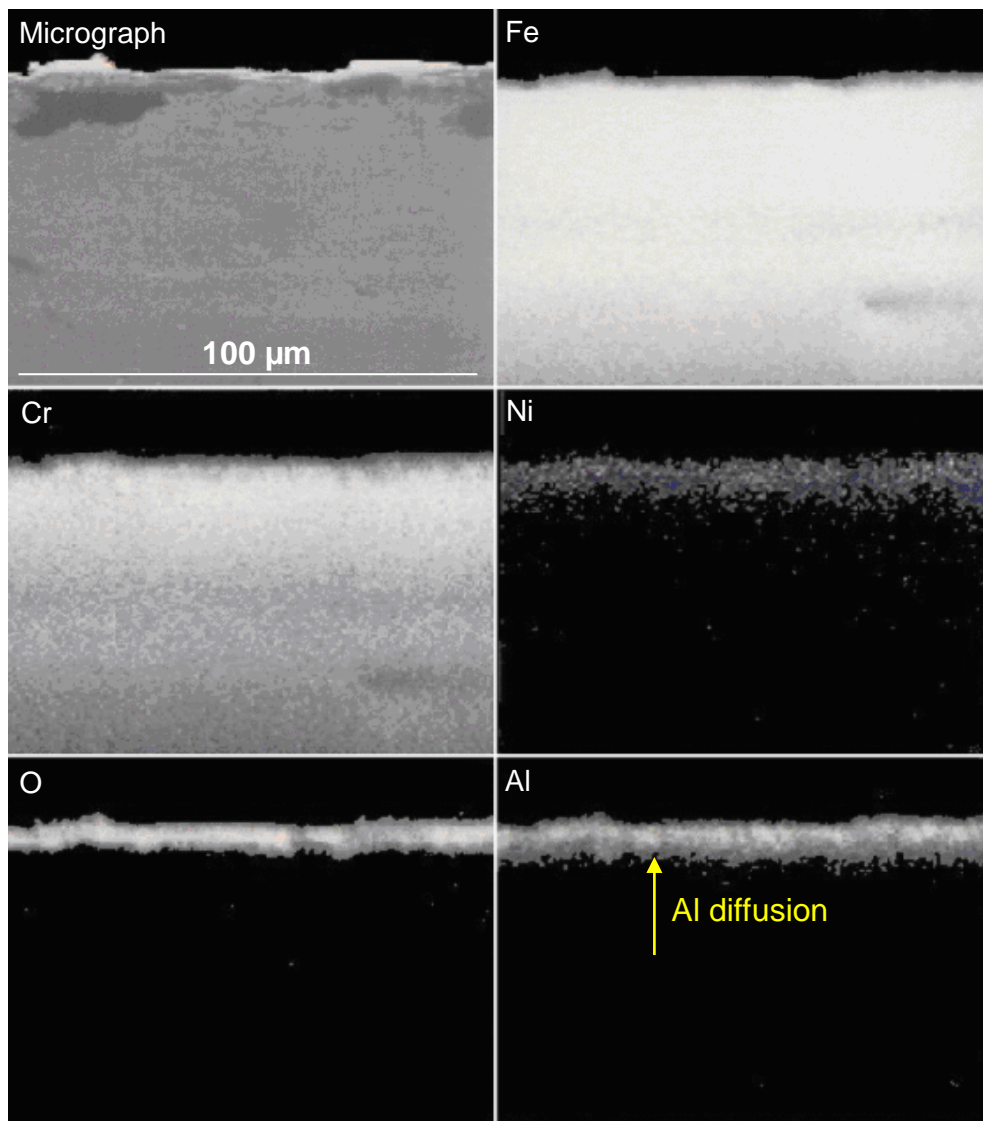
**Figure 5.82: Cross-sectional EDX element maps for Incoloy MA956 worn against Incoloy 800HT subsequent to wear at  $0.314 \text{ m.s}^{-1}$**

*(load = 7N, sliding distance = 4,522 m, temperature =  $750^\circ\text{C}$ )*



**Figure 5.83: Cross-sectional EDX element maps for Incoloy MA956 worn against Incoloy 800HT subsequent to wear at  $0.905 \text{ m.s}^{-1}$**

*(load = 7N, sliding distance = 4,522 m, temperature =  $750^\circ\text{C}$ )*



A far stronger signal was shown by aluminium in the glaze layers at both  $0.314 \text{ m.s}^{-1}$  and  $0.905 \text{ m.s}^{-1}$ . This observation indicates aluminium diffusion from the Incoloy MA956 sample material (aluminium is only present in trace amounts in the Incoloy 800HT counterface and thus its presence cannot be accounted for by transfer) to areas of glaze formation.

#### ***5.5.5 Autopoint EDX Analysis – Incoloy MA956 versus Incoloy 800HT***

Presented in Figure 5.84 are representative examples of the Autopoint EDX data obtained at  $0.314 \text{ m.s}^{-1}$  and  $0.905 \text{ m.s}^{-1}$ , slid for a total of 4,522 m at  $750^\circ\text{C}$ .

At  $0.314 \text{ m.s}^{-1} / 4,522 \text{ m}$ , a two-layer structure was observed on all samples examined, consisting of a glaze layer of no more than  $2 \mu\text{m}$  thickness and a mixed metal-oxide layer, extending to a depth of between 15 to  $20 \mu\text{m}$  ( $17$  to  $18 \mu\text{m}$  in the shown example). Immediately apparent were the negligible amounts of nickel ( $\sim 0.3\%$ ) in the glaze and debris layers - the composition of the debris layers were very close to that of the Incoloy MA956 sample with mean levels of iron at  $\sim 62\%$ , chromium at  $\sim 29\%$ , aluminium at  $\sim 7.5\%$  and trace amounts of silicon at  $\sim 1.4\%$ . This indicates that the Incoloy MA956 substrate was the near-exclusive source for the glaze and mixed metal-oxide debris material.

The levels of iron, chromium and aluminium were observed to be extremely variable within the mixed metal-oxide layer, with changes in iron levels at  $0.314 \text{ m.s}^{-1}$  coinciding with those in chromium (Figure 5.84a) – nickel levels remained near-negligible. Within the mixed debris layer, the highest concentrations of chromium occurred where there were minima in iron concentrations and vice versa. In the example presented in Figure 5.84a, starting from the interface between the debris and Incoloy MA956 substrate at  $17 \mu\text{m}$  depth and moving upwards towards the glaze layers at the surface, for the given test sample:

- at the interface between the debris and the Incoloy MA956 substrate, iron accounted for  $\sim 63\%$  of the metallic content and chromium accounted for  $\sim 28\%$ ;
- at  $14 \mu\text{m}$  depth, an iron minimum was encountered, with concentrations of  $\sim 40\%$  for iron and  $\sim 50\%$  for chromium;

- at 10  $\mu\text{m}$ , iron levels recovered to a peak value at which point chromium was at a minimum (Fe ~71%, Cr ~18%);
- iron values fell once again to a further minimum at 4  $\mu\text{m}$  depth, coincident with another mini-peak in chromium (Fe ~55%, Cr ~32%).

This is indicative of diffusion of either the iron or chromium within the debris layer, resulting in varying concentrations of both within the mixed metal-oxide layer.

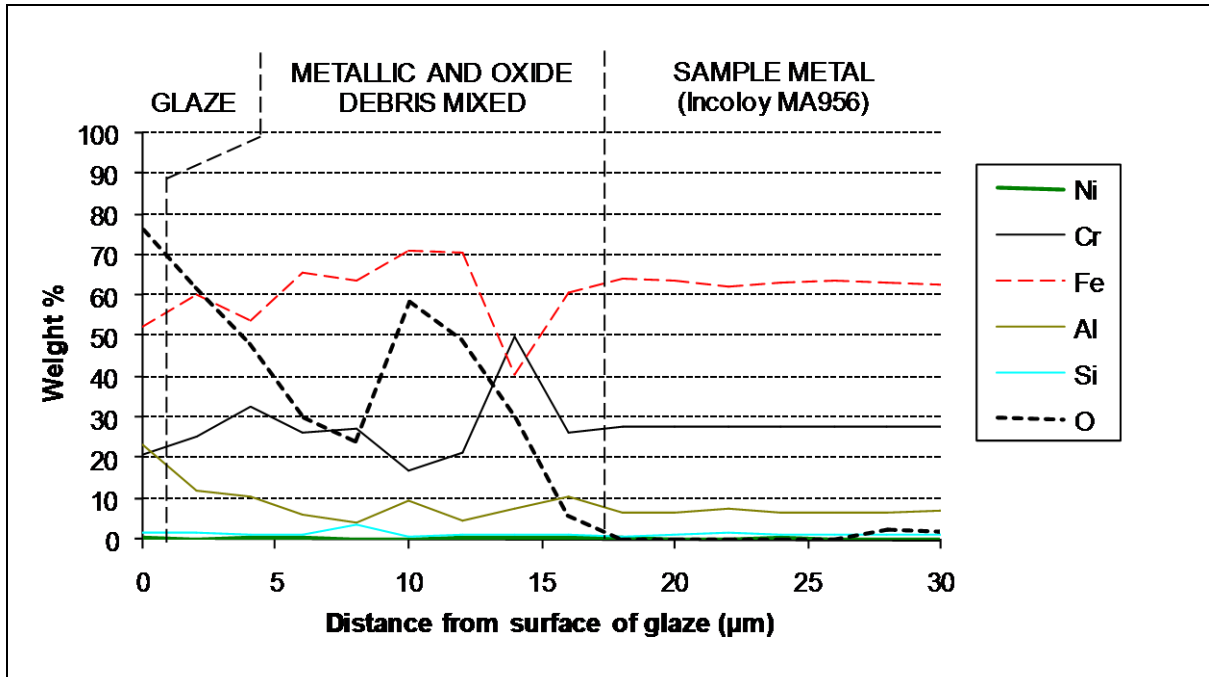
Up to this point, aluminium levels showed some variation, but tended to remain low. However, between 4 to 6  $\mu\text{m}$  depth and the surface (irrespective of sample analysed), both iron and in particular, chromium levels fell with increasing aluminium content. In the example presented in Figure 5.84b, as aluminium rose from ~10% of the metallic content at ~4  $\mu\text{m}$  depth up to ~22% in isolated areas of the glaze surface (though peak values of aluminium were normally no greater than ~12%), iron levels fell from ~55% to ~52% and chromium levels fell from ~32% to ~22% over the same specified distance. Composition values in other samples were similar, with compositions falling into a band 2 to 3% either side of those for the example presented in Figure 5.84b.

There was no clear trend at  $0.314 \text{ m.s}^{-1}$  regarding the iron / chromium / aluminium data with respect to oxygen content within the mixed metal-oxide layer, with oxygen levels increasing erratically from the Incoloy MA956 / debris interface towards the debris surface (although an oxygen peak at 10  $\mu\text{m}$  depth – 58% of the overall content – coincided with the metallic content maximum for iron of 71%). However, the highest oxygen concentrations were observed to match the highest aluminium concentrations at the glaze surface, with oxygen accounting for 78% of the overall content at this point and aluminium accounting for up to 22% of the metallic content in some isolated areas (though levels usually rose to no greater than ~12%). The data is therefore indicating that aluminium has diffused towards the surface, where it was being oxidised in preference to the iron and chromium.

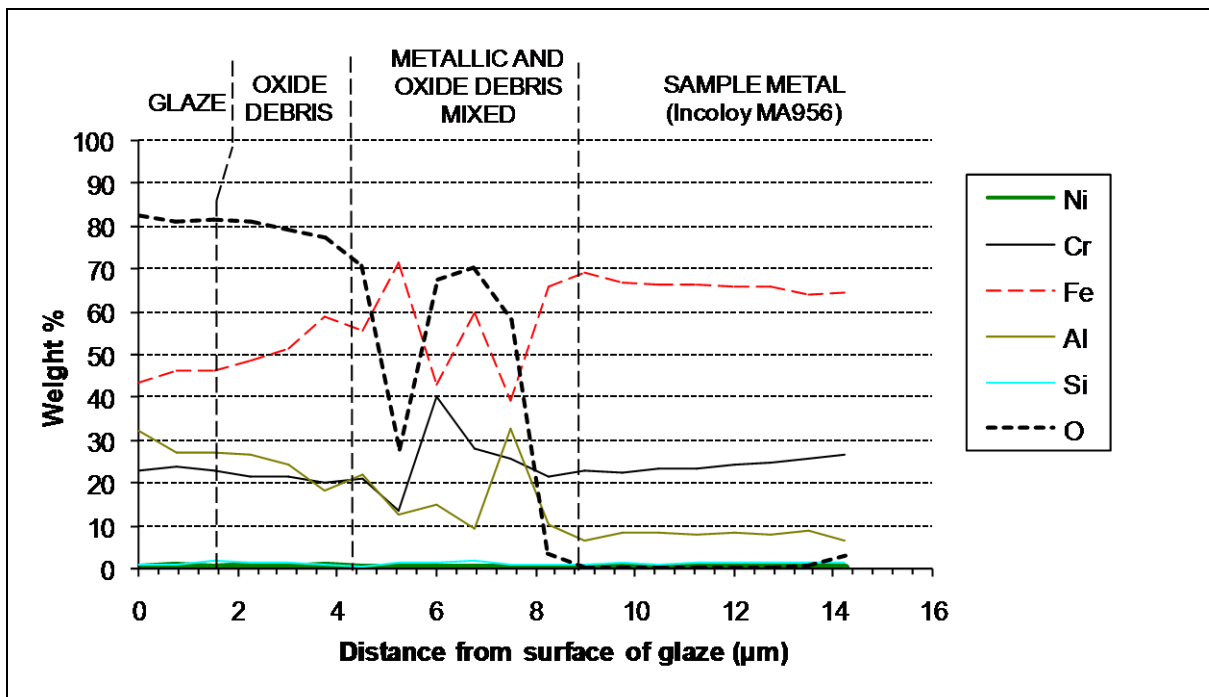
**Figure 5.84: Data from Autopoint EDX analysis for Incoloy MA956 versus Incoloy 800HT at sliding speeds of 0.314 and 0.905 m.s<sup>-1</sup> and 750°C**

Amounts of each substance present are expressed in terms of percentage of the non-oxygen content. Amount of oxygen is expressed in terms of percentage of the overall content. Data (sample size = 3) are for samples slid for a distance of 4,522 m.

(a) 0.314 m.s<sup>-1</sup>



(b) 0.905 m.s<sup>-1</sup>



Increasing the sliding speed to  $0.905 \text{ m.s}^{-1}$  resulted in a multi-layer structure, once again consisting of a glaze layer of no more than 1 to  $1.5 \mu\text{m}$  thickness, a completely oxidised intermediate layer of debris extending to between 4 and  $5 \mu\text{m}$ , and a mixed metal-oxide debris layer extending to the Incoloy MA956 / debris interface at  $7 \mu\text{m}$  to  $12 \mu\text{m}$  depth ( $\sim 9 \mu\text{m}$  in the shown example – Figure 5.84b). The debris layer at  $0.905 \text{ m.s}^{-1}$  (at least at glaze forming temperatures) was thus much thinner than at  $0.314 \text{ m.s}^{-1}$  (at  $15 \mu\text{m}$  to  $20 \mu\text{m}$  thickness).

For samples slid at  $0.905 \text{ m.s}^{-1}$ , there was again at best only a negligible amount of nickel present in the glaze layer. The dominance of iron (present to a mean value of  $\sim 56\%$ ), chromium (mean  $\sim 24\%$ ), aluminium (mean  $\sim 19\%$ ) and a trace amount of silicon ( $\sim 1.25\%$ ) indicated that Incoloy MA956 was the near-exclusive source of the glaze layer. Within the mixed debris layer (starting at  $\sim 9 \mu\text{m}$  depth), iron, chromium and aluminium levels were highly erratic, the iron minima coinciding with peaks of either aluminium (in the example presented in Figure 5.84b, at  $7.5 \mu\text{m}$  depth – iron accounted for 40% and aluminium for 32% of the metallic content) or chromium (in the example presented in Figure 5.84b, at  $6 \mu\text{m}$  depth – Fe 42%, Cr 40%). Nickel levels in the mixed debris layer were negligible, indicating no significant contribution from the Incoloy 800HT counterface.

Towards the surface, iron levels decreased (typically from  $\sim 70\%$  at  $\sim 5 \mu\text{m}$  depth to  $\sim 45\%$  at the glaze surface, with only a small amount of sample-to-sample variation) and chromium levels remained relatively constant (20% to 22%) as aluminium levels in all samples analysed increased from in general  $\sim 10\%$  of the total metallic content at  $7 \mu\text{m}$  to  $10 \mu\text{m}$  depth to as high as 32% on some areas of the surface of the glaze layer (more normal levels were 15-20%). The higher concentrations of aluminium at the surface of the glaze or other areas of high oxidation, were again indicative of diffusion towards the surface and preferential oxidation of this aluminium. Nickel levels were once again negligible within the glaze layers, indicating no significant inclusion of Incoloy 800HT counterface-sourced material.

Unlike  $0.314 \text{ m.s}^{-1}$ , there did appear at  $0.905 \text{ m.s}^{-1}$  to be some match between the variation of the iron content and the oxygen levels in the glaze and mixed debris layers, with peaks



in the iron content coincident with minima in the oxygen levels and vice versa. This was especially the case towards the surface – in the shown example (Figure 5.84b) at 5  $\mu\text{m}$  depth, the iron peak of 72% of metallic content matched a large fall in overall oxygen content to 28%. After this, iron's share of the metallic content decreased to 43% as aluminium's share of the metallic content increased to 32% and oxygen's share of the overall content increased to 82% towards the surface (further indicating preferential diffusion towards and oxidation of aluminium at the glaze surface).

#### 5.5.6 XRD Analysis – Incoloy MA956 versus Incoloy 800HT

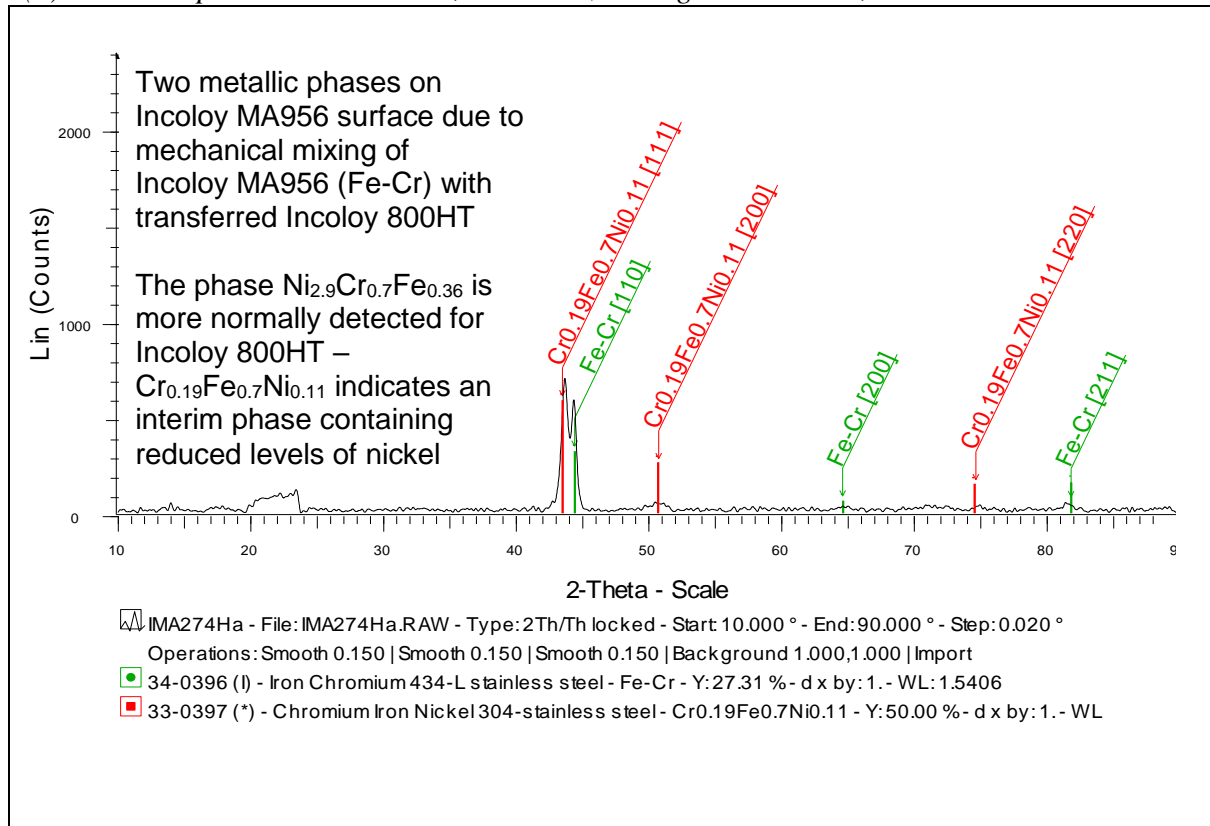
Regardless of sliding speed or temperature, XRD analysis indicated the presence of Fe-Cr in all cases, consistent with the predominantly iron-chromium Incoloy MA956 substrate. However, the presence of other phases depended very much on the temperature and the sliding speed used – this gave three distinct sets of results.

At room temperature and 270°C for both 0.314 and 0.905  $\text{m.s}^{-1}$ , two phases were detected, the aforementioned Fe-Cr and also  $\text{Cr}_{0.19}\text{Fe}_{0.7}\text{Ni}_{0.11}$  (Figures 5.85a and 5.86a). The presence of nickel in the latter phase indicated transfer of material from the Incoloy 800HT counterface, due to the complete absence of nickel in the Incoloy MA956 sample. This corresponds with the physical observation of a transfer layer at these temperatures, which EDX indicated was a mixed layer. In other instances (i.e. Nimonic 80A versus Incoloy 800HT), it has been more normal to obtain  $\text{Ni}_{2.9}\text{Cr}_{0.7}\text{Fe}_{0.36}$  as a nickel-containing phase – the reduced nickel  $\text{Cr}_{0.19}\text{Fe}_{0.7}\text{Ni}_{0.11}$  phase obtained with Incoloy MA956 slid against Incoloy 800HT may be a further indication of a mixed layer and thus was an indication of possible mechanical alloying.

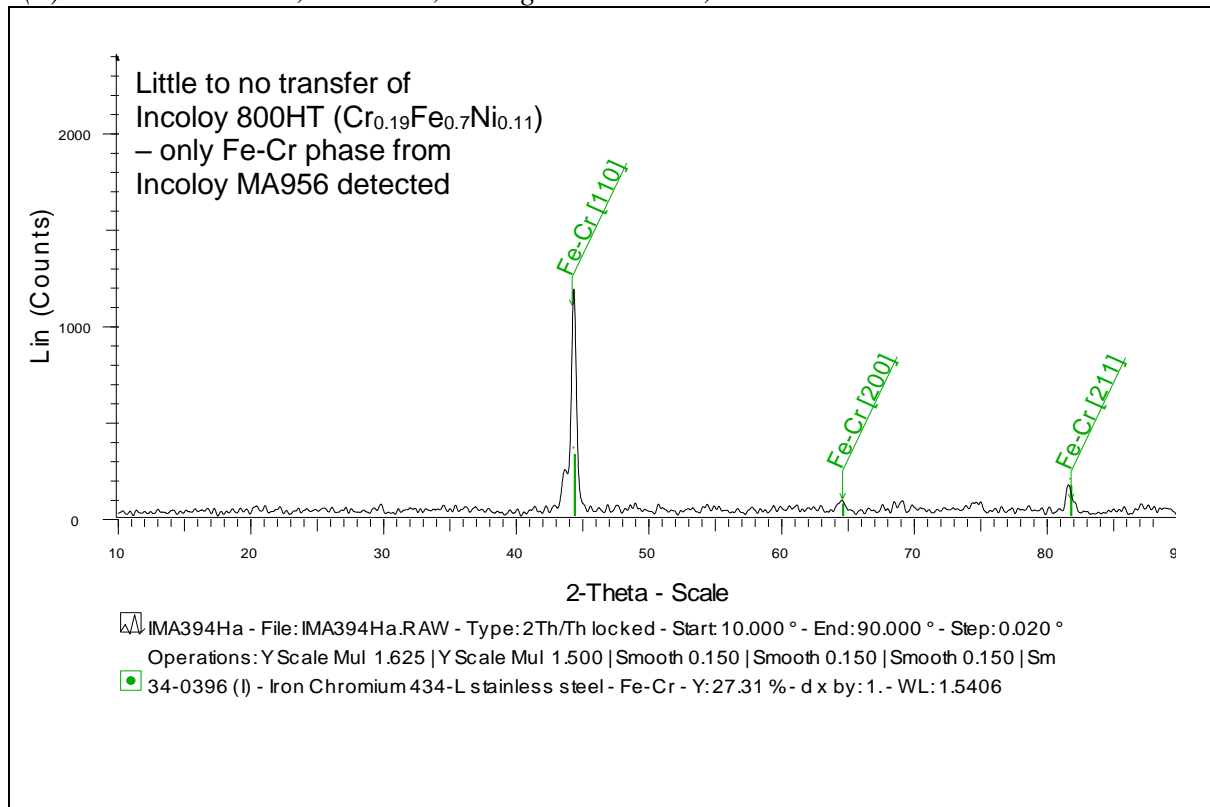
From 390°C (Figure 5.85b) up to the beginning of glaze formation at 630°C at 0.314  $\text{m.s}^{-1}$  and 690°C at 0.905  $\text{m.s}^{-1}$ , obtained results indicated the detection of only one metallic phase – Fe-Cr. This corresponds to the reduction in the transfer of material, as indicated by the observed loss of the transferred layer on the samples. The remaining nickel detected by EDX (in isolated patches of transfer) appears to be insufficient to be detected by XRD.

**Figure 5.85: XRD for Incoloy MA956 versus Incoloy 800HT –  $0.314 \text{ m.s}^{-1}$**

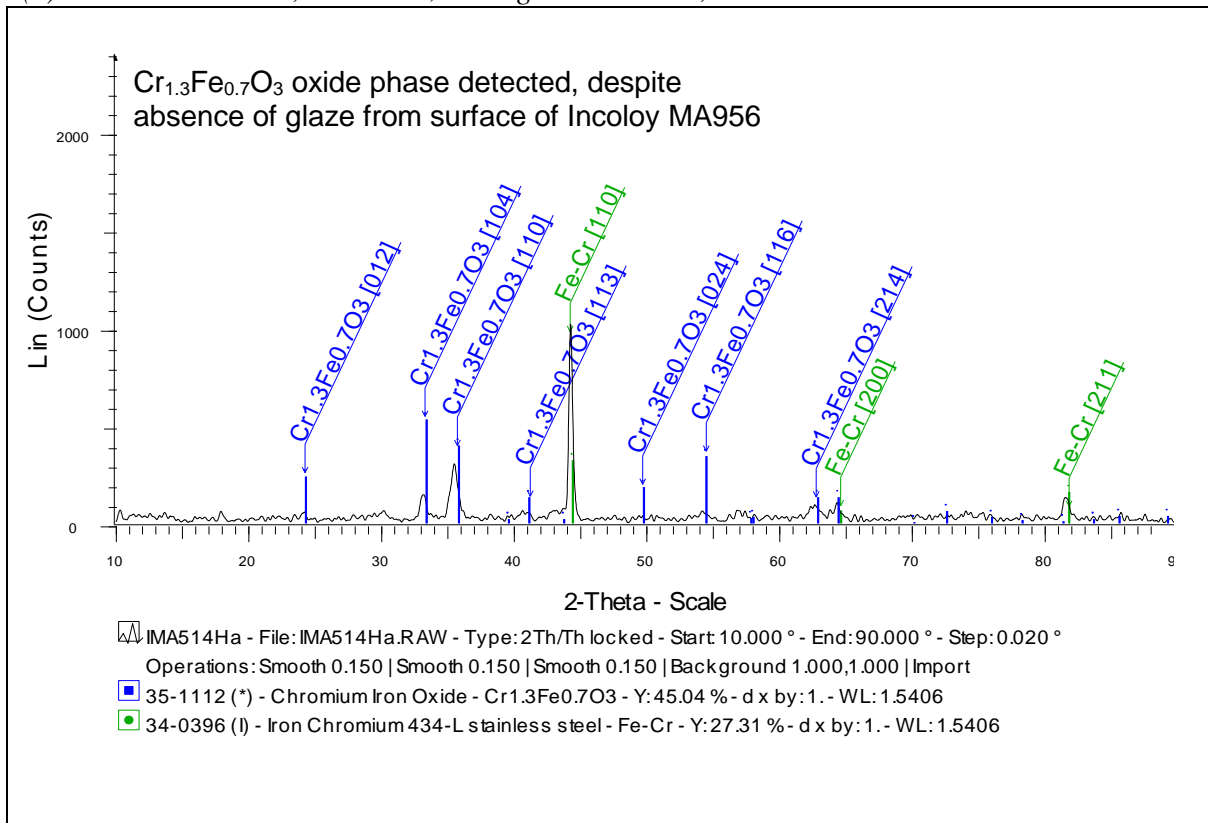
(a) Room temperature and  $270^\circ\text{C}$ , load = 7N, sliding distance = 4,522 m



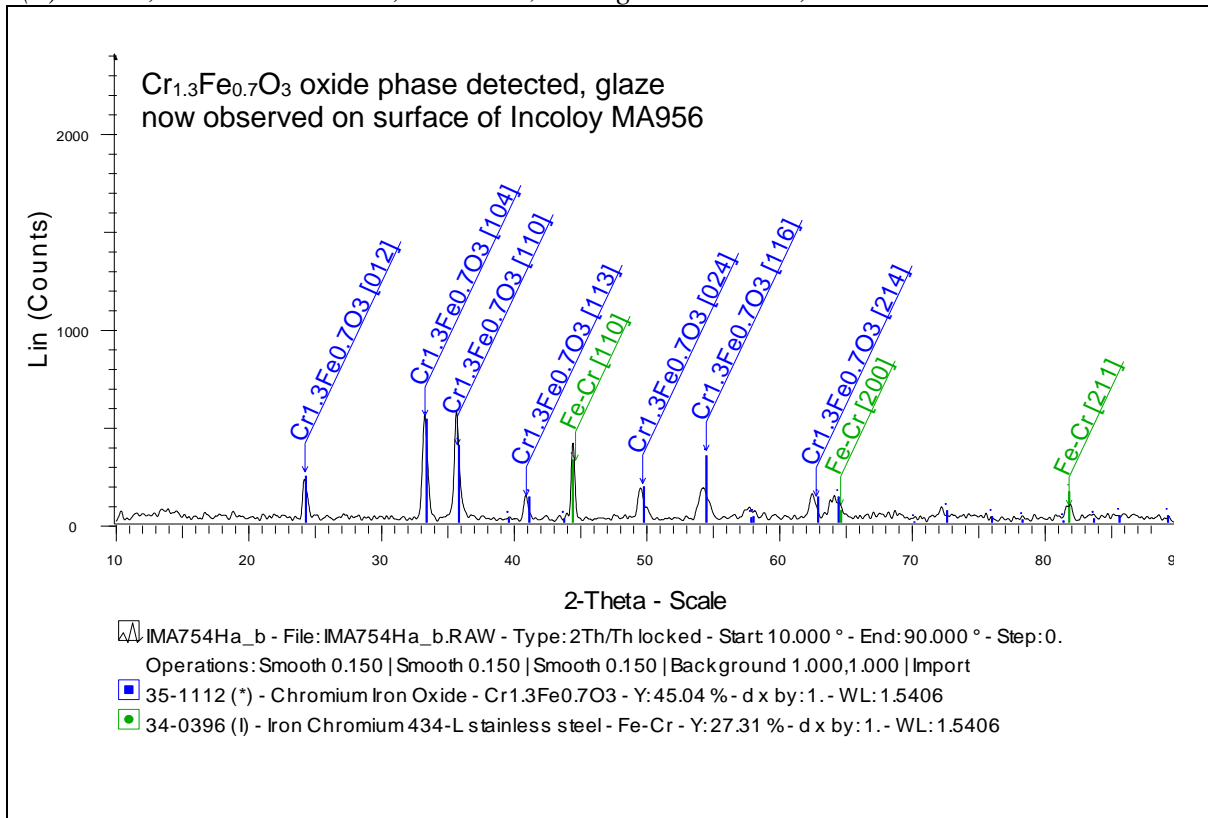
(b)  $390^\circ\text{C}$  and  $450^\circ\text{C}$ , load = 7N, sliding distance = 4,522 m



(c) 510°C and 570°C, load = 7N, sliding distance = 4,522 m

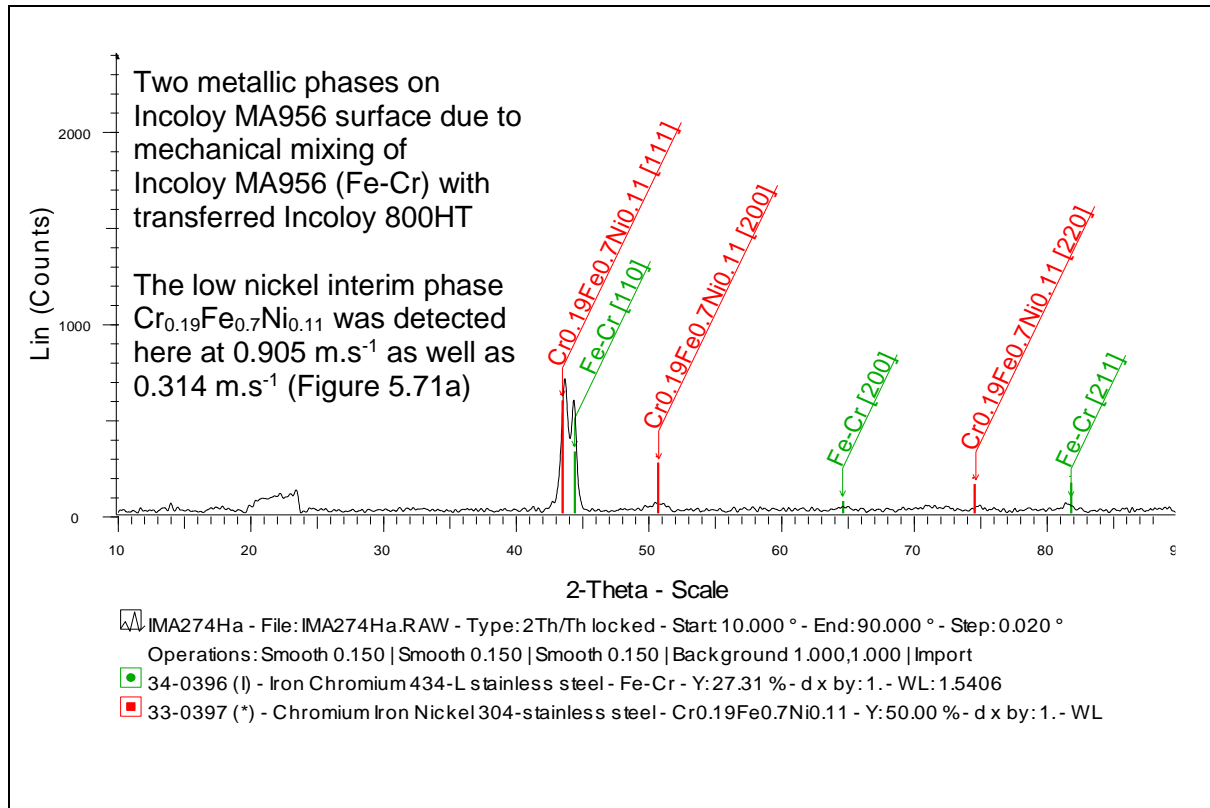


(d) 630°C, 690°C and 750°C, load = 7N, sliding distance = 4,522 m

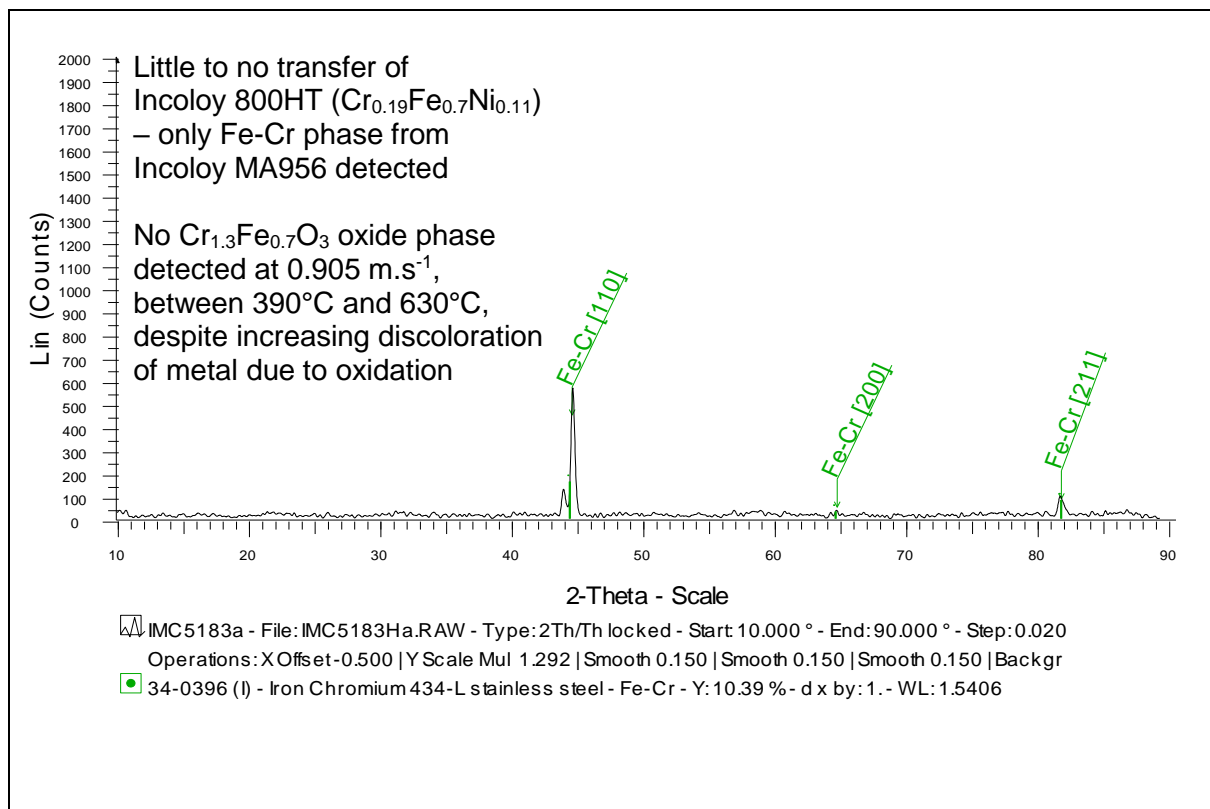


**Figure 5.86: XRD for Incoloy MA956 versus Incoloy 800HT – 0.905 m.s<sup>-1</sup>**

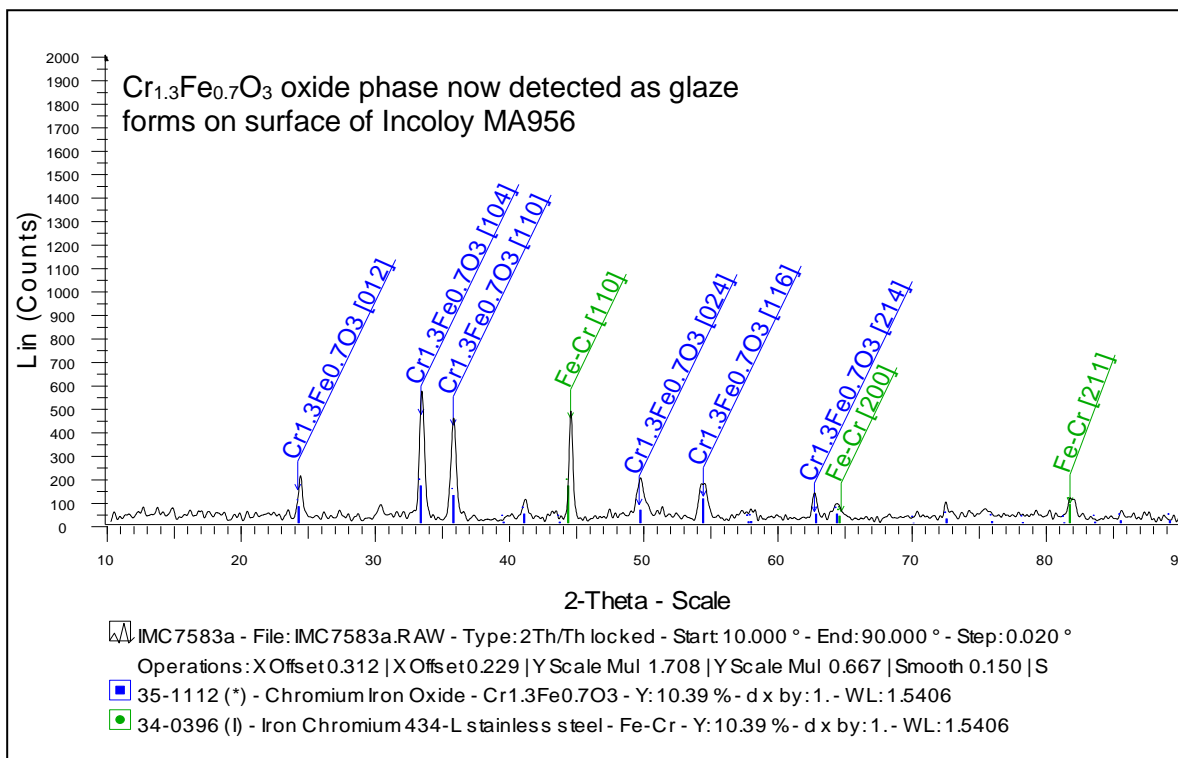
(a) Room temperature and 270°C, load = 7N, sliding distance = 4,522 m / 13,032 m



(b) 390, 450, 510, 570 and 630°C, load = 7N, sliding distance = 4,522 m / 13,032 m



(c) 690°C and 750°C, load = 7N, sliding distance = 4,522 m / 13,032 m



The presence of  $\text{Cr}_{1.3}\text{Fe}_{0.7}\text{O}_3$  was also detected from 510°C upwards (Figure 5.85c) on the  $0.314 \text{ m.s}^{-1}$  Incoloy MA956 samples (despite the absence of clear oxide layers at 510°C and 570°C). This was coincident with the slight charging due to the presence of limited oxide observed on the debris during SEM (Figure 5.79) and the discolouration of metallic surfaces due to oxidation between 390°C and 570°C (Figure 5.76). A stronger signal for  $\text{Cr}_{1.3}\text{Fe}_{0.7}\text{O}_3$  was obtained at temperatures (630°C, 690°C and 750°C) where glaze layers were observed to form on the Incoloy MA956 wear scar surfaces.

XRD analysis did not detect any oxide phase on samples slid at  $0.905 \text{ m.s}^{-1}$  between 510°C and 630°C (Figure 5.86b). This is despite increasing discolouration due to oxidation observed between 390°C and 630°C. At  $0.905 \text{ m.s}^{-1}$ , the  $\text{Cr}_{1.3}\text{Fe}_{0.7}\text{O}_3$  phase was only detected once the glaze layers started to develop at 690°C and 750°C (Figure 5.86c). Increasing sliding speed did not result in any observable changes in the oxide forming the glaze layers. The oxides continued to be sourced primarily from the Incoloy MA956, with no evidence of any nickel-containing oxide phase sourced from the Incoloy 800HT.

Glancing angle XRD was attempted on samples run at 750°C for sliding speeds of 0.314 m.s<sup>-1</sup> and 0.905 m.s<sup>-1</sup>, however, the highly uneven profile of the worn Incoloy MA956 samples at both sliding speeds did not allow for a smooth enough plot to obtain any clear results.

#### 5.5.7 Micro-hardness Testing – Incoloy MA956 versus Incoloy 800HT

At 0.314 m.s<sup>-1</sup>, evidence of enhanced hardening of subsurface layers was minimal (Figure 5.87a shows representative depth hardness profiles taken from samples slid at room temperature, 270°C, 510°C and 750°C), the hardness of these layers being only slightly greater than the underlying, undeformed bulk substrate. This was most pronounced at 750°C with values as high as ~5.1 GPa within the first 0.1 mm below the surface of the wear scar, decreasing to between 3.1 to 3.9 GPa between 0.1 mm and 1 mm. This pattern was less pronounced at room temperature (with peak values of no greater than ~4.5 GPa within 0.1 mm of the surface, falling to and settling between 3.5 GPa and 4.0 GPa between 0.1 mm and 0.5 mm) and 270°C (peak values were no greater than ~4.0 GPa within 0.1 mm of the surface, falling to between 2.9 GPa and 3.6 GPa between 0.1 mm and 0.5 mm), with hardness values becoming erratic after ~0.5 mm depth (varying between ~2.6 and ~4.3 GPa at both temperatures). No such pattern was evident with the 510°C data, although gradual declines in hardness from between 3.9 and 4.4 GPa in the subsurface area to between 3.5 and 3.6 GPa at 1 mm depth were noted at this temperature. No clear trends with temperature were noted.

At 0.905 m.s<sup>-1</sup> (Figure 5.87b shows representative depth hardness profiles taken from samples slid at room temperature, 270°C, 510°C and 750°C), evidence of subsurface hardening was less clear, with only 270°C showing a clear pattern indicating this. Peaks in hardness with the 270°C samples of as high as ~5.1 GPa within 0.1 mm of the wear scar surface were obtained, with values decreasing to in general between 3.8 and 4.1 GPa between 0.1 mm and 1 mm depth. A very gradual downward trend in hardness was also observed in samples tested at 510°C with increasing depth, with peak values in general of 4.2 GPa within 0.1 mm of the surface followed by steady decreases in hardness to 3.55 GPa at ~1 mm depth, without any sharp peak in hardness near the wear scar surface.

No clear pattern was observable in the sub-surface hardness profile data at room temperature or 750°C (sliding speed 0.905 m.s<sup>-1</sup>), with highly erratic values of hardness obtained from samples slid at each of these temperatures. Hardness values of generally between 2.9 GPa and 3.9 GPa were obtained, with variations in readings fluctuating as much as ~30% at room temperature and ~25% at 750°C.

As with Stellite 6 as a counterface material, Incoloy MA956 slid against an Incoloy 800HT counterface again showed far less of a tendency to increased subsurface hardness compared to Nimonic 80A as a sample material.

The mean values of hardness for the transfer layers (Table 5.7) at room temperature and 270°C of 5.82 GPa (room temperature / 0.314 m.s<sup>-1</sup>), 6.72 GPa (room temperature / 0.905 m.s<sup>-1</sup>), 7.11 GPa (270°C / 0.314 m.s<sup>-1</sup>) and 6.10 GPa (270°C / 0.905 m.s<sup>-1</sup>), were consistently higher than the hardness values obtained for both the Incoloy MA956 substrate (4.129 GPa) and the Incoloy 800HT counterface (2.15 GPa). The transfer layers that have formed on the surface of the Incoloy MA956 samples have thus undergone a significant degree of work-hardening.

Due to the absence of transfer layers on either the 0.314 m.s<sup>-1</sup> or 0.905 m.s<sup>-1</sup> samples at temperatures greater than 390°C (only isolated or patchy transfer was observed), no data is presented for temperatures higher than 270°C in Table 5.7.

A large difference in glaze layer hardness for the 750°C samples with sliding speed was indicated by the micro-hardness testing of the surface layers, with average values of 9.6 GPa at 0.314 m.s<sup>-1</sup> and 21.3 GPa at 0.905 m.s<sup>-1</sup>. These values compare with an average value of 4.1 GPa for the unworn substrate (Table 5.8). As with Nimonic 80A versus Incoloy 800HT, no collapse was observed in the glaze layer overlying the Incoloy MA956, with no indication of a substantial loose powdery layer between the glaze and the sample metal.



**Table 5.7: Hardness data for transfer layers at room temperature and 270°C, Incoloy MA956 versus Incoloy 800HT**

(load = 7N, sliding distance = 4,522 m, hardness values in GPa, Vickers micro-indenter - 50g, sample size = 5)

Room temp. / 0.314 m.s <sup>-1</sup>		Room temp. / 0.905 m.s <sup>-1</sup>	
6.313	Mean = 5.82 GPa	6.334	Mean = 6.72 GPa
4.429			
6.377			
5.963			
6.042			
270°C / 0.314 m.s <sup>-1</sup>		270°C / 0.905 m.s <sup>-1</sup>	
5.447	Mean = 7.11 GPa	6.144	Mean = 6.10 GPa
8.765			
4.651			
7.829			
8.836			

(Mean hardness of unworn Incoloy MA956 (sample) = 4.129 GPa,  
mean hardness of unworn Incoloy 800HT (counterface) = 2.15 GPa)

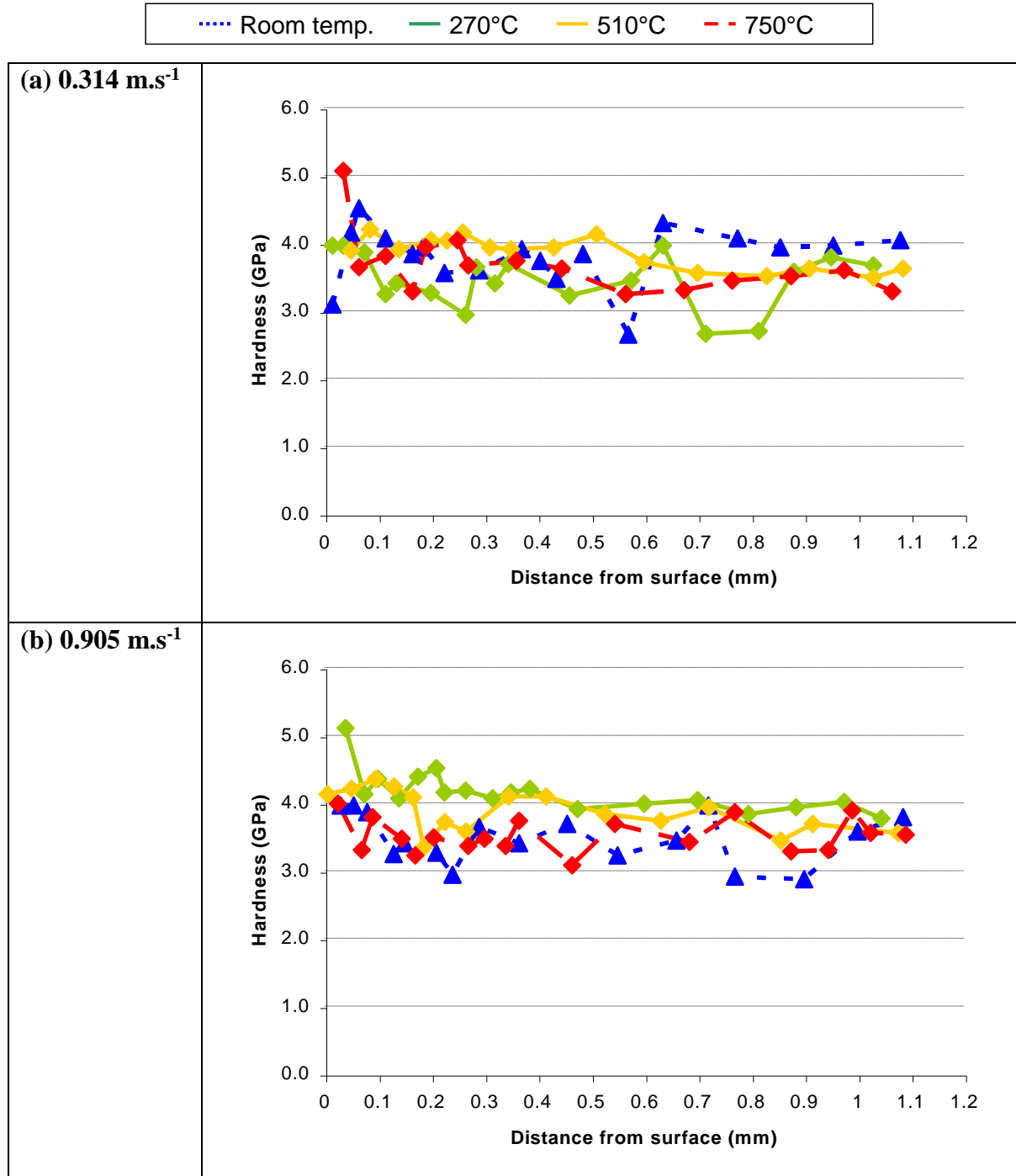
**Table 5.8: Hardness data for glaze and undeformed substrate, Incoloy MA956 versus Incoloy 800HT slid at 750°C**

(load = 7N, sliding distance = 4,522 m, hardness values in GPa, Vickers micro-indenter - 50g, sample size = 5)

Unworn substrate (preheated to 750°C for 4 hours)		Glaze formed at 0.314 m.s <sup>-1</sup>		Glaze formed at 0.905 m.s <sup>-1</sup>	
4.478	<b>Mean = 4.129 GPa</b>	6.110	<b>Mean = 9.63 GPa</b>	19.667	<b>Mean = 21.26 GPa</b>
3.667		7.185		35.659	
3.910		11.743		9.373	
4.237		11.611		17.542	
4.355		11.481		24.044	

**Figure 5.87: Subsurface layer hardness for samples slid at 0.314 and 0.905 m.s<sup>-1</sup>, Incoloy MA956 versus Incoloy 800HT**

(load = 7N, sliding distance = 4,522 m, hardness values in GPa, Vickers micro-indenter - 50g, sample size = 3)



### 5.5.8 *Sliding Without Reciprocation – Incoloy MA956 versus Incoloy 800HT, 510°C and 0.314 m.s<sup>-1</sup>*


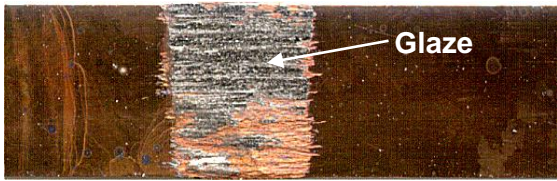
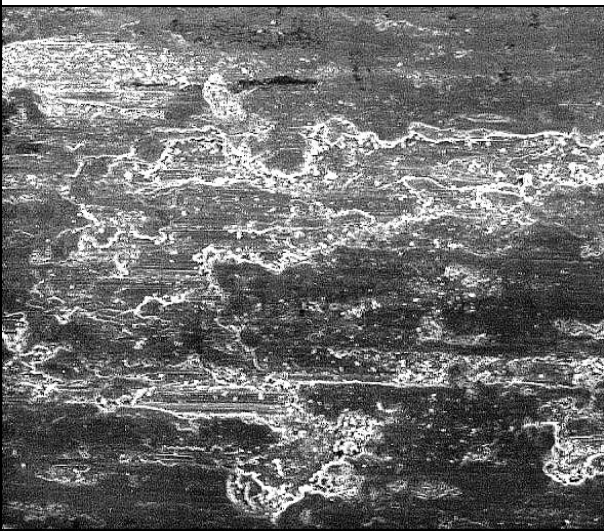
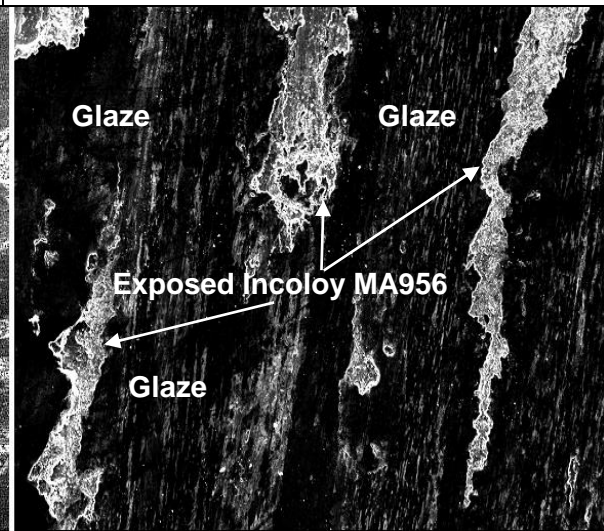
The sliding of Incoloy MA956 versus Incoloy 800HT (counterface) at 0.314 m.s<sup>-1</sup> and 510°C without reciprocation (sample size 3) led to formation of a patchy glaze layer on the surface of the Incoloy MA956 sample (Figure 5.88). The glaze layer directly overlay the Incoloy MA956, with no intermediate metallic transfer layer. This coincided with a significant reduction in wear – the mean recorded weight change after 4,522 m of sliding without reciprocation and only the counterface rotating was -0.030(0) g (wear rate between 0 and 4,522 m, 6.634 µg.m<sup>-1</sup>), compared to -0.108(0) g with reciprocation (wear rate 23.883 µg.m<sup>-1</sup>).

Coefficient of friction values for sliding without reciprocation for the Incoloy MA956 / Incoloy 800HT system varied between 0.57 and 0.63, compared to 0.57 and 0.65 for sliding with reciprocation – the formation of glaze without reciprocation did not have a significant effect on coefficient of friction. The highly variable, unsettled nature of the coefficient of friction data during and just after the ‘run-in’ period indicated that glaze formation did not occur until after on average 125 minutes or 2,355 m of sliding (Figure 5.89). Although sliding without reciprocation has clearly encouraged glaze formation, the reduction in frictional variability indicated that the rate of oxide formation was still sluggish.

EDX indicated the glaze layer was sourced almost exclusively from the Incoloy MA956 sample, consisting of ~60% iron, ~26% chromium, ~8% aluminium and only ~2.5% nickel. This was verified by XRD, which indicated the presence of the iron-chromium oxide phase Cr<sub>1.3</sub>Fe<sub>0.7</sub>O<sub>3</sub>, the same as that observed in the glaze formed with reciprocation between 630°C and 750°C.

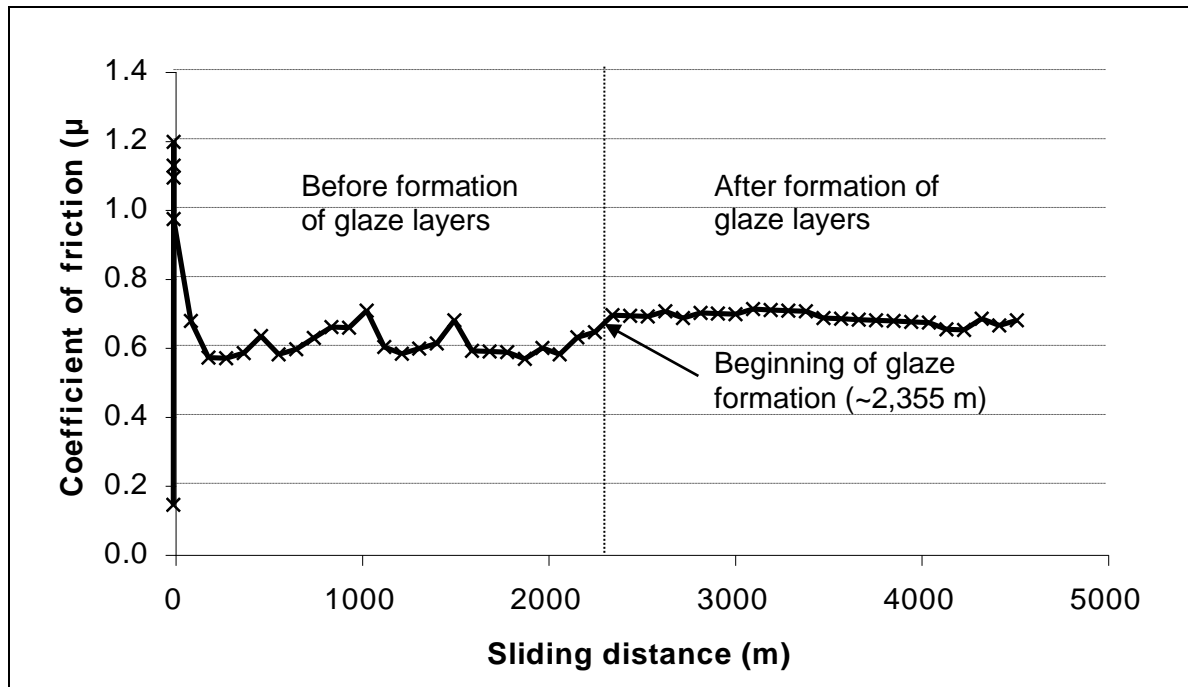
**Figure 5.88: Optical and SEM images of sample surfaces on sliding without reciprocation - Incoloy MA956 versus Incoloy 800HT at 510°C and 0.314 m.s<sup>-1</sup>**

(load = 7N, sliding distance = 4,522 m)

<p><b>With reciprocation</b></p> <p>No evidence of oxide debris accumulation or glaze formation – both the optical image and the SEM micrograph show no evidence of glaze build-up.</p> <p>Only sufficient oxide to discolour the surface and show up in XRD results as Cr<sub>1.3</sub>Fe<sub>0.7</sub>O<sub>3</sub> was present.</p> <p>Mean weight change = -0.108(0) g</p> <p>Coefficient of friction = 0.57 to 0.65</p>	<p><b>Without reciprocation</b></p> <p>Patchy Cr<sub>1.3</sub>Fe<sub>0.7</sub>O<sub>3</sub>-phase glaze formation, covering most of the wear scar surface.</p> <p>Mean weight change = -0.030(0) g</p> <p>Friction = 0.57 to 0.63</p>
 <p>18 mm</p>	 <p>Glaze</p> <p>5 mm</p>
 <p>x300 0510 20kV 100µm</p>	 <p>Glaze</p> <p>Glaze</p> <p>Exposed Incoloy MA956</p> <p>Glaze</p> <p>x300 0510 20kV 100µm</p>

**Figure 5.89: Coefficient of friction versus sliding distance for Incoloy MA956 versus Incoloy 800HT at 510°C and 0.314 m.s<sup>-1</sup> without reciprocation**

(load = 7N, sliding distance = 4,522 m, sample size for each data point = 3)



## 5.6 In-depth Nano-characterisation – Nimonic 80A versus Stellite 6

Previous experimental work has established that Nimonic 80A versus Stellite 6 at 0.314 m.s<sup>-1</sup> developed surface glaze layers at temperatures between 510°C and 750°C. At 750°C, compacted oxide formed on the wear scar surface at 0.314 m.s<sup>-1</sup> was observed to create a smooth adherent layer, with less evidence of breakaway than under other sliding conditions (Figures 5.3 and 5.4). Because of this, the 750°C case was selected for further in-depth characterisation work, using Transmission Electron Microscopy (TEM) and Scanning Tunnelling Microscopy (STM).

However, it was firstly necessary to establish more accurately the levels of hardness in the glaze layers formed at 0.314 m.s<sup>-1</sup> during sliding wear of the Nimonic 80A / Stellite 6 (counterface) system. On attempting micro-hardness testing, the Vickers diamond indenter used was more often than not able to penetrate the glaze layer, at best resulting in hardness values that were not much greater than the metallic substrate (Table 5.1). This problem was avoided by obtaining fresh data with a Hysitron nano-indenter. As well as testing Nimonic 80A samples slid against Stellite 6 at 0.314 m.s<sup>-1</sup> and 750°C, additional

samples were tested that had been slid for the same system at 510°C and also the Incoloy MA956 / Stellite 6 (counterface) system slid at 0.314 m.s<sup>-1</sup> and 750°C.

### ***5.6.1 Nano-indentation Testing – Nimonic 80A and Incoloy MA956 versus Stellite 6***

Table 5.9 shows the load used (nominal and actual values in  $\mu\text{N}$ ), modulus (in GPa) and hardness (also in GPa) obtained from the nano-indentation tests carried out on samples of Incoloy MA956 slid against Stellite 6 at 750°C and Nimonic 80A slid against Stellite 6 at 510°C and 750°C, using a sliding speed of 0.314 m.s<sup>-1</sup> in both cases.

On conducting nano-indentation on glaze layers formed by the sliding of Incoloy MA956 versus Stellite 6 at 750°C and 0.314 m.s<sup>-1</sup>, extremely high hardness values were obtained that were not too far removed from a theoretical hardness value of 28.98 GPa for bulk chromium oxide [116]. Samples 1, 2 and 5 gave nano-hardness values of 20.01, 17.51 and 28.39 GPa respectively, with a nominal test load of 5,000  $\mu\text{N}$ . Very high values for modulus of the glaze layers were also obtained during these nano-hardness tests, of 128.1 GPa for sample 1, 99.1 GPa for sample 2 and 133.8 GPa for sample 5, indicating a very high degree of sintering and little porosity in the nano-indentation areas. This was verifiable by earlier SEM studies (Figure 5.42), where large areas of glaze were observed to be smooth and with little porosity.

A very low value of nano-hardness was obtained for the Incoloy MA956 / 750°C / 0.314 m.s<sup>-1</sup> sample 4 at 6.80 GPa, with a value of 66.3 GPa for modulus. In this case, hardness tests were conducted in areas of extremely high porosity, this failing to offer support for the indenter even with a low applied load of 500  $\mu\text{N}$ . The data for samples 3 and 6 were unusable as the indenter easily penetrated the glaze at an applied test load of 10,000  $\mu\text{N}$ .

High values of hardness and slightly higher values of modulus were also obtained for glaze on Nimonic 80A samples slid against Stellite 6 at 750°C / 0.314 m.s<sup>-1</sup>. Samples 1, 2 and 3 gave nano-hardness values of 24.50, 27.4 and 16.62 GPa and modulus values of 130.2, 131.1, and 110.4 GPa with a nominal load of 5,000  $\mu\text{N}$ . Even with a reduced nominal load of 1,000  $\mu\text{N}$ , sample 4 gave a mean hardness value of 22.01 GPa and modulus value of 147.1 GPa.



The use of a reduced sliding temperature of 510°C for the Nimonic 80A / Stellite 6 (counterface) system at 0.314 m.s<sup>-1</sup> did not have any significant effect on hardness values, though modulus values were noticeably lower. Samples 1, 2, and 4 produced hardness values of 24.80, 24.26 and 26.03 GPa, and modulus values of 99.3, 98.0 and 102.2 GPa. The lower modulus values indicated greater porosity and reduced sintering at 510°C within the glaze layers – this was confirmed by SEM observations showing that samples slid at 510°C were a little more porous and less developed (Figures 5.5, 5.21 and 5.22). Only sample 3 at 510°C did not produce similarly high values of hardness (4.12 GPa) and modulus (51.6 GPa), due to a very high level of porosity in the main test area.

Comparison with micro-hardness values was not possible for Incoloy MA956 versus Stellite 6 at 750°C and 0.314 m.s<sup>-1</sup> (Table 5.9 – the loading / unloading curves for the tests are shown in the figures indicated in the table), and also Nimonic 80A versus Stellite 6 at 510°C and 0.314 m.s<sup>-1</sup>. During micro-hardness testing in each case, the indenter easily penetrated and broke up the glaze layer, thus meaning that it was impossible to obtain micro-hardness data. In the case of Nimonic 80A versus Stellite 6 at 750°C and 0.314 m.s<sup>-1</sup>, a mean hardness value of 6.44 GPa was obtained (maximum 7.32 GPa), far lower than the nano-hardness values obtained of 16.62 to 24.50 GPa – again, many tests were aborted during micro-hardness testing, due to the indenter penetrating the glaze layer.

### ***5.6.2 Nano-scale studies of glaze layers formed on Nimonic 80A samples (slid against a Stellite 6 counterface) at 750°C and 0.314 m.s<sup>-1</sup> using TEM and STM***

Figure 5.90 illustrates a cross-sectional composite transmission electron micrograph of the surface formed during wear testing at 750°C. The micrograph indicates that the wear-affected region consisted of three layers (total thickness ~3µm):

1. the top most layer (the glaze layer) showed the presence of uniform grain structure of size 5-15 nm, some of the grains displaying contrast – the dislocation density in this area was low;
2. the interfacial layer consisted of grains of size 10 – 20 nm and had a higher dislocation density; and
3. the layer just beneath the interfacial layer showed sub-surface deformation and the presence of elongated grains.



**Table 5.9: Nano-indentation data for glaze layers formed on Incoloy MA956 at 750°C, also Nimonic 80A at 510°C and 750°C when slid against Stellite 6**

Sample Material	Test number				Mean
Incoloy MA956 (750°C)	1 (Pass)	2 (Pass)	4 (Fail)	5 (Pass)	(Pass values only)
	Tests 3 and 6 (nominal test load 10,000 μN) failed due to penetration of indenter through glaze, data unusable				
Nominal load (μN)	1,000	5,000	500	1,000	-
Actual load (μN)	996.6	4,963.0	495.8	998.0	-
Hardness (GPa)	20.01	17.51	6.80 (f)	28.39	21.97
Modulus (GPa)	128.1	99.1	66.3 (f)	133.8	120.3
Other observations	Smooth glaze	Smooth glaze	Porosity	Smooth glaze	-
Nimonic 80A (510°C)	1 (Pass)	2 (Pass)	3 (Fail)	4 (Pass)	
Nominal load (μN)	5,000	5,000	5,000	5,000	-
Actual load (μN)	4,969.1	4,967.7	4,943.2	4,968.2	-
Hardness (GPa)	24.80	24.26	4.12 (f)	26.03	25.03
Modulus (GPa)	99.3	98.0	51.6 (f)	102.2	99.8
Other observations	Smooth glaze	Smooth glaze	Porosity	Smooth glaze	-
Nimonic 80A (750°C)	1 (Pass)	2 (Pass)	3 (Pass)	4 (Pass)	
Nominal load (μN)	5,000	5,000	5,000	1,000	-
Actual load (μN)	4,968.4	4,967.8	4,964.1	996.4	-
Hardness (GPa)	24.50	27.34	16.62	22.01	22.62
Modulus (GPa)	130.2	131.1	110.4	147.1	129.7
Other observations	Smooth glaze	Smooth glaze	Smooth glaze	Smooth glaze	-

(f) – Test failed, due to existence of flaws, porosity, etc. on the glaze surface.

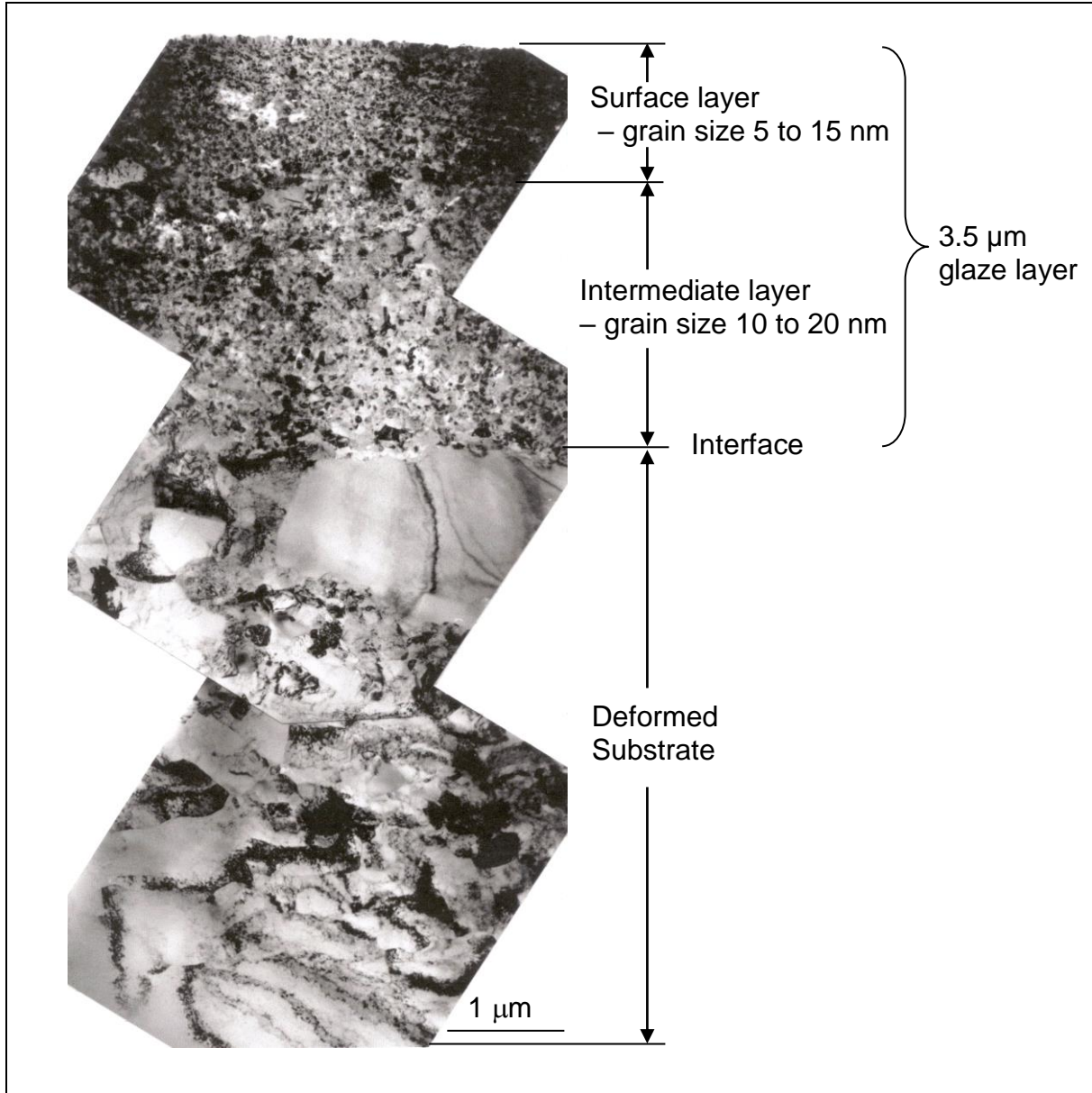
The structure of the glazed layer and the selected area diffraction (SAD) pattern are separately presented in Figure 5.91. The SAD pattern consists of spots arranged in concentric circles indicating the presence of small grains with high angle boundaries, multiple boundaries and large misorientations (formation of misorientated lattice fragmentation). The poorly defined boundaries indicate a non-equilibrium high-energy configuration. The indexed SAD pattern also revealed the presence of oxides of Ni, Cr and Co (Table 5.10) – TEM-EDS additionally indicated location-to-location variation in composition (Figure 5.92), supporting similar observations made during SEM-EDX during which erratic values of cobalt (between ~40 % and ~60%) and nickel (between ~7% and ~25%) were observed. The dark field image indicates phase differentiation within the glaze layer – this may have been due to areas of  $\text{Cr}_2\text{O}_3$  or even  $\text{CoCr}_2\text{O}_4$  /  $\text{Co}_3\text{O}_4$  within the largely NiO glaze layer identified in this region of the glaze.

The occurrence of sub-surface deformation is illustrated in Figure 5.93 – dislocations were observed in the deformed substrate. These dislocations were present as networks inside the deformed (elongated) grains. It was evident that shearing deformation took place in the substrate as a response to the sliding process.

The development of a nano-scale grain structure within the glaze layer was also confirmed by the use of STM topography (Figure 5.94), which indicated grain sizes of 5 to 10 nm – grain thickness was estimated at ~10 nm.

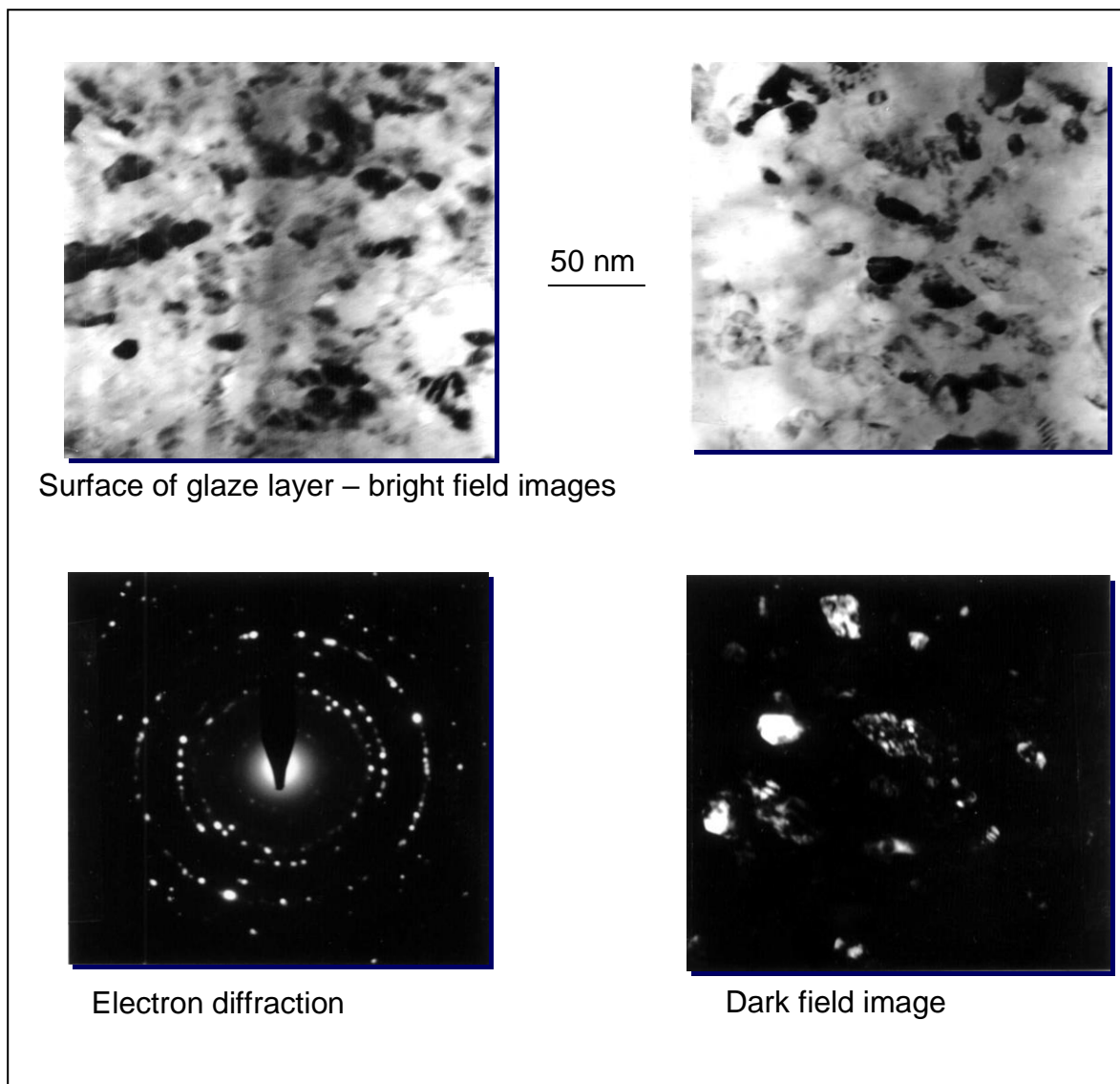
**Figure 5.90: TEM bright field image showing wear induced polycrystalline glaze layer and deformation of Nimonic 80A substrate**

(load = 7N, sliding speed =  $0.314 \text{ m.s}^{-1}$ , sliding distance = 4,522 m, temperature =  $750^\circ\text{C}$ )



**Figure 5.91: TEM morphological and structural details of glaze layer on Nimonic 80A**

(load = 7N, sliding speed =  $0.314 \text{ m.s}^{-1}$ , sliding distance = 4,522 m, temperature =  $750^\circ\text{C}$ )



**Table 5.10: Selected Area Diffraction (SAD) indexing data for glaze layer, produced by wear of Nimonic 80A versus Stellite 6**

(load = 7N, sliding speed =  $0.314 \text{ m.s}^{-1}$ , sliding distance = 4,522 m, temperature =  $750^\circ\text{C}$ )

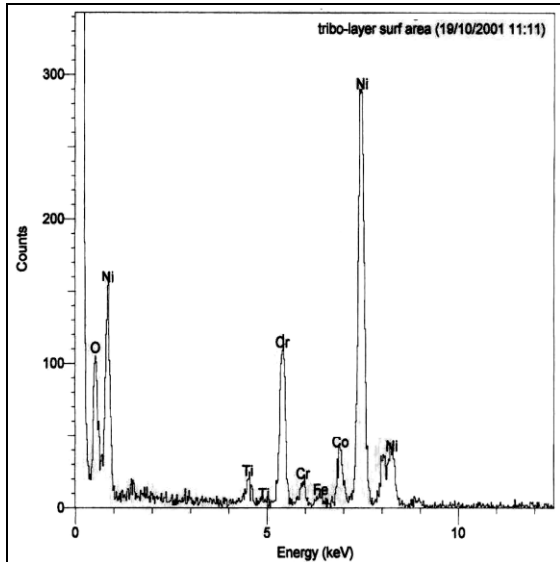
Ring No.	0.3702	0.2488	0.2095	0.1830	0.1676	0.1474	0.1279	0.1202	0.1044
d-sp nm	B	B	A	B	B	A	A	A	A
Index	0.3637	0.2489	0.2090	0.1824	0.1679	0.1480	0.1260	0.1210	0.1040
$ \Delta \%$	1.8	0.1	0.2	0.3	0.2	0.4	1.5	0.7	0.4

A – NiO (JCPD No. 22-1189); B –  $\text{Cr}_2\text{O}_3$  (JCPD No. 38-1479); Aperture:  $\varnothing 1.25 \mu\text{m}$

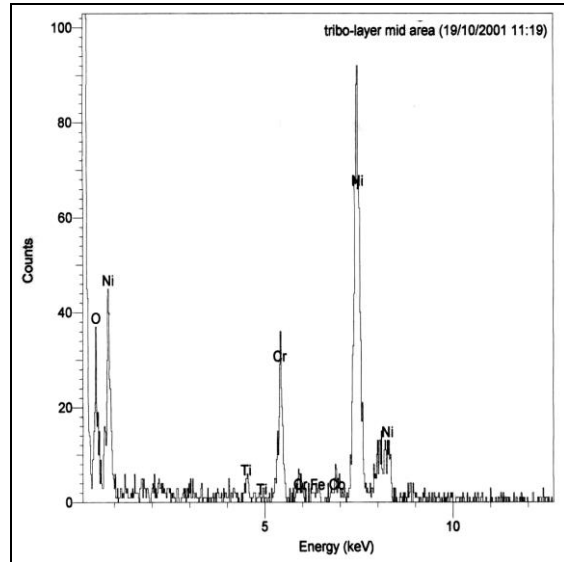
**Figure 5.92: TEM-EDS patterns for glaze and Nimonic 80A substrate**

(load = 7N, sliding speed =  $0.314 \text{ m.s}^{-1}$ , sliding distance = 4,522 m, temperature =  $750^\circ\text{C}$ )

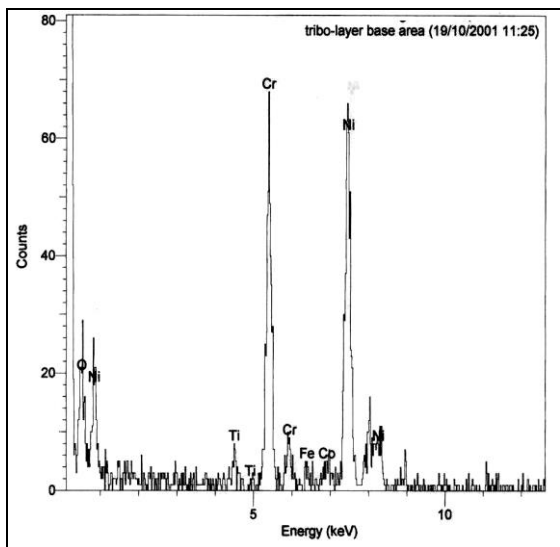
(a) Surface of glaze



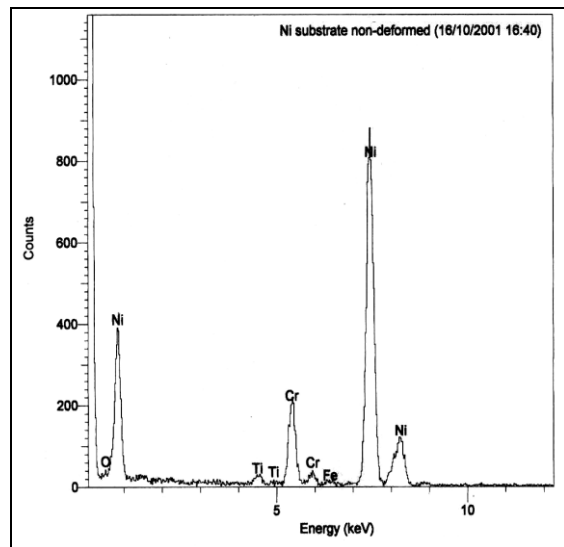
(b) Middle of glaze



(c) Base of glaze, near metal-glaze interface



(d) Metallic substrate

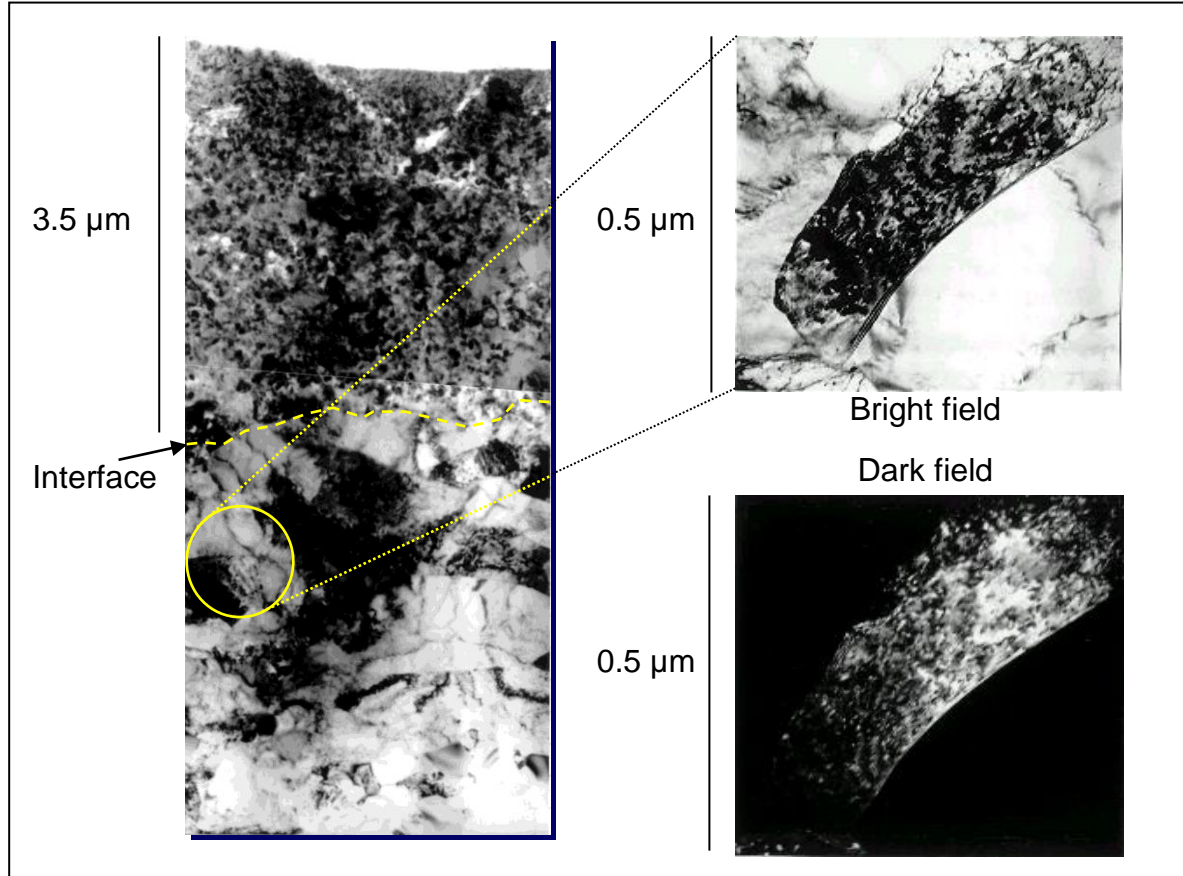


Glaze layers show the presence of Ni, Cr and Co, with variation in amounts from location to location

**Figure 5.93: TEM image showing interface of glaze layer / deformed Nimonic 80A substrate**

(load = 7N, sliding speed =  $0.314 \text{ m.s}^{-1}$ , sliding distance = 4,522 m, temperature =  $750^\circ\text{C}$ )

**(a) Elongation of grains in direction of sliding**

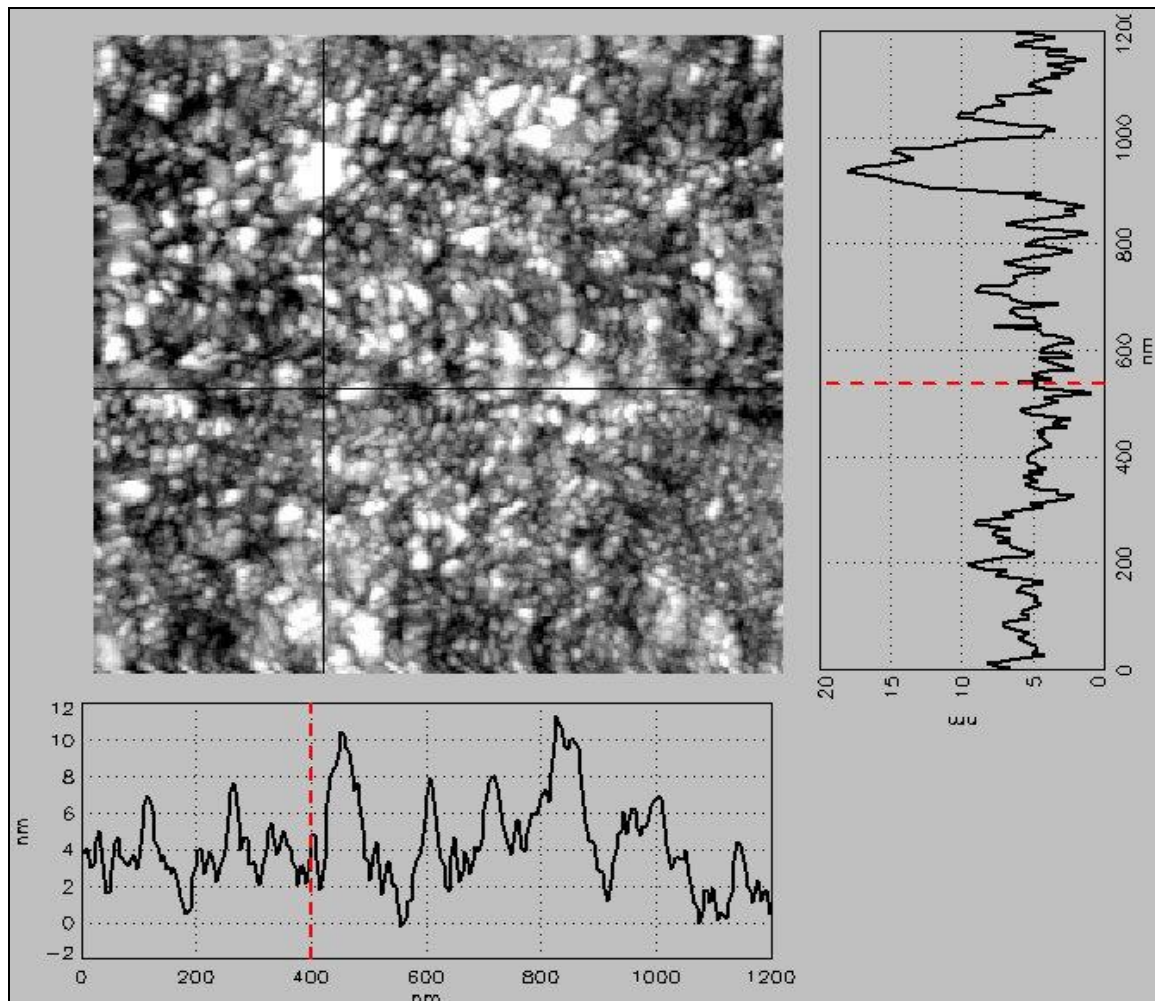


**(b) Twinning structure in the underlying substrate**





**Figure 5.94: STM surface line profile results on glaze layer formed on Nimonic 80A**  
(load = 7N, sliding speed =  $0.314 \text{ m.s}^{-1}$ , sliding distance = 4,522 m, temperature =  $750^\circ\text{C}$ )



STM indicates grain sizes of 5 to 10 nm at surface of glaze



## 6. DISCUSSION

This chapter is divided into five main sections, discussing the results of the experimental programme carried out in this research:

- **Section 6.1** discusses the effect of different sliding speeds on the wear behaviour of Nimonic 80A as a sample when slid against a Stellite 6 counterface over a range of temperatures from room temperature to 750°C. This section also considers glaze formation when pure Ni (Nickel 200™, 99% Ni) was used instead of Nimonic 80A as a sample against a Stellite 6 counterface.
- **Section 6.2** talks about the effect of different sliding speeds on the wear behaviour of Incoloy MA 956 versus Stellite 6 between room temperature and 750°C.
- **Section 6.3** looks at the effect of different sliding speeds on the Nimonic 80A versus Incoloy 800HT system between room temperature and 750°C.
- **Section 6.4** covers the effect of different sliding speeds between room temperature and 750°C on the Incoloy MA956 versus Incoloy 800HT system.
- **Section 6.5** discusses the information obtained from nano-characterisation work using STM, STS and TEM, carried out on glaze formed during the sliding of Nimonic 80A samples against Stellite 6 at 750°C and 0.314 m.s<sup>-1</sup>. The implications of the results from the nano-scale studies in relation to glaze formation theory are considered.

### 6.1 Nimonic 80A versus Stellite 6

#### 6.1.1 *Nimonic 80A versus Stellite 6 between Room Temperature and 750°C, at 0.314 m.s<sup>-1</sup>*

The formation of oxides and their subsequent transformation to glaze with increasing sliding distance and temperature significantly influenced the wear behaviour of Nimonic 80A / Stellite 6 (counterface) system at 0.314 m.s<sup>-1</sup>.

The observed rapid formation of oxide particles from the Stellite 6 surface separating the Nimonic 80A from Stellite 6 was responsible for the low wear of Nimonic 80A, even at room temperature and 270°C where glaze was not developed. At temperatures <390°C, the oxides predominantly resided on the Nimonic 80A surface as patches of loose particles; the

agglomeration of the particles increased with increasing sliding distance and temperature. It is to be noted that the oxide-covered areas on the Nimonic 80A surface displayed variable compositions; areas with low amounts of oxides contained mainly Ni (up to 60%) while the areas with large amounts of oxides showed predominantly the presence of Co (up to 50%) and Cr originating mainly from the Stellite 6 surface. These observations suggest that in the Nimonic 80A / Stellite 6 (counterface) system at  $0.314 \text{ m.s}^{-1}$ , wear predominantly occurred on the Stellite 6 surface.

As the temperature increased the nature of the oxide deposits changed. The loose particles underwent agglomeration and sintering at  $390^{\circ}\text{C}$ , with the onset of glaze formation becoming visible at  $450^{\circ}\text{C}$ . The extent of glaze formation and the coverage of the surface by glaze increased with temperature – the consolidated glaze formed at temperatures between  $510^{\circ}\text{C}$  and  $750^{\circ}\text{C}$ . Once such glaze was formed the wear of the system substantially reduced. Indeed weight gains were observed between  $510^{\circ}\text{C}$  and  $750^{\circ}\text{C}$  (0.000(9) g at  $510^{\circ}\text{C}$ , 0.001(4) g at  $630^{\circ}\text{C}$  and 0.001(0) g at  $690^{\circ}\text{C}$ ).

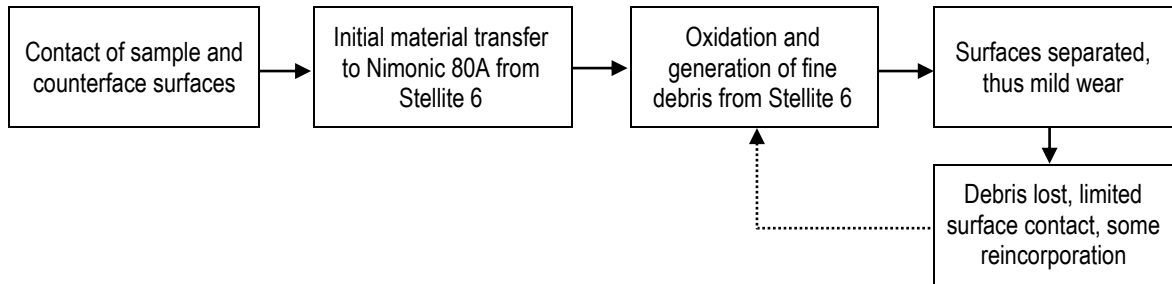
The glaze formed was nano-crystalline in nature and the mechanisms of formation (indicated in Figure 6.1) are explained in more detail in the subsequent Section 6.6.2.

Although it is difficult to ascertain the precise role of the chemical elements in the formation of glaze it is nevertheless important to note that the fully developed glaze (at  $750^{\circ}\text{C}$ ) contained 60% Co and 30% Cr, suggesting the presence of both  $\text{Co}_3\text{O}_4$  and  $\text{CoCr}_2\text{O}_4$  (the latter phase identified by XRD). A preferential role for Co-based oxide in glaze formation in the Nimonic 80A / Stellite 6 system is indicated.

One of the important observations is the preferential wear of the harder Stellite 6 (Figure 6.2) compared to the extremely limited wear of softer Nimonic 80A (Figures 5.1 and 5.25). It is suggested that the initial preferential wear of the harder Stellite 6 in the Nimonic 80A / Stellite 6 system was probably caused by a delamination type of mechanism, due to low fatigue crack growth resistance ( $da/dn$ ) and probably low  $K_{Ic}$  of the Stellite 6. The preferential wear of the Stellite 6 was demonstrated by the reversal of sample and counterface, when the Stellite 6 sample underwent high wear when worn against a Nimonic 80A counterface at  $0.314 \text{ m.s}^{-1}$  and  $750^{\circ}\text{C}$  (Figure 5.25).

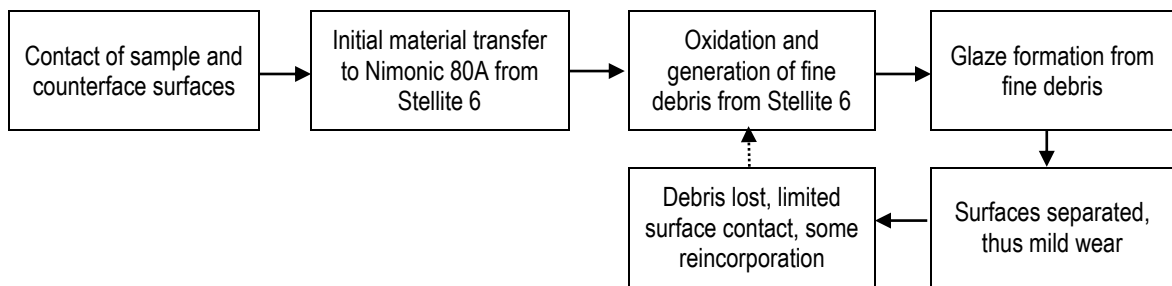
**Figure 6.1: Wear processes for Nimonic 80A versus Stellite 6 from room temperature to 750°C at 0.314 m.s<sup>-1</sup>**

*(a) Nimonic 80A worn with Stellite 6 counterface at room temperature, 270, 390 and 450°C*



After a brief period of contact at the very beginning of sliding, where there was transfer of material from the Stellite 6 counterface to the Nimonic 80A sample, the wear surfaces were separated by fine oxide debris, resulting in mild wear, low friction and low wear rates.

*(b) Nimonic 80A worn with Stellite 6 counterface at 510, 570, 630, 690 and 750°C*

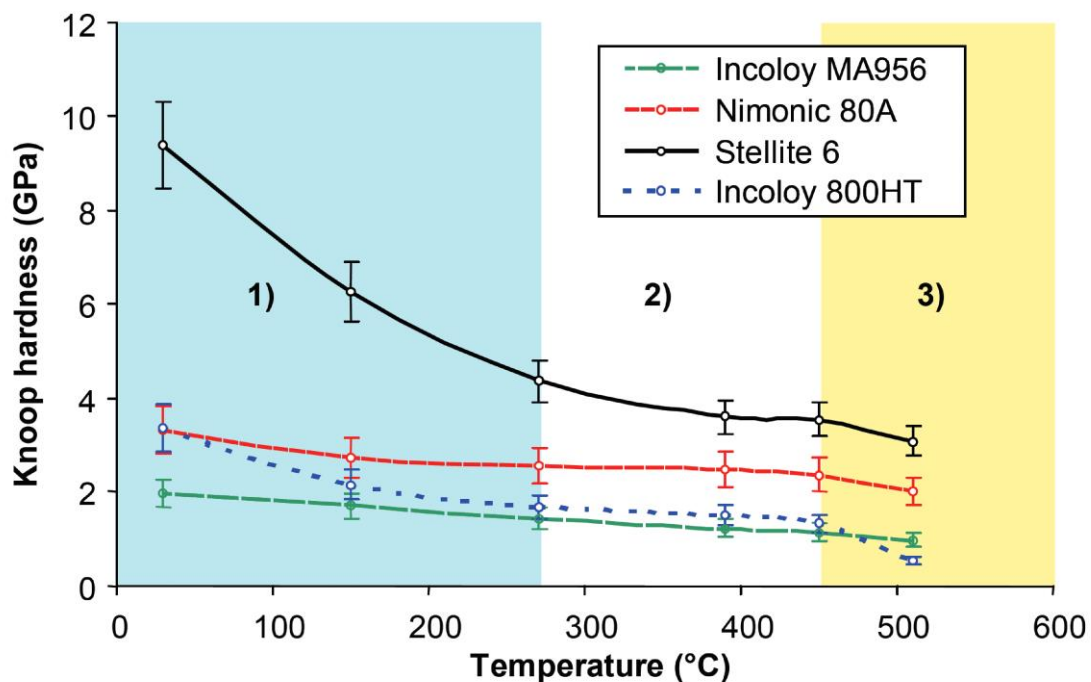


A similar process was followed at 510°C and above to that followed at between room temperature and 450°C. There is one obvious difference – that was the sintering of the fine oxide debris produced to form glaze layers.

Once the oxide debris from the Stellite 6 surface was generated and transferred to the Nimonic 80A surface, the oxide particles remained loose at room temperature to 390°C and did not develop into glaze. These oxides separating the surfaces were abrasive in nature, promoting further wear of the Stellite 6 surface. Another important observation that needs consideration is the enhanced wear of Stellite 6 at higher temperature (510°C to 750°C) leading to the generation of oxide debris and subsequent transfer to the Nimonic 80A surface facilitating the processes of rapid glaze formation and helping to sustain the formed glaze. This is demonstrated by the observed weight gain of Nimonic 80A after as little as 38 m of sliding at 510°C and 750°C (Figure 5.18), and the sustained integrity of the glaze at higher temperature (510°C and 750°C).

**Figure 6.2: Mean Knoop hardness (hot hardness, 50 g load, 12 s dwell time) from room temperature to 510°C [2], with wear regimes with respect to temperature identified for the Nimonic 80A / Stellite 6 and Incoloy MA956 / Stellite 6 systems**

1. Low temperature oxidational wear, moderate falls (large for Stellite 6) in hardness.
2. Low temperature oxidational wear at 0.314 m.s<sup>-1</sup>, metallic severe wear only at 0.905 m.s<sup>-1</sup>, little change in hardness.
3. Glaze formation for Nimonic 80A vs. Stellite 6 at 0.314 m.s<sup>-1</sup> with high oxidational wear replacing metallic severe wear at 0.905 m.s<sup>-1</sup>. Also, early glaze formation for Incoloy MA956 vs. Stellite 6, with extended early severe wear at 0.905 m.s<sup>-1</sup>.



	Mean Knoop hardness (GPa)			
Temperature (°C)	Stellite 6	Nimonic 80A	MA956	Incoloy 800
30	9.39	3.33	1.99	3.38
150	6.28	2.75	1.71	2.16
270	4.37	2.58	1.45	1.68
390	3.61	2.50	1.24	1.52
450	3.55	2.37	1.16	1.34
510	3.08	2.01	0.97	0.55

**Table 6.1: Free energies of formation for key oxides at 727°C formed under conditions of static oxidation [95]**

Oxide	$\Delta G_{727^\circ\text{C}}$ (kJ.mol <sup>-1</sup> )
$2\text{Al} + 1\frac{1}{2}\text{O}_2 \rightleftharpoons \text{Al}_2\text{O}_3$	-1362.4
$\text{Co} + \frac{1}{2}\text{O}_2 \rightleftharpoons \text{CoO}$	-163.3
$3\text{Co} + 2\text{O}_2 \rightleftharpoons \text{Co}_3\text{O}_4$	-525.0
$2\text{Cr} + 1\frac{1}{2}\text{O}_2 \rightleftharpoons \text{Cr}_2\text{O}_3$	-861.6
$\text{Fe} + \frac{1}{2}\text{O}_2 \rightleftharpoons \text{FeO}$ (dominant state above 500°C [14])	-197.2
$3\text{Fe} + 2\text{O}_2 \rightleftharpoons \text{Fe}_3\text{O}_4$ (favoured state between 200°C to 500°C)	-780.8
$2\text{Fe} + 1\frac{1}{2}\text{O}_2 \rightleftharpoons \text{Fe}_2\text{O}_3$ (favoured state below 200°C)	-556.8
$\text{Ni} + \frac{1}{2}\text{O}_2 \rightleftharpoons \text{NiO}$	-150.7
$\text{W} + \text{O}_2 \rightleftharpoons \text{WO}_2$	-405.7

In this context two issues are of importance. In the formation of higher temperature glaze (750°C) rich in Co and Cr oxide, the preferential oxidation of Co and Cr as a necessary condition for the formation glaze is indicated by  $\Delta G$  values in Table 6.1.

The second relevant issue which may cause the increased wear of Stellite 6 leading to increased debris generation facilitating glaze formation, is the hexagonal close-packed to face-centred cubic phase transformation in Stellite 6. Although it is known that Cr increases the transformation temperature by ~150°C to ~900°C [95], it is likely that the interfacial temperature generated by frictional heating and asperity interaction would be sufficient to cause the interface temperature to reach this level. It is also possible that other alloying elements may offset this increase in temperature. The formation of a face-centred cubic phase in Stellite 6 will lead to its easier (easy dislocation slip) deformation and a higher degree of material removal.

Once a sustained glaze is formed, the top part of the glaze undergoes back transfer to the Stellite 6 allowing the Stellite 6 also to develop a Co-based glaze (Figure 5.27). The result is a reduction of overall wear in the system.

The high sustainability of these glaze layers further indicated that the chromium carbides forming a second phase within the Stellite 6 (Figure 5.29) did not disrupt the glaze forming process despite their size (up to 15  $\mu\text{m}$ ). This is evidenced by the lack of sudden changes in coefficient of friction at  $0.314 \text{ m.s}^{-1}$  /  $750^\circ\text{C}$  indicating a breakdown in glaze once ‘steady state’ behaviour was established – Figures 5.2a and 5.26. The hardness levels of these carbides (up to 18 GPa – theoretically no greater than 18.7 GPa) were less than the high-Co/Cr oxides forming the glaze layers (between 20 GPa and 28 GPa – Table 5.9) on both sample and counterface surfaces, thus wear rate was dictated by the hardness of the glaze layers. The softer carbides therefore have been worn away and removed at the same rate as the oxides (which mostly underwent reincorporation as glaze continued to form) as sliding wear of the Stellite 6 continued. Also, as the carbides were worn away and did not penetrate beyond the surface of the Stellite 6 (Figure 5.29), they did not disrupt glaze formation on the opposing Nimonic 80A surface, as was observed elsewhere in the wear of other ‘two-phase’ materials [100].

### ***6.1.2 Nimonic 80A versus Stellite 6 between Room Temperature and $750^\circ\text{C}$ , at $0.905 \text{ m.s}^{-1}$***

At the higher sliding speed of  $0.905 \text{ m.s}^{-1}$ , the wear behaviour of Nimonic 80A against the Stellite 6 counterface showed a marked departure from that observed at the lower speed of  $0.314 \text{ m.s}^{-1}$  for the same system in the same temperature range – room temperature to  $750^\circ\text{C}$ .

At room temperature and  $270^\circ\text{C}$  (Figure 6.3a), the wear process at  $0.905 \text{ m.s}^{-1}$  was confined to the Stellite 6 surface. The loose  $\text{CoCr}_2\text{O}_4$  debris generated at  $0.905 \text{ m.s}^{-1}$  from the Stellite 6 surface residing on the Nimonic 80A surface did not develop into a glaze. Instead, the debris underwent deformation and spreading on the Nimonic 80A surface (Figures 5.3b and 5.4b), especially at  $270^\circ\text{C}$ . The deformed debris, although not forming a glaze, prevented metal-to-metal wear (contact between the Nimonic 80A sample and the

Stellite 6 counterface) and thus was responsible for the low wear rate at room temperature and 270°C.

The failure of the debris to undergo the level of sintering required for the formation of glaze was due to the low residence time of the debris between the wear interfaces (a large amount of debris was ejected at  $0.905 \text{ m.s}^{-1}$ ), reducing the contact times between the particles. Agglomeration and sintering require the particles to maintain their shape integrity, to be able to minimise their surface energy at the contact points between the particles. The deformed particles failed to satisfy this condition.

Between 390°C and 510°C, a severe wear mechanism dominated. The significant metal-to-metal wear of the Nimonic 80A surface accompanied by the production of large, flat, predominantly Nimonic 80A wear debris, indicates the operation of a delamination type of wear mechanism. The Nimonic 80A surface was completely devoid of the presence of wear debris, indicating zero debris retention between the wear interfaces. Although increasing temperature clearly increases the rate of oxidation, no glaze formation occurred due mainly to the low debris retention and low residence time of the debris on the Nimonic 80A surface. In the absence of glaze formation, the situation in this temperature range represented a classic high friction (Figure 5.2b) metal-to-metal contact scenario with wear occurring on the softer Nimonic 80A, probably aided by Nimonic 80A-sourced nickel and chromium oxides (NiO and Cr<sub>2</sub>O<sub>3</sub>) at 510°C.

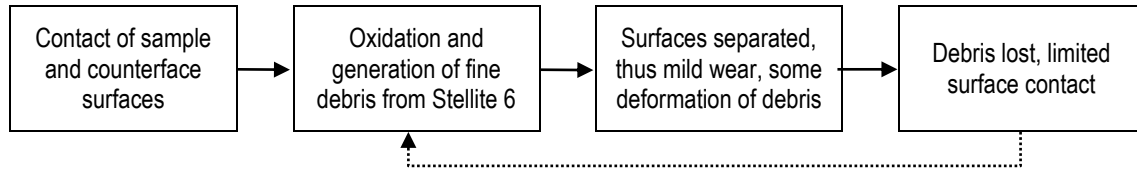
The severe wear mechanism continued to dominate at 570°C and 630°C, despite the generation of increasing levels of NiO and Cr<sub>2</sub>O<sub>3</sub> from the Nimonic 80A, particularly at 630°C. Contact was still metal-to-metal with continued production of large, flat, metallic debris indicating the operation of a delamination type mechanism. The NiO and Cr<sub>2</sub>O<sub>3</sub> produced assisted the wear processes as wear rates were observed to increase for extended sliding as more oxide debris was generated (Figure 5.1b).

The mechanisms for the Nimonic 80A / Stellite 6 system between 390°C and 630°C for a sliding speed of  $0.905 \text{ m.s}^{-1}$  are shown in schematic form in Figure 6.3b.



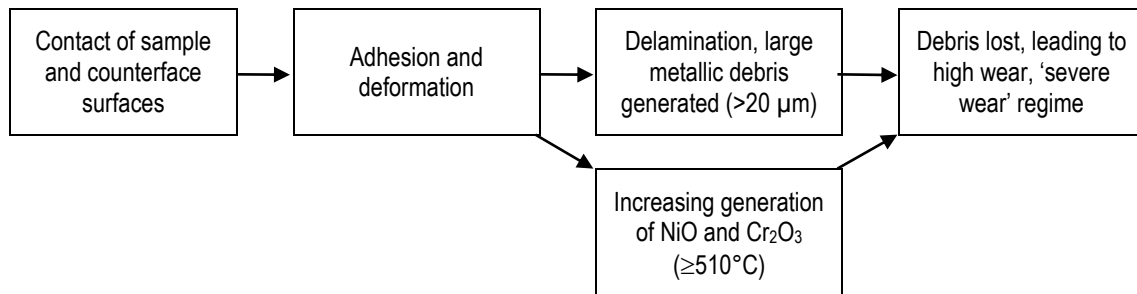
**Figure 6.3: Wear processes for Nimonic 80A versus Stellite 6 from room temperature to 750°C at 0.905 m.s<sup>-1</sup>**

(a) *Nimonic 80A worn with Stellite 6 counterface at room temperature and 270°C*



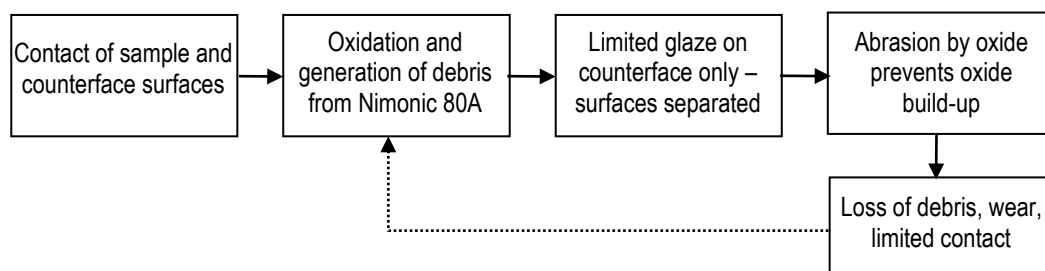
The wear surfaces were separated by fine oxide debris sourced from the Stellite 6, resulting in mild wear and low wear rates – the debris underwent some deformation and spreading. There is less debris present at 0.905 m.s<sup>-1</sup> than at 0.314 m.s<sup>-1</sup> due to high ejection rates.

(b) *Nimonic 80A worn with Stellite 6 counterface at 390, 450, 510, 570 and 630°C*



The large size flattened metallic debris generated by adhesion and delamination wear was unable to remain at the sliding interface – this led to further adhesion between wear surfaces and continued high wear. There was increasing generation of very fine NiO and Cr<sub>2</sub>O<sub>3</sub> from the Nimonic 80A between 510°C and 630°C, which had poor sintering characteristics and acted to assist the wear process.

(c) *Nimonic 80A worn with Stellite 6 counterface at 690°C and 750°C*



The poor sintering characteristics and abrasive action of the NiO / Cr<sub>2</sub>O<sub>3</sub> debris from Nimonic 80A, prevent the oxide debris building up into compacted oxide layers – the ploughing effect of carbides in the counterface proposed by Rose [2] can be discounted due to the presence of a patchy unstable NiO and Cr<sub>2</sub>O<sub>3</sub> glaze layer (only) on the counterface surface.

A change in the wear mechanism occurred at 690°C and 750°C, caused by further increases in the rate of NiO and Cr<sub>2</sub>O<sub>3</sub> generation from the Nimonic 80A surface. At these temperatures, the rate of formation of the oxides was sufficiently high to exceed the rate of debris elimination by ejection from the wear surfaces. Consequently debris retention between the wear interfaces was high enough to eliminate metal-to-metal contact, resulting in a technically mild wear regime (though wear levels remained high) reflected by lower friction values (Figure 5.2b). The large amount of NiO and Cr<sub>2</sub>O<sub>3</sub> did not form glaze (these oxides displayed a very low tendency to sinter and thus form glaze layers) on the Nimonic 80A surface and instead acted as agents to produce further wear by abrasion. The abrasive action of this debris resulted in a pattern of fine parallel wear groves on the highly worn surface of the Nimonic 80A at 690°C and 750°C (Figure 5.6).

Even when glaze was formed on the Stellite 6 surface (Figure 5.3b) by the NiO and Cr<sub>2</sub>O<sub>3</sub> generated from the Nimonic 80A surface (as demonstrated by swapping the sample and counterface materials – Figures 5.27 and 5.28), this glaze was abrasive in nature and promoted further wear of the Nimonic 80A surface.

It is instructive to note that Cr<sub>2</sub>O<sub>3</sub> generated from Nimonic 80A acted as a promoter of wear and disrupted the process of glaze formation. This is further evidenced by the fact that when Nickel 200™ (99% pure Ni) was worn against Stellite 6, the NiO produced rapidly formed a wear protective glaze on the surfaces of both the Nickel 200™ (99% pure Ni) and Stellite 6 in the absence of Cr<sub>2</sub>O<sub>3</sub> (Figures 5.34 and 5.35).

The mechanisms for the Nimonic 80A / Stellite 6 system at 690°C and 750°C for a sliding speed of 0.905 m.s<sup>-1</sup> are shown in Figure 6.3c.

The development of the glaze layer on the Stellite 6 conversely protected the surface of the Stellite 6 from high levels of wear (there was less wear of the Stellite 6 at 0.905 m.s<sup>-1</sup> than at 0.314 m.s<sup>-1</sup> – Figure 5.27), with only a brief period of metal-to-metal wear before the formation of the glaze layer. This additionally means that the enhanced wear of the Nimonic 80A at 690°C and 750°C is solely due to the abrasive action of the oxide debris. The NiO / Cr<sub>2</sub>O<sub>3</sub> glaze layer seals off the surface of the Stellite 6, thus the carbides in the

Stellite 6 cannot be assisting removal of material from the Nimonic 80A by ploughing, as proposed by Rose [2].

### **6.1.3 Wear Map for Nimonic 80A versus Stellite 6**

If the data from current and previous testing are looked at collectively with respect to sliding speed, it is possible to set up wear maps describing the wear behaviour of the Nimonic 80A versus Stellite 6 system as a function of sliding speed and temperature.

The following behaviour was observed at  $0.314 \text{ m.s}^{-1}$ :

- A low temperature mild wear regime existed between room temperature and  $450^{\circ}\text{C}$ , with the wear surfaces separated by a layer of discrete cobalt-chromium oxide particles, primarily from the Stellite 6.
- Mild wear persisted between  $510^{\circ}\text{C}$  and  $750^{\circ}\text{C}$ , with the oxide sintering to form comprehensive glaze layers. The primary source of debris was once again the Stellite 6.

Rose's data [2] collected at  $0.654 \text{ m.s}^{-1}$  suggest the following behaviour:

- A low temperature mild wear regime existed once again between room temperature and  $450^{\circ}\text{C}$ , with a layer of discrete cobalt-chromium oxide particles sourced primarily from the Stellite 6 separating the wear surfaces.
- Severe wear due to direct metal-to-metal contact between sample and counterface dominated between  $510^{\circ}\text{C}$  and  $630^{\circ}\text{C}$ . No oxide could be identified at  $510^{\circ}\text{C}$ , however, increasing levels of nickel and chromium oxide were evident at  $570^{\circ}\text{C}$  and  $630^{\circ}\text{C}$ .
- A mild wear regime was once again evident at  $690^{\circ}\text{C}$  and  $750^{\circ}\text{C}$  – although this was technically a mild wear regime with oxidational wear, Nimonic 80A wear levels remained high due to abrasion by large volumes of nickel and chromium oxide (displaying poor sintering characteristics) sourced from the Nimonic 80A (the material removed then became the abrasive agent). A high nickel-chromium oxide glaze layer existed only on the surface of the Stellite 6 counterface.

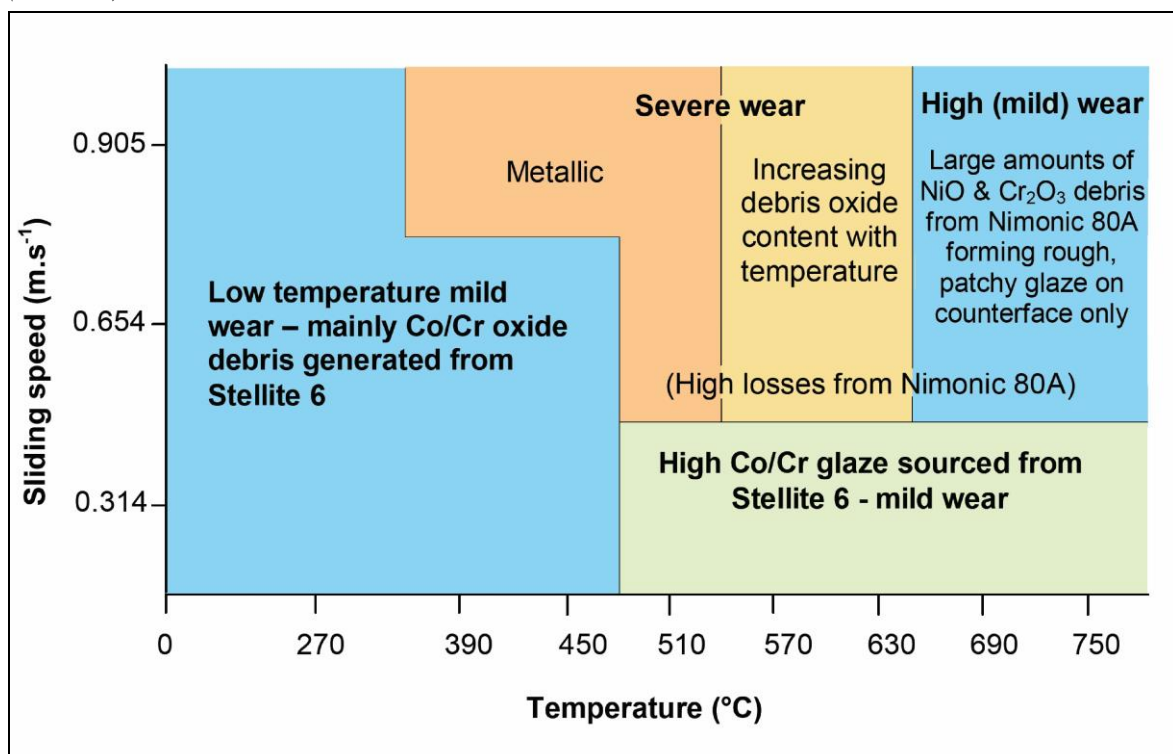
The following behaviour was observed at  $0.905 \text{ m.s}^{-1}$ :

- Low temperature mild wear existed only at room temperature and 270°C, with wear surfaces again separated by discrete cobalt-chromium oxide particles – the main source of debris was once again the Stellite 6.
- Severe wear due to direct metal-to-metal contact dominated between 390°C and 630°C. No oxide was observed between 390°C and 510°C, but at 570°C and especially 630°C, increasing levels of nickel and chromium oxide were observed.
- A mild wear regime was observed at 690°C and 750°C for 0.905 m.s<sup>-1</sup>. As at 0.654 m.s<sup>-1</sup>, this is technically a mild wear regime with oxidational wear, however, high losses from the Nimonic 80A were once again observed due to abrasion by large volumes of Nimonic 80A-sourced oxides. The nickel and chromium oxides produced showed poor sintering characteristics and instead of forming glaze layers, assisted the wear process. A high nickel and chromium oxide, rough patchy glaze layer was again evident only on the surface of the Stellite 6.

Given this information, it is therefore possible to construct the following wear map for Nimonic 80A when slid against Stellite 6 (Figure 6.4).

**Figure 6.4: Wear map for Nimonic 80A versus Stellite 6**

(load 7N)



#### 6.1.4 Elimination of Alloying Elements – Nickel 200<sup>TM</sup> versus Stellite 6 at 750°C

For the Nickel 200<sup>TM</sup> / Stellite 6 (counterface) system, wear of the Nickel 200<sup>TM</sup> was observed to be extremely low and a comprehensive NiO glaze was observed to form on both sample and counterface, with virtually no debris formation from the Stellite 6 – this was regardless of whether the sliding speed was 0.314 m.s<sup>-1</sup> or 0.905 m.s<sup>-1</sup>. It is suggested that the Nickel 200<sup>TM</sup> suffered initial wear and the NiO debris generated, quickly formed oxide glaze layers on both surfaces (Figure 5.34), rapidly reducing the overall wear of the system (Figure 5.32).

This contrasts markedly with the behaviour of the Nimonic 80A / Stellite 6 system, where the oxides generated from the Nimonic 80A failed to form a glaze at 750°C (glaze layers developed from the Stellite 6 oxide debris). There are two reasons depending on sliding speed:

1. At 0.314 m.s<sup>-1</sup>, wear of Stellite 6 occurred extremely rapidly and the surface of the Nimonic 80A was overwhelmingly covered with cobalt-chromium oxides sourced from the Stellite 6 (Figure 5.20), which developed into a protective glaze, preventing the generation of Nimonic 80A debris.
2. The second reason for the absence of Nimonic 80A-sourced glaze may be associated with inherent inability of the alloy debris (80% Ni, 20% Cr) to form a glaze. Some rough glaze containing nickel and chromium oxide debris (NiO and Cr<sub>2</sub>O<sub>3</sub>) did form a glaze layer on the surface of the Stellite 6 counterface, although this occurred only at 690°C and 750°C (Figure 5.4 shows the Stellite 6 counterface wear scar at 750°C).

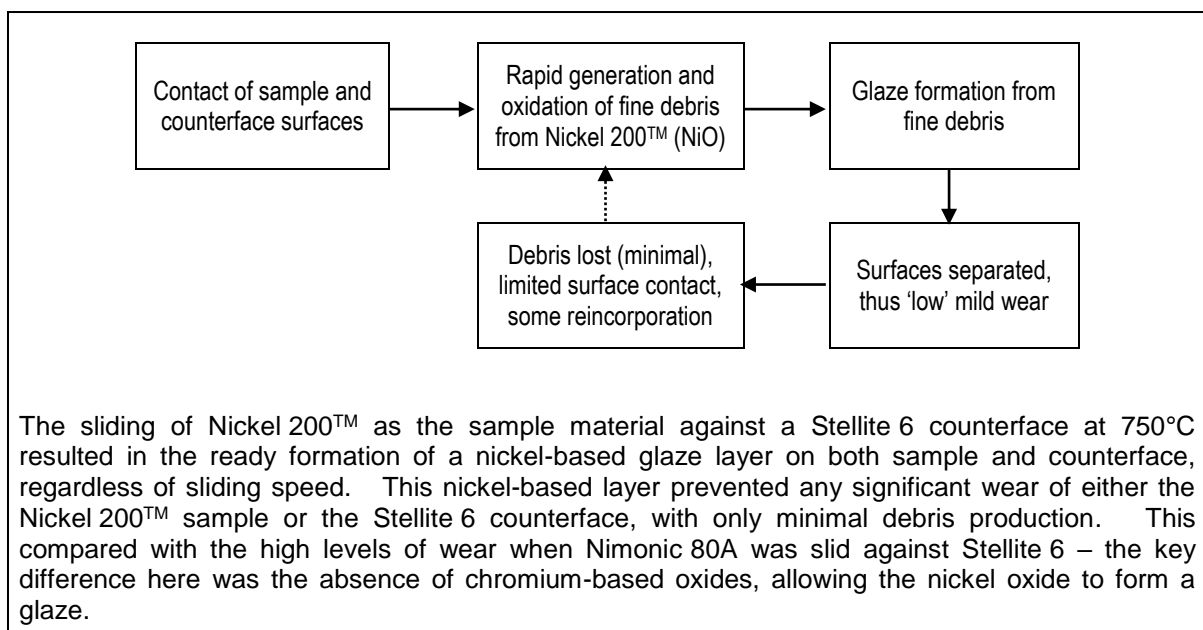
At 0.905 m.s<sup>-1</sup>, the key difference between the oxides produced by the Nickel 200<sup>TM</sup> / Stellite 6 system and the Nimonic 80A / Stellite 6 system is the presence of Cr<sub>2</sub>O<sub>3</sub> in the latter case, where glaze does not form. In addition to the poor sintering characteristics of the mixture of nickel and chromium oxides produced, there is clear evidence of an abrasive element in the oxides produced by the Nimonic 80A (Figure 5.6).

The abrasive component of the oxide clearly altered the morphology of the wear scar at 0.905 m.s<sup>-1</sup>. The highly torn and deformed metallic wear surfaces seen

between 390°C and 510°C in the absence of oxide, was replaced by the development of fine parallel grooves between 570°C and 750°C in the direction of sliding where oxide debris was observed (Figure 5.6 shows the SEM micrographs of the wear surfaces at 510°C, 570°C, 630°C and 690°C).

By substituting Nimonic 80A with Nickel 200<sup>TM</sup>, the oxide solely consisted of NiO, which readily formed glaze layers even at 0.905 m.s<sup>-1</sup>. Thus it can be concluded for the Nimonic 80A / Stellite 6 (counterface) system, that the poorer sintering characteristics and enhanced abrasive action are due to the presence of Cr<sub>2</sub>O<sub>3</sub>, in the nickel and chromium oxide debris sourced from the Nimonic 80A.

**Figure 6.5: Wear processes for Nickel 200<sup>TM</sup> slid against a Stellite 6 counterface at 750°C, for 0.314 and 0.905 m.s<sup>-1</sup>**



## 6.2 Incoloy MA956 versus Stellite 6

### 6.2.1 Incoloy MA956 versus Stellite 6 between Room Temperature and 750°C, at 0.314 m.s<sup>-1</sup>

At 0.314 m.s<sup>-1</sup>, the observed preferential wear of Stellite 6 (Sections 5.3.3 to 5.3.6 – Figures 5.44, 5.46, 5.48 and 5.49) at all temperatures (room temperature to 750°C) had a strong influence on the wear behaviour of the Incoloy MA956 / Stellite 6 (counterface) system, marked by extremely low wear of the Incoloy MA956 (Figure 5.38).

The oxide debris, produced preferentially from the Stellite 6 (with some incorporation of debris from the Incoloy MA956) and residing on the Incoloy MA956 surface (and on the Stellite 6 counterface surface), showed two types of behaviour depending on the temperature. At  $<390^{\circ}\text{C}$ , the debris existed as patches of particles separating the wear surfaces (Figure 5.40), hence reducing the wear of the Incoloy MA956 (Figure 5.38). The agglomeration and consolidation of the particles increased with increasing temperature and sliding distance with sintering first evident at  $390^{\circ}\text{C}$  and the onset of glaze formation occurring at  $450^{\circ}\text{C}$ . The consolidated glaze formed between  $450^{\circ}\text{C}$  and  $750^{\circ}\text{C}$  (Figure 5.40) was effective in further reducing the wear of the whole system (Figure 5.38). The formation of these glaze layers was similar to that observed in the case of the Nimonic 80A / Stellite 6 system.

Although the exact effect of each of the chemical elements in the glaze is uncertain, a key role for Co-based oxides is indicated in the development of rapidly forming wear protective glaze layers for the Incoloy MA956 / Stellite 6 system as it was for the Nimonic 80A / Stellite 6 system. The completely developed glaze in the Incoloy MA956 / Stellite 6 system (between  $450^{\circ}\text{C}$  and  $750^{\circ}\text{C}$ ) consisted of  $\sim 40\%$  Co and  $\sim 32\%$  Cr, again suggesting the presence of  $\text{Co}_3\text{O}_4$  and  $\text{CoCr}_2\text{O}_4$  (detected by XRD). However, the presence of higher levels of Fe (15-19% between  $450^{\circ}\text{C}$  and  $750^{\circ}\text{C}$ ) indicates a significant contribution to the glaze from the Incoloy MA956 – the role of the Fe at this time is, however, unclear.

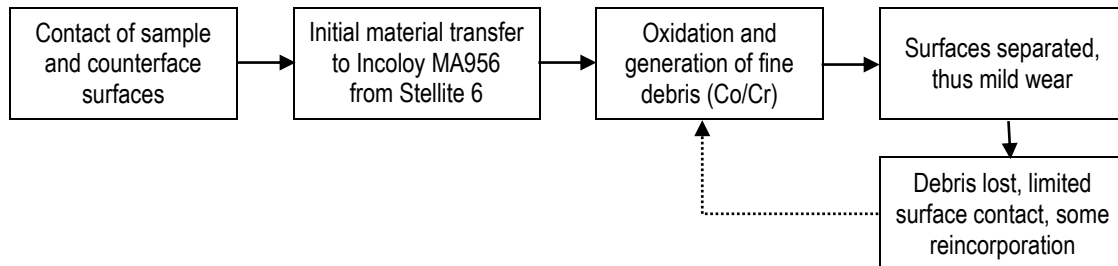
Preferential wear of the harder Stellite 6 in comparison to the softer Incoloy MA956 was again observed (Figure 5.38) as it had been for Nimonic 80A/Stellite 6. Removal of material by delamination mechanism was once again the most likely reason, due to low fatigue crack growth resistance ( $da/dn$ ) and probably low  $K_{Ic}$  of the Stellite 6.

Between room temperature and  $390^{\circ}\text{C}$ , where the oxides generated from the Stellite 6 did not develop into glaze, the abrasive nature of the loose oxides generated further promoted wear of the Stellite 6. As for the enhanced wear of the Stellite 6 at elevated temperatures ( $450^{\circ}\text{C}$  and greater), the  $\Delta G$  values in Table 6.1 once again indicate preferential oxidation of Co and Cr from the Stellite 6, which transferred to the Incoloy MA956, facilitating the rapid promotion of Co-based glaze formation and helped to sustain the glaze.



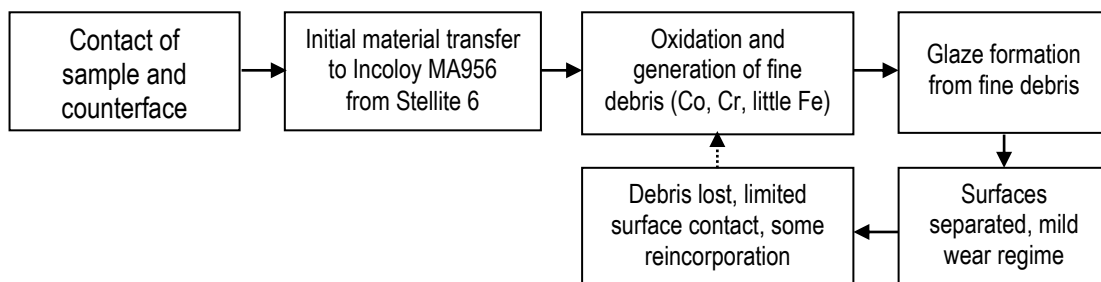
**Figure 6.6: Wear processes for Incoloy MA956 versus Stellite 6 from room temperature to 750°C at 0.314 m.s<sup>-1</sup>**

*(a) Incoloy MA956 worn with Stellite 6 counterface at room temperature, 270, 390 and 450°C*



The process followed by Incoloy MA956 versus Stellite 6 at 0.314 m.s<sup>-1</sup> was very similar to that followed by Nimonic 80A versus Stellite 6 at the same sliding speed. There was a brief period of contact at the very beginning of sliding, where there was a transfer of material from the Stellite 6 counterface to the Incoloy MA956 sample, after which the wear surfaces were separated by fine debris, resulting in mild wear and low wear rates.

*(b) Incoloy MA956 worn with Stellite 6 counterface at 510, 570, 630, 690 and 750°C*



A similar process was followed at 510°C and above, to that followed between room temperature and 450°C. There was one obvious difference – that being the sintering of the fine oxide debris produced to form glaze layers. Once again, this is analogous to the process followed at 0.314 m.s<sup>-1</sup> by Nimonic 80A versus Stellite 6.

The hexagonal close-packed to face-centred cubic phase transformation of Stellite 6 is also likely to be a factor in the generation of glaze debris – it is probable that the interfacial temperature has been raised sufficiently by frictional heating to promote this transformation. The formation of a face-centred cubic phase in Stellite 6 will lead to its easier (easy dislocation slip) deformation, leading to a higher degree of material removal – this is discussed in more detail for the Nimonic 80A / Stellite 6 system in Section 6.1.1.

The development of a sustained glaze on the Incoloy MA956 (there was no evidence of disruption from carbides within the Stellite 6) is then followed by the back-transfer of the top part of the glaze to the Stellite 6, facilitating the development of a Co-based glaze layer on the Stellite 6 surface. There is thus a reduction in the overall wear of the system.

### ***6.2.2 Incoloy MA956 versus Stellite 6 between Room Temperature and 750°C, at 0.905 m.s<sup>-1</sup>***

Between room temperature and 270°C, the presence of fine oxide debris particles (300 nm to 1 µm), prevented direct metal-to-metal contact between the sample and the counterface. Adhesion between the sample and counterface and deformation of the sample were thus kept to a minimum and sample weight losses remained very low as a consequence (Figure 5.38). The higher levels of iron and lower levels of cobalt in the oxides formed indicated that the Incoloy MA956 was now undergoing more wear and had become the primary source of debris at 0.905 m.s<sup>-1</sup>. The continued presence of cobalt in the debris indicated, however, that the Stellite 6 was still undergoing a limited amount of wear.

This situation (Figure 6.7a) was different from that observed for the Nimonic 80A / Stellite 6 (counterface) system under similar conditions in the sense that for the latter system, the surface was covered in Stellite 6-sourced debris.

This oxide debris retained on the Incoloy MA956 surface did not develop into a glaze. A limited amount of deformation and spreading of this oxide was observed on the Incoloy MA956 surface (Figures 5.41 and 5.42b), especially at 270°C. As discussed in Section 6.1.2, the deformed particles do not satisfy the conditions necessary for agglomeration and sintering. It is necessary for the particles to maintain their shape integrity, thus minimising their surface energy at the contact points between the particles. Only then can agglomeration and sintering occur and glaze layers develop.

A severe ‘metal-to-metal’ wear mechanism dominated at 390°C, with high wear and copious amounts of large, flat debris sourced from the Incoloy MA956 indicating wear by a delamination mechanism. The Incoloy MA956 metallic debris generated by metal-to-metal wear, however, were not retained on the wear surfaces. The low residence time of the debris and the low debris retention meant that no glaze formation could occur

from any oxide debris produced on either surface. Thus at 390°C, high friction metal-to-metal wear continued to occur with enhanced wear of the softer Incoloy MA956. This situation (Figure 6.7b) resembled that which occurred in the case of Nimonic 80A versus Stellite 6 at 390°C and 0.905 m.s<sup>-1</sup>.

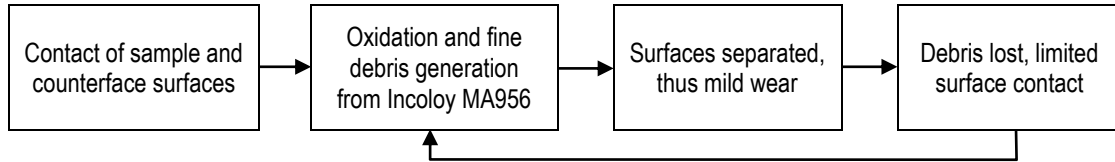
At 450°C and above (Figure 6.7c), the degree of severe wear diminished with increasing temperature, by the progressive development of glaze layers on the surface of the Incoloy MA956. At such temperatures, the rate of oxide debris generation was sufficient to exceed the rate of debris lost by ejection. Glaze layers were thus formed by increasing levels of debris retention (predominantly iron-chromium oxide particles – Cr<sub>1.3</sub>Fe<sub>0.7</sub>O<sub>3</sub> – produced from oxide forming on the surface of the Incoloy MA956) on the Incoloy MA956 surface. A limited amount of cobalt-chromium oxide (CoCr<sub>2</sub>O<sub>4</sub>) was also incorporated from the Stellite 6. Formation of this largely iron-based glaze separated the wear surfaces, allowing further oxidational wear and layer formation.

The static free energies of formation favour the development of cobalt and chromium oxides from the Stellite 6 – from Table 6.1,  $\Delta G_{727^\circ\text{C}}$  for  $2\text{Cr} + 1\frac{1}{2}\text{O}_2 \rightleftharpoons \text{Cr}_2\text{O}_3 = -861.6 \text{ kJ.mol}^{-1}$ ,  $\Delta G_{727^\circ\text{C}}$  for  $3\text{Co} + 2\text{O}_2 \rightleftharpoons \text{Co}_3\text{O}_4 = -525.0 \text{ kJ.mol}^{-1}$  and  $\Delta G_{727^\circ\text{C}}$  for  $\text{Fe} + \frac{1}{2}\text{O}_2 \rightleftharpoons \text{FeO} = -150.7 \text{ kJ.mol}^{-1}$  [95]. However, the increase in sliding speed from 0.314 m.s<sup>-1</sup> to 0.905 m.s<sup>-1</sup> resulted in a shift toward the formation of other oxides including iron from the Incoloy MA956.

EDX Mapping (Figure 5.49) and Autopoint EDX (Figure 5.50) also indicated the incorporation of aluminium within the glaze layer to levels as high as 24% at 0.905 m.s<sup>-1</sup> / 750°C, due to diffusion and preferential oxidation of aluminium from within the debris layers and possibly from the Incoloy MA956 sample material ( $\Delta G$  for  $2\text{Al} + 1\frac{1}{2}\text{O}_2 \rightleftharpoons \text{Al}_2\text{O}_3 = -1362.4$  – Table 6.1). Although the aluminium forms a small but significant part of the glaze at 0.905 m.s<sup>-1</sup> / 750°C, the effect of the aluminium on the properties and formation of the glaze is at this time uncertain.

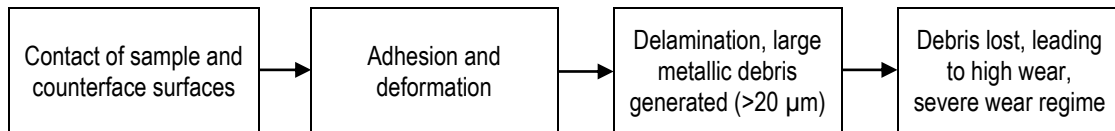
**Figure 6.7: Wear processes for Incoloy MA956 versus Stellite 6 from room temperature to 750°C at 0.905 m.s<sup>-1</sup>**

*(a) Incoloy MA956 worn with Stellite 6 counterface at room temperature and 270°C*



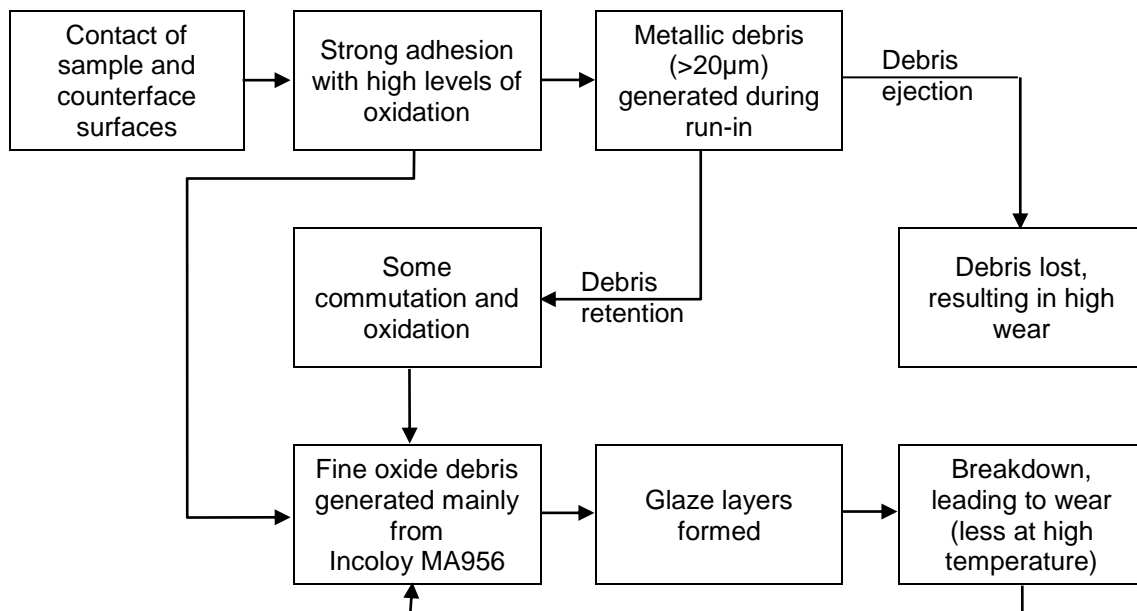
The wear surfaces were separated by fine debris, resulting in mild wear and low wear rates. At 0.905 m.s<sup>-1</sup>, the fine debris was primarily generated from the Incoloy MA956 rather than the Stellite 6. At 0.314 m.s<sup>-1</sup> (Figure 6.6), the primary source of the fine debris was the Stellite 6.

*(b) Incoloy MA956 worn with Stellite 6 counterface at 390°C*



The large size flattened metallic debris generated almost completely from the Incoloy MA956 by adhesion and delamination wear, was unable to remain at the sliding interface – this led to further adhesion between wear surfaces and continued high wear. There was no oxide debris present able to prevent the metallic surfaces from making contact.

*(c) Incoloy MA956 worn with Stellite 6 counterface at 450, 510, 570, 630, 690 and 750°C*



There was an initial period of high wear, referred to as the 'running-in' or 'run-in' period. The development of finer debris and a compacted oxide layer separated the surfaces – this prevents metallic adhesion and the production of large metallic debris that characterises run-in.

**Table 6.2: Summary of mean micro-hardness values for glaze and deformed substrate for Nimonic 80A and Incoloy MA956 versus Stellite 6 at 750°C**

(Vickers diamond indenter, 50 g for 12 s)

	Incoloy MA956	Nimonic 80A
<b>Glaze 0.314 m.s<sup>-1</sup></b>	Stellite 6-sourced glaze – mainly CoCr <sub>2</sub> O <sub>4</sub> – with underlying powdery layer  No data due to ready break-up of glaze layer during testing	6.45 GPa  Stellite 6-sourced glaze – mainly CoCr <sub>2</sub> O <sub>4</sub> – with underlying powdery layer
<b>Glaze 0.905 m.s<sup>-1</sup></b>	16.63 GPa  Incoloy MA956 sourced glaze – mainly Cr <sub>1.3</sub> Fe <sub>0.7</sub> O <sub>3</sub> – with direct adherence onto Incoloy MA956	No data due to lack of glaze formation on sample – NiO and Cr <sub>2</sub> O <sub>3</sub> loose debris (formed a rough, patchy glaze only on the Stellite 6 counterface)
<b>Substrate</b>	4.13 GPa	5.23 GPa

It is worthwhile to note that for the Incoloy MA956 / Stellite 6 system, on raising the sliding speed to 0.905 m.s<sup>-1</sup>, a mechanically more stable Incoloy MA956 sourced iron-chromium glaze with greater hardness was formed (Table 6.2). The greater mechanical stability of the Incoloy MA956 sourced iron-chromium glaze formed at 0.905 m.s<sup>-1</sup> is attributable to direct adherence of the oxide layers to the Incoloy MA956 wear surface.

As at 0.314 m.s<sup>-1</sup>, the development of a sustained glaze on the Incoloy MA956 (there was again no evidence of disruption from carbides within the Stellite 6) is then followed by the transfer of the top part of the glaze to the Stellite 6, facilitating the development of a glaze layer on the Stellite 6. However, at 0.905 m.s<sup>-1</sup> the transferred glaze is now predominantly iron-chromium based (sourced from the Incoloy MA956). A reduction in the overall wear of the system, however, still results.

### 6.2.3 Wear Map for Incoloy MA956 versus Stellite 6

If the data from current and previous testing are considered collectively with respect to sliding speed, it is possible to set up useful wear maps describing the variation of wear behaviour with sliding speed and temperature for Incoloy MA956 versus Stellite 6.

The following behaviour was observed at 0.314 m.s<sup>-1</sup>:

- A low temperature mild wear regime existed between room temperature and 450°C, with the wear surfaces separated by a layer of discrete mainly cobalt-chromium oxide particles, primarily from the Stellite 6.
- Mild wear persisted between 510°C and 750°C, with the mainly cobalt-chromium oxide sintering together to form comprehensive glaze layers. The primary source of debris was once again the Stellite 6. Very little evidence of any initial severe wear could be found.

Rose's data [2] collected at 0.654 m.s<sup>-1</sup> suggest the following behaviour:

- A low temperature mild wear regime existed once again between room temperature and 390°C. This debris was sourced primarily from the Stellite 6.
- A 'severe wear only' regime due to direct metal-to-metal contact between sample and counterface existed only at 450°C. No oxide could be identified at this temperature.
- Severe wear was observed initially on all samples between 510°C and 750°C. This severe wear phase became increasingly curtailed with increasing temperature, as Stellite 6-sourced oxide debris deposition and glaze formation became increasingly rapid. At 690°C and 750°C, there was very little evidence of severe wear before the onset of glaze formation and weight losses at these temperatures were consequently very low.

The following behaviour was observed at 0.905 m.s<sup>-1</sup>:

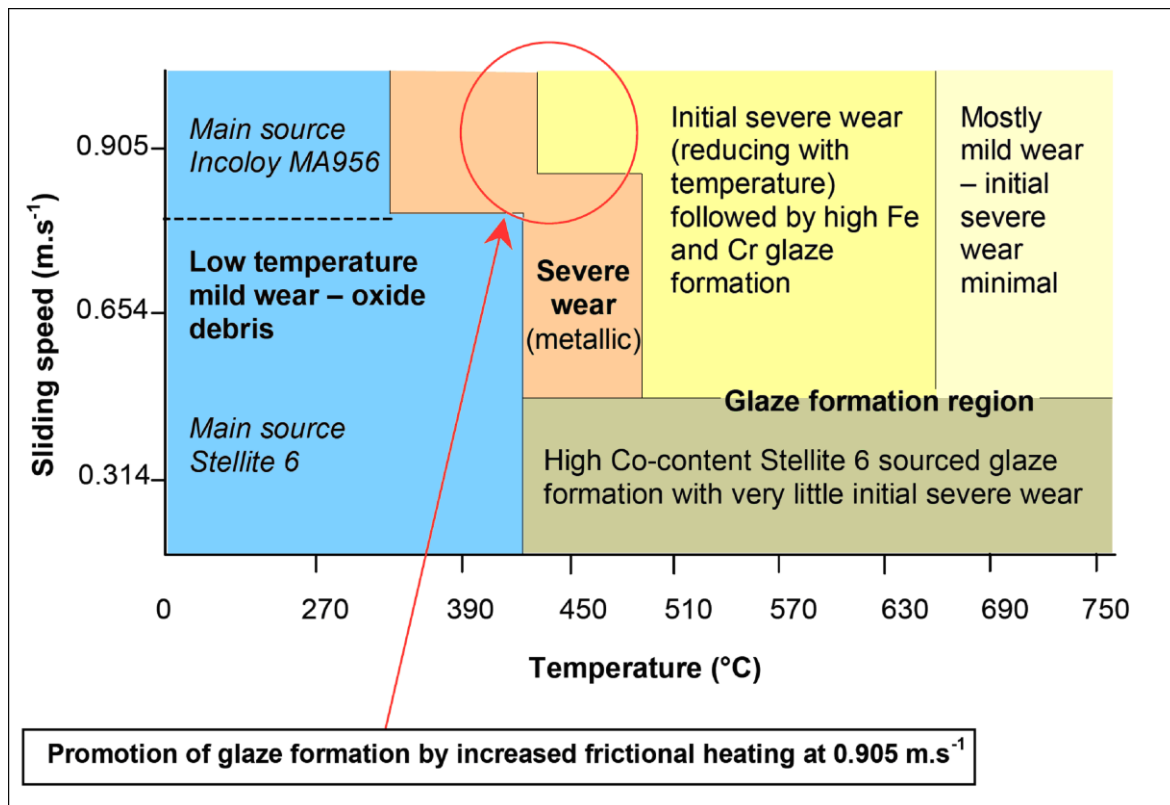
- Low temperature mild wear existed only at room temperature and 270°C, with wear surfaces again separated by discrete mainly iron-chromium oxide particles – the main source of debris was now the Incoloy MA956.
- 'Severe wear only' due to direct metal-to-metal contact was at 0.905 m.s<sup>-1</sup> observed at 390°C.
- Glaze formation was observed at 0.905 m.s<sup>-1</sup> at 450°C, after 13,032 m of sliding and an extended period of severe wear. This is 60°C lower than first observed for 0.654 m.s<sup>-1</sup> by Rose [2], due to the promotion of mainly iron-chromium oxide formation because of frictional heating.

- High losses due to severe wear became increasingly restricted on raising the temperature from 510°C to 750°C. The formation of wear protective glaze layers from Incoloy MA956-sourced mainly iron-chromium oxide occurred progressively earlier, until at 690°C and 750°C, there was very little evidence of severe wear before the onset of glaze. Weight losses at 690°C and 750°C were consequently very low.

Given this information, it is therefore possible to construct the following wear map for Incoloy MA956 when slid against Stellite 6 (Figure 6.8).

**Figure 6.8: Wear map for Incoloy MA956 versus Stellite 6**

(load 7N)





### 6.3 Nimonic 80A versus Incoloy 800HT

#### 6.3.1 *Nimonic 80A versus Incoloy 800HT between Room Temperature and 750°C, at 0.314 m.s<sup>-1</sup>*

Between room temperature and 750°C, the wear of Nimonic 80A worn against an Incoloy 800HT counterface was characterised by three wear regimes. At room temperature and 270°C, a severe wear, high transfer regime dominated (Figure 5.67) with an Incoloy 800HT-sourced metallic transfer layer forming across the surface of the Nimonic 80A. Severe wear continued to dominate between 390°C and 510°C, but with little metallic transfer and high wear of the Nimonic 80A. Nichromate-phase (Figure 5.51) glaze layer formation (the debris for this layer was sourced from the Incoloy 800HT counterface) was observed between 570°C and 750°C with some limited initial metallic transfer.

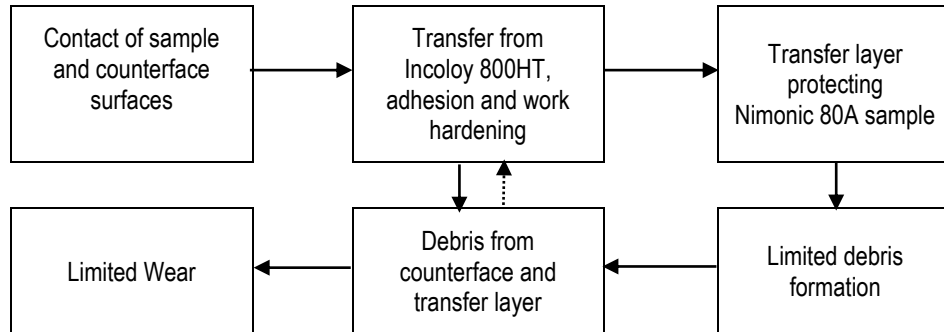
The dominant severe wear at room temperature and 270°C demonstrated by the complete absence of oxide debris and high friction coefficients (0.95 – 1.0), was characterised by high levels of transfer from the Incoloy 800HT to the Nimonic 80A, forming a work-hardened transfer layer (Table 5.5). This transfer layer (Figures 5.67 and 5.69), wholly sourced from the Incoloy 800HT counterface (EDX indicated a composition of ~44% Fe, ~30% Ni and ~24% Cr at room temperature) protected the surface of the Nimonic 80A (as described in Figure 6.9a) and weight losses from the Nimonic 80A remained low as a result. The flattened metallic debris (Figure 5.61), indicative of delamination wear, was formed either by direct removal from the highly worn Incoloy 800HT counterface or by limited removal from the Incoloy 800HT-sourced transfer layer on the Nimonic 80A (EDX of the debris indicated a composition of ~45% Fe, ~29% Ni and ~24% Cr at room temperature and 270°C).

The continued presence of severe wear between 390°C and 510°C (Figure 6.9b), accompanied by an increase in Nimonic 80A wear, was caused by:

- 1) the absence of a protective transfer layer (Figure 5.58) (resulting in a mixture of debris particles removed from both the Nimonic 80A and the Incoloy 800HT counterface);
- 2) increasing softening of the Nimonic 80A with increasing temperature (Figure 6.1).

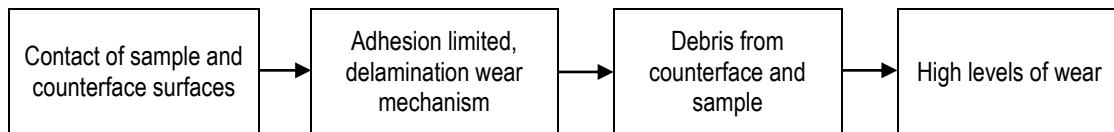
**Figure 6.9: Wear processes for Nimonic 80A versus Incoloy 800HT from room temperature to 750°C at 0.314 m.s<sup>-1</sup>**

*(a) Nimonic 80A worn with Incoloy 800HT at room temperature and 270°C*



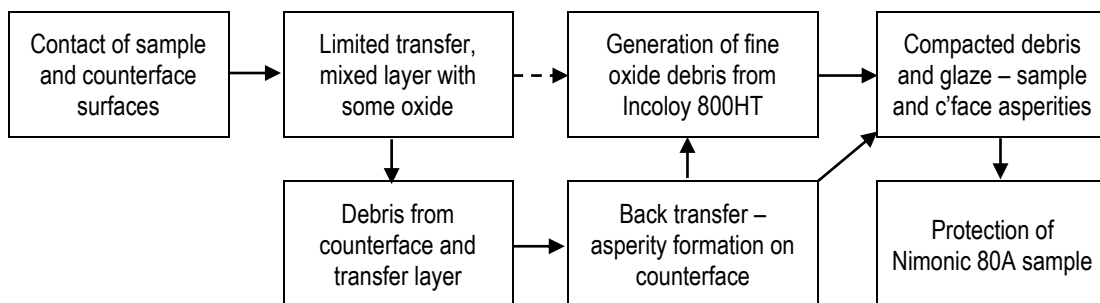
The Nimonic 80A sample material underwent very limited wear, with a transfer layer forming across the wear scar – most material losses were from the Incoloy 800HT counterface. Although wear was limited, because all the interactions occurring were metallic, this was a severe wear situation.

*(b) Nimonic 80A worn with Incoloy 800HT at 390°C, 450°C and 510°C*



Adhesion was extremely limited due to limited oxidation (visible only as discolouration – no oxide layers were formed), with only a few isolated patches of transferred material present on the Nimonic 80A sample. In the absence of the metallic transfer layers observed at room temperature and 270°C (or developed oxide layers as seen between 570°C and 750°C), wear of the Nimonic 80A increased and was at it's highest between 390°C and 510°C (and up to 570°C), with flat debris particles indicating wear by delamination.

*(c) Nimonic 80A worn with Incoloy 800HT at 570°C, 630°C, 690°C and 750°C*



A limited transfer layer was formed, mixed in nature, with increasing levels of oxidation towards the exposed surface – some back-transfer occurred at a later stage, accounting for asperities of Incoloy 800HT composition on the Incoloy 800HT counterface. Nichromate-phase (NiCr<sub>2</sub>O<sub>4</sub>) glaze formation then occurred due to the interaction of the asperities and the transfer layer. The more rapid development of the glaze progressively reduced wear between 570°C and 750°C.

The large, flattened nature of these debris (Figure 5.61) suggest material removal was by a delamination mechanism, regardless of whether the debris was sourced from the Nimonic 80A or the Incoloy 800HT.

The absence of the metallic transfer layer was due to increasing oxidation of the exposed surface of the Nimonic 80A with temperature (visible as discolouration on the wear surface – Figure 5.58 shows this clearly at 510°C), inhibiting adhesion of metallic debris from the Incoloy 800HT counterface to the Nimonic 80A wear surface. Also, the rate of oxidation was insufficient to overcome the low retention and residence times and high levels of debris ejection at the wear interface. Consequently the oxide was thus also unable to develop into significant debris layers and afforded no protection to the Nimonic 80A – the limited development and retention of the oxide in fact led to increased wear.

The effect of debris retention on the wear process was demonstrated by testing without Nimonic 80A sample reciprocation at 510°C with the rotating counterface sliding speed set to  $0.314 \text{ m.s}^{-1}$ . The increased debris retention allowed a patchy nichromate ( $\text{NiCr}_2\text{O}_4$ ) glaze layer to develop (Figure 5.71), indicating that a significant level of oxidation was occurring and it was the enhanced removal (with sample reciprocation) that was preventing the oxide from developing into glaze layers.

At temperatures of between 570°C and 750°C, enhanced oxidation of the Nimonic 80A and Incoloy 800HT surfaces when in contact led to the production of fine nickel-chromium-iron oxidational debris, sourced primarily from the Incoloy 800HT (Section 5.4.3). The development of this debris now happened at a rate in excess of that lost by ejection. The debris was thus able to build up and sinter on the wear surfaces to form wear resistant nichromate-phase ( $\text{NiCr}_2\text{O}_4$ ) glaze layers of high hardness (19.97 GPa at 750°C – Table 6.3) between 570°C and 750°C (Figure 5.67). The formation of these oxide layers became more rapid with increasing temperature, reducing the level of severe wear occurring at the beginning of sliding, as was apparent from the reduction in the size of the wear scar (Figure 5.58).

At 750°C, the glaze and other surface deposits formed a dual layer (Figure 6.10) overlying the Nimonic 80A (as shown by EDX mapping – Figure 5.64 – and Autopoint EDX –

Figure 5.66a). Severe wear produced a lower layer of mixed metal and oxide early in the wear process sourced from both the Nimonic 80A and the Incoloy 800HT counterface. As this layer continued to form, the oxide accounted for an increasing proportion of the material deposited. The Incoloy 800HT-sourced nichromate-phase glaze then developed overlying the mixed metal-oxide debris layer, due to interaction between this mixed metal-oxide layer and asperities on the Incoloy 800HT counterface. Optical studies (not shown) suggest that similar layer structures (glaze layer – mixed metal / oxide layer – substrate) formed at other glaze forming temperatures (570°C to 750°C).

**Table 6.3: Mean hardness values for glaze and deformed substrate for Nimonic 80A versus Incoloy 800HT at 750°C**

*(Vickers diamond indenter, 50 g for 12 s)*

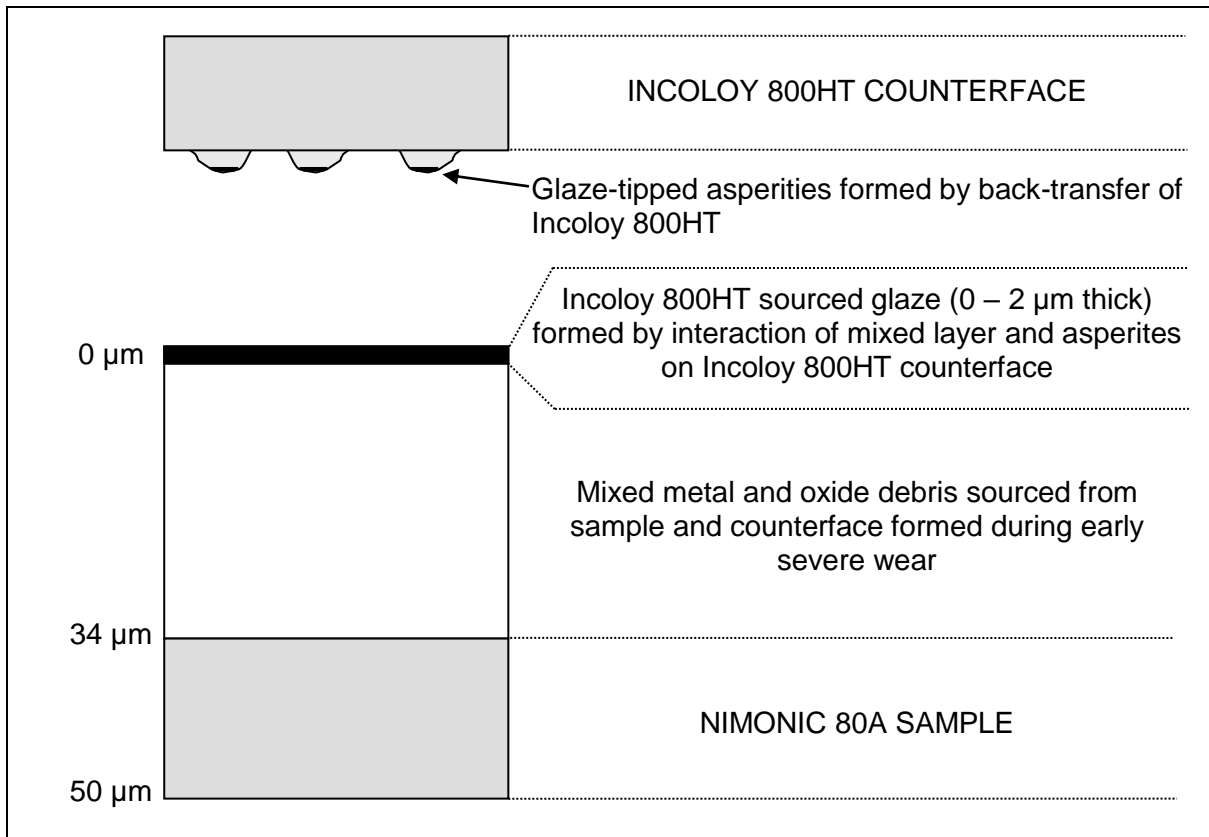
	Nimonic 80A
Glaze 0.314 m.s <sup>-1</sup>	19.97 GPa
Glaze 0.905 m.s <sup>-1</sup>	18.06 GPa
Substrate	5.23 GPa

The wear scar of the Incoloy 800HT counterface at glaze-forming temperatures (570°C to 750°C) was highly worn, due to the volume of material transferred to the Nimonic 80A. Some metallic material back-transferred and readhered to the Incoloy 800HT wear track to form the asperities, some of which rose up to 1.5 mm above the original surface of the wear scar (and thus could only have been created by back-transfer – Figure 6.11). As the asperities were the only areas to come into contact with the transfer layers on the sample, later glaze formation was thus restricted to the asperities.

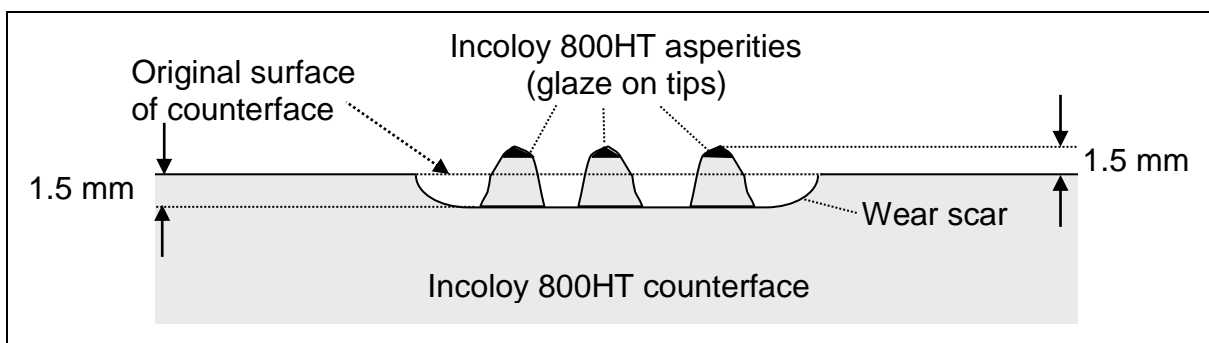
At 750°C, the glaze on the transfer layers on the Nimonic 80A matched that of the Incoloy 800HT. As the transfer layers underlying the glaze on the sample were of mixed composition, the only possible source of oxide of this composition was the Incoloy 800HT. The glaze layers on the counterface asperities were also of a composition consistent with the Incoloy 800HT (~29% Ni, ~23% Cr, ~42% Fe after 4,522 m), thus the back-transferred metallic asperities were also of Incoloy 800HT composition. The asperities must therefore form later in the sliding process, when Incoloy 800HT can no longer transfer to the

Nimonic 80A sample (i.e. when oxidation in the transfer layer inhibits adhesion of further metallic material). Glaze formation must only begin after back-transfer has created the asperities on the counterface and they have begun to interact with the highly oxidised layer on the surface of the Nimonic 80A.

**Figure 6.10: Layers formed on Nimonic 80A sample and Incoloy 800HT counterface at 750°C and 0.314 m.s<sup>-1</sup>**



**Figure 6.11: Wear scar cross-section on Incoloy 800HT counterface worn against a Nimonic 80A sample – 0.314 m.s<sup>-1</sup> and 0.905 m.s<sup>-1</sup>**



### 6.3.2 *Nimonic 80A versus Incoloy 800HT between Room Temperature and 750°C, at 0.905 m.s<sup>-1</sup>*

Two wear regimes were observed for the Nimonic 80A / Incoloy 800HT (counterface) system. A severe wear regime operated between room temperature and 570°C, with high levels of metallic transfer from the Incoloy 800HT to form a wear protective transfer layer on the Nimonic 80A (Figure 5.68). Between 630°C and 750°C, the observed formation of a nichromate-phase glaze layer (Figure 5.51 – material sourced from the Incoloy 800HT) producing a mild wear phase, was also preceded by a brief period of severe wear with high transfer from the Incoloy 800HT counterface to the Nimonic 80A.

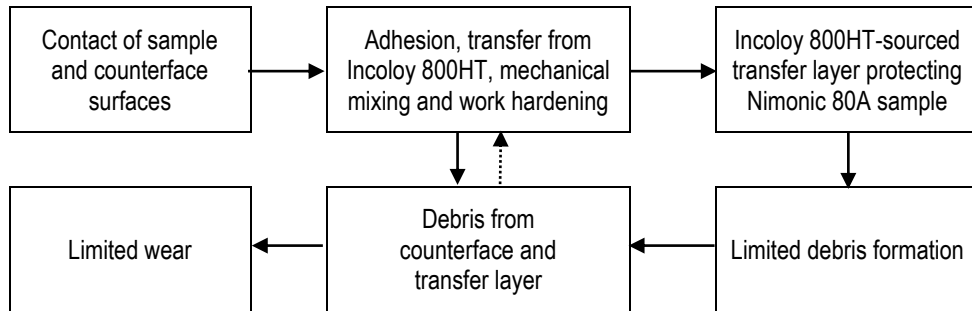
The initially occurring severe wear between room temperature and 750°C (high levels of friction of between 0.6 to 0.8 were observed – Figure 5.57b) by a delamination mechanism, led to the subsequent development of a wear-protective transfer layer (Figure 5.61b). Much of the material removed from the Incoloy 800HT was transferred to the surface of the Nimonic 80A, forming a metallic layer (Figure 5.59) that became work-hardened (Figure 5.82) and helped protect the surface of the Nimonic 80A from enhanced wear (Figure 6.12a).

Transfer levels were higher than at 0.314 m.s<sup>-1</sup>, directly due to the greater removal of Incoloy 800HT from the heavily worn counterface at 0.905 m.s<sup>-1</sup>. This transfer was at such a high level early in the wear process that sample weight increased during the first 4,522 m of sliding (Figure 5.55b).

Subsequently, the observed slight reductions in the Nimonic 80A sample weight were a direct result of the absence of large-scale transfer later in the sliding process (4,522 m to 13,032 m) coupled with very limited metallic material loss through wear (Figure 5.55b). This clearly indicates that the transfer layer was now protecting the Nimonic 80A from further enhanced wear. There was some continued transfer and redeposition from both sample and counterface during extended sliding up to 13,032 m, leading to mechanical mixing or alloying [37] in the transfer layer on the Nimonic 80A surface (Section 5.4.3). However, mixing was incomplete, with variable levels of nickel, chromium and iron indicating heterogeneity in the layer composition.

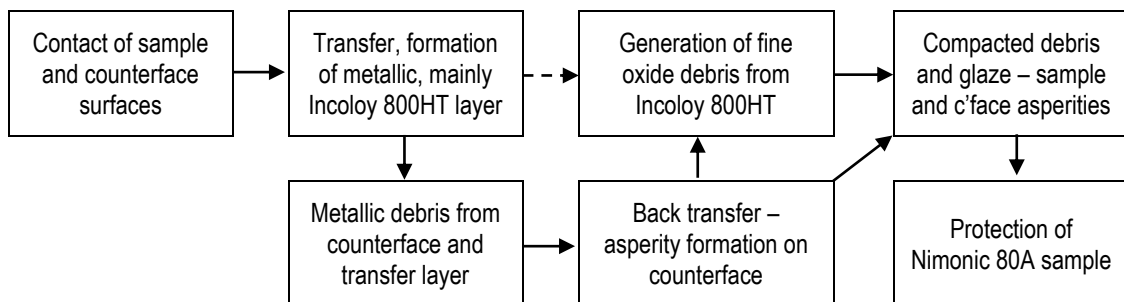
**Figure 6.12: Wear processes for Nimonic 80A versus Incoloy 800HT from room temperature to 750°C at 0.905 m.s<sup>-1</sup>**

*(a) Nimonic 80A worn with Incoloy 800HT at room temperature, 270°C, 390°C, 450°C, 510°C and 570°C*



The Nimonic 80A sample material underwent very limited wear, with a transfer layer forming across the wear scar, sourced from the Incoloy 800HT counterface. The level of transfer was such that there was a recorded weight gain for the sample, especially between 450°C and 570°C. The limited oxidation (visible as discolouration on samples slid at 390°C and above) did not have any visible effect on this metallic transfer.

*(b) Nimonic 80A worn with Incoloy 800HT at 630°C, 690°C and 750°C*



As at 0.314 m.s<sup>-1</sup>, a transfer layer was again formed, this time mainly of Incoloy 800HT (Figure 6.14) – increasing levels of oxide were detected towards the exposed surface. Once again, some back-transfer occurred, forming asperities of Incoloy 800HT composition on the Incoloy 800HT counterface. Nichromate-phase (NiCr<sub>2</sub>O<sub>4</sub>) glaze formation then resulted from interaction of the asperities and the transfer layer.

The increased wear of the Incoloy 800HT counterface and transfer to the Nimonic 80A with increased temperature between room temperature and 570°C (Figure 5.55), was probably caused by thermal softening of the Incoloy 800HT (Figure 6.1 shows a clear reduction of hardness of Incoloy 800HT with increasing temperature) allowing greater removal of material from the counterface.



The continued transfer of metallic Incoloy 800HT material at  $0.905 \text{ m.s}^{-1}$  between  $390^\circ\text{C}$  and  $570^\circ\text{C}$  (Figure 5.59) can be attributed to the reduced presence of oxide on the wear scar surface, caused by:

1. higher removal rates and lower residency times of debris at  $0.905 \text{ m.s}^{-1}$  preventing the development of surface oxidation that at  $0.314 \text{ m.s}^{-1}$  inhibited adhesion; and
2. any oxide developing on wear surfaces at  $0.905 \text{ m.s}^{-1}$  did not have time between surface contacts to develop sufficiently to inhibit or prevent adhesion of counterface material to the Nimonic 80A.

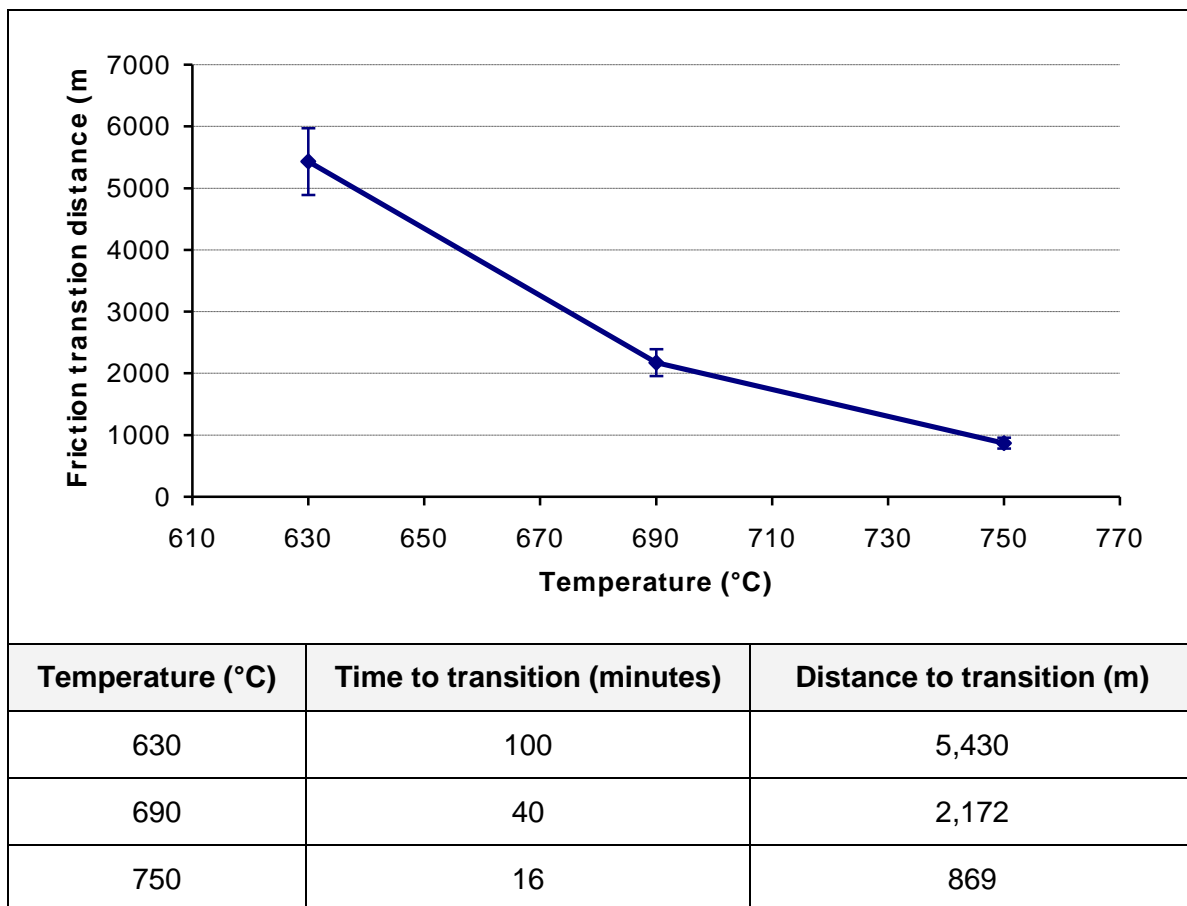
Although some discoloration due to oxidation still did occur, there was little indication that it interfered with the transfer and adhesion of Incoloy 800HT-sourced material to the surface of the Nimonic 80A.

At temperatures of  $630^\circ\text{C}$  and greater, wear resistant nichromate-phase ( $\text{NiCr}_2\text{O}_4$ ) nickel-chromium-iron oxide layers of high hardness ( $18.06 \text{ GPa}$  at  $750^\circ\text{C}$  – Table 6.3) developed from fine oxidational debris, formed as a result of enhanced oxidation of the contacting surfaces occurring at levels in excess of debris ejection rates (Figure 6.12b). The rate of development of these oxide layers increased with temperature, as indicated by the development of only a limited glaze layer after only  $13,032 \text{ m}$  of sliding at  $630^\circ\text{C}$ , compared to more comprehensive glaze layers (Figure 5.69) after only  $4,522 \text{ m}$  of sliding at  $690^\circ\text{C}$  and especially at  $750^\circ\text{C}$ . The time of transition of coefficient of friction values from ‘run-in’ (characterised by values of higher than  $0.8$  and sometimes greater than  $1$  due to metal-to-metal contact) to ‘steady-state’ mild wear (characterised by the separation of metallic surfaces by glaze layers and lower values of friction of between  $0.3$  and  $0.5$ ) also decreased as a direct consequence of glaze formation (Figure 6.13).

A multi-layered structure (Figure 6.14) formed at  $0.905 \text{ m.s}^{-1}$  (as shown by EDX mapping and Autopoint EDX – Figure 5.66b) from the debris deposited on the Nimonic 80A at  $750^\circ\text{C}$ , as it had at  $0.314 \text{ m.s}^{-1}$ . Severe wear dominated the early stages of the wear process at  $0.905 \text{ m.s}^{-1}$ , with a brief period of material removal and deposition from both the Nimonic 80A and the Incoloy 800HT counterface, resulting in the formation of a limited layer of mechanically mixed material [37]. The wear process was then dominated by the

transfer and partial oxidation of material from the Incoloy 800HT, from which a mixed metal-oxide layer developed. Later debris transferred from the Incoloy 800HT was completely oxidised – whether this was transferred as metal and later oxidised or alternatively transferred as oxide is unclear. The nichromate-phase glaze layer overlying this was formed due to interaction between the oxide transfer layer and asperities on the Incoloy 800HT counterface itself.

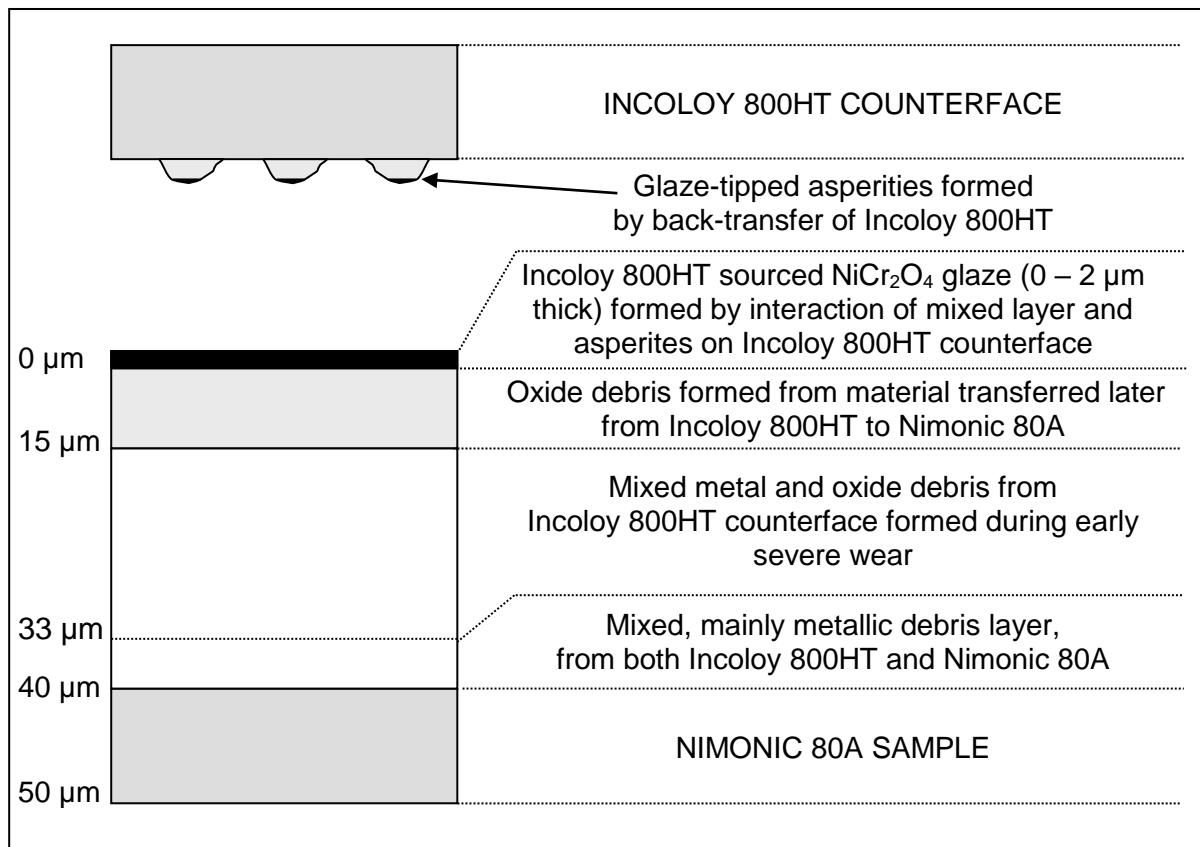
**Figure 6.13: Distance to transition in coefficient of friction from high variability (severe wear) to low variability (mild wear) at 630°C, 690°C and 750°C – Nimonic 80A versus Incoloy 800HT at 0.905 m.s<sup>-1</sup>**



Glaze formation at 0.905 m.s<sup>-1</sup> on the Incoloy 800HT counterface was identical to that observed at 0.314 m.s<sup>-1</sup>. Glaze of composition matching the Incoloy 800HT (~24% Ni, ~30% Cr, ~41% Fe after 4,522 m of sliding – the glaze was of almost identical composition after 13,032 m) developed only on the asperity tips on the counterface wear scar (after their formation), due to interaction of the asperity tips and the Incoloy 800HT-sourced transfer

layers on the Nimonic 80A samples. The height of the asperities (up to 1.5 mm above the unworn counterface surface – Figure 6.11) indicated they have been deposited on the wear scar surface after its formation, as a result of back-transfer of removed Incoloy 800HT material that was unable to adhere to the sample surface due to increasing oxidation.

**Figure 6.14: Layers formed on Nimonic 80A sample and Incoloy 800HT counterface at 750°C and 0.905 m.s<sup>-1</sup>**



### 6.3.3 Wear Map for Nimonic 80A versus Incoloy 800HT

As with Nimonic 80A and Incoloy MA956 when worn against Stellite 6, there is sufficient data to create a basic wear map for Nimonic 80A as the sample material slid against an Incoloy 800HT counterface.

The following behaviour was observed during the current study at 0.314 m.s<sup>-1</sup>:

1. At room temperature and 270°C, a severe wear regime was observed with high levels of transfer from the Incoloy 800HT to the Nimonic 80A sample forming a

transfer layer on the Nimonic 80A wear surface. This reduced wear of the Nimonic 80A.

2. Between 390°C and 510°C, severe wear continued to be observed. However, transfer was much reduced (due to surface oxidation reducing levels of adhesion) and no transfer layer was formed. Consequently, there was increased wear of the Nimonic 80A.
3. Between 570°C and 750°C, limited metallic transfer from the Incoloy 800HT counterface to the Nimonic 80A, formed a more mixed transfer layer. This was followed by mild wear and the formation of Incoloy 800HT-based nichromate-phase glaze layers on the transfer layer and the counterface (asperities only).

The following behaviour was observed at 0.654 m.s<sup>-1</sup> in previous work by Rose [2]:

1. A severe wear regime was observed between room temperature and 570°C, with high levels of transfer from the Incoloy 800HT to the Nimonic 80A sample. This formed a transfer layer on the Nimonic 80A wear surface, which reduced wear of the Nimonic 80A.
2. High levels of initial transfer from the Incoloy 800HT counterface to the Nimonic 80A were observed between 630°C and 750°C, which produced a predominantly Incoloy 800HT-based transfer layer. Glaze was then formed due to sliding between the transfer layer and the Incoloy 800HT counterface.

The following behaviour was observed during the current study at 0.905 m.s<sup>-1</sup>:

1. Severe wear with high levels of transfer from the Incoloy 800HT counterface to the Nimonic 80A was observed between room temperature and 570°C. The work-hardened transfer layer formed again protected the Nimonic 80A from high levels of wear.
2. Severe wear with transfer from the Incoloy 800HT counterface to form a transfer layer and low Nimonic 80A wear was again observed at 630°C after 4,522 m of

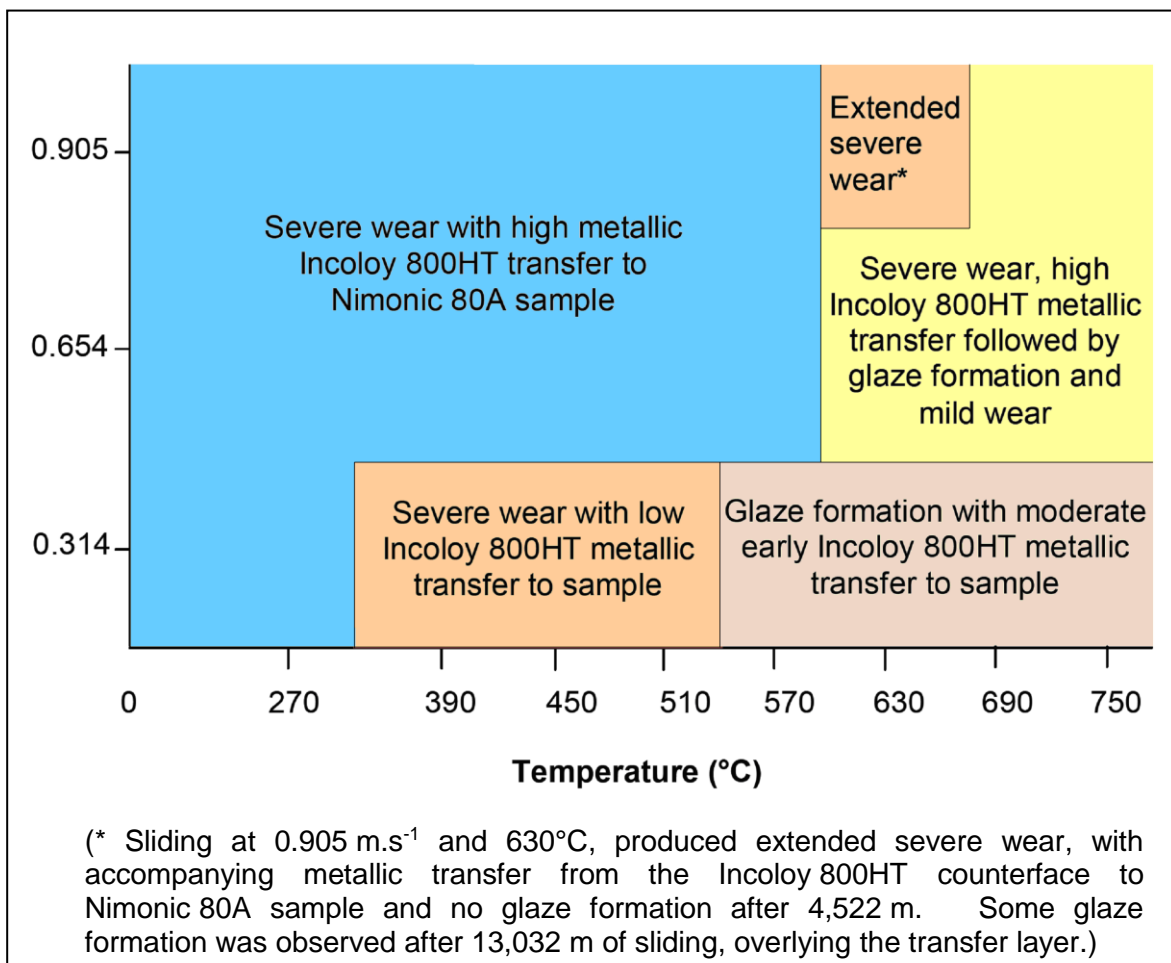
sliding. On continuing sliding up to 13,032 m, some nichromate-phase glaze formation was observed.

3. High levels of initial transfer to the Nimonic 80A from the Incoloy 800HT counterface were observed at 690°C and 750°C, producing a predominantly Incoloy 800HT-based transfer layer. Nichromate-phase glaze was then formed between the transfer layer and the Incoloy 800HT counterface.

It is therefore possible to construct the following wear map for Nimonic 80A when slid against Incoloy 800HT (Figure 6.15) from the observations made.

**Figure 6.15: Wear map for Nimonic 80A versus Incoloy 800HT**

(load 7N)



ERRATA: At 0.905 m.s<sup>-1</sup> and 630°C, 'patchy' glaze formation was observed after 4,522 m and 'limited' glaze formation after 13,032 m (Figure 6.15). Such glaze formation is reported in Section 5.4.2. The above caption incorrectly reports no glaze formation after 4,522 m. (Ian A. Inman, August 2010)

## 6.4 Incoloy MA956 versus Incoloy 800HT

### 6.4.1 *Incoloy MA956 versus Incoloy 800HT between Room Temperature and 750°C, at 0.314 m.s<sup>-1</sup>*

The sliding wear of Incoloy MA956 against Incoloy 800HT as the counterface material at 0.314 m.s<sup>-1</sup>, showed three distinct wear regimes over the temperature range room temperature to 750°C.

At room temperature and 270°C, moderate amounts of flattened metallic wear debris (Figure 5.79a) were produced by a severe wear ‘delamination’ mechanism, from both sample and counterface. Much of this metallic debris readhered to either the Incoloy MA956 sample or the Incoloy 800HT counterface, forming a mechanically-mixed metallic transfer layer (Figures 5.68a and 5.76), which became work-hardened due to sliding (Table 5.7) and limited the amount of wear (Figure 5.73). The mechanical mixing producing this layer was incomplete, with variable levels of nickel, chromium and iron indicating heterogeneity in the layer composition. The absence of oxide from either sliding surface at room temperature and 270°C indicated that oxidation did not play any significant part in the wear process (shown schematically in Figure 6.17a), either to protect the wear surfaces from high wear (as was the case with Incoloy MA956 versus Stellite 6) or to inhibit adhesion and prevent the build-up of the transfer layer on either surface.

Between 390°C and 570°C, both oxide (formed due to oxidation of the metallic surfaces as evidenced by surface discolouration – Figure 5.76) and metallic debris (produced by delamination wear – Figure 5.79a) were produced from both the Incoloy MA956 sample and Incoloy 800HT counterface surfaces. This debris was not retained due to low residency times and rapid ejection and thus the oxide debris was unable to form into compacted oxide wear-protective layers.

Although the oxide debris developing between 390°C and 570°C did not compact and sinter into wear-protective oxide layers (due to low residency and rapid ejection), the level of oxidation was sufficient to severely reduce metallic adhesion. Thus readhesion of the metallic debris to the wear surfaces was restricted to a few isolated areas and the metallic transfer layers formed at room temperature and 270°C did not develop between 390°C and 570°C (Figure 5.76 shows the 510°C example). The absence of both metallic and oxide

transfer layers led to increased wear of the unprotected surfaces of both the Incoloy MA956 and the Incoloy 800HT (Figure 6.17b).

Additionally, the hardness levels of both the Incoloy MA956 and Incoloy 800HT fell significantly with increasing temperature (Figure 6.1). This probably facilitated the easier removal of metallic material from both sample and counterface at higher temperature, in the absence of either metallic or compacted oxide layers.

The finding that the development of a wear protective compacted chromium-iron based oxide layer occurred by not reciprocating the sample (and only rotating the counterface – Figure 5.88) during testing, demonstrates the occurrence of a significant degree of oxidation at  $510^{\circ}\text{C} / 0.314 \text{ m.s}^{-1}$  and a higher level of debris retention. Thus reciprocation was responsible for causing debris ejection and prevented the formation of glaze layers.

At  $630^{\circ}\text{C}$  and  $690^{\circ}\text{C}$ , there was a further transition to a mild wear regime, albeit with an extended period of severe wear during the early stages of sliding. The increased production of Incoloy MA956-sourced fine oxide debris (Figures 5.76 and 5.78a) was able to occur at a sufficient rate to outstrip that lost by ejection. Thus the debris was able to build up and sinter to form wear protective glaze layers (Figures 5.76 and 5.78) of high hardness (9.62 GPa at  $750^{\circ}\text{C}$  – Table 6.4) on the surface of the Incoloy MA956.

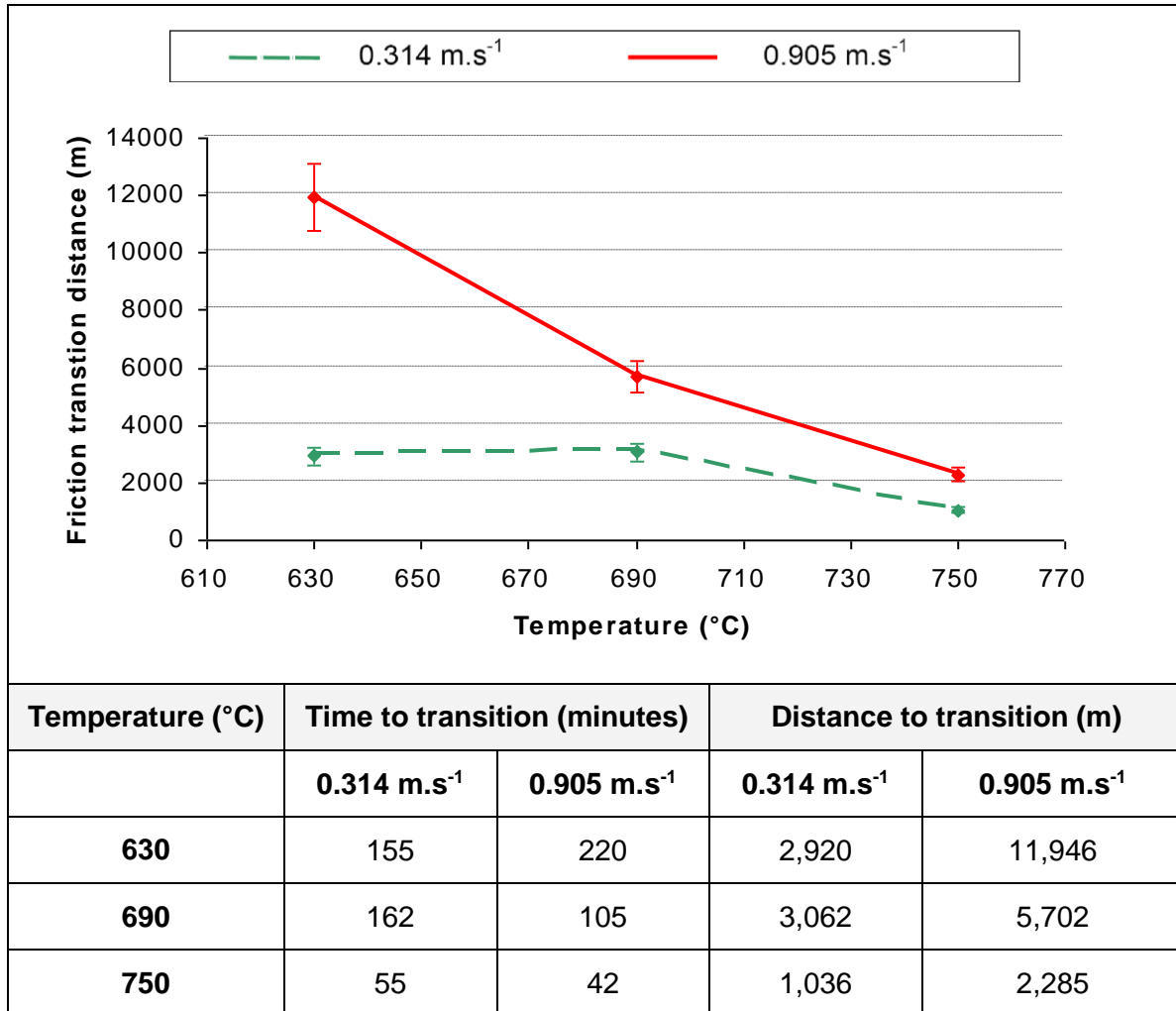
However, the level of debris ejection was still sufficient to heavily retard the build-up of oxide debris and the development of these oxide layers (as indicated by reductions of variability in friction – Figure 6.16), allowing for an extended period of severe wear (Figure 6.17c).

Further decreases in Incoloy MA956 and Incoloy 800HT strength between  $630^{\circ}\text{C}$  and  $750^{\circ}\text{C}$  allowed even greater removal of metallic (and oxide) material early during the wear process. The continued production of large, flattened metallic debris (Figure 5.79a) indicated that prior to later oxide layer development, wear was by a delamination mechanism.



**Figure 6.16: Distance to transition in coefficient of friction from high variability (severe wear) to low variability (mild wear) at 630°C, 690°C and 750°C – Incoloy MA956 versus Incoloy 800HT at 0.314 m.s<sup>-1</sup> and 0.905 m.s<sup>-1</sup>**

*(Time / distance to transition is the amount of sliding required before glaze formation occurred, thus reducing frictional variability.)*



**Table 6.4: Mean hardness values for glaze and deformed substrate for Incoloy MA956 versus Incoloy 800HT**

*(Vickers diamond indenter, 50 g for 12 s)*

	Incoloy MA956
Glaze 0.314 m.s <sup>-1</sup>	9.62 GPa
Glaze 0.905 m.s <sup>-1</sup>	21.26 GPa
Substrate	4.13 GPa

Only at 750°C did glaze formation occur rapidly enough (after 1,036 m of sliding – Figure 6.16) to restrict the amount of metallic debris removed during the early period of severe wear and reduce weight loss and wear rate.

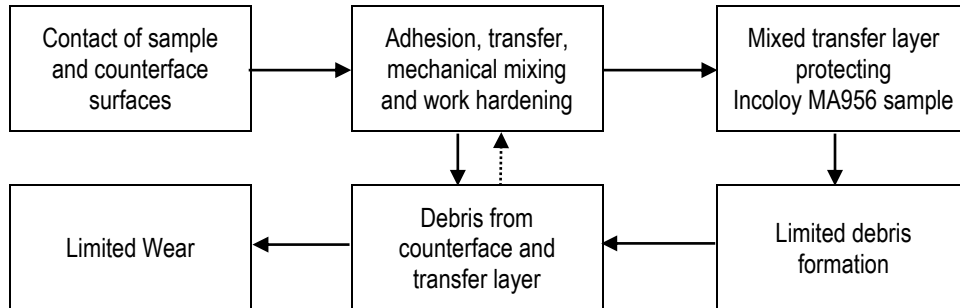
At 750°C, the observed multi-layer structure of the debris layers at 0.314 m.s<sup>-1</sup> shown by EDX mapping (Figure 5.82) and Autopoint EDX (Figure 5.84a), indicates debris development through a number of stages leading to the formation of a protective glaze layer (Figure 6.18c):

1. generation of metallic debris during the initial wear process from the Incoloy MA956 and its redeposition onto the surface of the sample, resulting in the development of a limited metallic debris layer adjacent to the undamaged Incoloy MA956 base metal;
2. progressive oxidation with increased sliding leading to subsequent depositions of debris comprising a mixture of metallic and oxide debris – the level of oxide found in the debris increased with further sliding;
3. generation of an Incoloy MA956-sourced Cr<sub>1.3</sub>Fe<sub>0.7</sub>O<sub>3</sub> phase fine debris (XRD – Figure 5.85) occurring later during the sliding process, due to sliding contact between this mixed layer and the Incoloy 800HT counterface;
4. sintering and compaction of this fine oxide after 1,036 m of sliding (Figure 6.16) into hardened glaze layers (hardness 9.62 GPa – Table 6.4), overlying the earlier metallic and mixed metal-oxide debris on the Incoloy MA956 sample surface and causing the onset of mild wear.

At 750°C, both the earlier metallic debris and the later oxide debris were iron-chromium based (typically 60-62% iron, 26-28% chromium and only 0-3% nickel), indicating that the material making up the layers was removed from and redeposited back onto the Incoloy MA956. There had been no intermixing of material from the Incoloy 800HT counterface at 750°C.

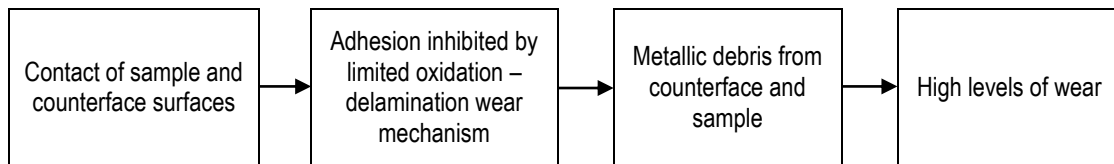
**Figure 6.17: Wear processes for Incoloy MA956 versus Incoloy 800HT from room temperature to 750°C at 0.314 m.s<sup>-1</sup>**

*(a) Incoloy MA956 worn with Incoloy 800HT at room temperature and 270°C*



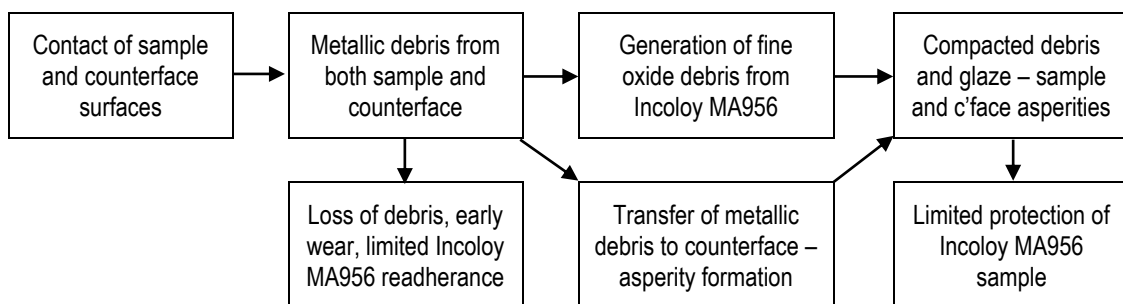
The Incoloy MA956 sample material underwent limited wear, with a transfer layer forming across the wear scar – most material losses were from the Incoloy 800HT counterface. Although wear was limited, because all the interactions occurring were metallic, this was a severe wear situation.

*(b) Incoloy MA956 worn with Incoloy 800HT at 390°C, 450°C, 510°C and 570°C*



Adhesion was extremely limited, with only a few isolated patches of transferred material present on the Incoloy MA956 sample. Flat debris particles of 20µm or greater indicated wear by delamination. Oxide was detectable by XRD from 510°C upwards and visible on surfaces as discolouration from 390°C – this oxide prevented adhesion, mixing and transfer of layers observed at room temperature and 270°C.

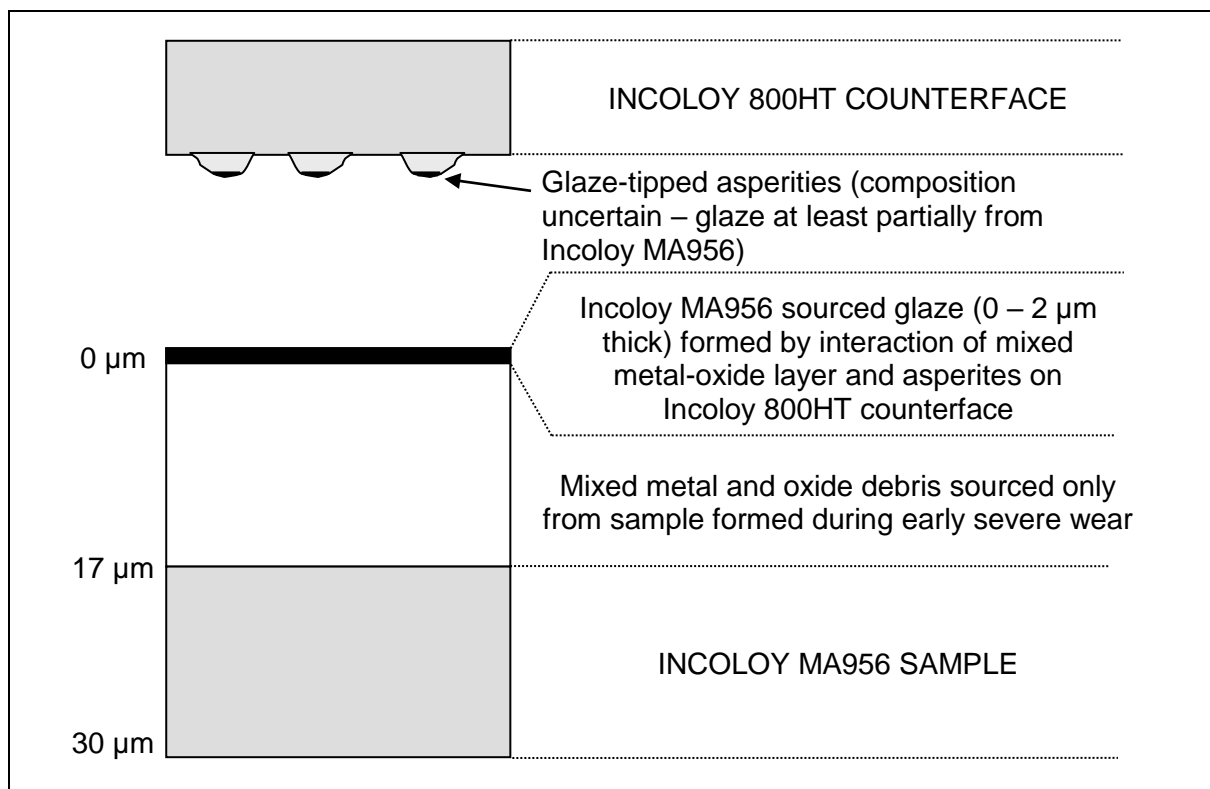
*(c) Incoloy MA956 worn with Incoloy 800HT at 630°C, 690°C and 750°C*



Early severe wear resulted in deep wear scars and early heavy material losses from both sample and counterface – some of this material readhered to the Incoloy 800HT counterface to form the observed asperities. Later glaze formation offered only limited protection to the Incoloy MA956 – the glaze formed across the Incoloy MA956 wear scar was sourced from the Incoloy MA956 itself. It is likely that the glaze on the counterface asperities was also sourced at least partially from the Incoloy MA956 (at 750°C, this glaze was of mixed composition).

The glaze layers formed at  $0.314 \text{ m.s}^{-1} / 750^{\circ}\text{C}$  with the Incoloy MA956 / Incoloy 800HT (counterface) system additionally had a higher than expected aluminium content (Figures 5.82 and 5.84), due to diffusion of aluminium to the glaze surface (as was observed with the Incoloy MA956 / Stellite 6 system at  $0.905 \text{ m.s}^{-1} / 750^{\circ}\text{C}$ ) where it underwent preferential oxidation ( $\Delta G$  for  $2\text{Al} + 1\frac{1}{2}\text{O}_2 \rightleftharpoons \text{Al}_2\text{O}_3 = -1362.4$  – Table 6.1). Aluminium content within the surface of the glaze commonly reached levels of  $\sim 12\%$ , with levels as high as  $\sim 24\%$  in some isolated areas. The source of this aluminium was the mixed Incoloy MA956-sourced metal-oxide debris layers underlying the glaze and possibly the undeformed Incoloy MA956 itself. Despite the high levels of aluminium, the effect of this aluminium on the formation and properties of the glaze layers is unclear at this time.

**Figure 6.18: Layers formed on Incoloy MA956 sample and Incoloy 800HT counterface at  $750^{\circ}\text{C}$  and  $0.314 \text{ m.s}^{-1}$**

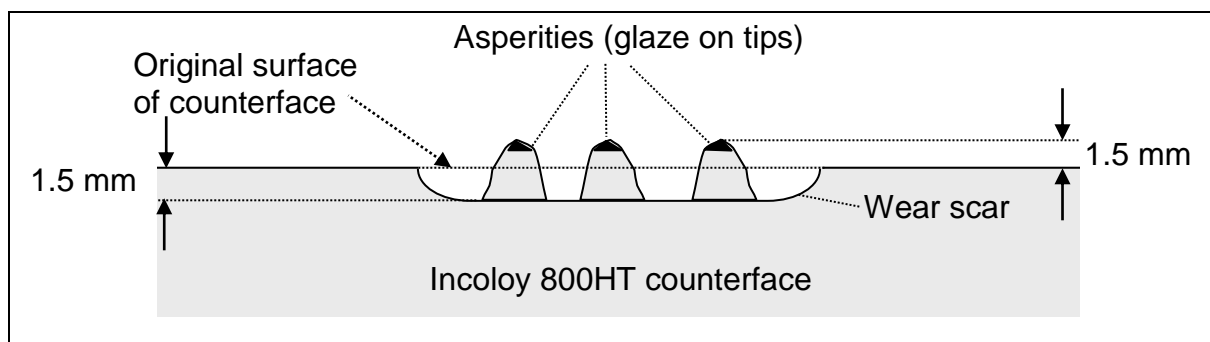


The Incoloy 800HT counterface at glaze forming temperatures ( $630^{\circ}\text{C}$  to  $750^{\circ}\text{C}$ ) underwent a limited degree of wear early in the sliding process, during which metallic material was deposited onto the wear track to form asperities (Figure 5.76). Subsequent development of glaze was restricted to the tips of these asperities (Figure 6.19), where they

were in contact with the Incoloy MA956 sample surface. At 750°C, this glaze has formed due to mixing of wholly Incoloy MA956-sourced glaze material transferred from the Incoloy MA956 sample with Incoloy 800HT-based debris, resulting in an intermediate composition oxide (~18% Ni, ~20% Cr, ~58% Fe) that adhered to the asperity tips. The wear patterns observed at 630°C and 690°C were almost identical to that observed at 750°C, thus indicating that the glaze on the asperity tips at these temperatures was also likely to at least in part transferred from the surface of the Incoloy MA956 – however, this is uncertain at this stage.

The source material of the metallic asperities formed on the Incoloy 800HT counterface wear track on which the glaze has formed is also unclear at this stage – the mixed composition of the glaze indicates they were either readhered Incoloy 800HT or a mixed Incoloy 800HT / Incoloy MA956 (from the sample) composition.

**Figure 6.19: Wear scar cross-section on Incoloy 800HT counterface worn against an Incoloy MA956 sample –  $0.314 \text{ m.s}^{-1}$  and  $0.905 \text{ m.s}^{-1}$**



#### **6.4.2 Incoloy MA956 versus Incoloy 800HT between Room Temperature and 750°C, at $0.905 \text{ m.s}^{-1}$**

The wear behaviour of Incoloy MA956 when slid against Incoloy 800HT between room temperature and 750°C at  $0.905 \text{ m.s}^{-1}$  was again marked by the occurrence of three wear regimes (as was observed at  $0.314 \text{ m.s}^{-1}$ ).

The wear regime between room temperature and 270°C was accompanied by the development of a layer (of no more than 9 µm thickness) on the Incoloy MA956 surface caused by intermixing of the metallic debris removed from both the sample and the

counterface. This layer underwent work-hardening (Table 5.8), conferring some degree of wear resistance to the Incoloy MA956 surface. The formation of flat, metallic debris from both surfaces indicated the operation of a delamination-type mechanism.

Between 390°C and 570°C at 0.905 m.s<sup>-1</sup>, both oxide (formed due to oxidation of the metallic surfaces and visible as discolouration – Figure 5.77) and metallic debris (formed by delamination wear – Figure 5.79b) were produced from both the Incoloy MA956 sample and Incoloy 800HT counterface surfaces. The low residency times of the debris and their rapid ejection prevented the development of compacted oxide wear-protective layers – at 0.905 m.s<sup>-1</sup>, the residency time of the debris was even less than at 0.314 m.s<sup>-1</sup>.

The higher levels of oxide ejection and lower residency times of the oxide debris at 0.905 m.s<sup>-1</sup> meant that the oxide formed was not able to restrict re-adhesion of the metallic debris to the same degree it had at 0.314 m.s<sup>-1</sup>. Therefore, a higher level of metallic debris was able to adhere to the wear surfaces and patchy metallic transfer layers were able to form (Figure 5.77). These patchy metallic transfer layers were now largely sourced from the Incoloy MA956 itself (reductions in nickel to ~3% indicated minimal contribution from the Incoloy 800HT counterface – the debris removed from the Incoloy MA956 was thus readhering after removal) and offered limited protection to the surface of the Incoloy MA956 sample. Wear was consequently less at 0.905 m.s<sup>-1</sup> than at 0.314 m.s<sup>-1</sup> (after 4,522 m of sliding) up to 630°C.

The hardness levels of both the Incoloy MA956 sample and the Incoloy 800HT counterface also decreased significantly with increasing temperature (Figure 6.1). This probably allowed the easier removal of metallic material from both surfaces, in the absence of either compacted oxide layers or comprehensive metallic transfer layers.

At 630°C and above, the wear regime at 0.905 m.s<sup>-1</sup> was characterised by a prolonged period of severe wear (a longer period than that observed at 0.314 m.s<sup>-1</sup>) caused by the delayed onset of glaze formation (after 11,956 m at 630°C, 5,702 m at 690°C and 2,285 m at 750°C – Figure 6.16). This delay was again due to the reduced residency time of the debris between the wear surfaces and the increased level of debris ejection – thus an extended critical period of sliding was needed to produce enough oxide debris to allow the

development of wear protective glaze layers. Only the more significant development and growth of a hardened glaze layer (21.25 GPa) led to a reduction in weight loss and wear rate after 13,032 m of sliding, most noticeably at 690°C.

The observed increase in weight loss and wear rate after 13,032 m and 750°C, can be attributed to increasing plastic flow of the Incoloy MA956 metallic substrate (Figure 5.77), reducing mechanical support for the glaze layers forming on the wear surface.

The development of a multi-layer structure at 0.905 m.s<sup>-1</sup> and 750°C (as indicated by the Autopoint data in Figure 5.84), indicates a number of stages of debris development (Figure 6.20c) leading up to the development of a protective glaze layer (Figure 6.21), similar to that observed at 0.314 m.s<sup>-1</sup>.

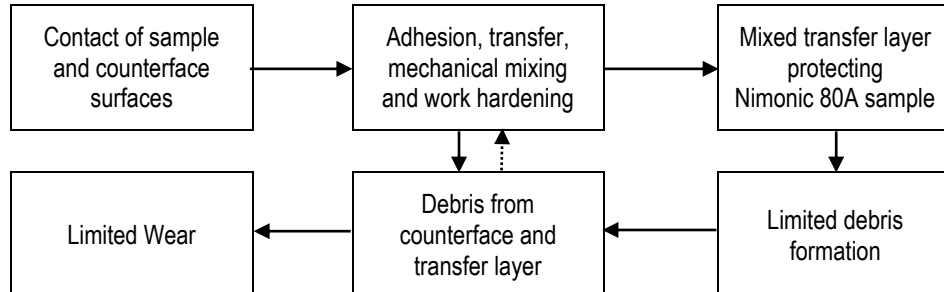
1. The generation and redeposition of metallic debris early during the wear process from the Incoloy MA956 has led to the development of a limited metallic debris layer.
2. Continuing oxidation with sliding has resulted in subsequent debris depositions being increasingly a mixture of metallic and oxide debris. Later deposits of debris were completely oxidised.
3. Finally, sliding between the completely oxidised upper part of this mixed layer and the Incoloy 800HT counterface has generated a fine Cr<sub>1.3</sub>Fe<sub>0.7</sub>O<sub>3</sub> phase debris (XRD – Figure 5.86), which have formed into glaze layers separating sample and counterface surfaces after ~2,285 m of sliding (Figure 6.16).

The sole source of both the earlier metallic debris and the later oxide debris was the Incoloy MA956 – the presence of only an iron-chromium oxide (~0.5% Ni, ~27% Cr, ~67% Fe) indicated no intermixing of material from the Incoloy 800HT counterface.



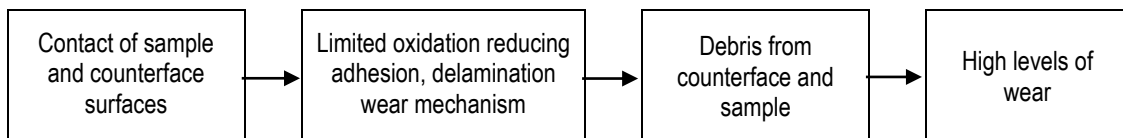
**Figure 6.20: Wear processes for Incoloy MA956 versus Incoloy 80HT from room temperature to 750°C at 0.905 m.s<sup>-1</sup>**

*(a) Incoloy MA956 worn with Incoloy 800HT at room temperature and 270°C*



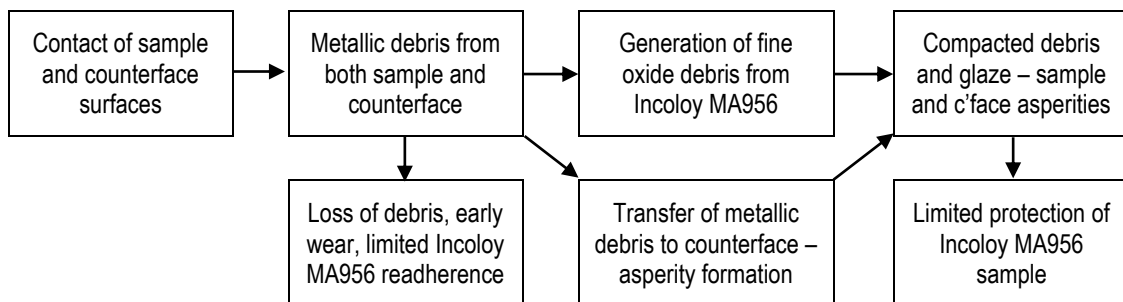
The Incoloy MA956 sample material underwent limited wear, with a transfer layer forming across the wear scar – most material losses were from the Incoloy 800HT counterface. Although wear was limited, because all the interactions occurring were metallic, as at 0.314 m.s<sup>-1</sup> (Figure 6.17) this is a severe wear situation.

*(b) Incoloy MA956 worn with Incoloy 800HT at 390°C, 450°C, 510°C, 570°C and 630°C*



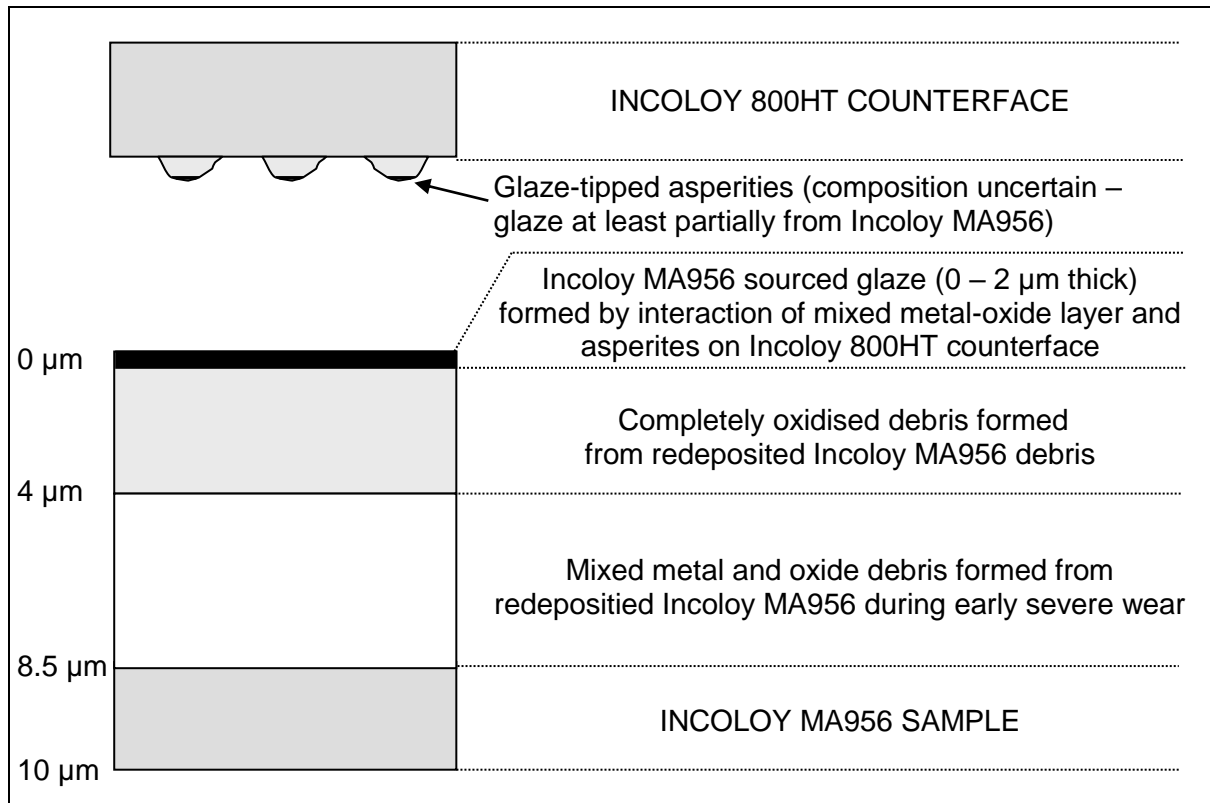
Oxidation was again apparent as discolouration from 390°C, however, it was less effective at preventing adhesion and limited, patchy metallic transfer layers formed. Although wear was still high, these limited transfer layers kept wear to a level less than at 0.314 m.s<sup>-1</sup> between 0 and 4,522 m (Figure 5.66). Extended sliding up to 13,032 m resulted in the removal of these transfer layers (especially at 570°C and 630°C) and increased levels of wear. Flat debris particles of 20µm or greater were generated, indicating wear by delamination.

*(c) Incoloy MA956 worn with Incoloy 800HT at 690°C and 750°C*



As at 0.314 m.s<sup>-1</sup>, early severe wear resulted in deep wear scars and early heavy material losses for both sample and counterface – some of this material readhered to the Incoloy 800HT counterface to form the observed asperities. Later glaze formation offered only limited protection to the Incoloy MA956 – the glaze that formed across the Incoloy MA956 wear scar (over only very limited layers of Incoloy MA956) was sourced from the Incoloy MA956 itself – it is likely therefore that the glaze on the counterface asperities was also sourced at least in part from the Incoloy MA956 (at 750°C, this glaze was of mixed composition). Additionally, it was observed that glaze formation was delayed at 690°C and 0.905 m.s<sup>-1</sup> – this was attributable to enhanced ejection of debris material at 0.905 m.s<sup>-1</sup>.

**Figure 6.21: Layers formed on Incoloy MA956 sample and Incoloy 800HT counterface at 750°C and 0.905 m.s<sup>-1</sup>**



The glaze layers formed at 0.905 m.s<sup>-1</sup> / 750°C also had a very high content of aluminium (Figures 5.83 and 5.84), due to diffusion and preferential oxidation of aluminium ( $\Delta G$  for  $2\text{Al} + 1\frac{1}{2}\text{O}_2 \rightleftharpoons \text{Al}_2\text{O}_3 = -1362.4$  – Table 6.1) from within the mixed metal-oxide debris layer and possibly the underlying Incoloy MA956 sample material (as was observed at 0.314 m.s<sup>-1</sup> / 750°C). As a consequence, some isolated areas of glaze contained up to ~32% aluminium at 0.905 m.s<sup>-1</sup> (though levels were more normally in the range 15 to 20%). Despite the high levels of aluminium, the effect of the high concentration of aluminium on the properties and formation of the glaze layers is uncertain at this time.

Glaze formation on the counterface at 0.905 m.s<sup>-1</sup> between 630°C and 750°C followed a similar route to that observed at 0.314 m.s<sup>-1</sup>. The counterface has undergone a moderate degree of wear prior to the deposition and adherence of metallic material onto the wear track to form asperities (Figure 5.77). The later development of glaze has been restricted to the tips of these asperities, where they have been in contact with the Incoloy MA956 sample surface (Figure 6.19). At 750°C, the formation of this glaze has occurred due to

transfer of Incoloy MA956-sourced glaze material that has mixed Incoloy 800HT-based debris, forming an intermediate composition oxide that has adhered to the asperity tips (~16% Ni, ~21% Cr, ~58% Fe after 4,522 m of sliding – the composition of the glaze after 13,032 m was near-identical). The near-identical wear patterns observed at 630°C and 690°C indicated that the glaze on the asperity tips at these temperatures was also at least in part transferred from the surface of the Incoloy MA956 – however, as at 0.314 m.s<sup>-1</sup>, this is uncertain at this stage.

The source material of the asperities in the Incoloy 800HT counterface wear track upon which the glaze has formed is not clear at this stage – at 0.905 m.s<sup>-1</sup> as at 0.314 m.s<sup>-1</sup>, the mixed composition of the glaze indicates they were either readhered Incoloy 800HT or composed of a mixture of Incoloy 800HT and Incoloy MA956 (from the sample).

#### **6.4.3 Wear Map for Incoloy MA956 versus Incoloy 800HT**

As with Nimonic 80A or Incoloy MA956 when worn against Stellite 6 and Nimonic 80A when slid against Incoloy 800HT, there are sufficient data to create a basic wear map for Incoloy MA956 as the sample material slid against Incoloy 800HT as the counterface material.

At 0.314 m.s<sup>-1</sup>:

1. A severe wear mechanism was dominant at room temperature and 270°C, with high levels of metallic transfer between the Incoloy MA956 and the Incoloy 800HT. This material formed a mixed transfer layer that protected the Incoloy MA956 from extended wear.
2. Severe wear continued, but with much reduced transfer up to 450°C. The lack of a protective transfer layer resulted in higher levels of weight loss from the Incoloy MA956. Adhesion is inhibited due to surface oxidation (observable as discolouration on wear surfaces).
3. Severe wear continued to be observed at 510°C and 570°C, but with an oxide phase now detectable (by XRD) – this oxide did not form into oxide layers, due to low residency and high ejection rates. Transfer from the Incoloy 800HT counterface was minimal due to this oxide with wear of the Incoloy MA956 increasing.

4. Glaze formation was clearly evident (the oxide sourced from the Incoloy MA956), preceded by a period of severe wear with limited transfer between 630°C and 750°C.

Rose [2] observed that at 0.654 m.s<sup>-1</sup>:

1. Severe wear dominated at room temperature and 270°C, accompanied by the development of a metallic transfer layer on the Incoloy MA956. This wear-protective transfer layer formed from material removed from both the Incoloy MA956 and the Incoloy 800HT.
2. Transfer levels were much reduced between 390°C and 630°C, with increased wear of the Incoloy MA956 due to the lack of a protective transfer layer. The metallic nature of remaining isolated areas of transfer and the debris indicated a severe wear mechanism. Some clear oxide development was observed on the wear scar surface at 630°C.
3. Glaze layers were observed to form after a period of severe wear at 690°C and 750°C, the oxide for these layers was sourced from the Incoloy MA956. The presence of these glaze layers reduced the rate of wear.

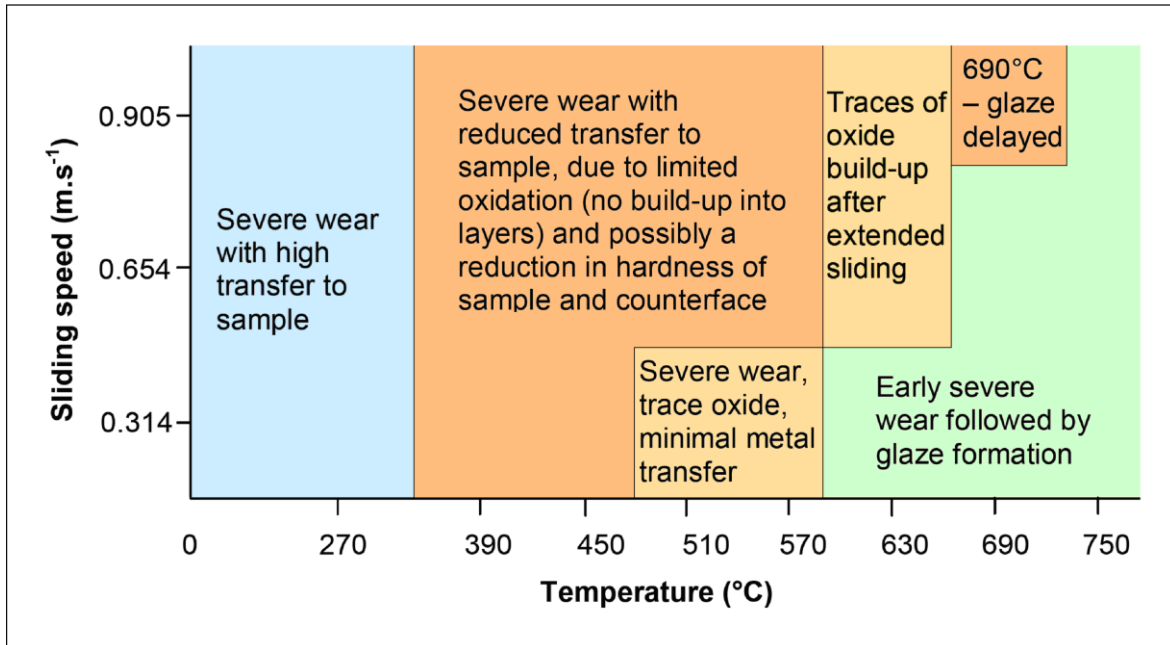
At 0.905 m.s<sup>-1</sup>:

1. High levels of metallic ‘severe’ wear were once again observed at room temperature and 270°C. A mechanically mixed work-hardened transfer layer once again formed, which protected the surface of the Incoloy MA956.
2. Increasing severe wear with much reduced transfer continued up to 630°C. This was due in part to surface oxidation (observable as discoloration) inhibiting adhesion of debris and the formation of a wear-protective transfer layer. Also, increasing softening of Incoloy MA956 and Incoloy 800HT with increasing temperature (Figure 6.1) allowed for the more ready removal of material from both. Clear traces of oxidation were observed on the wear scar after 13,032 m of sliding at 630°C.
3. Glaze formation was once again observed between 690°C and 750°C. However, the formation of the glaze was preceded by an extended period of severe wear, the length of which decreased with increasing temperature.

The wear map resulting from these observations is shown in Figure 6.22.

**Figure 6.22: Wear map for Incoloy MA956 versus Incoloy 800HT**

(load = 7N)



## 6.5 Nano-scale Studies of High Temperature Wear – Nimonic 80A / Stellite 6 at 750 $^{\circ}\text{C}$ and 0.314 $\text{m.s}^{-1}$

### 6.5.1 Nano-hardness of Glaze Layers – Nimonic 80A versus Stellite 6 and Incoloy MA956 versus Stellite 6

The recorded values of nano-hardness for both the Nimonic 80A / Stellite 6 and Incoloy MA956 systems slid at 750 $^{\circ}\text{C}$  (Table 6.5) are only slightly less than the theoretical bulk hardness of  $\text{Cr}_2\text{O}_3$  of 28.98 GPa [116]. The high hardness along with the high modulus values suggest an enhanced level of sintering with very low levels of porosity, giving an extremely wear-resistant glaze layer.

There is no significant difference between the hardness and modulus values for the glaze layers formed at 750 $^{\circ}\text{C}$ , for either the Nimonic 80A / Stellite 6 or Incoloy MA956 / Stellite 6 systems. This is not surprising, as the glaze layers overlying the samples for both systems are predominantly cobalt-chromium oxides sourced from the Stellite 6 counterface (Figure 5.10), with very similar routes of formation (Sections 6.1.1 and 6.2.1).

**Table 6.5: Mean nano-hardness and modulus values for glaze – Nimonic 80A / Stellite 6 (510°C and 750°C) and Incoloy MA956 / Stellite 6 (750°C)**

	<b>Nimonic 80A / Stellite 6, 510°C</b> (sample size = 3)	<b>Nimonic 80A / Stellite 6, 750°C</b> (sample size = 4)	<b>Incoloy MA956 / Stellite 6, 750°C</b> (sample size = 3)
<b>Mean Hardness (GPa)</b>	25.03	22.62	21.97
<b>Mean Modulus (GPa)</b>	99.8	129.7	120.3

Reducing the sliding temperature to 510°C for the Nimonic 80A / Stellite 6 system does not have a major effect on the hardness of the glaze layers produced. However, there is a sizeable reduction in modulus values, to ~76% of the modulus values obtained at 750°C. This is attributable to reduced sintering of the oxide debris on forming the glaze layers at 510°C – the glaze layers are thus ‘less stiff’ due to the higher residual porosity, as observed during SEM studies (Figures 5.21 and 5.22).

Despite the higher levels of hardness indicated by nano-hardness testing, some caution is still required in using nano-indentation as a tool to interpret the properties of the glaze layers. Due to the very small area of indentation during nano-hardness testing, collected data can be highly vulnerable to local inhomogeneities within the glaze layer.

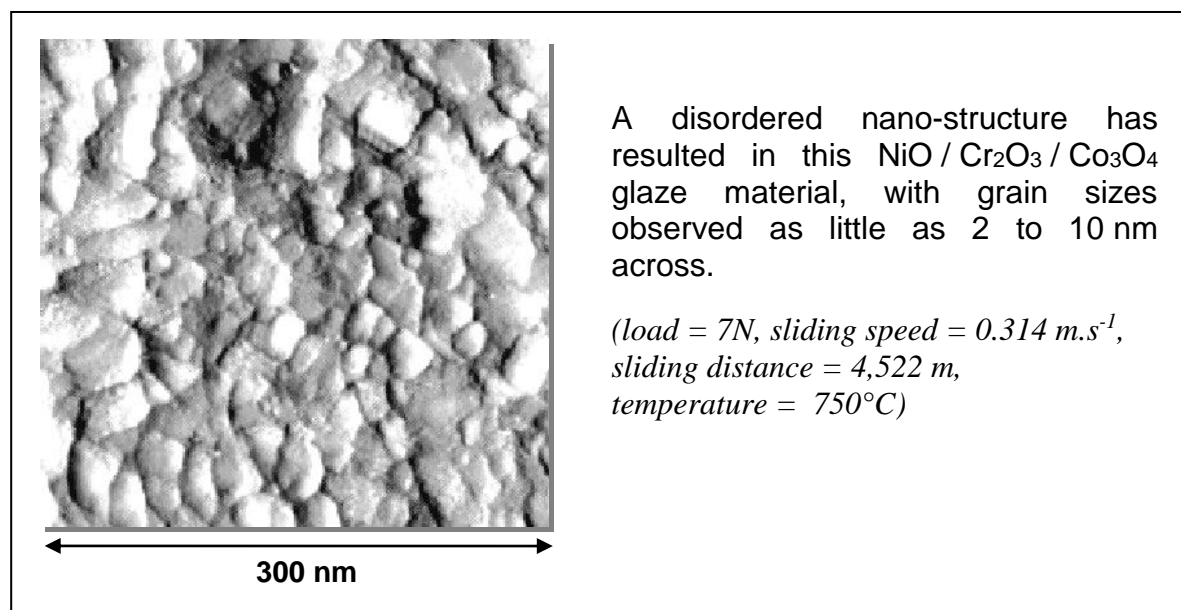
### 6.5.2 Nano-scale Characterisation of Glaze Layers – Nimonic 80A / Stellite 6 at $0.314 \text{ m.s}^{-1}$ and $750^\circ\text{C}$

The grain sizes of the glaze layer formed by the sliding of Nimonic 80A against Stellite 6 at  $750^\circ\text{C}$  and  $0.314 \text{ m.s}^{-1}$  for 4,522 m and studied using TEM and STM, clearly indicate the glaze layer to be a nano-structured material, with variations in this nano-scale structure (Figures 5.90 – 5.92). Early deposits of glaze (the  $2.5 \mu\text{m}$  immediately adjacent to the Nimonic 80A) of grain size 10 nm to 50 nm have been overlaid by later deposits (the  $1 \mu\text{m}$  surface layer), which have undergone further refinement with extended sliding to between 5 and 15 nm. Topographical analysis by STM shows further refinement at the very surface of the glaze to values of 2 to 10 nm (Figure 6.23).

The wear data (Figure 5.1) indicate minimal changes in weight at not only  $750^\circ\text{C}$ , but at temperatures as low as  $510^\circ\text{C}$ , (the lower end of the temperature range for more comprehensive glaze formation –  $510^\circ\text{C}$  to  $750^\circ\text{C}$ ), thus demonstrating the effectiveness of these nano-structured surfaces in conferring high wear resistance. From this, as stated in the work of Datta *et al.* [117], two main issues require further resolution and elaboration:

- i. the formation of these nano-structured surfaces; and
- ii. the effectiveness of such surfaces in conferring improved wear resistance.

**Figure 6.23: STM imaging of compacted oxide glaze formed during sliding wear of Nimonic 80A against Stellite 6**





The generation of ultra-fine structures during high temperature sliding wear has been observed in a number of systems [117-119], requiring a process of mechanical mixing, that involves a repeating cycle of welding, fracture and rewelding of debris generated. This may be predominantly from one or other surface, as seen in the Nimonic 80A / Stellite 6 system at  $0.314 \text{ m.s}^{-1}$  and  $750^\circ\text{C}$  (transfer from the Stellite 6 tended to dominate) or from both [117, 119].

Until recently, very few studies have been conducted into the evolution of the resulting microstructures and defect structures generated during high temperature sliding wear. Results from detailed TEM studies in this laboratory have allowed a greater understanding of the mechanisms of formation of these wear resistant, nano-structured surfaces.

Datta *et al.* [117, 119] suggested a series of ‘initial processes’ for the generation of a nano-structured glaze layer:

- i. deformation of the surface;
- ii. intermixing of the debris generated from the wear sample and counterface surfaces;
- iii. oxidation of the wear surfaces / debris;
- iv. further mixing; and
- v. repeated welding and fracture.

These processes were aided by high temperature oxidation and diffusion. Positron Annihilation studies [120] confirmed the presence of vacancy clusters consisting of five vacancies.

Once a glaze layer is established, the next step involves the deformation of these oxides and generation of dislocations resulting in the formation of sub-grains. These sub-grains are then further refined with increasing misorientation producing high angle boundaries (a process called “fragmentation”) and a non-equilibrium state results, indicated by poorly defined and irregular grain boundaries. High internal stresses are created within the grains, with dislocation density and arrangement dependent on grain size – smaller grains

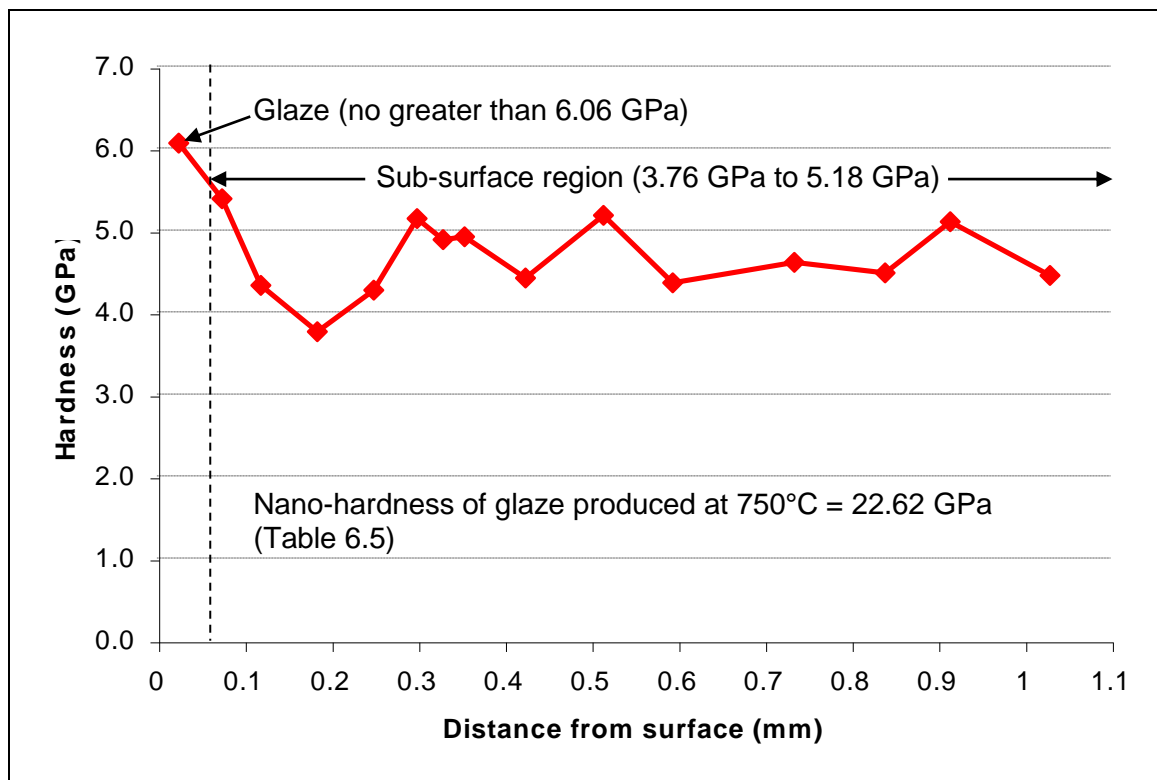
contain fewer dislocations [117,119]. The process leads to the formation of high-energy grain boundaries with a high defect density [121-125].

From the micro-hardness data (Figure 6.24), Datta *et al.* [117] reported no Hall-Petch softening, but neither was any significant hardening of the surface layers reported. Further investigation using nano-indentation did indicate a substantial degree of hardening (Table 6.5), however, the use of nano-hardness data to interpret results needs to be treated with caution, due to vulnerability to localised variations in the glaze layer brought about by the extremely localised nature of nano-indentation.

Such hardening can be attributed to the associated difficulties with dislocation generation in nano-sized grains [115,126,127] (as mentioned earlier, smaller grains contain fewer dislocations). As well as greater hardness, the presence of a nano-scale polycrystalline structure additionally infers improved fracture toughness [117,119] on the glaze material. All of these factors make debris generation an inefficient process.

**Figure 6.24: Surface and sub-surface layer micro-hardness for Nimonic 80A samples slid against Stellite 6 at  $0.314 \text{ m.s}^{-1}$  and  $750^\circ\text{C}$**

(load = 7N, sliding distance = 4,522 m, Vickers micro-indenter - 50g)



## 7. SUMMARY

### 7.1 Effect of Sliding Speed between Room Temperature and 750°C

#### 7.1.1 Nimonc 80A versus Stellite 6

##### 7.1.1.1 Nimonc 80A versus Stellite 6 at 0.314 m.s<sup>-1</sup>

- 1) At room temperature and 270°C, patches of loose chromium-cobalt oxide debris (CoCr<sub>2</sub>O<sub>4</sub>-phase – Figure 5.14a – sourced from the Stellite 6 counterface) developed on the surface of the Nimonc 80A sample (the micrographs – optical and SEM – are shown in Figures 5.3 and 5.5). These debris were retained at the wear interface and whilst protecting the Nimonc 80A from high wear (the wear rate was 0.626 µg.m<sup>-1</sup> between 0 and 4,522 m of sliding at room temperature and 0.539 µg.m<sup>-1</sup> at 270°C – Figure 5.1), they promoted further wear of the Stellite 6 counterface.
- 2) Agglomeration and sintering of the loose cobalt-chromium debris on the Nimonc 80A surface was first observed at 390°C, which on increasing the temperature to 450°C, was sufficient to result in the formation of some isolated patches of glaze (Figure 5.3). Wear rates remained low (Figure 5.1), at 0.184 µg.m<sup>-1</sup> at 390°C and -0.051 µg.m<sup>-1</sup> at 450°C, indicating that the oxide was continuing to protect the Nimonc 80A from wear.
- 3) Between 510°C and 750°C, rapid agglomeration and sintering of the debris occurred to form comprehensive wear-protective glaze layers (Figure 5.3) – at 510°C and 750°C, these developed within the first 38 m of sliding (Figures 5.20, 5.21 and 5.22). The CoCr<sub>2</sub>O<sub>4</sub>-phase oxide debris (XRD shown in Figure 5.14b) forming the glaze layers continued to be sourced from the Stellite 6, which underwent preferential wear during the early stage of the wear process. Very low, sometimes negative wear rates were obtained between 510°C and 750°C (-0.196 µg.m<sup>-1</sup> at 510°C, -0.312 µg.m<sup>-1</sup> at 630°C and -0.007 µg.m<sup>-1</sup> at 750°C – wear rate is for sliding between 0 and 4,522 m – Figure 5.1), indicating the wear protective nature of these glaze layers.
- 4) Some of this glaze then back-transferred to the Stellite 6, protecting both Nimonic 80A and Stellite 6 surfaces and resulting in an overall reduction in wear of both materials. This was demonstrated by the sliding of Stellite 6 as the sample against Nimonic 80A as the counterface (Figure 5.27). The carbides within the Stellite 6 did not disrupt glaze formation on either surface.

### 7.1.1.2 Nimonc 80A versus Stellite 6 at $0.905 \text{ m.s}^{-1}$

- 5) At room temperature and  $270^{\circ}\text{C}$ , wear levels remained low (for example, the wear rate between 0 and 4,522 m at  $270^{\circ}\text{C}$  was  $0.097 \mu\text{g.m}^{-1}$ ), due to the presence of loose oxide debris at the Nimonc 80A / Stellite 6 (counterface) interface separating the wear surfaces (Figure 5.4). No glaze formation was observed due to low residency times and low sliding temperature. There was no change in wear mode with extended sliding and wear remained low (indicated by a wear rate of  $0.029 \mu\text{g.m}^{-1}$  between 4,522 and 13,032 m at  $270^{\circ}\text{C}$ , not being significantly different to that between 0 and 4,522 m – Figure 5.1).
- 6) At  $390^{\circ}\text{C}$ ,  $450^{\circ}\text{C}$  and  $510^{\circ}\text{C}$ , a high friction severe wear regime dominated (with wear rates between 0 and 4,522 m of  $16.586 \mu\text{g.m}^{-1}$  at  $390^{\circ}\text{C}$  and  $19.604 \mu\text{g.m}^{-1}$  between 0 and 4,522 m at  $510^{\circ}\text{C}$  – Figure 5.1), accompanied by the production of a high level of metallic debris (by a delamination mechanism) from surface of the Nimonc 80A (Figure 5.7). No oxide layers were formed (the Nimonc 80A surface was heavily worn – Figure 5.4) due to a lack of debris retention and low debris residency times. This severe wear mode was maintained on extended sliding (at  $390^{\circ}\text{C}$ , a wear rate of  $16.299 \mu\text{g.m}^{-1}$  between 4,522 and 13,302 m was obtained; at  $510^{\circ}\text{C}$ , the wear rate between 4,522 and 13,032 m was  $22.564 \mu\text{g.m}^{-1}$  – values were similar to those observed between 0 and 4,522 m).
- 7) At  $570^{\circ}\text{C}$  and  $630^{\circ}\text{C}$ , the high levels of metallic debris produced predominantly from the Nimonc 80A were now accompanied by increasing levels of NiO and  $\text{Cr}_2\text{O}_3$ -phase debris production (XRD data for oxide debris at  $630^{\circ}\text{C}$  shown in Figure 5.15d), also sourced from the Nimonc 80A. These oxides did not readily sinter to form a glaze and in fact aggravated the wear process. This was reflected in the wear rates – at  $570^{\circ}\text{C}$  for example, the mean wear rate between 4,522 and 13,032 m was  $49.563 \mu\text{g.m}^{-1}$ , compared to  $13.907 \mu\text{g.m}^{-1}$  between 0 and 4,522 m (Figure 5.1).
- 8) At  $690^{\circ}\text{C}$  and  $750^{\circ}\text{C}$ , the extremely high levels of oxidation observed were now sufficient to exceed that eliminated by ejection. Debris residency times were thus now high enough to eliminate metal-to-metal contact, to produce a technically mild wear regime with low friction (Figure 5.2b).

- 9) However, the NiO and Cr<sub>2</sub>O<sub>3</sub>-phase oxides (XRD data in Figure 5.15d) produced at 690°C and 750°C did not form a glaze – even at 690°C and 750°C, these oxides displayed a very low tendency to sinter and thus form glaze layers. The mixture of loose NiO and Cr<sub>2</sub>O<sub>3</sub> oxides instead continued to assist the wear process, acting as abrasives on the surface of the Nimonc 80A, altering wear scar morphology from a worn metallic appearance at 510°C and 570°C to a grooved appearance at 690°C (Figure 5.6). Wear rates continued to increase with extended sliding as a result, increasing for example at 750°C from 17.653 µg.m<sup>-1</sup> between 0 and 4,522 m to 34.963 µg.m<sup>-1</sup> between 4,522 and 13,032 m (Figure 5.1).
- 10) The NiO and Cr<sub>2</sub>O<sub>3</sub>-phase oxides formed only a rough, patchy, unstable glaze on the surface of the Stellite 6, offering limited protection from wear to the Stellite 6 surface at 690°C and 750°C (Figure 5.4).

#### 7.1.1.3 Nickel 200<sup>TM</sup> versus Stellite 6 at 750°C

- 11) Nickel 200<sup>TM</sup> when worn against Stellite 6 at 750°C, exhibited extremely low wear (Figure 5.32) at both 0.314 m.s<sup>-1</sup> (with a recorded wear rate of -0.252 µg.m<sup>-1</sup> between 0 and 4,522 m) and 0.905 m.s<sup>-1</sup> (wear rate -0.184 µg.m<sup>-1</sup>), due to the formation of a NiO glaze (XRD data in Figure 5.36) sourced from the Nickel 200<sup>TM</sup> (optical and SEM micrographs in Figures 5.34 and 5.35) – sliding speed had no effect on the formation of this glaze layer. The glaze formed rapidly on both surfaces after initial wear of the Nickel 200<sup>TM</sup>.
- 12) Substitution of Nimonc 80A with Nickel 200<sup>TM</sup> allowed NiO glaze formation to occur due to:
  - a) the absence of rapid wear of the Stellite 6 at 0.314 m.s<sup>-1</sup> (thus no Co-Cr oxides were generated) when slid against Nickel 200<sup>TM</sup>;
  - b) at 0.905 m.s<sup>-1</sup>, there was an inherent inability of Nimonc 80A-sourced NiO and Cr<sub>2</sub>O<sub>3</sub> to sinter and form glaze when Nimonc 80A was the sample material – the substitution of Nimonc 80A with Nickel 200<sup>TM</sup> removed chromium from the wear system (at 0.905 m.s<sup>-1</sup>, debris was not being generated from the Stellite 6),

indicating that it was  $\text{Cr}_2\text{O}_3$  that was affecting the sintering characteristics of the Nimonic 80A-sourced oxide and was also acting as an abrasive agent.

### 7.1.2 *Incoloy MA956 versus Stellite 6*

#### 7.1.2.1 *Incoloy MA956 versus Stellite 6 at 0.314 m.s<sup>-1</sup>*

- 13) At room temperature and 270°C, loose patches of chromium-cobalt ( $\text{CoCr}_2\text{O}_4$ -phase) oxide debris were formed (Figures 5.40 and 5.42 show the optical and SEM micrographs respectively) which separated the wear surfaces and protected them from enhanced wear (the wear rate for 0 to 4,522 m of sliding was  $0.136 \mu\text{g.m}^{-1}$  at room temperature and  $0.101 \mu\text{g.m}^{-1}$  at 270°C – Figure 5.38). This debris was primarily generated from the Stellite 6, though a significant contribution was also made by the Incoloy MA956 sample (Figure 5.46).
- 14) The wear-protective loose Stellite 6-sourced chromium-cobalt ( $\text{CoCr}_2\text{O}_4$ -phase) debris persisted up to 450°C (Figure 5.40), with wear rates only slightly higher than at room temperature and 270°C – mean wear rates were recorded of  $0.545 \mu\text{g.m}^{-1}$  at 390°C and  $0.402 \mu\text{g.m}^{-1}$  at 450°C (Figure 5.38). However, sintering and agglomeration of this chromium-cobalt oxide debris was first observed at 390°C, with some isolated patches of glaze forming amongst the loose debris at 450°C.
- 15) Between 510°C and 750°C, rapid glaze development formed a comprehensive wear-protective layer (Figures 5.40 and 5.42) – wear rates decreased to negative values as a result (for example, mean wear rates were recorded at  $-0.130 \mu\text{g.m}^{-1}$  at 510°C,  $-0.335 \mu\text{g.m}^{-1}$  at 630°C and  $-0.150 \mu\text{g.m}^{-1}$  at 750°C – Figure 5.38). The Co-Cr oxide debris from which this glaze formed was still sourced primarily from the Stellite 6, though with a significant contribution from the Incoloy MA956 (Figure 5.46) – the effect of the iron sourced from Incoloy MA956 on the predominantly  $\text{CoCr}_2\text{O}_4$ -phase (XRD data in Figure 5.51b) oxide glaze is at this stage uncertain.
- 16) Some of this glaze was then back-transferred to the Stellite 6, protecting both Incoloy MA956 and Stellite 6 surfaces and resulting in an overall reduction in wear.

### 7.1.2.2 Incoloy MA956 versus Stellite 6 at 0.905 m.s<sup>-1</sup>

- 17) At room temperature and 270°C, low wear was maintained by the generation of oxide patches of Fe/Cr/Co oxide debris – optical and SEM micrographs are shown in Figures 5.41 and 5.42). This debris separated the Incoloy MA956 sample and Stellite 6 counterface and reduced wear (mean recorded wear rates were 0.462  $\mu\text{g.m}^{-1}$  between 0 and 4,522 m at room temperature and 0.411  $\mu\text{g.m}^{-1}$  at 270°C – Figure 5.38).

The primary source of the oxide debris at 0.905 m.s<sup>-1</sup> was now the Incoloy MA956 – increasing sliding speed from 0.314 m.s<sup>-1</sup> to 0.905 m.s<sup>-1</sup> resulted in a shift in the main source of the debris from the Stellite 6 to the Incoloy MA956. Extended wear did not result in a change of wear mode, as indicated by the minimal changes in wear rate (mean recorded wear rates between 4,522 and 13,032 m were 0.700  $\mu\text{g.m}^{-1}$  at room temperature and 0.127  $\mu\text{g.m}^{-1}$  at 270°C).

- 18) At 390°C, a high friction severe wear regime dominated with large quantities of metallic debris generated by a delamination mechanism predominantly from the surface of the Incoloy MA956 (the wear surface at 390°C and 0.905 m.s<sup>-1</sup> was of metallic appearance and highly damaged – Figures 5.41 and 5.42). No oxide layers were formed due to the lack of debris retention and low debris residency times. An increase in wear rate was observed on extended sliding (16.681  $\mu\text{g.m}^{-1}$  between 0 and 4,522 m, rising to 35.107  $\mu\text{g.m}^{-1}$  between 4,522 and 13,032 m – Figure 5.38), however, without an observable change in wear mode.

- 19) Between 450°C and 630°C, the level of severe wear progressively diminished as the increasing generation and retention of primarily Incoloy MA956-sourced iron-chromium oxide (Cr<sub>1.3</sub>Fe<sub>0.7</sub>O<sub>3</sub>-phase) debris with increasing temperature led to the progressively faster generation of mechanically stable, wear protective glaze layers on the Incoloy MA956 wear surface (Figures 5.41 and 5.42). Only a limited amount of chromium-cobalt oxide (CoCr<sub>2</sub>O<sub>4</sub>-phase) debris sourced from the Stellite 6 was transferred to and incorporated into the predominantly Incoloy MA956-sourced (FeCr<sub>2</sub>O<sub>4</sub>-phase) glaze layer at 0.905 m.s<sup>-1</sup> (Figure 5.47 – XRD shown in Figure 5.52c). This was reflected in the wear rate data (Figure 5.38) – at 450°C, the mean wear rate dropped from 32.675  $\mu\text{g.m}^{-1}$  between 0 and 4,522 m to -0.064  $\mu\text{g.m}^{-1}$



- between 4,522 and 13,032 m. At 510°C, a drop in wear rate from 18.330  $\mu\text{g.m}^{-1}$  to 4.318  $\mu\text{g.m}^{-1}$  was recorded – this pattern continued up to 630°C.
- 20) At 690°C and 750°C, extremely rapid generation of iron-chromium oxide ( $\text{FeCr}_2\text{O}_4$ -phase) debris predominantly from the surface of the Incoloy MA956 (Figure 5.47) and consequent formation of glaze (Figures 5.41 and 5.42), eliminated all but a very brief period of severe wear at the beginning of sliding. Again, only a limited amount of Stellite 6-sourced chromium-cobalt ( $\text{CoCr}_2\text{O}_4$ -phase) oxide was incorporated into the predominantly iron-chromium oxide ( $\text{FeCr}_2\text{O}_4$ -phase) glaze (XRD shown in Figure 5.52c). Wear rates at 690°C and 750°C were extremely low – at 690°C, wear rates of 0.243  $\mu\text{g.m}^{-1}$  between 0 and 4,522 m and 0.553  $\mu\text{g.m}^{-1}$  between 4,522 and 13,032 m were recorded. At 750°C, wear rates were 0.146  $\mu\text{g.m}^{-1}$  up to 4,522 m and 0.113  $\mu\text{g.m}^{-1}$  between 4,522 and 13,032 m respectively. The extremely low wear rates with minimal changes on extended sliding are indicative of a continuation of high temperature mild wear throughout sliding.
- 21) At 0.905  $\text{m.s}^{-1}$  / 750°C, the glaze layer also contained proportions of aluminium accounting for up to ~24%, due to diffusion and preferential oxidation of aluminium from within the debris layer and possibly the Incoloy MA956 sample material. However, it is unclear what affect this aluminium had on the properties or formation of the glaze.
- 22) The increase in sliding speed resulted in a shift in debris source from mainly the Stellite 6 at 0.314  $\text{m.s}^{-1}$  to predominantly the Incoloy MA956 at 0.905  $\text{m.s}^{-1}$ , regardless of temperature (Figures 5.46 and 5.47). This shift in source, resulting in a shift in composition from chromium-cobalt-based debris to iron-chromium-based debris, did not prevent the formation of the glaze.
- 23) Some of this glaze was then transferred to the Stellite 6, protecting both Incoloy MA956 and Stellite 6 surfaces and resulting in an overall reduction in wear.

### 7.1.3 *Nimonc 80A versus Incoloy 800HT*

#### 7.1.3.1 *Nimonc 80A versus Incoloy 800HT at 0.314 m.s<sup>-1</sup>*

- 24) At room temperature and 270°C, a severe wear mechanism was dominant with no production of oxide debris. Material removal was by a delamination-type mechanism, resulting in the production of large, flattened metallic debris that was primarily sourced from the Incoloy 800HT counterface. Much of this metallic debris adhered to the surface of the Nimonc 80A to form a hardened transfer layer (optical and SEM micrographs are shown in Figures 5.58 and 5.60a), which protected the surface of the Nimonc 80A and reduced wear – wear rates of 0.652  $\mu\text{g.m}^{-1}$  at room temperature and 1.656  $\mu\text{g.m}^{-1}$  at 270°C between 0 and 4,522 m of sliding were recorded (Figure 5.55).
- 25) At 390°C, 450°C and 510°C, some fine oxide debris was produced alongside the metallic debris – both the oxide debris and the metallic debris were of variable composition, some sourced from the Nimonc 80A sample and some from the Incoloy 800HT counterface. This oxide debris did not build up into wear protective oxide layers (only serving to discolour the wear surfaces) and was largely ejected from the Nimonc 80A / Incoloy 800HT (counterface) wear interface. It did, however, prevent the re-adhesion of the metallic debris, thus preventing the development of a metallic transfer layer (Figure 5.58). In the absence of either oxide or metallic transfer layers, the wear surfaces were not protected and wear consequently increased (Figure 5.55) – at 390°C, the wear rate was 12.370  $\mu\text{g.m}^{-1}$  up to 4,522 m of sliding, dropping slightly to 8.694  $\mu\text{g.m}^{-1}$  for up to 4,522 m of sliding at 510°C.
- 26) At temperatures of between 570°C and 750°C, oxide was produced in sufficient amounts to exceed that lost by ejection. Due to the increased residency of this oxide debris, wear protective nichromate ( $\text{NiCr}_2\text{O}_4$ -phase – XRD data in Figure 5.60b) glaze layers sourced almost exclusively from the Incoloy 800HT counterface, were thus able to develop on the Nimonc 80A wear scar (Figures 5.58 and 5.60) at a rate that increased with temperature. This increase in rate of oxide formation directly resulted in decreases in observed wear rate (Figure 5.55) – at 570°C, the mean wear rate was 6.454  $\mu\text{g.m}^{-1}$ , falling to -0.402  $\mu\text{g.m}^{-1}$  at 750°C (the negative value for wear indicating a net gain of material).

- 27) At 750°C, a dual-layered structure was produced by the sliding wear of Nimonc 80A against Incoloy 800HT at 0.314 m.s<sup>-1</sup> (this was clearly evident during Autopoint EDX analysis – Figure 5.66a). Firstly, during the early stages of wear, a mixed metal-oxide layer was formed by intermixing of material from both the Nimonc 80A and the Incoloy 800HT. This was overlaid at a later stage by a nichromate glaze layer, almost exclusively sourced from the Incoloy 800HT. Optical observations of Nimonc 80A samples slid against Incoloy 800HT at other glaze-forming temperatures (570°C, 630°C and 690°C) suggested that similar layered structures (glaze layer – mixed metal / oxide layer – substrate) were also formed.
- 28) The Incoloy 800HT counterface between 570°C and 750°C underwent a period of initial severe wear, at the end of which some of the metallic debris generated from the Incoloy 800HT counterface re-adhered to the Incoloy 800HT to form raised metallic asperities in the wear track. These asperities rose to 1.5 mm above the original surface of the unworn counterface. Glaze (also Incoloy 800HT-based) developed only on these asperities, due to interaction with the transfer layers on the Nimonc 80A sample (Figure 5.58).

#### **7.1.3.2 Nimonc 80A versus Incoloy 800HT at 0.905 m.s<sup>-1</sup>**

- 29) At room temperature and 270°C, wear was by a severe wear mechanism with no production of oxide debris. Material removal was by a delamination-type mechanism, resulting in the production of large, flattened metallic debris primarily sourced from the Incoloy 800HT counterface, which after 4,522 m of sliding was at a level greater than that at 0.314 m.s<sup>-1</sup>. A large proportion of the metallic debris adhered to the surface of the Nimonc 80A to form a hardened transfer layer (optical and SEM micrographs are shown in Figures 5.59 and 5.60b), which protected the surface of the Nimonc 80A and reduced wear. ‘Negative’ wear rates were obtained (due to deposition of material forming the metallic transfer layer) between 0 and 4,522 m (Figure 5.55), with values for wear rate of -1.988 µg.m<sup>-1</sup> at room temperature and -3.438 µg.m<sup>-1</sup> at 270°C.
- 30) Continued sliding up to 13,032 m at room temperature and 270°C resulted in only limited removal and readherance of debris, resulting in the development of a more

mechanically mixed metallic layer containing material from both the Nimonc 80A sample and Incoloy 800HT counterface. The metallic transfer layer continued to be wear protective with only slight losses (Figure 5.55), as indicated by the small but positive wear rates between 4,522 m and 13,032 m, of  $0.375 \mu\text{g.m}^{-1}$  at room temperature and  $0.421 \mu\text{g.m}^{-1}$  at  $270^\circ\text{C}$ .

- 31) Between  $390^\circ\text{C}$  and  $570^\circ\text{C}$ , some fine oxide debris was produced alongside the metallic debris. The increased ejection of the oxide debris at  $0.905 \text{ m.s}^{-1}$  compared to that at  $0.314 \text{ m.s}^{-1}$  meant that the oxide was less effective at preventing adhesion of metallic debris at the higher sliding speed. Consequently, a comprehensive metallic transfer layer was able to form at  $0.905 \text{ m.s}^{-1}$  (which was not able to form at  $0.314 \text{ m.s}^{-1}$ ), thus helping to protect the Nimonc 80A sample from extended wear at the expense of the Incoloy 800HT counterface (Figure 5.59).

This was reflected in the wear rates (Figure 5.55) with, for example, at  $450^\circ\text{C}$ , a large negative wear rate of  $-4.324 \mu\text{g.m}^{-1}$  between 0 and 4,522 m indicative of early (metallic) deposition and a small positive wear rate of  $1.659 \mu\text{g.m}^{-1}$  between 4,522 to 13,032 m due to only gradual removal of metal from the transfer layer.

- 32) Between  $630^\circ\text{C}$  and  $750^\circ\text{C}$ , oxide was produced at a sufficient rate at  $0.905 \text{ m.s}^{-1}$  to exceed that removed by ejection from the wear interface. The increased residency of the oxide thus allowed the development of an Incoloy 800HT-sourced nichromate ( $\text{NiCr}_2\text{O}_4$ -phase – XRD data in Figure 5.68b) glaze layer (Figures 5.59 and 5.60b), which as at  $0.314 \text{ m.s}^{-1}$ , protected the Nimonc 80A surface from wear. These glaze layers again developed more rapidly with temperature (changes in friction behaviour show this to be the case at  $0.905 \text{ m.s}^{-1}$  – Figure 5.57), though due to higher levels of debris ejection, their development was less rapid than at  $0.314 \text{ m.s}^{-1}$  – for this reason, glaze formation was not observed until  $630^\circ\text{C}$  at  $0.905 \text{ m.s}^{-1}$  (compared to  $570^\circ\text{C}$  at  $0.314 \text{ m.s}^{-1}$ ).

With the onset of glaze formation between  $630^\circ\text{C}$  and  $750^\circ\text{C}$ , the difference in wear rates began to decrease (Figure 5.55), with wear rate values at  $630^\circ\text{C}$  of  $1.997 \mu\text{g.m}^{-1}$  (4,522 to 13,032 m), compared to  $-2.702 \mu\text{g.m}^{-1}$  (0 to 4,522 m). The convergence of these values continued with increasing temperature as glaze formation became more rapid, with wear rates at  $750^\circ\text{C}$  of  $0.924 \mu\text{g.m}^{-1}$  between 0 and 4,522 m (due to some

limited severe wear during the initial stages of sliding) and  $-0.697 \mu\text{g.m}^{-1}$  between 4,522 and 13,032 m (as glaze layers continued to develop).

33) At  $750^{\circ}\text{C}$ , a multi-layered structure was produced by the sliding wear of Nimonc 80A against Incoloy 800HT at  $0.314 \text{ m.s}^{-1}$  (most evident by the use of Autopoint EDX – Figure 5.66b):

- a) a limited mechanically mixed metallic metal layer with material from both the Nimonc 80A sample and Incoloy 800HT counterface was formed during initial contact between the two surfaces;
- b) the wear process was then dominated by transfer from the Incoloy 800HT counterface, to form firstly a mixed metal-oxide layer then a completely oxidised layer (it is unclear whether the oxidised layer formed due to transfer of oxide or transfer of a mixture of metal and oxide which later underwent oxidation); and
- c) the nichromate ( $\text{NiCr}_2\text{O}_4$  – Figure 5.68b) glaze layer was then formed by interaction between the Incoloy 800HT-sourced oxide transfer layer on the Nimonc 80A and the Incoloy 800HT counterface after 869 m of sliding (Figure 5.57).

Optical observations of Nimonc 80A samples slid against Incoloy 800HT at other glaze-forming temperatures ( $630^{\circ}\text{C}$  and  $690^{\circ}\text{C}$ ) suggested that similar layered structures (glaze layer – mixed metal / oxide layer – substrate) were also formed.

34) The Incoloy 800HT counterface between  $630^{\circ}\text{C}$  and  $750^{\circ}\text{C}$  underwent a period of initial severe wear, at the end of which some of the metallic debris generated from the Incoloy 800HT readhered to form asperities in the wear track in a pattern identical to that observed at  $0.314 \text{ m.s}^{-1}$ . Glaze (Incoloy 800HT-based) developed only on these asperities as a result of interaction with the (Incoloy 800HT-sourced) transfer layers on the Nimonc 80A sample (Figure 5.59b).

#### 7.1.4 Incoloy MA956 versus Incoloy 800HT

##### 7.1.4.1 Incoloy MA956 versus Incoloy 800HT at 0.314 m.s<sup>-1</sup>

35) At room temperature and 270°C, the absence of oxide debris allowed direct contact between the Incoloy MA956 sample and Incoloy 800HT counterface. Severe wear by a delamination mechanism produced large metallic debris sourced from both the Incoloy MA956 and the Incoloy 800HT. This debris readhered to form a mechanically mixed transfer layer (optical and SEM micrographs are shown in Figures 5.76 and 5.78), which became work-hardened (Table 5.7) and limited the degree of wear – the heterogeneous composition of this layer indicated mixing was incomplete (XRD detected an interim composition Cr<sub>0.19</sub>Fe<sub>0.7</sub>Ni<sub>0.11</sub> phase – Figure 5.85a). The readhesion of this debris to form the transfer layer resulted in negligible wear rates at both room temperature and 270°C after 4,522 m of sliding (Figure 5.73).

36) Between 390°C and 570°C, both oxide and metallic debris were produced from both the Incoloy MA956 sample and the Incoloy 800HT counterface. Although the oxide debris produced did not form wear protective layers, it prevented readhesion of the metallic debris, thus preventing the formation of a metallic transfer layer (the 510°C / 4,522 m example is shown in Figure 5.76). Both the oxide and metallic debris were thus ejected (Figure 5.79). Reductions in hardness of both metals with temperature may also have facilitated easier removal of material.

In the absence of the debris and any wear protective layers, wear of both the Incoloy MA956 and the Incoloy 800HT increased (Figure 5.73). At 390°C, the wear rate at 0.314 m.s<sup>-1</sup> was recorded at 14.769 µg.m<sup>-1</sup> after 4,522 m of sliding. This rose to 23.893 µg.m<sup>-1</sup> at 510°C and 33.523 µg.m<sup>-1</sup> at 570°C (after 4,522 m).

37) At 630°C and 690°C, there was a further transition to a mild wear regime, due to increased production of Incoloy MA956-sourced (Cr<sub>1.3</sub>Fe<sub>0.7</sub>O<sub>3</sub>) debris outstripping that lost by ejection. The oxide was thus able to build up into wear-protective oxide layers (Figures 5.76 and 5.78). The high levels of debris ejection were still able to retard oxide build-up and there was still an initial extended period of severe wear at the beginning of sliding (Figure 5.75). The level of wear during this initial ‘severe wear’ phase was sufficient to continue the trend of increased wear with temperature

- (Figure 5.73) – the wear rate increased from  $44.829 \mu\text{g.m}^{-1}$  at  $630^\circ\text{C}$  to  $62.501 \mu\text{g.m}^{-1}$  at  $690^\circ\text{C}$  (sliding distance 4,522 m).
- 38) Only at  $750^\circ\text{C}$  did oxidation and glaze formation (Figures 5.76 and 5.78) occur rapidly enough to restrict metallic debris removal and severe wear during run-in (the oxide debris continued to be sourced from the Incoloy MA956), leading to a reduction in wear rate at this temperature (Figure 5.73) – the wear rate at  $750^\circ\text{C}$  was  $17.962 \mu\text{g.m}^{-1}$  (sliding distance 4,522 m) compared to  $62.501 \mu\text{g.m}^{-1}$  at  $690^\circ\text{C}$  (sliding distance 4,522 m).
- 39) Autopoint EDX indicated that a multi-layered structure was formed on the surface of the Incoloy MA956 sample on sliding at  $750^\circ\text{C}$  (Figure 5.84) and was composed of:
- a) a deformed metallic layer formed by removal of Incoloy MA956-sourced debris from and redeposition of this debris back onto the Incoloy MA956 sample during the early stages of wear;
  - b) an exclusively Incoloy MA956-sourced mixed metal-oxide layer, which developed by progressively greater oxidation of Incoloy MA956-sourced metallic debris with increased sliding distance, to produce some oxide debris slightly later in the wear process that mixed with the remaining metallic debris; and
  - c) a wear-protective oxide ( $\text{Cr}_{1.3}\text{Fe}_{0.7}\text{O}_3$ -phase – Figure 5.85d) glaze layer, produced after ~1,036 m of sliding (Figure 5.75) due to contact between the mixed metal-oxide debris layer and the Incoloy 800HT counterface – the Incoloy MA956-sourced mixed metal-oxide layer was the main source of the oxide in the glaze, there being no evidence of transfer from the Incoloy 800HT counterface.
- 40) At  $0.314 \text{ m.s}^{-1} / 750^\circ\text{C}$ , the glaze layer also contained proportions of aluminium in isolated areas accounting for as high as ~24% (though more normally, aluminium levels were no greater than ~12%), due to diffusion and preferential oxidation of aluminium from within debris layer and possibly the Incoloy MA956 sample material. The affect of the aluminium on the formation and properties of the glaze is, however, unclear.



- 41) The Incoloy 800HT counterface between 630°C and 750°C underwent a period of initial severe wear, during which metallic debris adhered to the wear track to form asperities (Figure 5.76). Subsequent glaze formation was restricted to the tips of the asperities, where they were in contact with the surface of the Incoloy MA956. Whether the asperities were redeposited Incoloy 800HT or were a mixed Incoloy MA956 / Incoloy 800HT composition is uncertain, however, the glaze was likely to be at least in part sourced from the Incoloy MA956 – glaze formed on the counterface at 750°C was of a composition intermediate between the Incoloy MA956 and the Incoloy 800HT.

#### 7.1.4.2 Incoloy MA956 versus Incoloy 800HT at 0.905 m.s<sup>-1</sup>

- 42) At room temperature and 270°C, the wear behaviour at 0.905 m.s<sup>-1</sup> was very similar to that at 0.314 m.s<sup>-1</sup> (i.e. severe wear), with metallic wear debris produced by a delamination mechanism from both the sample and the counterface. As at 0.314 m.s<sup>-1</sup>, no oxide was present to prevent metallic contact. Consequently, a mechanically mixed layer (XRD detected an interim composition Cr<sub>0.19</sub>Fe<sub>0.7</sub>Ni<sub>0.11</sub> phase – Figure 5.86a - mixing was again incomplete) was then formed by readhesion of the debris (Figures 5.77 and 5.78 show the optical and SEM micrographs), which became work-hardened (Table 5.7) due to the sliding action of the Incoloy MA956 sample against the Incoloy 800HT counterface.

The effect of the formation of the transfer layer on wear (leading to a reduction in wear rate on extended sliding between 4,522 m and 13,032 m) was reflected in the wear rate data (Figure 5.73). At room temperature, the wear rate fell from 1.045 µg.m<sup>-1</sup> between 0 and 4,522 m to -0.134 µg.m<sup>-1</sup> between 4,522 and 13,032 m. At 270°C, the reduction in wear rate was from 5.024 µg.m<sup>-1</sup> to 1.850 µg.m<sup>-1</sup>.

- 43) Between 390°C and 570°C, both oxide and metallic debris were produced at 0.905 m.s<sup>-1</sup> as it had at 0.314 m.s<sup>-1</sup> – once again, the oxide failed to form wear-protective layers. However, the higher levels of debris ejection and reduced residency times of debris at 0.905 m.s<sup>-1</sup>, meant that the oxide was not as effective at preventing the metal from readhering and patchy, primarily Incoloy MA956 transfer layers were able to form (Figures 5.77 and 5.78b show the 510°C case).

These layers offered a limited degree of protection to the Incoloy MA956 sample, which underwent less wear at  $0.905 \text{ m.s}^{-1}$  (after 4,522 m) than at  $0.314 \text{ m.s}^{-1}$  (after 4,522 m). For example, at  $390^\circ\text{C}$ , the wear rate decreased from  $14.769 \mu\text{g.m}^{-1}$  at  $0.314 \text{ m.s}^{-1}$  to  $9.928 \mu\text{g.m}^{-1}$  at  $0.905 \text{ m.s}^{-1}$ . At  $510^\circ\text{C}$ , the reduction in wear rate was from  $23.893 \mu\text{g.m}^{-1}$  at  $0.314 \text{ m.s}^{-1}$  to  $13.703 \mu\text{g.m}^{-1}$  at  $0.905 \text{ m.s}^{-1}$  (Figure 5.73).

However, the patchy transfer layers on the Incoloy MA956 samples formed between  $390^\circ\text{C}$  and  $570^\circ\text{C}$  at  $0.905 \text{ m.s}^{-1}$  were insufficient to have a significant effect on wear rate on extended sliding (4,522 to 13,032 m). For example, wear rates at  $390^\circ\text{C}$  actually rose very slightly from  $9.928 \mu\text{g.m}^{-1}$  between 0 and 4,522 m to  $11.866 \mu\text{g.m}^{-1}$  between 4,522 and 13,032 m. At  $510^\circ\text{C}$ , only a slight decrease in wear rate was observed, from  $13.703 \mu\text{g.m}^{-1}$  between 0 and 4,522 m to  $11.054 \mu\text{g.m}^{-1}$  between 4,522 m and 13,302 m.

- 44) At  $570^\circ\text{C}$  and  $630^\circ\text{C}$ , the patchy metallic transfer layers were observed only after 4,522 m of sliding. These transfer layers were removed on extended sliding up to 13,032 m, with accompanying increases in wear rate due to the loss of what little protection they offered. At  $570^\circ\text{C}$ , the wear rate increased from  $18.573 \mu\text{g.m}^{-1}$  between 0 and 4,522 m to  $27.838 \mu\text{g.m}^{-1}$  between 4,522 and 13,032 m. At  $630^\circ\text{C}$ , the increase was from  $29.011 \mu\text{g.m}^{-1}$  to  $41.477 \mu\text{g.m}^{-1}$ .
- 45) The readhesion of metallic debris for the Incoloy MA956 / Incoloy 800HT (counterface) system at  $0.905 \text{ m.s}^{-1}$  and between  $390^\circ\text{C}$  and  $570^\circ\text{C}$ , was less than that observed for equivalent conditions for Nimonc 80A versus Incoloy 800HT. The transfer layer formed on the surface of the Incoloy MA956 was patchier (Figures 5.77 and 5.78b show the  $510^\circ\text{C}$  case) and wear protection was also consequently less. At  $390^\circ\text{C}$ , the wear rate between 0 and 4,522 m for the Incoloy MA956 / Incoloy 800HT system was  $9.928 \mu\text{g.m}^{-1}$ , compared to  $-3.279 \mu\text{g.m}^{-1}$  over the same range for the Nimonc 80A / Incoloy 800HT system (the negative value of wear rate indicating a gain in material by the Nimonc 80A due to transfer from the Incoloy 800HT). At  $510^\circ\text{C}$ , the respective wear rates were  $13.703 \mu\text{g.m}^{-1}$  for the Incoloy MA956 / Incoloy 800HT system and  $-3.890 \mu\text{g.m}^{-1}$  for the Nimonc 80A / Incoloy 800HT system.
- 46) At  $630^\circ\text{C}$ ,  $690^\circ\text{C}$  and  $750^\circ\text{C}$ , there was a transition to a mild wear regime, brought about by the increased production of Incoloy MA956-sourced ( $\text{Cr}_{1.3}\text{Fe}_{0.7}\text{O}_3$ -phase –

XRD data shown in Figure 5.86c) oxide. However, reduced residency times and greater ejection of debris at  $0.905 \text{ m.s}^{-1}$  delayed the formation of glaze (optical and SEM micrographs for  $750^\circ\text{C}$  are shown in Figures 5.77 and 5.78b) from this oxide and an extended critical period was needed for the development of wear-protective glaze layers (Figure 5.75), compared to those formed at  $0.314 \text{ m.s}^{-1}$ . Only on reaching  $690^\circ\text{C}$ , did the onset of glaze formation begin to reduce the rate of wear (Figure 5.73), from  $56.970 \mu\text{g.m}^{-1}$  between 0 and 4,522 m to  $14.601 \mu\text{g.m}^{-1}$  between 4,522 and 13,032 m. At  $750^\circ\text{C}$ , the wear rate fell from  $73.413 \mu\text{g.m}^{-1}$  to  $42.728 \mu\text{g.m}^{-1}$ .

- 47) However, the enhanced glaze formation observed at both  $690^\circ\text{C}$  and  $750^\circ\text{C}$  (between 4,522 and 13,032 m) failed to prevent an increase in wear on increasing the sliding temperature from  $690^\circ\text{C}$  to  $750^\circ\text{C}$  (Figure 5.73), due to high levels of plastic flow of the underlying Incoloy MA956 substrate – this reduced the required mechanical support for the comprehensive glaze layers forming on the wear surface. The wear rate consequently increased from  $14.601 \mu\text{g.m}^{-1}$  between 4,522 and 13,032 m at  $690^\circ\text{C}$  to  $42.728 \mu\text{g.m}^{-1}$  between 4,522 and 13,032 m at  $750^\circ\text{C}$ .
- 48) A multi-layered structure was formed on the Incoloy MA956 sample surface at  $750^\circ\text{C}$  and  $0.905 \text{ m.s}^{-1}$  (after 4,522 m of sliding) and was composed of:
- a) a deformed, limited metallic layer developed during the early stages of sliding, due to the removal and redeposition of metallic Incoloy MA956 debris;
  - b) a mixed metal-oxide layer, formed at a later stage by progressively greater oxidation of the Incoloy MA956-sourced debris with increased sliding distance;
  - c) a wholly oxidised layer again sourced from the Incoloy MA956 developed later during the sliding process; and
  - d) a wear-protective iron-chromium ( $\text{Cr}_{1.3}\text{Fe}_{0.7}\text{O}_3$ -phase) glaze layer, formed after ~2,285 m of sliding (Figure 5.75) due to interaction of the underlying oxide debris layer with the Incoloy 800HT counterface – there was no detectable contribution to this glaze layer from the Incoloy 800HT.

This is very similar to the multi-layered structure formed at  $0.314 \text{ m.s}^{-1}$ , with the exception that there was a higher degree of oxidation, leading to the formation of the

wholly oxidised layer at  $0.905 \text{ m.s}^{-1}$ . The formation of this glaze layer was also greatly retarded due to the higher ejection rates and lower residency times at  $0.905 \text{ m.s}^{-1}$ , (forming after  $\sim 2,285 \text{ m}$  of sliding, compared to  $\sim 1,036 \text{ m}$  of sliding at  $0.314 \text{ m.s}^{-1}$  – Figure 5.75).

- 46) At  $0.905 \text{ m.s}^{-1} / 750^{\circ}\text{C}$ , the glaze layer also contained levels of aluminium accounting for as high as 32% in some isolated areas (though more normally, aluminium levels were no greater than 15% to 20%), due to diffusion and preferential oxidation of aluminium from within debris layer and possibly the Incoloy MA956 sample material. As at  $0.314 \text{ m.s}^{-1} / 750^{\circ}\text{C}$ , it is however unclear what affect the aluminium had on the formation and properties of the glaze.
- 47) Between  $630^{\circ}\text{C}$  and  $750^{\circ}\text{C}$  at  $0.905 \text{ m.s}^{-1}$ , the Incoloy 800HT counterface underwent a period of initial severe wear, during which metallic debris adhered to the wear track to form asperities as they had at  $0.314 \text{ m.s}^{-1}$ . Subsequent glaze formation was restricted to the tips of the asperities in the counterface wear track, where contact was made with the surface of the Incoloy MA956 (Figure 5.77b). As at  $0.314 \text{ m.s}^{-1}$ , whether the asperities were redeposited Incoloy 800HT or were a mixed Incoloy MA956 / Incoloy 800HT composition is not certain, however, the glaze was likely to be at least in part sourced from the Incoloy MA956 – glaze formation on the counterface at  $750^{\circ}\text{C}$  was of an intermediate composition between the Incoloy MA956 and the Incoloy 800HT.

## 7.2 In-depth and Nano-scale Studies of Nimonc 80A Samples worn against Stellite 6 at 750°C and 0.314 m.s<sup>-1</sup>

### 7.2.1 Nano-hardness of Glaze Layers – Nimonc 80A versus Stellite 6 and Incoloy MA956 versus Stellite 6

48) Nano-hardness testing succeeded in obtaining values of sample glaze layer hardness for combinations where it was not possible before – nano-hardness for successful tests were typically of the following values (the full data is presented in Table 5.9):

- a) For Incoloy MA956 versus Stellite 6 slid at 750°C, a mean value of 21.97 GPa was obtained, close to the theoretical value of hardness for bulk chromium oxide of 28.98 GPa [116].
- b) For Nimonc 80A versus Stellite 6 slid at 510°C, a mean value of 25.03 GPa was obtained.
- c) For Nimonc 80A versus Stellite 6 slid at 750°C, a mean value of 22.62 GPa was obtained, around four times higher than the values obtained for this combination during micro-hardness testing.

The reason for the more successful testing using nano-indentation, is that with the much smaller indenter and lower levels of load used, the indenter did not penetrate the glaze layer into any powdery layer or the substrate beneath. Hardness values between the three sets of data were not significantly different.

- 49) Nano-hardness testing of glaze layers could not be conducted with an applied load of more than 5,000 µN. Attempts to test at 10,000 µN resulted in the indenter penetrating the glaze layer in the same way as observed with micro-hardness testing.
- 50) The highest hardness values were obtained with smoother areas of glaze, apparently free of cracks and porosity, which resulted in much lower apparent values of hardness.
- 51) The modulus values for Nimonc 80A versus Stellite 6 at 750°C (the mean value was 129.7 GPa) were on average 8% greater than those for Incoloy MA956 versus Stellite 6 at 750°C (the mean value for successful tests was 120.3 GPa). However, the

level of data scatter means that this difference cannot be considered statistically significant.

- 52) The modulus values for Nimonc 80A versus Stellite 6 at 510°C (the mean value for successful tests was 99.8 GPa) was only 76% of those obtained at 750°C (the mean value for successful tests was 129.7 GPa). Even with the high level of data scatter, this is a significant difference – this is attributed to a higher level of porosity even in the smooth areas of glaze formed at 510°C, due to the sintering processes being less complete at this lower temperature.
- 53) Despite the higher levels of hardness indicated by nano-hardness, some caution is still required in using nano-indentation as a tool to interpret the properties of the glaze layers. There was still the possibility of variance in the data due to the extremely localised nature of nano-indentation, making the data collected vulnerable to localised changes in the physical nature of the glaze (i.e. the presence of porosity or hard particles, or variation in glaze thickness).

### ***7.2.2 Nano-scale Characterisation of Glaze Layers – Nimonc 80A / Stellite 6 at 0.314 m.s<sup>-1</sup> and 750°C***

- 54) The high temperature sliding wear of Nimonc 80A against Stellite 6 as a counterface alloy allowed the development of a wear resistant nano-structured glaze layer (Figures 5.90 and 5.94).
- 55) A process called “fragmentation” – involving deformation, generation of dislocations, formation of sub-grains and their increasing refinement causing increasing misorientation – was responsible for the formation of nano-structured grains.
- 56) The improved wear resistance of such a layer has been attributed to the absence of Hall-Petch softening and enhanced fracture toughness and hardness of the surface.

## 8. RECOMMENDATIONS FOR FURTHER WORK

The information generated in this study has allowed the construction of basic wear maps (Figures 6.4, 6.8, 6.15, 6.22). It has also been established that chemical composition can have a significant effect on the wear process. Also, the use of TEM and STM has given an insight at a nano-scale level into the behaviour of materials undergoing sliding and this nano-scale information has permitted an informed understanding of the mechanisms of glaze formation. However, the picture of the precise effects of individual elements and of environmental factors upon them (temperature, speed, load) on the glaze-forming process is still far from clear. It is also clear that the mechanisms involved are material specific.

The following studies are thus suggested in order to further the work carried out during the current experimental programme.

- 1) Further nano-scale work (using, for example, nano-indentation, TEM and STM) is necessary to ascertain the influence of temperature, speed and materials on glaze development.
- 2) The effectiveness of pre-oxidation of superalloys under conditions of limited debris retention has not as yet been fully explored – it is suggested that the experimental work carried out by Wood [2] on pre-oxidation of Incoloy MA956 is extended to other wear combinations.
- 3) The study of the effects of sliding speed has to date been restricted to wear behaviour at  $0.314 \text{ m.s}^{-1}$ ,  $0.654 \text{ m.s}^{-1}$  [2] and  $0.905 \text{ m.s}^{-1}$ . In order to obtain a greater understanding of the effects of sliding speed, it is necessary to increase the range of sliding speeds so that the effects of more subtle variations of sliding speed can be examined (possibly in combination with an adjustable load). This would be especially useful for the study of transitions of wear behaviour – for example, the transition from a low wear, glaze forming regime at  $0.314 \text{ m.s}^{-1}$  to a high wear, mixed sliding regime at  $0.905 \text{ m.s}^{-1}$  in the Nimonic 80A / Stellite 6 (counterface) system between  $630^{\circ}\text{C}$  and  $750^{\circ}\text{C}$ .
- 4) The wear rig is not at this time able to study the effects of sliding speed at less than  $0.314 \text{ m.s}^{-1}$  and greater than  $0.905 \text{ m.s}^{-1}$ . The modification of the wear rig is therefore



necessary to study wear behaviour of very low or very high sliding speeds under conditions of limited debris retention.

- 5) To date, sliding wear studies have largely been carried out on commercially available alloys that contain many minor alloying components that can have a significant effect on the nature of the wear process. Carrying out sliding wear tests using pure metals or controlled alloy combinations without minor alloying additions will allow a better understanding of the effects of individual components on oxide and glaze formation.
- 6) During the sliding of Incoloy MA956 against either Stellite 6 or Incoloy 800HT at high temperature (i.e 750°C), aluminium within the Incoloy 800HT showed a strong tendency to diffuse towards the wear interface and oxidise, resulting in high concentration of aluminium oxide within any oxide or glaze layers formed. The effects of such diffusion on the glaze forming process are not understood and it is recommended that in order to gain a greater understanding of this effect, that testing is repeated with modified alloys both absent of and containing controlled amounts of aluminium (and other elements susceptible to high levels of diffusion).
- 7) The sintering behaviour of the oxides has been shown to be of key importance during the formation of glaze layers. To better understand the formation of these glaze layers, the study is recommended of this sintering behaviour and the adhesion properties of fine oxide debris produced during sliding wear to surfaces at elevated temperatures – this could possibly be done by high temperature atomic force microscopy.
- 8) The use of techniques used within this thesis, such as Autopoint EDX and mapping has been restricted to the formation of oxide wear layers at 0.314 m.s<sup>-1</sup> and 0.905 m.s<sup>-1</sup> at 750°C under 7N load. These techniques could also be used to study the influence of temperature on individual components within the wear layers during wear layer development at other temperatures, under varying conditions of speed and load.

## REFERENCES

- [1] P.D. Wood – “The Effect of the Counterface on the Wear Resistance of Certain Alloys at Room Temperature and 750°C”, *Ph.D. Thesis*, SERG, Northumbria University (1997)
- [2] S.R. Rose – “Studies of the High Temperature Tribological Behaviour of Superalloys”, *Ph.D. Thesis*, AMRI, Northumbria University (2000)
- [3] P.D. Wood, P.K. Datta, J.S. Burnell-Gray and N. Wood – “Investigation Into the High Temperature Wear Properties of Alloys Contacting Against Different Counterfaces”, *Material Science Forum*, **Vols. 251-254** (1997) 467-474
- [4] F.H. Stott, D.S. Lin and G.C. Wood – “The Structure and Mechanism of Formation of the ‘Glaze’ Oxide Layers Produced on Nickel-Based Alloys during Wear at High Temperatures”, *Corrosion Science*, **Vol. 13** (1973) 449-469
- [5] F.H. Stott, J. Glascott and G.C. Wood – “Models for the Generation of Oxides during Sliding Wear”, *Proc Royal Society London A* **402** (1985) 167-186
- [6] J. Hall Stephens (Editor) – “Kempe’s Engineer’s Yearbook 2002”, *CMP Information Ltd.* (2001)
- [7] Leonardo Da Vinci – “Rollers for Friction Studies”, *Manoscritto L. Foglio 11 V.*
- [8] I.M. Hutchings – “Tribology: Friction and Wear of Engineering Materials”, *Edward Arnold* (1992)
- [9] J.F. Archard and W. Hirst – “The Wear of Metals under Unlubricated Conditions”, *Proc Royal Society London, A* **236** (1956) 397-410
- [10] J.I. Mc. Cool – “Comparison of Models for the Contact of Rough Surfaces” *Wear* **107** (1986) 37-60
- [11] J.A. Greenwood and J.B.P. Williamson – “Contact of Nominally Flat Surfaces”, *Proc. Royal Society London, A* **295** (1966) 300-319
- [12] A.R. Savkoor and G.A.D. Briggs – “The Effect of Tangential Force on the Contact of Elastic Solids” *Proc. Royal Society London, A* **356** (1977) 103-114
- [13] J.F. Archard and W. Hirst – “An Examination of a Mild Wear Process” *Proc. Royal Society London, A* **238** (1957) 515-528
- [14] T.F.J. Quinn – “Review of Oxidational Wear. Part 1: The Origins of Oxidational Wear” *Tribol. Int.*, **16** (1983) 257-270
- [15] H-K. Oh, K-H. Yeon, H.Y. Kim – “The Influence of Atmospheric Humidity on the Friction and Wear of Carbon Steels” *Journal of Materials Processing Technology*, **95** (1999) 10-16
- [16] J.F. Archard – “The Temperature of Rubbing Surfaces”, *Wear* **2** (1958/59) 438-455

- [17] J.K. Lancaster – “The Formation of Surface Films at the Transition Between Mild and Severe Metallic Wear”, *Proc. Royal Society London, A* **273** (1962) 466-483
- [18] J. Jiang, F.H. Stott and M.M. Stack – “The Effect of Partial Pressure of Oxygen on the Tribological Behaviour of a Nickel-Based Alloy, Nimonic 80A, at Elevated Temperature”, *Wear* **203-204** (1997) 615-625
- [19] F.H. Stott and G.C. Wood – “The Influence of Oxides on the Friction and Wear of Alloys”, *Tribo. Int.*, **11** (1978) 211-218
- [20] F.P. Bowden and D. Tabor – “Friction, an Introduction to Tribology” Publ. Heinemann, London (1973)
- [21] T.S. Eyre and D. Maynard – “Surface Aspects of Unlubricated Metal-to-Metal Wear” *Wear* **18**, (1971) 301-310
- [22] N.C. Welsh – “The Dry Wear of Steels 1, the General Pattern of Behaviour” *Phil. Trans.*, **257A** (1965) 31-50
- [23] N.C. Welsh – “The Dry Wear of Steels 2, Interpretation and Special Features” *Phil. Trans.*, **257A** (1965) 51-70
- [24] J.T. Burwell and C.D. Strang – “On the Empirical Law of Adhesive Wear”, *J. Applied Physics* **23** (1952) 18-28
- [25] K. Ludema – “Scuffing, Run-in and the Function of Surface Films, Particularly Oxides” *Review Paper for Interdisciplinary Collaboration in Tribology Project, NASA-Lewis* (1981)
- [26] D. Tabor – “Wear – A Critical Synoptic View” *Proc. Int. Conference on Wear of Materials, St. Louis, Missouri in April 1977, ASME* (1978) 1-10
- [27] E.C. Rabinowicz – “Friction and Wear of Materials” Publ. New York Wiley (1965)
- [28] C. Subramaniam – “Wear of Al-12.3 Wt% Si Alloy Slid Against Various Counterface Materials” *Scripta Metallurgica* **25** (1991) 1369-1374
- [29] C. Subramaniam – “Effects of Sliding Speed on the Unlubricated Wear Behaviour of Al -12.3 Wt. % Si Alloy” *Wear* **151** (1991) 97-110
- [30] C. Subramaniam – “On Mechanical Mixing during Dry Sliding of Aluminium – 12.3 Wt % Silicon Alloy Against Copper” *Wear* **161** (1993) 53-60
- [31] K.C. Ludema – “Third Bodies in Wear Models – Wear Particles: From the Cradle to the Grave”, *Proceedings of the 18<sup>th</sup> Leeds-Lyon Symposium on Tribology*, 3-6<sup>th</sup> September 1991, Lyon, France, Ed. D. Dowson, Publ. Elsevier, 155-160
- [32] E.J. Halling – “Principles of Tribology” *Publ. Macmillan Press*
- [33] N.P. Suh – “The Delamination Theory of Wear” *Wear* **25** (1973) 111-124

- 
- [34] H.C. Sin and N.P. Suh – “Subsurface Crack Propagation Due to Surface Traction in Sliding Wear” *J. App. Mech. Trans. ASME* **51** (1984) 317-323
- [35] D.A. Rigney and W.A. Glaeser – “The Significance of Near Surface Microstructure in the Wear Process” *Wear* **46** (1978) 241-250
- [36] S. Fayeulle, A.B. Vannes and L. Vincent – “First Body Behaviour before Debris Formation – Wear Particles: From the Cradle to the Grave”, *Proceedings of the 18<sup>th</sup> Leeds-Lyon Symposium of Tribology*, 3<sup>rd</sup> – 6<sup>th</sup> September 1991, Lyon, France, Ed. D. Dowson, Publ. Elsevier, 229-235
- [37] D.A. Rigney – “Transfer, Mixing and Associated Chemical and Mechanical Processes during the Sliding of Ductile Materials” *Wear* **245** (2000) 1 – 9
- [38] P.J. Blau – “Mechanisms for Traditional Friction and Wear Behaviour of Sliding Metals” *Wear* **72** (1981) 55-66
- [39] A. Iwabuchi – “The Role of Oxide Particles in the Fretting Wear of Mild Steel” *Wear* **151** (1990) 301-311
- [40] A. Iwabuchi, H. Kubosawa and K. Hori – “The Effect of Oxide Particles Supplied at the Interface before Sliding on the Severe – Mild Wear Transition”, *Wear* **128** (1988) 123-137
- [41] A. Iwabuchi, H. Kubosawa and K. Hori – “The Dependence of the Transition of Severe to Mild Wear on Load and Surface Roughness When the Oxide Particles Are Supplied before Sliding” *Wear* **139** (1990) 319-333
- [42] E.R. Leheup and R.E. Pendlebury – “Unlubricated Reciprocating Wear of Stainless Steel with an Interfacial Air Flow”, *Wear* **142** (1991) 351 – 372
- [43] C. Colombie, Y. Berthier, A. Floquet and L. Vincent “Fretting: Load Carrying Capacity of Wear Debris” *Trans. ASME* **106F** (1984) 194-201
- [44] K. Hiratsukam, T. Sasada and S. Norose – “The Magnetic Effect on the Wear of Metals” *Wear* **110** (1986) 251-261
- [45] N. Soda and T. Sasada – “Mechanisms of Lubrication by Surrounding Gas Molecules in Adhesive Wear” *ASME Trans., J. Lubr. Technol.*, **100,4** (1978) 492-499
- [46] W-Z Wu, J-D. Xing and J-Y. Su “An Investigation on Three Body Abrasive Wear Test at Elevated Temperature” *Wear* **210** (1997) 299-303
- [47] F.H. Stott and D.R.G. Mitchell – “The Influence of Coating on Wear at Elevated Temperatures” *Surface Engineering, Volume 1 Fundamentals of Coatings*, Ed. P.K. Datta and J.S. Gray, Royal Society of Chemistry (1993) 141-150
- [48] J.L. Sullivan and N.W. Granville – “Reciprocating Sliding Wear of 9% Cr Steel in Carbon Dioxide at Elevated Temperatures”, *Tribol. Int.*, **17** (1984) 63-71

- [49] J.S. Halliday and W. Hirst – “The Fretting Corrosion of Mild Steel” *Proc. Royal Society London, A* **236** (1956) 411-425
- [50] Nam. P. Suh and H.C. Sin – “The Genesis of Friction” *Wear* **69**, (1981) 91-114
- [51] S.L. Rice, F.A. Moslehy and J. Zhang – “The Role of Wear Particles in Modifying Coefficients of Friction – Wear Particles: From the Cradle to the Grave”, Proceedings of the 18<sup>th</sup> Leeds-Lyon Symposium on Tribology, 3-6<sup>th</sup> September 1991, Lyon, France, Ed. D. Dowson, Publ. Elsevier, 463-467
- [52] H. Hesmat – “The Rheology and Hydrodynamics of Dry Powder Lubrication” *Tribology Trans.* **34**, **3** (1991) 433-439
- [53] J. Jiang, F.H. Stott and M.M. Stack “Some Frictional Features Associated with the Sliding Wear of the Nickel-Base Alloy Nimonic 80A at Temperatures up to 250°C”, *Wear* **176** (1994) 185-194
- [54] F.H. Stott – “High-Temperature Sliding Wear of Metals”, *Trib. Int.*, **35** (2002) 489-495
- [55] D.J. Shaw – “Colloid and Surface Chemistry” Fourth Edition, Publ. Butterworth Heinemann (1992)
- [56] Y.H. Zhou, M. Harmelin, J. Bigot – “Sintering Behaviour of Ultra-Fine Fe, Ni and Fe-25 Wt. % Ni Powders”, *Scripta Metallurgica*, **23** (1989) 1391-1396
- [57] K.J. Bhansali – “Adhesive Wear of Nickel- and Cobalt-Base Alloys”, *Wear* **160** (1980) 95-110
- [58] K. Razavizadeh and T.S. Eyre – “Oxidative Wear of Aluminium Alloys”, *Wear* **79** (1982) 325-333
- [59] D.S. Lin, F.H. Stott, G.C. Wood, K.W. Wright and J.H. Allen – “The Friction and Wear Behaviour of Nickel-Based Alloys during High Temperature Wear”, *Wear* **24** (1973) 261-278
- [60] D.S. Lin, F.H. Stott, G.C. Wood – “The Effects of Friction and Wear Behaviour of Some Commercial Nickel Base Alloys”, *Trans ASLE* **17**, **4** (1973) 251-262
- [61] F.H. Stott, D.S. Lin, G.C. Wood – “The Wear and Friction of Nickel-Base Alloys under Oxidising Conditions”, *Proc. 5<sup>th</sup> Eur. Congr. on Corrosion* (1973) 452-455
- [62] F.H. Stott, D.S. Lin, G.C. Wood – “‘Glazes’ Produced on Nickel-Based Alloys during High Temperature Wear”, *Nature Physical Science*, **242** (April 2 1973) 75-77
- [63] F.H. Stott, D.S. Lin, G.C. Wood and C.W. Stevenson – “The Tribological Behaviour of Nickel and Nickel-Chromium Alloys at Temperature from 20 to 800°C”, *Wear* **36** (1976) 147-174
- [64] F.H. Stott, J. Glascott and G.C. Wood – “The Transition from Severe to Mild Sliding Wear for Fe-12%Cr-Base Alloys at Low Temperature”, *Wear* **97** (1984) 155-178

- [65] F.H. Stott, J. Glascott and G.C. Wood – “Factors Affecting the Progressive Development of Wear-Protective Oxides on Iron-Based Alloys during Sliding at Elevated Temperatures”, *Wear* **97** (1984) 93-106
- [66] F.H. Stott – “The Role of Oxidation in the Wear of Alloys”, *Tribology International*, **31** (1998) 61-71
- [67] D.J. Barnes, J.E. Wilson, F.H. Stott and G.C. Wood – “The Influence of Oxide Films on the Friction and Wear of Fe-5%Cr Alloy in Controlled Environments”, *Wear* **45** (1977) 161-176
- [68] D.J. Barnes, F.H. Stott and G.C. Wood – “The Frictional Behaviour of Iron and Iron-Chromium Alloys at Elevated Temperatures”, *Wear* **45** (1977) 199-209
- [69] D.J. Barnes, J.E. Wilson, F.H. Stott and G.C. Wood – “The Influence of Specimen Geometry and Sliding Mode on the Friction and Wear of Iron-Chromium Alloys in Controlled Environments”, *Wear* **45** (1977) 97-111
- [70] J. Jiang, F.H. Stott and M.M. Stack – “The Role of Triboparticles in Dry Sliding Wear”, *Tribo. Int.*, **Vol. 31, No. 5** (1998) 245-256
- [71] J. Jiang, F.H. Stott and M.M. Stack – “A Mathematical Model for Sliding Wear of Metals at Elevated Temperatures”, *Wear* **181** (1995) 20-31
- [72] J. Jiang, F.H. Stott, M.M. Stack – “Characterisation of Wear Scar Surfaces Using Combined Three-Dimensional Topographic Analysis and Contact Resistance Measurements”, *Tribo. Int.*, **Vol. 30, No. 7** (1997) 517-526
- [73] T.F.J. Quinn – “Oxidational Wear”, *Wear* **18** (1971) 413-419
- [74] T.F.J. Quinn – “Computational Methods Applied to Oxidational Wear”, *Wear* **199** (1996) 169-180
- [75] T.F.J. Quinn – “Oxidational Wear Modelling: Part 1”, *Wear* **153** (1992) 179-200
- [76] T.F.J. Quinn – “Oxidational Wear Modelling: Part 2 – The General Theory of Oxidational Wear”, *Wear* **175** (1994) 199-208
- [77] I. Garcia, A. Ramil and J.P. Celis – “A Mild Oxidation Model Valid for Discontinuous Contacts in Sliding Wear Tests: Role of Contact Frequency”, *Wear* **254** (2003) 429-440
- [78] B Chattopadhyay and G.C. Wood – “The Transient Oxidation of Alloys”, *Oxidat. Metals*, **2** (1970) 373-399
- [79] S.C. Lim and M.F. Ashby – “Wear-Mechanism Maps”, *Acta Metallurgica*, **35** (1987) 1-24
- [80] D.H. Buckley – “Influence of Chemisorbed Films on Adhesion and Friction of Clean Iron”, *NASA Center for Aerospace Information*, **NASA-TN-D-4775** (1968)



- [81] Feng, I-Ming and Uhlig – “Fretting Corrosion of Mild Steel in Air and in Nitrogen”, *Journal of Applied Mechanics*, **Vol 21, No.4** (1954) 395-400
- [82] K.H.R. Wright – “An Investigation of Fretting Corrosion”, *Proceedings of the Institution of Mechanical Engineers*, **Vol. 1B, No. 11** (1952-53) 556-574
- [83] R.B. Waterhouse – “Fretting Corrosion”, *Pergamon Press*, New York (1972)
- [84] R.C. Bill – “Fretting Wear of Iron, Nickel and Titanium under Varied Environmental Conditions”, *Wear of Materials*, ASME, New York (1979) 356-370
- [85] A.F. Smith – “The Unlubricated Reciprocating Sliding Wear of 316 Stainless Steel in CO<sub>2</sub> at 20 – 600°C”, *Tribo. Int.*, **19** (1986) 65-71
- [86] A. Iwabuchi, K. Hori, and H. Kudo – “The Effect of Temperature, Preoxidation and Presliding on the Transition from Severe Wear to Mild Wear for S45C Carbon Steel and SUS 304 Stainless Steel” *Proc. Int. Conf. Wear of Materials*, New York (1987) 211-220
- [87] K. Langgath, A. Kluge and H. Ryssel – “Wear of Steels After Implantation of Oxygen Ions Or Oxidation at 670K”, *Wear* **155** (1992) 343-351
- [88] J. Mølgaard and V.K. Srivastava – “The Activation Energy of Oxidation in Wear”, *Tribo. Int.*, **16** (1983) 305-314
- [89] J. Mølgaard – “A Discussion of Oxidation, Oxide Thickness and Oxide Transfer in Wear”, *Wear* **40** (1976) 277-291
- [90] H. So – “Characteristics of Wear Results Tested by Pin-on-Disc at Moderate to High Speeds”, *Tribo. Int.*, **Vol. 25, No. 5** (1996) 415-423
- [91] S.C. Lim – “Recent Development in Wear Maps”, *Tribo. Int.*, **Vol. 31, Nos. 1-3** (1998) 87-97
- [92] T.H.C. Childs – “The Sliding Wear Mechanisms of Metals, Mainly Steels”, *Tribo. Int.*, **13** (1980) 285-293
- [93] K. Kato and K. Hokkirigawa – “Abrasive Wear Diagram”, *Proc. Eurotrib '85, Vol. 4, Section 5.3, Elsevier, Amsterdam* (1985) 1-5
- [94] D.H. Buckley – “Adhesion, Friction and Wear of Cobalt and Cobalt-Base Alloys” *Cobalt* **38** (1968) 20-28
- [95] E.A. Brandes and G.B. Brook – “Smithells Metals Reference Book: Seventh Edition”, *Butterworth Heinemann* (1992)
- [96] F.H. Stott, C.W. Stevenson and G.C. Wood – “Friction and Wear Properties of Stellite 31 at Temperatures from 293 to 1074k” *Metals Tech.*, **4** (1977) 66-74
- [97] V. Kuzucu, M. Ceylan, H. Çelik and İ Aksoy – “Microstructure and Phase Analysis of Stellite 6 Plus 6 Wt.% Mo Alloy” *J. Mat. Proc. Tech.*, **69** (1997) 257-263



- 
- [98] H.So – “Wear Behaviours of Laser-Clad Stellite Alloy 6”, *Wear* **192** (1996) 78-84
  - [99] P. Crook and C.C. Li – “The Elevated Temperature Metal-to-Metal Wear Behaviour of Selected Hard Facing Alloys” *Wear of Materials*, **ASME Publication 110254**, (1983) 272-279
  - [100] M.Vardavoulis – “The Role of Hard Second Phases in the Mild Oxidational Wear Mechanism of High-Speed Steel Based Materials”, *Wear* **173** (1994) 105-114
  - [101] M. Bartsch, A. Wasilkowska, A. Czyrska-Filemonowicz and U. Messerschmidt – “Dislocation Dynamics in the Oxide Dispersion Strengthened Alloy Incoloy MA956”, *Mat. Sci. Eng.*, **A272** (1999) 152-162
  - [102] A. Fujita, M. Shinohara, M. Kamada and H. Yokota – “Improvement of Creep Rupture Ductility in Ni-Base Superalloy Nimonic 80A and Its Material Properties”, *Isij International*, **38** (1998) 291-299
  - [103] E.O. Ezugwu, Z.M. Wang and A.R. Machado – “The Machinability of Nickel Based Alloys: A Review”, *J. Mat. Proc. Tech.*, **86** (1999) 1-16
  - [104] A. Czyrska-Filemonowicz and B. Dubiel – “Mechanically Alloyed, Ferritic Oxide Dispersion Strengthened Alloys: Structures and Properties”, *J. Mat. Proc. Tech.*, **64** (1997) 53 -64
  - [105] Anon., Unpublished Work – *Special Metals (Wiggins) Ltd*
  - [106] M. Kerridge, J.K. Lancaster – “The Stages in a Process of Severe Metallic Wear”, *Proc. Royal Society London*, A **236** (1956) 250-264
  - [107] M. Sawa and D.A. Rigney – “Sliding Behaviour of Dual Phase Steels in Vacuum and in Air”, *Wear* **119** (1987) 369-390
  - [108] J.S. Benjamin, T.E. Volin – “The Mechanism of Mechanical Alloying”, *Metall. Trans.* **5** (1974) 1929-1934
  - [109] D.A. Rigney, L.H. Chen, M.G.S. Naylor, A.R. Rosenfield – “Wear Processes in Sliding Systems”, *Wear* **100** (1984) 195-219
  - [110] P. Heilmann, J. Don, T.C. Sun, D.A. Rigney, W.A. Glaeser – “Sliding Wear and Transfer”, *Wear* **91** (1983) 171-190
  - [111] L.H. Chen, D.A. Rigney – “Transfer during Unlubricated Sliding Wear of Selected Metal Systems”, *Wear* **105** (1985) 47-61
  - [112] A. Erdemir, C. Bindal, G.R. Fenske, C. Zuikey, A.R. Krauss and D.M. Gruen – “Friction and Wear Properties of Smooth Diamond Films Grown in Fullerene + Argon Plasmas”, *Diamond and Related Materials* **5** (1996) 923-931
  - [113] M.G. Gee and N.M. Jennet – “High Resolution Characterisation of Tribochemical Films on Alumina”, *Wear* **193** (1995) 133-145

- [114] W Czupryk – “Frictional Transfer of Iron in Oxidative Wear Conditions during Lubricated Sliding”, *Wear* **237** (2000) 288-294
- [115] D.G. Morris – “Mechanical Behaviour of Nanostructured Materials”, *Trans Tech Publications Ltd.* (1998)
- [116] J.F. Shackelford (Editor) – “The CRC Materials Science and Engineering Handbook”, *CRC Press* (1992)
- [117] I.A. Inman, S. Datta, H.L. Du, J.S. Burnell-Gray and Q. Luo – “Microscopy of Glazed Layers Formed during High Temperature Sliding Wear at 750°C”, *Wear* **254** (2003) 461-467
- [118] X.Y. Li, K.N. Tandon – “Microstructural Characterization of Mechanically Mixed Layer and Wear Debris in Sliding Wear of an Al-Alloy and an Al Based Composite”, *Wear* **245** (2000) 148–161
- [119] S. Datta, I.A. Inman, H.L. Du, Q. Luo – “Microscopy of Glazed Layers Formed during High Temperature Wear”, *Proceedings of the Invited Talk at the Institute of Materials*, Tribology Meeting, London, November 2001
- [120] P.K. Datta, H.L. Du, E. Kuzmann, I.A. Inman – “Near Surface Structural Changes of ‘Glaze’ Layers Formed during High Temperature Sliding Wear”, *to be published in Wear*
- [121] H. Gleiter – “Nanocrystalline Materials”, *Prog. Mater. Sci.* **33** (1989) 223–315
- [122] R.Z. Valiev, R.K. Islamgaliev, I.V. Alexandrov – “Bulk Nanostructured Materials from Severe Plastic Deformation”, *Prog. Mater. Sci.* **45** (2000) 103–189
- [123] T.C. Lowe, R.Z. Valiev – “Producing Nanoscale Microstructures through Severe Plastic Deformation”, *Journal of Materials Processing Technology* **52** (2000) 27–28
- [124] A.K. Ghosh, W. Huang – “Severe Deformation Based Progress for Grain Subdivision and Resulting Microstructures”, in: T.C. Lowe, R.Z. Valiev (Eds.), *Investigations and Applications of Severe Plastic Deformation*, Kluwer Academic Publishers, Dordrecht (2000) pp. 29–36
- [125] R.S. Mishra, S.X. McFadden, A.K. Mukherjee – “Analysis of Tensile Superplasticity in Nanomaterials”, *Mater. Sci. Forum* **304–306** (1999) 31–38
- [126] R.S. Mishra, A.K. Mukherjee – “Superplasticity in Nanomaterials”, in: A.K. Ghosh, T.R. Bieler (Eds.), *Superplasticity and Superplastic Forming*, Tms, Warrendale (1998) pp. 109–116
- [127] R.S. Mishra, S.X. McFadden, A.K. Mukherjee – “Tensile Superplasticity in Nanocrystalline Materials Produced by Severe Plastic Deformation”, in: T.C. Lowe, R.Z. Valiev (Eds.), *Investigations and Applications of Severe Plastic Deformation*, Kluwer Academic Publishers, Dordrecht (1994) pp. 231–240

## APPENDIX 1: Contacting the Author and Related Articles (not an official part of the thesis)

### A1.1 Contacting the Author

Should anyone have any comments or questions about the content of this thesis, the author may be contacted at '[ian.s.inman@gmail.com](mailto:ian.s.inman@gmail.com)' (correct the letters to obtain my e-mail address; the strange format is to stop spam e-mail readers detecting it).

The document is available in the following formats.

*Online (PDF):* <http://archive.org>

*Paper:* <http://dissertation.com>

### A1.2 Articles Directly Related to the Current Study

Clicking on any of the below will take you to a location from where the paper or document can be downloaded. Please note a fee may apply.

- [A] I.A. Inman, P.S. Datta, H.L. Du, C Kübel, P.D. Wood and F.T. Mahi – “High Temperature Tribocorrosion”, *reference module in “Materials Science and Materials Engineering”*, Elsevier Ltd. (2017)  
**SUPERCEDED VERSION:** I.A. Inman, P.S. Datta, H.L. Du, C Kübel and P.D. Wood – “High Temperature Tribocorrosion”, in: T. Richardson, B. Cottis, R. Lindsay, S. Lyon, D. Scantlebury, H. Stott and M. Graham (Eds.), *Corrosion Series – VOL 1: Types of High Temperature Corrosion*, Elsevier Ltd. (2010)
- [B] I.A. Inman, P.K. Datta – “Studies of High Temperature Sliding Wear of Metallic Dissimilar Interfaces IV: Nimonic 80A versus Incoloy 800HT”, *Tribology International* **44** (2011) 1902–1919 (Elsevier / Science Direct)
- [C] I.A. Inman, P.K. Datta – “Studies of High Temperature Sliding Wear of Metallic Dissimilar Interfaces III: Incoloy MA956 versus Incoloy 800HT”, *Tribology International* **43** (2010) 2051–2071 (Elsevier / Science Direct)
- [D] I.A. Inman, P.S. Datta – “Development of a Simple ‘Temperature versus Sliding Speed’ Wear Map for the Sliding Wear Behaviour of Dissimilar Metallic Interfaces II”, *Wear* **265** (2008) 1592–1605 (Elsevier / Science Direct)
- [E] I.A. Inman, S.R. Rose, P.K. Datta – “Studies of High Temperature Sliding Wear of Metallic Dissimilar Interfaces II: Incoloy MA956 versus Stellite 6”, *Tribology International* **39** (2006) 1361–1375 (Elsevier / Science Direct)

- [F] I.A. Inman, S.R. Rose, P.K. Datta – “Development of a Simple ‘Temperature versus Sliding Speed’ Wear Map for the Sliding Wear Behaviour of Dissimilar Metallic Interfaces”, *Wear* **260** (2006) 919–932 (Elsevier / Science Direct)
- [G] I.A. Inman, P.K. Datta, H.L. Du, Q. Luo, S. Piergalski – “Studies of high temperature sliding wear of metallic dissimilar interfaces”, *Tribology International* **38** (2005) 812–823 (Elsevier / Science Direct)
- [H] H.L. Du, P.K. Datta, I. Inman, E. Kuzmann, K. Süvegh, T. Marek, A. Vértes – “Investigations of microstructures and defect structures in wear affected region created on Nimonic 80A during high temperature wear”, *Tribology Letters* **18-3** (2005) 393-402 (Springer)
- [I] H.L. Du, P.K. Datta, I.A. Inman, R. Geurts, C. Kübel – “Microscopy of wear affected surface produced during sliding of Nimonic 80A against Stellite 6 at 20°C”, *Materials Science and Engineering* **A357** (2003) 412-422 (Elsevier / Science Direct)
- [J] I.A. Inman, S. Datta, H.L. Du, J.S. Burnell Gray, Q. Luo, S. Piergalski – “Microscopy of glazed layers formed during high temperature sliding wear at 750°C”, *Wear* **254** (2003) 461–467 (Elsevier / Science Direct)
- [K] I.A. Inman – "High Temperature ‘Like-on-like’ Sliding of Nimonic 80A under Conditions of Limited Debris Retention", Unpublished Work, Northumbria University (2003) – *this document is available for free download*

### A1.3 Other Related Work

The copyright of the two theses listed in references [O] and [P] resides with the named authors. Once again, clicking on any of the below will take you to a location from where the paper or document can be downloaded. Please note a fee may apply.

- [L] P.D.Wood, H.E.Evans, C.B.Ponton " Investigation into the Wear Behaviour of Stellite 6 during Rotation as an Unlubricated Bearing at 600°C", *Tribology International* **44** (2011) 1589-1597 (Elsevier / Science Direct)
- [M] P.D.Wood, H.E.Evans, C.B.Ponton "Investigation into the Wear Behavior of Tribaloy 400C during Rotation as an Unlubricated Bearing at 600°C from 2 Minutes to 12 Hours", *Wear* **269** (2010) 763–769 (Elsevier / Science Direct)
- [N] P.D. Wood, P.K. Datta, J.S. Burnell-Gray and N. Wood – “Investigation into the High Temperature Wear Properties of Alloys Contacting Against Different Counterfaces”, *Material Science Forum* **251-254** (1997) 467-474 (Scientific.net)
- [O] P.D. Wood – “The Effect of the Counterface on the Wear Resistance of Certain Alloys at Room Temperature and 750°C”, Ph.D. Thesis, SERG, Northumbria University (1997)
- [P] S.R. Rose – “Studies of the High Temperature Tribological Behaviour of Superalloys”, Ph.D. Thesis, AMRI, Northumbria University (2000)